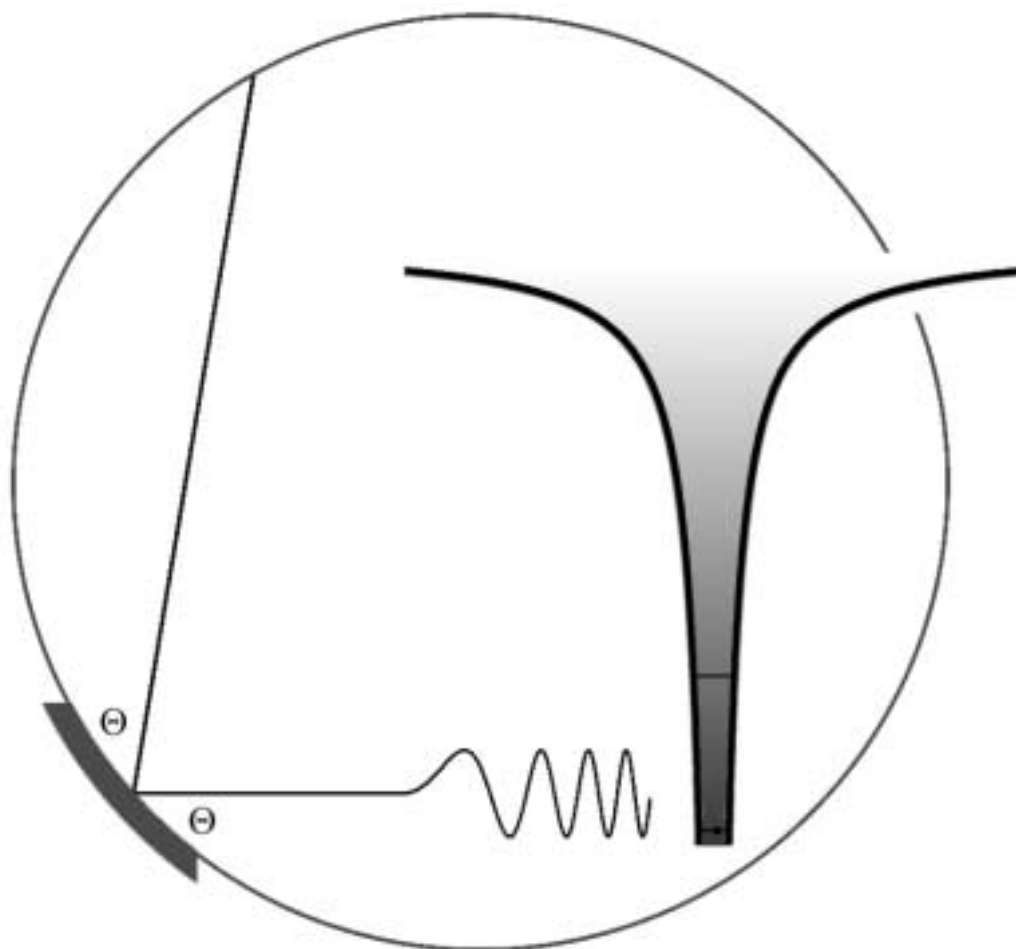


NIST Special Publication 972

Highly Charged Ions

Publications of the EBIT Project, 1993-2001

Atomic Physics Division, NIST, Gaithersburg, Maryland



Edited by: John D. Gillaspay
Laura P. Ratliff
James R. Roberts
Endre Takács

NIST Special Publication 972

Highly Charged Ions

Publications of the EBIT Project, 1993-2001
Atomic Physics Division, NIST, Gaithersburg, Maryland

Editors:
John D. Gillaspy
Laura P. Ratliff
James R. Roberts
Endre Takács

Atomic Physics Division
Physics Laboratory
National Institute of Standards and Technology
Gaithersburg, MD 20899-8420

July 2002



U.S. Department of Commerce
Donald L. Evans, Secretary

Technology Administration
Phillip J. Bond, Under Secretary of Commerce for Technology

National Institute of Standards and Technology
Arden L. Bement, Director

Certain commercial entities, equipment, or materials may be identified in this document in order to describe an experimental procedure or concept adequately. Such identification is not intended to imply recommendation or endorsement by the National Institute of Standards and Technology, nor is it intended to imply that the entities, materials, or equipment are necessarily the best available for the purpose.

National Institute of Standards and Technology Special Publication 972
Natl. Inst. Stand. Technol. Spec. Publ. 972, 319 pages (July 2002)
CODEN: NSPUE2

U.S. GOVERNMENT PRINTING OFFICE
WASHINGTON: 2002

For sale by the Superintendent of Documents, U.S. Government Printing Office
Internet: bookstore.gpo.gov — Phone: (202) 512-1800 — Fax: (202) 512-2250
Mail: Stop SSOP, Washington, DC 20402-0001

Preface

Assembled here are the publications of NIST Electron Beam Ion Trap (EBIT) project, from its inception through the end of 2001. They are grouped thematically, as indicated in the table of contents. In order to address some of the most frequently asked questions that are not fully answered in the papers themselves (When did this work begin? How much did it cost? Who worked on it?) a historical introduction is included. Other introductory material can be found on our web site at <http://physics.nist.gov/ebit>.

C

ontents

Historical introduction to the NIST EBIT project – J.D. Gillaspy	i
Remembering Mort Levine and the beginning of the EBIT – R. E. Marrs	vii

R

eviews and overviews

J.D. Gillaspy, J.R. Roberts, C.M., Brown, and U. Feldman The NIST EBIT: A progress report <i>AIP Conference Proceedings 274 Proc. VIth International Conference on the Physics of Highly Charged Ions, ed. by P. Richard, M. Stockli, and C.D. Lin, (AIP press, New York, 1993), p. 682.</i>	1
J.D. Gillaspy, J.R. Roberts, C.M., Brown, and U. Feldman Update on the NIST EBIT <i>National Institute of Standards and Technology Special Publication 850, Apr. 1993 (U.S. Government Printing Office, Washington, 1993).</i>	5
J.D. Gillaspy First results from the EBIT at NIST <i>Physica Scripta T71, 99 (1997).</i>	8
J.D. Gillaspy, Y. Aglitskiy, E.W. Bell, C.M. Brown, C.T. Chantler, R.D. Deslattes, U. Feldman, L.T. Hudson, J.M. Laming, E.S. Meyer, C.A. Morgan, A.I. Pikin, J.R. Roberts, L.P. Ratliff, F.G. Serpa, J. Sugar, and E. Takács Overview of the EBIT Program at NIST <i>Proceedings of Nobel Symposium 91, Physica Scripta T59, 392 (1995).</i>	13
J.D. Gillaspy Visible and UV light from highly charged ions: exotic matter advancing technology <i>IEEE LEOS Newsletter, August 1995, p. 19.</i>	17
J.D. Gillaspy EBIT spectra of highly stripped ions from the visible to the x-ray <i>Physica Scripta T65, 168 (1996).</i>	19

E. Takács, L.P. Ratliff, and J.D. Gillaspy X-ray, visible, and electron spectroscopy with the NIST EBIT <i>Hyperfine Interactions</i> 108 , 59 (1997).	26
E. Traebert, P. Beiersdorfer, S.B. Utter, J.D. Gillaspy, and F.G. Serpa Forbidden line wavelengths and transition probabilities measured using an electron beam ion trap (EBIT) <i>Proceedings of the 6th International Colloquium on Atomic Spectra and Oscillator Strengths for Astrophysical and Laboratory Plasmas, accepted for publication, University of Victoria, British Columbia (1998).</i>	40
L.P. Ratliff and J.R. Roberts Highly charged ion studies at the NIST EBIT <i>Trapping Highly Charged Ions: Fundamentals and Applications, ed. by J.D. Gillaspy, Nova Science Publishers, 257 (2001).</i>	44
J.D. Gillaspy Highly charged ions <i>Journal of Physics B: At. Mol. Opt. Phys.</i> 34 R93 (2001)	65
E. Takács and J.D. Gillaspy Trapped highly charged ion plasmas <i>Proceedings of the Non-neutral Plasmas Workshop 2001, ed. by C.F. Driscoll, F. Anderegg, L. Schweikhard, AIP Conference Proceedings Series (2001)</i>	103

Ultraviolet and visible radiation

C.A. Morgan, F.G. Serpa, E. Takács, E.S. Meyer, J.D. Gillaspy, J. Sugar, J.R. Roberts, C.M. Brown, U. Feldman Observation of visible and uv magnetic dipole transitions in highly-charged xenon and barium <i>Physical Review Letters</i> 74 , 1716 (1995).	117
H. Adler, E.S. Meyer, F.G. Serpa, E. Takács, and J.D. Gillaspy Fabry-Perot Spectroscopy of a visible magnetic dipole transition in Ba³⁴⁺ <i>Proceedings of the 7th International Conference on Highly Charged Ions, Nuclear Instruments and Methods in Physics Research B</i> 98 585 (1995).	121

F.G. Serpa, E.S. Meyer, C.A. Morgan, J.D. Gillaspy, J. Sugar, J.R. Roberts, C.M. Brown, U. Feldman Anomalous Z-dependence of a magnetic dipole transition in the Ti-like isoelectronic sequence <i>Physical Review A</i> 53 , 2220 (1996).	125
F.G. Serpa, E.W. Bell, E.S. Meyer, J.D. Gillaspy, and J.R. Roberts Kr spectra from an electron beam ion trap <i>Physical Review A</i> 55 , 1832 (1996).	130
F.G. Serpa, C.A. Morgan, E.S. Meyer, J.D. Gillaspy, E. Traebert, D.A. Church, and E. Takács Measurement of a magnetic dipole transition probability in highly charged Xe using an electron beam ion trap (EBIT) <i>Physical Review A</i> 55 , 4196 (1997).	134
F.G. Serpa, J.D. Gillaspy, and E. Traebert Lifetime measurements in the ground configuration of Ar¹³⁺ and Kr²²⁺ using an electron beam ion trap <i>Journal of Physics B: At. Mol. Opt. Phys.</i> 31 , 3345 (1998).	139
J. V. Porto, I. Kink, and J. D. Gillaspy UV light from the ground term of Ti-like Ytterbium, Tungsten, and Bismuth <i>Physical Review A</i> 61 , 054501 (2000)	147
J. V. Porto, I. Kink, and J. D. Gillaspy Direct imaging of highly charged ions in an electron beam ion trap <i>Review of Scientific Instruments</i> 71 , 3050 (2000).	151

X-ray radiation

E. Takács, E.S. Meyer, J.D. Gillaspy, J.R. Roberts, C.T. Chantler, L.T. Hudson, R.D. Deslattes, C.M. Brown, J.M. Laming, U. Feldman, J. Dubau, M.K. Inal Polarization measurements on a magnetic quadrupole line in Ne-like barium <i>Physical Review A</i> 54 , 1342 (1996).	161
D.J. McLaughlin, Y. Hahn, E. Takács, E.S. Meyer, J.D. Gillaspy Radiative and inner-shell dielectronic recombination in a highly charged barium ion <i>Physical Review A</i> 54 , 2040 (1996).	170

- Y. Aglitskiy, F.G. Serpa, E.S. Meyer, J.D. Gillaspay, and C.M. Brown 180
The use of a spherically curved crystal spectrometer for x-ray measurements on electron beam ion trap
Physica Scripta **58**, 178 (1998).
- C.T. Chantler, D. Paterson, L.T. Hudson, F.G. Serpa, J.D. Gillaspay, and R.D. Deslattes 184
Progress towards absolute x-ray spectroscopy on the NIST electron beam ion trap: current status and results
Physica Scripta **T73**, 87 (1997).
- C. T. Chantler, D. Paterson, L. T. Hudson, F. G. Serpa, J.D. Gillaspay, and E. Takács 187
Precision x-ray spectroscopy at the NIST electron beam ion trap: resolution of major systematic error
Physica Scripta **T80**, 440 (1999).
- C. T. Chantler, D. Paterson, L. T. Hudson, F. G. Serpa, J. D. Gillaspay, and E. Takács 190
Absolute measurement of the resonance lines in heliumlike vanadium on an electron-beam ion trap
Physical Review A **62**, 042501 (2000).
- E. Silver, H. Schnopper, S. Bandler, S. Murray, N. Madden, D. Landis, J. Beeman, E. Haller, M. Barbera, G. Tucker, J.D. Gillaspay, E. Takács, and J. Porto 203
Laboratory astrophysics and microanalysis with NTD-germanium-based x-ray microcalorimeters
Nuclear Instruments and Methods in Physics Research A **444** 156 (2000).
- E. Silver, H. Schnopper, S. Bandler, N. Brickhouse, S. Murray, M. Barbera, E. Takács, J.D. Gillaspay, J.V. Porto, I. Kink, J.M. Laming, N. Madden, D. Landis, J. Beeman, and E. Haller 208
Laboratory astrophysics survey of key diagnostic lines using a microcalorimeter on an electron beam ion trap
The Astrophysical Journal **541**, 495 (2000).
- I. Kink, J.M. Laming, E. Takács, J.V. Porto, J.D. Gillaspay, E. Silver, H. Schnopper, S. Bandler, M. Barbera, N. Brickhouse, S. Murray, N. Madden, D. Landis, J. Beeman, and E. Haller 214
Analysis of broadband x-ray spectra of highly charged krypton from a microcalorimeter detector of an electron-beam ion trap
Physical Review E, **63**, 046409 (2001).

- J.M. Laming, I. Kink, E. Takács, J.V. Porto, J.D. Gillaspy, E. Silver, H. Schnopper, S. Bandler, N. Brickhouse, S. Murray, M. Barbera, A. K. Bhatia, G. A. Doschek, N. Madden, D. Landis, J. Beeman, and E. Haller
Emission-line intensity ratios in FeXVII observed with a microcalorimeter on an electron beam ion trap
The Astrophysical Journal **545**, L161 (2000). 224
- I. Kink, J. M. Laming, E. Takács, J. V. Porto, J. D. Gillaspy, E. Silver, H. Schnopper, S. R. Bandler, M. Barbera, N. Brickhouse, S. Murray, N. Madden, D. Landis, J. Beeman, and E. E. Haller
Microcalorimeter/EBIT measurements of x-ray spectra of highly charged ions
Physica Scripta **T92** 454 (2001). 228

I on-surface interactions

- A.I. Pikin, C.A. Morgan, E.W. Bell, L.P. Ratliff, D.A. Church, and J.D. Gillaspy
A beam line for highly charged ions
Review of Scientific Instruments **67**, 2528 (1996). 231
- L.P. Ratliff, E.W. Bell, D.C. Parks, A.I. Pikin, and J.D. Gillaspy
Continuous highly-charged ion beams from the NIST EBIT
Review of Scientific Instruments **68**, 1998 (1997). 237
- E. Takács, Z. Ónodi-Szűcs, L.P. Ratliff, J.D. Gillaspy, and J. Pálinkás
X-ray emission for 3-137 keV Ar¹⁷⁺ impacting SiO₂
Nuclear Instruments and Methods in Physics Research B **124**, 431 (1997). 242
- H.-P. Cheng and J.D. Gillaspy
Nano-scale modification of silicon surfaces via coulomb explosion
Physical Review B **15**, 2628 (1997). 246
- H.-P. Cheng and J.D. Gillaspy
Large scale molecular dynamics simulation of a surface Coulomb explosion
AIP Conference Proceedings **392**, *Application of Accelerators in Research and Industry*, ed. by J.L. Duggan and I.L. Morgan (AIP Press, Woodbury, New York, 1997) p. 197. 255
- H.-P. Cheng and J. D. Gillaspy
Surface Coulomb explosions: The influence of initial charge distributions 259

- Computational Materials Science* **9**, 285, (1998).
D.C. Parks, M.P. Stockli, E.W. Bell, L.P. Ratliff, R.W. Schmieder, F.G. Serpa, and J.D. Gillaspay 271
Non-kinetic damage on insulating materials by highly charged ion bombardment
Nuclear Instruments and Methods in Physics Research B **134**, 46 (1998).
- J.D. Gillaspay, D.C. Parks, and L.P. Ratliff 278
Masked ion beam lithography with highly charged ions
Journal of Vacuum Science and Technology B **16**, 3294 (1998).
- L. P. Ratliff, R. Minniti, A. Bard, E. W. Bell, J. D. Gillaspay, D. Parks, A. J. Black, and G. M. Whitesides 282
Exposure of self-assembled monolayers to highly charged ions and metastable atoms
Applied Physics Letters **75**, 590 (1999).
- E. Takács, Z. Berényi, J. D. Gillaspay, L. P. Ratliff, R. Minniti, J. Pedulla, R. D. Deslattes, N. Stolterfoht 285
Separation of inner shell vacancy transfer mechanisms in collisions of slow Ar¹⁷⁺ ions with SiO₂
Journal of Physics B: At. Mol. Phys. **34**, 1277 (2001).
- L. P. Ratliff, J. D. Gillaspay 296
In situ imaging of highly charged ion irradiated mica
AIP conference proceedings, XVIth International Conference, ed. by J.L. Duggan and I.L. Morgan, (AIP press, New York, 2001), p. 935.
- R. Minniti, L. P. Ratliff, J. D. Gillaspay 300
In-situ observation of surface modification induced by highly charged ion bombardment
Physica Scripta **T92**, 22 (2001)

Historical introduction to the NIST EBIT project

The birth of the NIST EBIT may be traced to a discussion between Jim Roberts and Dick Deslattes prior to my arrival in 1988. Jim had been searching for new research directions for his Plasma Radiation group, and was encouraged by Dick to consider a new device called an "Electron Beam Ion Trap" (EBIT) that had just been developed at Berkeley and Livermore (see remarks by Ross Marrs, following this introduction). Jim traveled to California to see the original EBIT, and became convinced that NIST would benefit from being one of the first to embrace this new technology. On the day I arrived at NIST to join Jim's group, I was swept into a meeting in which he was already discussing the proposal to build an EBIT at NIST.

As plans developed, Jim teamed up with Josh Silver at the University of Oxford and Uri Feldman at the U.S. Naval Research Laboratory to have the components for two identical new EBITS designed and machined simultaneously. Mort Levine, recently retired from Lawrence Berkeley Laboratory, went to Oxford to lead the design work. In July of 1990, a contract was signed for \$165k for one set of "EBIT parts" (including \$35k for materials) to be fabricated by the Oxford Nuclear Physics Machine Shop and delivered to NIST. The contract was supplemented with a \$13k addition near the end of the 1-year fabrication period. Meanwhile, Jim specified the purchase of approximately \$100k in supporting electronics, vacuum pumps, and cryogenics, to be purchased in collaboration with the Naval Research Laboratory.

After completing my postdoc work on another project in Jim's group, he hired me to lead the EBIT project in 1991. Doug Alderson began to work part-time on the project as the group technician, helping me prepare the laboratory space. In April of 1992 the box of EBIT parts arrived. Charlie Brown, one of Uri Feldman's staff members, traveled to NIST periodically to work with me on the assembly. Eventually, we purchased another \$50k or so of additional hardware, to bring the EBIT into operation for a grand total of approximately \$330k.

Our vision was to create a facility that would last many years and that would be flexible enough to accommodate a wide range of experiments without major revision, so Charlie and I took the better part of a year to carefully assemble and align the components. Special attention was paid to cleanliness because we did not want to bake the vacuum system and damage some of the internal magnet systems. The extra effort paid off: we obtained an outgassing rate comparable to that of baked stainless steel, and we have never had to disassemble the core of the EBIT for any reason since. We have only opened the vacuum chamber occasionally to replace windows or to insert a fresh electron gun. One of the last views of the inside of the NIST EBIT is shown in the photograph in figure 1. Approximately 150 machined components make up the 6 major EBIT subsections that are shown.

Shortly after the system was assembled, the first NIST EBIT postdoc, Gino Serpa, arrived from Notre Dame and began helping with the external wiring. A few months later, Endre Takács came as a guest researcher from Keith Burnett's group at Oxford and began helping with the high voltage connections. Martin Laming visited from NRL to help install and debug some of the CAMAC electronics. Cornelius Morgan joined us from the University of Maryland, shortly after finishing his PhD, and began helping with the interlock systems. Our first trapped ions were obtained later in 1993 and our first major scientific results were submitted for publication in 1994.

Around this time, a major expansion of our EBIT work developed. Eric Meyer arrived from Harvard as our first NRC postdoctoral associate. Helmar Adler, a visitor from the Princeton Plasma Physics Laboratory (and former postdoc in another project in our group) carried out some experiments with Eric using a Fabry-Perot interferometer. Collaborations with Germany, Russia, Australia, Hungary and groups within NIST developed, as discussed below. At the same time, however, our collaborating scientists from NRL began to focus their work in other areas and became less involved with the EBIT. Two NRL technicians, Glenn Holland and Greg Boyer, continued to work on the construction of a metal ion injector for our EBIT, however. Recently, NRL participation has increased, as Martin Laming has become active in the planning and data analysis for the microcalorimeter collaboration discussed below.

In 1994, Elmar Träbert began a series of visits from Germany to carry out measurements of excited state lifetimes. Towards the end of this work (1998), we also did the first spatial imaging of the ion cloud inside our EBIT. Support for this collaboration was from a NATO International Scientific Exchange Grant and, later, the Alexander von Humboldt Foundation. Trey Porto arrived at the end of this period (1998) as an NRC postdoc and took the lead in developing the ion cloud imaging work.

Also 1994, Yefim Aglitskiy joined us half-time as a senior guest researcher from Russia. Yefim's colleague, Anatoly Faenov, also came for a short visit to do an x-ray spectroscopy experiment. The bulk of our x-ray spectroscopy, however, was done in collaboration with Dick Deslattes' group at NIST (which included Larry Hudson, Al Henins, Joe Pedulla, and Chris Chantler). After taking a position as a lecturer at the University of Melbourne in Australia, Chris returned periodically to carry out various x-ray experiments with us. We are currently co-PI's on a grant supporting this work from the Australian Research Council.

With a "competence" funding award in 1994 from the office of the NIST Director (Ray Kammer, retired), our research was expanded to address the emerging field of nanotechnology. Laura Ratliff was hired as the second permanent NIST EBIT staff physicist that year. In 1995 we extracted beams of highly charged ions from the top of our EBIT. Bob Schmieder, from Sandia National Lab, loaned us an air-operated atomic force microscope (AFM), and encouraged his postdoc, Dan Parks to join us as an NRC

associate. Cornelius Morgan began the design of an ion beamline, and Alexander Pikin later joined us from Russia (by way of Stockholm) to lead that effort. Ed Bell arrived as a JILA postdoc to help put the beamline designs into practice. By 1996, our 8 meter beamline was fully operational and producing record fluences of highly charged ions for experiments on surfaces. Joe McDonald and Joachim Steiger visited from Livermore to verify the beamline performance with an independent set of diagnostic hardware. The following year, Christiana Ruehlicke visited from Livermore, to carry out some experiments on protein fragmentation that required our very high beam fluences.

Some of our early ion-surface work was done in collaboration with Skip Berry and Stacy Mogren at the National Security Agency, using the analytical instruments that they had available at the Microelectronics Research Laboratory in Columbia, Maryland. By 1997, we had submitted our first ion-surface results for publication, and we purchased our own UHV AFM and scanning tunneling microscope. By 1998, this microscope was coupled to the EBIT beamline, and a new NRC postdoc, Ronnie Minniti, had developed a vibration isolation system and begun experiments with the microscope. By the following year, we submitted for publication the first atomic-scale images obtained in-vacuo of features induced by highly charged ions.

Between 1995 and 1998, Endre Takács was back in Hungary, but a U.S.-Hungarian Joint Fund grant made it possible for him to make periodic visits to NIST and bring, at various times, several of his students (Attila Báder, Zoltán Ónodi-Szűcs, Csilla Szabó, Zoltán Berényi, and Gábor Kuser). In 1999, Endre returned full time on a contract with MIT. It was during this later period that Csilla Szabó joined us again on a Fulbright Fellowship.

Jim Roberts retired from NIST in 1999, and I assumed his position as group leader. In that year, we also began to deploy the EBIT to support the x-ray astronomy missions of NASA, in collaboration with Eric Silver and Herb Schnopper from the Harvard-Smithsonian Center for Astrophysics and Marco Barbera from the Observatory of Palermo (Italy). Simon Bandler was the key postdoc from Harvard in this effort, and Frank Defreze was the supporting technician. Ilmar Kink joined us during this time on a postdoctoral fellowship from Sweden and worked together with Endre Takacs on this and various other experiments. The astrophysics work is currently supported by a NASA grant, for which we are co-investigators. Jim Roberts continues to work part time on the development of EBIT instrumentation.

Our most recent NRC postdoc, Jason Sanabia, joined us in 2001 from the University of Maryland and is working on ion-surface studies. Also this year, Hiro Tawara came from Japan (by way of Kansas State) as a senior guest researcher.

In addition to the people mentioned above, research has been carried out at the NIST EBIT by several other PhD students, Andrew Black (Harvard University) and David Patterson (University of Melbourne), undergraduates, David Fanning (Massachusetts Institute of Technology), Mark Scafonas (Saint Joseph's University), Cornelius Jackson (Norfolk State University), Chad Riland (University of Maryland),

Vivik Goel (Rice University), and Lashondria Dixon (Oklahoma State University and Southern University), and local high school students (Jessica Thomas, Brent Cezairliyan, Melissa Hao, Sam Jahanmir, Daniel Bates, and Gregory Vieira).

A number of additional people have repeatedly worked short-term on various aspects of the our EBIT program, including several NIST staff members (Jack Sugar, Yong-Ki Kim), outside visitors working in the lab (Ed Magee, Dave Knapp, John Seely, George Doschek, Andreas Bard, Gene Livingston, Curt Riemann, Jan Lorincik, David Church, Thomas Stoelker, Reinhold Schuch, Tony Calamai) and providing theoretical support (Hai-Ping Cheng, Nico Stolterfoht, Jacques Dubau). Others, participating remotely, are reflected in the co-author lists of the reprints contained in this document.

No list of EBIT team players would be complete without including the local management who have supported this work and provided us with their encouragement over the years: Wolfgang Wiese, Chief of the Atomic Physics Division at NIST, and Katharine Gebbie and Bill Ott, Director and Deputy Director of the Physics Laboratory at NIST.

My personal thanks go to all of you for daring to join in the EBIT adventure.

John Gillaspy,
Gaithersburg, MD; November, 2001



Figure 1. The NIST EBIT, just before final assembly of the 6 major subsections (clockwise from the bottom: electron gun, drift tube assembly, collector, liquid helium insert, liquid nitrogen shield, outer vacuum can).

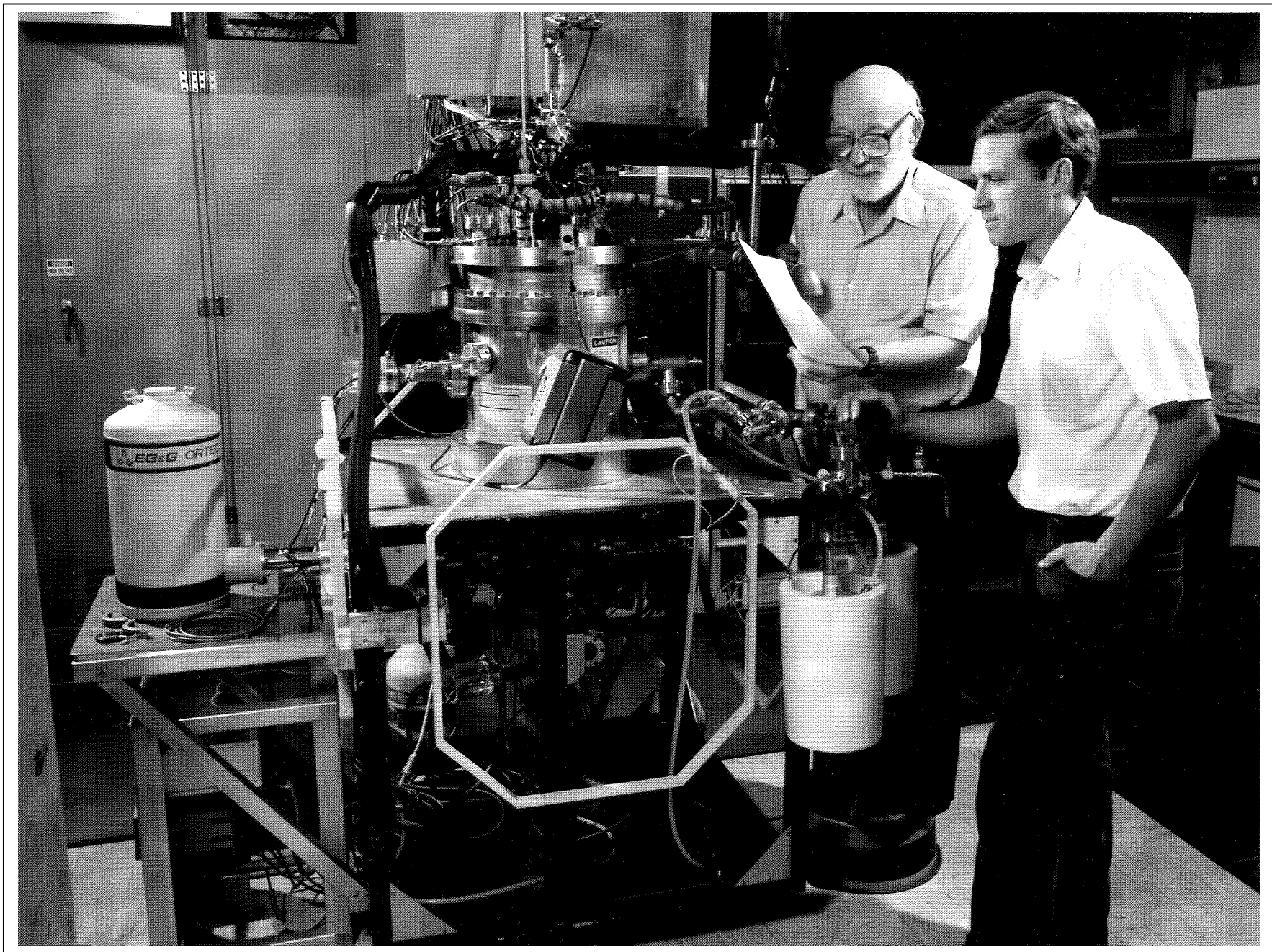


Figure 2. Mort Levine and Ross Marrs examine data from the first operational EBIT in California.

R

emembering Mort Levine and the beginnings of the EBIT

Mort Levine died in February 2001. During the period 1985 – 1986 Mort and I worked together on the development of the first electron beam ion trap (EBIT) at Lawrence Livermore National Laboratory. At the time, Mort was an employee of Lawrence Berkeley National Laboratory collaborating with several physicists at LLNL, including myself. This was the heyday of Star Wars and x-ray lasers at Livermore, and it became clear that more accurate measurements of energy levels and electron-ion collision cross sections in highly charged ions were necessary for the successful design of x-ray lasers. In this environment we knew that funding and management support would be available at Livermore for the development of tools for such measurements. We were aware of the production of very high ion charge states in an electron beam ion source (EBIS) in Russia, and the observation of x-rays from electron-ion collisions inside an EBIS in France. (We even had a private joke about exploiting the Russian “highly-charged-ion gap” to obtain funding.)

The conception of the EBIT was preceded by an attempt to use an EBIS at Berkeley for the study of highly charged ions. The Berkeley EBIS had been built as a cyclotron ion source and then abandoned, and was available at the time. It was a room temperature device that was unable to produce very high charge states. The solenoid magnet was made from split coils, which made it possible to look into the electron beam from the side. We started by studying the EBIS rather than using it. We built an imaging mirror for soft x-rays in an attempt to measure the size of the trapped ion distribution. We also measured rf emission with a probe inside the vacuum tank, and recorded extracted ions. Mort led these measurements, and Bob Schmieder (from Sandia at Livermore) and I drove over to Berkeley to participate. Mort had the most experience in plasma physics, and it seemed to me that he already knew that the performance of this EBIS would be degraded by plasma instabilities and that he was just looking for the evidence, which soon arrived. The lesson from this experience was that we needed to find a new tool for studying highly charged ions.

The experience with the Berkeley EBIS was our training ground. It gave us the knowledge and confidence to build a new type of machine. Bob Schmieder began the construction of a cryogenic EBIS at Sandia, and Mort and I began the construction of the EBIT at LLNL, which provided the money. The EBIT is the marriage of a cryogenic Penning trap with an EBIS electron beam. It was intended to be a small x-ray source for spectroscopy of trapped ions. It was not intended to be a source of ion beams, although it was later used for that purpose. We started the design by running computer calculations of magnetic fields and the propagation of space-charge-dominated electron beams. Mort found an excellent cryogenic engineer at Berkeley who worked with us and helped turn our “physics design” into a mechanical design. As a result, most of the EBIT parts were fabricated in the Berkeley shops and delivered to Livermore for final assembly.

Our experiences on the first day of EBIT operation are an example of the interaction of careful planning and the unexpected. We knew that the weak x-ray signal from trapped ions would be overwhelmed by bremsstrahlung if even a tiny fraction of the electron beam (or secondary electrons) struck solid material in the field of view of the x-ray detectors. Hence the drift tubes were designed with a larger diameter in the central section that is viewed by x-ray detectors. On the first day of operation we turned on the electron beam with no ion-trapping voltage applied to the drift tubes and looked for x-ray background with a Si(Li) detector, hoping that it would be small. We were relieved to find only a small x-ray count rate as we made adjustments to maximize electron beam transmission. Later, as we examined the x-ray spectrum, we were at first surprised to find x-ray lines at an energy greater than the electron beam energy, then excited as we realized the explanation. These lines turned out to be dielectronic recombination lines from highly charged barium ions. The barium came from the cathode of the electron gun, and the ions were trapped in an axial well generated by the space charge of the electron beam in our drift tube geometry. So we made our first highly charged ions by accident on the first day of operation, which the laboratory notebook records as 29 October 1986, arguably the “birth” date of the EBIT. As I remember it, Mort and I walked out to the parking lot together at the end of the day; as the evidence of our success began to sink in, Mort turned to me and said “we did it,” and so we had. Highly ionized barium, first made that day by serendipity, soon became the object of the first of many atomic physics measurements.

Mort continued working on the Livermore EBIT for several years after its initial operation. The machine that we first operated was a bare-bones version of what the facility later became as our understanding of the operation and capabilities of the EBIT grew and as more people joined the program and came from elsewhere as users. As we understood problems, such as high voltage breakdown caused by electrons trapped in magnet fringing fields, we modified parts to fix them. We built x-ray spectrometers to measure transition energies and invented ways to measure ionization cross-sections. One of the key EBIT concepts is the role of evaporative ion cooling, which Mort recognized and championed. We eventually developed an adjustable light gas cooling system, which is routinely used at Livermore to optimize the ionization balance and x-ray count rate. Without it, the production of the highest ion charge states would not be possible. After his retirement from LBNL and the EBIT program at Livermore, Mort served as a consultant for the design of the twin EBITs at Oxford and NIST.

Mort Levine was a colorful, enthusiastic, and unconventional person filled with many ideas and proposals, not all of which were accepted by his colleagues. However Mort challenged and stimulated those of us who worked with him. We discussed everything. It was an environment in which we could explore different approaches and change course if things didn't work. That is how the EBIT was developed, and it was fun.

Ross Marrs
Livermore, CA; October, 2001

R

Reviews and overviews

Ultraviolet and visible radiation

X-ray radiation

I on-surface interactions

R

reviews and overviews

THE NIST EBIT: A PROGRESS REPORT

J.D. Gillaspy* and J.R. Roberts
National Institute of Standards and Technology
Atomic Physics Division, Gaithersburg, MD 20899
and
C.M. Brown and U. Feldman
E. O. Hulburt Center for Space Research
Naval Research Laboratory, Washington, D. C. 20375

The invention of the Electron Beam Ion Trap (EBIT) at Livermore¹ has marked the emergence of a versatile new source for the spectroscopic study of highly charged ions. An EBIT can produce virtually any highly charged state of any atom on the periodic table, trap the ions in a controlled environment virtually free from inherent sources of systematic error, and selectively excite transitions with a well-defined monochromatic electron beam. During the past five years, the Livermore research program has successfully demonstrated many of the capabilities of the EBIT.² NIST and NRL are now in the process of constructing an EBIT facility on the east coast, at the NIST Gaithersburg site. In addition to benefiting our own research, the facility will also expand the availability of EBIT-based experiments for the scientific community in general.

The design of the NIST EBIT was created by Mort Levine and is based on the Livermore prototype which he helped develop. Notable changes include the addition of several field penetrators to drain electrons from peripheral Penning traps which were unintentionally formed by stray fields from the primary trap. The buildup of electrons in these peripheral traps is believed to have nucleated electrical breakdown and thus limited the ionization stage in the prototype EBIT at Livermore. The electrodes between the electron gun and the drift tubes have also been modified, as have the high voltage feed lines to the drift tubes which now enter from below rather than from above.

A detailed schematic diagram of the NIST EBIT is shown in figures 1 and 2. Projected operating parameters are given in Table 1. Currently, all primary components are on hand and assembly is in progress. We will bring the machine on-line during the coming year.

*Bitnet: Gillaspy@NBSenh, Internet: Gillaspy@enh.NIST.gov

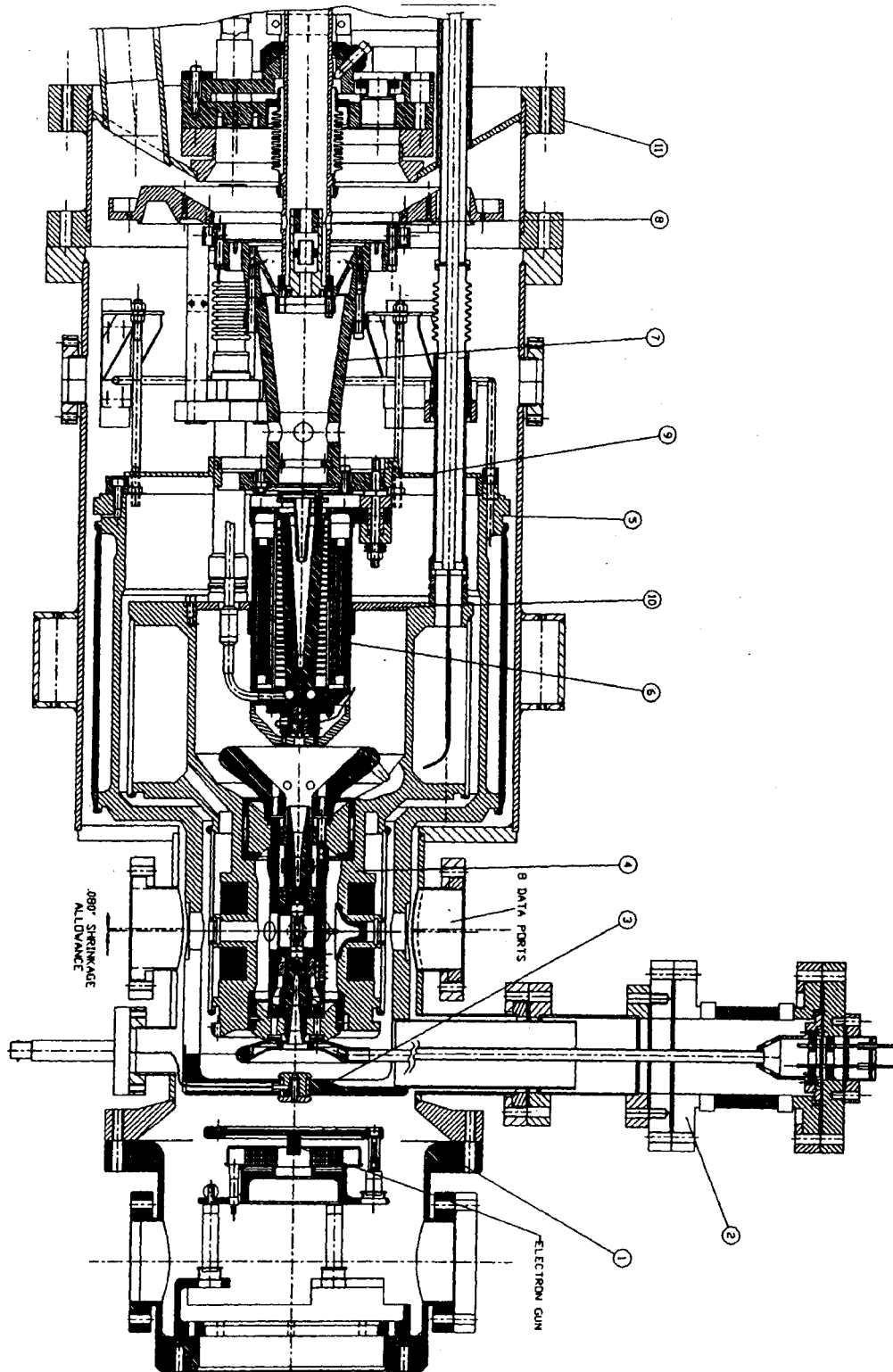


Figure 1. Cross-sectional side view of the NIST EBIT. Numbered components include electron gun assembly (1), high-voltage feed for drift tubes (2), transition electrode (3), superconducting magnet coil former (4), liquid nitrogen shield (5), collector magnet (6), and einzel lens (8). Overall height is approximately 1 meter.

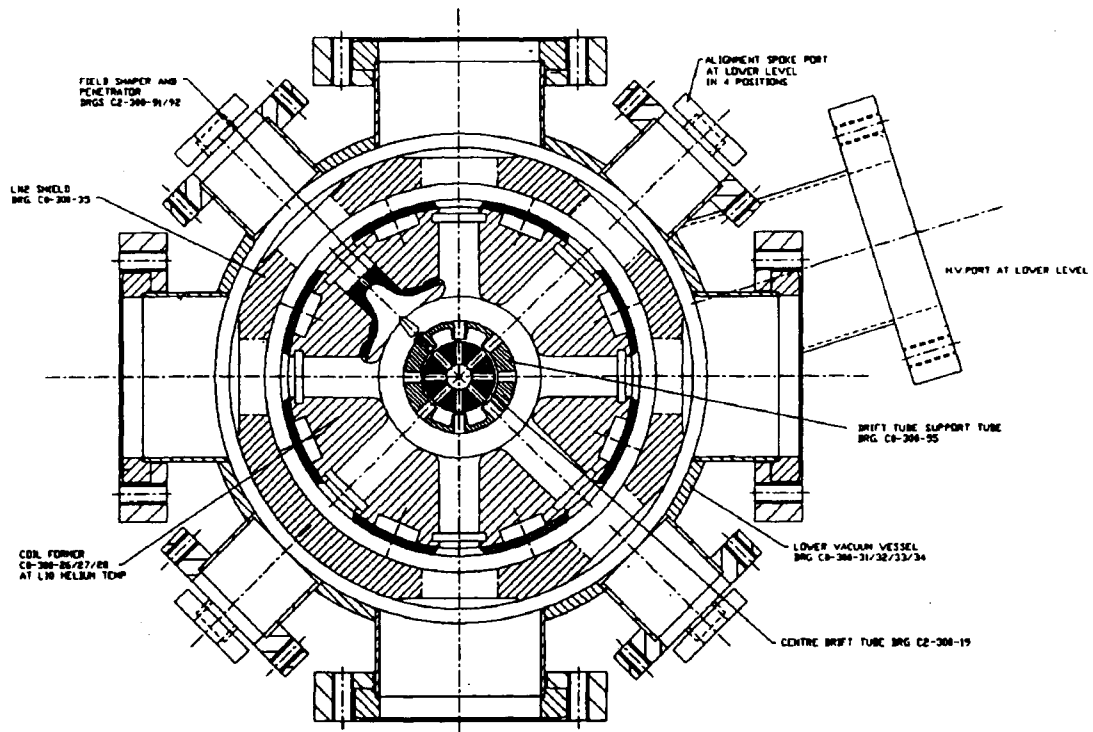


Figure 2. Cross-sectional view of the NIST EBIT, in the plane of the trap region. The distance between outer large flange faces is 27 cm. Seven of the ports will be equipped with a variety of windows to allow external observation from the visible to the x-ray regions of the spectrum.

Table 1. Projected characteristics of the NIST EBIT

Electron Beam Energy	700-50,000 eV
Electron Beam Resolution	50 eV
Electron Beam Current	10-200 mA
Electron Beam & Trap Radius	30 microns
Trap Length	2 cm
Number of Trapped Ions	40,000
Ion Density	$7 \times 10^8 \text{ cm}^{-3}$
Electron Density	$4 \times 10^{12} \text{ cm}^{-3}$
Current Density	5800 A/cm^2
Vacuum	$< 1 \times 10^{-12} \text{ torr}$
Maximum Trapping Time	5 hours

REFERENCES

1. M.A. Levine, R.E. Marrs, J.R. Henderson, D.A. Knapp, and M.B. Schneider, *Phys. Scr.*, **T22**, 157 (1988).
2. An essentially complete collection of the publications from the Livermore EBIT program through April 1992 is available as report UCRL-ID-110491 from the National Technical Information Service, U.S. Department of Commerce, 5285 Port Royal Rd., Springfield, VA 22161.

UPDATE ON THE NIST EBIT

J.D. Gillaspay* and J.R. Roberts
National Institute of Standards and Technology
Atomic Physics Division, Gaithersburg, MD 20899
and

C.M. Brown and U. Feldman
E. O. Hulburt Center for Space Research
Naval Research Laboratory, Washington, D. C. 20375

I. Introduction to EBIT.

A decade ago, the Electron Beam Ion Source (EBIS) was hailed as the most advanced method for producing highly charged ions [1]. A few years later, the EBIS concept was reevaluated and optimized for use as a spectroscopic source. The new device, the Electron Beam Ion Trap (EBIT) [2], produced a high density of ions in a relatively small volume with radial access ports. With this new geometry, plasma instabilities were removed and very high electron beam densities were achieved. These improvements boosted both the spectral brightness and the maximum attainable charge state, and furnished the atomic spectroscopy community with an important new laboratory source.

The spectra produced with an EBIT are very pure, consisting of lines from only a few charge states of essentially a single atomic species. The choice of charge state can be continuously varied by adjusting the electron beam energy. The ability to literally "dial up" a particular charge state greatly simplifies the identification of spectral lines. Virtually any highly charged state of any atom on the periodic table is accessible in this way.

In addition to operating the EBIT in a static mode where the electron beam energy is held constant and a spectrum is collected in order to determine accurate wavelengths, one can also use the precise and rapid control of the electron beam energy to carry out temporal studies of the emitted photons. This feature allows one to directly determine excited state lifetimes and to map out dielectronic recombination cross-sections.

A summary of the advantages of EBIT over conventional sources include:

1. Relatively few charge states.
2. No Doppler shifts
3. Insignificant Doppler broadening.
4. Insignificant density effects.
5. Very high charge states attainable.
6. Control over dielectronic satellites.
7. Slit-like source dimensions (60 μm x 2 cm) ideally suited to spectrometers.
8. Very little background signal.

9. High accuracy (21 ppm) wavelength measurements demonstrated.
10. Ultrahigh vacuum (10^{-10} Pa) maintained by cryogenic environment.
11. No cascade contamination in lifetime studies.

Although the spectral brightness of an EBIT is much weaker than that from powerful sources such as Tokamaks, the photon flux from an EBIT is nevertheless quite adequate for spectroscopic work when reasonable effort is taken to make use of efficient modern detection methods. A typical x-ray spectrum recorded with a solid state detector on an EBIT may only take a few seconds to collect. Very high precision studies of weak lines using crystal detectors may require many hours of data collection, however. Even in such cases the brightness is not usually of overriding concern since the source is under local control and operates reliably for long periods of time. Because the source is run by computer control, ions can be dumped from the trap and reloaded automatically at periodic intervals.

II. Present status of superconducting EBIT facilities.

The only full-scale EBIT devices in operation at this time are those at Livermore. The mechanical components for the NIST EBIT were made in Oxford England where an identical device is being put into operation [3]. The NIST EBIT will go into operation in Gaithersburg, Maryland during the coming year through a collaborative effort with the Naval Research Laboratory. An EBIT project is reportedly underway in Japan, although information about this project is scarce. A major EBIT project has been underway in the former Soviet Union at Dubna.⁴

Charge states as high as fully stripped Uranium are being actively pursued at Livermore where the prototype EBIT has been upgraded to operate above 150 keV. The NIST EBIT will begin operations under 50 keV, with possible upgrades in the future. Even at 50 keV, most of the states of any ion can be accessed.

The design of the NIST EBIT was developed by M. Levine and is based on his highly successful original work with the Livermore prototype. Detailed drawings, a discussion of the improvements that have been made, and a table of the projected operating conditions will be published in the proceedings of the VIth International Conference on the Physics of Highly-Charged Ions (HCI-92).

*Bitnet: Gillaspy@NBSenh, Internet: Gillaspy@enh.NIST.gov

- [1]. H. Winter, "The Production of Multiply Charged Ions for Atomic Physics Experiments" in Atomic Physics of Highly Charged Ions, R. Marrus (Ed.), 1983.

- [2]. M.A. Levine, R.E. Marrs, J.R. Henderson, D.A. Knapp, and M.B. Schneider, "The Electron Beam Ion Trap: A New Instrument for Atomic Physics Measurements," *Phys. Scr.*, T22, 157 (1988).
- [3]. J. Silver, private communication.
- [4]. Y. Aglitskiy, private communication.

First Results from the EBIT at NIST

J.D. Gillaspay¹

Atomic Physics Division, National Institute of Standards and Technology, Gaithersburg, MD 20899, USA

Received July 25, 1994; accepted August 2, 1996

Abstract

The Electron Beam Ion Trap (EBIT) facility at the National Institute of Standards and Technology (NIST) is now operational and producing atomic physics data. This report gives an overview of the design, operation, and performance of our EBIT. A preview of some of the first atomic physics results is given to illustrate the capabilities of the facility.

1. Introduction and background

The remarkable success of the Livermore group in constructing the first EBIT [1] and quickly obtaining a wide range of significant atomic physics results has stimulated a number of other laboratories to begin similar programs. Groups at the Clarendon Laboratory at Oxford, the Naval Research Laboratory in Washington D.C., and the NIST Physics Laboratory in Gaithersburg Maryland, were among the first to build EBITs following the initial Livermore success. In the summer of 1990, NIST contracted the Physics Department at Oxford to fabricate a duplicate set of EBIT components in parallel with the set for the Clarendon lab. M. Levine was brought in as a consultant to design a slightly modified version of the original Livermore EBIT and two sets of mechanical parts were produced under the direction of A. Holmes in the Nuclear Physics machine shop at Oxford. By the first quarter of 1992, one set of components was delivered to J.D. Silver's group at the Clarendon Lab and the other set of components was shipped to NIST where final assembly and integration with electronic components provided by NRL was begun by the NIST-NRL collaboration [2]. By the end of August 1993, the NIST-NRL EBIT was running with strong beam currents and producing clean X-ray spectra from neon-like barium, thereby demonstrating that the Livermore EBIT technology is readily transferable to other groups with no prior expertise with EBIT/EBIS devices. Our EBIT has subsequently been put through about a dozen test and experimental runs, some of the results of which are surveyed in the sections below. Parallel progress by the Oxford group has been described elsewhere [3].

A program to build another cryogenic EBIT was carried out in Russia [4]. Plans for additional large EBITs are underway in Japan [5], Germany [6], and perhaps Connecticut [7] and China as well. A number of small-scale "warm" EBITs, employing non-superconducting magnets, have also been constructed at various sites around the world including Russia [8], Japan [9], and France [10].

¹ Work performed with: Y. Aglitskiy, E. Bell, C.M. Brown, C. Chantler, R.D. Deslattes, U. Feldman, L. Hudson, J.M. Laming, E.S. Meyer, C.A. Morgan, J.R. Roberts, F.G. Serpa, J. Sugar, E. Takacs. The author's internet address is: Gillaspay@enh.nist.gov

2. Design and operation

Detailed scale drawings of our EBIT have been published in an early progress report [2] where the differences with the original EBIT are pointed out. Considerable room for improvement in the cryogenic design remains since the device continues to consume over 3 l/h of liquid helium. A schematic (not to scale) electrical diagram is shown in figure 1. The system of electrodes can be conceptually grouped into three sets: the electron gun, the drift tubes (DTs), and the collector assembly. The electron gun is a commercial dispenser-type unit with a 3 mm diameter curved cathode surface. Additional information and a diagram showing the internal structure of the electron gun can be found in ref. [11]. The DTs are shown in a detailed scale drawing in figure 2. They maintain thermal contact with the liquid helium bath through an annular sapphire insulator mounted in a compression fitting at the top of the DT assembly. The lower annular insulator is made of alumina. The shape of the outer shield is designed with two considerations in mind: reduce the electrostatic stress on the insulators, and reduce the possibility of having unintentionally trapped Penning electrons outside the DTs, a condition which might trigger high voltage breakdown. Although the electron gun and collector assemblies are presently referenced to earth ground through external connections, the internal mounting is entirely insulated from case ground, so the gun

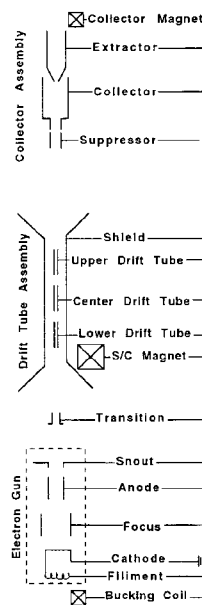


Fig. 1 Schematic diagram of EBIT electrodes and magnets.

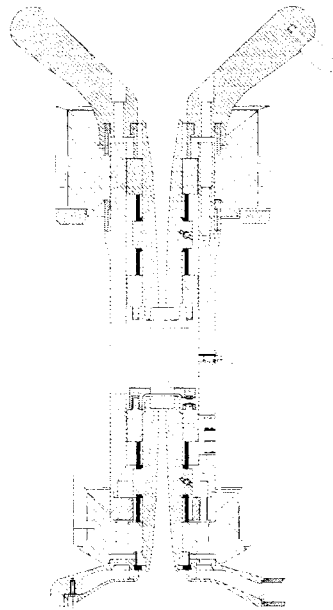


Fig. 2 Detailed scale drawing of EBIT drift tube assembly with high voltage insulators attached. The overall height of the assembly is 25.5 cm.

can be tied to the collector and floated down to negative high voltage in order to obtain greater electron beam energies in the future. The transition electrode helps guide the electrons through a small hole in the grounded cryogenic shield between the gun and the DT assembly. The primary magnet which surrounds the DTs produces a highly uniform 3 T field at 164 A. The collector and electron gun assemblies are surrounded by separate magnets which can be adjusted to cancel out the stray field from the superconducting magnet. The collector magnet is cooled by liquid nitrogen and the electron gun magnet is cooled by a chilled perfluorinated liquid which can withstand high voltages. The snout is a copper plated steel plate which helps shape the magnetic field lines near the electron gun.

During initial operation, spectra were obtained with all drift tubes connected to a single high voltage power supply, in which case the axial trap is formed solely by the variation in space charge potential between the DT and the electron beam due to the different inner diameters of the drift tubes. This provides a modest axial trapping potential of about 50 volts for 100 mA of beam current at 5 keV (the trap depth varies linearly with the beam current and inversely with the square root of the beam energy in this case). In order to increase the trap depth further, the two end drift tubes (end caps) are tied together and run a few hundred volts further from ground than the center drift tube. The X-ray signal strength as a function of end cap voltage is shown in figure 3. Although the DT shield is presently tied to the center DT, in future ion-extraction or injection modes of operation it will be operated a few hundred volts closer to ground in order to fully dump the trap. At present we have connected the snout electrode to the anode, although somewhat improved performance might be achieved if they were separately adjustable.

Tuning the EBIT is required in order to obtain optimal beam current and maximize the X-ray signal strength. Tuning is initiated by setting the electrode voltages and magnet

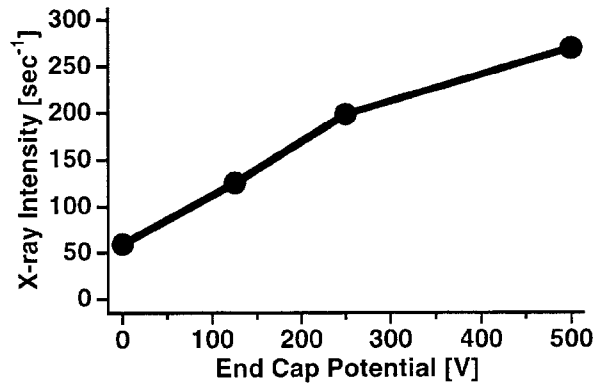


Fig. 3 Typical X-ray count rate as a function of end cap voltage. Data shown is the total count rate (number of counts in the peak channel multiplied by the number of channels corresponding to our detector-limited FWHM of 300 eV) for the strongest neon-like barium line (centered at 4.9 keV) as observed with a 0.13 cm² SiLi detector located 18 cm from the trap center. The EBIT was running at 125 mA electron beam current at 5 keV energy.

currents to the typical operating values shown in table I, and then slowly raising the anode voltage while monitoring the increasing beam current on the collector. The snout current, the key indicator of beam tuning quality, is constantly monitored and kept below 20 μ A. The anode voltage is interlocked to shut down (trip) automatically if the snout current rises above 80 μ A. Particularly during tuning, but even during normal operation, there are occasional unexplained bursts of current which lead to automatic shutdown. The snout is capacitively coupled into an oscilloscope which monitors occasional pulses of current which are below the trip threshold, but which seem to be correlated with trip frequency. With optimal tuning, the trip frequency can be of order 1/hour, but since the machine can be reset within a few seconds of a trip, reasonable operating environment can be obtained even with trip frequencies as high as 1/minute. When the cw snout current approaches 20 μ A, the EBIT is fine-tuned by adjusting the electrodes and magnets (primarily the transition voltage, bucking coil current, suppresser voltage, and focus). This fine-tuning lowers the snout current, after which the anode voltage can be raised to increase the beam current further. The procedure is iterated until no further gain is obtained. Once the proper settings for maximum beam current are obtained, the system can be varied from low to high currents without retuning. The experience at Livermore is that sets of horizontally oriented external shim coils around the DT region can be of critical importance for tuning, but

Table I. Typical electrode voltages and magnet currents for production of neon-like barium spectra.

Bucking Coil	18 A
Filament	6.3 V
Focus	-5 V
Transition	5.6 kV
Superconducting Magnet	164 A
Center Drift Tube	8 kV
Upper Drift Tube	8.5 kV
Lower Drift Tube	8.5 kV
Shield	8 kV
Suppresser	680 V
Collector	2 kV
Extractor	-1 kV
Collector Magnet	7 A

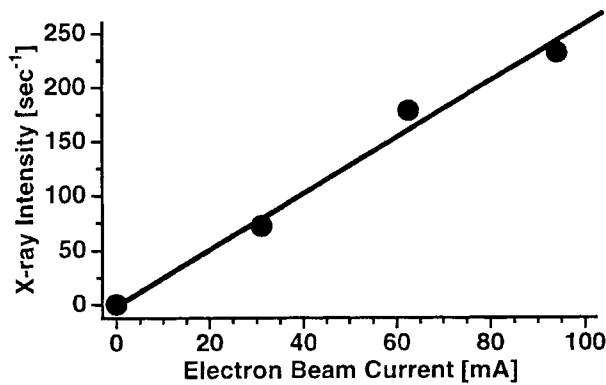


Fig. 4 Typical X-ray count rate as a function of electron beam current. Conditions are the same as in figure 3, except for the end caps which were held at 250 V. The straight line is a guide to the eye.

we find that when our EBIT is optimally aligned, the use of shim coils is unnecessary (minimum snout current obtained at zero shim current). This alignment is achieved by fine tuning the position of the DT assembly with the beam on, using a set of spring-loaded guide wires which are externally adjustable. The importance of successful tuning for spectroscopy is clear from the plot of photon count rate versus current shown in figure 4.

The present ranges of operating parameters are listed in table II. At low energies, as the DT voltage approaches the anode voltage, it becomes difficult to maintain snout currents below 20 μ A, and the beam current must be reduced. Figure 5 shows a summary of typical working beam currents obtained during a number of different days. The envelope of these currents is observed to roll off below a few keV.

It is well-known that spectroscopic signals from heavy ions (like barium) can be significantly enhanced by injecting lower mass elements (like nitrogen) into the EBIT in order to promote evaporative cooling [12]. A fortuitous small leak between our EBIT vacuum chamber and the liquid nitrogen lines to the collector walls seems to have provided nearly the ideal level of gas injection to cool our trapped barium ions. Later injection of additional nitrogen gas from a small atomic beam directed in through one of the side ports allowed only a modest additional increase in signal strength.

Additional introductory information about EBITs in general can be found in references [1, 13–14].

3. First Atomic Physics Results

Three atomic physics experiments are presently producing results from our EBIT in parallel: precision X-ray wavelength measurements, study of polarization of emitted X-rays, and observation and study of visible and near-uv light from magnetic dipole transitions within the ground term. The first two experiments employ Bragg crystal spectrometers in the Johann geometry [15] to study X-rays emitted from neon-like barium. The third experiment uses a scanning grating monochromator to study light from titanium-like and vanadium-like barium and xenon. In addition, we have a high-efficiency solid state (SiLi) detector monitoring the broadband X-ray emission from EBIT during all experiments. Examples of the spectra produced are shown in figures 6 and 7. An overview and discussion of the significance of our present work is

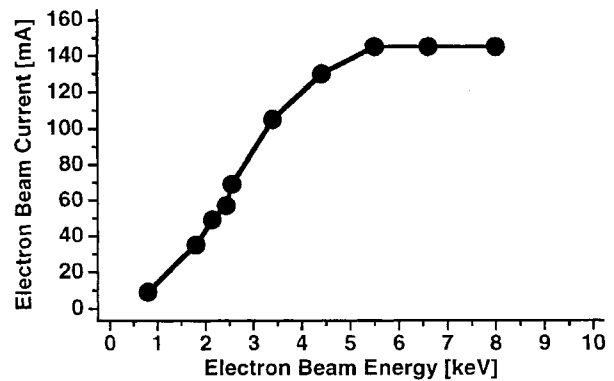


Fig. 5 Typical operating values of electron beam current as function of beam energy.

discussed below; detailed results will be presented in future publications.

To date, all precision X-ray wavelength measurements in EBITs have been made relative to other spectral lines which are also observed in EBIT and assumed to be known through *ab initio* calculations or by independent measurements in sources with very different X-ray production mechanisms than that in an EBIT. Variation between different types of sources, particularly with the strong polarization effects present in EBIT, has sometimes limited the accuracy of previous work, as described in ref. [19]. This fact, along with the desire for a measurement which is fully independent of theory, suggests the need for an improved approach. In the first experiment mentioned above we are attempting to use an external calibration source which will allow a direct tie to absolute length through the NIST measurement chain [16]. We are presently completing an extensive study of systematic errors associated with this method, and will soon have results to compare with unpublished [17] relative measurements taken on an independent EBIT at Livermore.

As mentioned in the previous paragraph, polarization effects due to the uniaxial electron beam can affect the interpretation and analysis of spectra in an EBIT. Additional polarization effects due to Zeeman shifts from the magnetic field are typically negligible for energetic X-ray transitions, but can become significant for visible and uv transitions. Previous studies have dealt with the X-ray polarization issue by first collecting data at one polarization, then modifying the spectrometer mounting to collect data with an orthogonal polarization at a later time [18]. In the second experiment

Table II. *Present performance parameters for the EBIT at NIST. The electron beam radius is assumed (from measurements taken on the Livermore EBIT) and the last two items are calculated. All other quantities are measured.*

Beam Energy	0.8–33 keV
Beam Current	0–155 mA
Beam Monochromaticity	< 90 eV
Magnetic Field	3 T
Trap Length	3 cm
Ions Trapped	Ba, Ar, N, Kr, Xe
Maximum Charge State	Ba ⁵⁴⁺
Vacuum at Top Flange	< 10 ⁻⁸ Pa (7x10 ⁻¹¹ torr)
Beam Radius	30 μ m
Electron Density	8x10 ¹² cm ⁻³ (@ 155 mA, 5 keV)
Current Density	5,500 A-cm ⁻² (@ 155 mA)

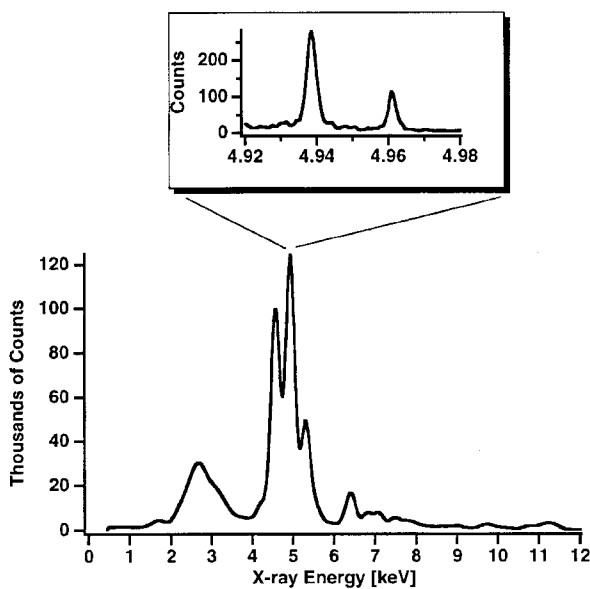


Fig. 6 Typical X-ray spectra of neon-like barium obtained from EBIT. The broadband spectrum was taken with a high-efficiency SiLi detector while spectrum in the inset (200x magnification on the horizontal axis) was taken with a high-resolution Bragg crystal spectrometer, and shows transitions to the ground state from the $J=1$ excited states $2p^{-1}_{3/2}3d_{5/2}$ (largest peak) and $2p^{-1}_{1/2}3s$ (smaller peak) fully resolved.

mentioned above, we are using two essentially identical Bragg crystal spectrometers to observe EBIT simultaneously in two orthogonal polarizations. With this configuration we do not need to correct for time variations in source operating conditions between measurements of the two polarizations. Another important consideration regarding polarization has to do with the population of levels by cascade from higher levels. This cascade feeding competes with direct population from electron-impact excitation and can have a large effect on the observed polarization [19]. Because the electron beam energy greatly affects the cascade feeding, the observed polarization can have a significant dependence on electron beam energy, and we are presently studying this dependence.

The last of our first three atomic physics experiments is carried out in a new spectral range for EBIT: the visible and near-uv. All previously reported spectroscopy in an EBIT has been at very short wavelengths, typically around 0.2 nm and below, although occasionally as high as 1 or 2 nm. By imaging the EBIT trap volume onto the slit of a grating spectrometer, we have been successful in obtaining spectra in the 320–450 nm range, and soon we expect to be able to extend these results out towards the infrared. The remarkable dearth of structure in these spectra over a broad wavelength range (fig. 7) greatly simplifies the identification of the lines. Although relatively rare, these long wavelength transitions can serve as important diagnostics both for the EBIT itself and for technologically important devices such as Tokamaks.

4. Future machine upgrades

In parallel with ongoing atomic physics experiments, we are constantly upgrading our EBIT to obtain more capabilities and improved performance. We are rapidly achieving higher voltages, and are almost certainly not yet at the limits of our machine in its present form. We have begun to put the system

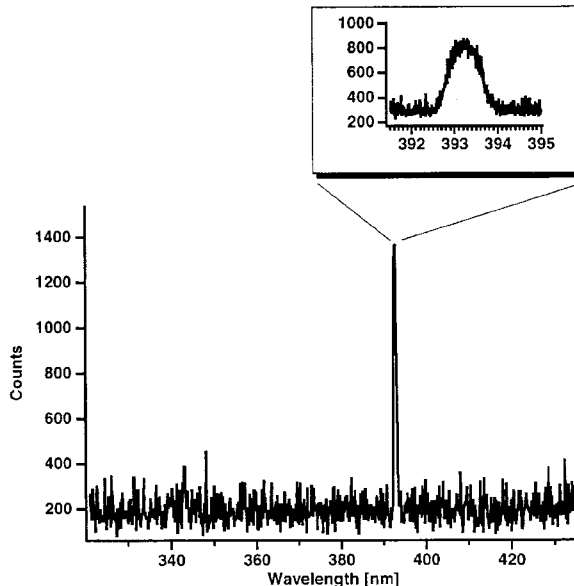


Fig. 7 Typical visible/near-uv spectra of titanium-like barium obtained from EBIT. The large peak is from the $J=2-3$ magnetic dipole transition within the ground term. The inset (10x magnification on the horizontal axis) shows a spectrum taken in the region of the large peak.

under computer control so voltages can be rapidly switched through preprogrammed sequences. A vacuum arc ion source (MEVVA) is being constructed which will allow us to inject and trap metal ions. We are beginning plans to build an “event mode” [20] data acquisition system which will allow efficient measurement of excited state lifetimes and cross sections for various atomic processes. We are also working to develop a new X-ray spectrometer for use on EBIT. Finally, we have recently begun a substantial effort to build an ion extraction beamline in order to investigate potential technological applications of highly charged ions interacting with surfaces. In parallel with this work, we [21] are planning to retrap ions into an external Kingdon trap in order to make possible additional atomic physics experiments.

Since this manuscript was submitted, substantial progress has been made on the three experiments and plans referred to in section 3 and 4. For an overview, see J.D. Gillaspay *et al.*, *Physica Scripta*, **T59**, 392 (1995), and for specifics see E. Takacs *et al.*, *Phys. Rev. A*, **54**, 1342 (1996) for X-ray polarization, C.A. Morgan *et al.*, *Phys. Rev. Lett.*, **74**, 1716 (1995) and F.G. Serpa *et al.*, *Phys. Rev. A*, **53**, 2220 (1996), for visible and near-uv light and MEVVA development, and A.I. Pikin *et al.*, *Rev. Sci. Am.*, **67**, 2528 (1996) for ion beamline development.

References

1. Levine, M.A., Marrs, R.E., Henderson, J.R., Knapp, D.A. and Schneider, M.B. *Physica Scripta* **T22**, 157 (1988).
2. Gillaspay, J.D., Roberts, J.R., Brown, C.M. and Feldman, U. “Proc. Vth International Conference on the Physics of Highly Charged Ions” (Edited by Richard, P., Stockli, M., Cocke, C.L. and Lin C.D.), **274**, p. 682 (AIP press, New York, 1993).
3. Silver, J.D. *et al.*, *Rev. Sci. Instrum.* **65**, 1072 (1994).
4. Aglitskiy Y. and Ovsyannikov V., private communication.
5. Ohtani, S., private communication.
6. Fussmann, G., private communication.

7. Smith, W.W., private communication
8. Antsiferov P.S. and Movshev, V.G., *Z. Phys.* **D21**, S317 (1991).
9. Kravis, S., this issue.
10. Briand, J.P. this issue
11. Knapp, D.A., Marrs, R.E., Elliott, S.R., Magee, E.W. and Zasadzinski, R., *Nucl. Instrum. Meth.* **A334**, 305 (1993).
12. Schneider, M.B., *et al.* "International Symposium on Electron Beam Ion Sources and Their Application" (Edited by Hershcovitch, A.), **188**, p.158 (AIP Press, NY, 1989).
13. Vogel, D., "Design and Operation of the Electron Beam Ion Trap", **UCRL-ID-104990** (National Technical Information Service, Springfield, VA, 1990).
14. Marrs, R.E., "Atomic, Molecular, and Optical Physics: Charged Particles" (Edited by F. B. Dunning and Randall G. Hulet), **29A**, p.391 (Academic Press, San Diego, 1995).
15. Brennan, S., *et al.*, *Rev. Sci. Instrum.* **60**, 2243 (1989).
16. Deslattes, R.D., *Nuc. Instrum. Meth.* **B31**, 51 (1988).
17. Beiersdorfer, P., private communication.
18. Henderson, J.R., *et al.*, *Phys. Rev. Lett.* **65**, 705 (1990).
19. Cowan, T.E., *et al.*, *Phys. Rev. Lett.* **66**, 1150 (1991).
20. Knapp, D.A., *Z. Phys.* **D21**, S143 (1991).
21. Yang L. and Church, D., "Proc. Vith International Conference on the Physics of Highly Charged Ions" (Edited by Richard, P. Stockli, M., Cocke, C.L. and Lin C.D.), **274**, p. 549 (AIP press, New York, 1993).

Overview of the Electron Beam Ion Trap Program at NIST

J. D. Gillaspy,¹ Y. Aglitskiy,² E. W. Bell,³ C. M. Brown,⁴ C. T. Chantler, R. D. Deslattes, U. Feldman,⁴ L. T. Hudson, J. M. Laming,^{4,8} E. S. Meyer, C. A. Morgan,⁵ A. I. Pikin,² J. R. Roberts, L. P. Ratliff, F. G. Serpa,⁶ J. Sugar and E. Takács⁷

National Institute of Standards and Technology, Gaithersburg, MD 20899, U.S.A.

Received August 19, 1994; accepted February 1, 1995

Abstract

This paper surveys the ongoing physics experiments at the Electron Beam Ion Trap (EBIT) facility at NIST, with particular attention paid to the underlying physical principles involved. In addition, some new data on the performance of our EBIT are presented, including results related to the determination of the trap width, ion temperature, and number of highly charged ions in the trap.

1. Introduction

With the Electron Beam Ion Trap (EBIT) at NIST now fully operational, a number of different experiments are progressing in parallel. This paper presents a survey of our current work and gives a preview of future plans. While an earlier paper [1] focused more on the general operation and performance of our EBIT, the present paper will focus on specific experiments. Detailed descriptions of the experiments surveyed here will appear in separate publications when the works are complete. Some additional material on machine performance is presented in the final section of this paper.

2. Survey of experiments

2.1. Tests of bound-state quantum electrodynamics (QED)

The importance of precise X-ray wavelength measurements for testing QED in the presence of the strong electric fields found in highly charged ions has been extensively reviewed

in the Proceedings of Nobel Symposium 85 [2]. The use of an EBIT to measure QED effects in highly charged ions under conditions free of Doppler shift corrections (the main systematic effect in most previous experiments) was pioneered by Beiersdorfer and colleagues [3]. Ideas for further EBIT work have been proposed by Silver [4]. Our activity in this area is guided by the theoretical work of Mohr [5] and Kim [6] and the experimental work of Deslattes [7]. Additional theoretical guidance is provided by outside groups such as that of Indelicato [8], Safronova [9], Dubau [10], and Drake [11]. Our particular interest in two-electron systems grows out of our desire to extend to very high charge states our previous work in neutral helium [12] and along the lower third of the helium-like isoelectronic sequence [13–15].

The fractional contribution of QED to binding energies typically increases quadratically as the charge state is increased with fixed electron number, and as the first reciprocal power of the principal quantum number ($1/n$) as n is reduced with fixed nuclear charge. The Z -scaling can be understood simply by combining the elementary Coulomb and angular momentum behaviour of electronic wavefunctions with the fact that large QED effects occur when an electron comes within a Compton wavelength of the nucleus (thereby allowing the infinite bare charge of the electron to become unscreened by the virtual positron-electron pairs which form the structure of the vacuum of space) (Table I).

As a prelude to our primary work in this area, we have undertaken a study of systematic errors associated with measuring the resonance lines of neon-like barium ($Q = 46+$) with the aid of an external calibration source. The X-ray spectrum of barium takes on a particular importance in EBITs because of its presence in the cathode of the electron guns frequently employed in such devices. If no other ions are injected, the trap will automatically fill up with barium, providing a convenient source of X-ray spectra

¹ Internet address: Gillaspy@enh.NIST.gov

² University of Maryland, College Park, MD 20742.

³ Joint Institute for Laboratory Astrophysics Boulder, CO 80309.

⁴ Naval Research Laboratory, Washington, DC 20375.

⁵ Texas A&M University, College Station, TX 77843.

⁶ University of Notre Dame, Notre Dame, IN 46556.

⁷ Institute of Nuclear Research (ATOMKI), Debrecen, Hungary.

⁸ Sachs Freeman Associates Inc., Landover, MD 20785.

Table I. Dependence of various atomic quantities on nuclear charge (Z). Some of the notes in the right-hand column refer to semiclassical arguments for circular electron orbits, but the results hold true generally. For a more precise analysis, refer to Ref. [20], for example

Physical parameter	Z-Scaling	Notes
Angular momentum ($r \times p$)	None	(Fundamentally quantized)
Linear momentum (p)	Z	(From $T = p^2/2m$ below, and $rp = \text{const}$)
Kinetic energy (T)	Z/r	(Coulomb-like, from the virial theorem)
Coulomb energy (U)	Z/r	(Definition)
Bohr radius (r)	$r \sim 1/Z$	(Consequence of first two items)
Coulomb wavelength (λ)	$1/Z^2$	($h\nu = U$; scaling holds for $\Delta n > 0$ transitions)
Electron fraction at nucleus (S)	Z^3	($1/r^3$ density of electronic wavefunction)
QED wavelength shift	Z^4	($Z^2 S$ from perturbation theory)
Fractional QED shift	Z^2	(Relative to Coulomb energy)

for diagnosing the performance of the EBIT. Although periodic trap-dumping can be used to remove the barium when it is unwanted, without this action barium provides a natural background spectrum whenever other elements are being studied in EBIT. With sufficient prior study, this natural background spectrum can be used as a built-in calibration reference.

Although many spectroscopic lines from highly charged barium ions have been studied by the Livermore group [16], precise wavelengths for the strongest lines observed in that work (the $2p-3d$ transitions in neon-like charge states) have not been published. We are presently measuring these lines using Bragg crystal spectrometers calibrated with external X-ray sources. QED effects for certain transitions in neon-like barium are predicted to become significant if wavelengths are measured to an accuracy of 0.1% or better [9].

2.2. X-ray polarization

Typically one associates polarized emission of photons with the presence of a strong external field which provides a quantization axis. Although the magnetic field in EBIT is "strong" by conventional standards (3 tesla), it is weak with regard to the very intense internal fields present in highly charged ions. It is interesting to compare the external field to the relativistically induced magnetic field that an electron sees as it orbits through the strong electric field provided by the nucleus. Because the Bohr radii which characterize highly charged ions are very small, the electrons are moving at velocities approaching the speed of light and the relativistically induced magnetic fields are strong. For an electron in the outermost shell of a neon-like barium ion, the induced fields are of order 7,000 tesla, and scale with the 4th power of Z . This 7,000 tesla field is the order of magnitude one would need to apply externally in order to affect the energy levels to an extent comparable to the spin-orbit splitting. With this in mind, it is easy to understand why highly charged ions are relatively unaffected by fields of order 3 tesla. An alternative way of looking at the problem is to note the ratio of a 3 tesla Zeeman shift to the transition energy. For the 5 keV resonance lines of neon-like barium, this ratio is of order 10^{-7} to 10^{-8} , a sufficiently small number that there is little hope of resolving it with present day X-ray spectroscopic techniques, and even if one could do so it would be fundamentally blurred by the natural widths of the lines themselves. This blurring of the lines typically has a strong dependence on nuclear charge ($\Delta v/v = Z^2$, for E1 transitions).

Although the presence of the magnetic field is often negligible for analyzing the emission of X-rays in EBIT, the uniaxial nature of the electron beam is highly significant, and actually provides a strong quantization axis for the polarized emission of radiation. Because atomic electrons are excited by impact with free electrons in the beam, momentum transfer considerations leave the ion in a preferentially aligned state. Upon spontaneous emission, the alignment of the ion is reflected in the polarization of the emitted radiation.

The situation is more complex if the electron beam is tuned to a sufficiently high energy to populate levels above the upper level of the transition of interest. In this case, cascade feeding becomes important, and one must take into

account all the various paths through the magnetic sublevels which feed the transition. Because increasing the electron beam energy can bring higher levels into consideration and change the cascade pattern, the polarization of the emitted radiation can depend significantly on the beam energy.

We are presently engaged in theoretical and experimental studies of this dependence of X-ray polarization on electron beam energy. Results of this study are important for testing the most sophisticated calculations of electron-impact excitation cross sections which contain information about the magnetic quantum sublevels. The analysis of polarized X-ray emission is being increasingly recognized for its importance in diagnosing technological devices such as Tokamak reactors as well.

2.3. Visible light spectroscopy

In a recent review paper [17], Marrs has remarked that one of the most exciting future developments in EBIT will be the extension of spectroscopy into the visible range of the spectrum. We have successfully done this by observing forbidden (M1) transitions within the ground term of titanium-like barium and xenon using a grating monochromator [18]. These transitions are of particular interest for their use in the remote monitoring of ion temperatures by Doppler broadening in large future tokamak fusion machines.

Because the light detected in these experiments arises from transitions between very close-lying levels, the wavelength is sensitive to small Zeeman shifts which are usually negligible in X-ray spectra. For the M1 transitions studied in our work, the Zeeman shifts appear at the 10^{-4} level of resolution, rather than the 10^{-7} - 10^{-8} level which is typical for the X-ray transitions discussed above.

When used to detect Doppler shifts, there are other advantages, though less fundamental, which visible light spectroscopy has over X-ray spectroscopy. Although the fractional resolution required to detect Doppler shifts from a moving ion is independent of wavelength, the availability of advanced refractive and reflective optics for visible light allows one to achieve both high efficiency and high resolution simultaneously. This opens up new opportunities, and makes the detection of Doppler shifts feasible with relative ease. For example, we have recently applied Fabry-Perot interferometry to achieve a resolution sufficient to see Doppler-blurred Zeeman broadening from ions in the trap (see Fig. 1 and Section 3.3 below).

The present accuracy of our measurement of the wavelengths of the visible light is sufficient to reveal large disagreements ($\sim 4\%$) with *ab initio* Dirac-Fock theoretical predictions [19]. Our present identification of these lines is confirmed by the isoelectronic behaviour of fitted calculations using the Cowan code [20]. This experiment should challenge theorists to improve their understanding of how electron-electron interaction affects level separations in a regime not widely addressed previously.

2.4. Ion-surface interactions for technology

The interaction of highly charged ions with surfaces has been studied for many years at accelerator facilities, and at least one company has come to produce a successful commercial product from this work [21]. Experiments with highly charged ions at accelerators, however, typically

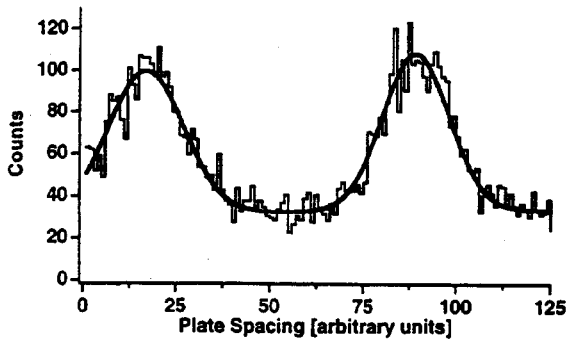


Fig. 1. Fabry-Perot interferometry (scanning mode) of the M1 transition near 400 nm in the ground term of titanium-like barium. The free spectral range (distance between peaks) is approximately 0.3 nm. The end cap potential on EBIT was 300 V.

involves high kinetic energy impact with surfaces. The use of EBITs (or EBISs [22]) to generate highly charged ions at rest in a small-scale laboratory environment offers new opportunities. Efforts in this area are underway at Livermore [23], Kansas State [24], and Hitachi Ltd. [25], as this technique may have application in the novel fabrication of technological devices. We have begun a concentrated program to assess the feasibility of using slow highly charged ions to fabricate an active electronic device such as a quantum dot diode. In collaboration with the recently formed Advanced Lithography Group consortium of industrial labs [26], we are also looking closely at the potential which highly charged ions may hold for future generations of projection lithography techniques.

3. New detail on EBIT device operation

Several earlier papers describe the operation of EBIT devices [1, 17, 27–28]. In this section we discuss several important parameters for which detailed data have not been published.

3.1. Trap size

Although it has often been said that the trap length for EBITs of the Berkeley-Livermore design is 2 cm, the actual length of the center drift tube is often longer (in our case, 3 cm). The external view of our trap is restricted by a 1.5 cm diameter hole in the surrounding liquid helium shield, so a typical detector will collect light from a section of the trap which is approximately 2 cm in length due to parallax at the edges. Using pinhole images of X-ray emissions, the Livermore group has measured the width of the electron beam to be 70 μm [28] but the width of the trapped ion cloud should be larger since the ion orbits are predicted to extend outside of the electron beam (Fig. 2). The X-ray imaging experiment is not affected by this because excited state lifetimes for typical X-ray transitions are of the order of femtoseconds, and therefore the ions travel less than 0.1 nm (a small fraction of an ion orbital cycle) before emitting a photon. By studying visible-wavelength photons from long-lived states, we are able to obtain data which determine the full spatial extent of the ion cloud. In this case, the ions can move through many orbital cycles before emitting a photon. To obtain data on the width of the ion cloud, we focused the center of EBIT onto the entrance slit of a grating monochromator which was mounted on a large precision trans-

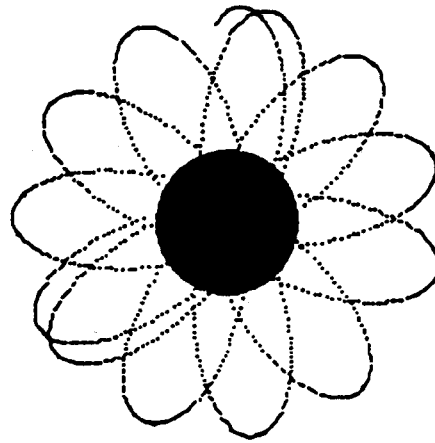


Fig. 2. Numerical simulation of an ion orbit through an electron beam with Gaussian density profile. Conditions: charge = 30 proton charges, Mass = 100 proton masses, magnetic field = 3 T, electron beam diameter containing 86% of charge = 60 μm (shown as shaded area in figure), drift tube diameter = 1 cm, space charge potential = 200 V, initial coordinates and velocity: $X_0 = Y_0 = 10 \mu\text{m}$, $v_0 = v_z = 4.0 \times 10^4 \text{ m/sec}$ (corresponding to an ion temperature of 1 keV).

lation stage. After adjusting the monochromator to be spectrally centered on one of the M1 transitions, we moved the spectrometer along a direction perpendicular to the line of sight into EBIT and monitored the strength of the observed signal. The result, shown in Fig. 3, is consistent with a 180 μm wide cloud of trapped ions, after correction for optical demagnification of the lens system. It should be possible to use this technique to monitor changes in the ion cloud width as the ion kinetic temperature is lowered by evaporative cooling.

3.2. Number of ions in the trap

The longstanding and vexing question of how many ions are in the trap has still not been definitively answered. Previous estimates based on calculation from spectroscopic data taking into account the solid angle of observation and other parameters, or on ion-extraction measurements, have yielded widely scattered values with large uncertainties. Recent work at Livermore using ion-cyclotron resonance [29] of the trapped ions may eventually yield highly reliable values, but present uncertainties seem to be as high as a factor of 10 [30]. In the meantime, the best estimate may be achieved from well-characterized measurements of an isolated spectral line. Since the location of a radiative recombination line can be adjusted by varying the electron beam

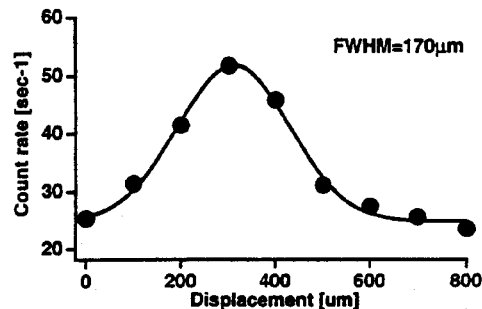


Fig. 3. Signal strength of visible light from Ti-like barium as a function of transverse position of a grating spectrometer.

energy in the EBIT, one can move such lines to a well-isolated region of the spectrum and obtain clear and clean results. Even more importantly, the radiative recombination cross sections can be calculated very accurately. With the number of EBIT laboratories growing, we suggest that a standardized procedure be adopted to compare the performance of different machines, as well as individual machines under varying circumstances. To this end, we present here detailed results for measurements taken on a particular radiative-recombination line in neon-like barium (Fig. 4), and infer a best estimate of 310000 ions in the trap from the following formula which relates the rate of photons detected (N_p) to the number of neon-like barium ions (N) in the trap:

$$N = \pi r^2 q N_p [f \Omega \varepsilon T I \lambda d\sigma(E, \theta)/d\omega]^{-1}$$

where ε is the efficiency of the detector, T is the transmission of the X-ray window at the photon energy, f is the fraction of ions in the trap which are unobscured, I is the electron beam current, r is the spatial FWHM of the electron beam, q is the charge of the electron, λ is an overlap factor which corrects for the spatial and temporal overlap of the ion cloud with the electron beam, $d\sigma(\varepsilon, \theta)/d\Omega$ is the differential cross section for emission of radiative-recombination photons (summed over the five sodium-like $n = 3$ levels contained within the finite resolution of the detector), E is the electron beam energy, θ is the angle of observation with respect to the electron beam, and Ω is the solid angle subtended by the detector. For our case, $\varepsilon = 100\%$ (SiLi detector @ 9 keV), $T = 100\%$ (0.007" thick Be foil at 9 keV), $f = 0.67$, $I = 100$ mA, $r = 35$ μ m, $\Omega = 5.8 \times 10^{-4}$ str (13 mm² detector at 18 cm distance), $\lambda = 18\%$ (estimated for 1 keV, Ba⁴⁶⁺ ions with 250 V applied end cap potential), $N_p = 10.86$ s⁻¹ (obtained by binning data into 10 eV wide channels for 20 minutes and fitting the peak with two Gaussians and a subtracted linear background), $d\sigma/d\Omega = 19.9 \times 10^{-28}$ m²/sr at $E = 5.69$ keV and $\theta = 90^\circ$ [31].

3.3. Ion temperature

The question of ion temperature – whether there is one, to begin with – is controversial due to the complex nature of the trap dynamics. If we assume an ion temperature, then the spectral linewidth observed can put an upper bound on its value. With adequate understanding of instrument pro-

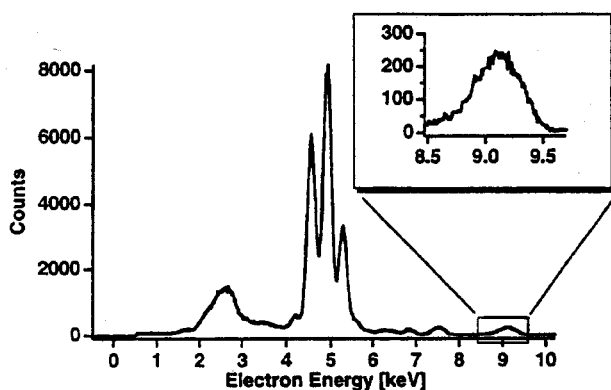


Fig. 4. X-ray spectrum show the radiative recombination line used to estimate the number of ions in the trap. The electron beam energy was set at 5.69 keV.

files and proper account for Zeeman broadening, the ion temperature can be accurately determined. Our preliminary Fabry-Perot data (Fig. 1 above) corresponds to an ion temperature below 1 keV. This ion temperature is a factor of 10 lower than the axial trap depth for an ion with charge 34+ contained by 300 V end cap potentials, suggesting the presence of strong evaporative cooling by interaction with lower charge state ions which see a shallower trap.

Acknowledgements

We thank Helmar Adler for collaboration in obtaining the Fabry-Perot data, and Yong-Ki Kim and Peter Mohr for theoretical support.

References

- Gillaspy, J. D., submitted, Proceedings of the VIth International Symposium on Electron Beam Ion Sources, Physica Scripta, 1994.
- "Heavy-Ion Spectroscopy and QED Effects in Atomic Systems" Proceedings of Nobel Symposium 85, (Edited by I. Lindgren, I. Martinsson, R. Schuch) Physica Scripta T46, 1993, p. 1-269, Royal Swedish Academy of Sciences, Stockholm, Sweden (1993).
- Beiersdorfer, P. *et al.*, Phys. Rev. A41, 3453 (1990).
- Silver, J. D. *et al.*, Rev. Sci. Instr., 65, 1072 (1994).
- Mohr, P., "Physics of Highly-Ionized Atoms" (Edited by R. Marrus) (Plenum, 1989), p. 111.
- Kim, Y.-K., Physica Scripta, T47, 54 (1993).
- Deslattes, R. D., Physica Scripta, T46, 9 (1993).
- Indelicato, P., Gorcex, O. and Desclaux, J. P., J. of Phys. B20, 651 (1987).
- Safronova, U. I., Safronova, M. S. and Bruch, R., Physica Scripta, 49, 446 (1994).
- Inal, M. K. and Dubau, J., J. Phys. B20, 4221 (1987).
- Drake, G. W. F., Adv. At. Mol. Phys. 18, 399 (1982).
- Sansonetti, C. J. and Gillaspay, J. D., Phys. Rev. A45, R1 (1992).
- Deslattes, R. D., Beyer, H. F. and Folkman, F., J. Phys. B17, L689 (1984).
- Chantler, C. T., D. Phil. Thesis, Oxford University (1990).
- Livingston, A. E., Galvez, E. J., Zacarias, A. S. and Serpa, F. G., AIP Conference Proceedings 274, "VIth International Conf. on the Physics of Highly Charged Ions" (Edited by P. Richard, M. Stockli, C. L. Cocke and C. D. Lin) (AIP, New York 1993), p. 402.
- Hutton, R. *et al.*, Phys. Rev. A, 44, 1836 (1991).
- Marrs, R. E., "Electron Beam Ion Traps", submitted to Meth. Exp. Phys., Livermore preprint # UCRL-JC-117432 (1994).
- Morgan, C. A. *et al.*, Phys. Rev. Lett., 74, 1716 (1995).
- Feldman, U., Indelicato, P. and Sugar, J., J. Opt. Soc. Am. B8, 3 (1991).
- Cowan, R. D., "Theory of Atomic Structure and Spectra" (University of California Press, Berkeley 1981).
- Fleischer, R. L., Price, P. B. and Walker, R. M., "Nuclear Tracks in Solids" (University of California Press, Berkeley 1975), p. 564.
- Donets, E. D., "The Physics and Technology of Ion Sources" (Edited by I. G. Brown) (Wiley, New York 1989), p. 245.
- Schneider, D., Briere, M. A., McDonald, J. and Biersack, J., Radiation Effects and Defects in Solids 127, 113 (1993).
- Parks, D. C., Bastaz, R., Schneider, S. W. and Stockli, M., J. Vac. Sci. and Technol., in press (1994).
- Mochiji, K., Itabashi, N., Yamamoto, S., Ochiai, I. and Okuno, K., Jpn. J. Appl. Phys., in press (1994).
- Loschner, H. *et al.*, Microlithography World, Spring, p. 4 (1994).
- Levine, M. A. *et al.*, Physica Scripta, T22, 157 (1988).
- Levine, M. A. *et al.*, "International Symposium on Electron Beam Ion Sources and Their Applications" (Edited by A. Hershovitch) (AIP, New York 1989), p. 82.
- Beiersdorfer, P., Beck, B., Elliott, S. and Marrs, R., Rapid Commun. in Mass Spect., 8, 141 (1994).
- Schweikhard, L. *et al.*, Rev. Sci. Instrum., Livermore preprint # UCRL-JC-116808, (1994).
- Saloman, E. B., Hubbell, J. H. and Scofield, J. H., At. Data Nucl. Data Tables 38, 1 (1988).

HOT TOPIC

Visible and UV light from Highly Charged Ions: Exotic Matter Advancing Technology

*J. D. Gillaspy
Atomic Physics Division, Physics Laboratory,
Technology Administration,
U.S. Department of Commerce,
National Institute of Standards and
Technology
Gaithersburg, MD 20899-0001
Gillaspy@enh.NIST.gov*

In a few laboratories scattered around the world, small devices the size of a filing cabinet are producing an exotic form of matter which may play a role in several future advanced technologies. These types of devices, Electron Beam Ion Traps (EBITs) [1], are capable of producing ions of virtually any possible charge state of any atom on the periodic table. The very highest charge states have strongly altered properties which make the ions not only an interesting curiosity, but also potentially useful. Alternative ways of producing the exotic highly charged ions (HCIs) require huge devices which are only affordable by a large national or corporate effort. The fairly recent development of EBIT technology brings R & D work with the most extreme HCIs down to a level which is affordable by the individual investigator or small private company.

Of the various potential applications for HCIs, one of the most proven is as an optical diagnostic for hot plasmas. Analysis of emission spectra from HCIs has long been used as a remote probe of the Sun, but this technique has now been brought down to Earth as scientists and engineers move closer to developing an electrical power generator which uses the same relatively safe and efficient process by which nature produces sunlight: nuclear fusion. Actively harnessing the power of the sun by creating a miniature "solar plasma in a bottle" here on earth, has been the focus of a major national effort for years [2]. Through an anticipated international collaboration, the ongoing fusion effort appears to be on the brink of reaching commercial viability in the early next century. Although the tiny EBIT device can produce plasmas in excess of 10,000,000 degrees Kelvin, as high as that in the sun or in fusion test reactors, the EBIT cannot contain enough material to itself be a useful energy production de-

vice. The core confinement chamber inside EBIT is only about as wide as a human hair, and a centimeter or two long, while fusion confinement chambers are large enough to walk around in. In addition, the density of the EBIT plasma is of order $10e9/cc$, much less than that required for commercial power production. One of the things that the EBIT can do very well, however, is provide a crisp, clear, and uncluttered laboratory view of the inner workings of nature in one of its more exotic and relatively inaccessible states: the highly charged plasma. Knowledge gained from EBIT studies can then be directly applied to improve fusion plasma diagnostic work.

A specific example of how EBIT can be used to help in the fusion effort is illustrated by some recent work we did involving the measurement of visible and near-ultraviolet light emission from HCIs. Although visible light is emitted copiously when neutral atoms are excited by thermal or electronic processes, the same is not true for HCIs. As atoms lose more and more of their outer electrons, the exposed remaining shells appear so tightly bound that the quantum energy level separations are thousands of electron-volts, rather than just a few electron-volts as they would be for separations which give rise to visible light emission. As a result, HCIs emit primarily in the X-ray region of the spectrum.

X-ray spectrometers are routinely deployed in fusion devices in order to monitor and diagnose conditions in the plasma. Information about plasma temperature and internal magnetic field, for example, can be obtained non-invasively from the Doppler and Zeeman widths of x-ray emission line profiles. It would be highly desirable to replace the x-ray spectrometers with visible light spectrometers in the future, however, for several reasons. First, one could then employ optical telecommunications technology, fiber optics in particular, to carry out truly remote diagnostics. With x-ray spectroscopy, the instruments must be located close to the confinement vessel walls in areas of high radiation which make them physically inaccessible to personnel during operation. Second, spectroscopic techniques are much

more advanced in the optical region, so more efficient and higher resolution measurements will be possible. Third, thin metal-foil x-ray windows used in test reactors may become impractical to use in scaled-up commercial versions of the reactors, while thick but transparent optical windows may offer an alternative. Finally, there are some fundamental advantages, such as the fact that Zeeman shifts appear as a larger fraction of the total wavelength when one observes optical emission from close-lying levels rather than x-ray emission from widely separated levels. All of these facts point towards optical diagnostics as the method of the future. The problem is: how does one get the HCIs to cooperate and give off the appropriate optical emission?

While ordinary visible light transitions are squeezed into the x-ray regime as the charge state is increased isoelectronically, RF and microwave transitions experience a similar shortening of wavelength, and can be squeezed into the visible and ultraviolet. Furthermore, transitions which would ordinarily be forbidden by the ordinary selection rules of quantum mechanics begin to become more and more allowed as higher order processes are brought into play in the presence of the strong internal electric fields which are characteristic of HCIs. Both of these facts open up possibilities for observing visible light from HCIs, even when the principle emission is limited to the x-ray regions of the spectrum.

While the typically strong dependence of wavelength on charge state can open up new possibilities, it can also lead to serious problems. If one finds a special case where a highly charged ion emits visible light, the wavelength will typically shift rapidly into the deep ultraviolet as the charge state is varied even slightly along an isoelectronic sequence. Since a variation in plasma temperature will alter the charge state, it would be desirable to have a single isoelectronic sequence which emits in the visible for a wide range of charge states. In order to have this, however, it would be necessary to violate nature's rule that wavelengths scale rapidly with charge.

A few years ago Uri Feldman from the Naval Research Laboratory teamed up with Jack Sugar and Paul Indeli-

cato at the National Institute of Standards and Technology to carry out an extensive search for an exception to nature's rule [3]. Using one of the most sophisticated computer codes available to simulate the atomic structure of highly ionized matter, the scientists sifted through scores of possibilities until they found the needle in the haystack. The code predicted that certain ordinarily forbidden transitions between the fine structure levels within the ground term of titanium-like ions—atoms stripped of all but the 22 innermost electrons—would produce visible light over a wide range of charge states for elements across the entire upper half of the periodic table. These transitions are forbidden because, to first order, the electric field component of an electromagnetic wave cannot connect states of identical parity. Instead, the magnetic component of the wave is required. Generally the magnetic component is rather ineffective, but, as mentioned above, the ordinary "rules of thumb" are highly distorted in HCIs. "Forbidden" transitions begin to be "allowed" at rates which scale in certain circumstances as rapidly as the tenth power of the charge. In extreme cases, the (formerly) "forbidden" transitions in HCIs can proceed even more rapidly than the "allowed" ones.

The special lines predicted in Ti-like ions remained an untested curiosity until early last year when the EBIT at

NIST was deployed to see if they really could be seen and whether they had the unusual properties which were predicted. In a recent issue of *Physical Review Letters* [4], we reported our findings that not only were the unusual lines clearly observable, but they were even more "visible" than expected, with wavelengths shifted approximately 5% back toward the red from their predicted location in the near-UV. In subsequent work, we have raised the charge state by up to 10 elementary charges, and find that although the wavelength offset is preserved, the scaling with charge is very similar to that predicted. We are presently measuring the lifetimes of the upper levels in order to further characterize this sequence. The reason for the wavelength offset has puzzled every theorist we have spoken to, including a cadre of the best who were present at last year's Nobel Symposium on Trapped Charged Particles [5]. This is just one of the presently unexplained puzzles which the highly charged form of Nature's "fourth state of matter" [6] (the plasma) presents us with.

Acknowledgments

I wish to thank my colleagues and postdocs listed on publications 1, 3, 4, & 5 below, as well as my Division Chief, Wolfgang Wiese, and Directors, Katharine Gebbie and Ray Kammer, for making this work possible.

For further reading

1. "The Electron Beam Ion Trap", R. E. Marrs, P. Beiersdorfer, and D. Schneider, *Physics Today*, 47, 27 (1995).
2. "Princeton Tokamak begins experiments with tritium-deuterium plasmas", B. Schwarzschild, cover photograph and news article, *Physics Today*, 47, 17 (1994).
3. "Magnetic dipole line from U LXXI ground-term levels predicted at 3200 Å", U. Feldman, P. Indelicato, and J. Sugar, *J. Opt. Soc. Am.* 8, 3 (1991).
4. "Observation of Visible and uv Magnetic Dipole Transitions in Highly Charged Xenon and Barium", C. A. Morgan, F. G. Serpa, E. Takacs, E. S. Meyer, J. D. Gillaspay, J. Sugar, J. R. Roberts, C. M. Brown, and U. Feldman, *Phys. Rev. Lett.*, 74, 1716 (1995).
5. "Overview of the EBIT Program at NIST", J. D. Gillaspay, Y. Aglitskiy, E. W. Bell, C. M. Brown, C. T. Chandler, R. D. Deslattes, U. Feldman, L. T. Hudson, J. M. Laming, E. S. Meyer, C. A. Morgan, A. I. Pikin, J. R. Roberts, L. P. Ratliff, F. G. Serpa, J. Sugar, and E. Takacs, *Proceedings of Nobel Symposium #91* (in press, *Physica Scripta*, 1995).
6. "The Fourth State of Matter: plasma dynamics and tomorrow's technology" B. Bova (New York, St. Martin's Press, 1971).

EBIT Spectra of Highly Stripped Ions from the Visible to the X-Ray

J. D. Gillaspay¹

Atomic Physics Division, National Institute of Standards and Technology, Gaithersburg, MD 20899, USA

Received October 3, 1995; accepted in revised form December 13, 1995

Abstract

This paper provides an updated review of the capabilities of the Electron Beam Ion Trap (EBIT) as an advanced light source for atomic spectroscopy. Recent developments extending the spectral range to over five orders of magnitude in wavelength are highlighted. Distinguishing features that make EBIT a powerful tool both for simplifying spectral analysis and for making precise and accurate measurements are discussed. Various limitations of the machine are also discussed, with the intent to provide an introductory guide for scientists who may be planning EBIT spectroscopy experiments for the first time.

1. What is an EBIT?

For the purpose of this paper, one may think of the EBIT as a high density monochromatic electron beam of variable energy, housed in a vacuum chamber small enough to fit in a closet. Atoms directed through the electron beam are ionized and subsequently trapped in an orbit around and through the beam. Subsequent ion-electron collisions excite transitions, causing the ions to fluoresce. More detailed descriptions of the operation and design of the EBIT can be found in the literature [1], including a popular account with color photographs [2], or on the World Wide Web EBIT home pages:

<http://physics.nist.gov/MajResFac/EBIT/ebit.html>
http://www-phys.lnl.gov/N_Div/ebit.html

2. The spectral range and simplicity of EBIT spectra

Since the last ASOSALP conference three years ago [3], the EBIT has continued to demonstrate itself as an increasingly powerful and versatile light source for atomic spectroscopy. Two developments in particular have dramatically expanded the spectral range of available data from EBIT sources. First, the development of the SuperEBIT at Livermore [4] has led to the production of spectra from energetic electronic transitions which emit all the way into the soft gamma-ray region of the spectrum (see Fig. 1) [5]. Second, the demonstration at NIST [6, 7] that an EBIT can be an effective source for visible and near-UV spectroscopy (see Fig. 2) of forbidden fine structure transitions in highly charged ions has extended the range of EBIT data to span over five orders of magnitude in wavelength.

One of the striking features of data taken with an EBIT is the often remarkable simplicity of the spectra. This is observed even out to both extremes of the available spectrum, as can be seen in both the soft gamma-ray data from Livermore and the visible and near-UV data from NIST. In

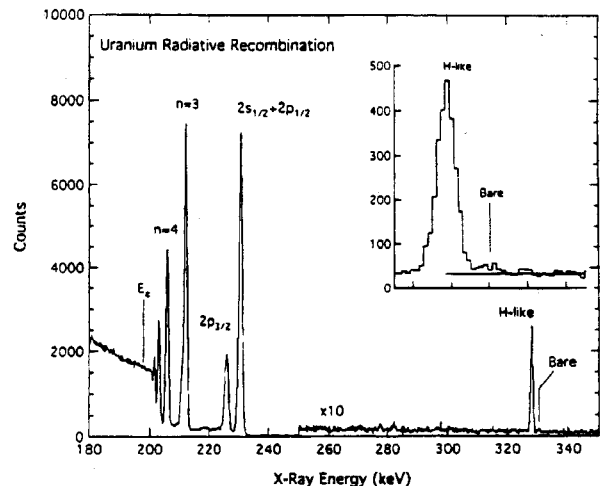


Fig. 1. Spectrum showing that an EBIT can produce the highest possible charge states, up to and including U^{92+} which emits photons with energy in excess of 300 keV (wavelengths < 0.004 nm) [5].

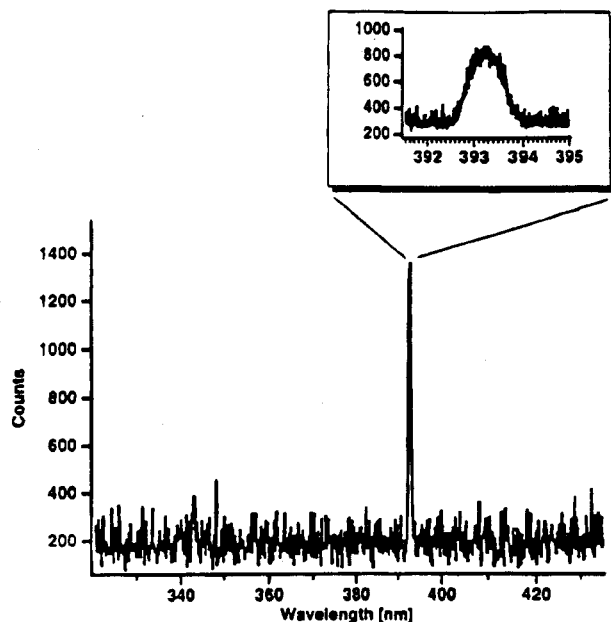


Fig. 2. Spectrum showing that an EBIT can also be used as a source for visible-light spectroscopy of highly charged ions. Here light from Ba^{34+} extending up to nearly 400 nm in wavelength is measured [7]. Inset shows the average of 10 higher-resolution (narrow slit) scans of 5 minutes each over the region where the strong line appears.

¹ Internet address: John.gillaspay@NIST.gov

the NIST barium data for example (Fig. 2) [7], only a single line appears over a very broad spectral range (320–440 nm). In both cases, a large part of the simplicity of the spectra arises from the purity and selectivity of the source, as will be illustrated more fully in the remainder of this paper.

3. How close to the ideal can an EBIT get?

3.1. Sketch of an ideal light source

An ideal spectroscopic light source would emit photons from a single atomic species, which has been prepared in a single charge state of any value, under conditions which selectively excites a single transition, with high brightness, and low density (to avoid collisions and absorption), with a small source size, running in continuous (rather than pulsed) mode, yet capable of being rapidly switched, and be inexpensive and easy to build. All real sources fall short of this ideal, sometimes for fundamental reasons (high brightness and low density, for example, are often contradictory). It has been suggested, however, that the EBIT goes further toward meeting all of these requirements than any other source [8]. The remainder of this section will address how close an EBIT source can approach the ideal spectroscopic light source. Section 4 will then address ways in which the performance of an EBIT falls short of the ideal.

3.2. An EBIT can produce any charge state

With electron beam energies near 200 keV, the SuperEBIT has recently produced spectra from radiative recombination onto bare uranium ($Q = 92+$, see Fig. 1) [5]. During the past eight years, a great deal of data has been taken from “midrange” charge states ($Q = 40$ – 60) where the EBIT runs with ease. Recently, data have been taken at NIST on charge states as low as $Q = 1$ (molecular nitrogen ions) [9] where the EBIT functions like a high-tech version of a simpler electron beam device which was built for just such a purpose decades ago (see Fig. 1 in Ref. [10]).

So far, EBITs have been used by the Livermore and NIST groups to obtain data from at least 44 elements (N, F, Ne, Al, Si, S, Cl, Ar, Sc, Ti, V, Cr, Mn, Fe, Co, Ni, Cu, Zn, Ge, Br, Kr, Rb, Y, Mo, Sn, Xe, Ba, Hf, Ta, W, Re, Ir, Pt, Au, Pb, Bi, Pr, Nd, Gd, Er, Tm, Yb, Th and U) and for at least 21 isoelectronic sequences (bare, H-like, He-like, Li-like, Be-like, B-like, C-like, N-like, O-like, F-like, Ne-like, Na-like, Mg-like, Al-like, Si-like, Sc-like, Ti-like, V-like, Co-like, Ni-like, Cu-like).

3.3. The EBIT has charge state selectivity

By varying a single knob, an EBIT can be adjusted to preferentially produce a selected charge state. Although other charge states are generally present, this varies depending on the proximity of nearby levels. The production of a single charge state with 97% purity has been demonstrated [11]. Even for non-optimal (open shell) configurations, it is possible to obtain a sizable degree of selectivity as evidenced by the visible light data from NIST (see Fig. 3).

Detailed computer simulations which predict the degree of charge state selectivity for all stages of ionization of all elements and under a wide range of conditions have been installed at all three of the major EBIT facilities (see Section 6 below) in order to help plan experiments and interpret observed results. These simulations are based on the orig-

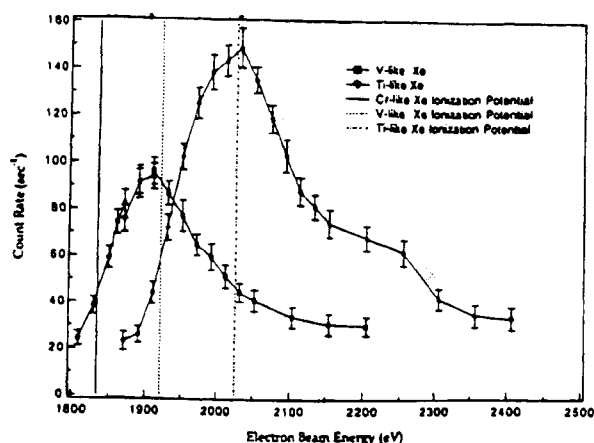


Fig. 3. Plot showing how charge states can be preferentially tuned in or out of the observed spectrum by adjusting the EBIT [6]. Shown is the variation in the intensity of two visible-light spectral lines from Xe^{32+} and Xe^{31+} as a function of electron beam energy. Because the excitation, fed by cascade from above, is approximately constant, the dependence of intensity on electron beam energy reflects the change in charge state abundance directly.

inal models from Livermore [12], but contain various refinements.

3.4. The EBIT has excitation selectivity

By adjusting the electron beam energy above or below an excitation threshold, spectral lines within a given charge state can be turned on or off. This is true not only for dielectronic recombination lines, but also for those directly excited by electron impact. Figure 4, for example, shows how a strong line in heliumlike iron can be extinguished by lowering the electron beam energy by 1% and how a second nearby line can then be extinguished by lowering the electron beam an additional 1% [13]. In this regard, the EBIT electron beam can be used much in the same way that a laser is used to selectively excite a transition, except in the case of the EBIT the direct excitation cross-section has only a sharp lower threshold, instead of a symmetric resonance structure. The degree of selectivity is limited by the energy spread of the electron beam, which is typically 50 eV, although it has been made as low as 16 eV [14] by compromising other aspects of the EBIT performance.

3.5. The EBIT provides a third dimension to spectroscopy

While the spectroscopy of highly charged ions using ordinary light sources typically consists of a simple two-dimensional data set composed of intensity *vs.* wavelength, the monochromatic nature of the electrons in the EBIT allow the spectra to be expanded along a third axis: electron beam energy. In this simple fact lies the key to understanding why an EBIT is such a useful spectroscopic source. Almost all the features of an EBIT can be traced to this single aspect of its design, and fully understanding a 3-dimensional plot of EBIT data (see Fig. 5) [see also Fig. 5 in Ref. 15] is a key test of understanding the EBIT in general.

The full significance of this third dimension is not easy to appreciate without careful consideration, particularly since many spectroscopic experiments need only sample a particular slice of the full three-dimensional phase space. Some of the unusual features of the EBIT which arise from the new

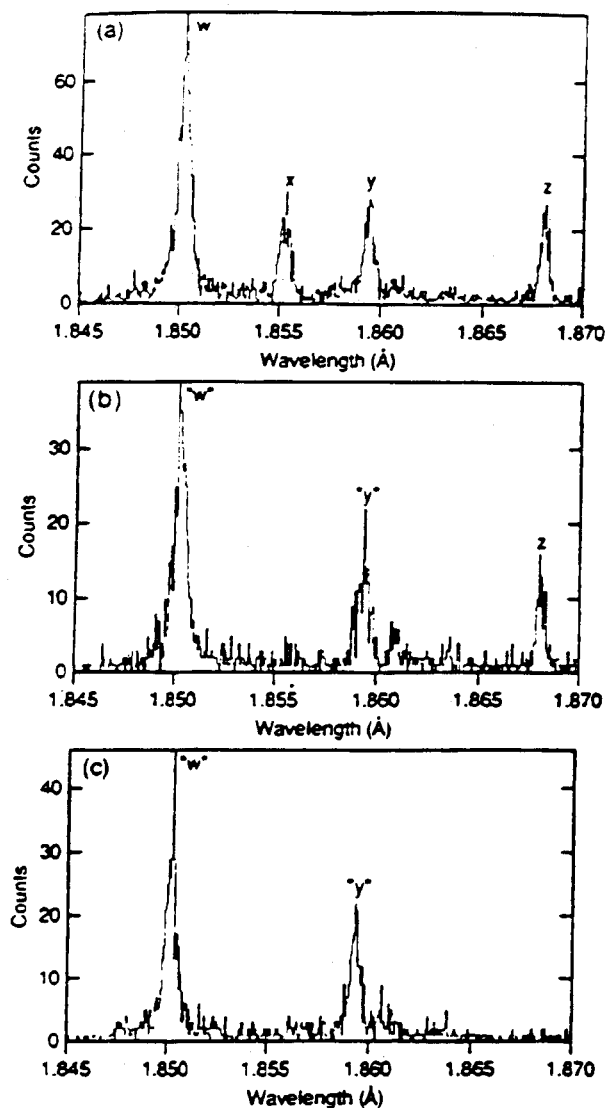


Fig. 4. Plot showing how, within a given charge state, spectral lines can be tuned in or out of the spectrum by adjusting the EBIT to bring the electron beam energy above or below the threshold for impact excitation [13]. Here, in the X-ray spectrum of helium-like iron (Fe^{24+}), lines "x" and "z" are extinguished by lowering the electron beam energy by 1% (b) and 2% (c) from the 6.74 keV value used to produce (a). Because the beam energy is far above the 2 keV threshold to produce the helium-like iron, the charge state distribution remains approximately constant.

dimension added by the electron beam energy are described in the remainder of this subsection.

The origin of the process by which a spectral line is formed can often be determined simply by observing its behavior as the EBIT control knobs are adjusted. No theoretical input or detailed understanding of the system is needed for this level of analysis. If a line appears abruptly and then disappears just as abruptly when the electron beam energy is varied by an amount equal to its energy width, then the line is probably a dielectronic recombination satellite. If a line moves continuously in photon energy as the electron beam energy is varied, it is probably a radiative recombination line. A judicious placing of the electron beam energy can localize and move radiative recombination emission out of the way, or turn off undesired satellites.

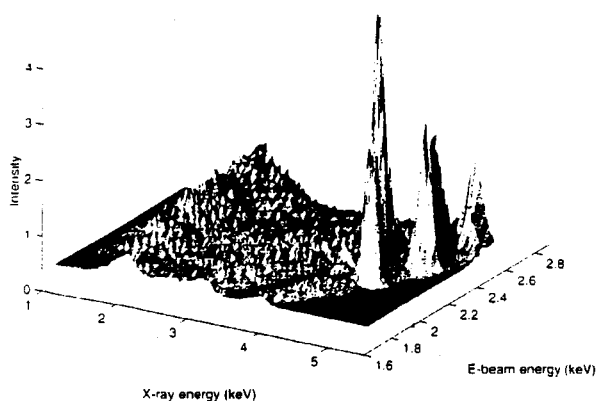


Fig. 5. Plot showing how spectra can be studied not only as a function of photon energy, but also (simultaneously) as a function of electron beam energy. The extra dimension provides an additional degree of control and an added axis for analysis which lies at the heart of many of the features of EBIT.

The tunable beam energy can also be used to enhance the effective resolution of a system which uses a low-resolution detector. Figure 4 in Ref. [16], for example, shows a spectrum with 50 eV resolution, taken with a solid state detector which has resolution of typically 200 eV. When viewed in three dimensions, the dielectronic recombination peaks can be seen to be asymmetric, with the widths along the photon and electron energy dimensions being 200 eV and 50 eV, respectively. Selecting information along the proper "cut" with an EBIT allows features to be resolved which would otherwise be fully blended.

3.6. The EBIT can be considered to be a bright source (sometimes)

The spectral brightness of the EBIT is perhaps the most misunderstood aspect of the device. When reviewing the literature, one can even find these apparently contradictory statements, both from knowledgeable members of EBIT research groups: "EBIT is a relatively weak X-ray source" [17], and "EBIT is a relatively bright source for emission spectroscopy" [8]. Both statements are correct, when taken from the appropriate point of view. In order to remove the subjectivity which necessarily comes with terms such as "bright" and "weak", I focus here on a more objective measure: how long does it take to acquire a useful spectrum? The answer depends on the experiment, but can vary from a second to several days, as described in more detail in the remainder of this subsection.

It is worth pointing out that signal strengths have improved dramatically since the first year of EBIT operation (around 1988) so anecdotal experience from that period should be considered atypical by current standards. Improvements have included both increases in beam current and the application of more efficient spectrometer geometries [18].

In the case of X-rays observed in low resolution (SiLi spectrometer with spectral resolution 2% at 7 keV), one can obtain useful spectra in one or two seconds, fast enough for real-time feedback when adjusting the EBIT to optimize its performance (see Fig. 4 in Ref. [19]). The count rate in a single spectral peak can be over 100 s^{-1} .

For visible light observed with moderate resolution (scanning grating monochromator with spectral resolution 0.2% at 400 nm) one can obtain useful spectra in 5 minutes (see inset of Fig. 2) even without the advantage of parallel detection. The count rate per spectral line can be over 10 s^{-1} .

For high resolution X-ray spectroscopy, one can obtain high quality data in 20 minutes to an hour (see Fig. 6). The count rate per spectral line can be over 1 s^{-1} .

3.7. The EBIT source shape can be optimal for many spectroscopic studies

The EBIT source shape is slit-like, approximately 3 cm long (the central 2 cm of which are visible from outside the EBIT vacuum chamber) and a fraction of a mm wide. The transverse dimension can vary depending on the excited state lifetime and the ion temperature. For the very fast lifetimes associated with X-ray transitions, light is effectively limited to the region of excitation determined by the electron beam itself (60 μm diameter, see Fig. 5 Ref. [20] for a direct measurement of the electron beam width using X-ray imaging). For visible and UV transitions with lifetimes longer than the time needed for an ion to traverse the electron beam (2 ns for 1 keV barium crossing a 60 μm electron beam), emission is spread over the entire trap region which can be 200 μm in diameter (see Fig. 3 of Ref. [19] for a measurement of the visible trap width). The narrow transverse dimension of the trap helps to increase its brightness, while at the same time allowing it to be efficiently imaged into a spectrometer (for example, the entrance slit of a grating spectrometer).

3.8. The EBIT is a very clean source

With a base level of evacuation 13 orders of magnitude below atmospheric pressure (10^{-8} Pa or 10^{-10} Torr) and a trap region surrounded by surfaces cooled to liquid helium temperature, the EBIT runs under conditions of very high

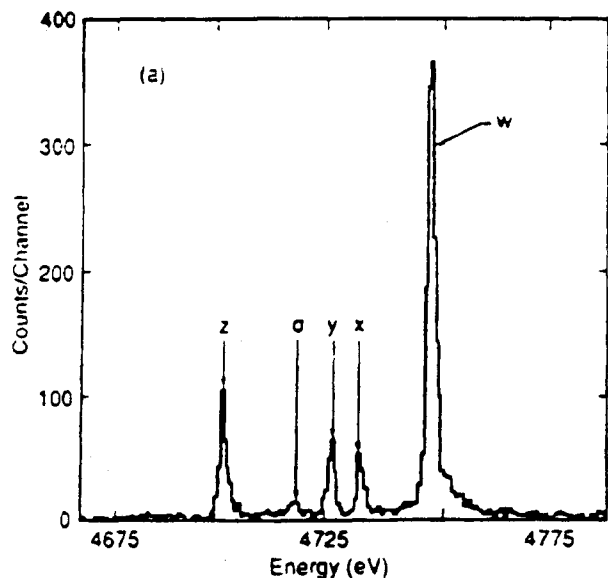


Fig. 6. Spectrum showing that EBIT is a bright enough source to allow high resolution X-ray spectra to be obtained in moderately short periods of time. This spectra was taken in 20 minutes with a von Hamos spectrometer with 0.06% energy resolution [18].

purity. Spectra are observed only from elements injected into the trap.

3.9. Doppler shifts are typically negligible in an EBIT

Although the ion temperature inside an EBIT can reach values that compare to the hottest plasmas produced on earth (1 keV $\approx 10\,000\,000$ K), the velocities are still only a small fraction of the speed of light ($v/c = 0.01\%$ for 1 keV barium) so Doppler broadening of typical X-ray transitions is smaller than both the natural linewidth and the typical instrument resolution. Furthermore, since the ions are trapped and excited in a symmetric potential at rest in the lab frame, there is no residual Doppler shift. At Livermore, ultra-high resolution X-ray spectrometers have been used to measure the Doppler broadening in select X-ray transitions (see Fig. 1 of Ref. [21]) while at NIST we have used a low-resolution optical interferometer to measure the Doppler broadening in visible light transitions (see Fig. 2 of Ref [22]). With evaporative cooling techniques, ion temperatures as low as 0.07 keV (50 times below the electron beam energy) have been obtained [21].

3.10. The EBIT is a sufficiently low density source that line profiles are unperturbed

Electron densities in an EBIT are about $4 \times 10^{12} \text{ cm}^{-3}$, comparable to that found in solar flares and Tokamak fusion devices (see Fig. 2, Ref. [23] for a comparison with other light sources). The number density of highly charged ions inside an EBIT is about 4 orders of magnitude lower than the electron density. This results in conditions in which self-absorption and collisional effects are negligible.

3.11. The EBIT is a steady, CW source

EBITs have been put into operation for extended experiments which continue 24 hours a day, 7 days a week. A single bunch of atoms can be injected and held in the trap for hours (see Fig. 7) [20] before the intensity of emitted light drops sufficiently to require reinjection of another bunch. Bunches can be injected at repetition rates of order 1 Hz if necessary.

3.12. The EBIT can be rapidly switched

Lifetime measurements are examples of experiments in which rapid switching times are desirable. Both electron beam energy and current in the EBIT can be switched, allowing the subsequent temporal decay of the intensity of the emitted light to be monitored in order to determine the

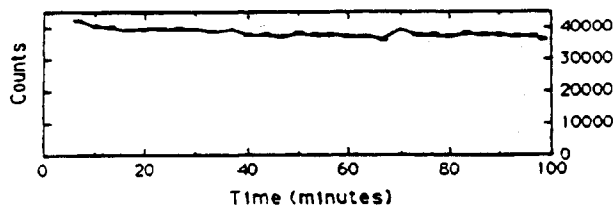


Fig. 7. Plot showing that ions can be trapped for hours inside EBIT. Here a single bunch of gold ions was injected into EBIT at $t = 0$, stripped to a high charge state ($Q = 37+$) in a fraction of a second, and then held in the trap for more than an hour as the intensity of the light emitted from the $n = 2-3$ transition lines was monitored. The $1/e$ decay time estimated from the data is approximately 4 hours.

lifetime of an excited state. In the case of current switching, the ions remain trapped by the 3 T magnetic field present inside the EBIT. At Livermore, electron beam energies have been switched with amplitudes of order 1 keV on time scales of order 10 ns to measure lifetimes between 6 μ s [24] and 90 μ s [25] with X-ray spectroscopy. At NIST, electron beam currents have been switched off to measure lifetimes of order 1 ms with visible light spectroscopy [26].

3.13. EBIT devices are relatively affordable and easy to build

Although construction of a new EBIT facility requires a significant investment in time and money, this effort is small compared to that of any other device that can approach its capabilities. A full-scale EBIT device can be fabricated for a few hundred thousand dollars, a figure which roughly matches the cost of the operating electronics and instrumentation. Development time can be avoided because EBITs are now available from commercial sources. Future developments can be expected to lower the cost greatly (designs are being developed, for example, for new EBITs which do not require any magnetic field [27]). For experimenters who wish to use existing EBIT devices in a collaborative way, facilities are available in several locations around the world (see Section 6 below).

4. Limitations

The previous discussion has emphasized how close to ideal conditions one can achieve with an EBIT. In typical practice, the situation may not be much different, but there are some limitations which should be kept in mind.

Lack of independence of all the variables can be one of the most troublesome limitations. Varying the electron beam energy, for example, not only adjusts the charge state, but also the range of levels accessible for excitation and (slightly) the trap depth. These limitations can be largely overcome by electronically automating the system to slew the electron beam rapidly between different energies, one energy to create the charge state, for example, and another to probe it. Such a system is available at all the major EBIT facilities. Duty cycle factors reduce the efficiency of data collection in this mode of operation.

Another compromise involves the amount of gas injected for evaporative cooling of the ion temperature – too much gas, and the vacuum level may be reduced enough that collisions will degrade the charge state purity. At the same time, evaporative cooling may be essential since it can improve the signal rate by orders of magnitude by allowing the ion density to be increased. Generally however, a good compromise can be reached in which the signal level is greatly enhanced while the charge state distribution is modified only slightly.

With present EBIT designs, the maximum obtainable electron beam currents diminish below 2 kV (see Fig. 4, Ref. [7]), limiting the production of low charge states in continuous trapped mode of operation. Useful data in CW trapping mode have been obtained for electron beam energies down to 0.67 keV [28]. Active [29] or passive transient methods can be used to circumvent the problem, but if one's primary goal is to study low charge states, other light sources should be considered as alternatives.

At the other end of the charge-state spectrum, it should be noted that work with the highest charge states (primarily the production of bare and hydrogenic charge states of heavy elements and the excitation of helium-like charge states in the heaviest elements) requires both a high energy (> 130 keV) electron beam and a vacuum level significantly beyond that of normal EBIT operation. While an EBIT can ionize a neutral atom up to a charge state of 50+ in a small fraction of a second, getting to 92+ can require several seconds, and signal rates can be weak. While an EBIT can produce and hold hundreds of thousands of ions with charge states of 50+, the number of bare uranium atoms produced and held so far is over four orders of magnitude lower. Experiments that approach the upper end of the EBIT's capability require an increasing amount of patience, but are feasible (the hydrogenic uranium data in Fig. 1 was acquired in just over one day using a high-efficiency Ge detector).

As mentioned in Section 4, charge state selectivity depends on the proximity (in energy) of the next ionization stage, and is not always near 100%. In an openshell system such as U^{67+} in which the ionization energy is 8 keV and the adjacent ionization stages are within 0.18 keV, one can expect the charge state distribution in the EBIT to have a full-width-half-maximum of 4, and a full-width-tenth-maximum of 7 (see Fig. 4b, Ref. [30]). This is only modestly better than that expected using the beam foil method to produce similar charge states in gold ions [31], although in the case of gold some of the nearby ionization stages are separated by much larger energies.

Another factor that must be considered with regard to charge state balance is that when the electron beam energy is scanned, the presence of localized dielectronic recombination (DR) resonances can abruptly modify the charge state distribution. Care must be taken to avoid such resonances when their presence could affect the results of a measurement, as is often the case. This task can be complicated by the fact that the electron beam energy can be unintentionally changed slightly when the current is adjusted, even if the drift tube voltages are held absolutely fixed (since the current affects the space charge correction to the electron beam energy [1]). The dependence of charge state distribution on proximity to DR resonances makes CW measurement of the DR profile as a function of electron beam energy a recursive problem. Virtually all of the problems mentioned in this paragraph, however, are overcome in the limit that the electron beam is scanned rapidly compared to the charge distribution relaxation time using "event-mode" techniques as described in the literature [15].

With regard to excitation selectivity, one must keep in mind that upper levels can be populated not only by direct excitation, but also by recombination (dielectronic or radiative) either directly to the upper level or to higher lying levels which may then allow cascade through the upper level of interest. Because of this, one cannot guarantee that a line will be extinguished simply by lowering the electron beam energy below the threshold for direct excitation. Either theoretical analysis or experimentation may be required to determine whether a particular line can be fully extinguished by varying the electron beam slightly.

Although the presence of a third dimension (electron beam energy) to aid in the analysis of spectra can be a great

tool, it also generates a large amount of phase space to probe. In cases where the desire is to collect as much data as possible in the shortest time available, the selectivity of an EBIT may not be fully desirable. Some experimenters may prefer a dense spectrum of lines over the selectivity and spectral purity provided by an EBIT. Electronically scanned modes of operation, however, can effectively collapse the third dimension and simulate any temperature distribution (as long as one neglects processes involving the simultaneous presence of two electrons of two different energies).

Conversely, the resolution obtained along the third dimension may not always be as high as desired. Dielectronic recombination resonances often have structure which cannot be fully resolved with the electron energy spread which is typical in an EBIT. This is one type of measurement in which accelerator based storage ring methods which employ electron coolers offer clear advantages over existing EBIT capability. Another limitation due to the EBIT's finite electron beam resolution is that very close lying dielectronic recombination satellites which arise from high-lying Rydberg levels cannot be switched off [32].

The times to acquire useful spectra mentioned in Section 3.6 above might all be multiplied by a factor of ten or more in order to correspond to a high statistics data set appropriate for a precision measurement. With sufficient instrument resolution, however, very high precision wavelength measurements can be obtained without many photons.

Although the slit-like source shape might be considered ideal for use with a ruled-grating spectrometer, some Bragg reflection X-ray spectrometers would be even better served by a point source with the same total flux.

The elemental purity provided by the ultra-high vacuum is compromised for at least one element due to the necessity to dope the electron gun cathode with barium in order to lower the work function. The cathode runs at high temperatures and is in a direct line of sight with the trap center. On time scales of many seconds, the trap accumulates significant amounts of barium which can show up in the spectrum. When this is a problem, the situation can be avoided almost entirely by periodically emptying the trap and rapidly refilling it with the desired element before the barium has time to reaccumulate; reduction of data accumulation rates due to the duty cycle for this procedure can be made negligible.

Although an EBIT can run uninterrupted for long periods, it does not always do so. More typically the operation is punctuated by occasional bursts of secondary current which inevitably end up appearing on the electron gun anode or auxiliary electrodes in that general proximity. These occurrences trip automatic shutdown protection in the power supplies, but recovery is typically immediate (seconds).

5. Future improvements

As a relatively recent development, the application of EBITs to their full capabilities is still in a rapid growth phase. A number of further improvements can be expected in the coming years, including the development of VUV spectroscopy with an EBIT, laser cooling and probing of ions in an EBIT [33, 34], Fourier-transform ion cyclotron resonance probes to precisely determine and control the number of

ions in the trap [35], faster switching times to measure processes on faster time scales, more efficient element injection, higher brightness, higher beam currents, and larger magnetic fields.

6. EBIT facilities worldwide

There are presently three major EBIT facilities which are active: Livermore [1], NIST [19], and Oxford [34]. The Livermore facility has been producing atomic physics data for 8 years and presently houses three EBITs of various sizes (an EBIT, a SuperEBIT, and a mini-EBIT). The Livermore team has published nearly 100 papers, the first 42 of which are reprinted in a compilation available from the National Technical Information Service [36]. The NIST EBIT facility began producing atomic physics data during the past year [6], and the Oxford facility is expected to produce data in the near future [37].

A SuperEBIT facility was nearing completion in Russia (Dubna) several years ago, but the effort is presently dormant [38]. A major EBIT facility is under construction in Japan (Tokyo) [39], and another is being planned in Germany (Berlin) [40]. Proposals have been made for at least one more facility in the U.S. (Connecticut) [41] and in Germany (Dresden) [42], France [43], and China.

References

1. Levine, M. A., Marrs, R. E., Henderson, J. R., Knapp, D. A. and Schneider, M. B., *Physica Scripta* **T22**, 157 (1988).
2. Marrs, R. E., Beiersdorfer, P. and Schneider, D., *Phys. Today* **47**, 27 (1994).
3. Lekrone, D. S. and Sugar, J. (Editors), *Physica Scripta* **T47**, (1993).
4. Knapp, D. A., Marrs, R. E., Elliott, S. R., Magee, E. W. and Zasadzinski, R., *Nucl. Instr. Meth.* **A334**, 305 (1993).
5. Marrs, R. E., Elliott, S. R. and Knapp, D. A., *Phys. Rev. Lett.* **72**, 4082 (1994).
6. Morgan, C. A. *et al.*, *Phys. Rev. Lett.* **74**, 1716 (1995).
7. Gillaspay, J. D., Proceedings of the Vth International Symposium on Electron Beam Ion Sources and Their Application, *Physica Scripta*, to be published.
8. Margolis, H. S., "Studies of Highly Ionized Atoms Using an Electron Beam Ion Trap", Ph.D. thesis, Oxford, 1994.
9. Serpa, F. G. *et al.*, to be published.
10. Srivastava, B. N. and Mirza, I. M. *Phys. Rev.* **176**, 137 (1968).
11. Chantrenne, S., Beiersdorfer, P., Cauble, R. and Schneider, M. B., *Phys. Rev. Lett.* **69**, 265 (1992).
12. Penetrante, B. M., Bardsley, J. N., DeWitt, D., Clark, M. and Schneider, D., *Phys. Rev.* **A43**, 4861 (1991).
13. Beiersdorfer, P. *et al.*, Proceedings of the ICPEAC XVII Conference, Brisbane, July 1991, p. 313.
14. DeWitt, D. R. *et al.*, *Phys. Rev. Lett.* **68**, 1694 (1992).
15. Knapp, D. A. *et al.*, *Phys. Rev.* **A47**, 2039 (1993).
16. Beiersdorfer, P., Phillips, T. W., Wong, K. L., Marrs, R. E. and Vogel, D. A., *Phys. Rev.* **A46**, 3812 (1992).
17. Beiersdorfer, P. and Wargelin, B. J., *Rev. Sci. Instrum.* **65**, 13 (1994).
18. Beiersdorfer, P. *et al.*, *Rev. Sci. Instrum.* **61**, 2338 (1990).
19. Gillaspay, J. D. *et al.*, Proceedings of Nobel Symposium 91, *Physica Scripta* **T59**, 392 (1995).
20. Schneider, M. B. *et al.*, International Symposium on Electron Beam Ion Sources and Their Application, (Edited by A. Hersheovitch), AIP Conference Proceedings No. 188, (AIP, New York 1989), p. 82.
21. Beiersdorfer, P., Decaux, V., Elliott, S. R., Widmann, K. and Wong, K., *Rev. Sci. Instrum.* **66**, 303 (1995).
22. Adler, H. *et al.*, *Nucl. Instr. Meth.* **B98**, 581 (1995).
23. Martinson, I., *Rep. Prog. Phys.* **52**, 157 (1989).
24. Crespo Lopez-Urrutia, J., Beiersdorfer, P., Widmann, K. and Decaux, V., Reported at 1995 DAMOP, Conference, and to be published.

25. Wargelin, B. J., Beiersdorfer, P. and Kahn, S. M., *Phys. Rev. Lett.* **71**, 2196 (1993).
26. Serpa, F. G. *et al.*, to be published.
27. Thomae, H., Becker, R., Bongers, H. and Kleinod, M., *Nucl. Instr. Meth.*, **B98**, 577 (1995).
28. Wargelin, B. J., A Study of Diagnostic X-ray Lines in Helium-like Neon Using an Electron Beam Ion Trap, Ph.D. thesis, University of California at Berkeley, 1993.
29. Decaux, V. and Beiersdorfer, P., *Physica Scripta* **T47**, 80 (1993).
30. Schneider, D. *et al.*, *Phys. Rev.* **A44**, 3119 (1991).
31. Chandler, G. A. *et al.*, *Phys. Rev.* **A39**, 656 (1989).
32. Beiersdorfer, P. *et al.*, *Z. Phys.* **D21**, S209 (1991).
33. Beiersdorfer, P., Proc. of the 15th International Conf. on X-ray and InnerShell Processes, AIP Conference Proceedings No. 215, (Edited by T. A. Carlson, M. O. Krause and S. T. Manson)(AIP, New York 1990), p. 648.
34. Silver, J. D. *et al.*, *Rev. Sci. Instrum.* **65**, 1072 (1994).
35. Beiersdorfer, P. *et al.*, *Nucl. Instr. Meth.* **B98**, 558 (1995).
36. "Selected Publications from the Electron Beam Ion Trap Program at Lawrence Livermore National Laboratory" (Edited by R. E. Marrs), UCRL-ID110491, available from National Technical Information Service, U.S. Department of Commerce, Springfield, VA 22161, as document DE92-018-232.
37. Silver, J., private communication, 1995.
38. Ovsyannikov, V. P., *et al.*, *Rev. Sci. Instrum.* **65**, 1132 (1994).
39. Ohtani, S., private communication, 1994.
40. Fussmann, G., private communication, 1994.
41. Smith, W. W., Pollack, E. and Kessel, Q. C., private communication, 1995.
42. Soff, G., private communication, 1995.
43. Briand, J. P., private communication, 1994.

X-ray, visible and electron spectroscopy with the NIST EBIT

E. Takács^{a,b}, L.P. Ratliff^a and J.D. Gillaspay^a

^a *Atomic Physics Division, National Institute of Standards and Technology, Gaithersburg, MD 20899, USA*

^b *Experimental Physics Department, Kossuth University, Bem tér 18/a, H-4026 Debrecen, Hungary*

An overview is given of recent activities at the NIST electron beam ion trap (EBIT) facility. The machine has been operational for almost three years. Important characteristics and demonstrated capabilities of our EBIT are presented. Selected results include experiments with trapped highly charged ions (X-ray and visible spectroscopy), and with extracted ions (ion-surface collision studies).

1. Introduction

Activity at the EBIT facility in Gaithersburg, MD at present can be divided into two broad categories. One category is associated with the spectroscopic investigation of the electromagnetic radiation emitted by highly charged ions created and trapped within the machine. In these measurements the ions are studied in situ at the place where they are created. The spectra exhibit the properties of the trap (hot plasma confined by magnetic and electric fields), the interaction between the electrons and the ions (excitation, ionization, and recombination processes), and the ions themselves (atomic structure). The second group of activities are associated with the extracted ions. In this case we use the EBIT as an ion source in which the highly charged species are created and then extracted for outside measurements. The extraction and beam transport is done by several electrostatic ion-optical elements and a magnet, which is used for separating the specific charge-state needed for the experiment. After a brief introduction to the machine, some selected results will be presented to give examples of the latest activities and to illustrate the capabilities of the EBIT laboratory at NIST.

2. The NIST EBIT facility

2.1. General

The electron beam ion trap at the Gaithersburg, MD site of the National Institute of Standards and Technology (NIST) was built jointly by NIST and the Naval Research Laboratory (NRL). There are earlier papers describing the properties of the machine [1,2], so only a brief introduction will be presented here.

The EBIT was built along the lines of the original design of the first Livermore machine [3] with a few modifications. The electron gun used can provide up to 160 mA of electron beam current. The beam compression at the drift tube region is accomplished by a pair of liquid helium cooled superconducting Helmholtz coils capable of producing magnetic fields up to 3 T. The voltage applied to the central drift tube determines the energy of the electron beam at the interaction region. The electrostatic trap potential in the axial direction can be up to 500 V deep. The highest demonstrated voltage applied to the central drift tube compared to the potential of the electron gun (ground potential) in our machine is 32 kV. Thus, the electron beam energy should be enough to strip off all but two electrons from atoms with atomic numbers up to about sixty and to create neon-like ions of all the naturally occurring elements.

Neutral gases are injected into the trap through one of the side ports facing the central drift tube. Ionized metal atoms – produced by a metal-vapor-vacuum-arc (MEVVA) ion source placed on the top of the EBIT – are injected along the axis of the machine parallel to the magnetic field lines. Electromagnetic radiation emitted from inside the EBIT is transmitted through beryllium and quartz window side ports for X-ray and visible spectroscopy, respectively. Examples from the palette of ions which has been created and studied in our machine include different ions of nitrogen, argon (up to 18+), krypton (up to 34+), xenon (up to 48+), barium (up to 46+), iron, gadolinium, and neodymium.

2.2. The extraction system

Although highly charged ions created and trapped inside the EBIT offer a great number of research opportunities (e.g., [4–14]), there are other experiments which require the ions to be extracted from the trap. These experiments include the study of ion-surface interactions by measuring surface damage, electron emission, and X-ray emission. Ion-gas interactions such as charge exchange and recoil-ion experiments may be studied as well. Recapturing ions into secondary ion traps is necessary for another important class of atomic physics experiments which can not be done in the presence of the electron beam (lifetime measurements of long-living excited-states, cold ion dynamics studies, and precision mass measurements, for example). For many of these types of experiments, data for highly charged ions are very sparse or non-existent. Finally, extracted ions may also be used to reveal important information about

the conditions inside the EBIT and, therefore, provide complementary information for spectroscopic studies being performed on ions trapped inside the machine.

A detailed description of the extraction and transport system can be found in [15]. An updated schematic of the beam line for the NIST EBIT is shown in fig. 1. Ions can be extracted from the trap into the beam line continuously or in pulses, typically 10 μ s to 100 ms long. The first ion-optical element in the beam line is a 90° electrostatic bender. There are other electrostatic elements to steer and align the beam (deflectors, einzel lenses) before it enters the charge-to-mass analyzing magnet. There is a four-jaw slit in the focal point in front of the magnet and a two-jaw slit in the focal point behind the magnet serving as entrance and exit slits of the analyzer. The entire system is fabricated from ultra-high-vacuum compatible materials and can be baked to at least 100°C. Vacuum pumps maintain a pressure in the beam line of about 10⁻⁶ Pa (10⁻⁸ Torr) or better to prevent significant losses from the ion beam due to charge-exchange collisions with residual gas in the beam line.

Ion beams of several highly charged ion species have been transported through the beam line and into the experimental chamber after the analyzing magnet. Measurements of the ion-beam current have been performed using two Faraday cups – located after the first electrostatic deflector and after the entrance slit of the analyzing magnet – which show that no ions are lost in this section of the beam line. Figure 2 shows an example of a charge-to-mass scan for 7.8 keV per charge Xe ions with the EBIT operated in a continuous-extraction mode.

Presently [16], the NIST EBIT beam line can deliver a continuous stream of 3,000,000 charge-to-mass selected highly-charged ions (Xe⁴⁴⁺) per second into a spot 3 mm in diameter. This number corresponds to a 21 pA beam current and exceeds any previously reported values of continuous-ion-beam currents extracted from an EBIT by several orders of magnitude. Since this beam current is 10 times higher than the value our group recently reported [15], we expect even further improvements. The system has also been operated in pulsed-beam mode. Operating at 2 Hz repetition rate, a change of the pulse width from 2.8 ms to 0.012 ms changes the time average current from 9.6 pA to 1.8 pA, respectively. This mode of running – important for retrap experiments – boosts the instantaneous beam current by several orders of magnitude.

3. X-ray spectroscopy

There are three X-ray instruments installed on the beryllium window side ports of the EBIT for wavelength and energy dispersive X-ray spectroscopy. Two of them are identical Johann-type bent crystal spectrometers for precision X-ray wavelengths and polarization studies. A description of the spectrometers and detectors can be found in refs. [17,18]. As a generic diagnostic tool and for measurements which require higher detection efficiencies but where the energy resolution is not so critical we use a Si(Li) detector.

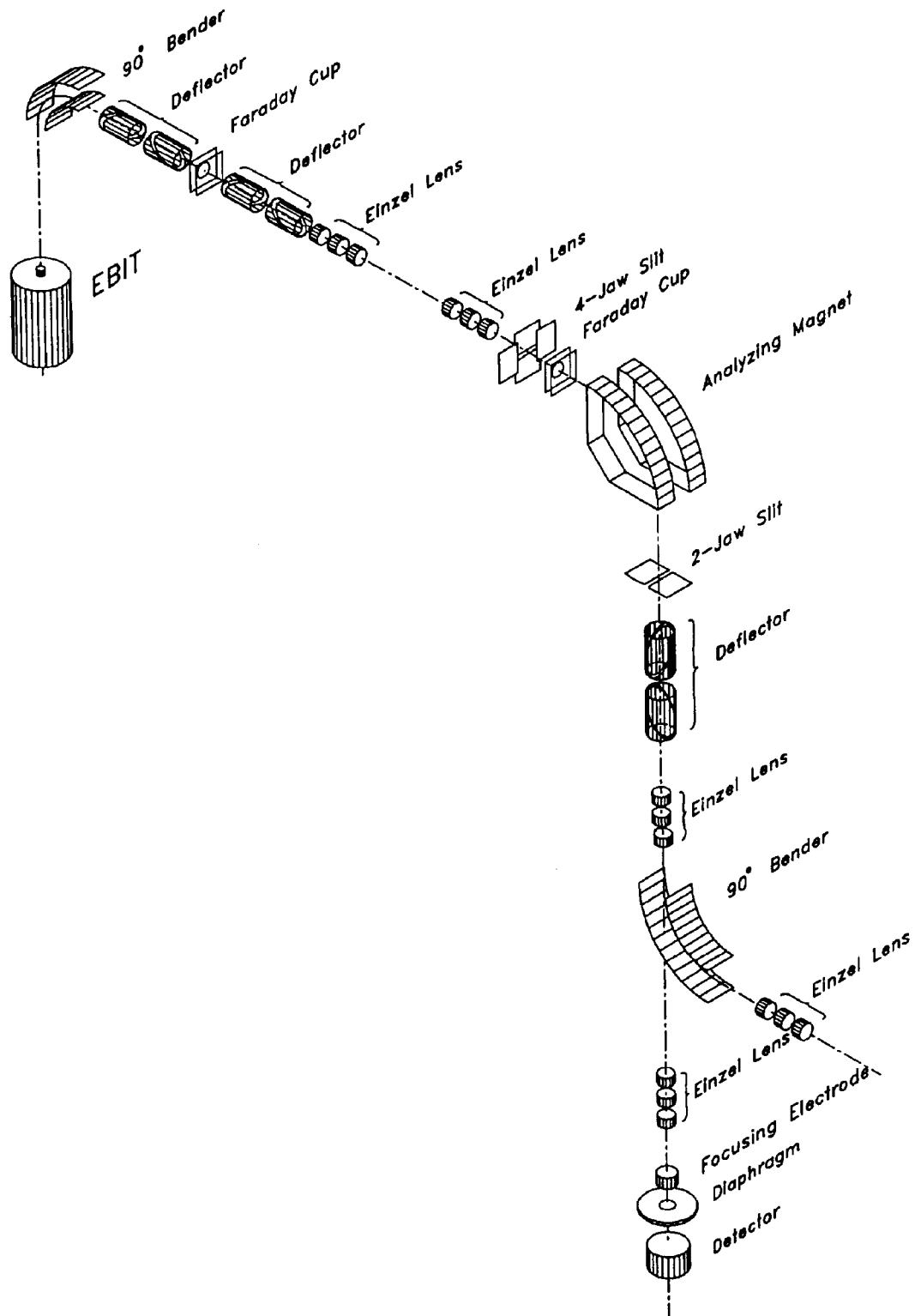


Fig. 1. The extraction and ion-transport system of the NIST EBIT facility. It consists of several electrostatic steering and focusing elements and a charge-to-mass analyzer magnet. At present the system can provide efficient transfer of highly charged ions into experimental chambers on two separate beamlines.

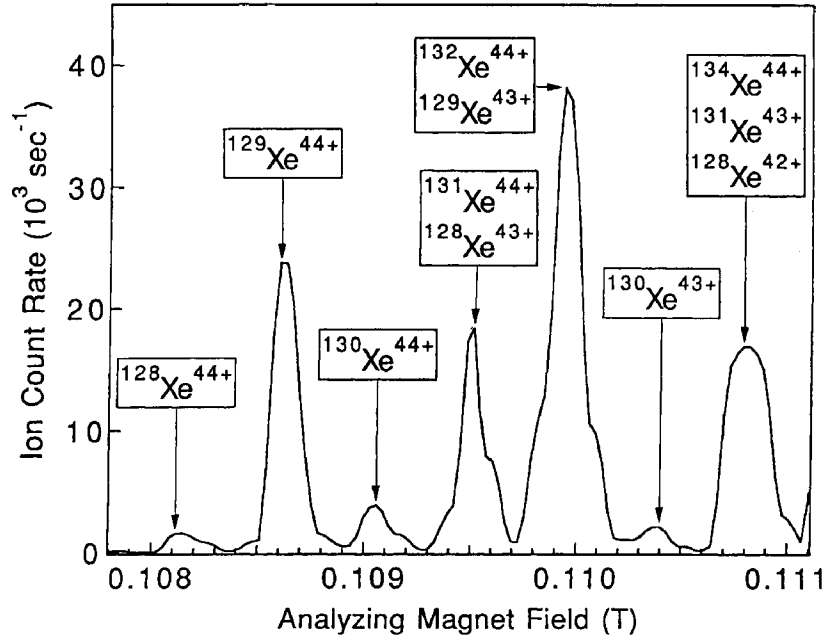
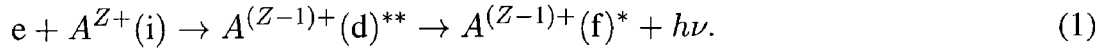


Fig. 2. Charge-to-mass analysis scan for 7.8 keV xenon ions. The isotopes in different charge states are depicted.

3.1. Inner shell dielectronic recombination in Sc-like barium

Dielectronic recombination (DR) is a resonant phenomenon and one of the fundamental processes in electron-ion collision physics. Due to the usually high relative cross sections corresponding to the DR process it plays an important role in determining the charge-state balance of ions in plasmas. The DR proceeds as



The first step involves a simultaneous continuum-to-bound and bound-to-bound electron transition. The bound-to-bound transition gives the resonant character of the process. The resulting doubly excited autoionizing state can relax by photon emission and the characteristic radiation is the signature of the process. According to eq. (1) DR can be detected by either measuring the X-ray photons ($h\nu$) [19] or measuring the recombined ions $A^{(Z-1)+}$ [20].

We would like to point out that measurement of the polarization or the angular distribution of the emitted X-rays provides information on the magnetic sublevels involved in the process. This information remains hidden in experiments where the detection is based on the number of recombined ions.

We started to explore the capabilities of our EBIT for measuring DR resonance processes by investigating the phenomenon in highly charged many-electron barium ions [19]. We used our Si(Li) detector to capture X-rays from resonant DR processes involving $2p \rightarrow 3d$ excitations of Sc-like barium (Ba^{35+}) and Ti-like barium (Ba^{34+}). The X-ray spectra shown in fig. 3 include several small peaks and a large peak which is

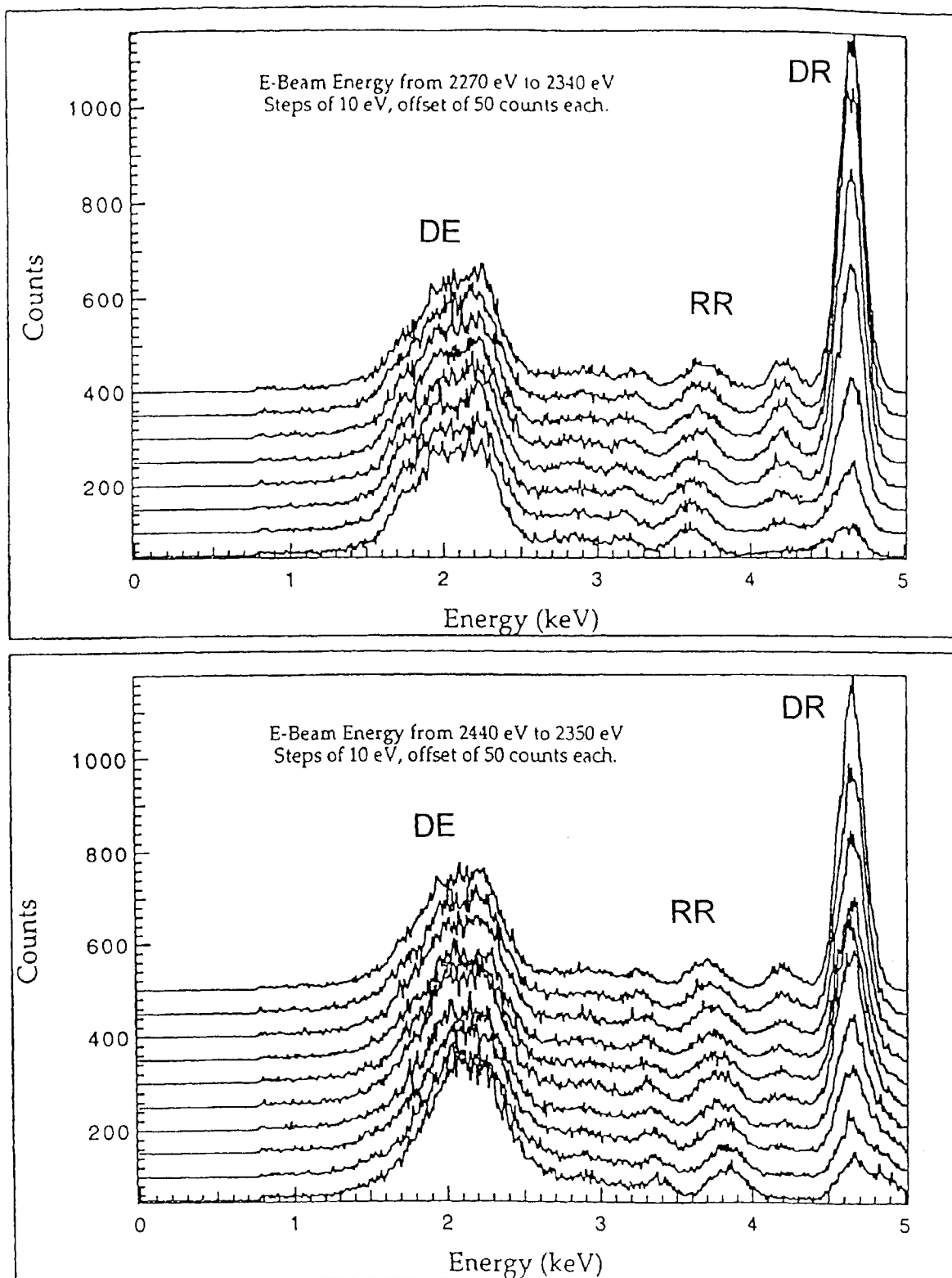


Fig. 3. The X-ray emission in Sc-like and Ti-like barium at around 4.6 keV becomes strong at a certain electron impact energy, a distinct signature of the dielectronic recombination process [19]. (DE: direct excitation, RR: radiative recombination, DR: dielectronic recombination.)

strong only at certain electron beam energies. The strong X-ray emission line observed at 4.6 keV appears when the electron beam energy is tuned close to 2.3 keV. At this beam energy the Ti-like and the Sc-like ions of barium are the main ions present in the EBIT. Calculations show that the smaller peaks (labeled RR) are from different radiative recombination (RR) processes and the large peak is due to the resonant inner shell excitation of a 2p electron to one of the 3d levels. The simultaneous measurement of the well-separated RR and DR lines allows the deduction of relative cross sections.

The calculations for the cross sections, done at the University of Connecticut, were based on the angular momentum average (AMA) approximation which is supposed to be justified when 3d levels are involved and also when the electron-beam energy spread is as large as a few tens of electron volts, as in our case. Including model calculations to account for our trap conditions (charge-state distribution balance, electron-ion overlap factor) we got good agreement between the measured and calculated cross sections. Details of the experimental and theoretical results can be found in [19].

In our EBIT the spread of the electron-beam energy was about 40–50 eV and the precision of the energy was 1–2 eV. Although this broad energy distribution seems to be several orders of magnitude larger than those reported at electron cooler facilities, we would like to note, however, that the center-of-mass impact energies are much larger in EBITs, too. This allows the observation of X-rays from inner-shell DR excitation processes, which are rarely observed at storage rings where the measurements usually extend up to only a few tens of eV center-of-mass energies. Using the scaling law for the energy spread given by [21] it can be shown that at such high energies the energy spread is “only” about ten times less in storage rings compared to EBITs.

3.2. Polarization of Ne-like barium X-rays

Polarized X-ray emission occurs when the electron charge cloud (wavefunction) of the ion – corresponding to the initial state of the transition – shows spatial anisotropy. This spatial anisotropy is quite common in astrophysical plasmas. In solar flares, ions and atoms can be excited by electrons moving along fixed magnetic field lines, which give rise to a preferred direction in space. Other examples include supernova shock waves, polar aurorae, and jets in active galactic nuclei. In a laboratory environment polarized X-ray emission can be observed in crossed beam and beam foil studies. In an EBIT the excitation of the ions also occurs in a spatially asymmetric way by the well collimated and directed electron beam. Since the spatial orientation of the electron cloud of the ion is sensitive to the excitation process, the polarization measurements are suggested as a method to pinpoint the presence or the importance of certain excitation channels.

For the polarization measurements our two Johann-type crystal spectrometers were operated simultaneously, with their respective reflection planes perpendicular to each other. The direction of observation was at 90° relative to the electron beam direction. For a Ge(220) ($2d = 0.400$ nm) crystal the Bragg angle is close to 45° for X-ray wavelengths around 0.28 nm. For these wavelengths the crystal is a near-perfect

polarizer. In the setup described above, the spectrometers simultaneously measure the parallel and perpendicular polarization components of the radiation. The intensity cross calibration of the two spectrometers can be done by comparing the measured intensities of a suitable unpolarized line.

In our case, we studied the electron beam energy dependence of the polarization of the $[(2p_{3/2})^{-1} 3s_{1/2}]_{J=2}$ to $[2p^6]_{J=0}$ magnetic-quadrupole (M2) X-ray emission in Ne-like barium. The energy of this line is around 4563 eV corresponding to a wavelength of 0.272 nm. Although the transition has a relatively small Einstein A -coefficient (about $3.0 \times 10^8 \text{ s}^{-1}$) the relative intensity of the line is comparable to that of the high Einstein A -coefficient lines. This is because of the strong cascade feeding of the upper level of the transition (driven by electron impact excitation to higher levels) and the fact that the number of decays per unit channel are bottlenecked by the electron impact excitation rates rather than the decay rates. For the intensity cross calibration we used the nearby $[(2p_{3/2})^{-1} 3s_{1/2}]_{J=1}$ to $[2p^6]_{J=0}$ electric-dipole (E1) line. Our model calculations show that this line is unpolarized to a very good approximation.

Figure 4 shows our results. In the electron impact energy range from 5.0 keV to 7.8 keV, the M2 line shows a strong negative polarization. We attributed the big change of polarization near 5.0 keV, as well as near 5.1–5.3 keV, to the presence of resonant excitation processes. These are not included in our calculations which show a general agreement with the trend of the data at the non-resonant electron beam energies. Details of the experiment can be found in [22].

4. Visible light spectroscopy

The well developed visible light spectroscopic techniques that serve as excellent tools for observations of electronic transitions in neutral atoms usually cannot be applied to the study of highly charged ions. The reason is that the energy differences between the same levels on an isoelectronic sequence increase rapidly with the nuclear charge Z (e.g., for E1 transitions the energy scales with Z^2). Although visible transitions in highly charged ions are thus hard to find, there is a strong need to locate them for practical applications, in particular for high-temperature plasma diagnostics. Such plasmas are present for example in the solar corona and in tokamaks. Local ion temperatures, bulk plasma velocities, direction and strength of local magnetic fields can all be inferred from Doppler and Zeeman broadening and shifts of spectral lines originating from these environments.

4.1. Observation of visible transitions in highly charged ions with a grating monochromator

We experimentally found visible transitions in highly charged barium and xenon which were theoretically predicted by Feldman et al. [23]. They predicted that there should be an unusual magnetic dipole transition between levels of the ground-term

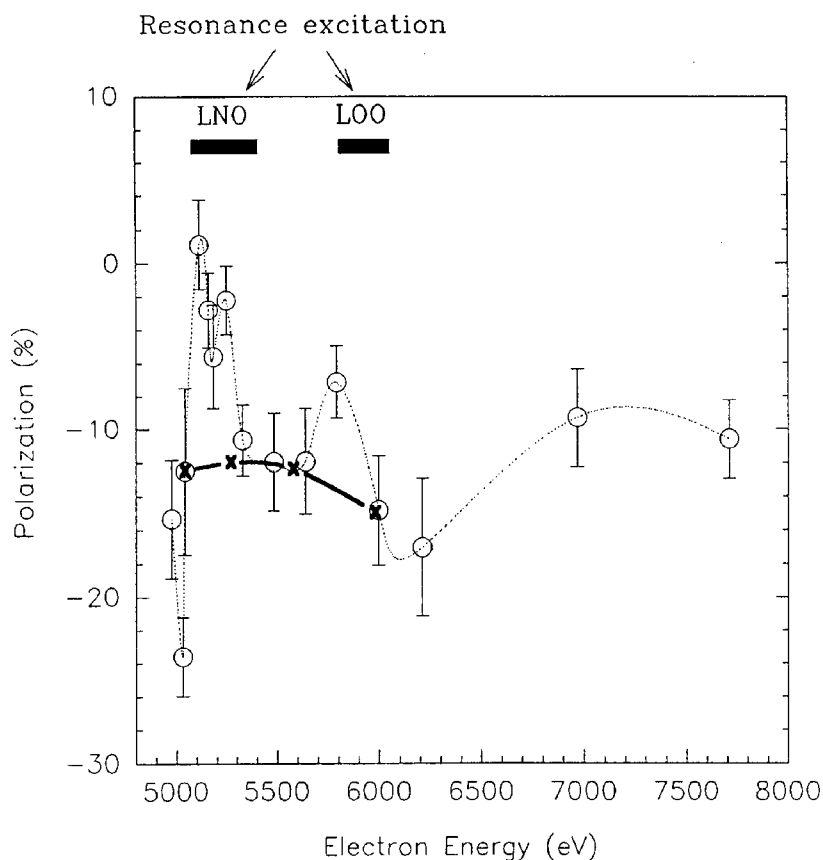


Fig. 4. The overall electron energy dependence of the polarization of the $[(2p_{3/2})^{-1} 3s_{1/2}]_{J=2} \rightarrow [2p^6]_{J=0}$ magnetic-quadrupole line in Ne-like barium. The solid line represents the calculations of Inal and Dubau which do not include resonant excitation processes [22]. In the energy ranges where the LNO and LOO resonant excitations take place, a big change in the polarization can be seen.

configuration of Ba^{34+} and Xe^{32+} . One of its unique properties is that this transition remains in the visible or near-UV region for a range of ions covering the entire upper half ($Z > 45$) of the periodic table. This fact makes the transition an unmatched candidate for hot plasma diagnosis and offers a great challenge for theorists who want to predict the transition energy using *ab initio* calculations.

Experimentally, we used a 0.25-m focal length, $f/3.5$ Ebert scanning monochromator with a blue-sensitive photomultiplier operated in photon-counting mode. The lines appeared at 393.24 nm and 413.93 nm wavelengths in Ba^{34+} and Xe^{32+} , respectively. The wavelength calibration was done by shining light from low-pressure discharge lamps (He, Hg, Ne, Ar, and Xe) through the EBIT from a port opposite to the spectrometer and by *in situ* measurements of nearly neutral krypton and argon lines. This calibration resulted in an overall 0.2 nm uncertainty for the wavelengths [24]. As a continuation of the first observation, our group went on to study the isoelectronic dependence of the transition energy [25].

4.2. Fabry–Perot spectroscopy

We used a Fabry–Perot instrument for a preliminary measurement of the previously observed $3d^4 \ ^5D_2$ – 5D_3 line in Ba^{34+} with improved resolution [26]. In our original study using the grating monochromator the 0.8 nm width of the line was dominated by the low resolving power of the instrument. However, if one wants to use this line for diagnosis of hot plasmas the instrument resolution has to be increased to allow observation of the Doppler and Zeeman effects.

In the experimental setup, light from the EBIT was transmitted through a quartz window side port and then collimated onto a plane Fabry–Perot interferometer. The instrument was followed by a 24.5 cm focal length fringe-imaging lens and a 4 mm central diameter aperture placed at the focal point. Behind the aperture the detection was done by the same photomultiplier used with the grating monochromator before. The wavelength scanning was done by precisely changing the mirror spacing using a piezoelectric element.

By fitting the data, shown in fig. 5, to Doppler broadened model line profiles, we deduced the temperature of the ions within our trap. We found that it is somewhat less but close to 1 keV. This conclusion is in agreement with the measurement of Beiersdorfer et al. [27] who used a high resolving power X-ray spectrometer to measure ion temperatures. It also agrees with our model calculations based on the numerical simulation of the charge state evolution within the EBIT using a code developed by Penetrante et al. [28]. We hope that with further studies using a higher resolution interferometer and different operating conditions of the EBIT, even lower temperatures can be achieved and measured down to the point where the Zeeman components of the line profile become visible. At that point the effects of local magnetic fields can be studied.

5. Electron spectroscopy with extracted ions

The extraction system described in section 2.2 efficiently transfers the ions created in the EBIT into experimental chambers. In the following, we report our preliminary study of the interaction of slow highly charged ions with solid surfaces by means of low energy electron spectroscopy.

There is a need to study ion-surface collision processes both for potential technological applications and from the perspective of fundamental research regarding the behavior of matter under the influence of extremely high and localized Coulomb fields. The availability of novel ion sources (EBIS, EBIT, ECR) has boosted the activity in this field of research in recent years and an enormous amount of progress was made in understanding the details of the processes governing the ion-surface interaction. There were especially important measurements done with (very) highly charged ions from an EBIT [29–31]. New exotic phenomena were reported, such as the formation of “hollow atoms” or the so-called “Coulomb explosion” on insulator surfaces.

FABRY-PEROT SCAN (F=15)

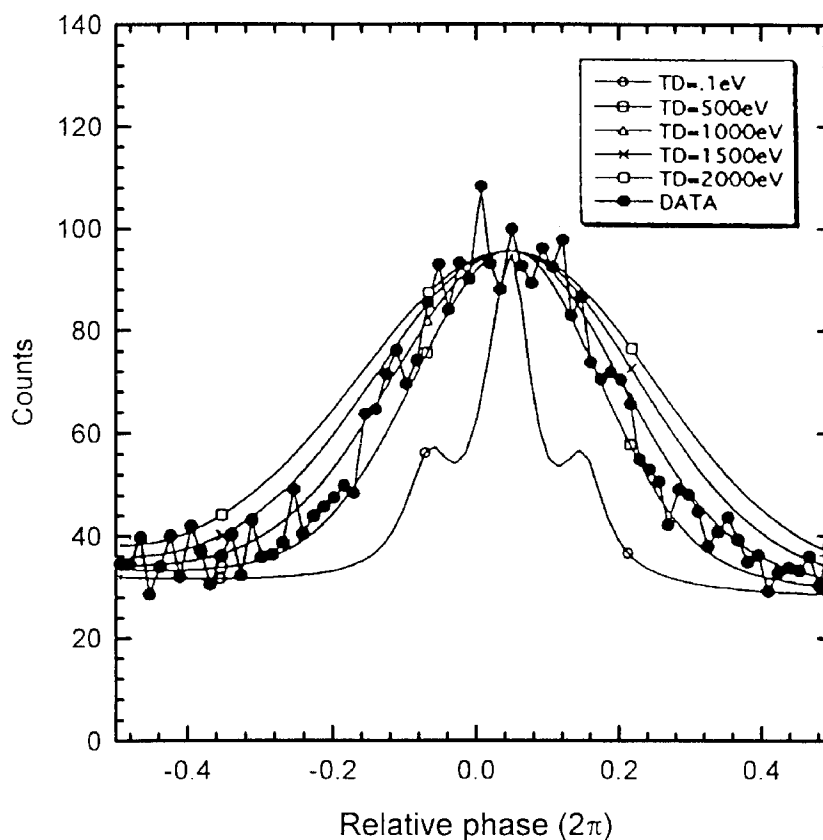


Fig. 5. Doppler broadened profile of the $3d^4 \ ^5D_2\text{--}^5D_3$ line in Ba^{34+} measured with a Fabry-Perot instrument. The calculated curves are the results of our simulations assuming different ion temperatures. The temperature of the ions in our trap is less than 1 keV [25]. (Note that a mislabeling of the horizontal axis in the original publication has been corrected; the results are unchanged.)

There are still several open questions, however, which need further and more detailed exploration. Recent reviews of the field can be found in [32–34].

When low-energy multiply charged ions are neutralized at solid surfaces, tens to several hundred-thousands of electron volts of atomic potential energy are dissipated, primarily via ejection of electrons. Using well-characterized surfaces, the quantitative analysis of these electrons can give detailed information about the atomic properties of both the projectile and the target, and about the collision mechanisms.

With the setup shown in fig. 6, a preliminary study of low energy electrons originating from the collisions of highly charged ions with surfaces was performed. The electron spectrometer was designed and developed at the Institute of Nuclear Research of the Hungarian Academy of Sciences, Debrecen, Hungary. During the measurements it was placed into a magnetically shielded container to reduce the effect of external magnetic fields which would distract the path of low energy electrons within the analyzer.

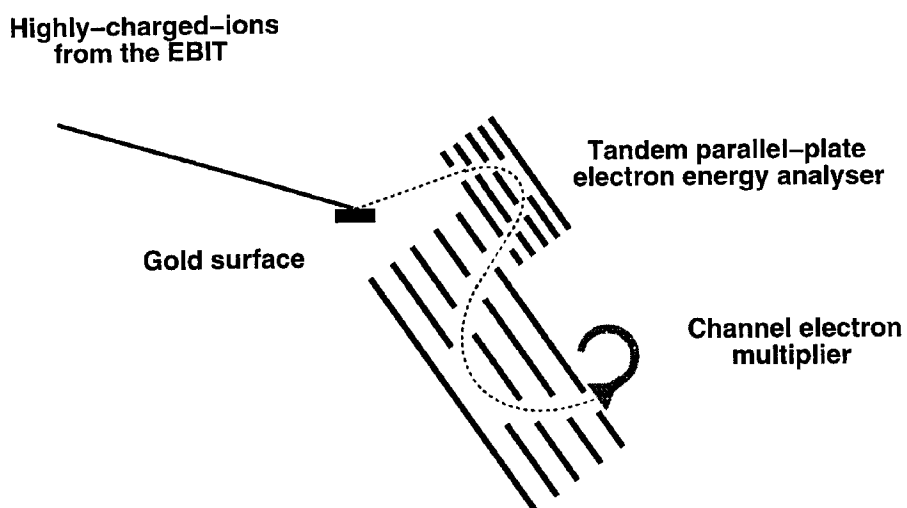


Fig. 6. Schematic of a parallel-plate electron analyzer equipped with a channel-electron-multiplier detector to study the interaction of highly charged ions with a polycrystalline gold surface.

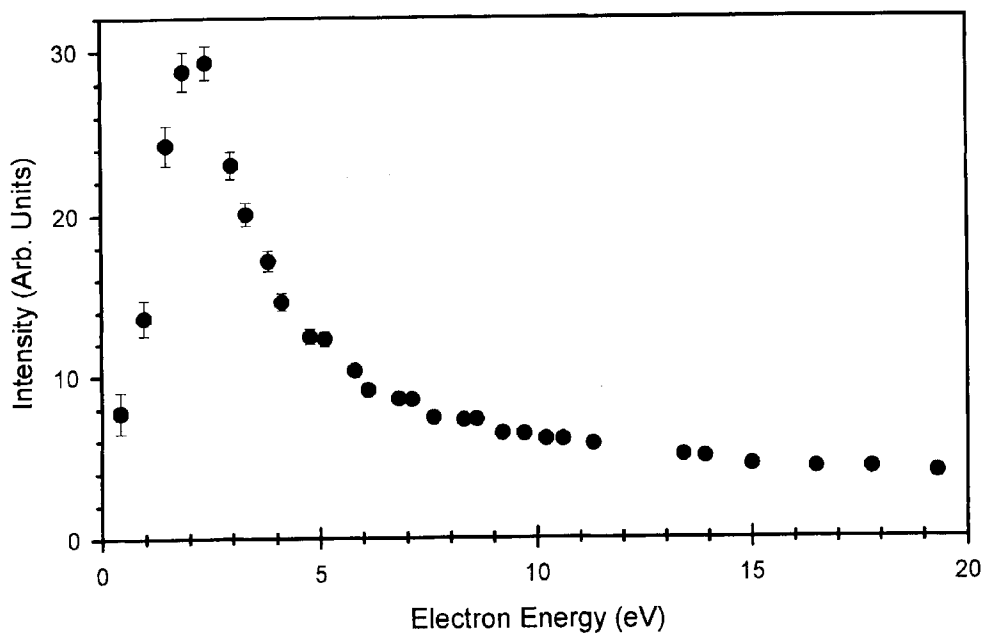


Fig. 7. Energy spectrum of low energy electrons taken with the setup in fig. 6. The low energy peak is consistent with the expected convoy electrons from Xe^{44+} colliding with a gold surface.

Electrons emerging in the grazing incidence collisions of Xe^{44+} ions with polycrystalline gold surfaces were energetically analyzed and detected. The preliminary spectra shown in fig. 7 suggest the presence of convoy electrons originating in the interaction. These electrons move with the speed of the specularly reflected projectile, because they occupy low-lying continuum energy states of the outgoing ion. In further experiments collective surface effects (image charge, surface plasmon effects) which distort and shift the convoy electron peak will be studied.

6. Summary

A general overview was presented to give some idea of the activities at the NIST EBIT facility which has been fully operational for about three years. Experiments centered around the in situ observation of ions have used different X-ray, UV and visible light detection techniques. The newly operational extraction system delivers energy- and mass-analyzed highly charged ions with currents unmatched by other instruments with similar overall capabilities.

Acknowledgements

Part of the work was done with the support of the Hungarian Science Foundation (OTKA, contract numbers: W 015012, F 013897, F 019344). One of the authors (E.T.) acknowledges the Foundation for the Hungarian Higher Education and Research for the support and the award of the Zoltán Magyar Fellowship for the years of 1995–1996. The results presented in this paper are the achievements of a large number of people from NIST, NRL and other collaborating groups whom we thank for their overall contributions. We thank A.I. Pikin for producing the updated schematic of the beamline and D.J. Alderson for assistance in constructing the magnetic shield for the electron spectroscopy measurements.

References

- [1] J.D. Gillaspay, J.R. Roberts, C.M. Brown and U. Feldman, in: *Proc. 6th Int. Conf. on the Physics of Highly Charged Ions-1992*, eds P. Richard, M. Stockli, C.L. Cocke and C.D. Lin, AIP Conf. Proc. No. 174 (AIP, New York, 1993) p. 682.
- [2] J.D. Gillaspay, in: *Proc. 5th Int. Colloquium on Atomic Spectra and Oscillator Strengths for Astrophysical and Laboratory Plasmas*, Physica Scripta (1996), in press; and in: *Proc. 6th Int. Symp. on Electron Beam Ion Sources*, Physica Scripta (1995), in press.
- [3] M.A. Levine, R.E. Marrs, J.R. Henderson, D.A. Knapp and M.B. Schneider, Phys. Scr. T22 (1988) 157.
- [4] R. Becker, E.D. Donets, M. Kleinod, H.S. Margolis and J.D. Silver, Rev. Sci. Instr. 67 (1996) 983.
- [5] H.S. Margolis, P.D. Groves, J.D. Silver and M.A. Levine, Hyp. Int. 99 (1996) 169.
- [6] H.S. Margolis, A.J. Varney, R.A. Jarjis and J.D. Silver, Nucl. Instrum. Methods B 98 (1995) 562.
- [7] J.D. Silver, A.J. Varney, H.S. Margolis, P.E.G. Baird, I.P. Grant, P.D. Groves, W.A. Hallett, A.T. Handford, P.J. Hirst, A.R. Holmes, D.J.H. Howie, R.A. Hunt, K.A. Nobbs, M. Roberts, W. Studholme, J.S. Wark, M.T. Williams, M.A. Levine, D.D. Dietrich, W.G. Graham, I.D. Williams, R. O'Neil and S.J. Rose, Rev. Sci. Instr. 65 (1994) 1072.
- [8] D. Vogel, P. Beiersdorfer, R. Marrs, K. Wong and R. Zasadzinski, Z. Phys. D (Suppl.) 21 (1991) S193
- [9] K.L. Wong, P. Beiersdorfer, D. Vogel, R. Marrs and M. Levine, Z. Phys. D (Suppl.) 21 (1991) S197.
- [10] R.E. Marrs, M.A. Levine, D.A. Knapp and J.R. Henderson, Phys. Rev. Lett. 60 (1988) 1715.
- [11] C.M. Brown, U. Feldman, G.A. Doschek, J.F. Seely, R.E. LaVilla, V.L. Jacobs, J.R. Henderson, D.A. Knapp, R.E. Marrs, P. Beiersdorfer and M.A. Levine, Phys. Rev. A 40 (1989) 4089.

- [12] D.A. Knapp, R.E. Marrs, M.A. Levine, C.L. Bennett, M.H. Chen, J.R. Henderson, M.B. Schneider and J.H. Scofield, *Phys. Rev. Lett.* 62 (1989) 2104.
- [13] D.A. Knapp, *Z. Phys. D (Suppl.)* 21 (1991) S143.
- [14] P. Beiersdorfer, D. Knapp, R.E. Marrs, S.R. Elliott and M.H. Chen, *Phys. Rev. Lett.* 71 (1993) 3939.
- [15] A.I. Pikin, C.A. Morgan, E.W. Bell, L.P. Ratliff, D.A. Church and J.D. Gillaspy, *Rev. Sci. Instrum.* 67 (1996) 2528.
- [16] L.P. Ratliff et al., to be published.
- [17] B.P. Duval, J. Barth, R.D. Deslattes, A. Henins and G.G. Luther, *Nucl. Instrum. Methods* 222 (1984) 274.
- [18] A. Henins, *Rev. Sci. Instrum.* 58 (1987) 1173.
- [19] D.J. McLaughlin, Y. Hahn, E. Takács, E.S. Meyer and J.D. Gillaspy, *Phys. Rev. A* 54 (1996) 2040.
- [20] W. Spies, O. Uwira, A. Mueller, J. Linkeman, L. Empacher, A. Frank, C. Kozucharov, P.H. Mokler, F. Bosch, O. Klepper, B. Franzke and M. Steck, in: *Physics of Highly Charged Ions*, eds F. Aumayr, G. Betz and H.P. Winter, Special Issue of *Nucl. Instrum. Methods B* 98 (1995) 158.
- [21] W. Zong, D.R. DeWitt, R. Schuch, H. Gao, S. Asp and E. Justiniano, *Hyp. Int.* 99 (1996) 325.
- [22] E. Takács, E.S. Meyer, J.D. Gillaspy, J.R. Roberts, C.T. Chantler, L.T. Hudson, R.D. Deslattes, C.M. Brown, J.M. Laming, U. Feldman, J. Dubau and M.K. Inal, *Phys. Rev. A* 54 (1996) 1342.
- [23] U. Feldman, P. Indelicato and J. Sugar, *J. Opt. Soc. Am. B* 8 (1991) 3.
- [24] C.A. Morgan, F.G. Serpa, E. Takács, E.S. Meyer, J.D. Gillaspy, J. Sugar and J.R. Roberts, *Phys. Rev. Lett.* 74 (1995) 1716.
- [25] F.G. Serpa, E.S. Meyer, C.A. Morgan, J.D. Gillaspy, J. Sugar and J.R. Roberts, *Phys. Rev. A* 53 (1996) 2220.
- [26] H. Adler, E.S. Meyer, F.G. Serpa, E. Takács, J.D. Gillaspy, C.M. Brown and U. Feldman, *Nucl. Instrum. Methods B* 98 (1995) 581.
- [27] P. Beiersdorfer, V. Decaux, S. Elliott, K. Widmann and K. Wong, *Nucl. Instrum. Methods B* 98 (1995) 566.
- [28] B.M. Penetrante, J.N. Bardsley, M.A. Levine, D.A. Knapp and R.E. Marrs, *Phys. Rev. A* 43 (1991) 4873.
- [29] F. Aumayr, H. Kurz, D. Schneider, M.E. Briere, J.W. McDonald and C.E. Cunningham, *Phys. Rev. Lett.* 71 (1993) 1943.
- [30] H. Kurz, F. Aumayr, D. Schneider, M.A. Briere and J.W. McDonald, *Phys. Rev. A* 49 (1994) 4693.
- [31] D.H.G. Schneider and M.A. Briere, *Phys. Scr.* 53 (1996) 228.
- [32] F. Aumayr and H.P. Winter, *Comm. At. Mol. Phys.* 29 (1994) 275.
- [33] P. Varga, *Comm. At. Mol. Phys.* 23 (1989) 111.
- [34] J. Burgdorfer, C. Reinhold, L. Hagg and F. Meyer, *Aust. J. Phys.* 49 (1996) 527.

FORBIDDEN LINE WAVELENGTHS AND TRANSITION PROBABILITIES MEASURED USING AN ELECTRON BEAM ION TRAP (EBIT)

E. Träbert

Experimentalphysik III, Ruhr-Universität Bochum, D-44780 Bochum, Germany

P. Beiersdorfer, S.B. Utter

Department of Physics and Space Technology,
Lawrence Livermore National Laboratory, Livermore, California 94501, U.S.A.

J.D. Gillaspy, F.G. Serpa

Physics Division, National Institute of Standards and Technology, Gaithersburg, Maryland 20899, U.S.A.

1. Introduction

Several coronal lines posed a long-standing riddle to earth-bound spectroscopists, until - following up on a suggestion by Grotrian (1937) - B. Edlén (1942) confirmed that their wavenumbers indeed corresponded to fine structure intervals in the ground configurations of highly charged ions like Fe X and Fe XI. This in turn caused turmoil in solar physics, because the corona must be much hotter than the underlying chromosphere in order to produce such ions.

X-ray and EUV spectra of the sun became available after World War II, by observations from sounding rockets and satellites. These spectra confirmed the presence of the highly charged ions. Laboratory observation of the (electric-dipole) forbidden lines, however, had to wait for the development of low-density plasma discharges such as the Tokamak fusion experiments, because in regular light sources, collisions would probably quench such long-lived levels. Since then, a fair number of forbidden transitions have been observed in the laboratory, and forbidden lines are being valued for plasma diagnostics.

While forbidden transitions in light ions are often found in astrophysical light sources, similar transitions in highly charged heavy ions such as Kr will be important for plasma machines like ITER, in which Kr will probably be used for radiative cooling and will therefore also be available for detailed diagnostics.

2. EBIT

Electron beam ion traps (EBIT) now offer novel ways to study such forbidden transitions:

- a) EBIT can produce any charge state ion of any element, with much simpler access and more elemental flexibility than at a large-scale fusion-oriented Tokamak or similar plasma experiment.
- b) EBIT can be switched from EBIT mode (with the electron beam on) to magnetic trapping mode (electron beam off, then working like a Penning ion trap) in less than 1 ms, permitting time-resolved studies and atomic lifetime measurements.

In explorative studies of visible spectra from the NIST and LLNL electron beam ion traps, a variety of ion species have been excited and stored. The spectra (see the Ar spectrum in figure 1, or Träbert *et al.* 1998 for spectra of Kr) are dominated by a number of forbidden lines.

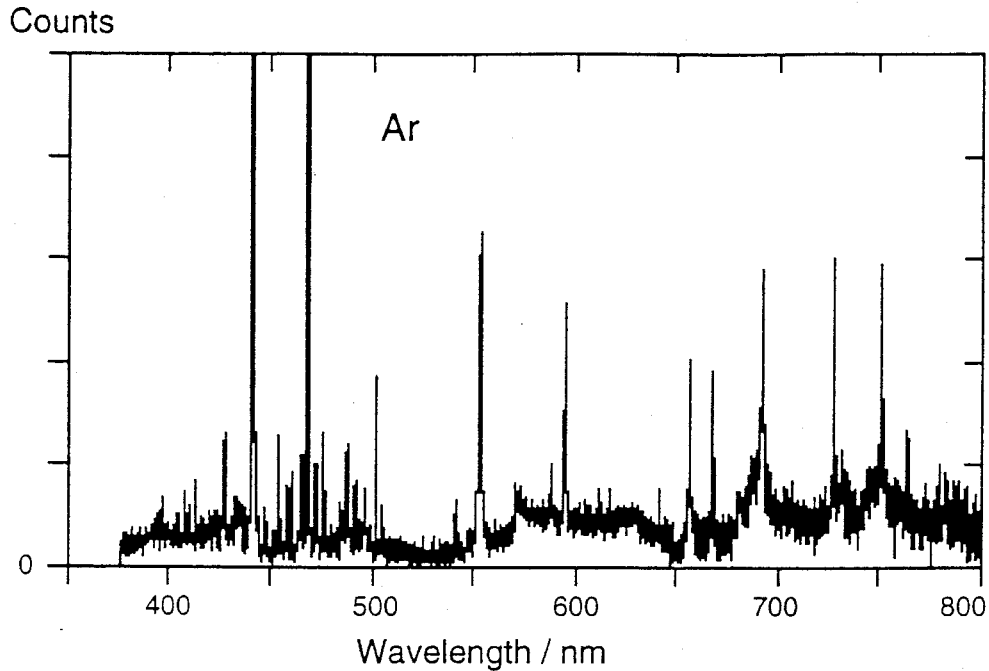


Fig. 1.-- Composite spectrum of Ar, measured at the LLNL SuperEBIT using a 1m normal incidence spectrometer equipped with a CCD camera (from Träbert *et al.* 1998).

Among the transitions studied for their wavelengths are the the $3s^2 3p^2 \ ^3P_1 - ^3P_2$ transition in Si-like Kr^{22+} and Mo^{28+} and the $3d^4 \ ^5D_2 - ^5D_3$ transition in several Ti-like ions from Xe^{32+} to Au^{57+} (Figure 2). The measured wavelengths, in comparison with calculated data, help to improve isoelectronic predictions for elements which may be present in future fusion test plasmas.

For several forbidden lines (the ground state fine structure transition in Ar^{13+} and the $3s^2 3p^2 \ ^3P_1 - ^3P_2$ transition in Si-like Kr^{22+}), transition probabilities have been measured, with about 5% uncertainties (Serpa *et al.* 1997, Serpa *et al.* 1998, Träbert *et al.* 1998). This is more precise than the predictions from most *ab initio* calculations (Cheng *et al.* 1979, Biémont and Bromage 1983, Huang 1985, Verhey *et al.* 1987), which usually need to be corrected for experimental fine structure intervals. However, better spectral resolution and improved light collection will be needed (and are in reach) to reach the desired level of 1% uncertainty.

Table 1. Results of Lifetime Measurements using EBIT

Ion	Upper level	Lifetime (ms)			Lifetime (ms)	
		Experiment	Theory as is		Theory after energy correction	
Ar^{13+}	$2s^2 2p \ ^2P_{3/2}^0$	8.7 ± 0.5	NIST	9.62 a		
				9.51 b		
				9.41 c	9.58	
Kr^{22+}	$3s^2 3p^2 \ ^3P_2$	5.7 ± 0.5	NIST	6.46 d	6.78	
				6.3 ± 0.3	LLNL	5.83 e
Xe^{32+}	$3d^4 \ ^5D_3$	2.15 ± 0.14	NIST	2.4 f		

a Verhey *et al.* 1987

b Froese Fischer 1983

c Cheng *et al.* 1979

d Biémont and Bromage 1983

e Huang 1985

f Feldman *et al.* 1991

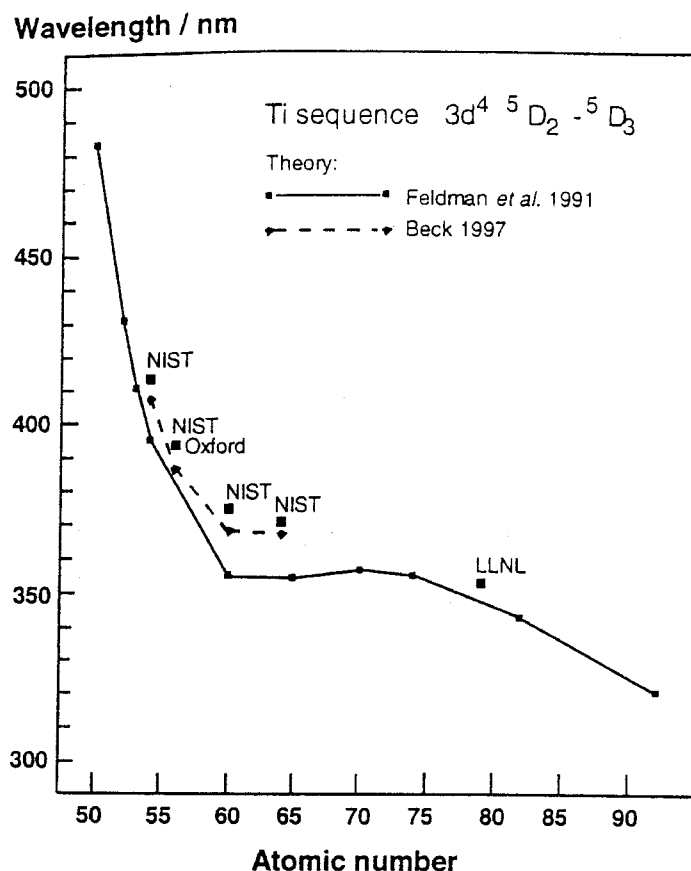


Fig. 2. -- Isoelectronic trend of the $3d^4 \ ^5D_2 - ^5D_3$ transition wavelength in Ti-like ions. Full line: Prediction by Feldman *et al.* (1991). Experimental data for Xe measured at NIST Morgan *et al.* 1995, Serpa *et al.* 1996), for Ba at NIST (Morgan *et al.* 1995) and at Oxford (Bieber *et al.* 1997), for Nd and Gd at NIST (Serpa *et al.* 1996) and for Au at LLNL (Träbert *et al.* 1998). Later MCDF calculations by Beck (1997) come closer to existing experimental results for Xe to Gd than the initial calculations by Feldman *et al.*, but give no further predictions.

3. Conclusion

Electron beam ion traps are quite suitable for the observation of forbidden transitions in the visible and permit lifetime measurements in the millisecond range. The precision for lifetime measurements reached so far is about 5%. In the x-ray range (with better detection efficiency and lower detector noise), EBIT has meanwhile yielded the first lifetime data with sub-percent precision. It is expected that after further development work at least the 1% range of uncertainty will be reached also for forbidden transitions in the visible spectrum. This is better than most applications require and severely tests theory.

4. Acknowledgments

This research has been supported by NATO (CRG 940181) and Humboldt Foundation Germany. Work at LLNL was performed under the auspices of USDoE (Contract No. W-7405-ENG-48). Conference participation would not have been possible without support by the German Research Association, DFG.

REFERENCES

- Beck, D.R. 1997, Phys. Rev. A **56**, 2428
- Bieber, D.J., Margolis, H.S., Oxley, P.K., and Silver, J.D. 1997, Physica Scripta, T **73**, 64
- Biémont, E., and Bromage, G.E. 1983, M.N.R.A.S., **205**, 1085
- Cheng, K.T., Kim, Y.-K., and Desclaux, J.P. 1979, At. Data Nucl. Data Tables, **24**, 111
- Edlén, B. 1942, Z. Astrophysik, **22**, 30
- Feldman, U., Indelicato, P., and Sugar, J. 1991, J. Opt. Soc. Am. B, **8**, 3
- Froese Fischer, C. 1983, J. Phys. B, **16**, 157
- Huang, K.-N. 1985, At. Data Nucl. Data Tables, **32**, 503
- Morgan, C.A., Serpa, F.G., Takács, E., Meyer, E.S., Gillaspy, J.D., Sugar, J., Roberts, J.R., Brown, C.M., and Feldman, U. 1995, Phys. Rev. Lett., **74**, 1716
- Serpa, F.G., Meyer, E.S., Morgan, C.A., Gillaspy, J.D., Sugar, J., and Roberts, J.R. 1996, Phys. Rev. A, **53**, 2220
- Serpa, F.G., Morgan, C.A., Meyer, E.S., Gillaspy, J.D., Träbert, E., Church, D.A., and Takács, E. 1997, Phys. Rev. A, **55**, 4196
- Serpa, F.G., Gillaspy, J.D., and Träbert, E. 1998, J. Phys. B: At. Mol. Opt. Phys., **31**, 3345
- Träbert, E., Beiersdorfer, P., Utter, S.B., and Crespo López-Urrutia, J.R. 1998, Physica Scripta, **58**, 599
- Verhey, T.R., Das, B.P., and Perger, W.F. 1987, J. Phys. B **20**, 3639

HIGHLY CHARGED ION STUDIES AT THE NIST EBIT*

L. P. Ratliff and J. R. Roberts

Atomic Physics Division, National Institute of Standards and Technology,
Gaithersburg, MD 20899-8421

INTRODUCTION

In this chapter we will discuss the application of the electron beam ion trap (EBIT) as a compact source of highly charged ions (HCIs) (see fig. 1) to various experiments conducted at the National Institute of Standards and Technology (NIST). These experiments were done in collaboration with several different groups. We will also give a very general overview of the NIST EBIT and the instrumentation for various types of experiments that have been conducted.

The highly charged ions in an EBIT are created when an intense beam (up to 4000 A/cm^2) of electrons collides with low velocity atoms or low charged ions. The ions are trapped by both axial and radial potential wells. Axially, along the electron beam axis, a well is formed by a series of three insulated drift tubes. Radially, a well is created by the space charge of the electron beam itself as well as by the magnetic field from a pair of superconducting Helmholtz coils. This essentially creates HCIs with a relatively small kinetic energy and allows two rather unique research opportunities. First, the ions can be studied spectroscopically while being trapped for relatively long periods of time inside the device. Second, the ions can be extracted into relatively low kinetic energy beams for collision studies. In the first category of experiments, spectrometers attached to the EBIT analyze the radiation (visible, ultraviolet, and x-ray) that is produced as the ions radiate as a result of excitations from collisions with the electrons. In this way, we can measure various absolute lifetimes and transition energies as well as relative cross sections, without many of the systematic errors due to large (relativistic) ion velocities. In the second category of experiments, ions are extracted into relatively low kinetic energy beams that bombard gas or solid targets. Although the ion velocities are much higher in this case than in many laboratory atom or ion beam experiments, they are much smaller than in accelerator experiments that deal with highly charged ions. Therefore, the EBIT allows observation of the phenomenology of collisions where the potential energy is comparable to, or even greater than the kinetic energy. An example is the analysis of ejected secondary particles, such as electrons, x-rays, ions, atoms, molecules or clusters, or when surface modification.

The chapter is organized as follows: a history section describes the chronology of the development of the NIST EBIT facility along with the experiments that have been performed there. The next section is a practical guide to the operation of the EBIT, a metal vapor arc to inject materials, and an extraction beam line. Finally, there is a brief conclusion.

* This contribution is a US government work and not subject to copyright.

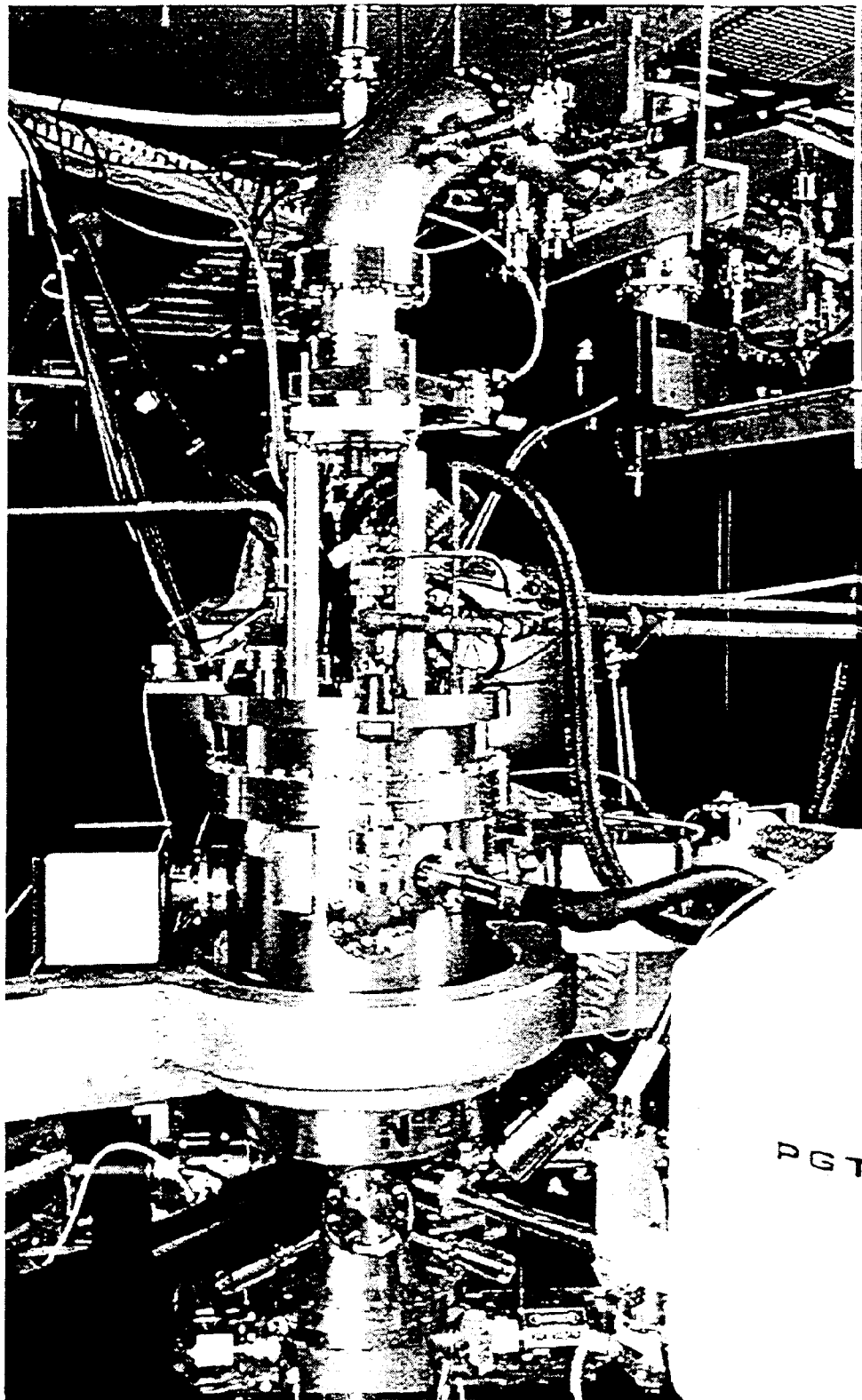


Fig. 1 Photograph of the NIST EBIT. The EBIT itself is held by an aluminum stand with an annular yoke. Also evident in the lower right of the picture is the liquid dewar for the Si(Li) detector. On top of the EBIT chamber and attached to the ceiling is the beginning section of a transfer beamline attached to the EBIT by a 90° elbow housing an electrostatic bender.

HISTORY

In 1988 the former National Bureau of Standards, NBS, was renamed the National Institute of Standards and Technology, NIST, and a substantial change in NIST's mission occurred as emphasized by Congress "to assist industry in the development of technology needed to improve product quality, to modernize manufacturing processes, to ensure product reliability and to facilitate rapid commercialization of products based on new scientific discoveries". As a result of this enhanced mission, new avenues for research and development were investigated at NIST. The Atomic Physics Division in the Physics Laboratory at NIST had developed an expertise in the investigation of atomic properties of ionized plasmas mainly by spectroscopic techniques for the Nation's magnetic fusion effort. It was reasoned that the theoretical and experimental techniques utilized in the magnetic fusion effort could be expanded to include other important areas of research that would be important to assist industry in the development of technology. Consultation with NIST colleagues lead us to contact researchers at the Lawrence Livermore National Laboratory (LLNL) who had recently brought online a new, compact reservoir of HCIs that emitted x-rays nearly continuously. This source was called the electron beam ion trap (EBIT). A very promising area that this device could impact and which was generic to the new NIST mission, was that of fundamental wavelength standards in the x-ray spectral region. Up to this time, the sources of highly charged ions utilized in research suffered from several fundamental problems, such as large Doppler shifts, wide Doppler spectral line profiles, and highly transient emission resulting in poor S/N statistics to name a few. After a few visits to the LLNL EBIT group, it was clear that the EBIT as a source of HCIs was unique and could provided new opportunities for the application of NIST measurement methods and techniques, especially in the area of high precision spectroscopic investigations of atomic (ionic) properties.

This situation was also seen as an opportunity to provide NIST with a unique research tool. It was realized that this source of highly charged ions could not only provide greater precision and accuracy in x-ray wavelength standards but the possibility to determine fundamental properties of highly charged ions, such as ionization, excitation and dielectronic recombination cross sections. These types of data were essential in the modeling of all highly ionized media from thermonuclear reactions to the evolution of stellar atmospheres.

The first order of business was the actual fabrication of a NIST EBIT. The EBIT program at LLNL had produced a workable EBIT that was designed and fabricated in conjunction with researchers and technicians at Lawrence Berkeley Laboratory. Simultaneous with the NIST inquiries about constructing a new EBIT based on the LLNL design, scientists from Oxford University, England became interested in a similar EBIT project for the Oxford Physics Department. It was decided at this point that NIST and Oxford would mount a joint effort to build two EBITs at the same time. With the cooperation of LLNL, by providing both NIST and Oxford with the original EBIT design drawings, Oxford University proceeded to fabricate two nearly identical EBITs, one of which was delivered to NIST in February 1992. The decision to modify the original EBIT as little as possible stemmed from the success of the LLNL EBIT and the idea "if it ain't broke don't fix it". Also a concern was the unknown stability properties of the ions trapped in the ~ 4000 A/cm² electron beam and the 3T magnetic field. However, for convenience and simplicity there were some modifications that were included. They were: 1) a redesign of the location of the high voltage input, 2) a modified design of the components for electron injection, 3) more observation ports, and 4) the inclusion of small, conducting appendages near and on the drift tube assembly. This latter modification was intended to improve stability by eliminating the build up of Penning electrons in the vicinity of the drift tubes. The build up of such electrons can provide a short-circuit, causing an unprogrammed shut down of the EBIT.

The next major undertaking was to put together the parts and make the device operational. Scientists at the Naval Research Laboratory (NRL) had demonstrated interest in collaborating with NIST on experiments of mutual interest in high precision and high accuracy x-ray spectra. Because the uniqueness of the EBIT was apparent to the researchers at NRL, a workshop was held before construction was begun at which research staff from both NIST and NRL presented and discussed ideas that could be applied to this new source of highly charged ions. As the result of this workshop, NRL decided to collaborate with NIST on the EBIT project by providing a portion of the electron beam control instrumentation and apparatus to make the EBIT function as a world class source of highly charged ions. It was also at this point that NIST hired a project leader and together with staff from NRL, the new EBIT and

some component parts were assembled. This NIST/NRL collaboration provided the scientific community an operational EBIT in September 1993.¹

The first efforts were repeats of experiments done at LLNL, to check that the modified EBIT design was operating appropriately.² A liquid nitrogen cooled Si(Li) x-ray detector with a resolution of approximately 175 eV and an operating range of 1 keV to 25 keV was used to observe broad spectral features of ions such as barium and xenon (see fig. 2). Barium is a contaminant given off by the heated electron gun cathode and xenon was injected as a gas into the vacuum. These preliminary experiments confirmed that the new EBIT was operational and performed better than expected.³ Other overview papers of the NIST EBIT early results include refs. 4, 5 and 6.

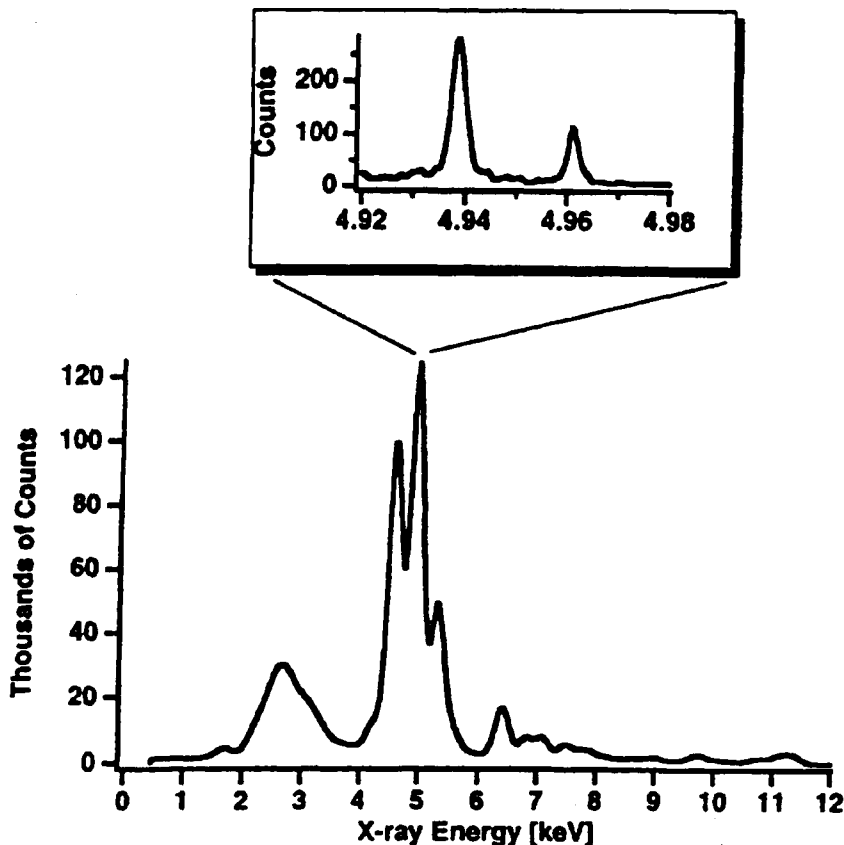


Fig. 2 The lower graph shows broadband x-ray spectra taken with a Si(Li) detector located at the trap region. The insert is the high-resolution spectrum taken with a Bragg crystal spectrometer showing the transitions from the $J=1$ excited states to the ground state in neon-like barium.

Using the same Si(Li) x-ray detector, dielectronic recombination (DR) and radiative recombination (RR) cross sections in Ba^{34+} and Ba^{35+} were studied.⁷ In this DR process, a continuum electron collisionally excites a 2p electron while it is simultaneously captured into the 3d (3s) orbital of the target ion. Then the 3d (or 3s) electron decays to the 2p vacancy of the recombined ion emitting a photon of 4.6 keV (or 4.0 keV). In addition to these DR peaks, the spectrum shows well defined radiative recombination peaks corresponding to emission from orbitals with $n = 3, 4,$ and 5 and a broad peak due to emission from higher orbitals (see fig. 3). The $n = 3$ RR peak overlaps with the 3d DR peak. The resonant nature of the DR excitation is seen by changing the electron beam energy by 100 eV (the energy spread of the electron beam is some tens of eV); the two DR peaks go away while the RR peaks show 100 eV shifts in energy. According to simulations of the conditions in the EBIT, most of the trapped barium atoms are in the charge states, $q = 34$ and $q = 35$. Calculations of the relative cross sections for this mixture of charge states, which

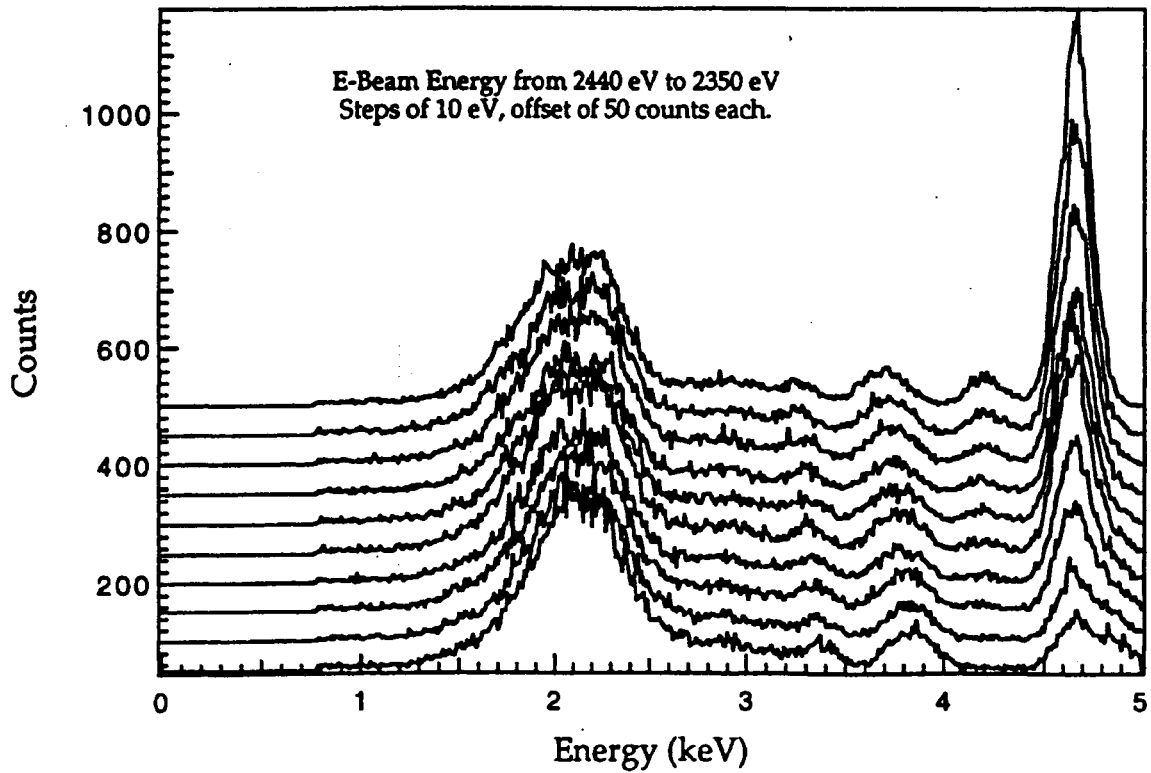
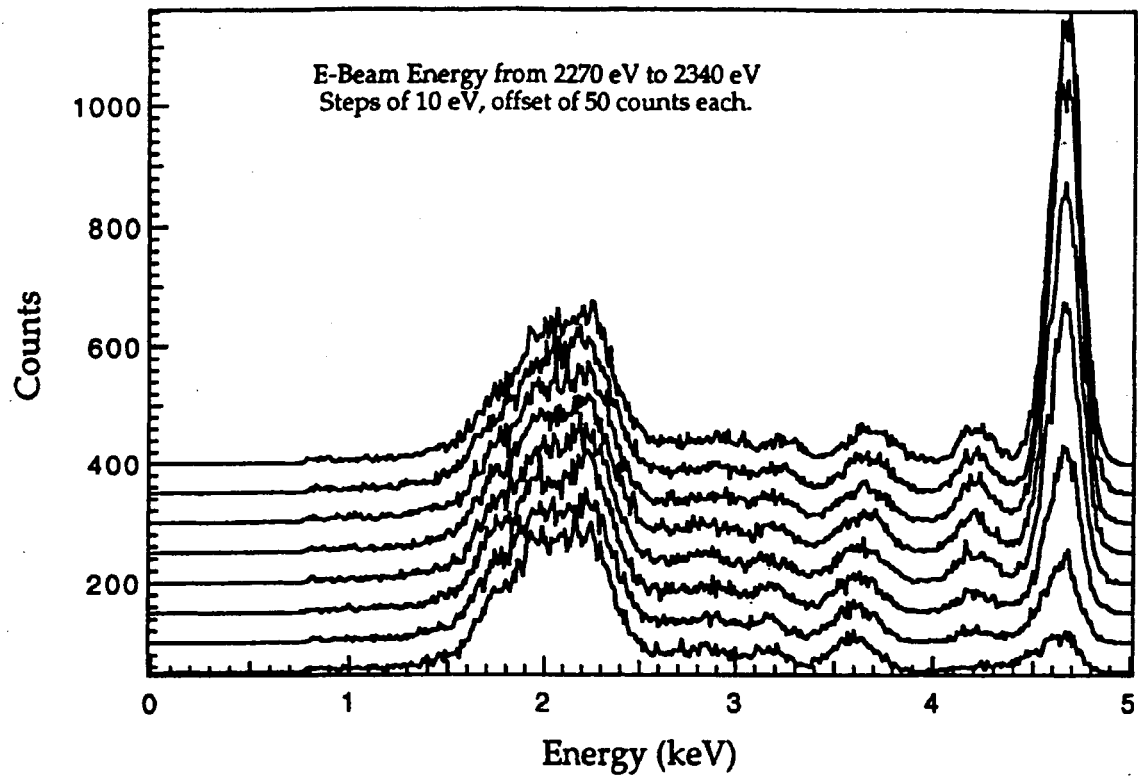


Fig. 3 Scandium-like barium spectra taken at varying electron-beam energies. The electron-beam is varied from 2270 eV to 2440 eV.

Two identical crystal spectrometers in the Johann configuration were used for high resolution x-ray spectroscopic studies.⁸ The spectrometers are fitted with bent germanium crystals with $2d = 0.400 \text{ } \mu\text{m}$ (2,2,0 family of planes). For incident radiation near 4.56 keV, the Bragg angle is near 45° , making the crystal a very good polarizer. Utilizing the two crystal spectrometers simultaneously and mounting them with their optical axes orthogonal allowed observation of polarization effects due to the directional nature of the electron beam. This "two-crystal" method of measuring polarization is insensitive to certain types of systematic errors that might have affected previous measurements. The spectral line studied was the magnetic quadrupole (M2) line, $2p^6 \text{ } ^1S_0 - 2p^5 ({}^2P_{3/2}^0)3s[3/2]_2^0$, in neon-like barium, Ba^{46+} . To account for differences in geometry and efficiency between the two detectors, the signals from the detectors are normalized using the nearby electric dipole (E1) line, which is essentially unpolarized. The polarization, P , is defined as: $P = (I_{\text{par}} - I_{\text{perp}})/(I_{\text{par}} + I_{\text{perp}})$, where I_{par} and I_{perp} are the intensities of the parallel and perpendicular polarized light measured at 90° from the electron beam axis. Aside from the regions where resonances occur in the cascade feeding of the upper state, strong negative polarization is measured in the range, 5 keV to 7.8 keV which is in good agreement with calculations (see fig. 4).⁹ We have also experimented with the implementation of new types of spectrometers for use on an EBIT. One such instrument is described in ref. 10.

The first observation of visible light from an EBIT¹¹ was made in 1993. Such visible spectroscopy from highly charged ions could be a valuable tool for diagnostics of high temperature plasmas, for example in nuclear fusion reactors and in the solar corona. It is beneficial to observe lines in the visible and near uv as they can be measured with standard, well established, optical techniques. Of specific interest were the predictions by Feldman et al.¹² Their calculations demonstrated that magnetic dipole (M1) line ($3d^4 \text{ } ^5D_2 - ^5D_3$) in the Ti-like isoelectronic sequence would remain in the visible/near uv spectral region for nearly half of the periodic table from $Z = 45$ to $Z = 92$. This would be particularly valuable to use for plasma diagnostics. Morgan *et al*¹¹ made the first measurements in this sequence and determined the wavelengths of barium and xenon to be 393.24 (20) μm and 413.94 (20) μm , respectively (see fig. 5). While these values are consistent with relativistic Hartree-Fock (HFR) calculations with a scaling factor of 93% (which is reasonable for highly charged ions), they differ by an unacceptable 5% from *ab initio*, multi-configuration, Dirac-Fock calculations. This M1 line in xenon was also observed using a Fabry-Perot spectrometer¹³ with a resolving power of 10^4 . In this case, an ion temperature of less than 1 keV was deduced from the Doppler width of the emitted spectral line. (see fig. 6). Additional observations of M1 spectral lines have been observed in krypton.¹⁴ In this experiment spectral lines of low charge state ions were observed along with the HCI M1 spectra.

In order to expand the range of ions available for study in the EBIT, a metal vapor vacuum arc, or MEVVA, ion source was added to the EBIT. The source was designed, built and tested at NRL and brought to NIST 1995. With the ability to inject metal ions into the EBIT, Serpa *et al*¹⁵ continued the investigation of the Ti-like isoelectronic sequence by adding measurements on neodymium ($\lambda = 375.3$ (2) μm) and gadolinium ($\lambda = 371.3$ (2) μm). Now with these four measured wavelengths in the sequence, the scale factors for the previous HFR calculation were refined and improved predictions were made for the isoelectronic series from xenon ($Z = 54$) to osmium ($Z = 76$).¹⁵

In 1995 researchers at NIST^{5, 16} developed a method for using the EBIT to measure lifetimes on the order of milliseconds. This temporal range is difficult to measure via the standard beam foil technique as it would require an unreasonably long flight tube. In this technique, the EBIT electron beam is switched on and off. When the beam is off, the fluorescence is monitored as a function of time. The decay curve (see fig. 7) is fitted with an exponential to extract a lifetime. Because the transitions that feed the upper state are extremely fast, there is no significant contribution to that population during the beam-off period. Careful diagnostics done by our group and the group at Livermore¹⁷ show that a certain portion of the decay is in fact due to the lifetime of the excited state of the ion. Using this technique, we measured magnetic dipole lifetimes for Xe^{32+} (2.15 (14) ms), Kr^{22+} (5.7 (5) ms) and Ar^{13+} (8.7 (5) ms).^{16, 18}

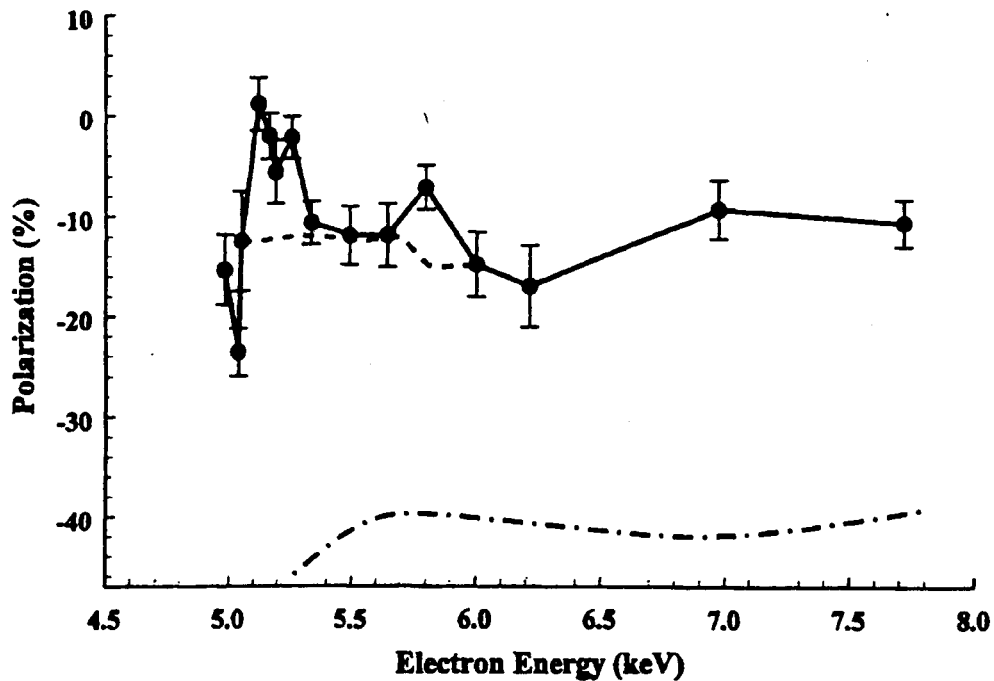


Fig. 4 Polarization measurements of a magnetic quadrupole transition (M2) in neon-like barium. The measurements were done with electron beam energies in the range of 5 keV to 7.8 keV.

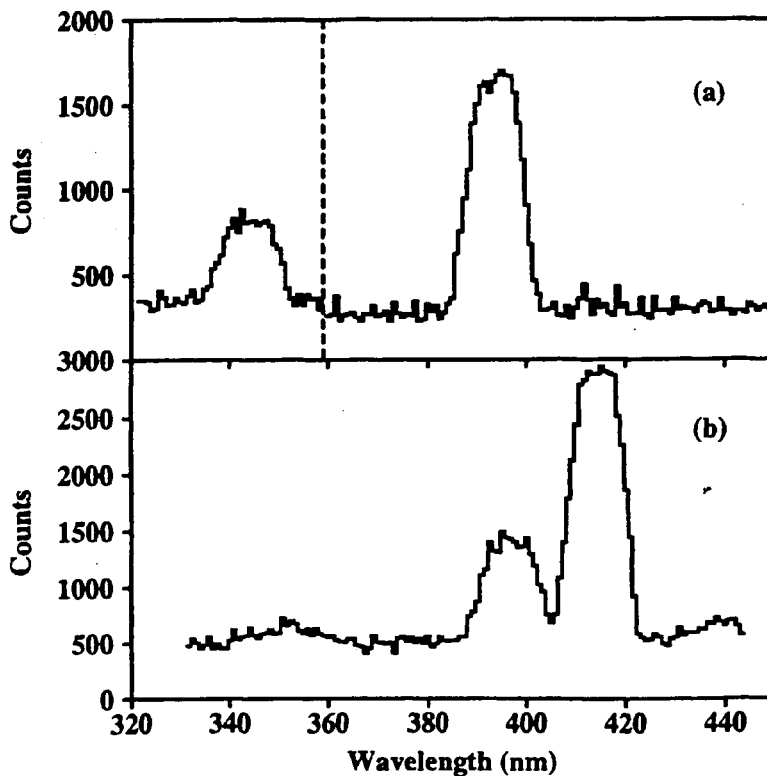


Fig. 5 A wavelength survey of barium (a) and xenon (b) showing magnetic dipole lines in the near ultraviolet spectral region for (a) Ba^{34+} and (b) Xe^{32+} and Xe^{31+} .

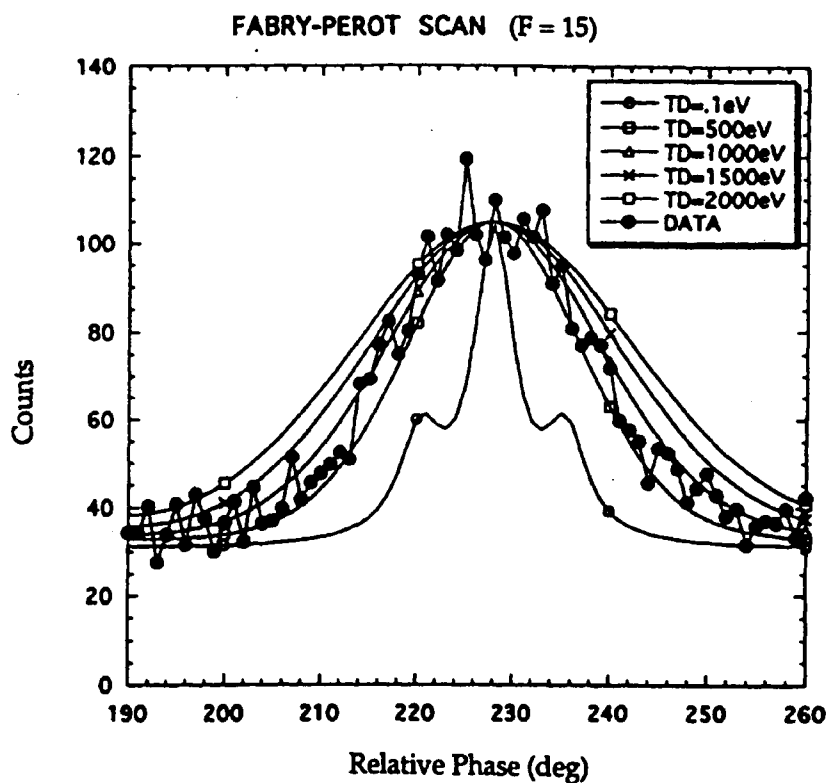


Fig. 6 Numerical simulations (—) at different ion temperatures, TD, and data (•) for Fabry-Perot scans of a Ba^{34+} magnetic dipole spectral line at $393.2 \mu\text{m}$.

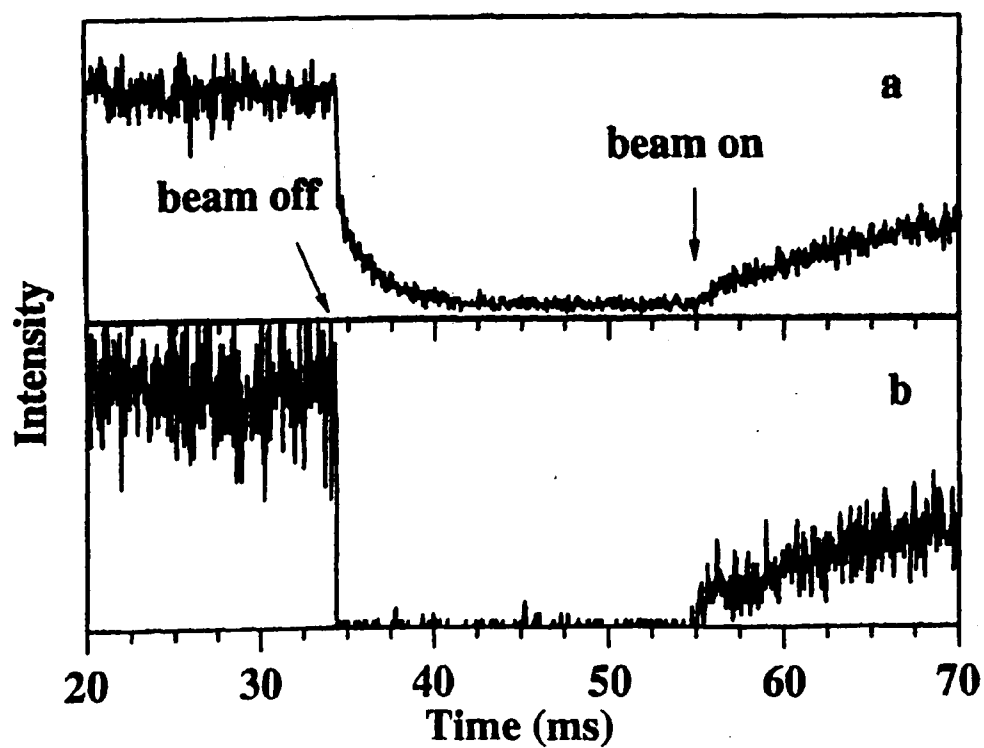


Fig. 7 The temporal evolution (a) of the magnetic dipole spectral line intensity at $413.94 \mu\text{m}$ from the Xe^{32+} and (b) of the x-rays detected by a Si(Li) detector for an optimized Xe^{32+} charge state.

In collaboration with the NIST Quantum Metrology Group, experimental work has been ongoing to measure the transition wavelengths in the x-ray spectral region with absolute accuracy at the 10 – 30 ppm level. There are two goals here. The first goal is to improve wavelength standards in the x-ray spectral region. The second goal is to measure Lamb shifts in hydrogenic systems with heavy nuclei; for a given number of electrons, the Lamb shift of an ion varies as the fourth power of its charge, so the magnitude of the Lamb shift of highly charged ions can be quite large. The measurements are done with one of the Johann bent-crystal spectrometers described previously.⁸ The calibration procedure employs an x-ray tube where an electron beam is focused onto a target foil. This foil is located directly opposite the EBIT trap region from the spectrometer entrance slit. The calibration x-rays travel through the EBIT to the spectrometer. The details of the absolute calibration are presented in ref. 19. The current status and results of this effort are also summarized in ref. 20.

Although the NIST EBIT program was begun to carry out high precision and accurate x-ray wavelength measurements, it was clear that there were other areas of research that were also exciting and that would benefit from the unique properties of an EBIT. One of these was the idea of extracting the HCIs from the trap and transporting them to another experimental chamber where the ions could interact with other matter, e.g., a material surface. In 1993 Schmieder and Bastasz²¹ from Sandia, published results from experiments done on the LLNL EBIT. They impacted HCIs onto a plastic (CR-39) surface and formed local damage sites. The surface was chemically etched in order to make the damage sites visible with a scanning electron microscope. This discovery led NIST to undertake the design and construction of a highly versatile transport ion beam line to systematically investigate the interaction of HCIs with surfaces.

The design and construction of this beam line proceeded in parallel with the ongoing spectroscopic experiments described previously, and in early 1996 it was essentially finished.²² This new beam line incorporated unique steering elements, movable Faraday cup detectors, several einzel lenses and an q/m charge-to-mass separator magnet. This magnet is capable of transporting almost any charge state of any element, except for the very lowest charge states of the highest mass elements at high velocity. For example, U^{8+} can be transmitted with 64 keV of kinetic energy at the highest magnetic field available in the separator magnet. At the end of the beam line are two chambers. One is used exclusively for the exposure of surfaces and the other, can be configured for a variety of experiments. With two target chambers at the end of the beam line and the spectrometers on the EBIT, it is easy to quickly switch among multiple experiments that can remain intact semi-permanently. This has attracted many collaborators with diverse interests to the NIST EBIT.

The performance of this beam line was outstanding and gave the highest fluxes ever observed in such a system.²² For example, we measured 21 pA of Xe^{44+} , three orders of magnitude more than had been reported for continuous mode operation of any EBIT at the time.²³ Previously, the time-averaged flux was observed to be much higher in pulsed mode operation than in the continuous mode. In pulsed mode, the ions are stored in the trap until a significant population of the desired charge state ion is accumulated. Then, the voltage on the center drift tube is raised, pushing the trapped ions over the barrier presented by the upper drift tube. In this way, ions are extracted from the trap in pulses as short as a few microseconds or as long as tens of milliseconds or more. This however can be a disadvantage for certain experiments. For example, experiments involving pulse-counting electronics might saturate for high intensity count rates. We have found that the NIST EBIT works quite well in what has been termed continuous leaky mode. That is, the upper drift tube potential is set below the lower drift tube potential and the ions with the highest energy are constantly escaping out the upper drift tube. We find that this method gives us the highest fluxes and the most stable beams.

With the beam line in place, we set out to understand the mechanism for surface damage with relatively low velocity, highly charged ions starting with the simple concept that follows. As the HCI approaches a surface, it starts to extract electrons from the material. Some of these electrons are bound in high lying states of the projectile HCI forming a "hollow atom". This type of atom will have many low-lying vacancies with most of the captured electrons in high lying states. The atom can decay via Auger or radiative processes and possibly extract more electrons from the material before its actual impact. If the surface is a good conductor, the electrons should be readily replaced from the bulk material, but an insulator could develop a locally charged region which would "Coulomb explode" leaving a crater at the surface.^{24,25,26}

We proceeded to expose several types of surfaces with highly charged ions and image their surfaces in collaboration with Schmieder from Sandia National Laboratory. In this collaboration, the experiments were performed using the NIST EBIT facility and an atomic force microscope (AFM) from the Sandia group.

We exposed the surfaces to the EBIT highly charged ions, removed them from the vacuum and imaged them in air. As our first surface to study we chose CR-39 to reproduce the results seen earlier by Schmieder and Bastasz.²¹ As expected, after etching in 5 N NaOH solution for 30 minutes at 50° C, we saw craters that were approximately 200 μm across using scanning electron microscope (SEM) and a field emission SEM (see fig. 8(a) and 8(b)). These craters can be seen with the naked eye as a haziness of the surface.

For subsequent experiments, we again chose insulating materials as we expected to see the largest effects with them. In order to see nanometer scale features, we required extremely smooth samples, so we chose mica, which is easily cleaved with adhesive tape. In previous studies at Livermore²⁷ and Kansas²⁸, hillocks were seen to result from HCl bombardment on mica. In collaboration with the Kansas group, we studied the effect of potential energy on the size of these hillocks and found that they increased approximately as the ion's potential energy to the 3/2 power.²⁸ (see fig. 9)

Recently, we studied a standard high-resolution resist, polymethylmethacrylate, or PMMA. We exposed the PMMA-coated silicon to Xe^{44+} , removed it from the vacuum and developed it in a solution of equal parts (by volume) of isopropyl alcohol and methyl isobutyl ketone at room temperature for 30 seconds. Figure 10 shows an AFM image of damage sites produced by multiple ion impacts through two dimensional array of nominally square holes; they are approximately 10 μm apart and 1 μm in diameter.²⁹ In another investigation, low doses of HCIs on PMMA were also done and single impact sites were imaged with an apparent width of approximately 24 μm . We have also investigated the effect of ion bombardment on the surface of the crystal amino acid, L-valine. (See the figures in the chapter by Edward Parilis within this volume.)

In collaboration with George Whitesides' group in the Chemistry Department of Harvard University, self assembled monolayers (SAMS) were also exposed with HCIs.³⁰ The samples consisted of silicon wafers coated with a thin titanium adhesion layer and then with 20 μm of gold. Self-assembled monolayers of dodecanethiol, $\text{CH}_3(\text{CH}_2)_{11}\text{SH}$, are grown in solution and removed from the solution just before they are put into the vacuum. They are then exposed with various fluences of Xe^{44+} ions. In this way, we found that a substantial exposure required 10^{11} ions/ cm^2 . This is approximately a factor of 10^5 less than the fluence required for a similar exposure with metastable argon atoms which have 5000 times less potential energy than the ions. Figure 11 shows a proof-of-principle of HCl masked lithography using hexadecanethiol SAMs over a 40 μm layer of gold bound to a silicon wafer with a chromium adhesion layer. The inset in figure 11 shows an edge roughness that appears to be limited by the quality of the mask used.

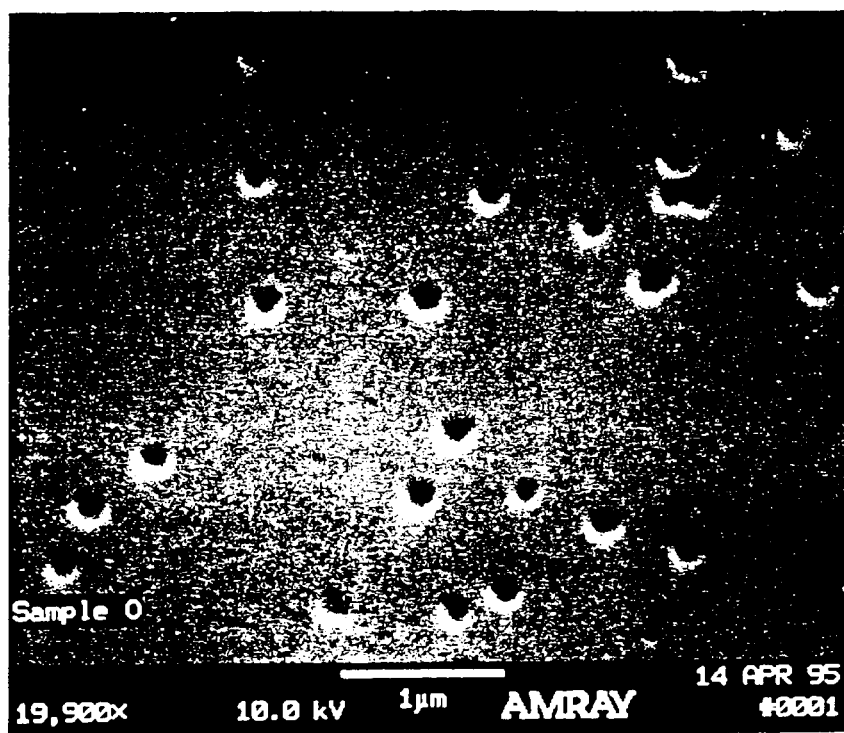
Using a compact, energy dispersive x-ray detector, we have measured the x-ray spectra from hydrogenic argon impacting silicon dioxide.³¹ This experiment represents the first investigation with x-ray spectroscopic methods of the effects of bombarding surfaces with HCIs from the NIST EBIT.

An ultra high vacuum (UHV) scanning tunneling/atomic force microscope (STM/AFM) and surface preparation chamber were added to the facility in 1997. This made NIST the only facility in the world in which one can use the very high charge state ions to expose surfaces and then image the surfaces without removing them from the vacuum. With this new capability, we can observe the structures created by ion bombardment before oxidation or environmental contamination can modify the structures.

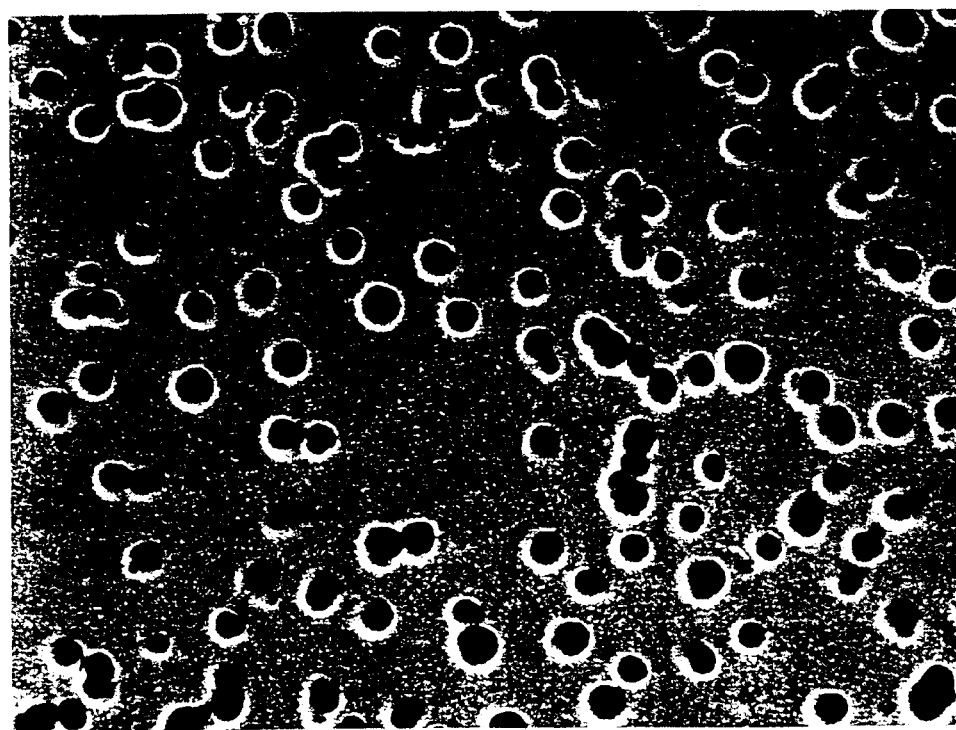
The most recent addition to the equipment for studying surfaces is a high spatial resolution ($\sim 15 \mu\text{m}$) movable intensified charge injection device (CID) detector system. This instrument images the ion beam at the location of the sample to accurately determine the spatial characteristics of the beam.

OPERATION

The EBIT facility can be thought of as four separate systems: 1) the EBIT itself, 2) the MEVVA ion source, 3) the beam line and 4) two target chambers and related equipment. This section is an overview of these systems.



a



b

Fig. 8 (a) Scanning electron microscope (SEM) and a (b) field emission SEM scans of an etched plastic, CR-39. The etched damage sites are approximately 200 µm in diameter.

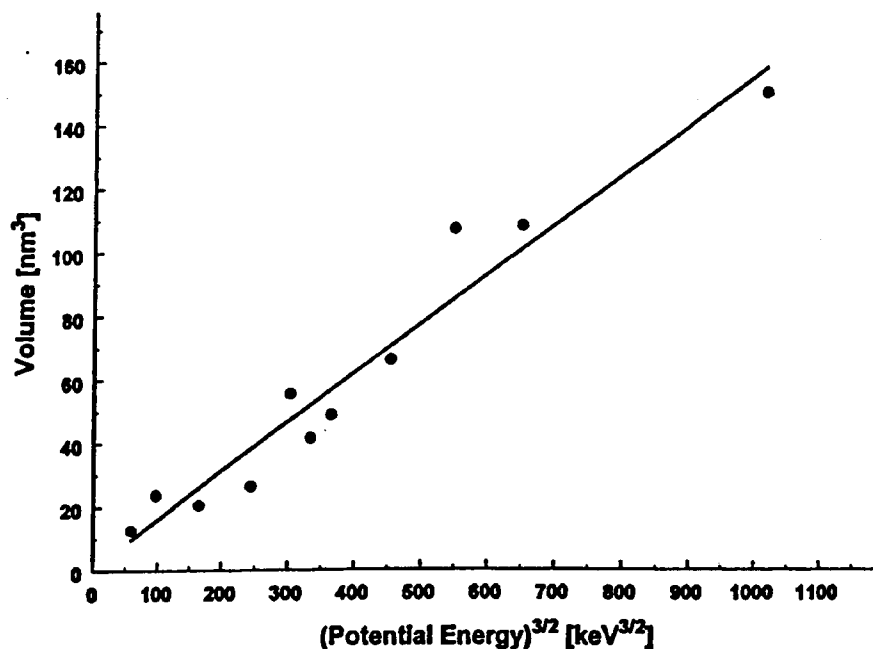


Fig. 9 A plot of the volume of damage hillocks in mica vs. the $3/2$ power of the potential energy of Xe^{+q} . The points (\bullet) represent the data for several different charge states from $30 \leq q \leq 50$ and the (—) a least squares fit to the data.

EBIT

The EBIT (see fig. 12) consists of three major components: the first includes the electron source, the drift tubes and the electron collector, the second comprises four magnetic field coils to shape the electron beam, and the third embodies the necessary support equipment. While it has been described in other publications, for completeness sake it will be described here as well. A beam of electrons from the electron gun travels through the drift tubes to the collector. Along the way, it is shaped by the various electric and magnetic fields. The EBIT is mounted vertically with spectrometers mounted around its circumference at the trap region and the extracted ion beam emerges from the top.

The electron gun is a commercial unit that consists of a cathode, an anode and a focusing electrode. The cathode is heated by a filament and is operated at ground potential. Electrons are extracted from the cathode when the anode is biased, normally at about 4.2 kV, and the focusing electrode shapes the beam. There is an electrode located near the electron gun that is normally held at the same potential as the anode. The purpose of this electrode, formerly called the snout, is to shape the magnetic field in the vicinity of the electron gun as well as to act as an electrostatic element. The transition electrode is located in the narrow opening of the grounded liquid nitrogen shield to prevent the ions from being influenced by the ground potential of the shield (see fig. 12).

The drift tube assembly consists of three cylindrical tubes enclosed by a cylindrical shield electrode. The electron energy in the trap region is the center drift tube voltage minus a correction due to the space charge of the electrons and ions in the trap. This correction is calculated by integrating Gauss' Law and, as an example, is ≤ 70 eV at 2 keV trap potential and 35 mA of electron current.¹¹ The collector electrode is biased at approximately +2 kV to attract the electrons that have passed through the drift tubes. A suppressor electrode located just below the collector prevents secondary electrons created in the collector from travelling back down into the EBIT. Just above the collector, the extractor electrode is at a negative voltage to aid in extracting the ions into a beam and to suppress the escape of secondary electrons from the top of the collector.

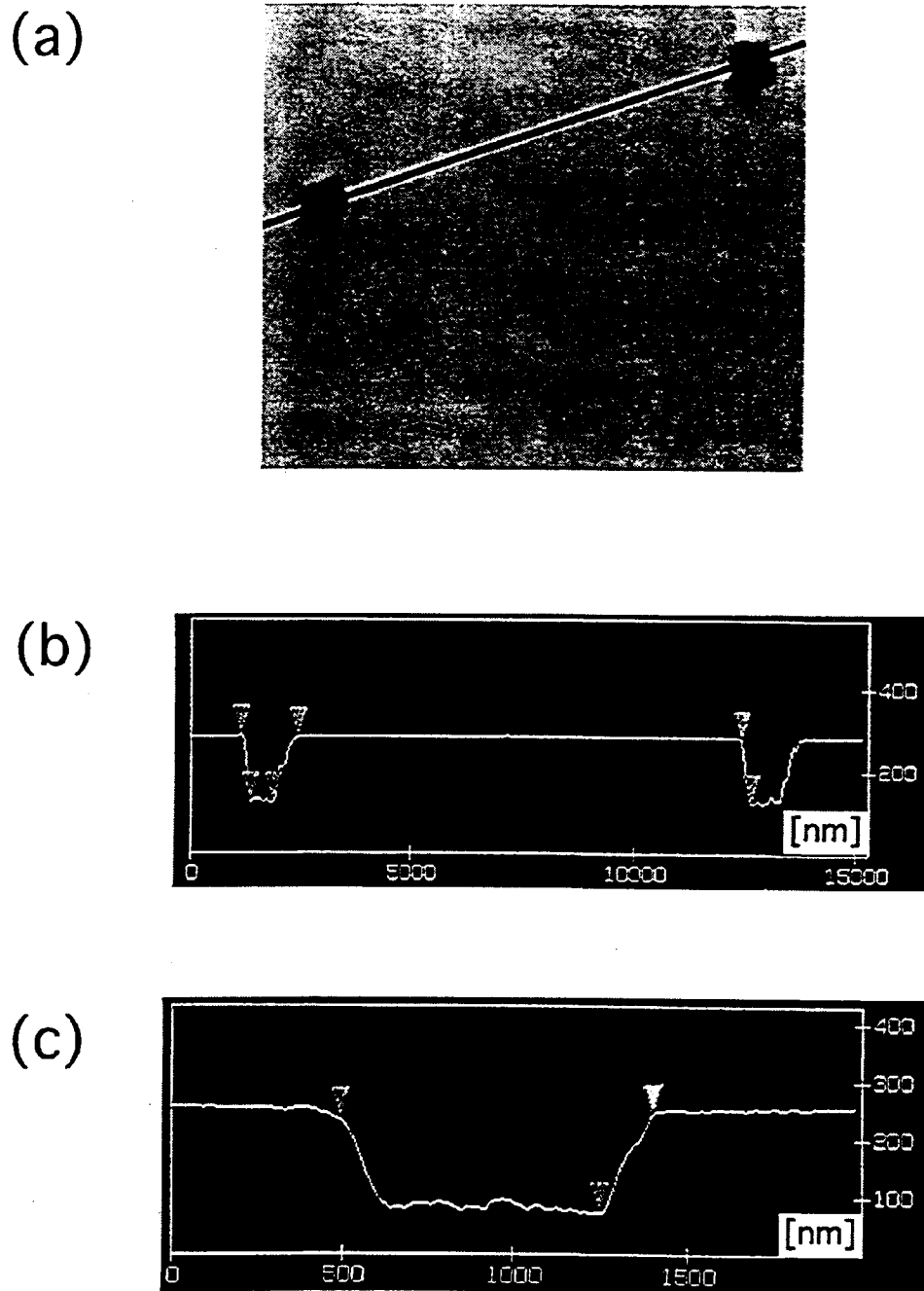


Fig. 10 An AFM image of damage sites produced by multiple ion impacts of $^{136}\text{Xe}^{44+}$ on a polymethylmethacrylate (PMMA) resist coated silicon wafer. A commercial stencil mask screened the wafer with a two dimensional array of square holes. Two sites are shown in top view (a) and depth profile (b); expanded view of a single site is shown in (c).

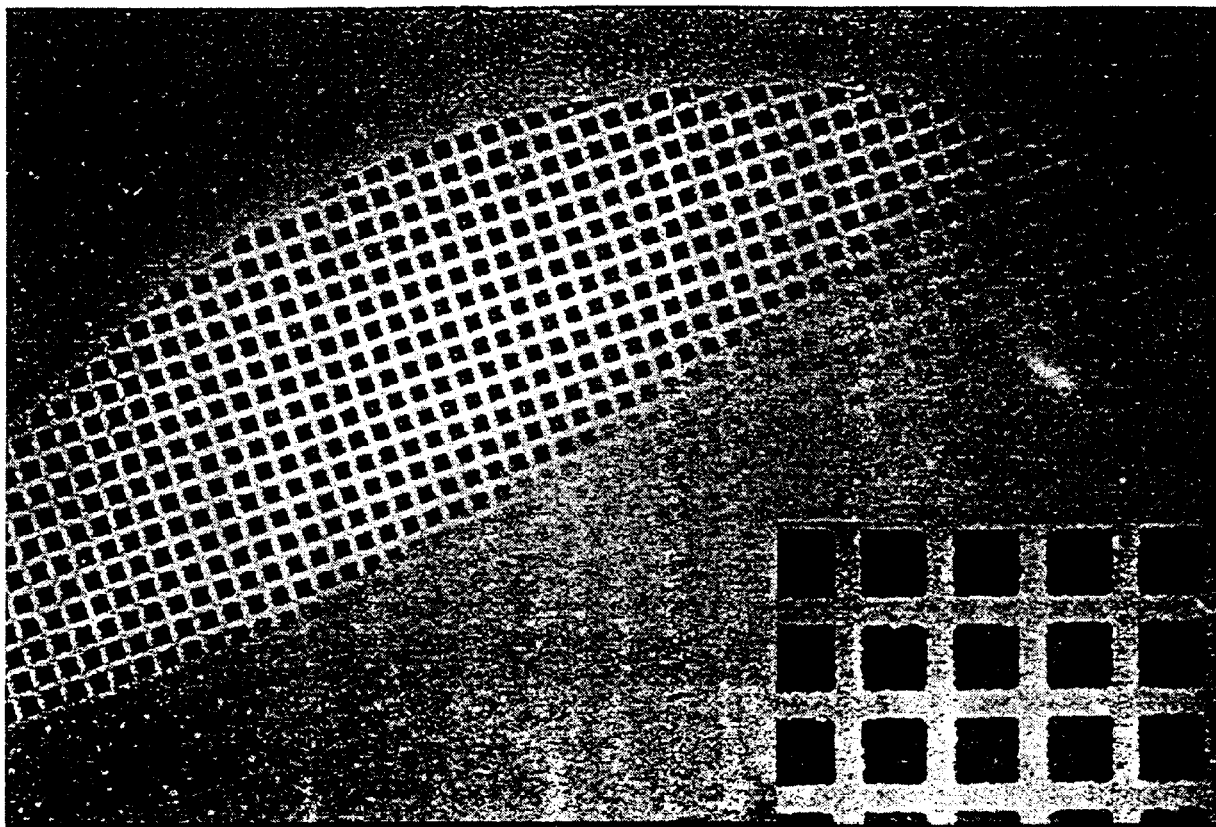


Fig. 11 A proof-of-principle of HCI masked lithography using hexadecanethiol SAMs. The insert demonstrates the edge roughness that appears to be limited by the quality of the mask. The squares are approximately 10 micrometers wide.

There are four magnetic field coils. The first is an electromagnet located in the electron gun region, called the bucking coil, which nulls the magnetic field from the superconducting magnet in the electron gun region. The next two are a pair of Helmholtz superconducting magnets that provide a field of 3 Tesla in the region of the drift tubes. This field constricts the electron beam to a filament $\sim 60 \mu\text{m}$ in diameter. The fourth is the collector magnet, surrounding the collector electrode, which helps to spread out the electron beam so that it will more uniformly distribute its energy.

A metal shielded room located in the corner of the laboratory houses four electrically floating systems for: 1) the EBIT drift tubes, 2) the collector magnet, 3) the MEVVA (see section on MEVVA) and 4) the ion beam imaging camera (see section on the Beamline). Each of these systems consists of an acrylic box that houses equipment such as power supplies, electronics, an isolation transformer and fiber optic transmitters and/or receivers. The fiber optic systems allow remote control of the power supplies located in the metal shielded room from a main control console. The voltages applied to the drift tubes (up to 500 V) float on top of the drift tube shield voltage that varies from $< 1 \text{ kV}$ to $> 30 \text{ kV}$ by way of HV voltage amplifiers and switching electronics. The collector magnet floats at the voltage of the collector electrode.

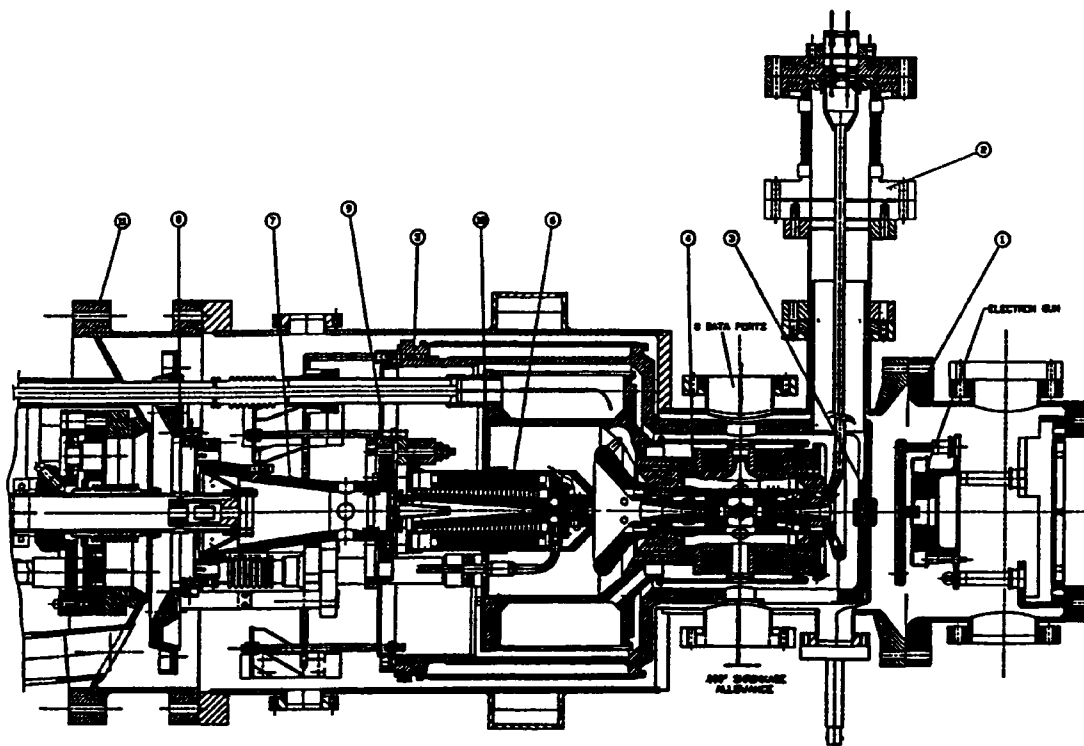


Fig. 12 A schematic cross section drawing of the EBIT showing; 1) the electron gun assembly, 2) the high voltage feed for the drift tubes, 3) the transition electrode, 4) the superconducting Helmholtz coil former and holder, 5) the liquid nitrogen shield, 6) the collector magnet, 7) collector suspension assembly, 8) einzel lens, 9) liquid nitrogen shield, 10) liquid helium dewar, 11) helium dewar support.

The cryogenic systems perform three functions. First, the liquid helium bath cools the Helmholtz magnet pair so that it is superconducting. Second, the liquid nitrogen cools the collector magnet so that it does not overheat, as well as providing an intermediate cooled jacket for the liquid helium. Third, the cold surfaces in the vacuum chamber condense gasses, reducing the base pressure from 10^{-7} Pa (10^{-9} Torr) (at room temperature) to $< 10^{-8}$ Pa (10^{-10} Torr).

Careful cryogenic system design is very important because of the humid air in the laboratory. Cold surfaces condense the water and form ice, both of which can cause problems for the electronics and high voltage equipment associated with the EBIT. For this reason, the liquid nitrogen feed lines are made of vacuum insulated pipe. The liquid nitrogen is transferred from a remote large dewar into a smaller dewar near the EBIT. This smaller dewar is designed so it is automatically filled during EBIT operation, thus guaranteeing that the intermediate jacket for the liquid nitrogen is always filled. This dewar also supplies liquid nitrogen to the collector magnet through an automatic valve. A thermocouple on the output of the collector magnet is used as feedback to control the valve. After the collector magnet, the liquid nitrogen is vented through a well-insulated line to the outdoors where a series of three large heat sinks warms it to its gaseous state. Unless the EBIT chamber is opened, the nitrogen shield and collector magnet are kept liquid nitrogen temperature constantly. This requires approximately 440 liters per day of liquid nitrogen.

Liquid helium is fed via a flexible, vacuum insulated transfer tube directly from a portable 250 liter storage dewar into the EBIT cryostat reservoir. During operation, the EBIT uses approximately 3.5 liters of helium per hour. For this reason, the cryostat is not kept at liquid helium temperature except when the EBIT is in use. Gaseous helium escapes through vent ports on the top of the EBIT. Heater tapes wound around these vent lines warm the helium exhaust and prevent water vapor condensation and icing.

MEVVA

The metal vapor vacuum arc (MEVVA)³² ion source can be used to inject nearly any metal ion into the EBIT. In the EBIT, these low-charge-state injected ions are further stripped. The MEVVA consists of five stainless steel electrodes: trigger, cathode, anode, extractor, and ground shield. These electrodes are arranged coaxially and are separated by ceramic spacers. A plasma is created when a capacitor is discharged between the trigger and cathode. Ions are accelerated to the anode and the extractor shapes the ion beam. The cathode electrode material determines the ion species that is created. We have used the following materials: Ti, V, Sc, Bi, Nd, Gd, W, and Fe.

The MEVVA is located directly above the EBIT and the metal ions are injected through a hole in the electrostatic bender of the beam line (see on Beam Line section). To inject ions, the MEVVA is triggered and the upper drift tube potential is lowered to permit the ions, to enter the trap region, and then quickly raised, to trap the ions. Typical timing sequencing and voltage values are described in detail in ref. 15.

Beam Line

A highly efficient beam line is used to transport ions extracted from the top of the EBIT.^{22,23} An electrostatic bender (see fig. 13) located above the EBIT bends the ion beam into the beam line. A fine wire mesh-covered hole in the upper plate of the bender allows ions from the MEVVA to be injected into the EBIT. Two sets of deflectors and two einzel lenses align and focus the ion beam into an analyzing sector magnet. This magnet bends the ions of a desired charge state by 90° and spatially separates the ions of different charge-to-mass ratios. Slits located at the entrance and exit of the magnet can be narrowed by translator feedthroughs to transmit only one charge-to-mass ratio.

After the sector magnet are a set of deflectors, a lens, and a second 90° electrostatic bender. This bender also has a fine wire mesh covered hole in the lower plate so that it can be biased to either bend or transmit the ion beam. Target chambers, for exposing surfaces to ions, are located both at the output of the bender as well as below it. Each chamber is equipped with an einzel lens, a second focusing electrode, and a plate with a 3 mm diameter aperture. The chamber below the bender is connected to an analysis chamber that houses a vacuum STM/AFM used for imaging surfaces that have been bombarded with ions.

To detect the ion beams, we use channel electron multipliers and Faraday cups. The electron multipliers, located in both target chambers, are capable of counting single ions and are useful for measuring low signal levels. They are also used for scanning the mass distribution. In this case the ion count is recorded while the current to the mass-analyzing sector magnet is ramped, resulting in a signal that measures the various species and their charge states present in the beam (see fig. 14). The Faraday cups measure absolute current and provide a useful verification of the signal measured by the multipliers. Faraday cups are located in the target chambers; they are mounted on motion feedthroughs and can be inserted into the beam just in front of the multipliers. Also, two movable Faraday cups are located in the beam, just after the first electrostatic bender and just before the magnet; these are used to monitor the ion current through the beam line to optimize the transmission through the various elements.

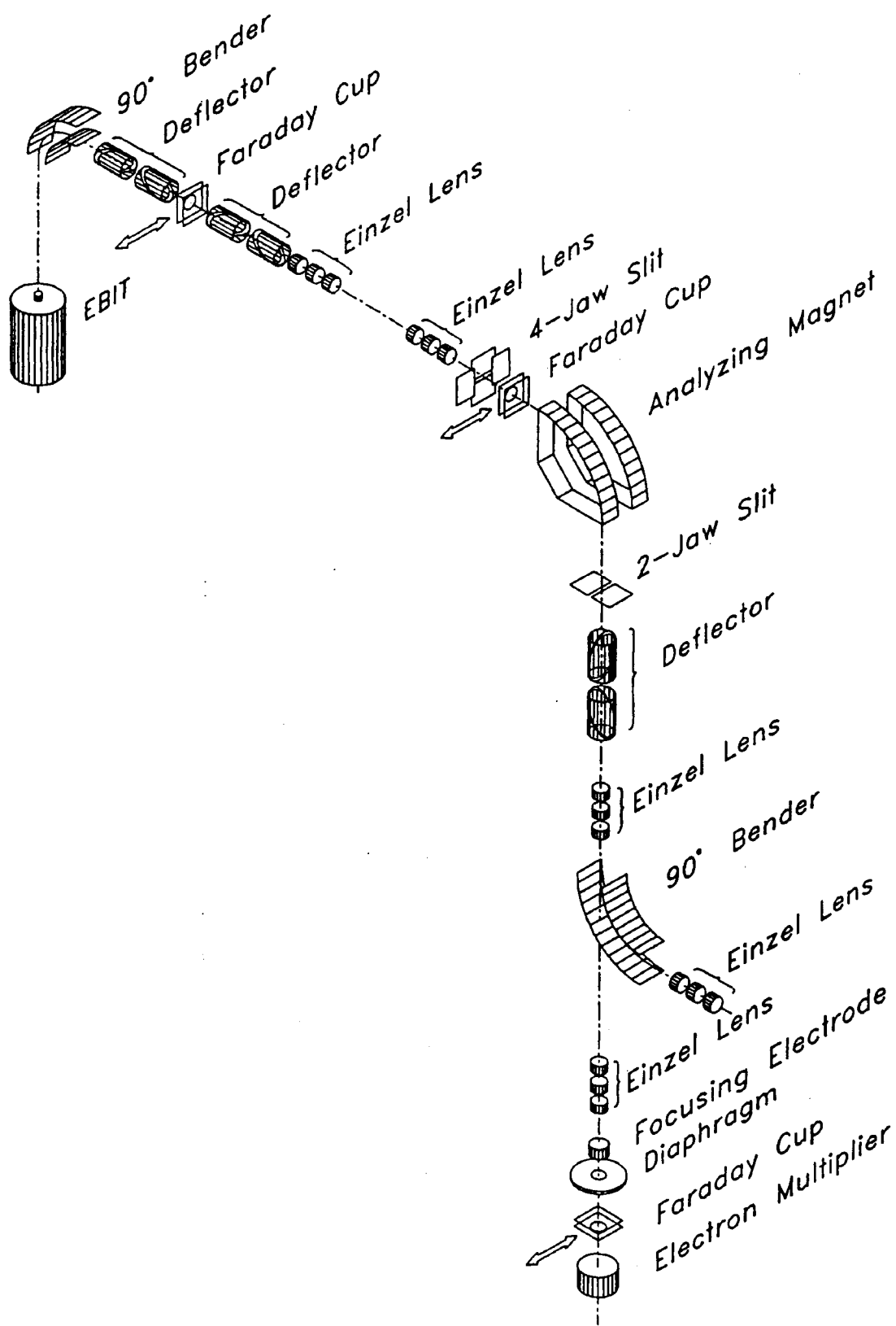


Fig. 13 A three dimensional schematic rendering of the EBIT beamline showing the major components.

In addition to the Faraday cups and channel electron multipliers, we have two imaging detectors. Each detector has a microchannel plate to intensify the signal from the ions. Just after the microchannel plate is a phosphor and a CID camera to allow for output. The image from the CID camera can be viewed on a video monitor or fed directly to a computer for analysis. One of the detectors can be mounted at various positions along the beam while the other is presently being installed permanently in the target chamber at the end of the beam line. This second detector is mounted on a motion feedthrough such that, when the target is removed, it can be inserted into the beam at the position of the target surface during exposure. In this way, we can know the spatial distribution of intensity along the beam near and at the target. For certain experiments, ions are decelerated (or accelerated) just before impacting the target. In this case, the target is biased at a negative (or positive) voltage relative to ground. To get an accurate measure of the beam profile, the imaging detector must be biased at this voltage as well. For this reason, the detector is electrically isolated and can be floated at potentials up to 10 kV.

CONCLUSION

In 1993 NIST successfully brought an EBIT on line based on a slightly modified design of the LLNL EBIT. Within one year successful experiments were being conducted involving several different types of experiment apparatus and collaborators from around the globe. After a five year period to establish a new competence within the newly Congressionally mandated NIST mission, the EBIT project was made a permanent facility at NIST with a wide range of objectives. These objectives encompass basic research studies on the physics of highly charged ions and the interaction of HCIs with surfaces.

The NIST EBIT facility has proven to be a very versatile instrument, but, we believe that we have only scratched the surface of its true versatility. There are important research avenues that we have not yet explored. One such avenue is high precision mass measurements (see the chapter in this volume by C. Carlberg). This would be a powerful technique for measuring fundamental constants, acquiring atomic reference data, and "weighing" chemical bonds and transition energies as well as contributing to a quantum standard of mass. In this concept for the EBIT, the ions are transferred to a precision hyperbolic Penning trap where the electric fields are very carefully characterized and stabilized. The ions in this secondary trap move at their resonant frequencies and this motion is monitored by measuring the induced image current on the trap electrodes. The current state-of-the-art for such measurements is on the very impressive 0.2 ppb level.³⁵ The use of HCIs rather than singly charged ions presents some advantages. The signal level would increase with the charge state and the resonant frequencies would increase, thereby increasing the resolution of the mass measurement. Another area would be to study the EBIT trap itself. Both experimental and model calculations could bear fruit on the understanding of the trap dynamics. This could possibly lead to revision in the basic EBIT design or mode of operation to make it more efficient or to permit the trap dynamics to be more accurately deconvolved from the fundamental atomic physics processes in the trap and allow more accurate measurements.

This chapter has served as an overview of the NIST EBIT project to date. Updated information on the progress of ongoing and future avenues of research can be gotten by accessing the NIST EBIT web page, <http://physics.nist.gov/MajResFac/EBIT/ebit.html> (case sensitive). This web page also has a list of the NIST EBIT publications, related web pages as well as other information.

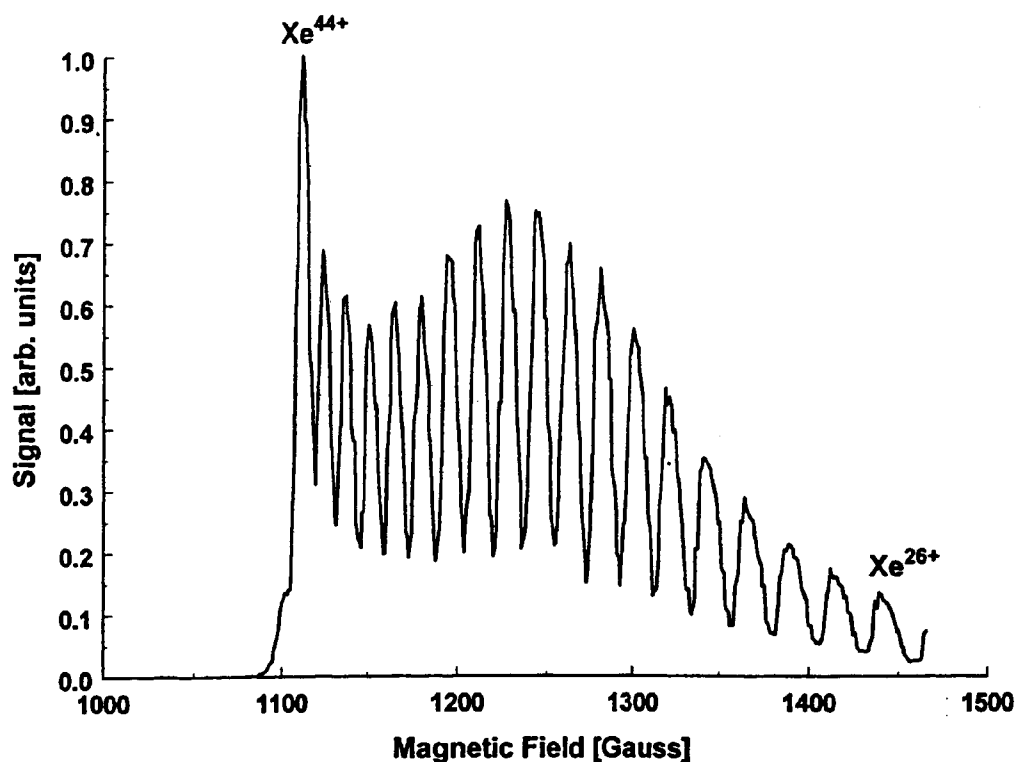


Fig. 14 A charge state distribution of extracted Xe ions from a scan of the sector magnet's field strength (voltage).

ACKNOWLEDGEMENTS

We would like to acknowledge the students, postdocs, guest scientists, collaborators, and NIST staff that have contributed to the success of the NIST EBIT project (those marked with a * have worked full-time for at least 1 year). Their affiliations can be found on the NIST EBIT web page. They are:

Helmar Adler
 Yefim Aglitskiy
 *Doug Alderson
 Attila Bader
 Andreas Bard
 *Edward Bell
 Zoltan Berenyi
 Skip Berry
 Andrew Black
 Greg Boyer
 Charles Brown
 Brent Cezairliyan
 Chris Chantler
 Hai-Ping Cheng
 David Church
 Richard Deslattes
 LaShondria Dixon
 George Doschek
 Jacques Dubau

Anatoly Faenov
 David Fanning
 Uri Feldman
 Walt Finkelstein
 Katherine Gebbie
 *John Gillaspay
 Vivik Goel
 Yukap Hahn
 Melissa Hao
 Glenn Holland
 Larry Hudson
 M. Inal
 Cornelius Jackson
 Sam Jahanmir
 Quentin Kessel
 Yong-Ki Kim
 Dave Knapp
 Martin Laming
 Mort Levine

Gene Livingston
 Jan Lorincik
 Ed Magee
 Joe McDonald
 Dan McLaughlin
 John Melngailis
 *Eric Meyer
 Stacy Mogren
 *Ronnie Minniti
 *Cornelius Morgan
 Mike Newman
 Jon Orloff
 Zoltan Onodi-szucs
 *Daniel Parks
 David Patterson
 Joe Pedulla
 *Alexander Pikin
 Ed Pollack
 *Trey Porto

*Laura Ratliff
 Curt Reimann
 Chad Riland
 James Roberts
 Christiana Ruhlicke
 Bob Schmieder
 Ryan Sears
 John Seely
 *Gino Serpa
 Dieter Schneider
 Win Smith
 Joachim Steiger
 Martin Stockli
 Jack Sugar
 *Endre Takacs
 Jessica Thomas
 Elmar Traebert
 George Whitesides
 Wolfgang Wiese

REFERENCES

1. Gillaspy, J. D., Roberts, J. R., Brown, C. M., and Feldman, U., "The NIST EBIT; A Progress Report", *AIP Conference Proceedings* 274, *Proc. VIth International Conference on the Physics of Highly Charged Ions* (Edited by P. Richard, M. Stockli, and C.D. Lin), p. 682 (AIP press, New York, 1993).
2. Gillaspy, J. D., "First Results from the EBIT at NIST", *Physica Scripta*, T71, 99 (1997).
3. Gillaspy, J. D., Aglitskiy, Y., Bell, E. W., Brown, C. M., Chantler, C. T., Deslattes, R. D., Feldman, U., Hudson, L. T., Laming, J. M., Meyer, E. S., Morgan, C. A., Pikin, A. I., Roberts, J. R., Ratliff, L. P., Serpa, F. G., Sugar, J., and Takács, E., "Overview of the Electron Beam Ion Trap Program at NIST", *Physica Scripta*, T59, 392 (1995).
4. Gillaspy, J. D., "Visible and UV light from Highly Charged Ions: Exotic Matter Advancing Technology, *IEEE LEOS*, 9 (August), 19 (1995).
5. Gillaspy, J. D., "EBIT Spectra of Highly Stripped Ions from the Visible to the X-ray", *Physica Scripta*, T65, 168 (1996).
6. Takács, E., Ratliff, L. P., and Gillaspy J. D., "X-ray, visible and electron spectroscopy with the NIST EBIT", *Hyperfine Interactions*, 108, 59 (1996).
7. McLaughlin, D. J., Hahn, Y., Takács, E., Meyer, E. S., and Gillaspy, J. D., "Radiative and Inner-Shell Dielectronic Recombination in a Highly Charged Barium Ion", *Phys. Rev. A*, 54, 2040 (1996).
8. Deslattes, R. D., "X-ray instrumentation for analysis of fluorescent and scattered radiation", *Rev. Sci. Instrum.* 63, 1128 (1992).
9. Takács, E., Meyer, E. S., Gillaspy, J. D., Roberts, J. R., Chantler, C. T., Hudson, L. T., Deslattes, R. D., Brown, C. M., Laming, J. M., Dubau, J., and Inal, M. K., "Polarization measurements on a magnetic quadrupole line in Ne-like barium", *Phys. Rev. A*, 54, 1342 (1996).
10. Aglitskiy, Y., Serpa, F. G., Meyer, E. S., Gillaspy, J. D., Brown, C. M., Faenov, A. Ya. And Pikuz, T. A., "The Use of a Spherically Curved Crystal Spectrometer for X-ray Measurements on Electron Beam Ion Trap", *Physica Scripta*, 58, 178 (1998).
11. Morgan, C. A., Serpa, F. G., Takács, E., Meyer, E. S., Gillaspy, J. D., Sugar, J., Roberts, J. R., Brown, C. M., Feldman, U., "Observation of visible and uv magnetic dipole transitions in highly-charged xenon and barium", *Phys. Rev. Lett.* 74, 1716 (1995).
12. Feldman, U., Indelicato, P. and Sugar, J., "Magnetic dipole line from U-LXXI ground-term levels predicted at 3200-Å" *J. Opt. Soc. Am. B*, 8, 3 (1991)
13. Adler, H., Meyer, E. S., Serpa, F. G., Takács, E., and Gillaspy, J. D., "Fabry-Perot Spectroscopy of a Visible Magnetic Dipole Transition in Ba³⁴⁺", *Nucl. Instrum. and Meth B*, 98, 581 (1995).
14. Serpa, F. G., Bell, E. W., Meyer, E. S., Gillaspy, J. D., Roberts, J. R., "Kr spectra from an electron-beam ion trap: 300 μm to 460 μm", *Phys. Rev. A*, 55, 1832 (1997).
15. Serpa, F. G., Meyer, E. S., Morgan, C. A., Gillaspy, J. D., Sugar, J., Roberts, J. R., Brown, C. M., and Feldman, U., "Anomalous Z dependence of a magnetic dipole transition in the Ti I isoelectronic sequence", *Phys. Rev. A*, 53, 2220, (1996).
16. Serpa, F. G., Morgan, C. A., Meyer, E. S., Gillaspy, J. D., Träbert, E., Church, D. A., and Takács, E., "Measurement of a magnetic dipole transition probability in highly charged Xe using an electron beam ion trap (EBIT)", *Phys. Rev. A*, 55, 4196 (1997).
17. Beiersdorfer, P., Schweikhard, L., Lopez-Urrutia, J. Crespo and Widmann, K., "The magnetic trapping mode of an electron beam ion trap: New opportunities for highly charged ion research", *Rev. Sci. Instrum.* 67, 3818 (1996).
18. Serpa, F. G., Gillaspy, J. D., and Träbert, E., "Lifetime measurements in the ground configuration of Ar¹³⁺ and Kr²²⁺ using an Electron Beam Ion Trap", *J. Phys. B*, 31, 3345 (1998).
19. Paterson, D. P., Chantler, C. T., Tran, C. Q., Hudson, L. T., Serpa, F. G. and Deslattes, R. D., "Absolute Calibration of and X-ray Spectrometer on the NIST Electron-Beam Ion Trap: Control, Design and Systematics". *Physica Scripta*, T73, 400 (1997).
20. Chantler, C. T., Paterson, D., Hudson, L. T., Serpa, F. G., Gillaspy, J. D., Deslattes, R. D., "Progress towards absolute X-ray spectroscopy on the NIST Electron-Beam Ion Trap: current status and results", *Physica Scripta*, T73, 87 (1997).
21. Schmieder, R. W. and Bastasz, R., "Surface Damage Caused by Single, Low-Energy, High-Charge-State Ions", *AIP Conference Proceedings* 274, *Proc. VIth International Conference on the Physics of*

- Highly Charged Ions* (Edited by P. Richard, M. Stockli, and C.D. Lin), p. 690 (AIP press, New York, 1993).
22. Pikin, A. I., Morgan, C. A., Bell, E. W., Ratliff, L. P., Church, D. A., and Gillaspy, J. D., "A Beam Line for Highly-Charged Ions Extracted from the NIST EBIT", *Rev. Sci. Instrum.*, **67**, 2528 (1996).
 23. Ratliff, L. P., Bell, E. W., Parks, D. C., Pikin, A. I., Gillaspy, J. D., "Continuous Highly-Charged Ion Beams from the NIST EBIT", *Rev. Sci. Instrum.*, **68**, 1998 (1997).
 24. Cheng, H. P. and Gillaspy, J. D., "Nano-scale Modification of Silicon Surfaces via Coulomb Explosion", *Phys. Rev. B*, **55**, 2628 (1996).
 25. Cheng, H. P. and Gillaspy, J. D., "Large Scale Molecular Dynamics Simulation of a Surface Coulomb Explosion", *Application of Accelerators in Research and Industry, AIP conference proceedings 392*, (Edited by J. L. Duggan and I. L. Morgan), p 197, (AIP Press, New York, 1997).
 26. Cheng, H. P., and Gillaspy, J. D., "Surface Coulomb Explosions: The Influence of Initial charge Distributions", *Computational Materials Science*, **9**, 285 (1998).
 27. Ruehlicke, C., Briere, M. A., Schneider, D., "AFM studies of a new type of radiation defect on mica surfaces caused by highly charged ion impact", *Nucl. Instrum. Meth. Phys. Res. B*, **99**, 52 (1995).
 28. Parks, D. C., Stockli, M. P., Bell, E. W., Ratliff, L. P., Schmieder, R. W., Serpa, F. G., and Gillaspy, J. D., "Non-kinetic Damage on Insulating Materials by Highly Charged Ion Bombardment", *Nucl. Instrum. and Meth. Phys. Res. B*, **134**, 46 (1998).
 29. Gillaspy, J. D., Parks, D. C., and Ratliff, L. P., "Highly Charged Ion Masked Ion Beam Lithography", *J. Vac. Sci. Technol. B*, **16**, 1 (1998).
 30. Ratliff, L. P., Minniti, R., Bard, A., Bell, E. W., Gillaspy, J. D., Parks, D., Black, A. J. and Whitesides, G. M., "Exposure of self-assembled monolayers to highly charged ions and metastable atoms", (to be Submitted).
 31. Takács, E., Onodi-Szucs, Z., Ratliff, L. P., Gillaspy, J. D., Pálincás, J., "X-ray emission for 3-137 keV Ar¹⁷⁺ impacting SiO₂", *Nucl. Instrum. Meth. Phys. Res. B*, **124**, 431 (1997).
 32. Brown, I. G., Galvin, J. E., Gavin, B. F. and MacGill, R. A., "Metal vapor vacuum arc ion source", *Rev. Sci. Instrum.* **57**, 1069 (1986).
 33. Natarajan, V., Boyce, K. R., DiFilippo, F., and Pritchard, D. E., "Precision Penning Trap Comparison of Nondoublets: Atomic Masses of H, D, and the Neutron", *Phys. Rev. Lett.* **71**, 1998 (1993).

TOPICAL REVIEW

Highly charged ions

J D Gillaspay

Atomic Physics Division, National Institute of Standards and Technology, Gaithersburg, MD 20899-8421, USA

E-mail: john.gillaspay@nist.gov

Received 5 April 2001, in final form 27 July 2001

Published 24 September 2001

Online at stacks.iop.org/JPhysB/34/R93**Abstract**

This paper reviews some of the fundamental properties of highly charged ions, the methods of producing them (with particular emphasis on tabletop devices), and their use as a tool for both basic science and applied technology. Topics discussed include: charge dependence and scaling laws along isoelectronic or isonuclear sequences (for wavefunction size or Bohr radius, ionization energy, dipole transition energy, relativistic fine structure, hyperfine structure, Zeeman effect, Stark effect, line intensities, linewidths, strength of parity violation, etc), changes in angular momentum coupling schemes, selection rules, interactions with surfaces, electron-impact ionization, the electron beam ion trap (EBIT), ion accelerators, atomic reference data, cosmic chronometers, laboratory x-ray astrophysics, vacuum polarization, solar flares, ion implantation, ion lithography, ion microprobes (SIMS and x-ray microscope), nuclear fusion diagnostics, nanotechnology, quantum computing, cancer therapy and biotechnology.

1. Introduction

Most of the universe consists of highly ionized matter (Fang and Canizares 2000). Because it is exceedingly rare on Earth, and because we are blindfolded from observing cosmic sources by the relatively high x-ray absorption of our atmosphere, the scientific study and application of highly ionized matter has been limited. Atomic physics and conventional ion beam technologies, for example, were developed in the virtual absence of laboratory access to highly charged ions. Today, however, powerful devices are available that can preferentially produce any ionization stage of any naturally occurring atom. Some of these devices (Levine *et al* 1988) are small enough to fit on a tabletop. Others are huge devices that produce ions travelling near the speed of light (Angert 1991, Stohlker *et al* 2000). These two extremes each have their own particular applications, but they share the property of providing a window into a part of the universe that is still relatively unexplored and that can be expected to impact a variety of fields.

This review covers a broad range of research with highly charged ions by using selected results from my own work and that of others to illustrate general concepts and provide an introduction to emerging applications. More details and breadth of coverage of the fundamentals can be found in comprehensive earlier reviews (Martinson 1989), books (Beyer *et al* 1997, Beyer and Shevelko 1999, Gillaspay 2001, Marrus 1982, 1988, Pal'chikov and Shevelko 1995) and conference proceedings (Lindgren *et al* 1992, Mokler *et al* 1998) for example.

After this introduction, section 2 covers the fundamental aspects of the ions themselves, while section 3 focuses on the experimental methods of producing them, with particular emphasis on the electron beam ion trap (EBIT). Section 4 provides an overview of a variety of applications in basic science and applied technology. Section 5 concludes with a summary table of the various scaling laws discussed in this paper, and some remarks about the future.

The functional definition of a 'highly charged ion' (HCI) varies. To many, it refers to any atom that is missing more than one or two electrons. To others, several dozen electrons must be missing before the label 'highly charged' is used. For the purposes of this review, I adopt the following definition: an HCI is any atom that has been stripped of a large number of electrons ($Q \gg 1$), so that the total energy yielded during reneutralization (E_0) is outside the realm of ordinary experience with laboratory ions ($E_0 \gg 10$ eV).

This definition overlaps with what are frequently referred to as *multiply charged* or *multicharged ions* at the lower end of this spectrum (typically $Q = 2-9$, with $E_0 < 1000$ eV), as well as what are sometimes called *very highly charged ions* at the upper end of the spectrum (e.g. $Q = 92$ with $E_0 \sim 750\,000$ eV). The tremendous variety of HCIs makes almost every generalized conclusion and 'rule of thumb' in the field suspect, but it also opens up an enormous range of possibilities for discovery.

2. Highly charged ions: fundamental aspects

2.1. Isoelectronic and isonuclear sequences

To explore the full range of phase space spanned by HCIs, one might first select a particular elemental species (atomic number Z) and then remove sequentially a number of electrons ($Q = 1, 2, 3, \dots$) to produce a series of ions with the same nucleus but a variety of N -electron structures ($N = Z - Q$). Since this is how the ions are actually produced, it is a natural way for an experimentalist to organize his data. This type of phase space cut through the (Z, Q) space of all possible HCIs is called an *isonuclear sequence*.

From the point of view of theory, however, scaling laws are often easier to understand by fixing the electronic number N , and varying the species Z . Data presented in this way are called an *isoelectronic sequence*. Conceptually, one may think of an isoelectronic sequence as starting with a particular neutral atom, and asking how the electronic properties of that atom change as the nuclear charge is increased in a series of unit steps.

An isoelectronic sequence, therefore, is like having a 'knob' on the nuclear charge that one can turn up, pulling the electronic cloud into a more tightly bound configuration and shrinking the size of the atom. An isonuclear sequence, on the other hand, is like peeling the layers of an onion away, to reveal the tightly bound cores of atoms. Both approaches lead to the same end result: an object with a highly compact spatial wavefunction (figure 1).

Because there are two 'charges', electronic (Q) and nuclear (Z), the phrase 'scaling with charge' is sometimes ambiguous. The more specific phrase 'scaling with Z ' refers to an isoelectronic sequence, while 'scaling with Q ' is most appropriate for an isonuclear sequence. Along an isoelectronic sequence, Z and Q differ by only a constant, so the two are sometimes

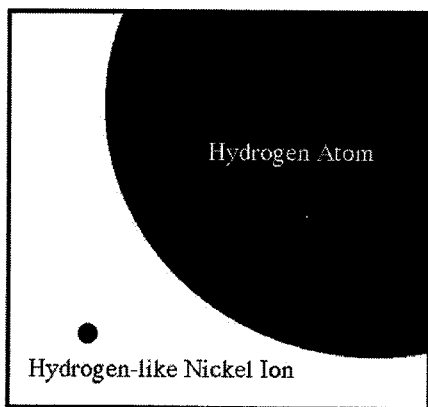


Figure 1. Schematic representation of the relative spatial extent of the wavefunction of a hydrogen-like nickel ion ($Z = 28$) compared with that of a hydrogen atom. The ratio is similar to the size of the planet Neptune compared with the size of the Sun.

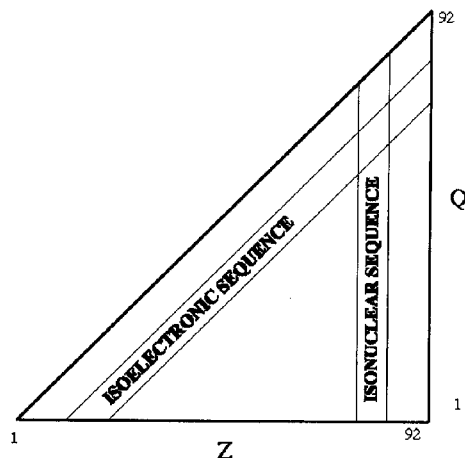


Figure 2. Schematic phase space plot of the range of all possible positive ions with nuclear charge Z and electronic charge $|Q| < Z$, up to $Q, Z = 100$. Examples of isoelectronic and isonuclear sequences are indicated.

used (loosely) interchangeably. In the limit of highly charged few-electron ions, $Z \sim Q$ so the two can be interchanged more correctly.

Isoelectronic sequences begin at $Z = N + 1$, while isonuclear sequences begin at $Q = 1$. Figure 2 illustrates schematically an isoelectronic sequence and an isonuclear sequence on a plot of the full (Z, Q) phase space for positive ions. Isotopes can be thought of as extending along a third axis that projects out of the page. Most laboratory experience is clustered around the bottom axis ('ordinary ions'). Negative ions (below the horizontal axis) are not shown because only a few of them are stable and they are not dealt with in this review. All of the positive ions, on the other hand, are predicted to be stable within the framework of elementary quantum mechanics. In most cases this prediction holds true, although quantum field theory describes a number of interesting exceptions that are described in sections 4.2 and 4.4 below. In discussing general scaling laws in this paper, I will consider one-electron (hydrogen-like) ions as the prototypical case.

2.2. Size

Perhaps the most fundamental and physically tangible aspect of an atom is its size (spatial extent of the electronic wavefunction). The great diversity of physical properties exhibited by the atoms across the periodic table emerges essentially from variations in the size and shape of the wavefunction. It is perhaps remarkable, then, that all atoms are roughly the same size: a few tenths of a nanometre. This ‘typical size of an atom’ is the first rule of thumb that must be abandoned in making the shift from neutral atoms to highly charged ions. U^{91+} , for example, has a wavefunction that is nearly 100 times more spatially compact than that of a hydrogen atom. This gives a sense of the great variation in physical properties that one can expect to find among HCIs.

A simple isoelectronic scaling law for one-electron ions predicts that the size of the wavefunction (Bohr radius = R) varies as the reciprocal of the ion charge,

$$\begin{aligned} R &\sim 1/Z \\ &\sim 1/(Q+1) \sim 1/Q \quad \text{for } Q \gg 1. \end{aligned} \quad (1)$$

Figure 1 is drawn to scale using this formula. When the approach to a one-electron ion is viewed along an isonuclear sequence, on the other hand, the relatively smooth scaling of size with Q indicated above gives way to abrupt jumps at closed-shell configurations.

For very highly charged ions, the wavefunction size becomes so small that one must begin to think about the ions in a qualitatively different way. The simplistic view of an HCI as a tiny Bohr atom with a charge is inadequate because the relevant length scales enter a new regime. Consider the hydrogen isoelectronic sequence. In the atomic limit, the system has planetary analogies that can be quite useful for gaining intuition. The electron orbits the nucleus at a characteristic distance that is large compared with both the spatial extent of the nucleus and the Compton wavelength of the electron (the fundamental length scale at which the electron ceases to behave as a point particle with finite charge). The ordinary hydrogen atom, like the solar system, is mainly empty space. At the high end of the isoelectronic sequence, however, the Bohr radius ($R \sim 50/Z$ pm) falls below the Compton wavelength (2 pm). Under these conditions, single-particle quantum mechanics begins to break down and semiclassical reasoning based on it becomes of limited value. Indeed, even the classical concept of a central Coulomb potential breaks down to some extent. Quantum field theory is required to describe the system. The resulting new picture is one in which the structure of the vacuum of space itself is significant. The concept of empty space is replaced by one in which everything is bathed in a sea of virtual positron–electron pairs, popping in and out of existence within the small window of time during which the Heisenberg uncertainty principle allows energy conservation to be violated. At short distance scales, it becomes apparent that the virtual sea of charge from the vacuum becomes polarized and screens the actual ‘bare’ charge of the electron. The closer one gets, the more the screening is avoided and the higher the electron charge appears to be. As the electron continues to ‘decloak’ from the vacuum at increasingly shorter length scales, the apparent charge that it carries rises significantly above the conventional value of 1.6×10^{-19} C, and ultimately approaches its bare value of infinity. The conceptual jump from a hydrogen atom to a hydrogen-like uranium ion is perhaps as great, or greater, than the jump from a classically orbiting planet to a quantum mechanical atom. For a more comprehensive introduction to the quantum field theory of HCIs, see Greiner *et al* (1985).

The reduction in size of an HCI with increasing Z results in a tremendous compression of the wavefunction density at the upper end of an isoelectronic sequence. The above scaling law for atomic size predicts that a hydrogen-like ($N = 1$) uranium atom ($Z = 92$) has an electronic density that is 780 000 times higher than that of a hydrogen atom. This compression

of the wavefunction into the space near the nucleus dramatically alters the relative importance of various physical effects that determine the atomic structure. The consequences of this are elaborated on in section 2.3 below.

A hint of the wavefunction compression that is so strong in HCIs is present even in the outer (valence) electrons of heavy *neutral* atoms. If an outer electron has zero angular momentum, then its wavefunction extends to the nucleus, and the electron can be thought of as spending a finite fraction of its time inside the orbits of the core electrons. During this time inside the core, the valence electron feels the full (unscreened) nuclear charge, and is pulled in closer toward the nucleus. In quantitative quantum mechanical terms, the probability density of a valence s-electron at the origin scales as Z (Foldy 1958). This linear scaling is a remnant of the full Z^3 scaling of an unscreened hydrogen-like ion.

This remnant scaling is one of the reasons that parity-violation experiments are done with heavy atoms. These atoms concentrate the valence electron wavefunction at the nucleus where the short-range interaction caused by the exchange of a massive vector Z -boson (weak neutral current) between the electron and a nucleon is non-zero. For neutral atoms, the observable in such experiments scales up as Z^3 , while for HCIs, it scales up as Z^5 (Fortson and Lewis 1984). There are also weak neutral current effects that occur between electrons (far from the nucleus), but these are generally smaller and thus have typically been neglected in experiments with neutral atoms (Bouchiat and Bouchiat 1974, Fortson and Lewis 1984). The compression of the electronic wavefunction throughout an HCI should amplify this effect as well. An additional advantage to using HCIs in parity-violation experiments is that the number of electrons can be reduced to a small value that can be accurately handled by theory. This is important because the experiments are based on observing interferences which require conventional atomic structure calculations to extract a quantitative value for the fundamental parity-violation parameter, the weak nuclear charge (Bouchiat and Bouchiat 1997). Theoretical issues and proposed experiments to use HCIs to test the parity-violating aspects of the standard model have been presented recently in the literature (Bednyakov *et al* 2000, Dunford 1996, Pindzola 1993, Schafer *et al* 1989, Zolotarev and Budker 1997).

2.3. Energy

2.3.1. Kinetic energy. The two different types of energies associated with ions, potential and kinetic, are sometimes confused, particularly when discussing beams of highly charged ions. Conventional ion beams used in the microelectronics industry or in materials science are comprised of singly charged ions with a kinetic energy in the keV to MeV range. This kinetic energy dominates the interaction of such ion beams with surfaces, and hence the internal (potential) energy liberated when the ion neutralizes itself upon contact with the surface is usually neglected. Since conventional ions carry only about 10 eV of potential energy (the ionization potential), neglecting it is a very good approximation. For beams of highly charged ions in the same kinetic energy range, however, the relative importance of kinetic energy to potential energy is reduced, or even inverted—sometimes by a large factor. The implications of an unusually large potential energy are discussed from an applications point of view in sections 4.6.2 and 4.6.3 below.

The kinetic energy that an HCI attains when it accelerates through an applied potential V is a factor of Q larger than it would be if it were singly charged. Modest voltages or stray electric fields can therefore have a large effect on the ion velocity. This effect can be exploited to produce fast ion beams relatively easily, as discussed in section 4.6.1 below. This effect can also lead to non-intuitive results in standard electrostatic ion beam optical elements. For example, a simple ‘velocity filter’, formed by passing a beam of a particular mass of ion

through an electric field normal to its direction of motion, and selecting only those ions that are bent by a particular angle, can actually pass ions with widely different velocities as long as they also have widely different charge states (conventionally assumed to be 1). For HCIs produced at rest along a potential gradient and accelerated to a different common potential, a simple velocity filter becomes an unusual type of filter that passes only those ions produced at specific locations in space, independent of the widely different velocities that they obtain after accelerating away from their point of origin. This effect is exploited in the efficient extraction of ion beams from the devices described in section 3.3 below.

The definition of a ‘fast’ and ‘slow’ HCI often varies, depending on an experimenter’s particular experience. A rather objective benchmark for the crossover from fast to slow is set by the orbital velocity of the outermost electrons in neutral atoms. This velocity is less than the speed of light by approximately a factor of $\alpha \sim 1/137$ (the fine structure constant). Processes such as charge capture by an HCI from a background gas molecule take on a very different character at collision velocities much above or below the crossover velocity of the target.

In addition to the fundamental difference between fast and slow ions described above, there is also a practical one: experiments at velocities far above the crossover velocity (‘fast ions’) require the use of large accelerator facilities, while those done with ‘slow ions’ can be done with table-top devices. This forms a natural division of the two research communities.

Within the accelerator community, ion velocity is often expressed in terms of the quantity ‘keV/u’, the ratio of the kinetic energy to the rest mass of the ion, with the mass measured in ‘u’ (unified atomic mass units) and the energy measured in ‘keV’ (joules divided by 1000 times the charge of the electron). This quantity (keV/u) is roughly equal to the kinetic energy divided by the number of nucleons (A), but it is often referred to simply as the ‘energy’ of the ions. Note that ions of the same charge but different mass, accelerated through a given electric field, will have the same energy but may have greatly different velocities. Dividing the energy by the mass, on the other hand, will uniquely specify a velocity factor, from which the velocity, v , can be extracted using the following expression:

$$\begin{aligned} \frac{\text{keV}}{u} \times 1.07 \times 10^{-6} &= \frac{T(v)}{m_0 c^2} = \frac{\sqrt{p^2 c^2 + m_0^2 c^4} - m_0 c^2}{m_0 c^2} \\ &= \sqrt{\frac{1}{1 - v^2/c^2}} - 1 = \frac{1}{2} \frac{v^2}{c^2} + \frac{3}{8} \frac{v^4}{c^4} + \frac{5}{16} \frac{v^6}{c^6} + \dots \end{aligned} \quad (2)$$

where $T(v)$ is the relativistic expression for kinetic energy (Lorrain and Corson 1970) and keV/u is the kinetic energy per unit rest mass, as described above. Sometimes the ‘u’ is dropped (implied), leading to possible confusion about whether energy or velocity is being specified. Another potentially confusing practice, particularly prevalent among the community of ‘table-top’ HCI researchers, is to normalize the kinetic energy by the ion charge, rather than the number of nucleons. The ion energy is then expressed in units of ‘keV/q’ ($q = Q$, the dimensionless ion charge state). This is frequently done because a variety of ion charge states may be created at a fixed potential and then accelerated to another potential, resulting in a variety of ion energies and velocities (but a single ‘keV/q’). Unfortunately, again, sometimes the denominator is implied, leading to potential confusion. As an example, to bring the various issues discussed above together, the crossover velocity for neutral target atoms (approximately equal to that of a hydrogen atom, $v_0 = 2.2 \times 10^6 \text{ m s}^{-1}$), corresponds to 25 keV/u, and can be produced by accelerating a typical hydrogen-like atom (with $A/Q \sim 2.5$) through a potential difference of approximately 62 kV.

Researchers studying the interaction of HCIs with surfaces have another benchmark velocity that defines what might be called ‘ultra-slow’ HCIs. This is the minimum impact

velocity (v_m) that an ion can have, under the influence of unscreened image charge acceleration by a surface. If one tries to perform an experiment by directing an ion beam onto a surface with velocity $v < v_m$, the ions will automatically accelerate to v_m shortly before impact. For very highly charged ions, v_m can be surprisingly close to the crossover velocity. For a typical surface, the energy gain due to image charge acceleration exceeds 1 eV by approximately a factor of $Q^{3/2}$ (Winter and Aumayr 1999). For the case of hydrogen-like xenon, the minimum impact velocity is about 1% of the crossover velocity. This 1% scales very weakly with charge (roughly as $Z^{1/4}$) along the hydrogen isoelectronic sequence, ranging from 0.3%–1.2% for $Z = 2$ –92. For a fixed atomic mass, the factor of 1% scales as $Q^{3/4}$, so for very low charge states v_m is many orders of magnitude less than v_0 .

The observation of impact velocities below v_m (down to zero) has been reported on imperfectly conducting surfaces (Briand *et al* 1997b, 2000). In fact, the observation of a so-called ‘trampoline effect’ has been reported, in which the net surface charge reverses its sign and causes an incident HCI to be repelled backwards after reaching a distance of several nanometres from the surface. This effect remains controversial, however, (Aumayr *et al* 1997, Briand *et al* 1997a).

2.3.2. Potential energy. To further complicate issues, there are two types of potential energy that are distinct for HCIs: the ionization energy and the neutralization energy. For an ordinary ion, these two are identical in magnitude, but for HCIs they can differ by more than a factor of ten. This is because ‘ionization energy’ is the energy required to remove *one* electron, producing the charge $Q + 1$ from an ion with one lower charge, while ‘neutralization energy’ is the energy released in replacing *all* of the missing electrons. The ionization energy is most relevant to the production of the ions, which typically occurs in a step-wise process (one electron removed after another), while the neutralization energy is more relevant to the impact of ions on surfaces.

The ionization energy (U) grows rapidly as the ion charge increases. Simple Coulomb potential scaling for one-electron ions predicts that there are two factors of charge involved, one that arises directly from the increased amount of nuclear charge and another from the reduced distance from that charge:

$$U(Z) \sim Z/R \sim Z/(1/Z) = Z^2. \quad (3)$$

For multielectron systems, the increase in U with charge along an isonuclear sequence will be reduced and less smooth, reflecting the atomic shell structure and the variation in electronic screening. All species of ions will approach a Q^2 enhancement of ionization potential in the high charge limit ($Q \rightarrow Z$). Figure 3 illustrates these aspects for the case of xenon.

The neutralization energy (E_0) is given by the sum of all the ionization energies of the charge states at and below that of the ion. Thus the energy E_0 is enhanced by two factors: the fact that it is the sum of several (numbering Q) ionization energies, and the fact that the individual ionization energies in the sum are themselves enhanced by the factor discussed above. Examples of the neutralization energy as a function of charge are presented in figure 4.

2.3.3. Photon energy. Another set of key energies associated with HCIs are those which separate the various eigenstates, and hence determine the wavelength of emitted light. Although all of the energy levels become more tightly bound as the charge increases isoelectronically, the deeper levels experience the largest change. Semiclassically, the concentric Bohr orbits of the electrons are pulled in towards a Coulomb singularity with a strong gradient, like matter falling into a black hole. The resulting tidal forces within the ion cause the energy levels to

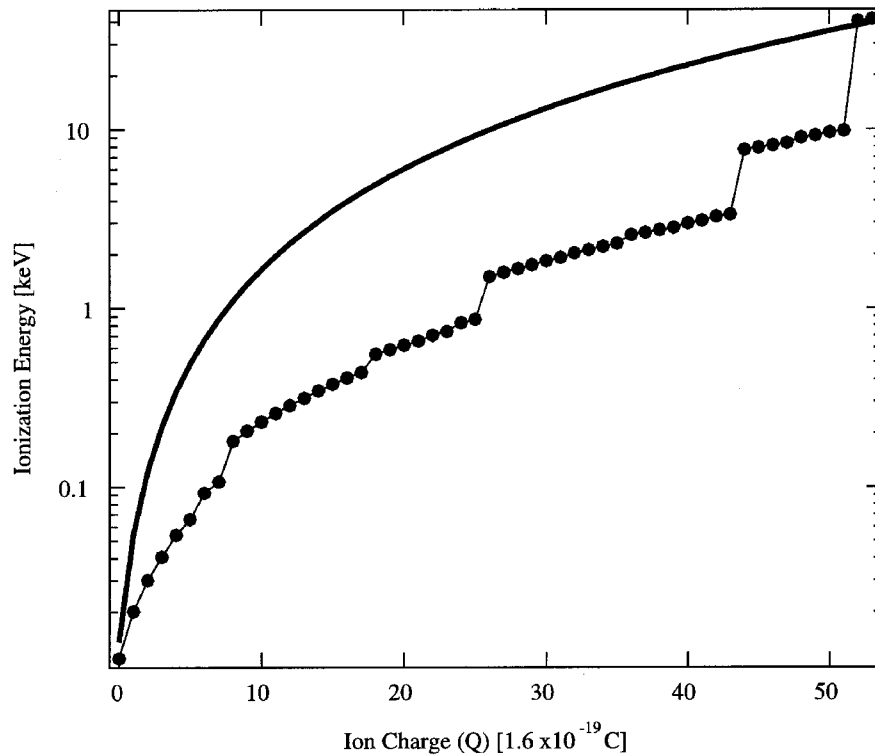


Figure 3. Ionization energy of xenon as a function of ion charge Q (isonuclear sequence). The smooth curve shows the scaled ionization potential of hydrogen, $0.0136Q^2$, for comparison (isoelectronic sequence).

become more separated. The resulting decrease in the wavelength of the emitted photons is dramatic, as shown by the example plotted in figure 5. The various spectral regions indicated in this plot are defined following the *Physics Vade Mecum* (Anderson 1981).

The rate at which photon energies scale up with charge can vary widely, depending on the terms in the Hamiltonian which lead to the separation of the energy levels in the first place. The separation between states with adjacent principal quantum numbers ($\Delta n = 1$) is determined primarily by the Coulomb potential, and therefore the Z^2 scaling described above for ionization potentials also applies to the photon energies. For transitions between fine structure levels ($\Delta n = 0$), however, the shifts in the energy levels are dominated by relativistic effects, which cause the photon energies to scale much more strongly with charge—typically as Z^4 .

To understand the Z^4 variation in photon energy for fine structure transitions, consider the formula for the relativistic energy of a free particle, expanded for velocities slow compared with the speed of light,

$$E = \sqrt{p^2c^2 + m_0^2c^4} \approx m_0c^2 + \frac{p^2}{2m_0} - \frac{p^4}{8m_0^3c^2} + \dots \quad (4)$$

The first and second terms give nothing new—just the rest mass and the classical kinetic energy. The third term, however, is the relativistic variation of mass that contributes to the fine structure shift. Because the orbital angular momentum ($l = r \times p$) is fixed by universal quantum numbers, p must increase as the atomic size (or semiclassically, the radius r of the orbit) decreases isoelectronically. For example, the velocity of electrons in the ground

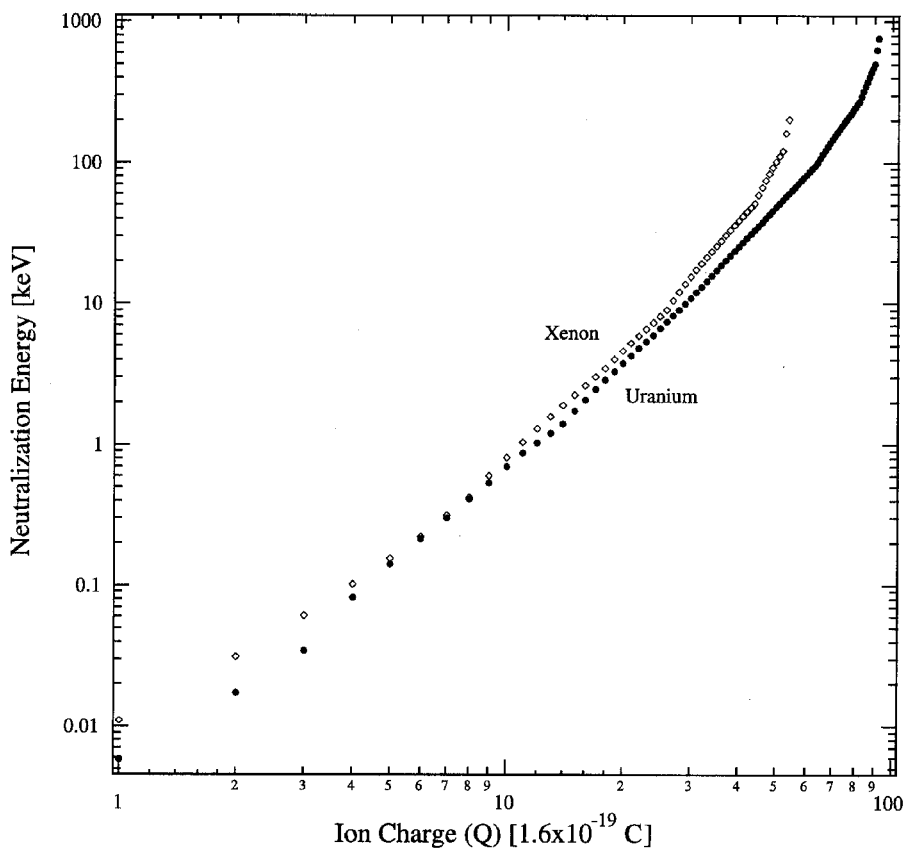


Figure 4. Neutralization energy for xenon and uranium as a function of ion charge. Note, by comparing with figure 3, that 40% of the neutralization energy of bare xenon comes from the two deepest energy levels. This fraction ranges from 100% to 34% across the periodic table of naturally occurring elements.

state of hydrogen-like ions is $v/c = \alpha Z$. Thus, the linear decrease in atomic size with increasing charge results in a linear increase in p , which produces the Z^4 scaling described above.

Even more illuminating is the part of the fine structure shift that is due to the spin-orbit interaction. This shift can be understood semiclassically as arising from the magnetic dipole interaction of the electron spin with the effective magnetic field generated in the reference frame of the orbiting electron by its motion through the electric field of the nucleus. This magnetic field is proportional to the vector product of the nuclear Coulomb field and the electron's orbital velocity, both of which scale up isoelectronically with Z :

$$B = cv \times E \sim Z \times Z^3 = Z^4. \quad (5)$$

In this expression, the electric field scales up with one power of Z because of the increased nuclear charge, and with two additional powers of Z because of the shrinking orbital radius which places the electron closer to the $1/r^2$ singularity at the nucleus. In summary, the overall scaling of the fine structure splitting is proportional to Z^4 , and therefore rapidly grows to become 'not-so-fine (or small)' in comparison with the principal splitting between energy levels ($\Delta n = 1$).

With these scaling laws in mind, it is easy to see how transitions that produce photons in the visible spectral range for neutral atoms rapidly scale up with charge to produce x-ray

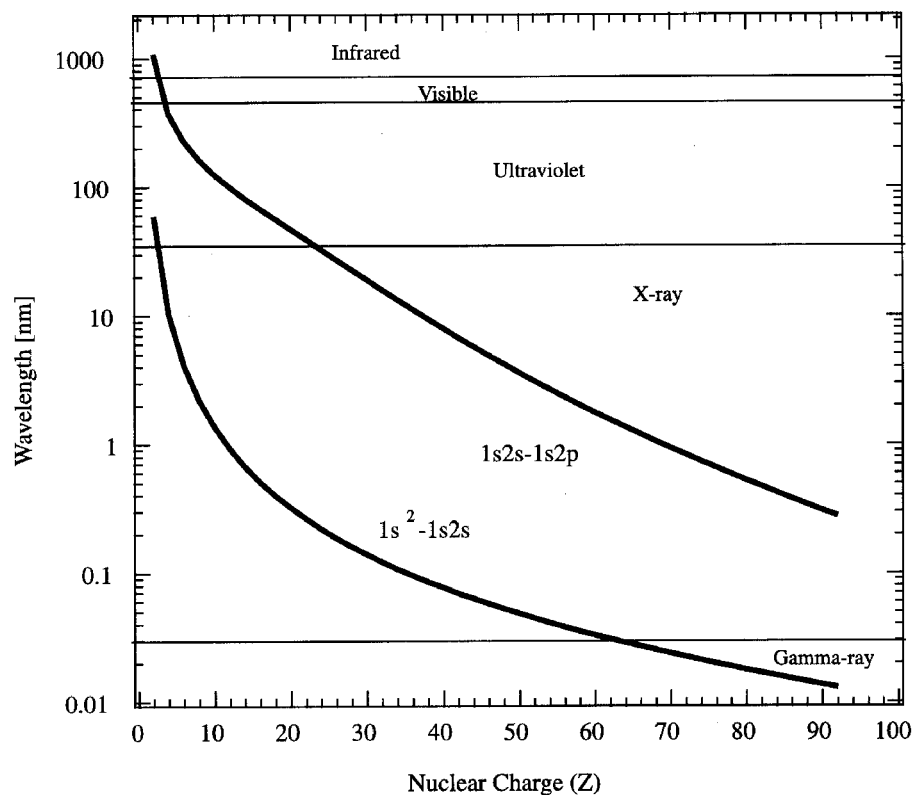


Figure 5. Examples of photon wavelength scaling with ion charge. Plotted are the calculated (Plante *et al* 1994) resonance lines ($1s^2-1s2p$, lower curve) and lines from the lowest-lying metastable triplet levels ($1s2s-1s2p$, upper curve) of helium-like ions.

photons in HCIs. A Z increase of only a factor of six under Z^4 scaling, for example, causes a green photon at $\lambda = 475$ nm to become a 3.4 keV x-ray ($\lambda = 0.36$ nm). The case of the $3d^4\ ^5D_2-^5D_3$ transition on the Ti-like sequence is one of a number of exceptions: an accidental crossing of energy levels gives rise to a nearly flat (Z -independent) variation of wavelength over a large portion of the periodic table (Feldman *et al* 1991, Porto *et al* 2000b).

There is another important contribution to the energy levels which scales in a way intermediate between the Z^2 dependence of the Coulomb interactions and the Z^4 dependence of the relativistic fine structure interaction: the hyperfine interaction. The origin of the hyperfine shift is the electrodynamic interaction of the orbiting charge and/or spin with the magnetic moment of the nucleus. The Z -scaling can be understood by considering the magnetic field generated at the nucleus by a circularly orbiting electron. This field follows directly from an integration of Maxwell's equations (or more simply, from the Biot-Savart law) and goes up as the inverse cube of the radius of the orbit. The linear scaling of Bohr radius with Z then directly leads to a Z^3 dependence of the hyperfine shifts.

For HCIs, the absolute magnitude of the hyperfine splitting grows so large that it enters the optical regime. High-resolution laser spectroscopy can then be used to probe the electronic structure so accurately that the atomic physics of HCIs impacts an entirely different field, nuclear physics. Information gained about the nucleus through very accurate measurements of electronic structure can be made to exceed the present experimental accuracy using other methods (Kuhl *et al* 1997). The hyperfine splitting in H-like bismuth has been measured using an HCI accelerator facility (Klaft *et al* 1994) and in H-like holmium and Li-like Bi using an electron beam ion trap (Lopez-Urrutia *et al* 1996, Beiersdorfer *et al* 1998).

Not all energy level shifts grow with increasing Z . The shifts due to external magnetic fields (the Zeeman effect) for example, actually decrease. The first-order (linear) Zeeman shift for the ground state of hydrogen-like ions has a weak Z dependence due to the effect of relativity. In the relativistic generalization of quantum mechanics, four wavefunctions (composed of two radial wavefunctions and two Pauli spinors) are required to fully describe even a single-electron atom or ion. Although one of the radial functions is typically small, its finite value leads to the variation with Z of the first-order Zeeman shift. The functional dependence of this variation is given by the following correction factor (Bethe and Salpeter 1977):

$$g_1 = \frac{1}{3} \left(1 + 2\sqrt{1 - (\alpha Z)^2} \right) \approx 1 - \frac{(\alpha Z)^2}{3} + \dots \quad (6)$$

If this factor is neglected, the first-order Zeeman shift is independent of Z , but even then it becomes relatively less significant in comparison to the overall energy scale as Z increases. The absolute scale of the first-order Zeeman shift is set by the product of the Bohr magneton and the magnetic field. The second-order Zeeman shifts (quadratic in magnetic field) scale much more strongly, decreasing as $1/Z^2$ for the ground state of hydrogen-like ions.

Shifts in the energy levels due to external electric fields (the Stark effect) also decrease with increasing Z . For non-degenerate levels, the Stark shift scales as $1/Z$. This scaling can be understood by considering the origin of the Stark shifts as a polarization of the electron cloud which produces an electric dipole moment, $q \times r$, which scales as $r \sim 1/Z$. In non-degenerate perturbation theory, the first-order shift scales as the matrix element of the dipole moment operator, and thus reflects the $1/Z$ scaling. For degenerate levels, such as those that arise in a simple treatment of the ground level of hydrogen-like ions for example, the first-order Stark shifts vanish. Degenerate perturbation theory can then be used to estimate the second-order shift, which arises from two dipole moment matrix elements, plus an energy denominator that scales as the level separations. The second-order shift thus scales as $1/Z \times 1/Z \times 1/Z^2 = 1/Z^4$. As the field approaches zero, linear shifts are eventually regained as radiative corrections lift the degeneracy on a fine scale.

In addition to the dramatic shifts in the *positions* of spectral lines described above, HCIs also display large changes in the relative *intensities* of the lines as well. With increasing charge, the quantum mechanical selection rules that suppress certain classes of transitions no longer apply, and transitions that are ordinarily ‘forbidden’ become relatively strong, sometimes becoming even stronger than the ordinary ‘allowed’ transitions (see section 2.6 below).

The energy distribution of radiation from HCIs changes in at least one more important way: spectral linewidth. While ordinary atoms typically have very sharp and well defined spectral emission lines, these become greatly broadened in HCIs, resulting in a spectrum that is considerably more ‘fuzzy’ than that of neutral atoms. This blurring of the emission spectrum is mandated by the Heisenberg uncertainty principle because the lifetimes of excited state levels decrease rapidly as the ion charge is increased. The Z -scaling of the lifetime (inverse linewidth) varies widely depending on the transition involved. The widths of hyperfine transitions, for example, scale as Z^9 . Intercombination transitions ($\Delta S \neq 0$) with $\Delta n = \pm 1$, have an even stronger scaling: Z^{10} . The widths of ordinary (electric-dipole) transitions scale as a more moderate Z^4 , but this is still significantly greater than the quadratic scaling of energy, so the relative sharpness of the emission spectrum still blurs with increasing charge: $\Delta E/E = Z^4/Z^2 = Z^2$.

2.4. Electric field

HCI's provide a simple system in which electrons are subject to some of the strongest electric fields available in the universe. Scaling up Coulomb's law as Z^3 (one factor of Z for nuclear charge, two more for reduced Bohr radius), the electric field experienced by a lone electron orbiting a uranium nucleus is approximately 10^{16} V cm⁻¹, the strongest static field available in any laboratory. Even the most intense laser fields are several orders of magnitudes less strong than this. The conditions inside HCI's thus provide a unique testing ground for 'strong-field quantum electrodynamics' (Greiner *et al* 1985). In addition, the residual strong fields that extend from HCI's to long distances form the basis for the emerging field of HCI-surface interactions, discussed below.

2.5. Angular momentum coupling

Because the outer electrons in neutral atoms interact primarily by electrostatic forces, the Hamiltonian is independent of spin (to first order). This gives rise to the ordinary LS -coupling scheme (Cowan 1981, Heckmann and Trabert 1989) in which eigenstates are well described by the independent quantum numbers corresponding to the total electron angular momentum (L) and total electron spin (S). Deviations from pure LS coupling can be described within the context of perturbation theory by expanding the eigenstates in terms of pure LS states; there will generally be a small admixture of nearby states with different quantum numbers. For HCI's, however, the admixture can become so large that an entirely different coupling scheme is called for. For example, there are states in magnesium-like manganese and oxygen-like copper in which the eigenfunctions are primarily comprised of a linear combination of two LS states, with virtually identical weights (equal to within a fraction of one per cent) (Gaigalas *et al* 1999). In cases like these, even discussing the situation qualitatively can become confusing. There have been cases where the admixtures were so large that theorists and experimentalists thought they were comparing results for a particular state when, in fact, they were talking about two physically different states. When the problem of state identification was clarified, entries in tables were switched and agreement between theory and experiment improved (Froese Fischer and Jonsson 2001).

The required change in coupling scheme is made clear by considering the relative importance of electrostatic (electron-electron) and relativistic effects (e.g. spin-orbit interaction). The spin-orbit interaction grows as Z^4 , as discussed above. The weaker Z^2 scaling of electron-electron interaction can be appreciated by considering that (1) it is inversely proportional to the distance between the two electrons and (2) the area of space that adjacent electrons on a spherical Bohr orbit have available to pass by each other scales as $4\pi R^2 \sim R^2 \sim Z^{-2}$. As the spin-orbit interaction becomes stronger with increasing Z , it becomes more appropriate to first couple the spin and angular momentum quantum numbers for each individual electron ($j = s + l$) and then take into account the electron-electron interaction by subsequently coupling the electrons together ($J = j_1 + j_2 + \dots$). The resulting natural transition from LS to jj coupling as Z is increased (isoelectronically) is evidenced by the smooth rearrangement of the energy eigenvalues plotted in figure 6. Standard spectroscopic notation (Cowan 1981, Heckmann and Trabert 1989) is used to label this figure.

2.6. Selection rules

The change from LS to jj coupling in HCI's is accompanied by a loss of familiar quantum mechanical selection rules. For example, electric dipole (E1) transitions can then take place even with a change of the total spin quantum number ($\Delta S \neq 0$). Furthermore, the requirement

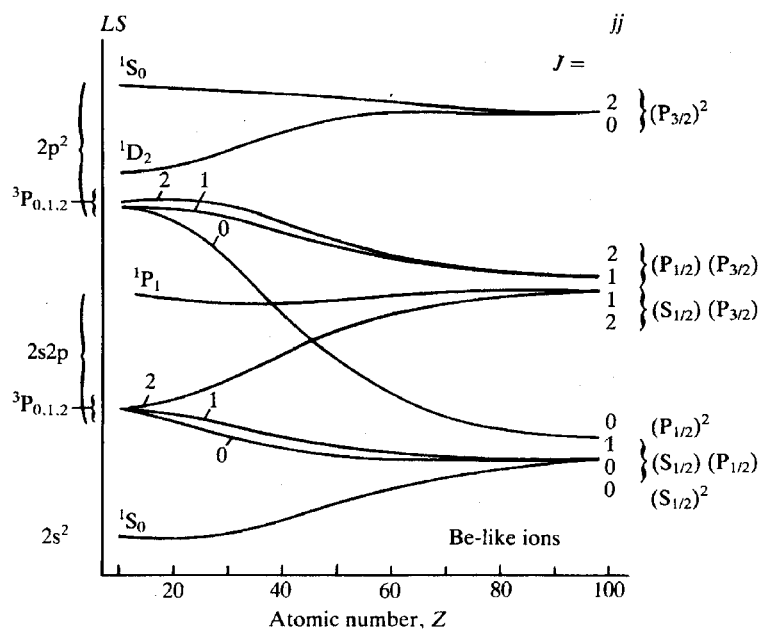


Figure 6. Variation of energy eigenvalues with Z , showing the crossover from LS to jj coupling in the case of Be-like ions, from Martinson and Curtis (1989).

that the total orbital angular momentum change by $\Delta L = 0, \pm 1$, with no $L = 0$ to $L = 1$ is relaxed. These and other changes in the selection rules are tabulated in Beyer *et al* (1997). A detailed discussion of the origin of the changes to the selection rules in terms of Racah tensors can be found in Heckmann and Trabert (1989).

2.7. Some issues on the theoretical foundations

Although the natural periodic table stops at $Z = 92$, and researchers have only been able to extend it by another 30% or less so far, it is of interest to consider what happens *in principle* at higher Z . In particular, what happens along the hydrogen-like isoelectronic sequence as Z rises above 137 (the reciprocal of the fine structure constant)? The most precisely tested theory in all of physics (quantum electrodynamics) predicts that at such high Z , the vacuum of space will become unstable and undergo a fundamentally new type of phase transition (Greiner *et al* 1985). One consequence is the spontaneous production of matter. This bizarre scenario is discussed further in section 4.4 below.

The phase transition at ultra-high Z is due to the existence of negative energy states. The effect of these states must be considered even at more moderate values of Z . A case in point is the ‘continuum dissolution’ problem. The Hamiltonian generalization of the Dirac equation to the case of two or more electrons becomes a problem once the interaction between the electrons is taken into account. If even a slight interaction term is allowed in the Hamiltonian, it can be shown that no bound state eigenfunctions exist. This problem is known as the ‘Brown–Ravenhall disease’, after the authors of the seminal paper entitled ‘on the interaction of two electrons’ that was published 50 years ago (Brown and Ravenhall 1951). Outside of a full field-theoretic treatment, the problem has still not gone away, although clever methods of effectively ignoring it in computations have been devised (Brown 1987). The *ad hoc* insertion of projection operators to forbid certain classes of transitions, for example, is one method of dealing with the problem (Sapirstein 1998). In a review paper on quantum electrodynamical

$Z^{-0}[Z\alpha]^2$	$Z^{-0}[Z\alpha]^4$	$Z^{-0}[Z\alpha]^6$	$\dots Z^{-0}[Z\alpha]^{2n}$
$Z^{-1}[Z\alpha]^2$	$Z^{-1}[Z\alpha]^4$	$Z^{-1}[Z\alpha]^6$	
$Z^{-2}[Z\alpha]^2$	$Z^{-2}[Z\alpha]^4$		
\vdots			\vdots
$Z^{-m}[Z\alpha]^2$			$Z^{-m}[Z\alpha]^{2n}$

Figure 7. Terms in the $Z\alpha$ and $1/Z$ expansion. The number of rows and columns extends to infinity ($n, m \rightarrow \infty$). Each box contains an infinite number of terms in the mass expansion (visualize along a z -axis extending out of the page). Each of the boxes in this three-dimensional matrix contains a set of Feynman diagrams. Figure after De Sousa Zacaris (1990).

effects in helium, Douglas and Kroll recount a bit of the history of how, before the work of Brown and Ravenhall, terms in the leading theoretical formulation (the Breit equation) were simply discarded in order to obtain agreement with experiments (Douglas and Kroll 1974).

Perhaps the most intriguing issue in the theoretical description of HCIs is the abundance of infinities that appear in the most rigorous calculations of the energy levels. Methods have been developed of handling these infinities so they will sum to finite values that, in the end, agree well with experimental measurements. The question of whether this procedure will continue to hold up under increasing experimental precision and widening breadth of application, is a topic of active research.

A more concrete look at the issues mentioned in the previous paragraph reveals several layers of infinities that can arise in the prediction of energy levels of HCIs. First, in one of the standard formalisms there is an expansion in the dimensionless parameter $Z\alpha$ (Z times the fine structure constant) that results in a sum of an infinite number of terms to calculate. For the realistic case of a finite mass nucleus, each of the terms in this expansion is itself represented by an infinite sum known as the ‘mass expansion’ (an expansion in the small dimensionless parameter given by the ratio of the mass of the electron to the mass of the proton). Each of the terms in the mass expansion is given, in turn, by the sum of one or more (sometimes a great many) Feynman diagrams, each of which itself can be, and frequently is, infinite in value (until renormalized). For multi-electron HCIs there is an additional expansion in α , which appears as an expansion in $1/Z$ when combined with the $Z\alpha$ expansion. Most current effort is focused on calculations represented by high-order Feynman diagrams, such as the two-loop binding correction (Eides and Shelyuto 1995, Pachucki 1994).

A useful way of organizing the $Z\alpha$ and the $1/Z$ expansion for a two-electron ion is shown in figure 7. Here, the first column gives the non-relativistic energy and the first row gives the sum of one-electron Dirac energies. Each box corresponds to a collection of Feynman diagrams. The well-known Breit interaction is located in the (2, 2) box marked $Z^{-1}[Z\alpha]^4$. There are serious concerns among theorists about whether the most complete theoretical treatments will hold up when measurements with increased precision become available at high Z .

2.8. Interactions with surfaces

The approach of a slow HCI to a surface presents an unusual experimental situation. The electrostatic pull of the HCI can be so great that it begins removing electrons from the surface even when it is dozens of atomic diameters away. These electrons are removed from a highly localized region of the surface, estimated to be on the order of 1–10 nm in diameter (Perez and Olson 1999). Many of the electrons that are removed swing around the ion and then travel back to the surface, not necessarily landing back at their point of origin because of the dynamical evolution of the ion–surface system in the meantime. In addition, some of the electrons are captured temporarily by the ion and become bound in high-lying Rydberg levels. This forms a so-called ‘hollow atom’ (Briand *et al* 2000, Khemliche *et al* 1998) in which most or all of the electrons are in an excited state. Hollow atoms have their electronic wavefunctions concentrated in a large shell that surrounds a relatively empty central core. The population of high-lying levels that results in a hollow atom can subsequently decay to lower levels, giving off either a photon or a secondary electron. Typically, the decay proceeds most rapidly through interaction with other bound electrons in an Auger process. Through the Auger decay, the partially neutralized ion automatically reionizes itself, as it continues to approach the surface. Part of the Auger-emitted electrons are directed back towards the surface in a diffuse beam, and part are ejected outwards away from the surface where they can be readily detected. In addition, there may be a great many low-energy electrons that are pulled from the surface and ejected outwards without undergoing an intermediate capture process by the ion. In experiments, up to several hundred electrons have been measured to be projected away from a surface by a single low velocity HCI (Schneider and Briere 1996). The HCI acts, in effect, like a miniature electron pump to remove a large number of electrons from a nanometre-sized region of the surface on a time scale that can be in the femtosecond range. The implications of this novel situation for the field of nanotechnology are discussed in sections 4.6 and 4.10 below.

There have been a number of efforts to develop quantitative models for the interaction of slow HCIs with surfaces, but these will not be discussed here. Most of the effort has been focused on predicting the dynamical evolution of the ion, rather than the long-time response of the surface. References to the former can be found in papers that develop the classical over-barrier model (Burgdorfer *et al* 1991), the extended classical over-barrier model (Ducree *et al* 1998), density functional theory (Arnau *et al* 1997), the close-coupling model (Bahrim and Thumm 2000), and cascade models (Stolterfoht *et al* 1999). Some models of surface response to HCI impact can be found in the references given in the last paragraph of section 4.6.2 below.

3. The production of HCIs

There are many possible ways of producing ionized atoms, some of which are quite exotic. In muon-induced ionization, for example, a muon is captured by a neutral atom and the atom responds by ejecting all of its electrons (Bacher *et al* 1989). This mechanism can produce an HCI in less than a femtosecond, and plays an important role in fundamental studies using exotic atoms (Siems *et al* 2000). The primary mechanisms for producing HCIs in the natural universe, however, are photoionization and electron-impact ionization (Giroux and Shapiro 1996). For the sort of precisely controlled laboratory work described in this review, electron-impact ionization is the primary method used.

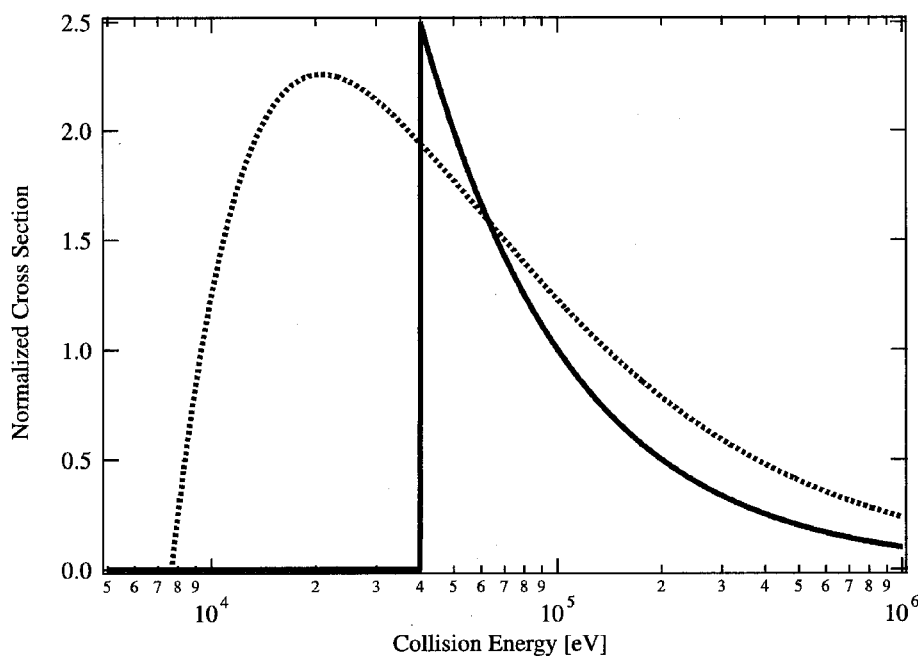


Figure 8. Energy dependence of typical electron-impact ionization (dotted curve) and excitation (full curve) cross sections for an HCI (see text).

3.1. Electron-impact ionization

In an electron-impact ionization process, electrons with high translational energy collide with an atom and remove a bound electron. This process continues in subsequent collisions, like the peeling of an onion, until the ionization energy becomes greater than the available translational energy. The projectile electron can be either a free electron, or bound to another atom or ion.

Electron-impact ionization proceeds easily for the first few electrons that are removed, but the process rapidly becomes more difficult as the charge increases. The difficulty is twofold: the more deeply bound electrons require more energy to remove (ionization cross sections decrease), and neutralizing collisions with background gas atoms thwart the step-wise progress towards the desired charge state (charge exchange cross sections increase). In addition, the effect of the latter is exacerbated by the former because of the increasing time between ionizing collisions.

The cross section for electron-impact ionization typically rises gradually from zero at a threshold equal to the ionization energy, and reaches a broad maximum at a factor of 2.5 to 3 above the threshold before falling slowly back towards zero. Figure 8 shows the ionization cross section for the removal of an electron from Xe^{44+} (to produce Xe^{45+}). In many cases, the ionization energy for the next-highest charge state will occur at a lower energy than the peak of the cross section, however, so the optimum electron energy to maximize the equilibrium amount of a particular charge state may occur at lower values than the peak of the cross section. In comparison, the electron impact *excitation* cross section typically rises abruptly to its peak value at threshold, before falling back towards zero at higher energies (figure 8). For excitation, the threshold is equal to the separation between the energy levels.

The magnitudes of the ionization and excitation cross sections for HCIs are typically much less than the classical elastic scattering cross section for a hydrogen atom ($\pi a_0^2 \approx 10^{-16} \text{ cm}^2$). When the vertical scale of figure 8 is multiplied by 10^{-21} cm^2 , the ionization cross section

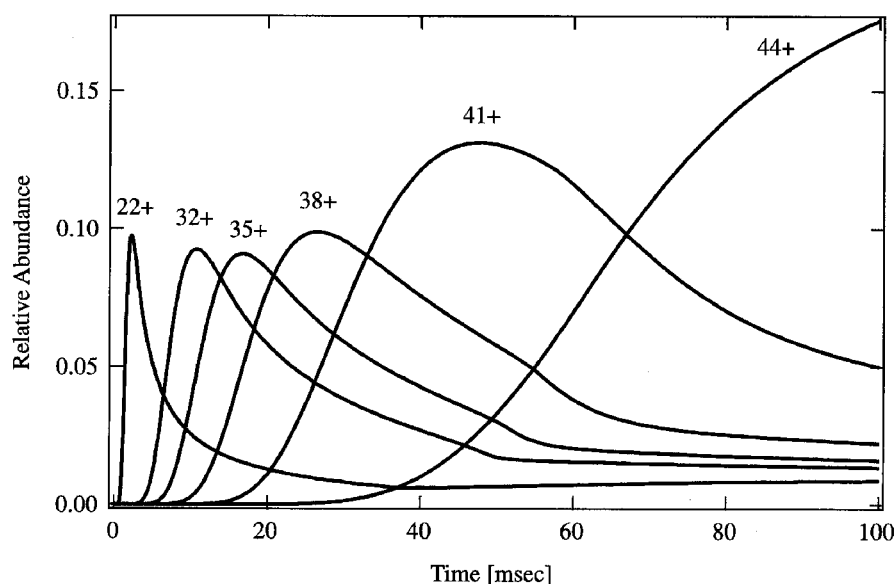


Figure 9. Time evolution of the charge states of xenon produced by an intense electron beam (see text).

shown corresponds to that of the Lotz formula (Lotz 1967). The peak value of the cross section predicted by the Lotz formula occurs at an electron energy equal to a factor of ‘e’ (~ 2.72) above the ionization energy I_0 , and has a value (in cm^2) approximately equal to

$$\sigma_{\max}(E = eI_0) = \frac{1.7 \times 10^{-14}}{I_0^2} \quad (7)$$

for I_0 measured in eV. Note that this formula is for a single electron, so the total cross section for ionization of any one of the N electrons in a given shell (all with approximately the same I_0) is given by this formula multiplied by N .

For dipole-allowed transitions, the order of magnitude of the peak of the excitation cross section can be estimated from the Van Regemorter (1962) formula, knowing only the transition energy and the oscillator strength. For more than an order of magnitude estimate, a more accurate computation may be required (Sampson and Zhang 1992). For a 4 keV transition and an oscillator strength of unity, this formula predicts that the peak of the excitation cross section would be roughly equal to that of the plotted ionization cross section. Because the peak of the excitation cross section scales as the inverse square of the transition energy, however, it should be reduced by a factor of 100 at the 40 keV energy shown in figure 8.

In order to give a feel for how sequential ionization proceeds, figure 9 shows the results of a numerical simulation which takes into account the dynamic evolution of the adjacent charge states under the influence of an intense electron beam. In this figure, the electrons are assumed to have a single energy (8000 eV) and direction, and a current density of 3900 A cm^{-2} . The physics included in the simulation is based on earlier work (Margolis *et al* 1997, Penetrante *et al* 1991).

Because the competing effect of ion neutralization by background gas becomes more severe as the ion charge increases, high vacuum systems are required for the production and transport of slow HCIs. The scaling of electron capture cross sections with increasing charge is not simple (Pal’chikov and Shevelko 1995), but for energies typical of the ions produced in table-top devices, they increase roughly linearly with charge. A more precise rule of thumb

leads to the following formula (Muller and Salzborn 1977) for the mean free path in metres of an ion of charge state Q (dimensionless), assuming a typical background gas like nitrogen (ionization potential ~ 12 eV) at a pressure p measured in hPa ($1 \text{ hPa} \approx 1 \text{ Torr}$),

$$\lambda = \frac{10^{-4} \times Q^{-1.17}}{p}. \quad (8)$$

For example, this formula predicts that at UHV conditions of $p \sim 10^{-10}$ hPa, a Xe^{44+} ion will have a mean free path $\lambda \sim 12\,000$ m and thus live for 60 s if the relative velocity through the gas is 200 m s^{-1} (corresponding to a room temperature kinetic energy, $\frac{1}{2}mv^2 = kT$). Moving at a more typical speed for an HCI (25 km s^{-1} , after acceleration through a 10 kV potential), this lifetime is shortened to 0.5 s. The vacuum requirements for HCIs are lessened in high-energy particle accelerators, because the cross sections decrease rapidly (e.g. $\sim v^{-7}$) as one goes into the very high velocity regime (Pal'chikov and Shevelko 1995).

3.2. Overview of laboratory devices

Martinson (1989) has reviewed the types of laboratory sources for HCIs in use prior to 1988. These fall largely into two categories: those that are relatively cheap, yet of limited ability (sparks, arcs and exploding wires, supplemented by hollow cathode and electrodeless discharges for the lowest charge states) and those that are very expensive and involve large national facilities (magnetically confined fusion devices, particle accelerators and multi-joule terawatt lasers). Fitting into a new class that falls in between these two extremes are the electron cyclotron resonance (ECR) ion sources (Geller 1996) and electron beam ion sources (EBIS) (Donets 1998). These two latter types of ion sources can produce rather high charge states, with a modest investment of resources. The newest source of HCIs to date, the electron beam ion trap (EBIT) (Levine *et al* 1988), has evolved out of the EBIS concept and is discussed in greater detail in a separate section below.

Recent advances in producing femtosecond tabletop lasers have made it possible to easily produce TW power levels, but the limited pulse length has prevented these lasers from becoming efficient methods of producing HCIs. Figure 10 shows the charge state distribution obtained from a 2 TW, 100 fs laser, in comparison to that produced by an EBIT (next section) and an ion accelerator.

3.3. The electron beam ion trap (EBIT)

The EBIT is a compact and relatively inexpensive device capable of producing and electromagnetically confining HCIs. A typical EBIT is almost 'table top' in size, costs less than a good electron microscope, and yet can remove most of the electrons from any naturally occurring atom on the periodic table. A somewhat larger EBIT (about twice the size) has been used to fully strip even the heaviest naturally occurring element (Marrs *et al* 1994b). Presently, there are cryogenic EBITs at Livermore (Marrs *et al* 1994a), NIST (Gillaspy *et al* 1995), Oxford (Silver *et al* 1994), Tokyo (Kuramoto *et al* 2000), Berlin (Biedermann *et al* 1997), Freiburg (Lopez-Urrutia *et al* 2000), Frankfurt (Zipfel *et al* 1998) and (very recently) Berkeley. A cryogenic EBIT was also built in Russia, but is currently out of service. Smaller 'warm' EBITs have been constructed at Livermore, Troitzk (Antsiferov and Movshev 1991), Dresden (Ovsyannikov *et al* 2000) and Paris (Khodja and Briand 1997). An additional cryogenic EBIT is under construction in Shanghai.

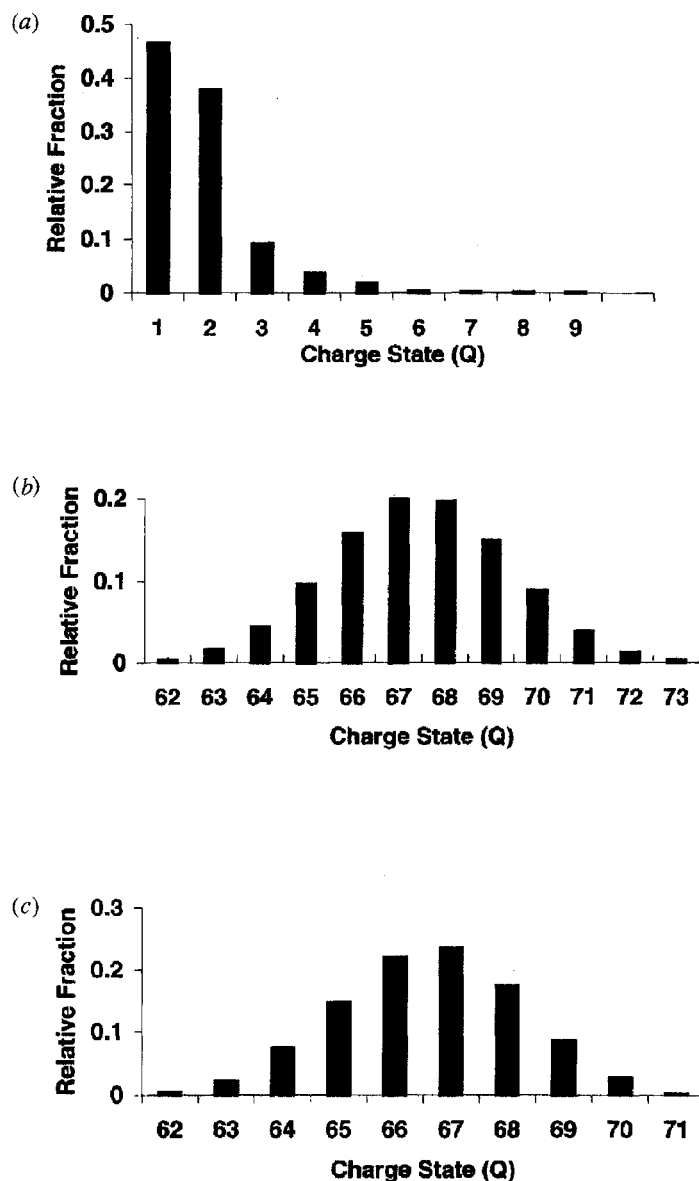


Figure 10. Charge state distribution from (a) a 2 TW, 100 fs laser incident on a tantalum target (Fournier *et al* 2000), (b) an ion accelerator producing 3 GeV gold ions (Chandler *et al* 1989) and (c) an EBIT producing uranium ions with 9 keV electron beam (Schneider *et al* 1991).

3.3.1. Comparison of EBIT to ion accelerators. From the most fundamental point of view, an EBIT functions as a miniature particle accelerator. In both cases, electric fields produce high-velocity charged particles which are then directed onto a target to cause collision-induced ionization. The ions are subsequently confined by magnetic and/or electric fields in an ultrahigh vacuum chamber. There is a great difference in scale and technical detail, however, between an EBIT and an ion accelerator. These differences essentially have to do with the relative motion of the laboratory and centre-of-mass reference frames.

In the case of an EBIT, the electrons are accelerated and the target atom/ions are at rest in the laboratory frame of reference. In the case of an ion accelerator, the roles are reversed, and the electrons are essentially at rest in the laboratory frame while the heavy ions are accelerated. In practice, the target electrons for the ion accelerator are those bound to atoms in a thin foil of solid material through which the ions pass. The fraction of the kinetic energy in the laboratory frame that is available for ionization is determined by the kinetic energy of the two collision partners in the centre-of-mass frame. For the case of the EBIT, the laboratory frame is already essentially in the centre-of-mass frame, so the energy fraction is 100%. For the case of the accelerator, the centre-of-mass frame is moving at near the speed of light through the laboratory frame, so most of the energy is unused. For a moving ion of mass M the fraction of laboratory energy available for ionization is given by,

$$\frac{E}{E_0} = 1 - \frac{M}{M + m} \quad (9)$$

where m is the mass of the electron at rest in the laboratory. For gold ions, this fraction is 3×10^{-6} , so in order to achieve 8 keV of ionization energy, one must accelerate the gold ions to 3 GeV (about 20% of the speed of light). This requires sophisticated alternating-field accelerator technology and a facility the size of a large building. In contrast, an EBIT can accelerate the relatively light electrons to 20% of the speed of light within a few centimetres using modest electrostatic fields produced by a commercially available voltage source. While the electron density in an EBIT is much less than the electron density in an ion accelerator target (beam foil), the interaction time is also much greater and these two factors tend to balance each other somewhat so that similar distributions of charge states are produced in both cases. Some examples of the equilibrium charge state distributions produced by an EBIT and an ion accelerator are shown in figure 10. For many high-precision spectroscopy experiments, the low velocity of the ions produced by an EBIT is advantageous because it renders Doppler shifts negligible. In other experiments, however, the high velocities of ions produced by an accelerator can be used to good advantage, as discussed elsewhere (Beyer and Shevelko 1999).

A storage ring is typically used in conjunction with an ion accelerator in order to capture the fast ions and recirculate them through an observation region. Such rings use large bending magnets to essentially form a large ion trap (with a typical circumference of 50 m). In an EBIT, the ions move much more slowly and can therefore be confined with a more modest effort. In fact, the electron beam that produces the ions in an EBIT, also generates a strong electric field which itself can be used to trap the ions in the radial direction. In effect, the electron accelerator that produces the ions is located *inside* the trap itself, so no additional effort is required to load the trap. Two small electrostatic mirrors separated by a few cm serve to reflect the ions back and forth along the axis of the electron beam, forming a ‘hall of mirrors’ that effectively extends the trap length to infinity as seen from the ion’s point of view. While the EBIT trap is thus something like a ring with infinite radius, in reality the ions are all localized in a small physical region of space in the laboratory. This makes it relatively efficient to collect light from the ions in order to study their structure and behaviour using standard spectroscopic techniques.

3.3.2. EBIT details. Some of the technical details of an actual EBIT are shown in figure 11. The design and operation of the device have been described in detail elsewhere (Gillaspy 1997, Levine *et al* 1988), so only a rough overview will be sketched below. An interactive online tutorial is available on the web¹. The most thorough description to date of the physics and technology that underlies an EBIT has been given by Currell (2001).

¹ <http://physics.nist.gov/MajResFac/EBIT/main.html>

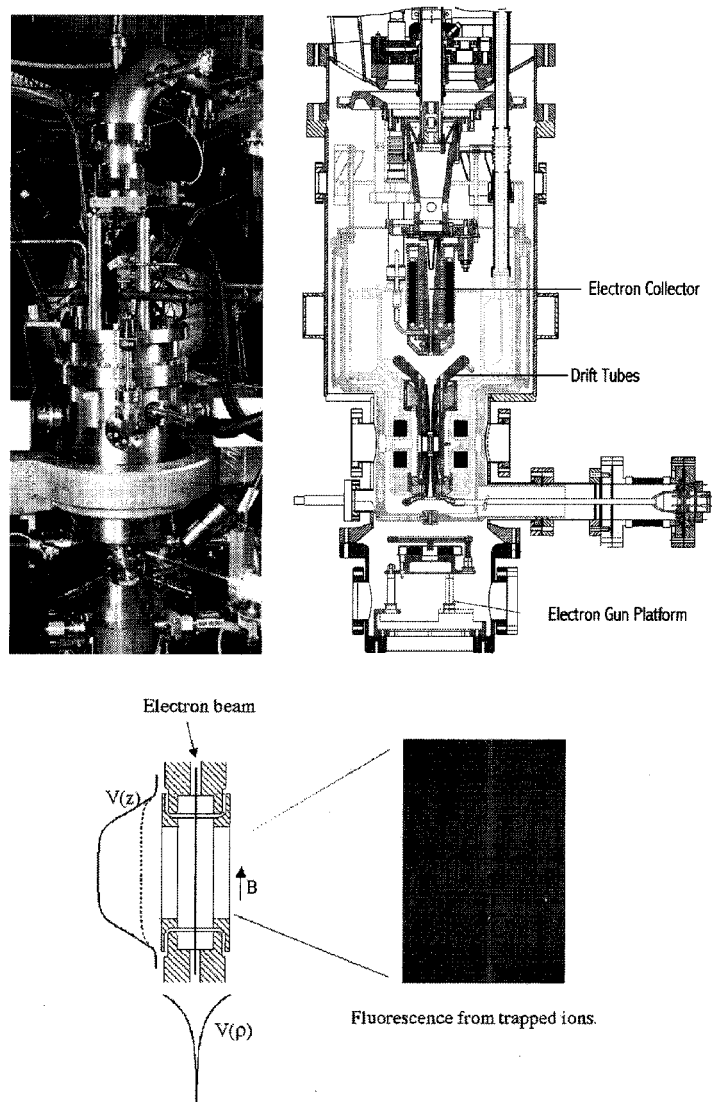


Figure 11. Upper, photograph of the electron beam ion trap at NIST, shown next to a cross sectional schematic (approximately 1 m in height). The photograph is reduced by a factor of two in order to show the ion extraction apparatus on top of the EBIT. Lower, detail of the drift tubes shown next to an enlarged image of the cloud of trapped ions (ion cloud approximately $200\ \mu\text{m}$ wide).

There are three primary subsections of an EBIT: (a) an electron gun to produce the beam; (b) a drift tube assembly to accelerate the beam to a specified energy; and (c) an electron collector to serve as a beam dump. In the EBIT shown in figure 11, the electron gun is a small unit, approximately 1 cm in diameter by 2 cm in length, with a 3 mm diameter cathode that produces about 150 mA of current. Although the original EBIT device was built with the electron gun permanently grounded, the one shown in figure 11 is mounted on a ‘floating’ (electrically isolated) high-voltage platform inside the main UHV vacuum chamber so that the electron gun ground lines can be operated at negative high voltage relative to the laboratory. This configuration makes it possible to provide a boost in the available beam energy, beyond the high voltage capability of the drift tube assembly described below. This is the principle that operates on a larger scale in the so-called ‘super-EBIT’ device to produce bare uranium ions (Marrs *et al* 1994b). In the super-EBIT, the electron gun rests on a large high-voltage

platform that is itself as large as an ordinary EBIT.

The primary magnetic field in the EBIT is a 3 T superconducting Helmholtz pair that is centred on the drift tubes. In the super-EBIT in Japan (Kuramoto *et al* 2000) this magnetic field is increased to 4.5 T. The magnetic field serves to compress the electron beam to a high density, approximately 4000 A cm^{-2} (Marrs *et al* 1994a) in the case shown. In addition, there is a smaller electromagnet built into the electron collector that runs at liquid nitrogen temperature, and another electromagnet in the electron gun region that runs at about 100 K above room temperature. The magnet surrounding the electron gun is used to cancel the stray field from the superconducting magnet, and then adjust the value of the small but finite residual magnetic field that is necessary at the cathode in order to efficiently couple the beam into the drift tube assembly without magnetic mirroring (Takacs *et al* 1996). High permeability metal in the electron gun region shapes the net field appropriately. Detail about the general design problem of coupling an electron beam into a strong magnetic field can be found in Becker (1995).

The drift tubes are cooled by thermal contact with a superconducting magnet assembly that is filled with liquid helium ($T = 4.2 \text{ K}$). Although generally the Wiedemann–Franz law links thermal and electrical conductivity, the choice of a suitably anomalous material (sapphire) allows good cooling and electrical isolation to be obtained simultaneously. The drift tubes are operated at 1–35 kV without any detected leakage current ($< 10 \mu\text{A}$).

The outer portion of the drift tube assembly is a large shield electrode that is specially shaped to reduce electrical breakdown to ground. Inside the shield there are three smaller electrodes which operate at differential voltages of up to 500 V from the shield voltage. These three electrodes form a variant of a cylindrical Penning trap (Gosh 1995). Raising the upper and lower electrode voltages with respect to the centre electrode forms a potential well that traps the ions in the axial direction. The electron beam is threaded through the central axis of the three inner drift tubes and produces an electric field that strongly supplements the radial magnetic trapping. The electron beam also provides a significant *axial* trapping potential because the centre and end drift tubes have different radii and therefore different amounts of surface charge induced by the space charge of the electron beam (or, equivalently, different locations of the virtual image charge). Because of the space charge and image charges, the electron beam energy at the trap centre is offset from that naively determined by the voltage placed on the drift tubes. In addition, the beam energy varies somewhat as a function of radius. These issues are discussed in more detail elsewhere (Currell 2001, Porto *et al* 2000a). Finally, the electron beam also provides the critical function of ionizing the atoms in the trap, and exciting them to electronic energy levels above the ground state in order to make them fluoresce.

In contrast to a conventional plasma which has a broad electron velocity distribution, the EBIT beam is closer to that of a delta-function (figure 12) and is directed along a well defined axis. This is extremely useful for sorting out differential cross sections for fundamental processes such as electron-impact ionization, excitation, and recombination. The energy of the electron beam can also be rapidly swept back and forth through a pattern that will synthesize an arbitrary electron distribution function (Savin *et al* 2000).

The electron collector functions by providing a retarding field that partially slows down the electrons and a magnet that spreads out the beam and allows it to be deposited over a large surface area that is cooled with liquid nitrogen. This action occurs inside a cylinder with end electrodes (essentially, an electron trap) to suppress the emission of secondary electrons.

All of the EBIT electrodes and magnets are annular about the primary electron beam axis so it is possible to look down from the top of the system and see the ions in the trap and, beyond it, the glow of the heated electron gun cathode. This configuration makes it possible to eject ions out of the top of the trap and direct them onto surfaces or inject them into secondary

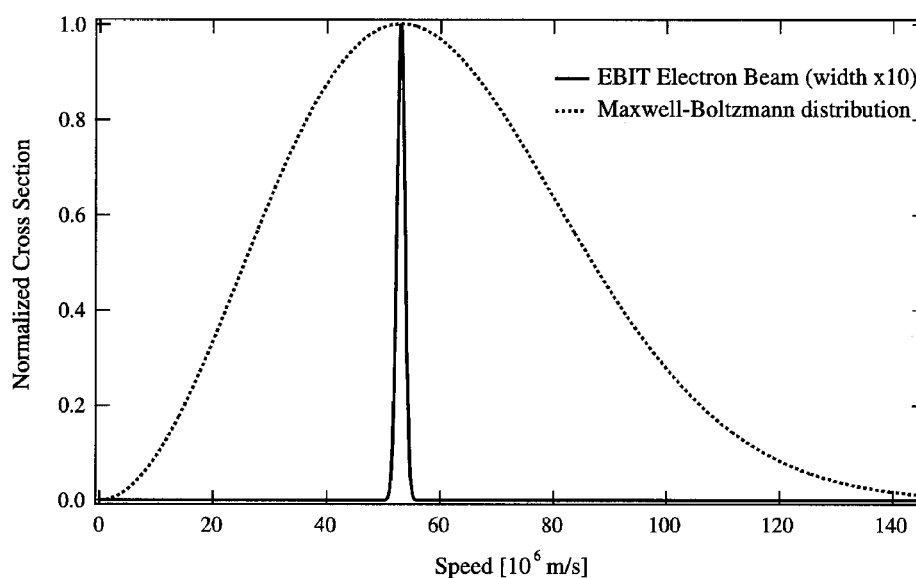


Figure 12. Electron beam velocity distribution in an EBIT compared with a Maxwell–Boltzmann distribution (non-relativistic). The temperature of the distribution and the peak of the beam velocity correspond to 8 keV. In order to make it visible on the plot, the beam width has been expanded by an order of magnitude (500 eV shown, 50 eV available in EBIT).

traps. A high efficiency ion beamline equipped with electrostatic and magnetic beam control components has been constructed to transport the ions to various other experiments in the laboratory; this system is of comparable complexity to the EBIT itself and is described in detail elsewhere (Pikin *et al* 1996, Ratliff *et al* 1997).

4. Applications

4.1. Atomic reference data

The most immediate application for HCIs is as a testbed for our understanding of the electronic structure of matter. Most of the atomic ‘data’ that are tabulated for use as input reference data for the development of new technologies are generated by calculations, not measured in experiments. Instead, benchmark experiments measure a sampling of representative cases in order to test and improve the underlying theory, upon which most of the reference data are then computed. This underscores the practical importance of having a highly robust underlying theory that can be applied with high confidence to a wide range of individual cases as the need arises.

As discussed in section 2 above, HCIs allow us to produce a subclass of atoms in which the basic physical parameters take on extreme values. Large deviations from model predictions that occur at these extreme values give clues to the nature of the deficiencies in our models and allow us to improve them in fundamental ways. This sort of quantum mechanical ‘shake test’ can be extremely important in the development of robust theories of atomic structure that will hold up to a high degree of confidence within the more limited realm of ordinary experience. As noted by Martinson and Curtis (1989), one can obtain a better understanding of neutral atoms by studying HCIs.

4.2. Cosmic chronometers

In the process of testing theories of ordinary matter under extreme conditions on Earth, one also obtains information that is relevant to a broader understanding of the cosmos. An interesting example is the effect of bound-state beta decay in the ‘cosmic chronometer’ provided by rhenium-187 (Bosch 1999). The time span of nucleosynthesis in our galaxy can be determined by the concentrations of decay products of rhenium-187 in meteorites. In the neutral charge state, rhenium has a half-life of 42×10^9 yr. During the course of the evolution of the galaxy, however, rhenium can spend a significant fraction of its life in a highly ionized state. Recent laboratory experiments at the GSI facility in Germany (Bosch *et al* 1996) have proven that the half-life of highly ionized rhenium is nine orders of magnitude shorter than that of the neutral state (33 yr, rather than 42×10^9 yr). The physical mechanism underlying the lifetime shortening is that beta decay can proceed more rapidly if the emitted electron does not escape the ion but is instead captured into an open electronic shell. If the open-shell is very deep, as it is in an HCI, the amount of work saved by not having to lift the electron out of the potential well is considerable.

The rhenium cosmic chronometer is presently being ‘reset’ to include the accurately measured value for the lifetime shortening due to the bound-state beta decay effect described above. Prior to the measurements, the nine orders of magnitude correction was applied using theoretical estimates. It can now be seen that these estimates were off by about a factor of two. Preliminary results for the rhenium clock recalibration reduce the estimated age of the universe by 10^9 yr. The implications, not only for cosmic geneology but also for shedding light on the future fate of our universe and the value of Einstein’s cosmological constant, are discussed by Bosch (1999).

4.3. X-ray astrophysics

A new era in deep space astrophysics began in 1999 when two x-ray observatories of unprecedented size and capability were launched into orbit: NASA’s Chandra and the European Space Agency’s XMM. Although previous x-ray missions had determined that the universe was rich in x-ray emission, they lacked the spectral and spatial resolution to clearly make out the details. The striking clarity of the data now arriving from the new x-ray observatories are the astrophysical equivalent of going from legally blind to 20–20 vision. Spectroscopically, it is reminiscent of the beginning of atomic physics in the early part of the 20th century when the richness of optical spectra from atoms on Earth was first being observed.

The x-ray data from Chandra and XMM contain a wealth of information about violent astrophysical processes that occur, for example, when stars explode, galaxies collide and matter falls into black holes. Radiation from the highly ionized matter that is produced in these circumstances has a complex spectral signature that challenges our understanding of the atomic physics and collision dynamics of HCIs. Because the Earth’s atmosphere is opaque to x-ray radiation, and because HCIs do not occur naturally on Earth, devices like the EBIT are valuable testbeds for developing both the x-ray telescope hardware itself (Silver *et al* 2000b) and the theoretical models that will be used to interpret the telescope observations (Gu *et al* 1999, Laming *et al* 2000, Silver *et al* 2000a). Indeed, with temperatures around 10 000 000 K, the ions produced and confined inside an EBIT rival the hottest and most reactive plasmas in the universe.

4.4. *The structure of the vacuum*

The idea that even an ideal vacuum is not just empty space has a long history. Descartes expressed this idea by saying ‘It is contrary to reason to say that there is a vacuum or a space in which there is absolutely nothing’. With the advent of quantum electrodynamics, well defined ways of subjecting the vacuum to quantitative physical experiments became possible. Perhaps the most remarkable aspect of the vacuum as described by quantum electrodynamics is that in the presence of a sufficiently strong electrostatic field, it is capable of generating real particles spontaneously. In effect, beyond a critical value, an electric field causes the ‘normal’ vacuum of ordinary experience to become unstable. This instability causes the vacuum to ‘decay’ in about 10^{-19} s (Greiner *et al* 1985) through a phase transition from a neutral to a charged state. The charged state is manifested by the spontaneous generation of positron–electron pairs. The Pauli exclusion principle stabilizes this emission and limits the number of emitted particles to a well defined finite value. An instructive gedanken experiment is presented by Greiner *et al* (1985) to give some physical insight as to what this means: imagine a box in which all particles are pumped out except for a bare HCl that is the source of a supercritical nuclear field. Within 10^{-19} s, two positrons and two electrons will spontaneously be generated out of the vacuum, the electrons will bind to the nuclear field, and the positrons are pumped out. The electronic cloud of the new HCl is the new charged vacuum, which is stable. If the two bound electrons are removed, the vacuum will emit two additional electrons (and two positrons) to re-establish the situation. In effect, nature begins generating a neutralizing stream of electrons spontaneously to prevent us from producing even higher charged ions. The supercritical fields at which this phase transition is predicted to occur can be generated in highly charged ions around $Z > 1/\alpha = 137$. The results of including the effect of the finite size of the nucleus shifts the onset of the transition to $Z > 173$ (the permutation of the last two digits is coincidental). It was previously thought that such a phase transition had already been observed in high-energy collisions of two heavy ions (temporarily forming a single superheavy nucleus) but it is now generally agreed that no experiments so far have achieved the necessary conditions long enough for the vacuum to decay (Schafer 1996). The study of highly charged ions with $Z < 92$ is a stepping stone on the way to this holy grail. Subcritical field effects such as wavelength shifts (Beiersdorfer *et al* 1998, Bosselmann *et al* 1999, Chantler *et al* 2000, Mohr *et al* 1998, Stohliker *et al* 2000) and changes in the g -factor (Haffner *et al* 2000) are subjects of active investigation presently.

4.5. *Solar physics and the Earth–Sun connection*

One of the first applications of the concept of an HCI in astronomy was to solve a longstanding problem summarized in the title of an article published in 1939 in the French journal *Scientia*: ‘A great enigma in current astronomical spectroscopy: the spectrum of emission lines in the solar corona’ (Swings 1939). In this paper, the author describes the struggle to explain dozens of unidentified emission lines observed during a solar eclipse. After essentially ruling out the speculations contained in 15 other papers, he essentially gave up and concluded that the problem was a grand enigma. Fawcett describes how Edlen resolved this enigma by identifying the lines as forbidden transitions in HCIs, calling it ‘perhaps the finest research in the annals of atomic spectroscopy’ (Fawcett 1981). The application of the spectra of HCIs to resolve many other problems in solar physics has continued through the years, and to date remains an important aspect of this field.

Currently, there is considerable interest in understanding and predicting certain aspects of solar flares because of the adverse effects they can have on earth. Powerful solar flares can

destroy the sensitive instruments in earth satellites if they are not powered down in advance. In May of 1998, it was reported that a solar flare permanently disabled a \$165 million satellite used by 45 million pagers in the US. Although optical observations of the Sun often provide hours of advance warning, sometimes the particles race towards the Earth at half the speed of light, allowing only a few minutes of warning. Even more disruptive than total destruction, perhaps, are transient problems that solar flares can inflict on commercial and military satellite behaviour. Energetic particles from flares can produce streaks of light in star-tracking navigation detectors, and make them point in improper and unstable directions (disrupting navigation) or change the electronic memory content and trigger unintended commands to be executed by onboard computer systems.

Even more challenging than protecting satellites is the problem of protecting humans in space. During a solar flare, astronauts can be exposed to lethal doses of radiation, and airline passengers and crews of commercial jets flying at high latitudes can be subject to significantly elevated doses (equivalent to dozens of chest x-rays per flight).

Finally, solar storms can disrupt the upper atmosphere of the Earth to such an extent that high-frequency radio transmission is blacked out. In addition, associated changes in the Earth's magnetic field can be inductively picked up by transcontinental power grids and lead to electrical blackouts. On March 13, 1989, for example, the entire Hydro Quebec system, which serves more than 6 million customers, was blacked out for a sustained period of time, and most of the neighbouring systems in the United States came close to experiencing the same sort of outage. The National Oceanic and Atmospheric Administration of the US Department of Commerce routinely issues online space weather alerts, warnings, and forecasts because of their potential impact on Earth².

The spectroscopy of HCIs plays an important role in research directed towards understanding solar flares, and in providing real-time diagnostics to predict their influence on Earth (Drake *et al* 1999, Laming *et al* 2000).

4.6. Microelectronics and nanotechnology

The microelectronics industry continues to be a major driver for the development of new techniques in the area of nanotechnology. Because ion beams are widely used in the fabrication of microelectronic devices, this area is a natural one to benefit from the unique characteristics of HCIs. Of particular interest are slow HCIs that can be produced with small and inexpensive devices. In the US, research to explore these applications began around 1992 (Schmieder and Bastasz 1993), and has been carried out recently at university and government laboratories that make up the Research Association for Multiply-Charged Ion-Surface Interaction Studies³: Lawrence Livermore National Laboratory (Schenkel *et al* 1999b), Oak Ridge National Laboratory (Meyer and Morozov 1999), National Institute of Standards and Technology (Gillaspy *et al* 1998), J R McDonald Laboratory at Kansas State University (Bahrim and Thumm 2000, Parks *et al* 1998), University of Florida (Cheng and Gillaspay 1997) and Cornell (Beebe and Kostroun 1992). In Europe, research in this area has been carried out largely within the Human Capital and Mobility Network of the European Union (Arnau *et al* 1997). A number of US and international patents have been issued⁴ and small

² <http://www.sec.noaa.gov/>

³ <http://www.phys.ksu.edu/area/jrm/ramcisis.html>

⁴ US patents: 5 327 475 (Ruxam Inc., 1994; lithography), 5 625 195 (France Telecom, 1997; implantation), 5 849 093 (1998; cleaning and smoothing). French patents: 2 757 881 and 2764 110 (Universite Pierre et Marie Curie, 1998 and 1999; etching, cleaning, and nanomanufacturing), 2 793 264 (X-ion, 2001; cleaning and microfabrication). Japanese patents: 9 199 457 (Hitachi, 1997; cleaning), 8 213 363 (Hitachi, 1996; lithography), 7 280 755 (Hitachi, 1995; electron spectroscopy) 7 230 985 and 6 326 060 (Hitachi, 1995 and 1994; etching). See also, French patent application 2 800 477

companies have been formed in France (Borsoni *et al* 2000), the US and the UK specifically to explore the possible commercialization of the new HCI-based technology. Some larger existing companies in the US and Japan (Itabashi *et al* 1995, Mochiji *et al* 1994, 1996) are also exploring the possibilities to a more limited degree. In the subsections below, several applications for HCIs produced with small sources are discussed in more detail. Reviews of related applications using very fast ions produced with large devices such as ion accelerators have been published previously in a special issue of the MRS Bulletin (Fischer and Metzger 2000), in books (Fleischer 1998) and in review articles (Fischer and Spohr 1983).

4.6.1. Ion implantation. The most common use of ion beams in microelectronics manufacturing today is ion implantation, a process in which high velocity ion beams are injected into materials. The ions are typically accelerated to a well defined velocity by traversing an electrostatic potential formed by high-voltage power supplies. One of the industry trends is to produce ions beams with higher velocities, but eventually the size and cost of the accelerating structures and power supplies becomes prohibitive. By using an HCI of the same species instead, one can obtain a Q -times higher ion energy with the same voltage. For example, Xe^{44+} is routinely produced using high voltages of only 8 kV, but when the ion is accelerated through the same 8 kV potential, it reaches an energy of over 350 keV. The advantages in cost, size and safety can be huge, even for relatively modest Q . The development of ion implanters that use multiply charged ions have already been built and reported in the literature by several industry laboratories (Amemiya *et al* 1998, Horsky 1998, Matsuda and Tanjyo 1996). These researchers used selected ions in the range from $Z = 5$ to $Z = 33$.

4.6.2. Ion lithography. The key step in microelectronics fabrication is lithography, an area dominated by optical techniques. Diffraction is currently limiting decreasing feature size, so making a shift to particle beam methods where diffraction is reduced by many orders of magnitude is being considered. Electron beams can be focused to very small spots, but because of their relatively small mass, they scatter through large angles when they enter solid materials (much like ping-pong balls scattering off a bowling ball). This scattering results in features that are much larger than the electron beam spot size. The heavier mass of ions makes them preferable, in this regard, to electron beams. Focused ion beam (FIB) systems have been used to produce 8 nm features (Kubena *et al* 1991). FIBs are commercially available, but their throughput for lithographic applications is low. High-throughput systems in which large-diameter beams are projected through a stencil mask to produce 50 nm resolution features are in the development stage. The economic and technical advantages of such ion projection lithography systems have been reviewed recently (Berry 1998, Kaesmaier and Loschner 2000, Kaesmaier *et al* 1999).

Beam focusing and rastering can be effectively applied to high- Z and/or high- Q ions as well, as demonstrated in figure 13 (Fischer and Metzger 2000). Unfortunately, high-throughput methods using masks cannot be effectively used with fast ion beams because of problems with required mask thickness and edge scattering (Fischer and Metzger 2000). Both of these problems can be avoided, however, by using the potential energy carried by slow HCIs to pattern surfaces. The mask need only be a small fraction of a micrometre thick to stop the sort of HCIs produced by an EBIT, for example. Furthermore, the electrons captured by an HCI during edge scattering will tend to neutralize it, thereby ‘turning off’ its ability to use the potential energy to modify subsequent surfaces it hits.

(X-ion, 2001; lithography and reticle) and associated Australian and world patent applications. See also footnotes 5 and 8 below.



Figure 13. A pointillist portrait of William Helmholtz, painted with high-velocity krypton ions. Each dot is formed by the impact of an individual ion. The width of the head is approximately $250\ \mu\text{m}$, about twice the width of a human hair. Figure courtesy of B Fischer (Fischer and Metzger 2000).

Masked ion beam lithography using HCIs was first demonstrated in 1998 (Gillaspy *et al* 1998), but many open questions remain to be studied before its potential value can be accurately assessed. In special cases, such as thin-film or shallow-junction applications in which uniform features with circular cross sections in the 1–100 nm range are required, HCIs might be put to use immediately (see section 4.10 below, for example). Atomic force microscope images of a lithographic resist material (PMMA) exposed to Xe^{44+} ions show that single HCIs can produce 24 nm wide dots with essentially 100% efficiency (Gillaspy *et al* 1998). Studies on an aluminosilicate compound (mica) have shown that features of a similar size can be produced, and that the dot size can be varied by adjusting the ion charge state up or down (Parks *et al* 1998). Figure 14 shows a pattern produced on a silicon wafer using HCIs and a sensitive ultra-thin self-assembled monolayer resist (Ratliff *et al* 1999). Taking into account the measured sensitivity of this resist to the HCIs and the currently available beam fluence (up to $3 \times 10^6\ \text{Xe}^{44+}/\text{s}$), the portion of the pattern shown in figure 14 should require about 1 min to produce. Next-generation EBIT-type HCI sources are being designed to improve on this by several orders of magnitude (Marrs 1999). One commercial organization is currently using HCIs from a high-fluence ECR ion source to produce silicon oxide nanodots for potential application in high-density memory devices (Borsoni *et al* 2000).

The features produced on surfaces by conventional ions seem to be rather different from those produced by HCIs. This is reasonable given that the physical mechanisms appear to be quite different. In the case of HCIs, a tremendous amount of potential energy seems to

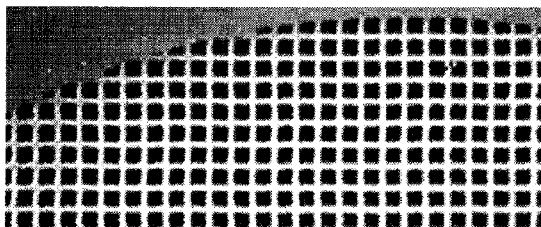


Figure 14. An array of $10\ \mu\text{m}$ gold squares patterned on a silicon wafer using Xe^{44+} ions, viewed in wide-angle with a light microscope. Close-up images taken with an electron microscope have been published elsewhere (Ratliff *et al* 1999).

be deposited in the first few atomic layers near the surface, and the kinetic energy seems to be largely irrelevant. Studies in mica in which the kinetic energy of the HCIs was varied by several orders of magnitude showed no significant change in the surface features, while varying the potential energy caused the dots to shrink in size and vanish into the detection limit. The physical picture that is emerging suggests that individual HCIs can produce fundamentally uniform nanoscale structures even in the limit that the ion energy is reduced towards zero. This may have important implications for lithographic patterning of shallow-junction devices, and other cases in which deep ion damage to the underlying substrate must be avoided.

Modelling the permanent changes caused to a surface by an HCI is still at a primitive stage of development. While considerable work has been carried out by atomic physicists to model the neutralization of the ion during its approach to the surface (see section 2.8), this work has stopped short of attempting to predict the response (dynamic motion) of the atoms which make up the surface. An initial step in the latter direction has been made by using a supercomputer to compute the motion of over 34 000 atoms surrounding a locally charged region of a surface which is assumed to be produced by a single incident HCI. Colour-coded atomic scale images of this molecular dynamics simulation, showing with sub-femtosecond time resolution the production of 10 nm diameter craters over the course of 10 s to 100 s of femtoseconds, are published elsewhere (Cheng and Gillaspay 1997). Subsequent refinement of the simulation (Hedstrom and Cheng 2000), including charge flow, confirms the basic predictions of the earlier work. These simulations suggest that the cratering of the surface should be absent in materials that have a very rapid electronic response (metals, for example). The possibility of exploiting this material-specific response to develop a novel type of method of surface patterning is being explored commercially (LeRoux *et al* 2000).

4.6.3. Ion microprobes. The most developed technological application for HCIs at present is in the area of surface microprobes. The possibility of using HCIs to upgrade conventional secondary ion mass spectrometry (SIMS) probes was discussed in 1993 through a Cooperative Research and Development Agreement between the Advanced Lithography Group and the National Institute of Standards and Technology. Independent work at the Lawrence Livermore National Laboratory demonstrated the feasibility and advantages of this method through laboratory experiments (Hamza *et al* 1999, Schenkel *et al* 1999a, b, 1998, Schenkel 2000). In addition, several patents have been issued to companies and universities in Japan⁵ and an established US surface analysis company has become involved in developing this application⁶.

⁵ US patents: 5 714 757 (Hitachi 1998; SIMS), 5 528 034 (University of Tokyo 1996; SIMS), Japanese patents: 8 166 362 (Hitachi 1995; SIMS).

⁶ Charles Evans and Associates, Sunnyvale CA; research supported in part by NIST SBIR contract <http://www.rdc.noaa.gov/~amd/abstracts1999.pdf> (identification of this company name is not intended to imply recommendation or endorsement by the National Institute of Standards and Technology of any product or service).

An alternative development in the general area of ion-based microprobes involves the use of HCIs to power a projection x-ray microscope (Marrs *et al* 1998). In an initial test of this idea, bare and hydrogen-like argon ions from the Livermore EBIT were focused onto a 20 μm spot, where they produced a point source of 3 keV x-rays that was used to image a nickel wire mesh. See also the last paragraph of section 4.9 below for possible medical applications of this type of imaging device.

It has been proposed that a next-generation EBIT with relatively modest upgrades (Marrs 1999) will result in an HCI-based microscope with x-ray fluxes equal to that used for scanning x-ray microscopy at the National Synchrotron Light Source and the Cornell High Energy Synchrotron Light Source. The ultimate resolution of an HCI-based x-ray microscope remains to be determined, but the possibility of localizing the truly point-source x-ray emission from individual ion impacts using secondary charged particle imaging correlated with spatially sensitive x-ray detection is a tantalizing possibility (Bruch *et al* 1998).

4.7. Quantum computing

Recently, a great deal of attention has been devoted to the possibility of creating a new type of computer that is based on the non-intuitive aspects of quantum mechanics that are not contained in the laws of classical physics (Sackett *et al* 2000). Quantum computing can be highly efficient because it relies on the parallel evolution of multicomponent wavefunctions. Reading out the results of the computation, however, requires a measurement which collapses the wavefunction and leads to a fundamental loss of information during that particular computation cycle. There are a few highly specialized computations, however, for which a major gain in efficiency over conventional computers can, in principle, be realized. Because one of these specialized applications is of critical importance for national security (decrypting encoded messages) a large amount of effort has been directed toward the long-range goal of realizing a quantum computer in a variety of physical systems. One of the most advanced schemes for quantum computing uses trapped ions (Sackett *et al* 2000). In all of the work done to date, the ions have been singly charged. Some advantages of using highly charged ions have been outlined in the literature previously (Gruber *et al* 2000, 2001, Wineland *et al* 1998). It is unclear, at present, whether the value of the improvements would outweigh the added difficulty of using highly charged ions. It appears that no direct experimental activity in the area of quantum computing with highly charged ions has been pursued to date.

4.8. Energy technology: fusion

Harnessing the mechanism of energy production used by the Sun, nuclear fusion, has been an active area of research for several decades. The power generated by experimental fusion reactors has increased steadily during the past 20 years, increasing at a rate that exceeds the more well known progress in the semiconductor industry (Moore's law). Today, conditions are close to those necessary for a commercial fusion power plant, so part of the scientific effort is shifting towards engineering design issues.

HCIs may play an important role as a diagnostic tool for monitoring the conditions inside fusion plasmas. Although x-ray spectral lines are often used in these diagnostics, optical lines have significant advantages over them (Denne and Hinnov 1987). Working together with scientists from the Princeton Plasma Physics Laboratory, the NIST EBIT group has explored the possible use of visible light emitted by highly charged titanium-like ions as a monitor of the temperature (Doppler width) and magnetic field (Zeeman shifts) inside a hot plasma (Adler *et al* 1995). In particular, the $J = 2$ to $J = 3$ fine structure transitions within the ground term

of these ions seems particularly promising because they appear to violate the usual photon energy scaling laws (see section 2.3.3 above). This allows one to keep the spectral emission in the visible and near-UV for a wide range of plasma temperatures (Feldman *et al* 1991, Porto *et al* 2000b). More conventional optical diagnostic lines are rather narrowly tailored to specific temperatures and rapidly fade out as the temperature is varied. When this happens on the titanium-like sequence, the signal can be regained by shifting to one higher or lower value of Z in the diagnostic species.

One of the advantages of using optical lines in place of x-ray lines for fusion diagnostics is that the associated measurement technology is much more developed in the optical regime. Fibre optics can be used, for example, to efficiently collect photons and direct them into remotely located measuring instruments, thereby removing the need to conduct experiments near the high-radiation core of a reactor vessel. In addition, the relatively narrow natural widths make optical lines preferable to x-ray lines for precise determination of the temperature and the magnetic field.

Table-top ion traps are useful devices for carrying out spectroscopic research in support of the fusion work that takes place at large national plasma facilities, but could the little traps be used themselves to obtain fusion conditions? The reactivity per unit volume would seem to be too low, but a method of boosting the density considerably and actually overcoming the Brillouin limit has been seriously discussed in the literature (Barnes *et al* 1993). Recently, experimental data from a table-top trap have been presented which suggest that the Brillouin limit has been exceeded by one order of magnitude (Zhuang *et al* 2000).

4.9. Medicine

The results of many research studies indicate that ion beams are a particularly effective method of treating cancer and other tumours of the body. One of the main reasons is that high doses can be delivered to the tumour with relatively little damage to surrounding healthy tissue. The physical basis for this is clear:

- (a) ion beams can be precisely directed at the tumor target;
- (b) the ion beam energy can be precisely adjusted to come to rest inside the tumor target; and
- (c) the deposition of kinetic energy of an ion peaks dramatically near the end of its trajectory (figure 15).

The last two factors, in particular, make it possible to deliver more dose to the tumour with fewer side effects than is possible using conventional radiation treatments, thereby improving the clinical outcome.

The first treatment of patients with ion beams took place in 1954, in a physics research laboratory in Berkeley. From that time until the Bevalac accelerator was shut down in 1992, approximately 2000 patients were treated at this location. Over 8000 additional patients have been treated at the Harvard Cyclotron Laboratory, since 1961. Based on these and several other research programmes, the first hospital-based ion beam treatment facility was constructed in 1990 in Loma Linda, California. This facility was designed to treat over 1000 patients per year, using proton beams. As an outgrowth of the Harvard programme, the Massachusetts General Hospital recently opened a new proton-beam therapy centre that is also designed to treat about 1000 patients per year. Over a dozen other ion beam treatment facilities, mainly operating at existing physics research facilities, are in operation around the world. To date, over 30 000 patients worldwide had been treated with ion beams, most of them protons. Reviews and references to these and other developments, as well as lists of new ion therapy facilities under

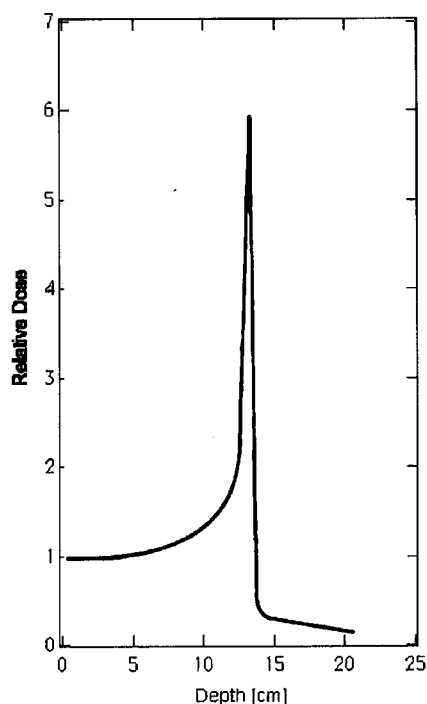


Figure 15. Relative dose of energy deposited at various depths in human tissue by nitrogen ions with an initial velocity of 66% of the speed of light (310 MeV u^{-1}). Figure after Kraft *et al* (1991).

construction can be found in the literature (Chu *et al* 1993, Kraft 2000, Miller 1995) or online from the Proton Therapy Cooperative Group⁷.

Although most of the past experience is with proton beams, there are clinical advantages to using higher- Z ion beams instead. A limited amount of heavy-ion beam therapy has already been carried out at a number of facilities, with very promising results. The first dedicated treatment facility to use heavy ions was recently constructed in Chiba, Japan; they have already treated over 700 patients. Construction of new facilities for ion therapy is being pursued particularly vigorously in Japan where cancer is the leading cause of death (Soga 2000).

The GSI facility in Germany has been treating a small number of patients with heavy ions since 1997 (Scholz 2000, Stelzer 1998). A precise beam positioning and energy control system has been developed there in order to more accurately deposit the ion energy into the tumor volume and minimize the damage to healthy surrounding tissue. The effectiveness of the GSI work was apparent from the outcome of the first patient treated at the facility. This patient had a very large brain tumor and a poor prognosis. After treatment, the tumor fully disappeared and the side effects were minimal. In a recent report on the clinical outcome of 23 patients treated at GSI through September of 1999 (Debus *et al* 2000), the local tumour control rate (full remission and non-recurrence at the treated tumor site) was 94% at 1 yr after treatment. Over 70 patients have now been treated at this location.

Currently, limiting factors in the more widespread application of high- Z ion therapy for tumours is cost and available technical expertise. Research into more efficient and inexpensive ways of producing the necessary ion beams is needed. HCIs have an important role to play

⁷ <http://neurosurgery.mgh.harvard.edu/hcl/ptles.htm>

in this. In Frankfurt, for example, work is underway to produce a 'MEDEBIS' (a medical electron beam ion source) for this purpose (Kester *et al* 1996, 1997).

Although high- Z ions for medical therapy are produced in ultra-high vacuum conditions, they are eventually delivered to the patient by passing through a thin metal window and a considerable column of air, both of which influence the charge state. For high velocities the ions can maintain a high charge state, or even increase it, while travelling through the air because of the stripping effect of the energetic ion-atom collisions (Betz 1972).

In addition to the applications of HCIs for cancer therapy, there are also possible applications for their use in medical imaging. In particular, the areas of breast cancer (mammography) and heart disease (coronary angiography) have been targeted in a recent patent⁸ for the HCI-powered x-ray microscope mentioned in section 4.6.3 above.

4.10. Biotechnology

The crossroads of nanotechnology and biology is becoming a fruitful area of interdisciplinary research. A fundamental length scale for this research is the distance spanned by a single helical turn of a DNA molecule: 3.4 nm. This length scale is large compared with the atomic scale, yet small compared with current microfabrication technology. Leaders in the biotechnology industry have predicted that genomic sciences will benefit greatly from the development of new methods of manipulating matter on these nanometre-length scales (Haseltine 2000).

Protein sequencing is an area of biotechnology that is in need of better tools to fragment large molecules into smaller units. Preliminary experiments involving the use of beams of HCIs for DNA fragmentation have been carried out by C Ruehlicke using the EBITs and atomic force microscope facilities at NIST (Ruehlicke *et al* 1997) and Livermore (Ruehlicke *et al* 1998).

There is a large demand from the biosciences community for new analysis methods. Mass spectrometry is an established technique that is widely used, but there are significant limitations associated with the difficulty in producing gaseous ions of organic molecules. Shock-wave desorption using fast atomic ion beams (Daya *et al* 1997, Johnson and Sundqvist 1992, Reimann 1995) or slow HCIs may be a method of overcoming some of these limitations. Preliminary observations of HCI-induced desorption of the amino acid L-valine have been presented in figure 11 of chapter 17 of Gillaspay (2001).

The production of artificial supported membranes for use in biotechnology experiments is an active area of research (Plant 1999). One of the key steps is to produce uniform holes (pores) in the support for the insertion of membrane proteins. The diameters of these holes are on the order of 10 nm and smaller. At NIST, researchers in the Atomic Physics Division and the Biotechnology Division have been collaborating on some preliminary experiments to assess the feasibility of using HCIs to produce these small holes in thin materials.

5. Conclusion

The field of HCI research has developed considerably in the past decade. The motivation for much of this work derives from the scaling rules summarized in table 1. These rules reflect the fact that as the ion charge is increased, some phenomena are dramatically enhanced while others are reduced. Some numerical values to set the absolute scale of a few of the scaling rules are given in table 2.

⁸ US patent 6 115 452 (Regents of the University of California 2000; imaging).

Table 1. Summary of scaling rules for various physical processes discussed in this paper. See text for definitions of terms and notes on range of applicability.

Bohr radius	Z^{-1}
Electron density at nucleus, neutral atom	Z
Electron density at nucleus, HCl	Z^3
Parity-violation, HCl	Z^5
Kinetic energy of HCl accelerated through an electrostatic potential	Q
Minimum impact kinetic energy under image acceleration	$Q^{3/2}$
Ionization energy (I)	Z^2
Photon energy, $\Delta n = 1$ transitions	Z^2
Photon energy, $\Delta n = 0$ (fine structure) transitions	Z^4
Orbital angular momentum of electron	Z
Orbital velocity of 1S electron in hydrogen-like ion	$c\alpha Z$
Zeeman shift	Z^0
Zeeman shift, relativistic correction factor	$1 - 0.33(\alpha Z)^2$
Stark shift, first order (non-degenerate)	Z^{-1}
Stark shift, second order (degenerate)	Z^{-4}
Linewidth of hyperfine transitions	Z^9
Linewidth of intercombination transitions	Z^{10}
Linewidth of electric dipole transitions	Z^4
Relative line blurring, $\Delta\lambda/\lambda$, of electric dipole transitions	Z^2
Electric field experienced by bound electron	Z^3
Electron-electron interaction within ion	Z^2
Peak location of ionization cross section (Lotz)	$I \sim Z^2$
Peak magnitude of ionization cross section (Lotz)	$I^{-2} \sim Z^{-4}$
Peak location of excitation cross section, electric dipole	$\Delta E \sim Z^2$
Peak magnitude of excitation cross section, electric dipole	$\Delta E^{-2} \sim Z^{-4}$
Mean free path through background gas, slow ions	Q
Mean free path through background gas, fast ions	Q/v^7

Table 2. Summary of numerical values of selected quantities discussed in this paper. See text for definitions of terms and notes on range of applicability.

Bohr radius (cf Compton wavelength of electron, $\lambda_c = 2.43 \times 10^{-12}$ m)	$\sim 22\lambda_c Z^{-1}$
Charge of the electron, at distances $\gg \lambda_c$	1.60×10^{-19} C
Charge of the electron, at distances $\ll \lambda_c$	∞
Crossover velocity dividing 'fast' and 'slow' ions	$v_0 = 2 \times 10^6$ m s $^{-1}$
Velocity gain from image charge, hydrogenlike	0.3–1.2% v_0
Energy gain from image charge acceleration	$\sim 1 \times Q^{3/2}$ eV
Neutralization energy of U $^{1+}$	6 eV
Neutralization energy of U $^{92+}$	763 000 eV
Electric field felt by 1s electron, hydrogenlike uranium	10^{16} V cm $^{-1}$
Critical Z for spontaneous generation of matter (point nucleus)	137
Critical Z for spontaneous generation of matter (finite nucleus)	173
Diameter of surface region modified by slow HCl impact	~ 10 nm
Peak location of ionization cross section (I = ionization energy)	$2.72 \times I$
Peak magnitude of ionization cross section	Equation (7)
Mean free path through background gas, slow ions	Equation (8)

At the 85th Nobel symposium in 1992, Joe Sucher suggested that just as the progression of technology can be described by 'ages' (stone age, bronze age, etc) so too does science enter into ages in which new progress is enabled by some underlying development. Sucher

coined a new term to describe a change that had taken place in atomic physics research: 'We entered and are still in the midst of a veritable second flowering, which I will call the ion age' (Sucher 1993). At the same symposium, another speaker (Briand 1993) made reference to the then-new EBIT devices that were beginning to make it relatively easy and inexpensive to produce very highly charged ions. Meanwhile, half way around the world, a new heavy-ion accelerator dedicated to the treatment of cancer patients was gearing up (Myers 1993). These and other developments helped foster new connections between researchers in fundamental atomic physics and other fields such as materials science and the life sciences.

Since the 1992 Nobel symposium the quality and number of tools available to study HCIs has increased considerably. There are now in operation or under construction, nearly a dozen EBITs around the world. In addition, these and other methods of producing and studying HCIs, such as particle accelerators and storage rings, have improved their capabilities dramatically. A cursory look at the remaining open questions and possibilities for future research makes it clear that the ion age has just begun.

Acknowledgments

I thank Zoltan Berenyi for help with some of the figures, Pam Novosel for help with the references and figures, Indrek Martinson and Bernd Fischer for providing original copies of their figures, and Peter Mohr, Endre Takacs, and John Woodward for critical readings of the manuscript.

References

- Adler H, Meyer E S, Serpa F G, Takacs E, Gillaspay J D, Brown C M and Feldman U 1995 *Nucl. Instrum. Methods B* **98** 581–4
- Amemiya K, Ito J and Tokiguchi K 1998 *J. Vac. Sci. Technol. A* **16** 472–6
- Anderson H, 1981 *Physics Vade Mecum* (New York: American Institute of Physics)
- Angert N 1991 *Nucl. Tracks Rad. Meas.* **19** 871–4
- Antsiferov P S and Movshev V G 1991 *Z. Phys. D* **21** S317–S318
- Arnau A *et al* 1997 *Surf. Sci. Rep.* **27** 117–239
- Aumayr F, Winter H P, Limburg J, Hoekstra R and Morgenstern R 1997 *Phys. Rev. Lett.* **79** 2590–600
- Bacher R, Blum P, Gotta D, Heitlinger K, Schneider M, Missimer J and Simons L M 1989 *Phys. Rev. A* **39** 1610–20
- Bahrim B and Thumm U 2000 *Surf. Sci.* **451** 1–6
- Barnes D C, Nebel R A and Turner L 1993 *Phys. Fluids B* **5** 3651–60
- Becker R 1995 *Handbook of Ion Sources* ed B Wolf (Boca Raton, FL: Chemical Rubber Company) p 157–82
- Bednyakov I, Labzowsky L, Plunien G, Soff G and Karasiev V 2000 *Phys. Rev. A* **61** 012103
- Beebe E N and Kostroun V O 1992 *Rev. Sci. Instrum.* **63** 3399–411
- Beiersdorfer P, Osterheld A L, Scofield J H, Lopez-Urrutia J R C and Widmann K 1998 *Phys. Rev. Lett.* **80** 3022–5
- Berry I L 1998 *J. Vac. Sci. Technol. B* **16** 2444–8
- Bethe H and Salpeter E 1977 *Quantum Mechanics of One- and Two-Electron Atoms* (New York: Plenum)
- Betz H D 1972 *Rev. Mod. Phys.* **44** 465–539
- Beyer H, Kluge H and Shevelko V P 1997 *X-Ray Radiation of Highly Charged Ions* (Berlin: Springer)
- Beyer H and Shevelko V P 1999 *Atomic Physics with Heavy Ions* (Berlin: Springer)
- Biedermann C, Forster A, Fussmann G and Radtke R 1997 *Phys. Scr. T* **73** 360–1
- Borsoni G, Gros-Jean M, Korwin-Pawlowski M L, Laffitte R, Le Roux V and Vallier L 2000 *J. Vac. Sci. Technol. B* **18** 3535–8
- Bosch F 1999 *Phys. Scr. T* **80A** 28–34
- Bosch F *et al* 1996 *Phys. Rev. Lett.* **77** 5190–3
- Bosselmann P, Staude U, Horn D, Schartner K H, Folkmann F, Livingston A E and Mokler P H 1999 *Phys. Rev. A* **59** 1874–83
- Bouchiat M A and Bouchiat C 1974 *J. Physique* **35** 899–927
- 1997 *Rep. Prog. Phys.* **60** 1351–96

- Briand J P 1993 *Phys. Scr.* T **46** 157–61
- Briand J P, Giardino G, Borsoni G, Le Roux V, Bechu N, Dreuil S, Tuske O and Machicoane G 2000 *Rev. Sci. Instrum.* **71** 627–30
- Briand J P, Thuriez S, Giardino G, Borsoni G, Froment M, Eddrief M and Sebenne C 1997a *Phys. Rev. Lett.* **79** 2591–1
- Briand J P, Thuriez S, Giardino G, Borsoni G, LeRoux V, Froment M, Eddrief M, deVilleneuve C, DetatBan B and Sebenne C 1997b *Phys. Rev. A* **55** R2523-6
- Brown G E 1987 *Phys. Scr.* **36** 71–6
- Brown G E and Ravenhall D G 1951 *Proc. R. Soc.* **208**
- Bruch R, Afanasyeva N, Kano P and Schneider D 1998 *Nanotechnology* **9** 346–51
- Burgdorfer J, Lerner P and Meyer F W 1991 *Phys. Rev. A* **44** 5674–85
- Chandler G A, Chen M H, Dietrich D D, Egan P O, Zioc K P, Mokler P H, Reusch S and Hoffmann D H H 1989 *Phys. Rev. A* **39** 565–9
- Chantler C T, Paterson D, Hudson L T, Serpa F G, Gillaspay J D and Takacs E 2000 *Phys. Rev. A* **6204** 2501
- Cheng H P and Gillaspay J D 1997 *Phys. Rev. B* **55** 2628–36
- Chu W T, Ludewigt B A and Renner T R 1993 *Rev. Sci. Instrum.* **64** 2055–122
- Cowan R 1981 *The Theory of Atomic Structure and Spectra* (Berkeley, CA: University of California)
- Currell F J 2001 *Trapping Highly Charged Ions: Fundamentals and Applications* ed J D Gillaspay (New York: Nova Science)
- Daya D *et al* 1997 *Radiat. Meas.* **28** 101–10
- de Sousa Zacaris A 1990 Spectroscopic tests of quantumelectrodynamic interactions in helium-like chlorine and nickel *MS Thesis* University of Notre Dame
- Debus J, Haberer T, Schulz-Ertner D, Jakel O, Wenz F, Enghardt W, Schlegel W, Kraft G and Wannenmacher M 2000 *Strahlenther. Onkol.* **176** 211–6
- Denne B and Hinnov E 1987 *Phys. Scr.* **35** 811–8
- Donets E D 1998 *Rev. Sci. Instrum.* **69** 614–9
- Douglas M and Kroll N M 1974 *Ann. Phys.* **82** 89–155
- Drake J J, Swartz D A, Beiersdorfer P, Brown G V and Kahn S M 1999 *Astrophys. J.* **521** 839–43
- Ducree J J, Casali F and Thumm U 1998 *Phys. Rev. A* **57** 338–50
- Dunford R W 1996 *Phys. Rev. A* **54** 3820–3
- Eides M I and Shelyuto V A 1995 *Phys. Rev. A* **52** 954–61
- Fang T T and Canizares C R 2000 *Astrophys. J.* **539** 532–9
- Fawcett B C 1981 *Phys. Scr.* **24** 663–80
- Feldman U, Indelicato P and Sugar J 1991 *J. Opt. Soc. Am. B* **8** 3–5
- Fischer B E and Metzger S 2000 *MRS Bull.* **25** 39–42
- Fischer B E and Spohr R 1983 *Rev. Mod. Phys.* **55** 907–48
- Fleischer R L 1998 *Tracks to Innovation: Nuclear Tracks in Science and Technology* (New York: Springer)
- Foldy L 1958 *Phys. Rev.* **111** 1093
- Fortson E N and Lewis L L 1984 *Phys. Rep. Rev. Sec. Phys. Lett.* **113** 289–344
- Fournier P *et al* 2000 *Rev. Sci. Instrum.* **71** 1405–8
- Froese Fischer C and Jonsson P 2001 *Theochem. J. Mol. Struct.* **537** 55–62
- Gaigalas G, Karpuskiene R and Rudzikas Z 1999 *Phys. Scr. T* **80B** 472–3
- Geller R 1996 *Electron Cyclotron Resonance Ion Sources and ECR Plasmas* (Philadelphia, PA: IOP Publishing)
- Gillaspay J 2001 *Trapping Highly Charged Ions: Fundamentals and Applications* (New York: Nova Science)
- 1997 *Phys. Scr. T* **71** 99–103
- Gillaspay J D, Parks D C and Ratliff L P 1998 *J. Vac. Sci. Technol. B* **16** 3294–7
- Gillaspay J D *et al* 1995 *Phys. Scr. T* **59** 392–5
- Giroux M L and Shapiro P R 1996 *Astrophys. J. Suppl.* **102** 191–238
- Gosh P K 1995 *Ion Traps* (New York: Oxford University Press)
- Greiner W, Muller B and Rafelski J 1985 *Quantum Electrodynamics of Strong Fields* (Berlin: Springer)
- Gruber L, Holder J P, Beck B R, Steiger J, McDonald J W, Glassman J, DeWitt H, Church D A and Schneider D 2000 *Hyperfine Interact.* **127** 215–22
- Gruber L, Holder J P, Steiger J, Beck B R, DeWitt H E, Glassman J, McDonald J W, Church D A and Schneider D 2001 *Phys. Rev. Lett.* **86** 636–9
- Gu M F, Kahn S M, Savin D W, Beiersdorfer P, Brown G V, Liedahl D A, Reed K J, Bhalla C P and Grabbe S R 1999 *Astrophys. J.* **518** 1002–9
- Haffner H, Beier T, Hermanspahn N, Kluge H J, Quint W, Stahl S, Verdu J and Werth G 2000 *Phys. Rev. Lett.* **85** 5308–11
- Hamza A V, Schenkel T, Barnes A V and Schneider D H 1999 *J. Vac. Sci. Technol. A* **17** 303–5

- Haseltine W 2000 What's Next in Genomics Research? *NIST Technology Services Seminar*
- Heckmann P H and Trabert E 1989 *Introduction to the Spectroscopy of Atoms* (Amsterdam: North-Holland)
- Hedstrom M and Cheng H P 2000 *J. Phys. Chem. B* **104** 4633–41
- Horsky T N 1998 *Rev. Sci. Instrum.* **69** 1688–90
- Itabashi N, Mochiji K, Shimizu H, Ohtani S, Kato Y, Tanuma H and Kobayashi N 1995 *Japan. J. Appl. Phys. Part 1* **34** 6861–5
- Johnson R E and Sundqvist B U R 1992 *Phys. Today* **45** 28–36
- Kaesmaier R and Loschner H 2000 *Microelectron. Eng.* **53** 37–45
- Kaesmaier R, Loschner H, Stengl G, Wolfe J C and Ruchhoeft P 1999 *J. Vac. Sci. Technol. B* **17** 3091–7
- Kester O, Becker R and Kleinod M 1996 *Rev. Sci. Instrum.* **67** 1165–7
- 1997 *Phys. Scr. T* **71** 107–12
- Khemliche H, Schlatholter T, Hoekstra R, Morgenstern R and Schippers S 1998 *Phys. Rev. Lett.* **81** 1219–22
- Khodja H and Briand J P 1997 *Phys. Scr. T* **71** 113–6
- Klaft I, Borneis S, Engel T, Fricke B, Grieser R, Huber G, Kuhl T, Marx D, Neumann R, Schroder S, Seelig P and Volker L 1994 *Phys. Rev. Lett.* **73** 2425–7
- Kraft G 2000 *Nucl. Instrum. Methods A* **454** 1–10
- Kraft G *et al* 1991 *Nucl. Tracks Radiat. Meas.* **19** 911–4
- Kubena R L, Ward J W, Stratton F P, Joyce R J and Atkinson G M 1991 *J. Vac. Sci. Technol. B* **9** 3079–83
- Kuhl T *et al* 1997 *Nucl. Phys. A* **626** 235C–40C
- Kuramoto H *et al* 2000 *Rev. Sci. Instrum.* **71** 687–9
- Laming J M *et al* 2000 *Astrophys. J.* **545** L161–4
- LeRoux V, Borsoni G and Korwin-Pawlowski M L 2000 A reflection lithography using multicharged ions, *Conf. on Micro- and Nano-Engineering* (Jena)
- Levine M A, Marrs R E, Henderson J R, Knapp D A and Schneider M B 1988 *Phys. Scr. T* **22** 157–63
- Lindgren I, Martinson I and Schuch, R (ed) 1992 Heavy-ion spectroscopy and QED effects in atomic systems *Proc. Nobel Symp. 1985 (Saltsjobaden)* *Phys. Scr. T* **46**
- Lopez-Urrutia J R C, Bapat B, Feuerstein B, Werdich A and Ullrich J 2000 *Hyperfine Interact.* **127** 497–501
- Lopez-Urrutia J R C, Beiersdorfer P, Savin D W and Widmann K 1996 *Phys. Rev. Lett.* **77** 826–9
- Lorrain P and Corson D 1970 *Electromagnetic Fields and Waves* (San Francisco, CA: Freeman)
- Lotz W 1967 *Z. Phys.* **206** 205–11
- Margolis H S, Oxley P K, Varney A J, Groves P D and Silver J D 1997 *Phys. Scr. T* **73** 375–7
- Marrs R E 1999 *Nucl. Instrum. Methods B* **149** 182–94
- Marrs R E, Beiersdorfer P and Schneider D 1994a *Phys. Today* **47** 27–34
- Marrs R E, Elliott S R and Knapp D A 1994b *Phys. Rev. Lett.* **72** 4082–5
- Marrs R E, Schneider D H and McDonald J W 1998 *Rev. Sci. Instrum.* **69** 204–9
- Marrs R 1982 *Atomic Physics of Highly Ionized Atoms* (New York: Plenum)
- 1988 *Physics of Highly-Ionized Atoms* (New York: Plenum)
- Martinson I 1989 *Rep. Prog. Phys.* **52** 157
- Martinson I and Curtis L J 1989 *Contemp. Phys.* **30** 173–85
- Matsuda K and Tanjyo M 1996 *Rev. Sci. Instrum.* **67** 901–4
- Meyer F W and Morozov V A 1999 *Nucl. Instrum. Methods B* **157** 297–303
- Miller D W 1995 *Med. Phys.* **22** 1943–54
- Mochiji K, Itabashi N, Yamamoto S, Ochiai I and Okuno K 1994 *Japan. J. Appl. Phys. Part 1* **33** 7108–11
- Mochiji K, Itabashi N, Yamamoto S, Shimizu H, Ohtani S, Kato Y, Tanuma H, Okuno K and Kobayashi N 1996 *Surf. Sci.* **358** 673–7
- Mohr P J, Plunien G and Soff G 1998 *Phys. Rep. Rev. Sec. Phys. Lett.* **293** 228–369
- Mokler P H, Bosch F, Stohlker T and Wolf A (ed) 1998 *Proc. 9th Int. Conf. on the Physics of Highly Charged Ions (Bensheim)* Germany *Phys. Scr. T* **80A/B**
- Muller A and Salzborn E 1977 *Phys. Lett. A* **62** 391–4
- Myers F S 1993 *Phys. World* **6** 8–8
- Ovsyannikov V P, Zschornack G, Grossmann F, Landgraf S, Ullmann F and Werner T 2000 *Rev. Sci. Instrum.* **71** 690–2
- Pachucki K 1994 *Phys. Rev. Lett.* **72** 3154–7
- Pal'chikov V. G and Shevelko V P 1995 *Reference Data on Multicharged Ions* (Berlin: Springer)
- Parks D C, Stockli M P, Bell E W, Ratliff L P, Schmieder R W, Serpa F G and Gillaspay J D 1998 *Nucl. Instrum. Methods B* **134** 46–52
- Penetrante B M, Bardsley J N, Dewitt D, Clark M and Schneider D 1991 *Phys. Rev. A* **43** 4861–72
- Perez J A and Olson R E 1999 *Application of Accelerators in Research and Industry: Proc. 15th Int. Conf.* ed J L

- Duggan and I L Morgan (New York: American Institute of Physics)
- Pikin A I, Morgan C A, Bell E W, Ratliff L P, Church D A and Gillaspay J D 1996 *Rev. Sci. Instrum.* **67** 2528–33
- Pindzola M S 1993 *Phys. Rev. A* **47** 4856–8
- Plant A L 1999 *Langmuir* **15** 5128–35
- Plante D R, Johnson W R and Sapirstein J 1994 *Phys. Rev. A* **49** 3519–30
- Porto J V, Kink I and Gillaspay J D 2000a *Rev. Sci. Instrum.* **71** 3050–8
- 2000b *Phys. Rev. A* **6105** 4501
- Ratliff L P, Bell E W, Parks D C, Pikin A I and Gillaspay J D 1997 *Rev. Sci. Instrum.* **68** 1998–2002
- Ratliff L P, Minniti R, Bard A, Bell E W, Gillaspay J D, Parks D, Black A J and Whitesides G M 1999 *Appl. Phys. Lett.* **75** 590–2
- Reimann C T 1995 *Nucl. Instrum. Methods B* **95** 181–91
- Ruehlicke C, Ratliff L P, Schneider D H and Gillaspay J D 1997 unpublished
- Ruehlicke C, Schneider D, Schneider M, DuBois R D and Balhorn R 1998 *Nanotechnology* **9** 251–6
- Sackett C A *et al* C 2000 *Nature* **404** 256–9
- Sampson D H and Zhang H L 1992 *Phys. Rev. A* **45** 1556–61
- Sapirstein J 1998 *Rev. Mod. Phys.* **70** 55–76
- Savin D W, Beiersdorfer P, Kahn S M, Beck B R, Brown G V, Gu M F, Liedahl D A and Scofield J H 2000 *Rev. Sci. Instrum.* **71** 3362–72
- Schafer A 1996 *Nucl. Instrum. Methods B* **119** 48–54
- Schafer A, Soff G, Indelicato P, Muller B and Greiner W 1989 *Phys. Rev. A* **40** 7362–5
- Schenkel T, Hamza A V, Barnes A V and Schneider D H 1999b *Prog. Surf. Sci.* **61** 23–84
- Schenkel T, Hamza A V, Barnes A V, Schneider D H, Walsh D S and Doyle B L 1998 *J. Vac. Sci. Technol. A* **16** 1384–7
- Schenkel T, Newman M W, Niedermayr T R, Machicoane G A, McDonald J W, Barnes A V, Hamza A V, Banks J C, Doyle B L and Wu K J 2000 *Nucl. Instrum. Methods B* **161** 65–75
- Schenkel T *et al* 1999a *Phys. Scr. T* **80A** 73–5
- Schmieder R W and Bastasz R J 1993 *AIP Conf. Proc. 274: 6th Int. Conf. on the Physics of Highly Charged Ions* ed P Richard, M Stockli, C L Cocke and C D Lin (New York: AIP) p 675–81
- Schneider D, Clark M W, Penetrante B M, McDonald J, Dewitt D and Bardsley J N 1991 *Phys. Rev. A* **44** 3119–24
- Schneider D H G and Briere M A 1996 *Phys. Scr.* **53** 228–42
- Scholz M 2000 *Nucl. Instrum. Methods B* **161** 76–82
- Siems T *et al* 2000 *Phys. Rev. Lett.* **84** 4573–6
- Silver E *et al* 2000a *Astrophys. J.* **541** 495–500
- 2000b *Nucl. Instrum. Methods A* **444** 156–60
- Silver J D *et al* 1994 *Rev. Sci. Instrum.* **65** 1072–4
- Soga F 2000 *Rev. Sci. Instrum.* **71** 1056–60
- Stelzer H 1998 *Nucl. Phys. B* 650–7
- Stohlker T *et al* 2000 *Phys. Rev. Lett.* **85** 3109–12
- Stolterfoht N, Bremer J H and Muino R D 1999 *Int. J. Mass Spectrom.* **192** 425–36
- Sucher J 1993 *Phys. Scr. T* **46** 239–42
- Swings P 1939 *Scientia* **65** 72
- Takacs E *et al* 1996 *Phys. Rev. A* **54** 1342–50
- Van Regemorter H 1962 *Astrophys. J.* **136** 906
- Wineland D J, Monroe C, Itano W M, Leibfried D, King B E and Meekhof D M 1998 *J. Res. Natl Inst. Stand. Technol.* **103** 259–328
- Winter H and Aumayr F 1999 *J. Phys. B: At. Mol. Opt. Phys.* **32** R39–65
- Zhuang G, Liu W D, Yu C X, Zheng J, Fu C J, Xie J L, Zhao K, Bai B, Liang X P, Zhao S J and Chi J 2000 *Phys. Plasmas* **7** 3912–6
- Zipfel B, Becker R, Kleinod M and Rao R 1998 *Hyperfine Interact.* **115** 193–200
- Zolotarev M and Budker D 1997 *Phys. Rev. Lett.* **78** 4717–20

Trapped Highly Charged Ion Plasmas

E. Takács¹ and J. D. Gillaspay²

National Institute of Standards and Technology, Gaithersburg, MD 20899

Abstract. Electron Beam Ion Trap (EBIT) devices and their special features are reviewed with attention to applications in highly charged ion plasma research. EBIT properties are presented based on information extracted from a variety of experiments reported in the literature. Topics discussed include typical parameters (Debye length, Wigner-Seitz radius, Coulomb coupling parameter, density, temperature, etc.), magnetic trapping mode, ion cloud shape, rotation, and evaporative cooling. We conclude that the quantitative understanding of highly charged ion plasmas inside an EBIT requires improved modeling and advanced diagnostic techniques.

INTRODUCTION

Heavy ions with dozens of electrons removed, so-called highly charged ions, have a wide range of potential applications. Imagine an atomic system that is stripped to its core, with only a few electrons remaining at most. The electronic binding energy that must be overcome to further ionize such a system can be over a thousand times higher than that in ordinary ions or atoms. Even more striking, the potential energy liberated when such a highly charged ion re-neutralizes itself can be nearly a million times larger than that of a conventional ion.

Because many atomic properties scale with high powers of the nuclear charge, ions along an isoelectronic sequence (ions with different nuclear charges, but the same number of electrons) quickly enter exotic regimes where conventional intuition fails. Forbidden electronic transitions can become stronger than those allowed by electric dipole selection rules, and energy levels can become strongly affected by the structure of the vacuum [1,2].

The enormous amount of free potential energy and ultra-compact size that highly charged ions possess is as unique as their exotic atomic structure. When such ions approach surfaces, their strong electrostatic pull on bulk electrons can be felt many atomic diameters away. As a result, highly charged ions are very effective in modifying or breaking chemical bonds and crystal structures on the nanometer length scale [3].

The natural curiosity to study such exotic ions in the extreme strong field limit was one of the driving forces to build a device, such as an Electron Beam Ion Trap (EBIT), that can be accommodated in a small laboratory. The first EBIT was put into operation at the Lawrence Livermore National Laboratory [4,5] almost fifteen years ago. Shortly after this, the National Institute of Standards and Technology (NIST) became the

¹ Also at Massachusetts Institute of Technology, Cambridge, MA 02139 and University of Debrecen, Debrecen, Bem tér 18, Hungary, H-4026, E-mail: endre.takacs@nist.gov ² E-mail: john.gillaspay@nist.gov

second place in the world to have a working EBIT [6,7], followed by new constructions in several other laboratories [8-12].

EBITs are not the only machines that can create ions in high charge states, but certainly they are one of the most versatile, offering great control over the experimental conditions in which highly charged ions are produced. The success of the EBIT is proven by the numerous widely-cited experiments that have been carried out by since its inception [4,5,13-18].

Although the device is still in the process of rapid evolution, the fact that current small-scale EBITs can already produce millions of highly charged ions per second suggests that applications that take advantage of the unusual properties of very highly charged ions should be pursued. Some of the basic scientific studies which will underlie applications of such exotic ions are being carried out by the highly charged ion community, while more immediate applications are being pursued by industrial entrepreneurs [19] (and references contained in [2]).

As EBIT devices may one day be capable of producing much larger numbers of highly charged ions, it is interesting to survey the capabilities and properties of the present machines to help further the development of possible future designs. The basic mechanisms of ion production and operation of the EBIT is theoretically understood; the evolution of the charge states and the dynamical ionization and recombination balance between the neighboring charges can qualitatively be accounted for with model calculations [20-23]. However, there are indications in several experiments that a quantitative understanding remains to be developed.

Detailed understanding of EBIT properties is hampered by the fact that only a limited number of experiments have been performed that specifically target the properties of the highly charged plasma inside an EBIT. There is, however, a large database of indirect information contained in other types of measurements. In the present paper, we will attempt to put these pieces of information together in a coherent manner to provide a general experimental overview of the detailed operation and features of an EBIT. We will also point out some discrepancies that have accumulated in the fifteen years of experience with the device that might point to a better understanding of its operation and that could possibly even be exploited in future applications. We hope that with this summary we will stimulate people from the broader scientific community to contribute to a cross-disciplinary attack on some of the problems, and in particular to put forward advanced diagnostic and modeling ideas that will ultimately help to realize new applications for highly charged ions.

HIGHLY CHARGED ION BEAMS AND CLOUDS

Most of the applications that take advantage of highly charged ions require large numbers ions in the form of high quality clouds or beams. EBITs, in this sense, already qualify as one of the best devices to study. The source region is rather simple and well controllable, and is qualitatively similar to the precision controlled traps that the non-neutral plasma community uses. Understanding the basic properties of these traps can serve as a foundation for designing new, innovative highly charged ion devices. However, as in atomic structure, it might well be that conventional plasma

properties have to be rethought in the highly charged ion regime, in which case existing EBITs could be used as test-beds for these ideas.

Some members of the conventional non-neutral plasma community have argued that highly charged ions could offer some attractive possibilities for the study of strongly coupled systems at relatively high temperatures [24]. Some of the advantages of using highly charged ions in quantum information schemes have also been discussed [25]. One of the first steps towards these goals was the experimental realization of a highly charged ion crystal in a precision trap that was filled with ions from an EBIT [26,27]. Some of the cooling schemes applicable to highly charged ions have already been put into operation in an EBIT [28-30].

Another interesting possibility is related to the quest for crystalline ion beams with high center-of-mass energies (>1 MeV, but with small relative energy <1 eV). These beams would provide the unprecedented quality and brightness sought in many applications [31-33]. The idea of creating crystalline ion beams in storage rings was proposed more than fifteen years ago [34]. Despite some promising results [35,36], the experimental realization in high-energy devices appears to be still lacking [32].

An alternative approach to the crystalline ion beam problem [37] was recently experimentally realized [32] in a small-scale storage ring. The idea is to first create a crystalline ion cloud at rest using methods and tools that are applied in strongly coupled ion cloud studies, and then to accelerate it to high energies without destroying the ordered structure. The experiment, which used singly charged ions and laser cooling to create the ion crystals at rest, was able to demonstrate acceleration to about 1 eV energy [32]. It is believed that scaled-up versions of this scheme can be used as high-energy storage rings.

Direct laser cooling of highly charged ions is problematic because of the scarcity of visible transitions. It has recently been demonstrated, however, that sympathetic laser cooling can be equally effective [38]. This alternative cooling technique has also been shown to be very effective for highly charged ions [26,27]. In addition, there may be other, non-laser based cooling schemes that have yet to be fully developed [45,46].

One of the major differences between Penning traps and EBITs is the presence of a monoenergetic, high-energy, high-density electron beam at the center of the trap. Some groups, however, have modified their Penning traps to include an electron beam [39-42]. These works are not motivated by the desire to create highly charged ions, but rather to create better confinement conditions and more dense plasmas for applications such as alternative nuclear fusion devices. The dense electron beam creates a steep spatial ion density gradient that helps to locally overcome the density limitations posed by the Brillouin limit [39,40]. Similar gradients have been observed in recent EBIT experiments [43,44]. Furthermore, typical ion densities found in EBITs (see below) are already above the Brillouin limit.

The possibility of creating high ion cloud densities and high brilliance beams using present EBITs without auxiliary laser cooling may not be that far-fetched. Recent model calculations [45,46] suggest that evaporative cooling could be significantly enhanced under certain conditions, and thus even the strongly correlated regime might be achievable this way.

ELECTRON BEAM ION TRAPS

The basic operational principle and the details of the EBIT components can be found in several recent reviews [47,48]. These papers give a design and modeling point of view of the operation of the present-day EBITs. In the present work, we would like to review a few experiments that determined some of the important operating parameters of the machine. In some cases these results were not even the main goal of the particular experiment, but rather a byproduct. Since these experiments were done with different machines, using different types of ions, and different experimental techniques, their direct comparison might not be justified in all cases. However, a semi-comprehensive review of the data might help to shed some light on the capabilities of EBITs and to give a general feel for the operating parameter ranges.

Operation

The creation of highly charged ions in an EBIT is based on the interactions of ions with a high density electron beam of about 1 keV to 30 keV energy. The electron beam is produced by a commercial electron gun and is highly compressed by a pair of superconducting magnets producing homogenous field of about 3 T in the center of the machine. Neutral atoms or singly charged ions are injected into a three element Penning trap and then are stripped of most of their bound electrons during consecutive interactions with the electron beam. The average ionization stage in equilibrium can be selected by properly choosing the energy of the electron beam. Radially the ions are confined by both the electric field of the electron beam and the high magnetic field. The effect of the magnetic field dominates only for large distances from the electron beam. Once the ions of the desired charge state are produced, the electron beam can be used for exciting electronic transitions for spectroscopic studies, or it can be turned off completely, leaving the axial confinement solely to the magnetic field [49,50]. Details of the modeling of ion creation [47] and the trapping dynamics [48] are described elsewhere. The NIST EBIT is also equipped with a highly efficient ion extraction and transport system, with a built-in charge-to-mass ratio separator. This system can be used for diagnostic purposes to infer charge state distributions inside the trap, or as a facility for ion-surface and ion-gas collision experiments.

In the following paragraph we summarize the typical plasma parameters of EBIT ion clouds. The measurements that provided the input for these determinations will be presented in later sections.

Typical plasma parameters

Plasma conditions created in EBITs are similar to those of the solar corona. Electron densities are around 10^{12} cm⁻³ and electron energies are approximately equal to (or above) those found in 10 million Kelvin temperature plasmas. One distinctive difference is that in the EBIT the electron energy is monoenergetic, with a width of only about 16 eV [70] to 70 eV [71]. A typical relative energy spread, $\Delta E/E$, is under

1 %. The narrow energy spread is the key to creating a charge state distribution that only includes a few ionization stages. In the case of ions with closed shell electronic configurations, close to 100 % charge state purity can be achieved [77]. In a more typical case, there would be a distribution of charge states present. The charge-to-mass spectrum of extracted ions [72,73] can be used to monitor the degree of charge state purity.

Typical measured densities of particular charge states in multi-component EBIT ion clouds range from $5 \times 10^8 \text{ cm}^{-3}$ to $1 \times 10^{10} \text{ cm}^{-3}$ [7,61]. Local ion densities can be higher than these values because of the steep gradient in the space charge potential of the electron beam. Typical measured ion temperatures are between 70 eV [65] and 700 eV [66, 64], increasing as the ion charge increases.

The Debye length for typical ion densities (n) and temperatures (T) inside an EBIT,

$$\lambda_D = \sqrt{\frac{\epsilon_0 kT}{nq^2}} \quad (1)$$

is around 20 μm to 60 μm . This value is relatively small mainly because of the high charge (q) of the ions. The size of the ion cloud is 2 to 20 times this value.

The average distance between ions of a particular charge state is given by the Wigner-Seitz radius,

$$a = \sqrt[3]{\frac{3}{4\pi n}} \quad (2)$$

about 3 μm to 8 μm . These Debye lengths and Wigner-Seitz radii are similar to those for typical singly charged ion plasmas, but other parameters that scale with the ion charge can be very different. One such parameter that scales quadratically with ion charge is the average potential energy between neighboring ions:

$$V_a = \frac{q^2}{4\pi\epsilon_0 a} \quad (3)$$

For ions of high charge-states this can be 3 or 4 orders of magnitude higher than for singly charged systems. It can be more than 1 eV in absolute value. This leads to another strongly scaling quantity, the Coulomb coupling parameter:

$$\Gamma = \frac{q^2}{4\pi\epsilon_0 a kT} \quad (4)$$

Because of the high ion charge, even at temperatures close to 1 million Kelvin Γ is more than 0.01. If the cloud could be cooled to room temperature, Γ would be around 50, which is well into the range where liquid phase behavior is predicted [60].

EXPERIMENTAL CHARACTERIZATION OF EBITS

Although there have been over 300 EBIT publications since the first one in 1988, relatively few experiments have been performed to date that determine the parameters described in the previous section. In the following subsections, we discuss these few experiments, and point to corresponding theoretical work.

Electron beam

The spatial distribution of the electron beam has been measured using a variant of an x-ray pinhole camera [5, 74, 75], and using Thomson scattering [76]. The x-ray imaging experiments rely on the fact that excited state lifetimes in highly charged ions are so short that x-rays are emitted essentially instantaneously at the location that they interact with the electron beam. A map of the x-ray emission from the ions, therefore, reflects the electron beam density distribution directly. The measurements are in rough agreement with predictions based on Herrmann theory [51], although there have been some discrepancies on the order of 20 %. Generally, it has been assumed that the electron beam spatial distribution is Gaussian, with a radius r_H containing 80 % of the electron beam given by,

$$r_H = \frac{r_B}{\sqrt{2}} \sqrt{1 + \sqrt{1 + 4\left(\frac{8mkT_c r_c^2}{e^2 B^2 r_B^4} + \frac{B_c^2 r_c^4}{B^2 r_B^4}\right)}} \quad (5)$$

where B_c is the magnetic field in the electron gun cathode region; T_c is the temperature of the cathode; r_c is the radius of the cathode; B is the magnetic field at the central drift tube; m is the rest mass of the electron; k is the Boltzmann constant; r_B is the Brillouin radius:

$$r_B = \sqrt{\frac{I_e \sqrt{E_e}}{4.74 \cdot 10^5 \cdot \pi B^2}} \quad (6)$$

determined by the electron current, I_e , and the electron energy, E_e .

In order to understand the presence of the parameter B_c in the above expression, it is useful to consider some further details of the EBIT design. The electrons are emitted from a heated cathode in a Pierce-type electron gun configuration [4,5,48] located in the fringing field region of the main trap magnet. The electrons are accelerated towards a positively biased drift tube region (the trap center) by a series of guiding electrodes. It has typically been assumed that the maximum current density is achieved by minimizing the radius in expression (5), implying that the field at the cathode should be zero. In this case, however, the trap magnet acts as a magnetic mirror, and a significant number of electrons will be reflected back away from the trap. We have shown that theoretically the optimum field is actually a few tenths of a mT (a few gauss) [52]. The control of the magnetic field is aided by a steel plate placed above

the electron gun, and a coil built into a sealed chamber that surrounds the electron gun [5,52]. The magnitudes of the various EBIT parameters ($r_c \sim 1.5$ mm, $T_c \sim 1000$ K, for example) allow one to simplify expression (5) considerably to,

$$r_H \approx \left(\frac{8mkT_c r_c^2}{e^2 B^2} \right)^{1/4} \quad (7)$$

On its way towards the drift tubes, the electron beam is compressed by the increasing magnetic field. Model calculations show that the 3 T magnetic field in the trap region is homogenous over the 3 cm long ion trap region to better than 0.05 % [44].

Magnetic trapping

The early EBIT papers stated that the ions were trapped in the radial direction by the electrostatic field provided by the electron beam (see, for example [5]). The magnetic field was presented as a technical detail needed to adiabatically compress the electron beam to high densities at the trap center. From the onset of our work [7,50], however, we have taken a somewhat different view, which emphasizes the direct effect of the magnetic field on the ion confinement. With this point of view, we first reported an experiment that demonstrated that an EBIT can be used to measure some properties of highly charged ions (excited state lifetimes, for example) more efficiently when the electron beam is turned off [50]. This work was stimulated by some related work on ion cloud diagnostics at Livermore [53-57]. Both the atomic lifetime measurements and the cloud diagnostic studies showed that after an initial expansion, the ion cloud stabilized after the electron beam was turned off. Only trap losses like cross-field diffusion and charge exchange with the background gas then lead to a decrease of the ion signal. Similar issues have been studied more thoroughly outside of the EBIT community e.g. [24, 60]. We suggest that using an EBIT to produce highly charged ions, and then switching to the “magnetic trapping mode” of operation might be particularly interesting for many advanced plasma studies.

Ion cloud shape

It is only recently that an image of the measured ion cloud shape has been reported [2]. Most of the experiments have simply used the EBIT as a light source or as an ion source for atomic physics or ion-surface studies, with relatively little effort allocated to study the macroscopic properties of the ion cloud itself. Ironically, much of the work that *has* been published rests on assumptions about the spatial distribution of the ions in the cloud.

The first systematic study of the ion cloud shape was published recently [43]. This work used a CCD camera and an optical lens system. Data was collapsed along the axis of the electron beam to produce a 1-dimensional cross sectional image with improved signal-to-noise ratio. Complimentary data, taken under rather different EBIT

operating conditions, have been reported in the PhD thesis of M. Tarbutt [44]. Both of these works were predated by some spatial information that was obtained by Serpa *et al.* [50] in connection with the measurement of excited-state atomic lifetimes. In this work, the entire spectrometer table was mounted on sliding rails and was moved perpendicular to the EBIT observation direction by piezoelectric translators, allowing the transverse distribution of light at the entrance slit of the spectrometer to be mapped out. Some earlier unpublished work using CCD imaging was briefly described in a Livermore annual report [58].

The lack of any work in imaging the ion cloud immediately after the first EBIT came online can be partly understood by realizing that it was quite a few years before the first visible-light spectroscopy was done on an EBIT [18]. The reason for this is that the scaling laws cause most of the transition energies to shift into the x-ray energy range as the ion charge is increased. There are a few unusual transitions, however, that stay in the visible range, because of a fortuitous energy-level crossing. One of these transitions has been predicted [59] and found [18] in the Ti-like isoelectronic sequence. There are also transitions that during their rapid scaling to shorter wavelengths from the infrared or microwave range, pass through the visible range at a particular charge state or narrow range of charge states. Notable examples of the latter are visible hyperfine transitions in high Z elements.

Another requirement for cloud imaging is that the line should have a lifetime that is long compared to the time it takes the ion to complete several cycles of its motion (the cyclotron frequency varies from $1.2 \times 10^7 \text{ s}^{-1}$ to $1.3 \times 10^8 \text{ s}^{-1}$ for ions ranging from U^{10+} to Ar^{18+}). This condition is necessary, because electron impact excitation can only take place inside the electron beam. As mentioned above, if the emitting transition has a short lifetime (like in most of the x-ray lines), the image only reflects the product of the electron and ion densities, not the full ion cloud shape.

The cloud imaging experiments of Porto *et al.* [43] used Ar^{13+} , Xe^{31+} , and Xe^{32+} ions and the experiments of Tarbutt [44] used Ar^{10+} ions for the measurements. Both experiments concluded that the ion cloud has a density distribution that sharply peaks in the center of the EBIT. Porto *et al.* assumed thermal equilibrium for the ion cloud to model the shape of the measured distribution in the self-consistent field of the electron beam and the ion clouds. The fits suggest that the ions may indeed be close to thermal equilibrium. The temperatures obtained from the fits fall within expected values [43]. At lower trapping voltages, the experimentally obtained widths became wider than what is expected for even the maximum possible temperatures, which was interpreted as a signature that the ion cloud is non-thermal.

Ion cloud rotation

The possible collective rotation of the ion cloud has not been taken into account in any of the previous work with EBITs. Clouds of highly charged ions in thermal equilibrium in a pure magnetic field with densities close to the Brillouin limit should rotate collectively at half the cyclotron angular frequency [60]. How this situation is modified by the presence of the electron beam has yet to be studied in detail.

Ion number and density

The ion densities can be measured by detecting x-rays originating from processes with well-known cross sections, assuming the electron density is known. One of these is the so-called radiative recombination, which can be calculated to better than few percent accuracy [13]. This method was used by Gillaspy *et al.* [7] and by Margolis *et al.* [61] to determine the number Ba^{46+} ions in the trap (3.1×10^5) or, with fewer assumptions, the ion density ($1.0 \times 10^8 \text{ cm}^{-3} - 1.1 \times 10^9 \text{ cm}^{-3}$). Margolis *et al.* [61] also measured densities of $1.3 \times 10^{10} \text{ cm}^{-3}$ and $0.7 \times 10^{10} \text{ cm}^{-3}$ for Ar^{16+} and Ar^{17+} ions respectively using the same method.

A different technique was used by Schweikard *et al.* [54] to determine the number of ions inside the EBIT. In [54] electrical probes were inserted into the EBIT to detect ion cyclotron resonance (ICR) signals induced by the ions. From the induced currents, the number of ions is inferred to be 10^5 to 10^6 for high charge state Kr ions (Kr^{34+} , Kr^{35+} , and Kr^{36+}). Using these numbers and assuming approximately 10^3 cm^3 for the volume of the ion cloud, we infer $10^8 \text{ cm}^{-3} - 10^9 \text{ cm}^{-3}$ for the average ion densities, in reasonable agreement with the results of the x-ray method.

It should be noted that the estimated densities using the ICR method are averages over the entire ion cloud, whereas the x-ray method samples only the region where the electron beam overlaps with the ion cloud. Because of the density gradient, the x-ray method should yield higher values than the average density. A better determination of the local ion densities could be performed by combining either of these methods with imaging techniques.

Charge state distribution

The evolution of the charge state distribution when the electron beam is on is determined by a set of coupled differential equations including source and loss terms for each charge state [20]. Once equilibrium is reached, recombination with electrons to produce lower charge states and re-ionization keep a balance between the neighboring charge states. Model calculations can account for the qualitative behavior of the time dependence, however discrepancies have been reported in several cases [62,63]. One of the critical issues that comes up in many experiments is the overlap factor between the electron beam and the ion cloud [20,63]. The modeling of this parameter relies on the knowledge of the properties of the ion cloud. As it has been shown in the imaging experiments [43,44], this can be very complicated, especially if non-thermal clouds are present. Further understanding calls for advanced modeling of the highly charged ion cloud.

Ion temperatures

A routine procedure in spectroscopy to determine ion temperatures is the measurement of the Doppler broadening of spectral lines. This method assumes that the emitting ions are in thermal equilibrium, a condition that might not be satisfied in some cases as suggested by the direct imaging results. Collective ion cloud rotation

could also cause spectral line broadenings, which might explain why the experiments have not indicated very low temperatures, even in cases where the axial potential barrier was very small. Nevertheless, the broadening of a relatively narrow spectral line, measured by high-resolution instruments, gives a general idea about the temperature ranges that highly charged ions are subjected to in EBITs.

The NIST EBIT group [7,64] used a Fabry-Perot spectrometer to measure the width of a visible magnetic dipole transition in Ba^{34+} . The experimental results indicated an ion temperature between 500 eV and 1000 eV. These values are much less than what the depth of the potential trap would allow, which for such a high charge-state amounted to about 17 keV (the reason for this reduced temperature is given in the next section). Similar conclusions were drawn from the x-ray line-width measurements of Beiersdorfer *et al.* [65,66] using Ti^{20+} ions. In these cases, the measured widths indicated equilibrium temperatures of 70 eV - 700 eV. Although the temperatures showed a dependence on the axial trap depth, the measured values were generally smaller than the possible temperatures Ti^{20+} ions were allowed to take, similarly to the observation of the NIST group using Ba^{34+} ions. Neither of the measurements took into account the possible collective rotation of the ion cloud, so the actual ion temperatures could have been even lower than those inferred from the measurements.

Evaporative cooling

The interaction of the ions with the dense and energetic electron beam continuously pumps energy into the cloud via inelastic collisions at a rate of a few keV/s [20]. At this rate of heating, most of the ions would quickly boil out of the trap. However, evaporative cooling of the higher charge state ions by elastic collisions with lower charge state ions that preferentially escape the trap strongly modifies this situation. Evaporative cooling of heavy ions can be even more efficient using lighter ions purposely injected into the trap. These lighter ions can be rapidly stripped bare, after which their charge state evolution is truncated.

Evaporative cooling of highly charged gold (Au^{69+} , Au^{68+} , Au^{67+} , etc.) by low charge state Ti ions (maximum Ti^{22+}) was successfully demonstrated by Schneider *et al.* [67]. Using this method, trapping times of several hours have been observed, demonstrating the presence of a strong cooling mechanism. Model calculations of the effect [69] predicted that highly charged heavy ions can be trapped for indefinitely in this way.

Conventional evaporative cooling in an EBIT [67-69], as described above, differs from evaporative cooling in neutral atom traps in that there is no time-dependence of the trap potentials. This cooling is not lossy because it depends on collisions with lower charge state ions that “see” a different trap depth. There have been two recent model investigations [45,46], which propose improved evaporative cooling schemes for an EBIT using time-dependent potentials. Because of the long-range nature of the strong Coulomb interaction, evaporative cooling works very differently in the case of highly charged, compared to the neutral atom case. At low temperatures, instead of getting weaker, the evaporative cooling mechanism can be accelerated, leading to very low achievable temperatures.

REFERENCES

- [1] I. Martinson, *Reports of Progress in Physics* **52** (1989) 157.
- [2] J.D. Gillaspay, *Journal of Physics B: Atomic, Molecular and Optical Physics* **34** (2001) R93.
- [3] R. Minniti, L.P. Ratliff, J.D. Gillaspay, *Physica Scripta* **T92** (2001) 22.
- [4] M.A. Levine, R.E. Marrs, J.R. Henderson, D.A. Knapp, and M.B. Schneider, *Physica Scripta* **T22** (1988) 157
- [5] M.A. Levine, R.E. Marrs, J.N. Bardsley, P. Beiersdorfer, C.L. Bennett, M.H. Chen, T. Cowan, D. Dietrich, J.R. Henderson, D.A. Knapp, A. Osterheld, B.M. Penetrante, M.B. Schneider, and J.H. Scofield, *Nuclear Instruments and Methods in Physics Research B* **43** (1989) 431.
- [6] J.D. Gillaspay, J.R. Roberts, C.M. Brown, and U. Feldman, *Proceedings of the VIth International Conference on the Physics of Highly Charged Ions*, eds. P. Richard, M. Stockli, and C.D. Lin, (AIP press, New York, 1993), *AIP Conference Proceedings* **274** (1993) 682.
- [7] J.D. Gillaspay, Y. Aglitskiy, E.W. Bell, C.M. Brown, C.T. Chantler, R.D. Deslattes, U. Feldman, L.T. Hudson, J.M. Laming, E.S. Meyer, C.A. Morgan, A.I. Pikin, J.R. Roberts, L.P. Ratliff, F.G. Serpa, J. Sugar and E. Takács, *Physica Scripta* **T59** (1995) 392.
- [8] J.D. Silver, A.J. Varney, H.S. Margolis, P.E.G. Baird, I.P. Grant, P.D. Groves, W.A. Hallett, A.T. Handford, P.J. Hirst, A.R. Holmes, D.J.H. Howie, R.A. Hunt, K.A. Nobbs, M. Roberts, W. Studholme, J.S. Wark, M.T. Williams, M.A. Levine, D.D. Dietrich, W.G. Graham, I.D. Williams, R. Oneil, and S.J. Rose, *Review of Scientific Instruments* **65** (1994) 1072.
- [9] C. Biedermann, A. Forster, G. Fussmann, and R. Radtke, *Physica Scripta* **T73** (1997) 360.
- [10] F.J. Currell, J. Asada, K. Ishii, A. Minoh, K. Motohashi, N. Nakamura, K. Nishizawa, S. Ohtani, K. Okazaki, M. Sakurai, H. Shiraishi, S. Tsurubuchi, and H. Watanabe, *Journal of the Physical Society of Japan* **65** (1996) 3186.
- [11] T. Werner, G. Zschornack, F. Grossmann, V.P. Ovsyannikov, and F. Ullmann, *Nuclear Instruments and Methods in Physics Research B* **178** (2001) 260.
- [12] J.R.C. Lopez-Urrutia, B. Bapat, I. Draganic, A. Werdich, and J. Ullrich, *Physica Scripta* **T92** (2001) 110.
- [13] R.E. Marrs, M.A. Levine, D.A. Knapp, and J.R. Henderson, *Physical Review Letters* **60** (1988) 1715.
- [14] P. Beiersdorfer, S. Vongoleler, M. Bitter, E. Hinnov, R. Bell, S. Bernabei, J. Felt, K.W. Hill, R. Hulse, J. Stevens, S. Suckewer, J. Timberlake, A. Wouters, M.H. Chen, J.H. Scofield, D.D. Dietrich, M. Gerassimenko, E. Silver, R.S. Walling, and P.L. Hagelstein, *Physical Review A* **37** (1988) 4153.
- [15] J.R. Henderson, P. Beiersdorfer, C.L. Bennett, S. Chantrenne, D.A. Knapp, R.E. Marrs, M.B. Schneider, K.L. Wong, G.A. Doschek, J.F. Seely, C.M. Brown, R.E. LaVilla, J. Dubau, and M.A. Levine, *Physical Review Letters* **65** (1990) 705.
- [16] D. Schneider, D. Dewitt, M.W. Clark, R. Schuch, C.L. Cocke, R. Schneider, K.J. Reed, M.H. Chen, R.E. Marrs, M. Levine, and R. Fortner, *Physical Review A* **42** (1990) 3889
- [17] R.E. Marrs, S.R. Elliott, and D.A. Knapp, *Physical Review Letters* **72** (1994) 4082
- [18] C.A. Morgan, F.G. Serpa, E. Takács, E.S. Meyer, J.D. Gillaspay, J. Sugar, J.R. Roberts, C.M. Brown and U. Feldman, *Physical Review Letters* **74** (1995) 1716.
- [19] G. Borsoni, N. Bechu, M. Gros-Jean, M.L. Korwin-Pawłowski, R. Laffitte, V. Le Roux, L. Vallier, N. Rochat, and C. Wyon, *Microelectronics Reliability* **41** (2001) 1063.
- [20] B. M. Penetrante, J. N. Bardsley, D. DeWitt, M. Clark, and D. Schneider, *Physical Review A* **43** (1991) 4861.
- [21] B. M. Penetrante, D. Schneider, R. E. Marrs, and J. N. Bardsley, *Review of Scientific Instruments* **63** (1992) 2806
- [22] H.S. Margolis, *D.Phil. Thesis, Oxford University*, 1994.
- [23] I.V. Kalagin, D. Küchler, V.P. Ovsyannikov, and G. Zschornack, *Plasma Sources in Science and Technology* **7** (1998) 441.
- [24] X.P. Huang, J. J. Bollinger, W.M. Itano, J.N. Tan, B. Jelenkovic, T.B. Mitchell, and D.J. Wineland, *Hyperfine Interactions* **115** (1998) 41.
- [25] D.J. Wineland, C. Monroe, W.M. Itano, D. Leibfried, B.E. King, and D.M. Meekhof, *Journal of Research of the National Institute of Standards and Technology* **103** (1998) 259.
- [26] L. Gruber, J.P. Holder, J. Steiger, B.R. Beck, H.E. DeWitt, J. Glassman, J.W. McDonald, D.A. Church, and D. Schneider, *Physical Review Letters* **86** (2001) 636.
- [27] J.P. Holder, L. Gruber, H.E. DeWitt, B.R. Beck, D.A. Church, and D. Schneider, *Physica Scripta* **T92** (2001) 158.
- [28] B. M. Penetrante, J. N. Bardsley, M. A. Levine, D. A. Knapp and R. E. Marrs, *Physical Review A* **43** (1991) 4873.
- [29] B. M. Penetrante, M. A. Levine, and J. N. Bardsley, *Proceedings of the International Symposium on Electron Beam Ion Sources and their Applications*, ed. A. Herschovitch (AIP press, New York, 1989), *AIP Conference Proceedings* **188** (1989) 145.
- [30] R. E. Marrs, *Review of Scientific Instruments* **67** (1996) 941.

- [31] T. Schatz, U. Schramm, and D. Habs, *Hyperfine Interactions* **115** (1998) 29.
- [32] T. Schatz, U. Schramm, and D. Habs, *Nature* **412** (2001) 717.
- [33] J. Beebe-Wang, N. Elander, and R. Schuch, *Physica Scripta* **57** (1998) 36.
- [34] J. P. Schiffer and P. Kienle, *Zeitschrift für Physik A, Atoms and Nuclei* **321** (1985) 181.
- [35] M. Steck, K. Beckert, H. Eickhoff, B. Franzke, F. Nolden, H. Reich, B. Schlitt, and T. Winkler, *Physical Review Letters* **77** (2001) 3803.
- [36] R.W. Hasse, *Physical Review Letters* **83** (2001) 3430.
- [37] R. Blumel and P.E. Smaldino, *Physics Letters A* **260** (1999) 495.
- [38] P. Bove, L. Horneaker, C. Brodersen, M. Drewsen, J. S. Hangst, and J. P. Schiffer, *Physical Review Letters* **82** (1999) 2071.
- [39] D.C. Barnes, R.A. Nebel, and L. Turner, *Physics of Fluids B* **5** (1993) 3651.
- [40] G. Zhuang, W. Liu, C. Yu, J. Zheng, C. Fu, J. Xie, K. Zhao, B. Bai, X. Liang, S. Zhao, and J. Chi, *Physics of Plasmas* **7** (2000) 3912.
- [41] R.G. Greaves, M.D. Tinkle, and C.M. Surko, *Physical Review Letters* **74** (1995) 90.
- [42] M. H. Holzscheiter, *Physica Scripta* **T59** (1995) 69.
- [43] J.V. Porto, I. Kink, and J.D. Gillaspay, *Review of Scientific Instruments* **71** (2000) 3050.
- [44] M.R. Tarbutt, *D.Phil. Thesis, Oxford University*, 2000.
- [45] R.E. Marrs, *Nuclear Instruments and Methods in Physics Research B* **149** (1999) 182.
- [46] T. Kinugawa, F.J. Currell, and S. Ohtani, *Journal of Physical Society of Japan* **68** (1999) 3763.
- [47] F.J. Currell, *Trapping Highly Charged Ions: Fundamentals and Applications* ed. J.D. Gillaspay (New York: Nova Science), 2001.
- [48] G. Fussmann, C. Biedermann, and R. Radtke, *Advanced Technologies Based on Wave and Beam Generated Plasmas* eds. H. Schluter and A. Shivarova (Kluwer Academic Publishers), 1999, 429.
- [49] L. Schweikhard, P. Beiersdorfer, G. V. Brown, J. R. Crespo Lopez-Urrutia, S. B. Utter, and K. Widmann, *Nuclear Instruments and Methods in Physics Research B* **142** (1998) 245.
- [50] F.G. Serpa, C.A. Morgan, E.S. Meyer, J.D. Gillaspay, E. Trabert, D.A. Church, and E. Takács, *Physical Review A* **55** (1997) 4196.
- [51] G.J. Hermann, *Journal of Applied Physics* **29** (1958) 127.
- [52] E. Takács, E. S. Meyer, J. D. Gillaspay, J. R. Roberts, C. T. Chantler, L. T. Hudson, R. D. Deslattes, C. M. Brown, J. M. Laming, J. Dubau, and M. K. Inal, *Physical Review A* **54** (1996) 1342.
- [53] P. Beiersdorfer, B. Beck, S. Elliott, and L. Schweikhard, *Rapid Communications in Mass Spectrometry* **8** (1994) 141.
- [54] L. Schweikhard, J. Ziegler, P. Beiersdorfer, B. Beck, St. Becker, and S. Elliott, *Review of Scientific Instruments* **66** (1995) 448.
- [55] P. Beiersdorfer, St. Becker, B. Beck, S. Elliott, K. Widmann, and L. Schweikhard, *Nuclear Instruments and Methods in Physics Research B* **98** (1995) 558.
- [56] P. Beiersdorfer, B. Beck, St. Becker, and L. Schweikhard, *International Journal of Mass Spectrometry and Ion Process* **157/158** (1996) 149.
- [57] P. Beiersdorfer, L. Schweikhard, J. Crespo Lopez-Urrutia, and K. Widmann, *Review of Scientific Instruments* **67** (1996) 3818.
- [58] Electron Beam Ion Trap, *Annual Report 1994, Lawrence Livermore National Laboratory*, ed. D. Schneider, UCRL-ID-121572, 1995.
- [59] U. Feldman, P. Indelicato, and J. Sugar, *Journal of the Optical Society of America B* **8** (1991) 3.
- [60] T.M. O'Neil, *Physica Scripta* **T59** (1995) 341.
- [61] H. S. Margolis, A. J. Varney, R. A. Jarjis, and J. D. Silver, *Nuclear Instruments and Methods in Physics Research B* **98** (1995) 562.
- [62] N.J. Peacock, R. Bamsley, M.G. O'Mullane, M.R. Tarbutt, D. Crosby, J.D. Silver, and J.A. Rainnie, *Review of Scientific Instruments* **72** (2001) 1250.
- [63] E. Takács, Z. Berényi, Cs. Szabó, J.D. Gillaspay, and A.G. Calamai, *to be published*, 2001.
- [64] H. Adler, E.S. Meyer, F.G. Serpa, E. Takács, J.D. Gillaspay, C.M. Brown, and U. Feldman, *Nuclear Instruments and Methods in Physics Research B* **98** (1995) 581.
- [65] P. Beiersdorfer, V. Decaux, and K. Widmann, *Nuclear Instruments and Methods in Physics Research B* **98** (1995) 566.
- [66] P. Beiersdorfer, V. Decaux, S. R. Elliott, and K. Widmann, *Review of Scientific Instruments* **66** (1995) 303.
- [67] M.B. Schneider, M.A. Levine, C.L. Bennett, J.R. Henderson, D.A. Knapp, and R.E. Marrs, *Proceedings of the International Symposium on Electron Beam Ion Sources and their Applications*, ed. A. Herschovitch (AIP press, New York, 1989), AIP Conference Proceedings **188** (1989) 158.
- [68] B. M. Penetrante, J. N. Bardsley, M.A. Levine, D.A. Knapp, and R.E. Marrs, *Physical Review A* **43** (1991) 4873.

- [69] D. Schneider, M.W. Clark, B.M. Penetrante, J. McDonald, D. DeWitt and J. N. Bardsley, *Physical Review A* **44** (1991) 3119.
- [70] D. DeWitt, D. Schneider, M.H. Chen, M.W. Clark, J.W. McDonald, and M.B. Schneider, *Physical Review Letters* **68** (1992) 1694.
- [71] R.E. Marrs, M.A. Levine, D.A. Knapp, and J.R. Henderson, *Electronic and Atomic Collisions*, eds. H.B. Gilbody, W.R. Newell, F.H. Read, and A.C.H. Smith (Elsevier Science Publishers B.V.), 1988.
- [72] A.I. Pikin, C.A. Morgan, E.W. Bell, L.P. Ratliff, D.A. Church, and J.D. Gillaspay, *Review of Scientific Instruments* **67** (1996) 2528.
- [73] L.P. Ratliff, E.W. Bell, D.C. Parks, A.I. Pikin, and J.D. Gillaspay, *Review of Scientific Instruments* **68** (1997) 1998.
- [74] D.A. Knapp, R.E. Marrs, S.R. Elliott, E.W. Magee, and R. Zasadinski, *Nuclear Instruments and Methods in Physics Research A* **334** (1993) 305.
- [75] S.B. Utter, P. Beiersdorfer, J.R.C. Lopez-Urrutia, and K. Widmann, *Nuclear Instruments and Methods in Physics Research A* **428** (1993) 276.
- [76] H. Kuramoto, I. Yamada, H. Watanabe, M. Sawasaki, C. Yamada, and S. Ohtani, *Physica Scripta* **T92** (2001) 351.
- [77] S. Chantrenne, P. Beiersdorfer, R. Cauble, and M.B. Schneider, *Physical Review Letters* **69** (1992) 265.

Ultraviolet and visible radiation

Observation of Visible and uv Magnetic Dipole Transitions in Highly Charged Xenon and Barium

C. A. Morgan,* F. G. Serpa,† E. Takács,‡ E. S. Meyer, J. D. Gillaspay, J. Sugar, and J. R. Roberts
Atomic Physics Division, National Institute of Standards and Technology, Gaithersburg, Maryland 20899

C. M. Brown and U. Feldman

E. O. Hulbert Center for Space Research, Naval Research Laboratory, Washington, D.C. 20375-5000

(Received 27 May 1994)

We have observed an unusual transition which is predicted to result in visible and near-uv emission from very highly charged titaniumlike ions spanning the entire upper half of the periodic table. Measurements of the wavelengths of the $3d^4\ ^5D_2\text{-}^3D_3$ transitions in Ba^{+34} and Xe^{+32} are in surprisingly poor agreement with *ab initio* calculations. This work was carried out in an electron beam ion trap and demonstrates that such a device can be an important tool for visible spectroscopy of highly charged ions.

PACS numbers: 32.70.-n, 31.25.-v, 52.25.-b, 52.70.Kz

Although ions having identical numbers of electrons display similar spectral structure, the scale of many atomic properties changes dramatically as the nuclear charge (Z) is increased along an isoelectronic sequence. One example is the rapid decrease in transition wavelengths leading to the characteristic emission of light in the x-ray region of the spectrum for very highly charged ions. It was therefore unusual when Feldman, Indelicato, and Sugar [1] reported calculations predicting a small set of observable visible and near-uv magnetic dipole ($M1$) lines for highly charged ions in the titaniumlike isoelectronic sequence. The upper levels of these transitions lie within the ground term, and, therefore, in low density plasmas ($\leq 10^{13}\text{ cm}^{-3}$), where competition from electron collisions is negligible, a large fraction of excited levels should decay to them and result in intense forbidden lines. Even more intriguing is the fact that these lines are predicted to remain in the visible or near-uv region of the spectrum for a range of ions covering the entire upper half of the periodic table ($45 \leq Z \leq 92$). To our knowledge, this is the only candidate sequence of strong lines with visible or near-uv wavelengths persisting over the 1 to 10 keV range of ionization energies. Once measured, the lines are easily located even with low resolution spectrometers. In this Letter, we report the first observation and measurement of these unusual lines.

Interest in visible and near-uv forbidden transitions in highly charged ion is not only academic; there are important practical applications, particularly in high temperature plasma diagnostics. Long wavelength forbidden transitions have been seen in the solar corona [2,3] and in tokamaks [4-7], and they have been used extensively to probe a variety of properties for both kinds of plasmas. For example, local ion temperatures and bulk plasma velocities can be inferred from the substantial Doppler widths and shifts of these lines [5,6,8]. It is also possible to determine the direction and magnitude of internal magnetic fields from polarization measurements or from Zeeman shifting or broadening of the line profiles [9-11]. The

visible and near-uv transitions are preferred, since they can usually be measured more accurately and because refractive optics and polarizers can be efficiently employed. Most of the visible and near-uv diagnostic lines used to date come from ions with the ns^2np^k ($n = 2, 3$) ground configurations [12]. Unfortunately, these lines are expected to move to much shorter wavelengths in the high- Z (high ionization energy) elements of the sequence appropriate to the next generation of high temperature fusion devices. Thus, such lines will no longer be as easy to measure and will lose much of their value as diagnostic tools. The high radiation levels expected near these new devices will make remote diagnostic using fiber optics desirable, thereby increasing the need for visible or near-uv diagnostic lines.

In the present work, ions were created at the joint National Institute of Standards and Technology and Naval Research Laboratory Electron Beam Ion Trap (NIST-NRL EBIT) [13]. The trap is based upon the design of the Lawrence Livermore National Laboratory EBIT [14] and consists of three cylindrical drift tubes through which nearly monochromatic ($\sim 50\text{ eV}$ spread) and intense ($\sim 2000\text{ A cm}^{-2}$) electron beam passes. The electron beam is focused to a small diameter ($\sim 60\ \mu\text{m}$) by a 3 T axial magnetic field, and the electron energy is determined by the potential applied to the center drift tube. The ions are trapped axially along a 2 cm length by biasing the end drift tubes 250 V above the center drift tube; they are confined radially by the space charge potential of the electron beam and by the magnetic field. Injected atoms are converted to ions via collisions with the electron beam. A specific charge state can be preferentially produced by tuning the beam energy to just below its ionization potential. This capability for producing and trapping very highly charged ions in a small-scale laboratory device has made the EBIT a valuable source for x-ray spectroscopy [15]. The low effective electron density inside the EBIT ($\sim 10^{12}\text{ cm}^{-3}$), however, also makes it ideal for studying weak, forbidden transitions

within the ground terms of highly charged ions. We have now demonstrated this potential by using the EBIT for visible and near-uv spectroscopy of such transitions.

Barium and xenon were studied because they are easily introduced into the EBIT. Barium is emitted continuously from the heated cathode of the electron gun, and xenon can be loaded by directing a stream of neutral gas into the trap region through a side port. The electron beam energy required to maximize production of titaniumlike barium and xenon ions in the EBIT is 2.259 and 2.026 keV [16], respectively. Although the electron beam energy is determined by the center drift tube potential, the exact energy is somewhat less than this potential due to beam space charge defects. For a 35 mA beam, we estimate this space charge correction to vary from 72 to 63 eV as the center drift tube potential is varied from 1880 to 2570 V. For a higher current beam, the space charge correction is proportionately higher.

Light emitted from the trap was imaged by a pair of lenses onto a 250 μm entrance slit of a 0.25 m focal length, $f/3.5$ Ebert scanning monochromator. The magnification factor of the lens system was 0.8. A blue-sensitive photomultiplier was mounted behind a 500 μm exit slit and operated in photon-counting mode. With a 2360 grooves per mm grating, the instrumental width of the monochromator was 0.8 nm. The Doppler width of the spectra from the trapped ions is estimated to be less than 0.08 nm, and any Zeeman shifts less than 0.04 nm.

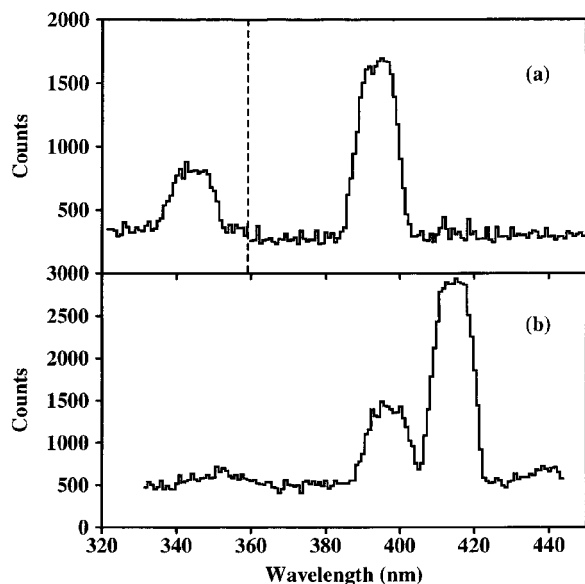


FIG. 1. Broad survey spectral scans with high (10 nm, monochromator slits removed) bandpass for (a) the $3d^4\ ^5D_2-^5D_3$ transition in Ba^{+34} (right peak) and the $3d^5\ ^4G_{7/2}-^4G_{9/2}$ transition in Ba^{+33} (left peak), and (b) the corresponding transitions in Xe^{+32} and Xe^{+31} . The EBIT drift tubes were set at 2378 and 2277 V for the portions of the spectrum in (a) to the right and left of the dotted line, respectively, and at 2144 V for the entire spectrum in (b). The electron beam current was 50 mA throughout.

The wavelength range studied here (320 to 443 nm) was limited at the lower end by the diminishing transmission of the lenses. Calibration of the monochromator's wavelength scale was performed by shining light from a number of low pressure discharge lamps, including mercury, helium, neon, argon, and xenon, through the EBIT from a port opposite the spectrometer. Argon and krypton were also injected, ionized, and trapped during the course of the experiment to observe previously reported [12,17] $M1$ lines *in situ*. In this case, a relatively dense stream of gas was flowed continuously into the EBIT. This broadened the charge state distribution by providing a significant flux of neutral atoms from which steady state populations of the lower charge states, specifically Ar^{+13} and Kr^{+22} , could be formed. Such low charge state ions could not otherwise be made, since the EBIT electron beam became unstable at energies below 1 keV. Our *in situ* measurement of the krypton line yielded 384.08(20) nm, and that of the argon line yielded 441.32(20) nm. These are to be compared with their literature values [12,17] of 384.09(3) nm and 441.24(2) nm, respectively. We estimate the overall uncertainty in our wavelength calibration to be ± 0.2 nm.

Initially, broad survey scans (340–440 nm) with wide spectral bandpass (10 nm, monochromator slits removed) were conducted (Fig. 1). These were followed by narrower scans in the regions where prominent spectral features appeared (e.g., Fig. 2). Finally, the monochromator was adjusted to the peak of the observed lines, and the magnitude of their signal was recorded as a function of electron beam energy. The well controlled conditions in the EBIT produced only a few lines in the survey spectra and greatly simplified the task of identifying them.

There are no previously measured and identified lines from titaniumlike, vanadiumlike, and neighboring $3d^N$ shell ions of barium and xenon. It was not possible, therefore, to confirm the presence of these ions in the trap by observing an experimentally known transition. The existence of trapped barium and xenon was confirmed,

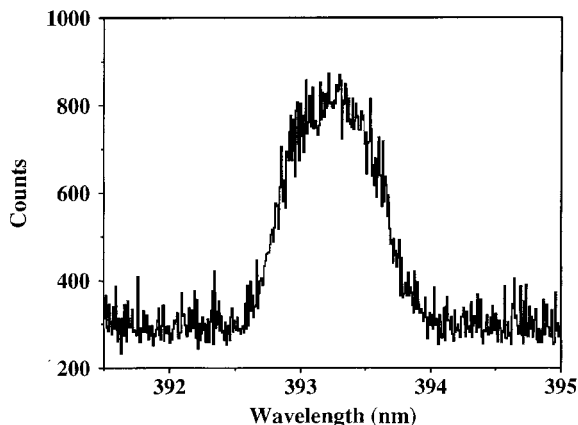


FIG. 2. $3d^4\ ^5D_2-^5D_3$ transition in titaniumlike Ba^{+34} . The profile shown is the sum of 10 individual scans, each of which was accumulated in 5 min with a drift tube potential of 2378 V.

however, by the observation of known x-ray lines from a higher charge state (Ne-like) in high-resolution spectra [18] at increased electron beam energies. Furthermore, the features seen in low-resolution x-ray spectra, taken simultaneously with our uv data, were consistent with theoretical predictions [we used the GRASP² multiconfiguration Dirac-Fock (MCDF) code] [19] for radiative recombination into, and transitions between, levels in $3d^N$ shell ions of Ba and Xe. These were the only charge states of Ba and Xe whose predicted features were consistent with the observed low-resolution spectra.

In Fig. 3, we show energy level diagrams for the barium ions produced in our study. The corresponding diagram for xenon ions, although not shown, is very similar. After a tentative identification of the prominent spectral feature at 393.24 nm (Figs. 1 and 2) as the titaniumlike barium line, whose wavelength was originally predicted [1] to be 377.8 nm, we used the Cowan relativistic Hartree-Fock (HFR) atomic structure code with electron correlation correction [20] to improve the prediction. For the $3d^N$ configuration, the two Slater integrals, $F^2(3d3d)$ and $F^4(3d3d)$, and the $5d$ spin-orbit integral (ζ) determine the energy level positions. We scaled the F^k parameters to make the code's predicted wavelength match that of the tentatively identified line exactly. This scaling factor turned out to be 93% of the *ab initio* HFR values. This is a relatively modest adjustment since scale factors between 90% and 95% are typically required for highly charged ions [20]. Using the 93% scaling, a calculation of the $3d^4 5D_2-5D_3$ transition in titaniumlike Xe⁺³² gives a value of 409.4 nm. This is within 5 nm of a strong line recorded during Xe injection, with the electron beam energy tuned to produce Xe⁺³². As presented in Fig. 3, the $J = 3$ level can decay via the $J = 2$ or the $J = 4$ levels. Calculations using the Cowan code indicate that the A values for the $J = 2-3$ transition in xenon and barium are approximately 400 s^{-1} . The A value for the $J = 3-4$ transition, however, is only 2 s^{-1} in xenon and 17 s^{-1} in barium. Therefore, most of

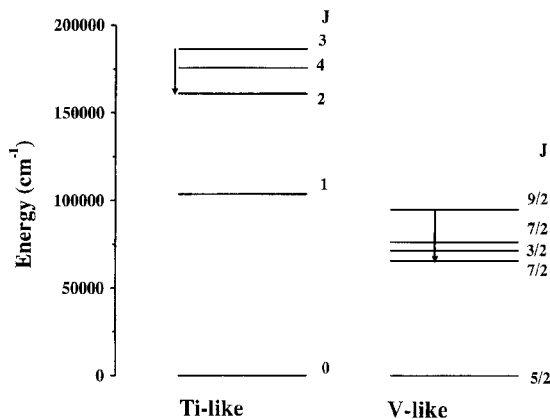


FIG. 3. Energy level diagrams of the lowest levels in the ground terms of titaniumlike and vanadiumlike barium. The level energies were calculated using the Cowan code and arrows indicate visible and near-uv $M1$ transitions.

the decays from the $J = 3$ level will proceed via the $J = 2-3$ channel, and the transition should be easily observable under our plasma conditions.

As a separate check on the scaling factor, we calculated the $3d^8$ levels of ironlike Sn⁺²⁴, the closest highly charged ion of the $3d^N$ shell ($2 \leq N \leq 8$) in which the energies of all the levels of the ground configuration are experimentally known. Using the same 93% F^k parameter scaling for the $3d^8$ configuration, we find agreement with the previously measured values [21] to within 1%.

After observing the titaniumlike barium line, we conducted a theoretical search for other observable $M1$ transitions arising from the $3d^N$ ground configurations. This involved completing calculations for the other charge states of barium and xenon from calciumlike to ironlike ions, using the 93% scaling of the F^k parameters. By examining the calculated wavelengths and branching ratios, we predicted that only one more line should be observable, specifically a $3d^5 4G_{7/2}-4G_{9/2}$ transition in vanadiumlike barium and xenon. The wavelength of this line is predicted to decrease rapidly with increasing Z and to leave the near-uv spectral range ($\geq 300 \text{ nm}$) for ions with $Z \geq 58$.

These predictions prompted us to take a survey scan at shorter wavelengths, with the electron beam energy tuned to produce vanadiumlike barium. A single prominent feature was found, and the wavelength fell very close to the calculation (Table I). Later, when a survey scan was made in xenon, the vanadiumlike line was also found near the predicted location. Thus the wavelengths of all four prominent features recorded in the survey spectra matched the scaled theoretical values closely (Table I).

It should be noted that the noble atomic gases (argon, krypton, xenon) were introduced separately into the EBIT, with sufficient time between loadings to allow the previous gas to be removed by a combination of cryogenic and ion pumping. Features associated with ions of any one of these species were not seen in the spectra of the others. Further evidence for the proper identification of these lines came from the measurement of their ampli-

TABLE I. Predicted and measured wavelengths of visible and near-uv $M1$ forbidden transitions in titaniumlike Ba⁺³⁴ and Xe⁺³² and vanadiumlike Ba⁺³³ and Xe⁺³¹.

Ion	Transition	Wavelength ^a (nm)		A^c (s^{-1})
		Calculated ^c	Measured	
Ba ⁺³⁴	$3d^4 5D_2-5D_3$	393.2 ^b	393.24 ± 0.20	433
Xe ⁺³²	$3d^4 5D_2-5D_3$	409.4	413.94 ± 0.20	434
Ba ⁺³³	$3d^5 4G_{7/2}-4G_{9/2}$	341.4	343.57 ± 0.20	425
Xe ⁺³¹	$3d^5 4G_{7/2}-4G_{9/2}$	394.3	396.25 ± 0.20	311

^aWavelengths in air.

^bThe F^k scaling in the Cowan code was adjusted to 93% so that the calculated and measured wavelengths of this line were equal.

^cCalculated with Cowan code using a 93% scaling of the $F^2(3d3d)$ and $F^4(3d3d)$ Slater integrals.

tudes as a function of electron beam energy. Because the ionization potentials of the nearby charge states are only separated by about 100 eV in both barium and xenon, the populations of these various charge states, and hence the signal strengths of the corresponding emission lines, are expected to change quickly with beam energy. This was seen in our measurements (e.g., Fig. 4) where it was found that all of the identified lines exhibited the expected behavior with electron beam energy, following the predicted [22] population densities of their parent ions.

Although our scaled HFR calculations reproduce the experimental data quite well, a state-of-the-art, fully *ab initio*, MCDF calculation [23] fails to yield good agreement [16]. To our knowledge, there is no other case in which a fully relativistic calculation disagrees with transition energies of highly charged ions ($q \geq +30$) by as much as 5%. The measurements reported here therefore present an important challenge to theorists seeking to predict accurately atomic structure from first principles.

In summary, we have observed a special set of lines from highly charged ions which are expected to persist in the visible and the near-uv range of the spectrum over a large range of nuclear charge states. It is anticipated that this will have important practical application for remote diagnosis in the next generation of high temperature plasma fusion devices. Measurement of these lines also provides a sensitive probe of atomic structure theory applied to a range of ions where the accuracy has been limited by a scarcity of experimental data.

We would like to thank Yong-Ki Kim for carrying out *ab initio* calculations of ionization energies and transition wavelengths. We would also like to thank Mort Levine, Ross Marrs, Dave Knapp, Ed Magee, and the rest of the Livermore EBIT team for guidance during construction of the NIST-NRL EBIT facility. This work was supported

in part by the Office of Fusion Energy of the U.S. Department of Energy.

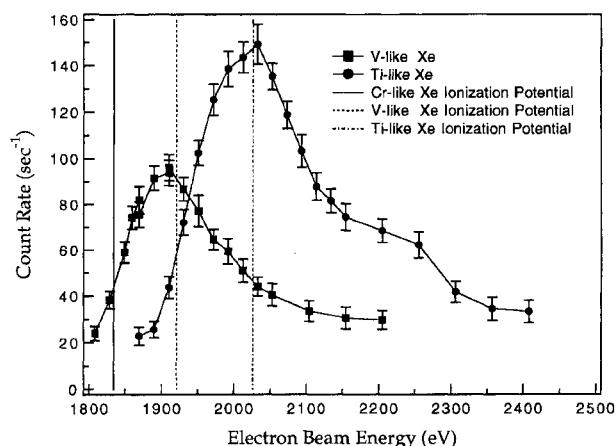


FIG. 4. Amplitudes of the $3d^4\ ^5D_2\text{-}^5D_3$ observed titaniumlike and $3d^5\ ^4G_{7/2}\text{-}^4G_{9/2}$ vanadiumlike transitions in xenon versus electron beam energy, for 35 mA of electron beam current. The corresponding ionization energies are shown by vertical lines.

*Permanent address: Texas A&M University, College Station, TX 77843.

†Permanent address: University of Notre Dame, Notre Dame, IN 46556.

‡Permanent address: Institute of Nuclear Research of the Hungarian Academy of Sciences (ATOMKI), H-4001 Debrecen, Pf. 51, Hungary.

- [1] U. Feldman, P. Indelicato, and J. Sugar, *J. Opt. Soc. Am. B* **8**, 3 (1991).
- [2] B. Edlen, *Z. Astrophys.* **22**, 30 (1942).
- [3] U. Feldman, *Phys. Scr.* **24**, 681 (1981).
- [4] G. A. Doschek and U. Feldman, *J. Appl. Phys.* **47**, 3083 (1976).
- [5] S. Suckewer, *Phys. Scr.* **23**, 71 (1981).
- [6] S. Suckewer *et al.*, *Nucl. Fusion* **24**, 815 (1981).
- [7] E. Hinnov, S. Suckewer, S. Cohen, and K. Sato, *Phys. Rev. A* **25**, 2293 (1982).
- [8] K. Ida and S. Hidekuma, *Rev. Sci. Instrum.* **60**, 867 (1989).
- [9] U. Feldman, J. F. Seely, N. R. Sheely, Jr., S. Suckewer, and A. M. Title, *J. Appl. Phys.* **56**, 2512 (1984).
- [10] D. Wróblewski, L. K. Huang, H. W. Moos, and P. E. Phillips, *Phys. Rev. Lett.* **61**, 1724 (1988).
- [11] D. Wróblewski, L. K. Huang, H. W. Moos, and P. E. Phillips, *Rev. Sci. Instrum.* **59**, 1632 (1988).
- [12] V. Kaufman and J. Sugar, *J. Phys. Chem. Ref. Data* **15**, 321 (1986).
- [13] J. D. Gillaspay, J. R. Roberts, C. M. Brown, and U. Feldman, in *Proceedings of the 6th International Conference on the Physics of Highly Charged Ions—1992*, edited by P. Richard, M. Stöckli, C. L. Cocke, and C. D. Lin AIP Conf. Proc. No. 274 (AIP, New York, 1993), p. 682.
- [14] M. A. Levine, R. E. Marrs, J. R. Henderson, D. A. Knapp, and M. B. Schneider, *Phys. Scr.* **T22**, 157 (1988).
- [15] P. Beiersdorfer, in *Proceedings of the 15th International Conference on X-Ray and Inner-Shell Processes—1990*, edited by T. A. Carlson, M. O. Krause, and S. T. Manson, AIP Conf. Proc. No. 215 (AIP, New York, 1990), p. 648.
- [16] Y.-K. Kim (private communication).
- [17] A. Dollfus, *C.R. Acad. Sci. Paris* **245**, 2011 (1957).
- [18] J. D. Gillaspay, in *Proceedings of the 6th International Symposium on Electron Beam Ion Sources and Their Applications, 1994* (to be published).
- [19] F. A. Parpia, I. P. Grant, and C. F. Fischer, GRASP² (private communication).
- [20] R. D. Cowan, *The Theory of Atomic Structure and Spectra* (University of California Press, Berkeley, CA, 1981), p. 456.
- [21] J. O. Ekberg, U. Feldman, and J. Reader, *J. Opt. Soc. Am. A* **5**, 1275 (1988).
- [22] B. M. Penetrante, J. N. Bardsley, D. DeWitt, M. Clark, and D. Schneider, *Phys. Rev. A* **43**, 4861 (1991); H. Margolis (private communication).
- [23] Y.-K. Kim, *Phys. Scr.* **T47**, 54 (1993).



ELSEVIER

Fabry–Perot spectroscopy of a visible magnetic dipole transition in Ba³⁴⁺

H. Adler^a, E.S. Meyer^{b,*}, F.G. Serpa^b, E. Takacs^b, J.D. Gillaspay^b, C.M. Brown^c,
U. Feldman^c

^a Princeton Plasma Physics Laboratory, P.O. Box 451, Princeton, NJ 08543, USA

^b Atomic Physics Division, National Institute of Standards and Technology, Gaithersburg, MD 20899, USA

^c E.O. Hurlburt Center for Space Research, Naval Research Laboratory, Washington, DC 20375, USA

Abstract

We are using Fabry–Perot interferometry to study visible lines from highly-charged ions created and trapped within an electron beam ion trap (EBIT). The $3d^{45}D_2-5D_3$ titanium-like barium (Ba³⁴⁺) line at 3932(2) Å was recently measured in Ref. [1] (C.A. Morgan et al., Phys. Rev. Lett. 74 (1995) 1716) using a grating monochromator. We present preliminary Fabry–Perot spectra of this line with significantly improved resolution. The Doppler-broadened 1 Å line width is consistent with an expected ion temperature of less than 1 keV. We discuss the possibility of resolving Zeeman splittings, and of using these visible lines as a diagnostic in high temperature, low density plasmas, like those that exist in tokamaks and the EBIT itself.

1. Introduction

In 1991, Feldman, Indelicato, and Sugar [2] predicted an uninterrupted isoelectronic sequence of visible and near-UV forbidden lines extending all the way from titanium-like silver (Ag²⁵⁺), with an ionization potential of 1.3 keV, to titanium-like uranium (U⁷⁰⁺), with an ionization potential of 8.2 keV. These lines correspond to a magnetic dipole (M1) transition from the $J = 3$ to the $J = 2$ level within the $3d^{45}D$ ground configuration of the titanium-like ion. For all lines of the sequence, the calculated wavelengths lie in the range from 3200 to 6100 Å [2].

Recently, an electron beam ion trap (EBIT) was used to observe these lines in barium (Ba³⁴⁺) and xenon (Xe³²⁺) at wavelengths of 3932(2) Å and 4139(2) Å, respectively [1]. In addition to providing confirmation for the predictions of Feldman et al. (although with a 4% discrepancy in transition energy), the experiment represents the first time that an EBIT has been used to measure previously unknown visible transitions in highly-charged ions. In Ref. [1], a grating monochromator was used to measure the lines, and the resulting widths – roughly 8 Å – were dominated by the low resolving power of the instrument.

Higher resolution measurements of these lines, however, should have several applications. Of immediate interest is their utility for diagnosing hot plasmas, since a measurement of Doppler broadening gives a determination of local ion temperature, and a measurement of the Zeeman shift or splitting gives a determination of local magnetic field strength. Studies of these lines also have application in atomic theory. Because the transition energies are small compared with typical binding energies within the ion, high resolution measurements provide a sensitive test of atomic-structure calculations. In fact, there is currently a very large discrepancy between the observed wavelength of the Ba³⁴⁺ line and the predictions of a fully relativistic atomic code [3].

In light of these important applications, we have undertaken a higher resolution study of the Ba³⁴⁺ line using a Fabry–Perot interferometer. We have found that this technique is quite feasible for EBIT studies, and that in fact some of the unique properties of the EBIT simplify the analysis.

2. Doppler broadening

Even though ion temperature plays an important role in the operation and efficiency of the EBIT as an ion source, until recently there had been no direct measurement of the temperature of ions trapped within an EBIT. The Doppler

* Corresponding author.

width of a line emitted from ions of mass M at temperature T is given by [4].

$$\Delta\lambda = \lambda\sqrt{8k_{\text{B}}T \ln 2 / (Mc^2)}, \quad (1)$$

where k_{B} is Boltzmann's constant, and c is the speed of light. Beiersdorfer et al. [5] have just reported a crystal spectrometer measurement of the Doppler broadening in the $1s^2^1S_0-1s2p^3P_1$ X-ray transition in helium-like titanium (Ti^{20+}). With resolving powers up to $\lambda/\Delta\lambda \approx 22000$, they were able to measure temperatures down to 130 eV. Such a high resolving power is near the state-of-the-art for X-ray spectroscopy, but easy to achieve in a visible measurement, especially with a Fabry–Perot instrument.

3. Zeeman effects

Ions trapped in an EBIT are immersed in a fairly strong axial magnetic field used for focusing the electron beam. We typically operate at the limit of our magnet – 3 tesla (although we have successfully created and trapped ions down to 1.5 T), since ion production and excitation rates increase quickly with field strength. Though the effect of a 3-T field on transition wavelengths and lifetimes is negligible for X-ray studies, Zeeman shifts can be a significant fraction of the total transition energy for visible lines.

A magnetic dipole transition from a $J = 3$ level to a $J = 2$ level should contain 15 distinct Zeeman lines: five with $\Delta m = -1$; five with $\Delta m = 0$; and five with $\Delta m = +1$. The Zeeman shift for any one of these lines is given by

$$\Delta = -B\mu_0 g_{J=3} m_{J=3} - (-B\mu_0 g_{J=2} m_{J=2}), \quad (2)$$

where B is the magnetic field, $\mu_0 = 5.7883 \times 10^{-5}$ eV/T is the Bohr magneton, and $g_{J=3}$ and $g_{J=2}$ are the Landé g -factors for the $J = 3$ and $J = 2$ levels, respectively. The Cowan atomic structure programs [4] give $g_{J=3} \approx 1.282$ and $g_{J=2} \approx 1.373$ for the $3d^4^5D$ levels in Ba^{34+} (see Ref. [1] for a description of the scaling parameters used with the code). Thus, the shifts in the barium lines for $B = 3$ T are given by

$$\Delta = -2.226 \times 10^{-4} \text{ eV } m_{J=3} + 2.384 \times 10^{-4} \text{ eV } m_{J=2}. \quad (3)$$

The major splittings, corresponding to the separations of the centers of gravity of components with $\Delta m = -1, 0$ or $+1$, display the normal triplet structure with separations of the order of 2.3×10^{-4} eV. This corresponds to a full-width separation in wavelength of $\Delta\lambda \approx 0.6 \text{ \AA}$ at 3932 \AA , giving $\Delta\lambda/\lambda \approx 1.5 \times 10^{-4}$. The finer splittings within each group are much smaller – approximately 0.15×10^{-4} eV, or about 6.5% of the larger splittings.

Both the polarization and intensity of the emitted line radiation depend upon Δm , and the intensity further de-

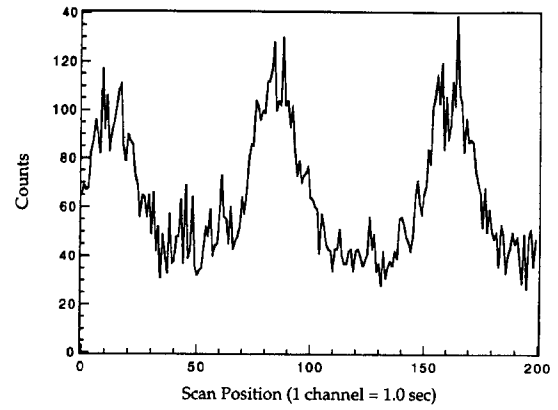


Fig. 1. Fringe data for the Ba^{34+} line, averaged over 16 scans. The scan period was 200 s, and counts were histogrammed into 1 s channels. The distance between peaks is $3.0(1) \text{ \AA}$, corresponding to $\Delta\nu = 19.4(5) \text{ cm}^{-1}$.

pends upon m_j for the upper state. For observation perpendicular to the field, and assuming uniform level population, the relative intensities are given by the following standard formulas [6]:

$$\begin{aligned} I_{\pi}(\Delta m = 0) &= J^2 - m^2 = 9 - m^2; \\ I_{\sigma}(\Delta m = -1) &= (J + m)(J - 1 + m)/4 \\ &= (m + 3)(m + 2)/4; \\ I_{\sigma}(\Delta m = +1) &= (J - m)(J - 1 - m)/4 \\ &= (3 - m)(2 - m)/4. \end{aligned} \quad (4)$$

By observing at 90° to the magnetic field direction as we do, the σ -components ($\Delta m = \pm 1$) should be linearly-polarized parallel to the field axis, and the π -components ($\Delta m = 0$) should be linearly-polarized perpendicular to the field axis [4].

4. Experiment

A typical scan of the titanium-like barium line is shown in Fig. 1. Light from the EBIT is transmitted through a quartz window side port and then collimated onto a plane Fabry–Perot interferometer. The Fabry–Perot is then followed by a fringe-imaging lens (24.5 cm focal length) and a central aperture 4 mm in diameter placed at the focal point. Behind the aperture, the light is detected by a photomultiplier tube operating in single-photon counting mode. The plot in Fig. 1 was created by repeatedly scanning the Fabry–Perot mirror spacing d with a piezoelectric element while histogramming photon counts versus scan position. The total acquisition time for the spectrum was about 40 min. By temperature controlling the Fabry–Perot plates, we were able to reduce any drift over the time of a scan to a negligible level.

Using the 6328-Å line of a He–Ne laser as a reference, we found a finesse of $F = 22$. Taking into account the change in flatness finesse, parallelism finesse, reflectivity, and pinhole finesse with wavelength, we extrapolated a value of $F = 15$ for the finesse of the interferometer at 3932 Å. Chromatic aberration in the optics, however, could have lowered the finesse substantially by causing the image focus to shift away from the pinhole. After doing a ray tracing analysis, we estimate that this effect can give at most a factor of two reduction in the pinhole finesse. This leads to an overall lower bound of $F = 9$ for the total finesse. The free spectral range $\Delta\sigma = c/2d = 19.4(5) \text{ cm}^{-1}$ (3.0(1) Å at 3932 Å) was made large (by moving the Fabry–Perot plates as close together as possible) because of the very large Doppler width expected for the barium line. We determined d and thus $\Delta\sigma$ by using a standard technique in which the Fabry–Perot is tilted and the distance between fringes in the back reflection of an incident laser is measured [7]. Later, the accuracy of this measurement was confirmed by measuring a closely-spaced pair of lines at 4044 Å and 4047 Å from a potassium discharge lamp. The uncertainty shown in $\Delta\sigma$ is 1-sigma systematic error arising from our tilt-technique measurement.

The Ba^{34+} charge state was created by biasing the center drift tube electrode to 2350 V, which corresponds to an electron beam energy of about 2250 eV (the energy reduction is due to space charge effects). This energy is just below the titanium-like state's ionization potential. The end cap electrodes were biased at 500 V to give an axial trap depth of 17 keV. With the electron beam current fixed at 50 mA, the counting rate achieved for the barium line is of order 200/s, which is roughly equal to our dark count background. This counting rate compares favorably with previous precision X-ray measurements we have made using a Bragg crystal spectrometer.

5. Discussion

In Fig. 2, we compare numerical simulations of the Doppler- and finesse-broadened Zeeman lines for a number of different ion temperatures with our data. The Zeeman components are expected to be blurred by Doppler broadening due to the substantial temperature of the ions in the EBIT. Comparison of our measurements with calculations indicate that the ion temperature is less than 1 keV, in agreement with the predictions of a numerical simulation of EBIT charge-state evolution developed by Penetrante et al. [8].

The scarcity of visible lines in the highly-charged ions produced in EBIT greatly simplifies the analysis of Fabry–Perot spectra. Furthermore, the precise control over the electron beam energy that one has with the EBIT allows fine control over emitting charge state density. This

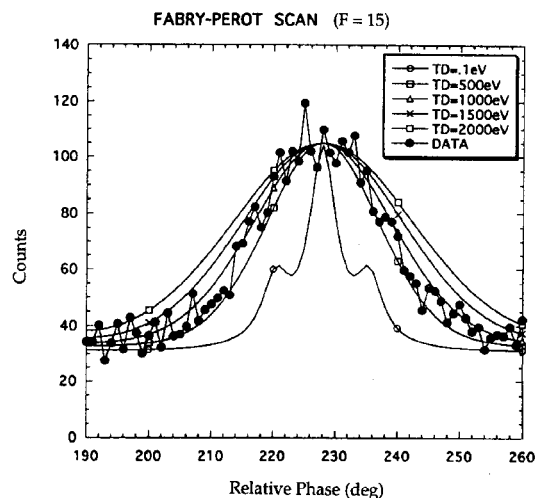


Fig. 2. Simulations of the line profile for different ion temperatures TD and for a Fabry–Perot finesse of $F = 15$. The data is the sum of two separate peaks from Fig. 1. A best fit appears to lie between $TD = 1000$ eV and $TD = 500$ eV, indicating that the ion temperature lies between these two values. At a very low temperature ($TD = 0.1$ eV), the Zeeman-induced triplet structure can be seen, although broadened somewhat by the finite finesse.

selectivity helps with confirming line identifications without resorting to a wavelength prefilter.

For our first measurements, we achieved a resolving power of 10^4 , good enough to get a crude measurement of ion temperature. We expect there is room to improve by perhaps another factor of ten by either using a higher finesse instrument or working at a larger mirror spacing d . Resolution of Zeeman splittings should be possible by using a shallower trap in order to enhance evaporative cooling (reduce T). Studying ions further up the titanium-like sequence with larger mass will also help to reduce the Doppler width (increase M).

In the future, we plan to extend our measurements to tungsten, uranium, and various rare earth metals along the titanium-like sequence. We also plan to employ polarizers in order to separate the different Zeeman lines. For example, eliminating the $\Delta m = 0$ (π -) component will make it much easier to resolve the Zeeman splitting between the orthogonally-polarized σ -component lines.

Our discussion of relative Zeeman intensities above assumed that the different m_J sublevels of the upper state are populated equally. This might not be true in an EBIT, since the excitation source (the electron beam) is uni-directional and can create preferential populations in certain m_J sublevels. As the upper level of the visible transition is populated primarily by cascades, it is difficult to calculate exactly how much effect this will have on the polarization of the visible emission. We are pursuing extensive calculations now and hope to include these effects in a later study.

In conclusion, we have used a Fabry–Perot interferometer to study highly-charged ions created and stored inside

an EBIT. Because of the low energy of visible transitions, it should be possible to resolve Zeeman shifts as well as to measure magnetic field-induced polarization. The inherently high resolution of spectroscopic techniques in the visible makes it straightforward to measure Doppler broadening and determine the temperature of the emitting ions, and the line we have measured should have applications in tokamaks as well as EBITs.

Acknowledgements

We thank J. Sugar for calculating the Landé g -factors for the $J = 3$ and $J = 2$ levels in titanium-like barium, and we thank J.R. Roberts for helpful discussions and a careful reading of this manuscript.

References

- [1] C.A. Morgan, F.G. Serpa, E. Takacs, E.S. Meyer, J. Sugar, J.R. Roberts, J.D. Gillaspay, C.M. Brown and U. Feldman, *Phys. Rev. Lett.* 74 (1995) 1716.
- [2] U. Feldman, P. Indelicato and J. Sugar, *J. Opt. Soc. Am. B* 8 (1991) 3.
- [3] Yong-Ki Kim, private communication (1994).
- [4] R.D. Cowan, *The Theory of Atomic Structure and Spectra* (University of California Press, Berkeley, 1981).
- [5] P. Beiersdorfer, V. Decaux, S. Elliott, K. Widmann, K. Wong, preprint, 1994; also, these Proceedings (7th Int. Conf. on the Physics of Highly Charged Ions (HCI-94), Vienna, Austria, 1994) *Nucl. Instr. and Meth. B* 98 (1995).
- [6] I.I. Sobelman, *Atomic Spectra and Radiative Transitions* (Springer, Berlin, 1979).
- [7] Burleigh Instruments Inc., private communication (1994).
- [8] B.M. Penetrante, J.N. Bardsley, M.A. Levine, D.A. Knapp and R.E. Marrs, *Phys. Rev. A* 43 (1991) 4873; we thank H. Margolis for providing a port of the original Fortran source code to C.

Anomalous Z dependence of a magnetic dipole transition in the Ti I isoelectronic sequence

F. G. Serpa,* E. S. Meyer, C. A. Morgan,† J. D. Gillaspay, J. Sugar, and J. R. Roberts
Atomic Physics Division, National Institute of Standards and Technology, Gaithersburg, Maryland 20899-0001

C. M. Brown and U. Feldman

E. O. Hulburt Center for Space Research, Naval Research Laboratory, Washington, D.C. 20375-5000

(Received 20 October 1995)

In isoelectronic sequences, transition wavelengths ordinarily move rapidly to shorter wavelengths as Z increases. However, it has been predicted that a particular sequence of magnetic dipole ($M1$) transition wavelengths for the Ti-like ions, Xe^{+32} through U^{+70} , remain relatively constant in the 320–400-nm range. In the present paper we extend the experimental identifications of the Ti-like $M1$ transitions from Ba and Xe to Nd (Nd^{+38}) and Gd (Gd^{+42}) to verify this behavior. Using the newly acquired wavelengths to adjust atomic parameters, we have also calculated improved wavelengths for all such $M1$ transitions between Xe ($Z=54$) and Os ($Z=76$).

PACS number(s): 32.30.Jc, 32.10.-f, 52.70.-m, 31.25.-v

I. INTRODUCTION

Since it is common for the wavelengths in isoelectronic sequences of ionic transitions to move rapidly to shorter wavelengths as Z increases, wavelengths are typically within the range of optical instruments for only a few members of a sequence. They shift into the vacuum ultraviolet and soft x-ray spectral regions, becoming much more difficult to use as plasma diagnostic probes. Previously, Feldman, Indelicato, and Desclaux [1] reported results from a survey of atomic transitions that violate this general wavelength scaling behavior and that would be suitable for plasma diagnostics in future high-energy Tokamak fusion devices. This search was aimed at finding transitions that fulfill the following requirements: (a) the wavelengths should be ≥ 250 nm so that transmission optics can be employed; (b) the lines should be reasonably intense and arise from the lowest term of the ground configuration, and (c) the emitting ion should have an ionization potential in the 5–10-keV range. The survey included all promising isoelectronic sequences and was based on calculations using a Dirac-Fock code of Desclaux and co-workers [2,3], including all refinements [4,5]. Feldman, Indelicato, and Desclaux [1] discovered only one set of transitions in only one isoelectronic sequence that fulfilled the stated requirements. They found that the wavelengths of the $M1$, $3d^4\ ^5D_2-^5D_3$ transitions in the Ti-like ions Xe (Xe^{+32}) through U (U^{+70}) are in the 320–400-nm range, satisfying the first requirement. Since the 5D is the lowest term of the Ti-like ground configuration, $3d^4$, and since the spontaneous decay rates of the transition are sufficiently high, the second requirement is also fulfilled. The last requirement is fulfilled for all ions with atomic numbers $Z \geq 75$.

However, *ab initio* calculations often are not sufficiently accurate to unambiguously identify the transition wave-

lengths when compared with experimental observations, especially where there exists more than one ion stage in the experiment. Therefore, it is necessary to make experimental observations along an isoelectronic sequence in incremental steps to compare with theoretical calculations to assure that further predictions are as accurate as possible.

In a recent paper [6], spectra of highly ionized Xe and Ba in the 320–400-nm range were produced with an electron beam ion trap (EBIT). Each spectrum (see Fig. 1 [6]) contained only two lines, one of which was identified as the predicted Ti-like $M1$ transition, thus providing the first experimental verification of the prediction. The wavelength agreement between the calculations using the Dirac-Fock code of Desclaux and co-workers [2,3] and the experimental values was within 5%, and within 4 nm or 1% with the predictions of the Hartree-Fock code of Cowan [7] when the electrostatic integrals were scaled to 93% of their *ab initio* values. For highly charged ions, the comparison of Cowan's code calculations with experimental values typically requires that the electrostatic integrals be scaled from 90% to 95% of their *ab initio* values [7]. This scaling arises from the interaction of the configuration under investigation with energetically distant perturbers.

In this paper we extend the identification of the Ti-like $M1$ transitions to Nd^{+38} and Gd^{+42} . Using the experimentally acquired wavelengths, we established scaling factors for the electrostatic integrals in the Cowan code for elements $Z=54-76$. From these scaling factors, improved predictions of wavelengths for Ti-like $M1$ transitions within the $3d^4$ ground configuration between Xe ($Z=54$) and Os ($Z=76$) have been obtained.

II. EXPERIMENT

The EBIT at the National Institute of Standards and Technology (NIST), a joint project between NIST and the Naval Research Laboratory (NRL), was used as the source of excited highly charged ions in this work [8,9]. The desired ion stage is produced by successive electron impact ionization from an accelerated electron beam. This beam is produced by

*Permanent address: University of Notre Dame, Notre Dame, IN 46556.

†Permanent address: Texas A&M University, College Station, TX 77843.

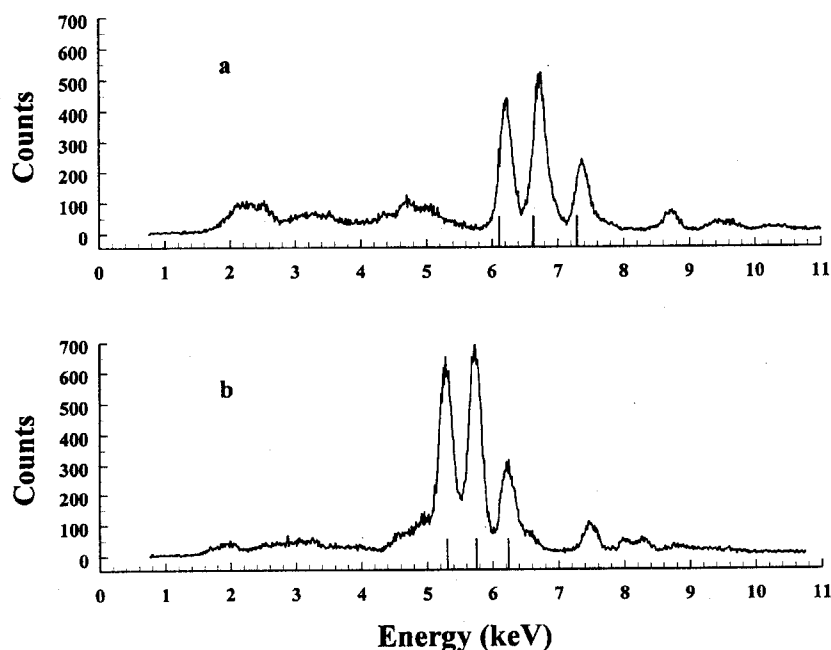


FIG. 1. X-ray spectra in keV of (a) Gd and (b) Nd taken with a Si(Li) detector during injection at 10 kV accelerating potential. The tick marks along the abscissa correspond to calculated transition energies between excited levels and the ground state. The calculations were done with the GRASP² code [14].

a electron gun that provides currents up to ~ 150 mA. A pair of superconducting magnets in a Helmholtz configuration, producing a uniform axial magnetic field of 3 T, compresses the electron beam to a diameter of ~ 60 μm resulting in a current density of ~ 5000 A/cm². Together the electron beam and the magnetic field produce a radial trap for the ions. Axial trapping of the ions along the electron beam axis is provided by raising the two ends of three collinear, insulated drift tubes to a positive potential with respect to the center drift tube bias potential. Together this results in a cylindrical trap ~ 30 mm long and ~ 200 μm in diameter [10] in the direction of the electron beam. A variable voltage between 2 and 20 kV applied to the drift tubes defines an accelerating potential for the electron beam. A correction of approximately -100 eV must be applied to this energy due to the net space charge of the electrons and the positive ions in the trap. The precise energy of the electron beam (~ 50 -eV width) is determined from the variable accelerating potential, the center drift tube bias voltage, and the space-charge correction. By adjusting the accelerating voltage slightly below the ionization energy of the desired ion, the population of a specific charge state can be optimized.

Desired elements are introduced into the trap region in various ways. Due to the composition of the electron gun cathode, Ba is naturally present and is injected slowly in our EBIT. Other elements must be introduced externally either by gas injection or by means of a metal vapor vacuum arc (MEVVA) source. The MEVVA attaches to the top of the EBIT vacuum chamber along the electron beam axis, approximately 1.5 m above the trap region. The operation of the MEVVA has been described in detail previously [11,12]. In brief, the MEVVA consists of a central trigger electrode, a cylindrical cathode, an anode, and extractor plates and is modeled after the Livermore MEVVA design [13]. The composition of the cathode determines the species to be injected. The trigger, cathode, and anode all operate at or slightly above the voltage of the drift tubes to assure that the injected ions will have enough energy to reach the trap. A pulse of

several kilovolts and a few microseconds in duration is applied to the trigger electrode. The resulting discharge generates a small amount of plasma between the cathode and trigger. This plasma, containing low charge states of the species being injected, is accelerated towards the trap. An einzel lens between the MEVVA and the trap provides additional focusing to increase the number of ions arriving at the trap.

A set of eight, 25-mm-high by 2.5-mm-wide, radially positioned slots in the central drift tube provide openings for radiation emanating radially from the trap region. Four 120-mm-diam and four 38-mm-diam knife-edge flanges in the vacuum vessel allow for radial viewing access to the trap region. One of the ports is blocked by a device to suppress the buildup of electrons [8]. A Si(Li) detector, with an energy resolution of ~ 190 eV, is used to monitor the x-ray spectra through one of the radial ports. This port has a 0.13-mm-thick beryllium window to act as the vacuum interface. Wavelengths above 300 nm were also observed radially through a quartz window port. Wavelength dispersion of this spectra was achieved with a 0.3-m focal length, $f/5.3$ Czerny-Turner scanning monochromator, with a 1200-groove/mm grating resulting in a reciprocal linear dispersion of 2.6 nm/mm. A low noise, 12-stage, 50-mm-diam, end-on photomultiplier was placed at the monochromator exit slit. A commercial cooler was used to reduce the temperature of the photomultiplier to about -25 $^{\circ}\text{C}$. This cooling and a magnetic defocuser surrounding the photomultiplier to reduce the active cathode area decreased the detector noise to about 3 counts/s. Because of the detector sensitivity to stray magnetic fields from the EBIT superconducting magnet, two 50-mm-diam (150- and 175-mm focal length) fused silica plano-convex lenses were used to image light from the trap to a new position about 850 mm away from the EBIT. This combination of lenses produced a demagnification of ~ 0.8 and transmitted $\sim 30\%$ of the light incident on the first lens. The monochromator was attached to an optical table, which was fully adjustable in the horizontal plane, and moved independently from the two lenses. Two translation stages with a

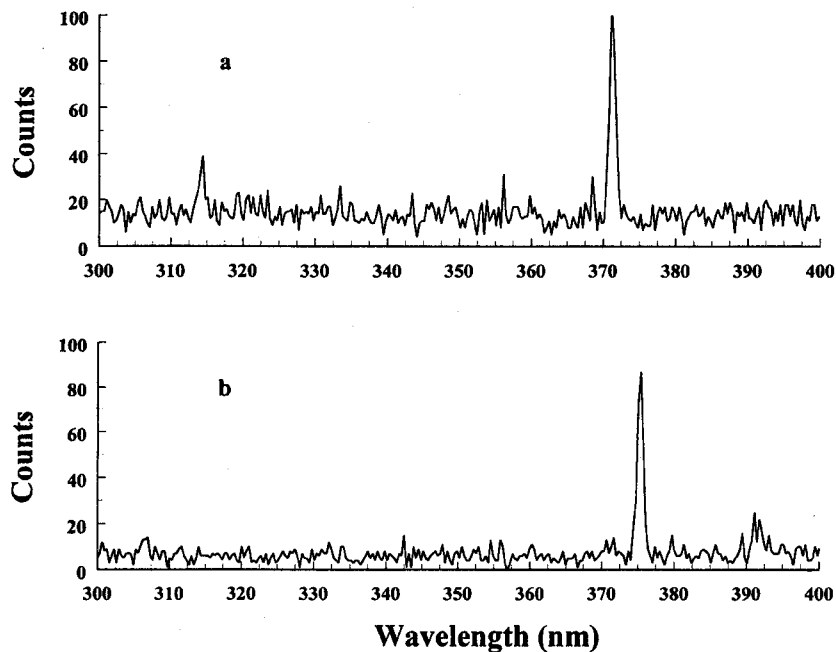


FIG. 2. Survey of emission spectra in the 300–400-nm range obtained with a scanning monochromator for (a) Gd and (b) Nd.

resolution $\leq 10 \mu\text{m}$ were used to translate the monochromator and optical table assembly and placed the monochromator's entrance slit at the trap image formed by the lenses.

For the present experiment, Gd and Nd were injected separately into the EBIT using the MEVVA. The main accelerating voltage and the MEVVA anode voltage were set to 10 keV, appropriate to produce Ne-like Nd and Gd. The upper, middle, and lower drift tubes were at +500, +100, and +500 V, with respect to the main accelerating voltage. To load the trap with ions, first the upper drift tube offset voltage was reduced to zero, which combined with the offset of +100 V on the middle drift tube, forced any residual ions out of the trap. After 2 ms, a pulse was transmitted through a fiber optic to trigger the MEVVA, and 15 μs later the upper drift tube offset voltage was raised again to +500 V to trap the injected ions. This cycle was repeated about every 2 s and trapping was confirmed by observing the corresponding x-ray spectra.

III. DATA

X-ray spectra of Gd obtained with the Si(Li) detector are shown in Fig. 1(a). The transition energies to the ground state from the $2p^5(^2P_{1/2})3d(1/2,3/2)_1, 2p^5(^2P_{3/2})3s(3/2, 1/2)_1$ and $2p^5(^2P_{3/2})3d(3/2,5/2)_1$ levels (in $j-j$ coupling) of Ne-like Gd were obtained from calculations using the multiconfigurational Dirac-Fock (MCDF) code GRASP² [14] and yielded 6.11, 6.63, and 7.29 keV, respectively. This agrees with the main peaks in Fig. 1(a) at 6.2, 6.7, and 7.4 keV. Similar calculations for Ne-like Nd give 5.31, 5.75, and 6.24 keV for the same transitions and are also in agreement with our measured values of 5.34, 5.78, and 6.27 keV [see Fig. 1(b)]. In order to obtain the desired Ti-like charge state, a similar timing sequence of events described above was followed. Ions were injected with a 10-kV accelerating potential, and 3 ms after the upper drift tube bias was raised, the total center drift tube voltage was lowered to the Ti-like

ionization energy. The total duration of each cycle was about 2 s. Wavelength survey scans were made between 300 and 400 nm for Nd and Gd (see Fig. 2). The Gd scan was taken at a 3.34-keV drift tube voltage, a 63-mA electron beam current, and with a 400- μm entrance and exit slit widths. It showed a prominent peak at 371.3 nm [Fig. 2(a)] and a weaker peak at ~ 314.4 nm [Fig. 2(a)]. The Nd scan was taken at a drift tube voltage of 2.77 keV, 49-mA electron beam current, and 600- μm entrance and exit slits. It showed a main peak at ~ 375.3 nm and a weaker feature at ~ 391.0 nm [Fig. 2(b)]. We identified the stronger peaks as the $3d^4\ ^5D_2 - ^5D_3$ M1 transition.

By setting the monochromator to the wavelength of the Gd M1 peak at 371.3 nm and varying the accelerating potential, we observed the dependence of the line intensity on drift tube potential. A plot of this line intensity is shown in

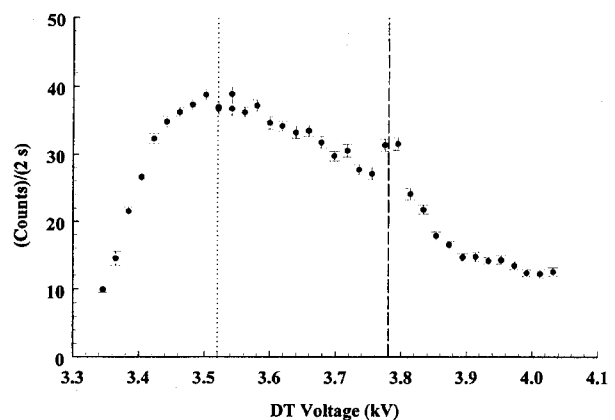


FIG. 3. Detector signal from the M1 line of Ti-like Gd as a function of the voltage of the middle drift tube. The dotted line indicates the voltage corresponding to maximum intensity and the dashed line indicates the voltage corresponding to the dielectronic recombination feature.

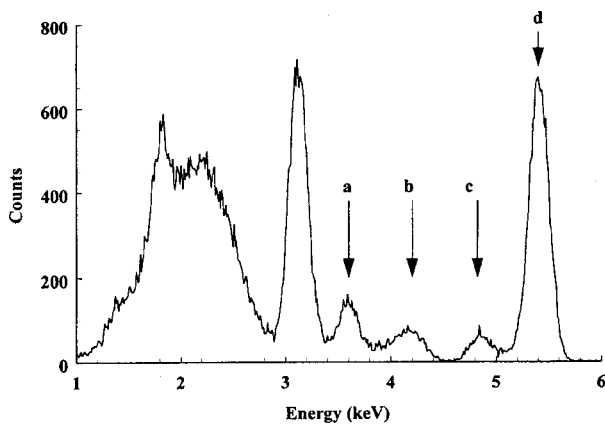


FIG. 4. X-ray spectra in keV of highly ionized Nd observed during the $M1$ line scan. The peaks labeled a and b are consistent with radiative recombination into the $n=5$ and 4 shells, respectively, for Ti-like Nd. The peaks labeled c and d are due to dielectronic recombination into the Ti-like charge state.

Fig. 3, where the horizontal axis has been corrected for the 100-V offset applied to the middle drift tube but has not been adjusted for the space-charge effects. The vertical axis shows the detector signal, which has been normalized for temporal variations in the number of trapped ions over the time of acquiring this data. The normalization is derived from the ratio of the peak signals (at 3.52 keV) at the beginning and end of the data acquisition. The data exhibit the expected behavior for the Ti-like charge state, as derived from computer simulations of the charge-state balance in the trap as a function of beam energy [15]. The experimental maximum found at a central drift tube voltage of 3.52 keV is about 100 V higher than the beam energy of the simulation. This is in agreement with an expected space-charge correction of about -100 V. The plot also shows a small peak at higher drift tube voltage. We attribute this to an enhancement of the Ti-like population due to dielectronic recombination (DR) from the Sc-like charge state; the resonant capture of an electron into the $3d$ shell with the excitation of a $2p_{1/2}$ electron to the $3d$ shell would require an electron energy of about 3.69 keV, according to our MCDF calculations. Again this is 100 V lower than the 3.78-keV energy observed and is consistent with our estimate of the space-charge correction.

As a further confirmation of the charge-state identification, an x-ray spectrum taken with the Si(Li) detector during the Nd scan is shown in Fig. 4. The peaks labeled a and b are due to radiative recombination into Ti-like Nd with the captured electron in the $n=5$ and 4 shell, respectively. Our MCDF calculations predict 3.6 and 4.2 keV for peaks a and b , respectively. The peaks labeled c and d are due to DR into the Ti-like charge state, where an electron is captured into the $3d$ shell and a $2p_{3/2}$ electron is excited to the $3d$ shell. The observed energy of peaks c and d agrees with our MCDF calculations for the decay of a $3s$ (4.8 keV) or $3d$ (5.3 keV) electron to fill the hole left in the $2p_{3/2}$ shell by the DR process.

Higher-resolution wavelength scans were made using narrower slit widths to better determine the $M1$ transition wavelengths, as well as to observe other features present at shorter wavelength in Gd. The monochromator wavelength scale

TABLE I. Scaling factors and calculated and observed wavelengths for the $3d^4(^5D_2-^5D_3)$ Ti-like $M1$ transitions. All wavelengths are in nm and the uncertainties are listed in parentheses.

Z	Element	Scale factor	$\lambda(2-3)_{\text{calc}}$	λ_{expt}
54	Xe	0.922	413.0	413.9(2) ^a
56	Ba	0.930	393.2	393.2(2) ^a
60	Nd	0.946	374.9	375.3(2) ^b
64	Gd	0.962	368.6	371.3(2) ^b
68	Er	0.978	363.6	
72	Hf	0.994	356.2	
74	W	1.000	352.4	
76	Os	1.000	350.7	

^aReference [6].

^bThis work.

was calibrated by viewing a low-pressure He discharge lamp through the radial viewport located on the side of the EBIT opposite the monochromator. The wavelength range used was 296.7–435.8 nm. Also, by injecting small amounts of Ar and Kr gas into the EBIT, *in situ* calibration lines could be observed. The $\text{Ar}^{+23}2s^22p^2P_{1/2-2}P_{3/2}$ and the $\text{Kr}^{+22}3s^23p^2^3P_{1-3}P_2$ $M1$ transitions were observed at 441.24(2) and 384.09(2) nm, respectively [17]. The wavelength uncertainties determined from these two wavelength calibrations, along with a possible systematic wavelength shift from the data acquisition, were added in quadrature to give an overall uncertainty of $\leq \pm 0.2$ nm.

IV. DISCUSSION AND CONCLUSION

For the Gd $3d^4^5D_2-^5D_3$ $M1$ transition, the experimental value differed from its predicted value by about 10 nm when fixed scaling was used for the electrostatic integrals in the Cowan code [7]. To improve the agreement, we used the measured Gd $M1$ line and the previously observed lines (Ref. [6]), and adjusted the electrostatic integrals in the Cowan code by a linear variation of the scale factor = 0.922 + 0.004($Z-54$) (see Table I). This gave the best fit to the known wavelengths over the range from $Z=54$ (0.922) to $Z=74$ (1.000). For $Z \geq 74$, this factor is set equal to one, i.e., no scaling, due to the far configuration-interaction effects approaching zero at high ionization. This variation of the scale factors not only fit our observed wavelengths but also correctly predicted the wavelength of the $M1$ line for Nd, which we subsequently observed. Such variation of the scale factor for the electrostatic integrals is a commonly observed behavior along an isoelectronic sequence. For example, in the investigation of the Zn sequence by Litzen and Reader [16], similar increases with Z of the scale factor for the electrostatic integrals, F^2 , were found. At W, the Cowan code wavelength equals that obtained in Ref. [1] from the Dirac-Fock code of Desclaux and co-workers.

In Gd we also found a weaker peak at 314.4 nm. This peak has a similar beam energy dependence as the $M1$ line, which suggests that it also belongs to this Ti-like charge state. A candidate for this is the $3d^4^5D_4-^5D_3$ $M1$ transition, which competes with the $3d^4^5D_2-^5D_3$ for line strength at high Z [1]. An observation of other members of this isoelectronic sequence is needed to confirm this identification.

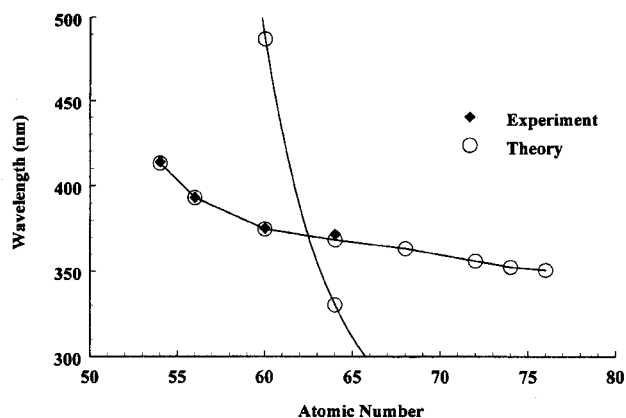


FIG. 5. Z dependence of Ti-like $M1$ lines as a function of atomic number. The flatter curve represents the $3d^4 \ ^5D_2-^5D_3$ transitions and the steeper curve represents the $3d^4 \ ^5D_4-^5D_3$ transitions. Open circles correspond to the wavelengths calculated with the scaled Hartree-Fock code of Cowan [7] and the filled diamonds represent experimental observations.

At lower central drift tube potentials, a second weak peak appeared at 320.8 nm, suggesting that it belongs to a lower charge state, e.g., V-like Gd.

Figure 5 is a plot of the calculated wavelengths (open circles) of the $M1$ transitions, $3d^4 \ ^5D_2-^5D_3$ and

$3d^4 \ ^5D_4-^5D_3$ obtained with the Hartree-Fock code of Cowan using the scaling in Table I. This figure illustrates the normal behavior of the $M1$ lines as a function of atomic number, i.e., a very rapid change in the wavelengths of the $3d^4 \ ^5D_4-^5D_3$ transitions, while the anomalous Z dependence is portrayed by the small change in the wavelengths of the $3d^4 \ ^5D_2-^5D_3$ transitions. This figure also includes the observed wavelengths (filled diamonds). Table I lists the data for the $3d^4 \ ^5D_2-^5D_3$ transitions, together with the experimental scale factors. Another observation at higher Z (such as W) would help extend and confirm the present isoelectronic sequence of $M1$ lines for the $3d^4$ configuration, and would likely be of great importance for future tokamak diagnostics.

In conclusion, we have measured and identified the $3d^4 \ ^5D_2-^5D_3$ $M1$ transitions for Nd^{+38} and Gd^{+42} . These measurements extend our previous work for $Z=54$ and 56, and confirm the suppressed Z dependence for these $M1$ transition wavelengths along the Ti-like isoelectronic sequence. To date, we know of no *ab initio* calculations that can predict these wavelengths with an accuracy comparable to the scaled Hartree-Fock code of Cowan.

ACKNOWLEDGMENT

We would like to thank C. Boyer and G. Holland for their technical assistance in constructing and implementing the MEVVA.

-
- [1] U. Feldman, P. Indelicato, and J. Sugar, *J. Opt. Soc. Am. B* **8**, 3 (1991).
 - [2] J. P. Desclaux, *Comput. Phys. Commun.* **9**, 31 (1975).
 - [3] P. Indelicato, O. Gorceix, and J. P. Desclaux, *J. Phys. B* **20**, 651 (1987).
 - [4] O. Gorceix, P. Indelicato, and J. P. Desclaux, *J. Phys. B* **20**, 639 (1987).
 - [5] P. Indelicato, *J. Phys. (Paris) Colloq.* **150**, C-239 (1989).
 - [6] C. A. Morgan *et al.*, *Phys. Rev. Lett.* **74**, 1716 (1995).
 - [7] R. D. Cowan, *The Theory of Atomic Structure and Spectra* (Univ. California Press, Berkeley, California, 1981).
 - [8] J. D. Gillaspay *et al.*, in *Vlth International Conference on Physics of Highly Charged Ions*, edited by P. Richard *et al.*, AIP Conf. Proc. No. 247 (AIP, New York, 1993), p. 682.
 - [9] R. E. Marrs, P. Beiersdorfer, and D. Schneider, *Phys. Today* **47** (10), 27 (1994).
 - [10] J. D. Gillaspay *et al.*, *Phys. Scr.*, **T59**, 392 (1995).
 - [11] I. G. Brown *et al.*, *Appl. Phys. Lett.* **49**, 1019 (1986).
 - [12] I. G. Brown *et al.*, *Rev. Sci. Instrum.* **57**, 1069 (1986).
 - [13] A. M. Levine *et al.*, *Phys. Scr.* **T22**, 157 (1988).
 - [14] F. A. Parpia, I. P. Grant, and C. F. Fischer, GRASP² (private communication).
 - [15] D. Knapp (private communication).
 - [16] U. Litzen and J. Reader, *Phys. Rev. A* **36**, 5159 (1987).
 - [17] V. Kaufman and J. Sugar, *J. Phys. Chem. Ref. Data* **15**, 321 (1986).

Kr spectra from an electron-beam ion trap: 300 nm to 460 nm

F. G. Serpa,* E. W. Bell,[†] E. S. Meyer,[‡] J. D. Gillaspay, and J. R. Roberts

Atomic Physics Division, National Institute of Standards and Technology, Gaithersburg, Maryland 20899

(Received 9 October 1996)

Kr spectra from 300 nm to 460 nm produced in an electron-beam ion trap (EBIT) are reported in this work. The spectra include magnetic dipole ($M1$) transitions from Kr XXIII and Kr XXII, as well as electric dipole ($E1$) lines of Kr II and Kr III. Two new capabilities of the EBIT at the National Institute of Standards and Technology, time resolved data acquisition and extracted ion analysis, are used to aid in the charge state identification. [S1050-2947(97)03503-8]

PACS number(s): 32.30.Jc, 32.10.-f, 31.25.Eb, 31.25.Jf

I. INTRODUCTION

Recent developments in electron beam ion trap (EBIT) spectroscopy have shown the importance of the EBIT as a source of magnetic dipole ($M1$) transitions in the visible or near-uv [1,2]. Magnetic dipole transitions arising between levels of the ground configuration of highly charged ions are not only useful as diagnostic tools for tokamaks [3–5] and in the study of the solar corona [6,7], but also have academic interest since *ab initio* calculations fail to account for the observed wavelengths [5,8]. Many such transitions remain unobserved, particularly for charge states with ionization energies below 2 keV [9]. Measurements of such lines are important because they make significant impact on the elaboration of spectral [10] and energy level [11] databases. They are also important for improving predictions along isoelectronic sequences [9] and provide a challenge for *ab initio* calculations.

In the present work we report spectra from 300 nm to 460 nm obtained with the EBIT during injection of Kr gas. Our data include two $M1$ transitions, one of which has not been previously observed. These $M1$ lines arise from transitions between the levels of the ground configuration of Kr XXIII ($3s^23p^2$) and Kr XXII ($3s^23p^3$). A new ion extraction, transport, and charge-to-mass analysis system at the National Institute of Standards and Technology (NIST) [12] was used to obtain information about the distribution of ion charge states within the EBIT. Data from the extraction system together with time resolved data were used to aid in charge state identification. Lines of singly and doubly ionized Kr were also present in our spectra and were used for *in situ* wavelength calibration.

II. EXPERIMENTAL SETUP

The EBIT at NIST was used as the source of excited highly charged ions in this work [13,14]. The desired ion

stage is produced by successive electron-impact ionization from an accelerated electron beam, produced by a electron gun which provides currents up to ~ 150 mA. A pair of superconducting magnets in a Helmholtz configuration produces an axial magnetic field of 3 T in the trap region and compresses the electron beam to a diameter of ~ 60 μm , resulting in a current density of ~ 5000 A/cm². Together the electron beam and the magnetic field produce a radial trap for the ions. Axial trapping of the ions along the electron beam axis is provided by raising the two ends of three collinear, insulated drift tubes to a positive potential with respect to the center drift tube bias potential. Together this traps a cylindrical ion cloud ~ 30 mm long and ~ 200 μm in diameter [15], oriented along the direction of the electron beam. A variable bias voltage from 2 kV to 20 kV is applied to the drift tubes to define an accelerating potential for the electron beam. A correction of approximately -100 eV must be applied to this energy in order to account for the net space charge of the electrons and the positive ions in the trap in this particular experiment. The precise energy of the electron beam (~ 50 eV width) is determined from the accelerating bias potential, the center drift tube floating voltage, and the space charge correction. By adjusting the accelerating voltage slightly below the ionization energy of the desired ion, the relative population of a specific charge state can be optimized.

A gas injection system connected to a lateral port, that looks directly into the trap, is used to introduce krypton atoms into the EBIT from a direction perpendicular to the trap. The gas injection system consists of a tunable gas leak, two pump chambers, and three collinear apertures. The apertures are used to define the differential pumping of the chambers and for rough alignment of the gas stream. The first aperture (0.318 cm in diameter) is located 67.7 cm from the trap and separates the gas leak from the first chamber. The second aperture (1.27 cm diameter) is located 44.5 cm from the trap and separates the first and second chambers. The last aperture (0.318 cm diameter) is located 32.1 cm from the trap and separates the second chamber and the injection port to the EBIT. The gas leak allows for tuning of the amount of gas injected, which is monitored by an ion gauge located in the chamber between the first and second apertures. Typical gas injection pressure values for this experiment were $\sim 5 \times 10^{-4}$ Pa to $\sim 2 \times 10^{-3}$ Pa. Each chamber is pumped by a turbo pump with a pumping speed of about 50 l/sec.

*Permanent address: Physics Department, University of Notre Dame, Notre Dame, IN 46556.

[†]Present address: Diamond Semiconductor Group, 14 Blackburn Center, Gloucester, MA 01930.

[‡]Permanent address: D.E. Shaw Co., 120 West 45th, New York, NY 10036.

The detection system is described in detail elsewhere [1,2]. Briefly, a cooled, low noise photomultiplier was used for photon detection, and a scanning monochromator was used for wavelength selection. Radiation emanating from the trap was imaged onto the entrance slits of the scanning monochromator using a set of two plano-convex lenses; this was necessary to keep the photomultiplier away from any stray magnetic field from the superconducting magnet and to improve the signal. The entire optical table which supports the monochromator was attached to two perpendicular translation stages which can be positioned with a resolution better than $10\ \mu\text{m}$. These translation stages were used to place the monochromator's entrance slit at the image of the trap produced by the lens system.

The trap was emptied of ions at preset time intervals by sending a fast pulse to the middle drift tube. This pulse raised the middle drift tube floating voltage above the upper and lower drift tube floating voltages in less than 1 ms, kept it constant for ~ 0.1 ms, and lowered it back to its initial value again in less than 1 ms, so that the total duration of the pulse was less than 2 ms. Time resolved data were acquired by setting the monochromator to a particular wavelength and accumulating data over thousands of such cycles. Photons arriving at the photomultiplier were time-stamped with a resolution better than 0.1 ms. The timing electronics were designed using CAMAC modules controlled by a list processor interfaced to a computer.

The ion extraction and transport system [12] was used to obtain information about the distribution of ion charge states within the EBIT. Briefly, the trap was emptied on-axis, allowing the ions to be extracted from the EBIT along the magnetic field lines, after which a series of electrostatic elements focused and aligned the ion beam before sending it through a charge to mass ratio analyzing magnet. The charge states were separated using the magnet and a detector counted the number of ions transported through the magnet for a particular value of the magnetic field. By successively stepping the magnetic field and emptying the trap, a plot of the relative populations of the charge states present in the trap was obtained.

III. DATA

Figure 1 shows a Kr spectrum taken at a drift tube voltage of 10 kV. The upper, middle, and lower drift tubes floating voltages were set at 450 V, 0 V, and 500 V, respectively. The entrance and exit slits of the monochromator were set to $500\ \mu\text{m}$. The data shown took about 2 hours to accumulate and are the sum of seven spectral scans, each one with a different time between unloading the trap, ranging from 5 ms to 60 ms. We identify the peak at 384 nm to be the $3s^23p^2\ ^3P_1 \leftarrow ^3P_2$ transition in Kr XXIII and the peak at 346.47 nm to be the $3s^23p^3\ ^2D_{3/2} \leftarrow ^2D_{5/2}$ transition in Kr XXII. Most of the remaining spectrum, except the peak at 402.58 nm, can be attributed to Kr II and Kr III. The 384-nm line was predicted to be at 383.2(40) by Kaufman and Sugar [9] and observed first by Roberts *et al.* [20] in a tokamak. The line at 346.47 nm has not been previously observed but was predicted [9] to be at 344.6(30) nm. Only one other *M*1 line is predicted in Ref. [9] for the range of 300 nm to 400 nm, a line at 313.4 nm which was not observed.

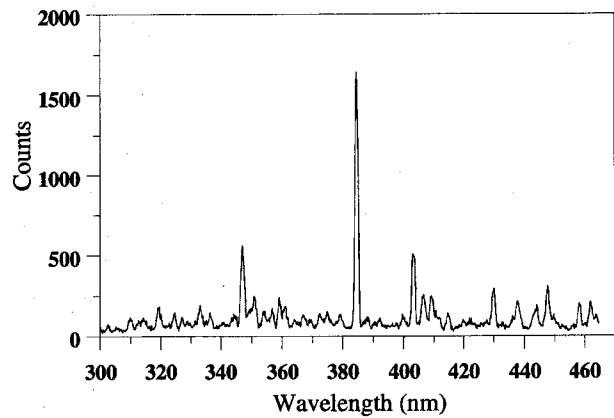


FIG. 1. Survey spectrum from 300 nm to 460 nm taken during Kr gas injection at an electron beam energy of ~ 10 keV, and $500\text{-}\mu\text{m}$ slits.

Extracted ion data are shown in Fig. 2, where ion beam intensity is plotted as a function of analyzing magnetic field. The plot shows the different charge states present in the trap as well as their relative populations. The peaks corresponding to Kr XXIII and Kr XXII are indicated with arrows in the plot. Weaker peaks near the main peaks indicate the presence of less abundant Kr isotopes in the trap. The electron beam energy used during extraction (10 keV) did not maximize the relative populations of these charge states but allowed us to increase the electron beam current and thus the absolute signal of these charge states compared to that obtained at lower currents. This particular plot was obtained while emptying the trap every 40 ms.

Another way of aiding charge state identification is to compare the temporal buildup of the individual line intensities. Time resolved data (Fig. 3) were taken for the 384-nm (Kr XXIII), 346.47-nm (Kr XXII), 402.58-nm, and 429.3-nm (Kr II) lines with an electron beam energy of approximately 5 kV, a current of 84 mA, and a pressure of 2×10^{-3} Pa in the gas injection system. Data corresponding to different transitions have been normalized so that all the plots reach the same equilibrium value for long times. The plots show the trap being emptied near the 20-ms mark. The 346.47-nm line shows a time evolution consistent with our charge state iden-

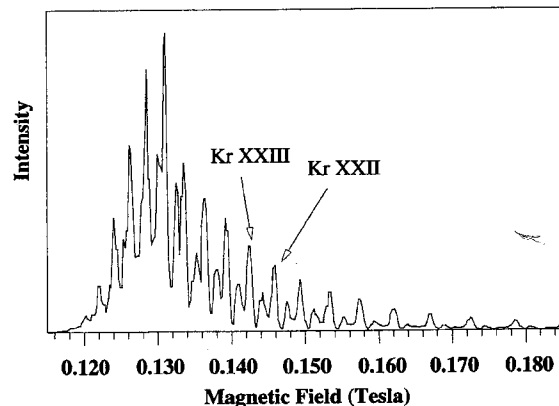


FIG. 2. Extracted ion beam intensity vs magnetic field. The two arrows show the peaks corresponding to Kr XXIII and Kr XXII.

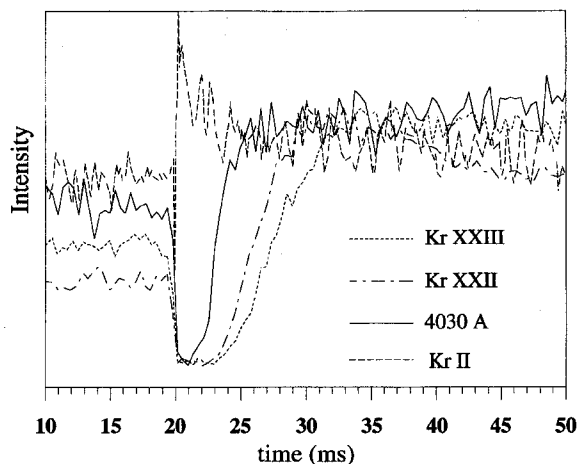


FIG. 3. Time resolved spectral intensity of various lines. The trap is being emptied near the 20-ms mark.

tification (Kr XXII), i.e., it rises just before the Kr XXIII line, as would be expected for a sequential ionization process such as electron impact inside the EBIT. The data also suggest that the unidentified line at 402.58 nm belongs to a charge state lower than Kr XXII. Using the tabulated energy levels of Kr [11] we searched for possible $M1$ transitions arising from the ground state term and found no suitable candidate for this unidentified line. The lack of energy levels for the $3p^6 3d^n$ ($n=2$ to 8) charge states of Kr makes the identification difficult. A possible candidate for this line was proposed in a similar spectroscopic study [16] carried out in a partially overlapping spectral region by the Livermore group using their EBIT. The identification proposed by that group is the magnetic dipole ($M1$) $2p^5 3d^3 P_1 \leftarrow ^3 P_2$ transition in Kr XIX. The upper level of this transition ($^3 P_2$) is low enough to be easily populated by direct electron impact excitation or through cascading, and because of its angular momentum cannot decay to the ground state ($2p^6$) via $E1$. Calculated energy levels [17] as well as solar coronal identification of lines [18] arising from the first excited configuration of the Ar isoelectronic sequence exist in the literature but only up to Ar-like Ni. The extrapolated energy difference to Kr XIX is in reasonable agreement with our measurement but further observations along the isoelectronic sequence are required for a definite identification. The time behavior of the Kr II line is consistent with a fast rise of this low charge state right after the middle drift tube voltage is raised and lowered.

Scans of the lines at 346.47 nm and 402.58 nm were taken with an electron beam energy of ~ 10 keV, a current of 141 mA, and 100- μm entrance and exit slits. Figure 4 shows two such scans, both of which also show smaller features at lower wavelengths that we identify as Kr II and Kr III. We use these *in situ* lines for wavelength calibrations instead of lines from a conventional stationary light source to eliminate the uncertainty introduced by the wavelength shifts due to the placement of the stationary source outside the EBIT. In order to use these lower charge state lines for wavelength calibration, the influence of the magnetic and electric field on their transition wavelength should be considered. The effect of the magnetic field (Zeeman effect) is to remove the m

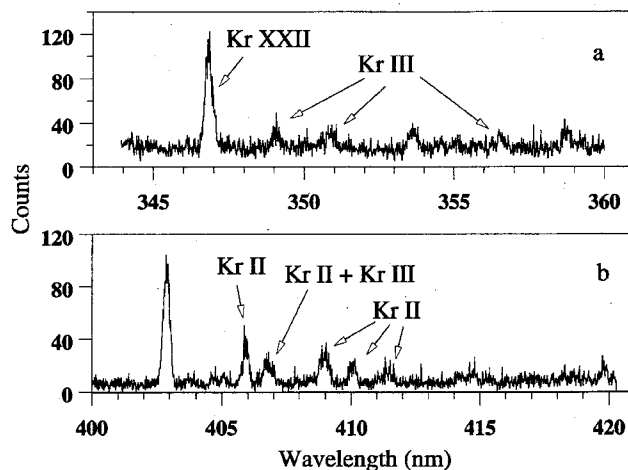


FIG. 4. Spectral scans taken with 100- μm entrance and exit slits. Peaks are labeled with their respective charge state identification.

degeneracy. Considering that only transitions with $|\Delta m|=1$ are allowed for $E1$ and $M1$ transitions, we estimate that the magnetic components of the lines shift by approximately 0.027 nm and 0.075 nm (3 cm^{-1}) for lines at 300 nm and 500 nm, respectively. These shifts are symmetric so there is no net shift but an overall broadening of the line [19]. We estimate this broadening due to the Zeeman effect to be about 6 cm^{-1} . To consider the effects of the electric field (Stark effect) inside the EBIT we estimate the electron density to be $\sim 4 \times 10^{12} \text{ cm}^{-3}$ ($7 \times 10^{-1} \text{ C/m}^3$) and conclude that the maximum macroscopic electric field from the electron beam is $\sim 1 \times 10^3 \text{ kV/m}$. The actual total electric field will be smaller than this, depending on the degree of neutralization of the trap. Assuming 20% neutralization of the trap, we obtain a value of $8 \times 10^2 \text{ kV/m}$. Another possible contribution to the electric field comes from the voltage differential between the central drift tube and the endcaps. Assuming a potential difference of about 400 V in a distance of about one-tenth of the trap length (0.2 cm), we obtain an electric field of about 200 kV/m in the small region of the voltage drop. This is smaller than the electron beam contribution. The Stark effect does not produce a shift in first order (except for hydrogen), so in general the shifts are proportional to the square of the electric field. The Kr lines used for calibration were $s^2 p^4(^1D)5s \leftarrow s^2 p^4(^1D)5p$ and $s^2 p^4(^3P)5s \leftarrow s^2 p^4(^3P)5p$ for Kr II, and $s^2 p^3(^2D)4d \leftarrow (^2D)5p$ and $s^2 p^3(^4S)5s \leftarrow (^4S)5p$ for Kr III. Di Rocco *et al.* [21] have measured line shifts due to the microscopic Stark effect in similar lines of Kr II and Kr III in a pinched

TABLE I. Different contributions to the uncertainties. All values quoted in nanometers. The final uncertainties ($1-\sigma$ level) are computed by combining the individual uncertainties in quadrature.

Line (nm)	Calibration/Fitting	Reproducibility	Uncertainty
346.47	0.05	0.04	0.06
402.58	0.02	0.04	0.05

discharge. They estimate the electric field to be 5×10^4 kV/m. All the shifts are smaller than 1 cm^{-1} . Using this value and the fact that the shifts are proportional to the square of the electric field, we estimate negligible shifts due to the Stark effect in the EBIT for low charge states of Kr.

By using the low charge states of Kr as wavelength calibration lines, we obtain 346.47(6) nm for the Kr XXII line and 402.58(5) nm for the unidentified line. The quoted wavelengths are measured in air and the uncertainties are the result of adding in quadrature the uncertainties from the fits and reproducibility at the one standard deviation uncertainty level. Table I shows the different contributions to the final uncertainties.

In conclusion, we have shown how the EBIT is an important source not only of $M1$ lines for highly charged ions, but also for lines in moderately charged ions as well, even when the electron beam energy is well beyond that required to optimize the production of the moderately charged ions. A previously unobserved $M1$ line in Kr XXII was measured. The usefulness of the ion extraction system and time resolved data as charge state identification tools was also shown.

ACKNOWLEDGMENTS

We would like to thank E. Träbert for helpful discussions.

-
- [1] C. A. Morgan, F. G. Serpa, E. Takács, E. S. Meyer, J. D. Gillaspay, J. Sugar, J. R. Roberts, C. M. Brown, and U. Feldman, *Phys. Rev. Lett.* **74**, 1716 (1995).
 - [2] F. G. Serpa, E. S. Meyer, C. A. Morgan, J. D. Gillaspay, J. Sugar, J. R. Roberts, C. M. Brown, and U. Feldman, *Phys. Rev. A* **53**, 2220 (1996).
 - [3] S. Suckewer and E. Hinnov, *Phys. Rev. Lett.* **41**, 756 (1978).
 - [4] R. U. Datla, J. R. Roberts, W. L. Rowan, and J. B. Mann, *Phys. Rev. A* **34**, 4751 (1986).
 - [5] K. H. Burrell, R. J. Groebner, N. H. Brooks, and L. Rottler, *Phys. Rev. A* **29**, 1343 (1984).
 - [6] B. Edlén, *Ark. Mat. Astr. Fys.* **28B**, 1 (1941).
 - [7] B. Edlén, *Z. Astrophys.* **22**, 30 (1942).
 - [8] U. Feldman, P. Indelicato, and J. Sugar, *J. Opt. Soc. Am. B* **8**, 3 (1991).
 - [9] V. Kaufman and J. Sugar, *J. Phys. Chem. Ref. Data* **15**, 1 (1986).
 - [10] T. Shirai, K. Okazaki, and J. Sugar, *J. Phys. Chem. Ref. Data* **24**, 1577 (1995).
 - [11] J. Sugar and A. Musgrove, *J. Phys. Chem. Ref. Data* **20**, 859 (1991).
 - [12] A. I. Pikin, C. A. Morgan, E. W. Bell, L. P. Ratliff, D. A. Church, and J. D. Gillaspay, *Rev. Sci. Instrum.* **67**, 2528 (1996).
 - [13] J. D. Gillaspay, J. R. Roberts, C. M. Brown, and U. Feldman, in *VIIth International Conference on the Physics of Highly Charged Ions*, edited by P. Richard, M. Stockli, C. L. Cocke, and C. D. Lin, AIP Conf. Proc. No. 274 (AIP, New York, 1992), p. 682.
 - [14] R. E. Marrs, P. Beiersdorfer, and D. Schneider, *Phys. Today*, **47**(10), 27 (1994).
 - [15] J. D. Gillaspay, Y. Aglitskiy, E. W. Bell, C. M. Brown, C. T. Chantler, R. D. Deslattes, U. Feldman, L. T. Hudson, J. M. Laming, E. S. Meyer, C. A. Morgan, A. I. Pikin, J. R. Roberts, L. P. Ratliff, F. G. Serpa, and E. Takács, *Phys. Scr.* **T59**, 392 (1995).
 - [16] J. R. Crespo López-Urrutia, P. Beiersdorfer, K. Widmann, and V. Decaux, in *10th APS Topical Conference on Atomic Processes in Plasmas, Program and Abstracts, A5* (Lawrence Livermore National Laboratory, San Francisco, 1996).
 - [17] W. J. Wagner and L. L. House, *Astrophys. J.* **166**, 683 (1971).
 - [18] L. Å. Svensson, J. O. Ekberg, and B. Edlén, *Solar Phys.* **34**, 173 (1974).
 - [19] I. I. Sobelman, *Atomic Spectra and Radiative Transitions*, 2nd ed. (Springer Verlag, Berlin, 1992).
 - [20] J. R. Roberts, T. L. Pittman, J. Sugar, V. Kaufman, and W. L. Rowan, *Phys. Rev. A* **35**, 2591 (1987).
 - [21] H. O. Di Rocco, G. Bertuccelli, J. Reyna Almandos, F. Bredice, and M. Gallardo, *J. Quant. Spectrosc. Radiat. Trans.* **41**, 161 (1989).

Measurement of a magnetic-dipole transition probability in Xe^{32+} using an electron-beam ion trap

F. G. Serpa,* C. A. Morgan, E. S. Meyer,† and J. D. Gillaspay
Atomic Physics Division, National Institute of Standards and Technology, Gaithersburg, Maryland 20899-0001

E. Träbert
Experimentalphysik III, Ruhr-Universität Bochum, D-44780 Bochum, Germany

D. A. Church
Physics Department, Texas A&M University, College Station, Texas 77843-4242

E. Takács
Experimental Physics Department, Kossuth University, Bem ter 18/a, Debrecen H-4026, Hungary
and Institute for Nuclear Research of the Hungarian Academy of Sciences (ATOMKI), Bem ter 18/c, Debrecen, H-4026, Hungary
(Received 21 January 1996)

The transition probability for the $3d^4\ ^5D_2 \leftarrow\ ^5D_3$ magnetic-dipole transition in Ti-like Xe (Xe^{32+}) has been measured using an electron-beam ion trap. The unusually weak dependence of the transition energy on nuclear charge Z , and the fact that the transition wavelength remains in the 320- to 400-nm range for $54 < Z < 92$, makes this transition promising as a plasma diagnostic tool. Our measurement of the transition probability yields $465(30)\ \text{s}^{-1}$, corresponding to a lifetime of 2.15(14) ms, in good agreement with the theoretical value of 2.4 ms. [S1050-2947(97)07506-9]

PACS number(s): 32.30.Jc, 32.10.-f, 52.70.-m, 31.25.-v

I. INTRODUCTION

The transition probability between atomic levels is needed in order to determine particle densities from absolute emission or absorption measurements. In plasma diagnostics to avoid the complications of self-absorption, optically thin lines are preferred, that is, regular lines of low transition probability, like spin-forbidden intercombination or electric-dipole-forbidden magnetic-dipole (M1) transitions. It is also preferred that the lines be in the visible or near-uv range of the spectrum, so that high-resolution interferometric techniques can be employed in order to derive a maximum of information, including line shapes and widths.

Such M1 transitions, without faster competing decays, occur in the ground configurations of many ions. These then require relatively low excitation energies and thus are easily excited in plasmas. Many M1 transitions have been observed in Tokamak spectra where their long wavelengths have been used for the determination of quantities, such as ion temperature [1,2]. Unfortunately, however, the wavelength of most M1 transitions varies strongly with the nuclear charge of the ion along a given isoelectronic sequence, as the associated level intervals result from the relativistic fine-structure splitting with its Z^4 scaling in simple systems. This makes the search for, and identification of, such M1 transitions difficult for ions beyond those rather simple cases for which the identification of solar corona lines was possible [3-6]. However,

in a lengthy search of computed data Feldman, Indelicato, and Sugar found a particular system in which a single M1 transition had an almost constant wavelength and transition probability over a wide range of nuclear charges [7]. This transition, $3d^4\ ^5D_2 \leftarrow\ ^5D_3$ in Ti-like ions (Fig. 1), was subsequently identified in spectra recorded at the National Institute of Standards and Technology (NIST) electron-beam ion trap (EBIT) facility [8,9] at Gaithersburg. In this work we report a measurement of the associated transition probability, predicted to be about $420\ \text{s}^{-1}$ [10] that corresponds to a lifetime of about 2.4 ms. This prediction was obtained with the Cowan code using the scaled parameters for the radial integrals obtained in Ref. [9]. A similar calculation using the multiconfigurational Dirac-Fock GRASP² code [11] without any scaling of radial integrals yields 1.97 ms for the lifetime.

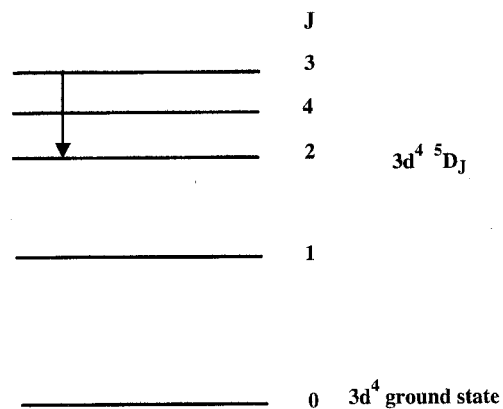


FIG. 1. Lowest levels of a Ti-like ion, indicating the $3d^4\ ^5D_2 \leftarrow\ ^5D_3$ M1 transition of interest at 413.94 nm

*Permanent address: University of Notre Dame, Notre Dame, IN 46556.

†Permanent address: D. E. Shaw Co., 120 West 45th, New York, NY 10036.

The standard method for lifetime measurements in highly charged ions, beam-foil spectroscopy, does not permit the measurement of such long lifetimes because it would require extremely long flight paths [12]. The technique of slow ion beams [13] needs to be developed further before it can be used for the ms time range. Hence, the present options are the use of an ion storage ring [14–16], ion retrapping from an ion source [17,18], or an EBIT. The last approach was chosen here.

For lifetime measurements using an EBIT, two approaches have been developed. The first relies on trapping highly charged ions by the electric and magnetic fields produced by the electron beam, drift tube potentials, and the superconducting magnet (“electron trapping mode” [19]). The ion excitation process is modulated for sufficiently separated levels by tuning the electron-beam energy above or below the excitation threshold. Lifetime measurements on the $1s2s^3S_1$ level in several He-like ions have been performed at Lawrence Livermore National Laboratory (LLNL) by exploiting this technique [20]. However, this technique does not work for transitions between levels of the ground configuration, because here the level excitation threshold can be insignificant compared to that for production of the ion itself.

A second approach, discussed in Ref. [21], has been developed in parallel at LLNL and at NIST. In this technique, the electron beam current is temporarily switched off so that the ions are confined radially only by the magnetic field, as in a Penning trap, while longitudinal confinement is provided by the drift tube potentials (the EBIT “magnetic trapping mode” [22,19]). The LLNL group has done extensive systematic tests on this confinement mode. In particular, they have shown, using an ion-cyclotron resonance probe and x-ray spectroscopy [22–25], that most of the ions remain in the trap immediately after the beam is switched off, but eventually leave the trap with a time constant of greater than 1.5 s. They also confirmed the validity of the lifetime measurement technique on N^{5+} by comparing the result obtained in an EBIT [3.92(13) ms at the one standard deviation level] to the accurate value previously obtained in a storage ring experiment [3.90(5) ms also at the one standard deviation level] [19,14].

II. EXPERIMENTAL SETUP

The EBIT at NIST [26,27] was used as the source of excited highly charged ions in this work. In this source, the desired ion is produced by successive electron-impact ionization from an accelerated electron beam, produced by a electron gun which provides currents up to ~ 150 mA. A pair of superconducting magnets in a Helmholtz configuration produces an axial magnetic field of 3 T in the trap region and compresses the electron beam to a diameter of ~ 60 μm , resulting in a current density of ~ 5000 A/cm². Together the electron beam and the magnetic field produce a radial trap for the ions. Axial trapping of the ions along the electron-beam axis is provided by raising the two ends of three collinear, insulated drift tubes to a positive potential with respect to the center drift tube bias potential. This traps a cylindrical ion cloud ~ 30 mm long and ~ 200 μm in diameter [28], oriented along the direction of the electron beam.

A variable bias voltage of 2 to 20 kV is applied to the drift tubes to define an accelerating potential for the electron beam. A correction on the order of 100 eV must be applied to this energy in order to account for the net space charge of the electrons and the positive ions in the trap. The precise energy of the electron beam (~ 50 eV width) is therefore determined from the accelerating bias potential, the center drift tube floating voltage and the space-charge correction. By adjusting the accelerating voltage slightly below the ionization energy of the desired ion, we can optimize the relative population of a specific charge state.

A gas injection system connected to a lateral port that looks directly into the trap was used to introduce xenon atoms into the EBIT from a direction perpendicular to the trap. The gas injection system consists of a tunable gas leak, two pump chambers, and three collinear apertures. The apertures are used to define the differential pumping of the chambers and for rough alignment of the gas stream. The first aperture (0.318 cm diameter) is located 67.7 cm from the trap and separates the gas leak from the first chamber. The second aperture (1.27 cm diameter) is located 44.5 cm from the trap and separates the first and second chambers. The last aperture (0.318 cm diameter) is located 32.1 cm from the trap and separates the second chamber and the injection port to the EBIT. The gas leak allows for tuning of the amount of gas injected, which is monitored by an ion gauge located in the chamber between the first and second apertures. Each chamber is pumped by a turbo pump with a pumping speed of about 50 l/s.

The detection system is described in detail elsewhere [8,9]. Briefly, a cooled, low noise photomultiplier was used for photon detection, and a scanning monochromator was used for wavelength selection. Radiation from the trap was imaged onto the entrance slits of the monochromator by two plano-convex lenses; this was necessary to keep the photomultiplier away from the stray magnetic field from the superconducting magnet. The two lens system produced a demagnification of ~ 0.8 . The entire optical table which supported the monochromator was attached to two perpendicular translation stages which could be positioned with a precision better than 10 μm . These translation stages were used to place the monochromator’s entrance slit at the image of the trap produced by the lens system. A Si(Li) detector with an energy resolution of ~ 190 eV, was used to monitor the x rays through one of the radial ports.

III. LIFETIME MEASUREMENT

For the lifetime measurements, we set the drift tube voltage that defines the bulk of the electron-beam energy to 2.172 keV in order to obtain a strong signal from the Ti-like Xe transition. The gas injection pressure of Xe in the first gas injection chamber was changed from run to run. This pressure was varied between 2×10^{-5} Pa ($\sim 2 \times 10^{-7}$ Torr) and 4×10^{-4} Pa ($\sim 4 \times 10^{-6}$ Torr) of Xe, but did not significantly affect the pressure in the EBIT outside of the trap region, which remained lower than $\sim 5 \times 10^{-8}$ Pa ($\sim 5 \times 10^{-10}$ Torr). A typical electron-beam current for this experiment was about 60 mA. The anode voltage that defines the electron-beam current was driven by a function generator that switched the current off in about 50 μs , kept it at zero

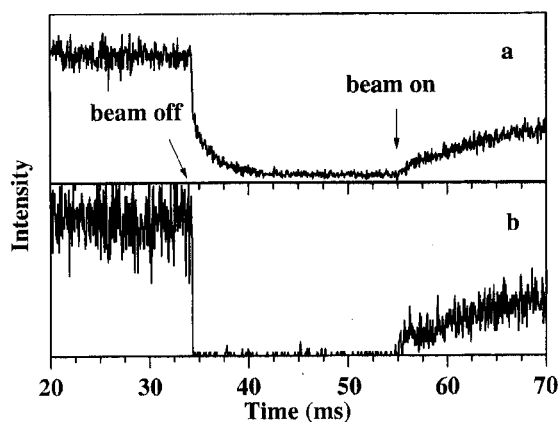


FIG. 2. (a) Time evolution of the visible light signal from Ti-like Xe. The electron-beam current was switched off and on where indicated by the arrows. (b) X-ray time dependence.

for about 20 ms to allow the transition to decay, and finally switched back on in about 50 μ s. The current was then held constant for about 200 ms to allow the signal to recover. Time-resolved data were acquired by setting the monochromator to the transition wavelength and accumulating synchronized data over many thousands of cycles. The entrance and exit slits of the monochromator were set at 500 μ m. Photons arriving at the photomultiplier or x rays detected by the Si(Li) detector were time stamped with a resolution better than 50 μ s. The timing electronics were constructed from computer automated measurement of control (CAMAC) modules controlled by a list processor interfaced to a computer.

IV. DATA

Data were recorded in both the visible and x-ray spectral ranges. While the visible light, detected in narrow band, offered information on the long-lived level of interest, the x rays, detected in broadband, reflected the total ion population in the trap while the beam was on rather than the charge state and level of interest. For a sample of both the x rays and visible light, see Fig. 2. The short lifetimes associated with the x rays allow us to confirm that the electron beam was switched off rapidly. In an EBIT, a multitude of processes build up to a steady state which yields the extended flat part of our signal curve. When the electron-beam current is suddenly switched off, so is the ion excitation. Consequently, the signal drops, with a time constant corresponding to the lifetime of the observed level. In addition, there may be an initial rapid drop due to ions moving out of the observation region. If all the ion cloud dynamics were reversible in 50 μ s, the signal recovery after suddenly switching the electron-beam current back on would be much more rapid than the observations. For extraction of the atomic lifetime, we evaluate only the decay part of the signal curve; we discuss the recovery part of the curve below.

V. DECAY CURVE EVALUATION

The decay curve of the visible signal shows an initial steep fall that extends over about 0.1 ms. We note that this signal loss is over an order of magnitude less than that seen

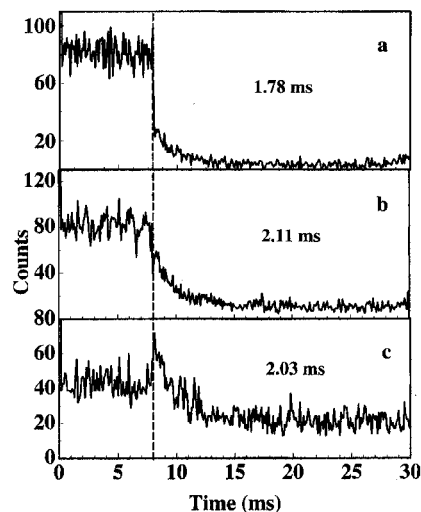


FIG. 3. Time evolution of the visible signal for three different positions of the entrance slit (200 μ m wide). (a) Centered on electron beam. Integration time \sim 60 min. (b) Shifted by 200 μ m from center. Integration time \sim 108 min. (c) Shifted by 400 μ m from center. Integration time \sim 124 min. The dotted line indicates the time at which the electron beam was switched off.

in the LLNL experiments on nitrogen [22,19]. This steep fall can be interpreted either as an actual loss of ions from the trap as the beam is switched off or as a loss of ions from the viewing region of the detection system. The latter would arise from an ion cloud expansion when the electron-beam component of the trapping potential is switched off. Our experimental setup permits access to a viewing region of up to \sim 2 mm in width. The 500- μ m slit setting used for most of the measurements restricts the viewing region to \sim 625 μ m. In order to observe the ion cloud expansion and quantify the effect of a restricted viewing region on the lifetimes we narrowed the slits to 200 μ m and translated the spectrometer in a direction perpendicular to the viewing axis. Figure 3 shows three sets of data at different entrance slit positions and their respective fitted lifetimes. The expected ion expansion, when the electron beam is switched off, can be seen directly in Fig. 3(c). From the decay constants obtained from the data in these tests and the one from a run with 1-mm slits (2.01 ms), we obtain a standard deviation of 0.14 ms for the decay constant. This uncertainty of about 7% includes the uncertainty due to reproducibility. The final quoted value for the lifetime is the average from five different data sets taken with 500- μ m slits centered on the electron beam. The standard deviation from these measurements is also a measurement of the uncertainty due to reproducibility and agrees with the 0.14-ms uncertainty obtained above from the different slit positions.

The data were fitted to a single exponential function plus a background representing the detector dark rate. Successive initial data points were omitted to study the influence of the rapid switching of the electron beam on the data evaluation; after very few points were removed (corresponding to \sim 0.1 ms) the fit results became stable. Figure 4 shows a typical fit to a data set and the corresponding residuals. Similarly the tail of the decay was truncated to find out about a hypothetical slow decay component (perhaps relating to ion loss from

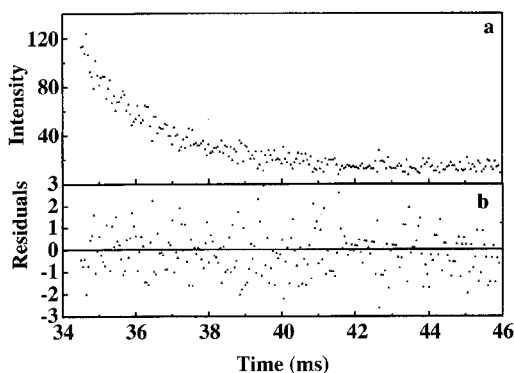


FIG. 4. (a) Fit of one data set to a single exponential plus a constant background ($\chi_r^2=0.95$). Same time scale as Fig. 2. (b) Normalized residuals $(y_{\text{fit}} - y)/\sqrt{y}$.

the trap), but no second decay component could be extracted. By comparing fits from different runs we found no significant dependence for pressures below 4×10^{-4} Pa ($\sim 4 \times 10^{-6}$ Torr) at the gas injection chamber.

An extensive computation was made to assure that the lifetime was not influenced by slow cascading from higher levels. Since E1 transitions are much faster than M1 transitions, we restricted the simulation to configurations that could contribute to slow M1 transitions. Only levels of the $3p^6 3d^4$ configuration contribute to such transitions, since the levels of $3p^6 3d^3 4s$ can decay to $3p^6 3d^4$ through two E1 transitions via the $3p^5 3d^5$ configuration. The GRASP² code [11] was used to calculate the energy levels and transition probabilities among the 34 levels belonging to $3p^6 3d^4$. We assumed a range of initial populations [equally populated, statistically populated ($2J+1$), and proportional to J] for the levels and found that the predicted contributions to the lifetime from cascading were smaller than 1%.

Based on the statistics, reproducibility, viewing region, and various truncation exercises discussed above we obtained a lifetime of 2.15(14) ms, at the one standard deviation level. This is considered to be in good agreement with a theoretical value of 2.4 ms [10].

The lack of symmetry of the decay and the recovery part

of the signal upon switching the electron-beam current off and on indicates that the ions do not reassemble quickly into the electron beam where they can be reexcited. A variation between 5 and 40 ms of the time interval during which the electron beam is switched off yielded no recognizable differences in this behavior. Apparently the ion cloud needs a few hundred ms to reestablish the steady state. Such an effect suggests that there are irreversible processes at work, which might involve geometry and ion cloud dynamics.

VI. CONCLUSION

The present study completes the quest [7] for, the identification and wavelength measurement [8,9], and now the transition rate measurement of a line particularly suited for plasma diagnostics of future high-temperature tokamaks. As the theoretical expression for the probability of such M1 transitions depends mostly on angular-momentum factors and the transition energy, this dependence has now been corroborated and a suitable benchmark been provided for similar transitions. It needs to be stressed, however, that *ab initio* calculations do not have enough accuracy to predict these fine-structure intervals, and thus the M1 transition energies, with anything close to spectroscopic accuracy.

The magnetic trapping mode of EBIT operation has demonstrated its usefulness for lifetime measurements in the ms range. Improvements that are anticipated for future work include faster electron beam-current switching to measure shorter lifetimes, online diagnostics to monitor the spatial distribution of the ion cloud in the trap, and further investigation and modeling of the ion cloud dynamics and its perturbation by the electron-beam switching.

ACKNOWLEDGMENTS

We thank the LLNL EBIT group for communicating their findings prior to publication. This work has been partially supported by a NATO Collaborative Research Grant No. CRG 940181. D.A. Church was given financial support from Texas A&M University. E. Takács acknowledges the Foundation for Hungarian Higher Education and Scientific Research and the Hungarian Science Foundation (OTKA, Contract No. F 019344) and NIST for support.

- [1] E. Hinnov, S. Suckewer, S. Cohen, and K. Sato, *Phys. Rev. A* **25**, 2293 (1994).
- [2] B. Edlén, *Phys. Scr.* **T8**, 5 (1984).
- [3] B. Edlén, *Ark. Mat. Astron. Fys.* **28B**, 1 (1941).
- [4] B. Edlén, *Z. Astrophys.* **22**, 30 (1942).
- [5] V. Kaufman and B. Edlén, *J. Phys. Chem. Ref. Data* **3**, 825 (1974).
- [6] V. Kaufman and J. Sugar, *J. Phys. Chem. Ref. Data* **15**, 321 (1986).
- [7] U. Feldman, P. Indelicato, and J. Sugar, *J. Opt. Soc. Am. B* **8**, 3 (1991).
- [8] C.A. Morgan, F.G. Serpa, E. Takács, E.S. Meyer, J.D. Gillaspay, J. Sugar, J.R. Roberts, C.M. Brown, and U. Feldman, *Phys. Rev. Lett.* **74**, 1716 (1995).
- [9] F.G. Serpa, E.S. Meyer, C.A. Morgan, J.D. Gillaspay, J. Sugar,

J.R. Roberts, C.M. Brown, and U. Feldman, *Phys. Rev. A* **53**, 2220 (1996).

- [10] J. Sugar (private communication).
- [11] F.A. Parpia, I.P. Grant, and C.F. Fischer, GRASP² (private communication).
- [12] E. Träbert, *Nucl. Instrum. Methods B* **98**, 10 (1995).
- [13] G. Hubricht and E. Träbert, *Z. Phys. D* **7**, 243 (1987).
- [14] H.T. Schmidt, P. Forck, M. Grieser, D. Habs, J. Kenntner, G. Miersch, R. Repnow, U. Schramm, T. Schüssler, D. Schwalm, and A. Wolf, *Phys. Rev. Lett.* **72**, 1616 (1994).
- [15] J. Doerfert, E. Träbert, J. Granzow, A. Wolf, J. Kenntner, D. Habs, M. Grieser, T. Schüßler, U. Schramm, and P. Forck, *Nucl. Instrum. Methods B* **98**, 53 (1995).
- [16] J. Doerfert, E. Träbert, and A. Wolf, *Hyperfine Int.* **99**, 155 (1996).

- [17] L. Yang and D.A. Church, *Phys. Rev. Lett.* **70**, 3860 (1993).
- [18] L. Yang, D.A. Church, S. Tu, and J. Jin, *Phys. Rev. A* **50**, 177 (1994).
- [19] P. Beiersdorfer, L. Schweikhard, J. Crespo Lopez-Urrutia, and K. Widmann, *Rev. Sci. Instrum.* **67**, 3818 (1996).
- [20] B.J. Wargelin, P. Beiersdorfer, and S.M. Kahn, *Phys. Rev. Lett.* **71**, 2196 (1993).
- [21] J.D. Gillaspay, *Phys. Scr.* **T65**, 168 (1996).
- [22] P. Beiersdorfer, B. Beck, St. Becker, and L. Schweikhard, *Int. J. Mass Spectrom. Ion Processes* **157-158**, 149 (1996).
- [23] P. Beiersdorfer, St. Becker, B. Beck, S. Elliott, K. Widmann, and L. Schweikhard, *Nucl. Instrum. Methods B* **98**, 558 (1995).
- [24] L. Schweikhard, J. Ziegler, P. Beiersdorfer, B. Beck, St. Becker, and S. Elliott, *Rev. Sci. Instrum.* **66**, 448 (1995).
- [25] P. Beiersdorfer, B. Beck, R.E. Marrs, S.R. Elliott, and L. Schweikhard, *Mass Spectrom.* **8**, 141 (1994).
- [26] J.D. Gillaspay, J.R. Roberts, C.M. Brown, and U. Feldman, in *VIIth International Conference on the Physics of Highly Charged Ions*, edited by P. Richard, M. Stockli, C.L. Cocke, and C.D. Lins, AIP Conf. Proc. No. 274 (AIP, New York, 1993), p. 682.
- [27] R.E. Marrs, P. Beiersdorfer, and D. Schneider, *Phys. Today* **47(10)**, 27 (1994).
- [28] J.D. Gillaspay, Y. Aglitskiy, E.W. Bell, C.M. Brown, C.T. Chantler, R.D. Deslattes, U. Feldman, L.T. Hudson, J.M. Laming, E.S. Meyer, C.A. Morgan, A.I. Pikin, J.R. Roberts, L.P. Ratliff, F.G. Serpa, J. Sugar, and E. Takács, *Phys. Scr.* **T59**, 392 (1995).

Lifetime measurements in the ground configuration of Ar^{13+} and Kr^{22+} using an electron beam ion trap

F G Serpa†§, J D Gillaspay† and E Träbert‡

† Atomic Physics Division, National Institute of Standards and Technology, Gaithersburg, MD 20899-0001, USA

‡ Experimentalphysik III, Ruhr-Universität Bochum, D-44780 Bochum, Germany

Received 6 February 1998

Abstract. We have measured the radiative lifetimes for the $2s^22p^2P_{3/2}$ level of Ar^{13+} and the $3s^23p^2^3P_2$ level of Kr^{22+} . These measurements were performed by monitoring the temporal behaviour of their associated radiative decays during magnetic trapping mode in an electron beam ion trap (EBIT). Our lifetime results, 8.7(5) ms for Ar^{13+} and 5.7(5) ms for Kr^{22+} , are compared with theory.

1. Introduction

Radiation originating from the ground configuration of highly charged ions is an important source of information for astrophysical and laboratory plasmas. In low-density plasmas, such as those encountered in tokamaks, the solar corona and other astronomical objects, the main decay channel for excited levels of the ground state configuration is through magnetic dipole (M1) transitions [1, 2]. The lifetimes associated with these electric-dipole (E1) forbidden transitions are much longer than those for levels with E1-allowed transitions, and can be as long as many milliseconds. The traditional method for lifetime measurements, beam-foil, cannot be employed due to the extremely long flight paths which would be needed [3], while the technique of slow ion beams [4] needs to be developed further before it can be used for the millisecond time range. Heavy-ion storage rings, a tool recently utilized for lifetime measurements in the millisecond range [5], may be severely limited by the available ion beam currents for highly charged species and by geometrical constraints which cause a low detection efficiency. Consequently, calculations of these transition probabilities have been the main source for such M1 transition rate data until quite recently. Many such calculations, involving different approaches, have appeared in the literature [6–12], but the dearth of measurements has made comparison with experiment difficult. Thus, the measurement of these transition probabilities is crucial not only in providing the experimental data needed for the understanding and modelling of plasma sources such as fusion devices or the solar corona, but also in testing sophisticated calculations. Such measurements have become possible only quite recently [13–15]. In a previous paper [15] (paper I), we reported one such measurement in an electron beam ion trap (EBIT) that relied on the trapping of ions in the ‘magnetic trapping mode’ [16–18]. In this paper we report two new measurements in highly charged ions that determine the lifetime of the $2s^22p^2P_{3/2}$ level in the B-like ion Ar^{13+} and of the $3s^23p^2^3P_2$ level in the Si-like ion Kr^{22+} .

§ Permanent address: University of Notre Dame, Notre Dame, IN 46556, USA.

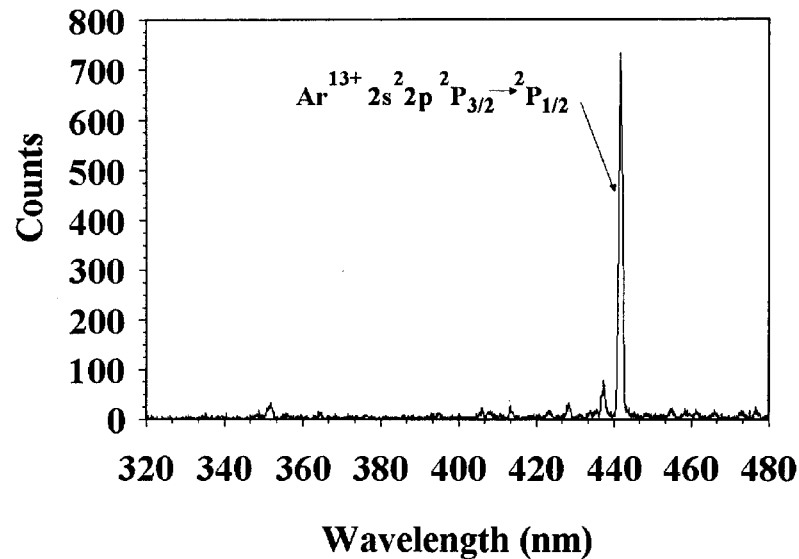


Figure 1. Survey scan from 320 to 480 nm. The scan was taken at an electron beam energy of 3.7 keV and at an Ar pressure of 1.3×10^{-5} Pa (1×10^{-7} Torr) in the gas injection chamber.

The ground state configuration of $\text{Ar}^{13+} 2s^2 2p$ consists of two levels, $^2P_{3/2}$ and $^2P_{1/2}$. These levels are degenerate in the non-relativistic limit, but split due to relativistic effects (fine structure). Since these states have the same parity, the upper level cannot decay radiatively through an E1 transition so it decays to the $^2P_{1/2}$ level either via an M1 or an electric quadrupole (E2) transition. The corresponding spectral line at 441.24 nm was first observed by Lyot *et al* [19] in the solar corona and subsequently identified by Edlén [20]. Since the M1 decay is about five orders of magnitude faster than the E2 decay, the lifetime of the $^2P_{3/2}$ state is essentially the inverse of the transition probability of the M1 branch. This transition probability is predicted [7] to be $\sim 103.97 \text{ s}^{-1}$, which translates into a lifetime of $\sim 9.62 \text{ ms}$. We expect the transition to be prominent since higher excited states can only decay into these two states. Another advantage of the simplicity of this system is that there are no other long-lived low-lying levels. This precludes the possibility of slow cascades from within the ground term and therefore facilitates the direct measurement of the associated lifetime. A survey scan from 320 to 480 nm during Ar gas injection is shown in figure 1. The scan shows the prominence of the $^2P_{3/2} \rightarrow ^2P_{1/2}$ transition and some weaker Ar II and Ar III lines.

The ground state configuration of $\text{Kr}^{22+} 3s^2 3p^2$ consists of five levels. Again, all these levels have the same parity, so that the levels can only decay via M1 or E2 transitions. Figure 2 shows a level diagram of these states, together with their main decay channels and associated transition probabilities, taken from Biémont *et al* [8]. The 3P_2 level decays primarily to the 3P_1 level via an M1 transition (150 s^{-1}) as well as a slower (4.83 s^{-1}) E2 decay component to the 3P_0 level. These two decay branches translate into a predicted lifetime of 6.46 ms for the 3P_2 state. The $^3P_2 \rightarrow ^3P_1$ transition was first observed and identified by Roberts *et al* [21] in a tokamak at 384.09(3) nm. This transition is particularly interesting because it is the only one in the $3s^2 3p^2$ ground state configuration that remains above $\sim 90 \text{ nm}$ as nuclear charge (Z) is increased along the isoelectronic sequence (284.1 nm at Mo^{28+} ; $\sim 130 \text{ nm}$ at W^{60+}) [8]. This makes it a candidate for high-resolution observation for plasma diagnostics since visible and near-UV transitions can usually be measured accurately

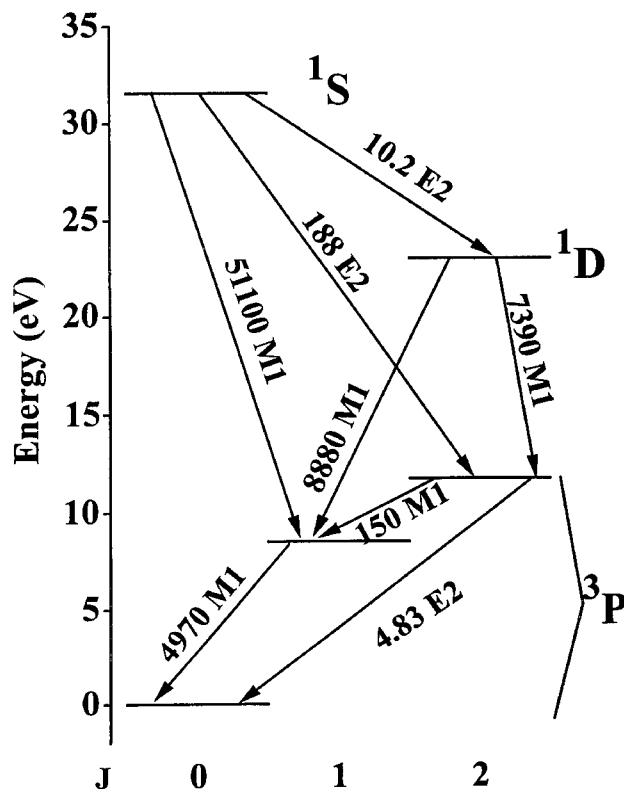


Figure 2. Diagram showing the five levels of the ground configuration of Kr^{22+} , their decay type and calculated [8] transition probabilities (in s^{-1}). In the case where a level can decay through M1 and E2 the fastest branch is indicated.

and because refractive optics and polarizers can be employed efficiently. This transition has also been shown to be prominent in EBIT [22]. Figure 2 also shows possible cascade effects into the $3P_2$ state from the $1S_0$ and $1D_2$ states. The $1D_2$ level decays primarily to the $3P_2$ and $3P_1$ levels with a transition probability of about $8000 s^{-1}$ for each branch; this is significantly faster than the transition probability associated with the $3P_2$ ($\sim 150 s^{-1}$) decay. The $1S_0$ level has two main decay channels, to $3P_2$ and $3P_1$, the latter being much faster ($\sim 51\,100 s^{-1}$), and therefore should not affect the measurement significantly. Nevertheless, in order to assess the influence of these cascades in our measurement, we modelled the system including all five levels and the possible transitions connecting them. We used different models for the initial populations of the levels (equally populated, statistically populated and populated proportional to $J + 1$) and found no significant effects concerning the decay of interest at the 1% level.

2. Experimental set-up and procedure

The experimental procedure and set-up was the same as the one described previously [23]. The EBIT at NIST [24, 25] was used as the source of excited highly charged ions. In this source, ions in the desired charge state are produced from neutral atoms by successive electron-impact ionization effected by collisions with the accelerated electrons from an electron gun which provides currents of up to ~ 150 mA. A pair of superconducting magnets

in a Helmholtz configuration produce an axial magnetic field of 3 T in the trap region and compress the electron beam to a diameter of $\sim 60 \mu\text{m}$, resulting in a current density of $\sim 5000 \text{ A cm}^{-2}$. Together, the electron beam (by its attractive Coulomb potential and the partial space-charge compensation) and the magnetic field (via Lorentz forces) provide a radial trap for the ions. Axial trapping of the ions along the electron beam axis is provided by raising the two end tubes of three collinear, insulated drift tubes to a positive potential with respect to the centre drift tube bias potential. This traps a cylindrical ion cloud $\sim 30 \text{ mm}$ long and $\sim 200 \mu\text{m}$ in diameter [26], which is oriented along the direction of the electron beam. A variable bias voltage of $\sim 1.5 \text{ kV}$ to $\sim 20 \text{ kV}$ is applied to the drift tubes to define an accelerating potential for the electron beam. A correction of the order of 100 eV must be applied to this energy in order to account for the net space charge of the electrons and the positive ions in the trap. The precise energy of the electron beam ($\sim 50 \text{ eV}$ width) is therefore determined from the accelerating bias potential, the centre drift tube floating voltage and the space-charge correction. By adjusting the accelerating voltage slightly below the ionization energy of the desired ion, we can optimize the relative population of a specific charge state. A gas injection system was connected to a lateral port that looks directly into the trap and is used to introduce neutral krypton and argon atoms into the EBIT from a direction perpendicular to the trap axis.

The detection system has also been described in detail elsewhere [27]. In brief, a cooled, low-noise photomultiplier was used for photon detection, and a scanning monochromator was used for wavelength selection. Radiation from the trap was imaged onto the entrance slit of the monochromator by two plano-convex lenses; this was necessary in order to keep the photomultiplier away from the stray magnetic field of the superconducting magnet. The two-lens system produced a demagnification of ~ 0.8 . The entire optical table which supported the monochromator was attached to two perpendicular translation stages which could be positioned with a precision of better than $10 \mu\text{m}$. These translation stages were used to place the monochromator's entrance slit at the image of the trap produced by the lens system. A Si(Li) detector with an energy resolution of $\sim 190 \text{ eV}$ was used to monitor the x-rays from the same trap volume through one of the radial ports.

3. Lifetime measurement

The ionization potential of Ar^{13+} is 756 eV. Trying to maximize the relative population of this charge state by setting the electron beam energy slightly below this ionization potential will force the EBIT to run at low electron beam current. We opted to set the electron beam energy to much higher values in order to increase the current and therefore to obtain a stronger overall signal from the transition. Different electron beam energies were used for Ar in order to search for possible systematic effects. Typical values for the electron beam energy and collector current were 1.5 keV at 30 mA, 8 keV at 118.6 mA and 5 keV at 70.2 mA. In the case of Kr^{22+} , the ionization potential is 1.05 keV. Therefore, it was possible to run at electron energies close to the energy at which the relative population of Kr^{22+} is maximized. A typical electron beam energy and collector current for Kr was 1.4 keV at 30 mA. The gas injection pressure of Ar and Kr in the first chamber of the injection system was changed from run to run. This pressure was varied between $6.6 \times 10^{-5} \text{ Pa}$ ($5 \times 10^{-7} \text{ Torr}$) and $4 \times 10^{-4} \text{ Pa}$ ($3 \times 10^{-6} \text{ Torr}$), but did not significantly affect the pressure in the EBIT above the trap region, which remained lower than $6.6 \times 10^{-8} \text{ Pa}$ ($5 \times 10^{-10} \text{ Torr}$). The anode voltage that defines the electron beam current was driven by a function generator that switched the current off in about $50 \mu\text{s}$, kept it at zero for about 80 ms to allow the level population to decay and finally switched it back on within about $50 \mu\text{s}$. The current

was then held constant for about 280 ms to allow the signal to recover. Time-resolved data were acquired by setting the monochromator to the transition wavelength and accumulating synchronized data over many thousands of cycles using an 'event mode' data acquisition system [15]. The entrance and exit slits of the monochromator were set to $500 \mu\text{m}$, which translates into a bandpass of 1.3 nm. Photons arriving at the photomultiplier or x-rays detected by the Si(Li) detector were time-stamped with a resolution of better than $50 \mu\text{s}$.

4. Data analysis

Data sets (see figure 3) show the temporal behaviour of the signal observed, in this case on the $2s^22p \ ^2P_{3/2} \rightarrow \ ^2P_{1/2}$ transition in Ar^{13+} . The figure shows an initial fast decay immediately after the electron beam is switched off at time $t \sim 19 \text{ ms}$. Then the signal decays exponentially for about 50 ms and begins to recover at $t \sim 72 \text{ ms}$ when the beam is switched back on. The observed decay curves were fitted by either one or two exponentials plus a constant background and covered a time interval of about six lifetimes of the level of interest. Both single- and double-exponential fits gave similar results for the primary decay component within the quoted uncertainties. X-ray data from the SiLi detector were used to determine the exact time at which the switching occurs by observing the sudden decay of the prompt x-rays. In order to take into account the initial drop in signal, the data were truncated stepwise until the fitted lifetime value stabilized. Typically, after about less than 1 ms the fit was stable and produced reasonable reduced chi-squared values near unity. In order to check for collisional quenching and other effects, results from the different runs were compared and showed no dependence on beam energy or on pressure over the range studied. Figure 4 shows the lifetimes values obtained from different runs as a function of pressure for the $2s^22p \ ^2P_{3/2}$ level in Ar^{13+} . Figure 5 shows the spread for the fitted lifetimes for the $3s^23p^2 \ ^3P_2$ level in Kr^{22+} . The results of the measurements are summarized in table 1, where calculated values have been included for comparison. Since the transition probabilities depend on the third power of the energy separation, a second column has been added to the calculations where the transition probabilities have been modified by

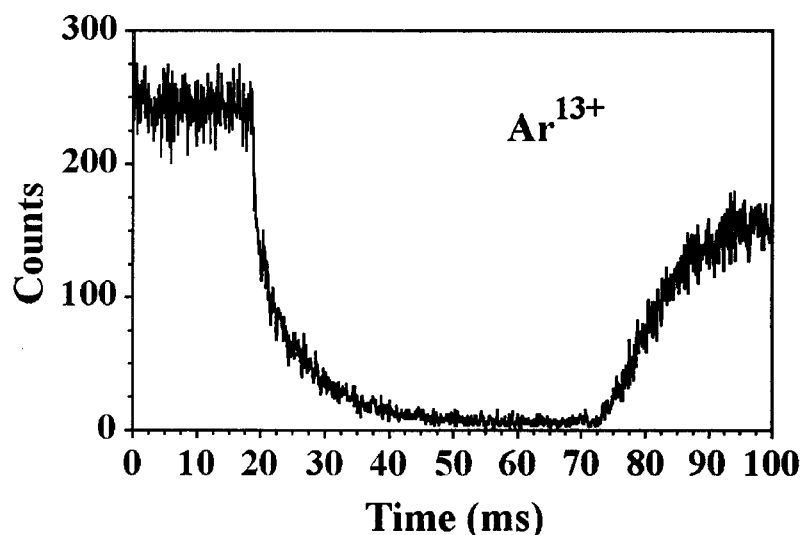


Figure 3. Temporal dependence of the light emitted at 441.24 nm from the $^2P_{3/2} \rightarrow \ ^2P_{1/2}$ transition in Ar^{13+} .

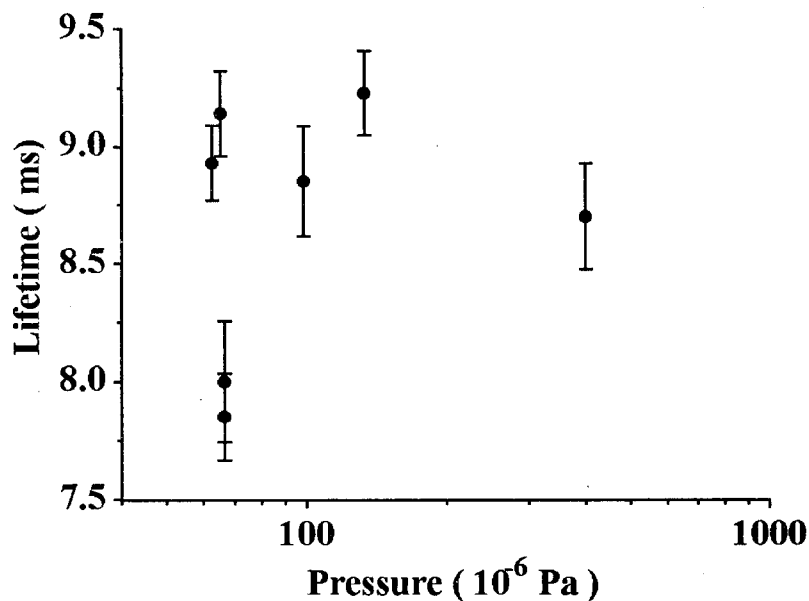


Figure 4. Lifetime as a function of gas injection pressure for the $^2P_{3/2}$ state of Ar^{13+} . Pressure shown on a logarithmic scale.

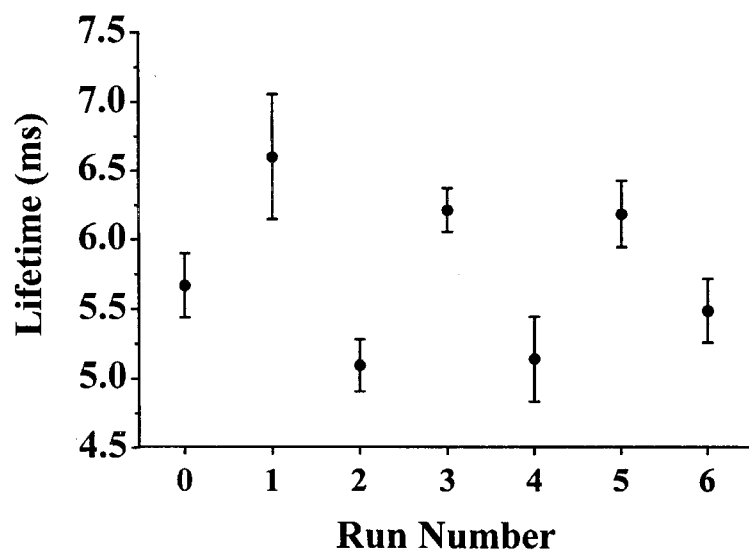


Figure 5. Fitted lifetimes for the $3s^2 3p^2 \ ^3P_2$ state of Kr^{22+} obtained from different runs. The error bars shown for each point are the uncertainties from the fitting procedure.

using the accepted experimental value for the transition energies, in the cases where a discrepancy between the calculations and experiment would make a difference. Our value for the radiative lifetime of the $2s^2 2p \ ^2P_{3/2}$ level in Ar^{13+} is about one and a half standard uncertainties [28] lower than the available calculations. Results are quoted to one standard uncertainty, obtained from the standard deviation from the weighted average of the lifetimes obtained from different runs, so that fitting and reproducibility effects are included. The experimental radiative lifetime for the $3s^2 3p^2 \ ^3P_2$ level in Kr^{22+} is lower than the result of

Table 1. Radiative lifetimes for the $3s^23p^2\ ^3P_2$ level of Kr^{22+} and the $2s^22p\ ^2P_{3/2}$ level of Ar^{13+} . The final column shows the modified calculated radiated lifetimes obtained from the transition probabilities, where the experimental values for the energy separations have been used instead of the calculated ones.

Ion	Level	Experiment (ms)	Calculation (ms)	Mod.
Ar^{13+}	$2s^22p\ ^2P_{3/2}$	8.7(5) ^a	9.62 ^b	
			9.51 ^c	
			9.41 ^d	9.58 ^d
Kr^{22+}	$3s^23p^2\ ^3P_2$	5.7(5) ^a	5.83 ^e	6.69 ^e
			6.46 ^f	6.78 ^f

^a This work.

^b Verhey [7]. Wavelength not available in the paper.

^c Froese Fischer [6]. Modification did not affect the result.

^d Cheng [12].

^e Huang [10].

^f Biémont [8].

^g Radiative lifetimes shown are the inverse of the sum of the transition probabilities to the 3P_1 and the 3P_0 states.

relativistic calculations of Biémont [8] by about one and a half standard uncertainties, but it agrees well with a more recent calculation by Huang [10] that includes relativistic effects as well as the Breit interaction and Lamb shift contributions. Unfortunately Huang's energy separations disagree with experiment by as much as 5%, so that the modified calculated transition probability is higher than our measurement by about one and a half standard uncertainties.

5. Conclusion

We have reported two new lifetime measurements of excited states within the ground configuration of Ar^{13+} and Kr^{22+} using an electron beam ion trap. These results, with uncertainties at the $\sim 8\%$ level, provide data in a region where measurements are scarce. We find that our results for the total radiative lifetimes are about one and a half standard uncertainties below the theoretical values in both cases.

Acknowledgment

This work has been partially supported by a NATO Collaborative Research grant no CRG 940181.

References

- [1] Hinnov E, Suckewer S, Cohen S and Sato K 1994 *Phys. Rev. A* **25** 2293
- [2] Edlén B 1984 *Phys. Scr.* **T 8** 5
- [3] Träbert E 1995 *Nucl. Instrum. Methods B* **98** 10
- [4] Hubricht G and Träbert E 1987 *Z. Phys.* **D 7** 243
- [5] Doerfert J, Träbert E, Wolf A, Schwalm D and Uwira O 1977 *Phys. Rev. A* **78** 4355
- [6] Froese Fischer C 1983 *J. Phys. B: At. Mol. Phys.* **16** 157
- [7] Verhey T R, Das B P and Perger W F 1987 *J. Phys. B: At. Mol. Phys.* **20** 3639
- [8] Biémont E and Bromage G E 1983 *Mon. Not. R. Astron. Soc.* **205** 1085
- [9] Sugar J and Kaufman V 1984 *J. Opt. Soc. Am.* **B 1** 218

- [10] Huang K-N 1985 *At. Data Nucl. Data Tables* **32** 503
- [11] Curtis L J 1989 *Phys. Rev. A* **40** 6958
- [12] Cheng K T, Kim Y-K and Desclaux J P 1979 *At. Data Nucl. Data Tables* **24** 111
- [13] Yang L and Church D A 1993 *Phys. Rev. Lett.* **70** 3860
- [14] Yang L, Church D A, Tu S and Jin J 1994 *Phys. Rev. A* **50** 177
- [15] Serpa F G, Morgan C A, Meyer E S, Gillaspay J D, Träbert E, Church D A and Takács E 1997 *Phys. Rev. A* **55** 4196
- [16] Beiersdorfer P, Beck B, Becker St and Schweikhard L 1996 *Int. J. Mass Spectrom. Ion Processes* **157–158** 149
- [17] Beiersdorfer P, Schweikhard L, Crespo Lopez-Urrutia J and Widmann K 1996 *Rev. Sci. Instrum.* **67** 3818
- [18] Gillaspay J D 1996 *Phys. Scr. T* **65** 168
- [19] Lyot B and Dollfus A 1953 *C. R. Acad. Sci., Paris* **237** 855
- [20] Edlén B 1954 *Mon. Not. R. Astron. Soc.* **114** 700
- [21] Roberts J R, Pittman T L, Sugar J, Kaufman V and Rowan W L 1987 *Phys. Rev. A* **35** 2591
- [22] Serpa F G, Bell E W, Meyer E S, Gillaspay J D and Roberts J R 1997 *Phys. Rev. A* **55** 1832
- [23] Serpa F G, Meyer E S, Morgan C A, Gillaspay J D, Sugar J, Roberts J R, Brown C M and Feldman U 1996 *Phys. Rev. A* **53** 2220
- [24] Gillaspay J D 1997 *Phys. Scr. T* **71** 99
- [25] Marrs R E, Beiersdorfer P and Schneider D 1994 *Phys. Today* **47** 27
- [26] Gillaspay J D et al 1995 *Phys. Scr. T* **59** 392
- [27] Morgan C A, Serpa F G, Takács E, Meyer E S, Gillaspay J D, Sugar J, Roberts J R, Brown C M and Feldman U 1995 *Phys. Rev. Lett.* **74** 1716
- [28] Taylor B N and Kuyatt C E 1994 Guidelines for evaluating and expressing the uncertainty of NIST measurement results *NIST Technical Note* 1297

UV light from the ground term of Ti-like ytterbium, tungsten, and bismuth

J. V. Porto, I. Kink, and J. D. Gillaspay

National Institute of Standards and Technology, Gaithersburg, Maryland 20899-8421

(Received 24 September 1999; published 7 April 2000)

We have used an electron-beam ion trap to measure the wavelength of the $J=2-3$ magnetic dipole transition in the $3d^4$ ground term of Ti-like ytterbium, tungsten, and bismuth. This fills in a gap in previous measurements along this isoelectronic sequence, as well as extending previous work to the highest Z yet. With the addition of our results, measurements of this line now cover a sufficient range of Z to allow an interpolation of reliable wavelength estimates for the unmeasured members of the isoelectronic sequence from $Z=52$ to 83. We provide a table of these wavelengths for each member of the sequence in this range, and compare the measured wavelengths to recent calculations. Our results show that a long-standing discrepancy between prediction and experiment disappears in the high- Z limit.

PACS number(s): 32.30.Jc, 32.10.-f, 52.70-m, 31.25.-v

Since Feldman, Indelicato, and Sugar made the surprising prediction [1] that a visible-near-uv transition in the ground term of the Ti-like isoelectronic sequence was nearly Z independent over the upper half of the Periodic Table, several experimental measurements were made to test this calculation [2-4]. The predicted line arises from an $M1$ transition between the lowest $J=2$ and 3 levels of the $3d^4$ ground configuration, and the radiative decay rates are high enough to make the line reasonably strong under most plasma conditions. In addition to being a curiosity (transitions of this sort typically scale as Z^4), there is significant interest in these lines because their unexpected weak dependence on Z makes them potentially important for plasma diagnostics [1-5]. The unusual nature of these lines also makes them useful for testing relatively uncharted aspects of many-body atomic calculations.

The original Dirac-Fock calculations, which included correlations among all M -shell electrons, disagree with experiment by as much as 5% for $Z=60$ [3]. This is a surprisingly large discrepancy for such a relativistic calculation of a highly charged ion, the error presumably arising from missing correlation effects. Subsequent calculations [6] for $54 \leq Z \leq 64$, which included correlations via excitations to virtual subshells, reduced the discrepancy in this range of Z to $\approx 1.5\%$. In recent years relativistic many-body atomic calculations have improved dramatically [7,8] and it is essential to have high-quality experimental data over as wide a range of Z as possible to compare with the calculations. Systems like the Ti-like sequence, where many-body effects are very important and the visible transition can be measured accurately, are particularly well suited as tests of the theory. In addition, since the $J=2-3$ optical transition ($\Delta E \approx 3$ eV) arises from a small difference between relatively large energies ($E \approx 80$ eV for tungsten), the Ti-like system serves as a good test of effects which influence the $J=2$ and 3 states differently. Very recent multiconfiguration Dirac-Fock (MCDF) calculations of this line in the very high- Z ions tungsten and bismuth [9] provide strong motivation for measuring them.

Electron-beam ion traps (EBIT's) are versatile tools for measuring atomic properties over an extremely wide range of charge states. There have been measurements of the $J=2-3$ line previously reported for five different Ti-like ions:

four in the range from Xe ($Z=52$) to Gd ($Z=64$) [2,3] and a single measurement at Au ($Z=79$) [4]. Some of these measurements were confirmed in subsequent experiments in independent labs [10,11]. Reference [11] also provided an interesting qualitative explanation for the unusually weak Z dependence of this line. The goal of this study was to measure wavelengths near $Z=70$ and above $Z=80$ in order to provide data over the entire region of the isoelectronic sequence where the line exists. The experimental arrangement is similar to that described in previous measurements [3]. Cylindrical high-voltage drift tube electrodes surrounding the trap region provide the accelerating potential for a narrow, intense electron beam which is confined by a 3T magnetic field. A metal vapor vacuum arc (MEVVA) source produces low-charged Yb, W, or Bi ions, which are injected into the EBIT, trapped, and further ionized by the electron beam. The spectrometer we used is a 0.3-m focal length Czerny-Turner scanning monochromator with a linear dispersion of 2.6 nm/mm, coupled to a cooled, blue-sensitive photomultiplier [3]. At the operating temperature of -25 °C, the background count rate for the photomultiplier was 3 or 4 Hz. The charge state of interest was optimized by adjusting the electron energy to be just below the ionization potentials of the ion, which were calculated to be 4246 eV for Yb^{48+} , 4920 eV for W^{52+} , and 6662 for Bi^{61+} [12]. For the ytterbium and tungsten measurements, nitrogen was introduced into the trap to provide low-mass, low-charged ions for evaporative cooling of the heavy, highly charged ions [13]. During the bismuth measurement, we found that weak lines in some charge state of nitrogen were blended with the Ti-like bismuth line, so argon was used as a cooling gas. In all cases, the gas was expanded into the trap region through a 3.2-mm-diameter hole 16 cm from the trap, from a chamber at $\sim 1.3 \times 10^{-4}$ Pa.

In these measurements, the identification of the $J=2-3$ line was aided by the fact that the line disappeared when the MEVVA ion loading was stopped, and that the threshold for observation of the measured lines was at the ionization energy for the production of the ion. (See Fig. 1 for the energy dependence of the tungsten line, and Fig. 2 for the spectra.) Due to the presence of the electron beam, there is a space-charge correction which decreases the actual energy of the

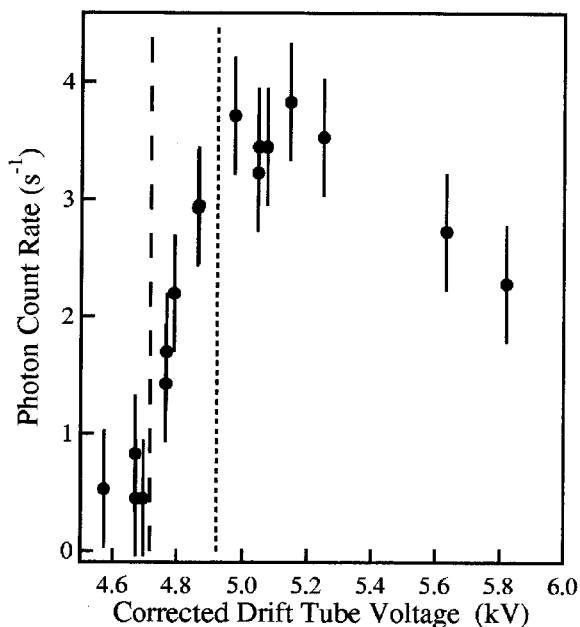


FIG. 1. Plot of the intensity of the observed $J=2-3$ $M1$ transition in W^{52+} as a function of electron-beam energy. The drift tube voltage has been corrected for an estimated 220-V space charge shift. The dashed line represents the ionization potential for W^{51+} (i.e., the threshold for production of W^{52+}), and the dotted line represents the ionization potential for the Ti-like state, W^{52+} .

electrons in the trap region, and this shift in the accelerating potential has been included in the data of Fig. 1. At operating conditions of 90 mA and ~ 5 kV, the space-charge offset is calculated to be -220 V. This estimate does not include the

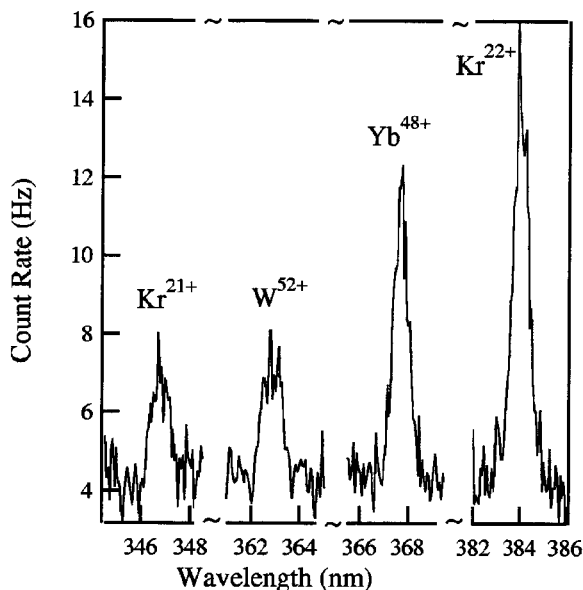


FIG. 2. Selected parts of the observed spectra during the ytterbium, tungsten, and krypton measurements. The spectrometer slits in these measurements were $300 \mu\text{m}$, and each peak represents an average of four scans.

partial neutralization of the electron beam by the ions, and therefore the shifted electron energies serve as lower bounds. We note that while the addition of the cooling gas increases the total number of metal ions (Yb, W, or Bi) in the trap, it usually lowers the average charge state at a given beam energy (due to charge exchange with the neutral gas). With the cooling gas, the electron-beam energy which maximizes any given charge state is raised to higher values. This fact can be seen in Fig. 1, where the maximum signal intensity from the W^{52+} occurs at a beam energy above the ionization potential for the ion. We note that the bismuth line had the correct threshold, and disappeared when the MEVVA ion loading stopped, but the intensity did not decrease even when the beam energy was as high as 10 kV, which is significantly above the ionization potential for Ti-like bismuth. We attribute this behavior to the increased charge exchange cross section for the highly charged Bi^{61+} , which pushes the charge-state balance to lower charges.

During the ytterbium and tungsten measurements, the calibration of the spectrometer was checked *in situ* against two previously measured lines in Kr which are on either side of the two Ti-like lines that we measured: the $3s^23p^3D_{3/2-2}D_{5/2}$ line in Kr^{21+} at 346.47(6) nm [14], and the $3s^23p^2^3P_1-^3P_2$ line in Kr^{22+} at 384.09(3) nm [15]. All four lines were measured with $300\text{-}\mu\text{m}$ entrance and exit slits on the spectrometer, but the Yb and the 384-nm Kr lines were also measured with 150 and $100\text{-}\mu\text{m}$ slits in order to measure slit-dependent systematics. During the tungsten run, the calibration lines indicated a 0.2-nm systematic offset in wavelengths, possibly due to misalignment of the spectrometer. The tungsten data were therefore shifted to correct for this offset. In the bismuth measurement, nearby transitions in N^{3+} were also used for calibration: the three lines arising from the $^3S-^3P$ multiplet of the $3s-3p$ transition array at 347.87, 348.30, and 348.49 nm [16]. The bismuth and calibration spectra were taken with $250\text{-}\mu\text{m}$ slits in order to be able to resolve the closely spaced nitrogen lines.

One interesting aspect of the Ti-like sequence is that the $J=4$ level, which is the highest energy level of the ground term at low Z , crosses both the $J=3$ and 2 levels as Z is increased. Unfortunately, at high Z the unobserved UV $J=4-3$ transition competes with the $J=2-3$ transition we observe, and at $Z=74$ (tungsten) the branching ratio to the $J=2$ level drops to only 16% [17]. With entrance and exit slits of $300 \mu\text{m}$, the maximum count rate we observed for the $J=2-3$ line in W^{52+} was only 4 Hz, which is more than four times smaller than the rate measured on the same line in Gd^{42+} under similar conditions [3]. For bismuth ($Z=83$) there is a further factor of 2 decrease in signal, making measurements of this line in such a high charge state even more difficult. The combined standard uncertainty ($1-\sigma$ level) arising from the calibration, peak fitting and reproducibility considerations are 0.15 nm for Yb^{48+} and Bi^{61+} and 0.2 nm for W^{52+} .

The measured wavelength for the $3d^4 J=2-3$ line in Yb^{48+} , W^{52+} , and Bi^{61+} , along with previously measured wavelengths for the same transition at different Z 's, are shown in Fig. 3. We had previously found [3], that a scaling of the electrostatic integrals in the relativistic Cowan code

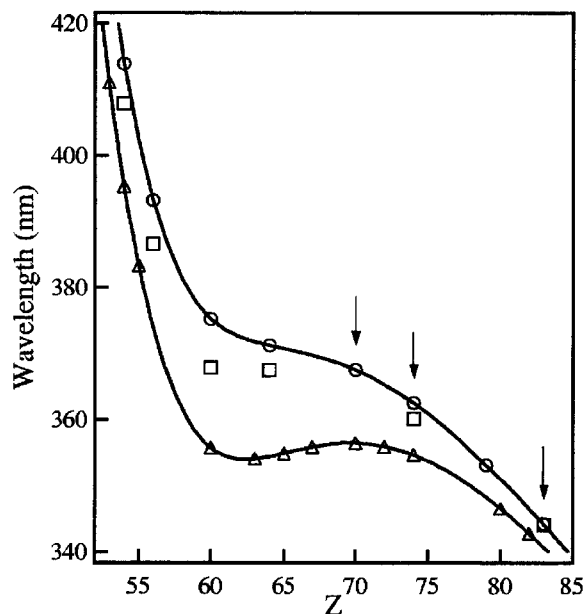


FIG. 3. Plot of the measured wavelengths of the $J=2-3$ $M1$ transitions in the $3d^4$ configuration of the Ti-like isoelectronic sequence (circles), including the new measurements of Yb^{48+} , W^{52+} , and Bi^{61+} , which are indicated by arrows. (The measurements for $Z \leq 64$ are from Refs. [2,3], and the measurement at $Z=79$ is from Ref. [4].) The calculations of Refs. [1,17] (triangles) and [6,9] (squares) are also shown. The solid curve through the open circles is a cubic spline of the calculations, and the solid line through the measured points is the estimate described in the text.

[18], which was linear in Z , described the measured wavelengths for Z between 52 and 64. Extending this scaling to higher Z but with the scale factor capped at 1.0, however, failed to provide good agreement, since errors quickly exceeded 5%. In contrast, MCDF calculations improve at higher Z , as can be seen in Fig. 4, where we have plotted the relative error of the calculations of Indelicato and co-workers [1,17] and of Beck [6,9]. Although the discrepancy between the measurements and theory is not expected to have a simple functional dependence on Z , it is fairly smooth and the calculations approach experiment at higher Z . The recent calculation of Beck at $Z=83$ [9] is in very good agreement with our measurement.

With the addition of the three measurements that we report here, the relatively smooth discrepancy between measurement and calculation can be used as an estimate of the unmeasured wavelengths for $52 \leq Z \leq 83$. In the absence of a clear functional dependence for the wavelengths, we used a simple cubic spline interpolation to estimate the difference between the data and the calculated curve shown in Fig. 3; the result is shown in Fig. 4. Using this interpolation, the wavelengths of the other Ti-like ions in this range of Z were estimated, and the resulting values are given in Table I and shown in Fig. 3. We include two points for $Z \leq 53$ which involve extrapolations beyond the measured values. It is difficult to estimate robust errors for the interpolation and extrapolation, but we made consistency checks by removing each data point individually from the ensemble and reinter-

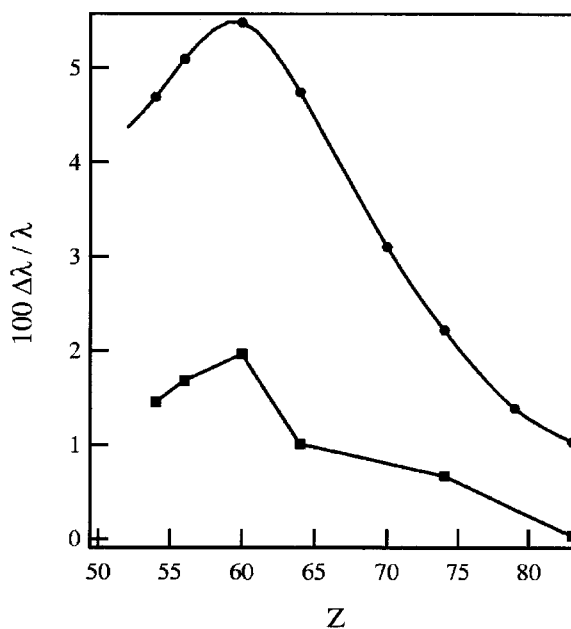


FIG. 4. Plot of the difference between calculated data and measurements (see Fig 3). The circles are from the calculations of Refs. [1,17], and the squares are from the calculations of Refs. [6,9]. The line through the circles is a cubic interpolation constrained to pass through all the measured points.

polating to predict the removed point. With the exception of the measured end points at $Z=54$ and 83 (which become extrapolations once the end data points are removed) and the point of maximum curvature at $Z=60$, the estimated values are within 0.1% (<0.4 nm) of the measured values. In all cases (including the extrapolation from $Z=79$ to 83) the fits to subsets of the data predict the eliminated points to within 0.2% (<0.8 nm). We expect the estimates to be more ac-

TABLE I. Table of measured and interpolated values for the wavelengths of the $J=2-3$ transition within the ground term of the Ti-like isoelectronic sequence. A conservative estimate for the uncertainty in the interpolated values is 0.8 nm. (See the discussion in the text.) Measured wavelengths are indicated as (a) Ref. [2], (b) Ref. [3], (c) this work, and (d) Ref. [4].

Z	λ (nm)	Z	λ (nm)	Z	λ (nm)
52	449.4	63	371.9	74(c)	362.6(2)
53	429.6	64(b)	371.3(2)	75	361.0
54(a)	413.9(2)	65	370.8	76	359.2
55	402.2	66	370.3	77	357.4
56(a)	393.2(2)	67	369.8	78	355.3
57	386.5	68	369.2	79(d)	353.2(2)
58	381.4	69	368.5	80	351.1
59	377.8	70(c)	367.64(15)	81	348.9
60(b)	375.3(2)	71	366.5	82	346.6
61	373.6	72	365.3	83(c)	344.29(15)
62	372.6	73	364.0		

curate than this when all the measured points are used (particularly for $63 < Z < 83$), and the uncertainty for most points is likely to be limited by the 0.2-nm uncertainty in the measured wavelengths. Nonetheless, we take 0.8 nm as a conservative estimate for the uncertainty of the entire range studied. Thus the interpolation provides a 0.2% estimate of the lowest Ti-like $3d^4$ $J=2-3$ transitions for $52 \leq Z \leq 83$.

We would like to thank Y. -K. Kim for helpful discussions and for performing atomic structure calculations that aided this experiment. We thank D.J. Alderson for assistance in operating the EBIT and F.G. Serpa for assistance with the spectrometer. I.K. acknowledges support from the Swedish Foundation for International Cooperation in Research and Higher Education (STINT).

-
- [1] U. Feldman, P. Indelicato, and J. Sugar, *J. Opt. Soc. Am. B* **8**, 3 (1991).
- [2] C.A. Morgan, F.G. Serpa, E. Takács, E.S. Meyer, J.D. Gillaspy, J. Sugar, J.R. Roberts, C.M. Brown, and U. Feldman, *Phys. Rev. Lett.* **74**, 1719 (1995).
- [3] F.G. Serpa, E.S. Meyer, C.A. Morgan, J.D. Gillaspy, J. Sugar, J.R. Roberts, C.M. Brown, and U. Feldman, *Phys. Rev. A* **53**, 2220 (1996).
- [4] E. Träbert, P. Beiersdorfer, S.B. Utter, and J.R. Crespo Lopez-Urrutia, *Phys. Scr.* **58**, 599 (1998).
- [5] F. Parente, J.P. Marques, and P. Indelicato, *Europhys. Lett.* **26**, 437 (1994).
- [6] D.R. Beck, *Phys. Rev. A* **56**, 2428 (1997).
- [7] P. Indelicato, S. Boucard, and E. Lindroth, *Eur. Phys. J. D* **3**, 29 (1998).
- [8] J. Saperstein, *Rev. Mod. Phys.* **70**, 55 (1998).
- [9] D.R. Beck, *Phys. Rev. A* **60**, 3304 (1999).
- [10] D.J. Bieber, H.S. Margolis, P.K. Oxley, and J.D. Silver, *Phys. Scr.* **73**, 64 (1997).
- [11] D. Kato, C. Yamada, T. Fukami, I. Ikuta, H. Watanabe, K. Okazaki, S. Tsurubuchi, K. Motohashi, and S. Ohtani, *Phys. Scr.* **80**, 446 (1999).
- [12] Y. K. Kim, (private communication).
- [13] M. B. Schneider, M. A. Levine, C. L. Bennett, J. R. Henderson, and R. E. Marrs, in *International Symposium on Electron Beam Ion Sources and Their Applications*, edited by A. Herscovitch, AIP Conf. Proc. No. 188 (AIP, New York, 1989), p. 158.
- [14] F.G. Serpa, E.W. Bell, E.S. Meyer, J.D. Gillaspy, and J.R. Roberts, *Phys. Rev. A* **56**, 2428 (1997).
- [15] V. Kaufman and J. Sugar, *J. Phys. Chem. Ref. Data* **15**, 321 (1986).
- [16] R. Hallin, *Ark. Fys.* **32**, 201 (1966).
- [17] P. Indelicato, *Phys. Scr.* **T65**, 57 (1996).
- [18] R. D. Cowan, *The Theory of Atomic Structure and Spectra* (University California Press, Berkeley, CA, 1981).

Direct imaging of highly charged ions in an electron beam ion trap

J. V. Porto,^{a)} I. Kink, and J. D. Gillaspay

National Institute of Standards and Technology, 100 Bureau Dr. Stop 842, Gaithersburg, Maryland 20899-8421

(Received 29 March 2000; accepted for publication 10 May 2000)

We have directly observed the ion cloud distribution in an electron beam ion trap using visible and ultraviolet fluorescence from lines in the ground term of Ar^{13+} , Xe^{31+} and Xe^{32+} ions. Using a gated intensified charge coupled device camera, we have the capability to measure both static and dynamic ion cloud distributions. The images provide information about the trapped highly charged ions which is difficult to obtain by other methods. To demonstrate the usefulness of the technique, we took images of static ion clouds under different conditions and compared the distributions to a simple model. We also recorded time resolved images which show that we can monitor the relaxation of the ion cloud toward equilibrium when the trapping conditions are suddenly changed. The information provided by such measurements can be used to improve models of ion cloud dynamics and, combined with modeling, these techniques can help improve measurements of atomic data using electron beam ion traps. [S0034-6748(00)04208-8]

I. INTRODUCTION

Electron beam ion traps (EBITs) have proven to be valuable devices for research involving x-ray spectroscopy of highly charged ions.¹⁻³ There are currently at least eight major EBIT facilities in operation around the world, and more are being planned. Because EBITs have been used largely (and very successfully) as static light sources, however, experimental studies of the geometry and motion of the ion cloud within the traps have been scarce. This has been one of the key limitations which has prevented EBITs from being used to measure absolute (without recourse to normalization) cross sections of atomic collision processes. X-ray fluorescence of ions has been successfully used to image the *electron* distribution in the electron beam of an EBIT,⁴ but the short lifetime of x-ray transitions precludes the possibility of measuring the entire ion cloud distribution. The extension of spectroscopic studies with an EBIT from the x-ray into the visible regime,⁵ where long-lived excited states can be probed, has opened up the possibility of directly imaging the full ion cloud. With direct knowledge of the ion cloud distribution absolute cross sections can in principle be obtained. In addition, EBITs have begun to be used in a transient mode of operation to either form pulsed beams of highly charged ions^{6,7} or measure excited state atomic lifetimes.⁸⁻¹⁰ In light of these developments, the lack of experimental knowledge about the geometry and dynamics of the ion cloud inside an EBIT has become apparent. In this article, we present the results of a study in which the ion cloud is directly imaged in visible and UV light with a charge coupled device (CCD) camera, and the dynamical motion of the cloud is studied under a variety of conditions.

II. EXPERIMENT

The National Institute of Standards and Technology (NIST) EBIT has been described elsewhere,¹¹ and we describe here only the aspects relevant for the current study. The EBIT consists of a narrow electron beam (radius $a \approx 35 \mu\text{m}$) confined by a 3 T magnetic field which is used to ionize and trap ions at high charge states, producing ions with charges up to $+73e$. In the experiments described here, the electron beam was subject to a constant flux of neutral gas which, when ionized, provides the source of ions in the trap. The space charge of the electron beam provides a trapping potential in the radial direction ρ , and three cylindrically symmetric electrodes surrounding the beam provide a trapping potential in the axial direction z (see Fig. 1). A positive voltage V_E applied to the middle of the three electrodes relative to the electron gun determines the energy of the electron beam. The voltage V_z of the two end cap electrodes relative to the middle electrode is used to control the axial trap depth. The combined trap potential $V(\rho, z)$ is nearly independent of z in the 3 cm space between the two end cap electrodes. In the radial direction the potential is logarithmic in ρ for $\rho > a$ (see Fig. 2). Inside the electron beam the potential depends on the density distribution of electrons, as we discuss in more detail below. The trapping potential depends on the ion cloud distribution as well since the ions will partly neutralize the electron beam space charge at high ion densities. In addition to the electrostatic potential, the constant magnetic field also plays a role in confining the ions. The end cap electrode voltages can be switched rapidly, allowing for fast axial dumping of ions. Both the radial and axial trapping potentials have typical depths of up to a couple of hundred volts per charge. The resulting trapped ion cloud is long (30 mm) and narrow (typically between 0.07 and 1 mm in diameter).

The imaging system consists of two coaxial lenses operated at nearly infinite conjugation, with the electron beam

^{a)} Author to whom correspondence should be addressed; electronic mail: trey@nist.gov

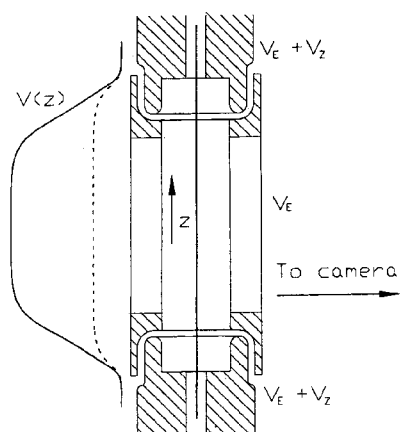


FIG. 1. Cross section of the cylindrical EBIT trapping electrodes. The trap consists of an electron beam threading three drift tubes. The upper and lower drift tubes are held at a potential of $V_E + V_z$, while the middle drift tube is held at V_E . The resulting axial potential is indicated schematically. The dashed line represents the image potential formed by the electron beam and the internal geometry of the electrodes. The solid line represents the total potential including the voltage V_z applied to the end caps. The resulting radial potential is shown in Fig. 2.

near the focus of the first lens (focal length $f=20$ cm) and the camera imaging plane near the focus of the second ($f=35$ cm). The lenses were placed 1 cm from each other and the total distance between the electron beam and camera plane varied between 55 and 65 cm, depending on the choice of magnification. The lenses were standard cemented achromats, chosen to minimize spherical aberrations on the blue side of the visible spectrum. The magnification depended on the placement of the camera and electron beam relative to the

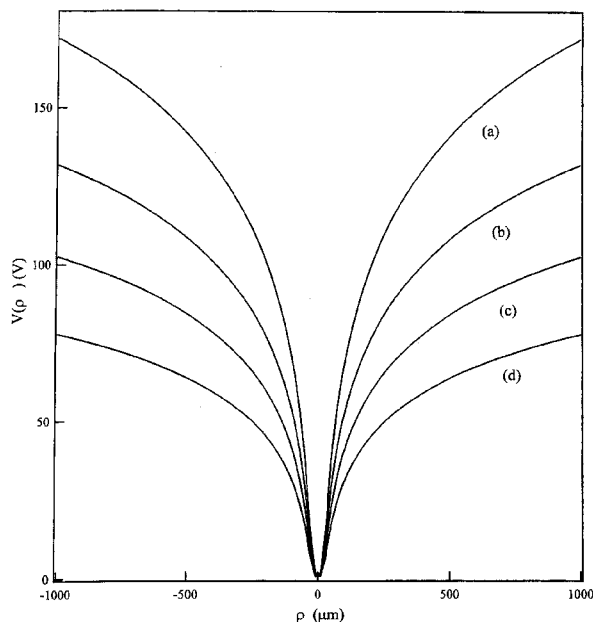


FIG. 2. Examples of the EBIT radial space charge trapping potential. The plots are for the conditions of the four static measurements described in the text and listed in Table II.

TABLE I. Transitions used to image trapped ions.

Ion	Transition	λ (nm)	Lifetime (ms)
Ar ¹³⁺	$2p^2 P_{1/2} - ^2P_{3/2}$	441.2 ^a	8.7(5) ^b
Xe ³¹⁺	$3d^5 ^4G_{7/2} - ^4G_{9/2}$	396.3 ^c	~ 3 ^d
Xe ³²⁺	$3d^4 ^5D_2 - ^5D_3$	413.9 ^c	2.15(14) ^c

^aReference 19.

^bReference 20.

^cReference 21.

^dReference 22.

^eReference 23.

lenses and was measured independently. Images were taken at magnifications of 1.75 and 2.65. At these magnifications, a single pixel corresponded to 15.3 and 10.1 μm , respectively. The spatial resolution was determined to be about twice the pixel size by imaging a 75 μm pinhole under various conditions. In addition, two *in situ* tests of the magnification were made in order to roughly check the calibration of the magnification. An image of the entrance slit of a previously calibrated optical spectrometer¹² was projected into the EBIT and subsequently re-imaged onto the CCD. In addition, the slit in the drift tube electrode was imaged. Both measurements confirmed the overall magnification of the system.

Narrow band interference filters ($\Delta\lambda=10$ nm) were used to isolate the particular line of the charge state of interest. Simultaneous measurements with a spectrometer indicate that contamination from lines from low charged states that fall within the 10 nm width of the filter were small but measurable, particularly for Ar¹³⁺. However, their influence will be largely ignored throughout this article. The camera used was a commercial intensified CCD which could be gated on and off within a few nanoseconds. We took advantage of the vertical symmetry of the ion cloud distributions by operating the camera in "full vertical binning" mode. In this mode the two-dimensional image is projected along the symmetry axis of the EBIT into the last row of the CCD before being digitized, capturing the radial distribution while averaging over the homogeneous axial distribution. Full two-dimensional images were taken in order to check the camera and EBIT alignment and assure that the full vertical binning mode did not distort the radial image significantly. For the data presented here, the misalignment was less than 2 pixels out of 580, which corresponds to an angle of less than 0.2°. The total collection time required to produce a single vertically binned image was typically about 10 min. In addition to the imaging system, a visible/UV spectrometer and solid state x-ray detector are also attached to the EBIT on different ports.¹¹

III. ION CLOUD DISTRIBUTIONS

We studied ion cloud distributions by observing fine structure transitions in the ground term of three different ions: Ar¹³⁺, Xe³¹⁺ and Xe³²⁺ (see Table I). The transitions are excited by the electron beam and the lifetimes are all more than 1 ms. By contrast, ion motion in the azimuthal direction (due to the magnetic field and the radial electric field) has orbital periods that range from several nanosec-

lematic in solar and astrophysical spectra, are harder for us to check experimentally because of the problems of charge exchange in our experiment enhancing the $2p^6-2p^53s$ intensities.

These effects of charge exchange may however allow the measurement of state selective charge-exchange cross sections, relative to those for electron-impact excitation or ionization. As well as applications of neutral beam heating in tokamaks, we expect such data to be very useful in interpretation of cometary x-ray spectra [46–48]. Here, neutral material outgassing from the comet nucleus encounters highly charged ions in the solar wind. The ensuing charge-exchange collisions populate highly excited states of the solar wind ions, followed by x-ray emission as these states radiatively decay. An astrophysically relevant experiment would require trapped ions of C, N, O, or Ne, and the admission to the EBIT chamber of the appropriate neutral gas, i.e., H_2O , CO_2 , etc.

Among our line identifications are several lines with potential for electron-density diagnostics. The density sensitivity arises because the relative populations among the different levels of the ground configurations varies with density. If this results in higher population accumulating in a level of higher angular momentum (i.e., the $2s^22p^2P_{3/2}$ in Kr XXXII, the $2s^22p^2^3P_2$ in Kr XXXI, or the $2s^22p^3^2D_{5/2}$ in Kr XXX) than the ground level, then excitations to levels among the $n=3$ configurations with higher angular momentum than are possible from the ground state alone, result. Hence new lines from these high angular momentum level states become visible at higher densities.

In Fig. 3(a) we show two line intensity ratios in Kr XXXII that vary as a result of $n=3$, $j=5/2$ levels becoming excited, calculated for an electron temperature of 2×10^7 K. The electron densities over which this ratio varies is $10^{19} - 10^{21} \text{ cm}^{-3}$, which is the relevant density range for high Z underdense plasma radiators. This should be very useful, since the density diagnostic available in the Kr K -shell spectrum, the ratio of the $1s^2^1S_0-1s2p^3P_2$ to either of the $1s^2^1S_0-1s2p^1^3P_1$ lines only becomes sensitive at densities greater than 10^{21} cm^{-3} , i.e., higher than is usually achieved in such experiments. One solution to this is to suspend pellets of material of slightly lower Z in the Xe filled enclosure, so that the corresponding He-like transitions are sensitive in the right range. This would be most appropriate in the hottest regions of the Xe enclosure, since Kr and similar ions will be ionized beyond the B-like charge state, but elsewhere the B-like density diagnostic we discuss might be preferable. We note that previously discussed L shell diagnostics in Xe [6,49] for the electron temperature are still dependent on the electron density, due to the density sensitivity of the dielectronic recombination process and the ionization balance itself in such experiments. The density diagnostic we identify is much less dependent on the electron temperature, and would go some way towards resolving such ambiguities.

Further density sensitive line ratios at the same electron temperature in Kr XXXI and Kr XXX are plotted in Fig. 3(b), which may have applications to tokamak plasmas with density in the range $10^{12} - 10^{14} \text{ cm}^{-3}$.

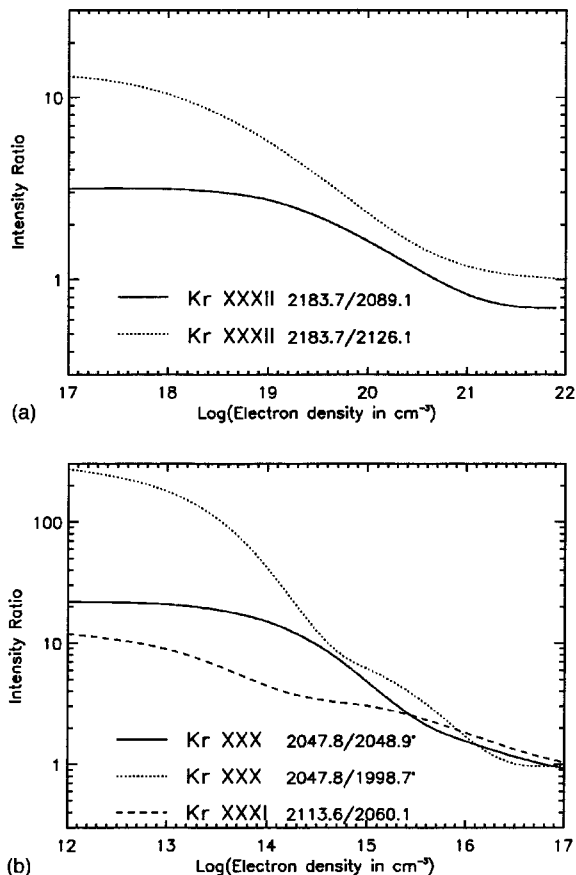


FIG. 3. Electron-density ($\log_{10}n_e$) dependence of line intensity ratios at electron temperature $T_e=2 \times 10^7$ K calculated with a model described in Sec. IV for selected transitions in Kr XXX–XXXII (identified in Table II).

VI. CONCLUSION

We have demonstrated the value of using an EBIT plasma model for the analysis of complex and only partially resolved x-ray spectra obtained with a broadband high-resolution x-ray detector. This approach can be applied in the determination of numerous physical characteristics of the EBIT plasma, such as measurements of important reaction rates and the validation of diagnostic line ratios. In this paper we have identified many new lines in the spectra of L -shell Kr ions, some with diagnostic potential applicable in other fields of plasma physics, and have made progress towards understanding conditions in the EBIT trap itself.

ACKNOWLEDGMENTS

The authors thank D. J. Alderson for his technical support. I.K. acknowledges support from the Swedish Foundation for Cooperation in Research and Higher Education (STINT). J.M.L. was supported by NASA Contract W 19353 (Applied Information Systems Research Program) and ONR/NRL 6.1 Research Option ‘‘Solar Magnetism and the Earth’s Environment.’’

ments presented here.) The radius ρ_0 is typically taken to be the radius of the electron beam a . The offset V_0 can be chosen in order to satisfy boundary conditions appropriate for thermal distributions, namely that $V(\rho=0)=0$. In this case V_0 represents the potential at the radius of the electron beam relative to the center of the trap, and it is relatively insensitive to the electron distribution $n_e(\rho)$. For example, for a constant electron density distribution V_0 is given by

$$V_0 = \frac{\lambda}{4\pi\epsilon_0}. \quad (2)$$

For a Gaussian beam distribution of the same width and total linear charge density, we calculate V_0 to be

$$V_0 = 1.08 \frac{\lambda}{4\pi\epsilon_0} \quad (3)$$

and we expect any reasonable distribution to have a similar offset V_0 . The total radial potential can therefore be approximated as

$$\frac{V(\rho)}{V_0} \approx \begin{cases} 2 \ln(\rho/a) + 1 & \rho > a \\ (\rho/a)^2 & \rho \leq a \end{cases}, \quad (4)$$

where $V_0 = \lambda/4\pi\epsilon_0$. This is equivalent to modeling the electron distribution as a constant density $\lambda/4\pi\epsilon_0$ for $\rho < a$. The total trap depth in the radial direction is given by Eq. (4) evaluated at the inner radius R of the trap electrodes, $\Delta V_\rho = V(R)$.

In the axial direction the trap electrodes provide a radially independent, nearly square well potential. The walls of this axial potential lie outside the field of view of our camera, and do not directly affect the visible ion distribution, apart from determining the overall temperature. Given the very fast axial motion of an individual ion, any ion with enough velocity in the z direction to escape the trap will do so within between 1 and 100 μs , so the trap depth ΔV_z determines the largest possible axial velocity in the trap. In addition to the applied end cap voltage V_z , the axial trap depth ΔV_z has an additional contribution V_{im} arising from the geometry of the trap. The additional potential is an image charge effect arising from the electron beam passing through the constriction of the radial opening in the trap electrodes from the inner diameter of the trap ($R=5$ mm) to the inner diameter of the end cap electrodes ($r=1.5$ mm): $\Delta V_z = V_z + V_{\text{im}}$ (see Fig. 1). This offset is determined by the logarithm of the ratio of inner electrode radii. It also scales with $\lambda/4\pi\epsilon_0$, and is given by

$$\frac{V_{\text{im}}}{V_0} \approx \ln\left(\frac{5 \text{ mm}}{1.5 \text{ mm}}\right) \approx 2.4. \quad (5)$$

The axial image charge potential is smaller than the radial space charge contribution, and is typically less than 30 or 40 V.

If the ion densities are not small, then the image potential from the ions themselves must also be added to the trap. The distributions of all the ion charge states $n_i(\rho)$ are not necessarily known, but under the assumption that the ions are in thermal equilibrium, the shape of the individual ion distributions $n_i(\rho)$ can be determined self-consistently by

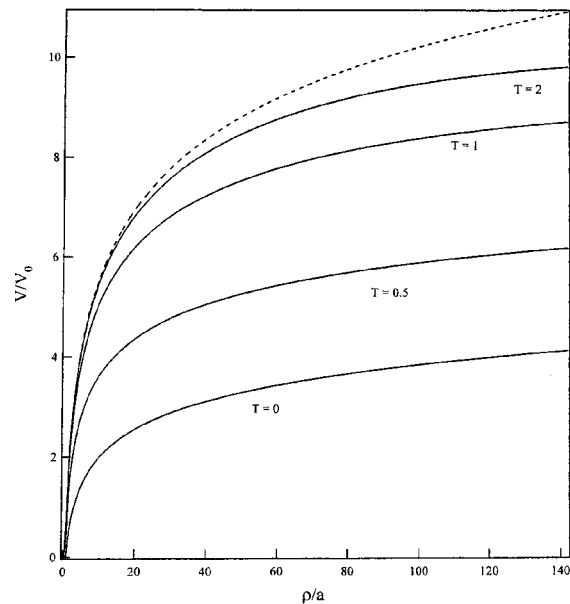


FIG. 5. The self-consistent solution for the total electric potential arising from the electron beam and an ion cloud in thermal equilibrium. The dashed line represents the potential from the electrons only (i.e., no neutralization). The solid lines represent the potential including an ion cloud containing 65% of the total charge of the electron beam, with different scaled temperatures as indicated. The scaled temperature is given by kT/QV_0 .

requiring that they obey Boltzmann distributions. At low temperatures where the ions are concentrated near the electron beam, we expect the total potential depth to scale approximately with the total linear charge density $\lambda_{\text{tot}} = \lambda_e + \lambda_{\text{ion}}$. At higher temperatures the degree of neutralization will be less since the ions do not overlap well with the electron beam. A simple model which shows this effect assumes that there is only one charge state Q_i in the trap. Figure 5 shows the total combined potential from the electron beam and a self-consistently determined thermal distribution of ions which has 65% of the total charge of the electron beam. At low ion temperature, the total potential depth is neutralized by roughly 65%, but at the highest temperatures the potential compensation is only 10%. We also find that due to this weak neutralization, the *shape* of the ion cloud at higher temperature has a surprisingly weak dependence on the number of ions in the trap.

Regardless of the exact form of each $n_i(\rho)$, trapped ions always weaken the radial confinement and lower the total radial trap depth ΔV_ρ at a given temperature. Since ΔV_ρ is entirely due to the electron space charge but only a portion of ΔV_z is, the addition of the ion space charge decreases ΔV_ρ relative to ΔV_z . Given the right conditions, changes in the value of $\Delta V_\rho/\Delta V_z$ as the trap is increasingly neutralized should be observable, providing a rough measure of the electron beam neutralization by ions. Due to the insensitivity of the trap potential to high temperature ion clouds (as argued above and demonstrated in Fig. 5) a decrease in ΔV_ρ is likely to be more easily observable for cold ion clouds. Indeed, for the ion clouds described here, we do not see a weakening of ΔV_ρ .

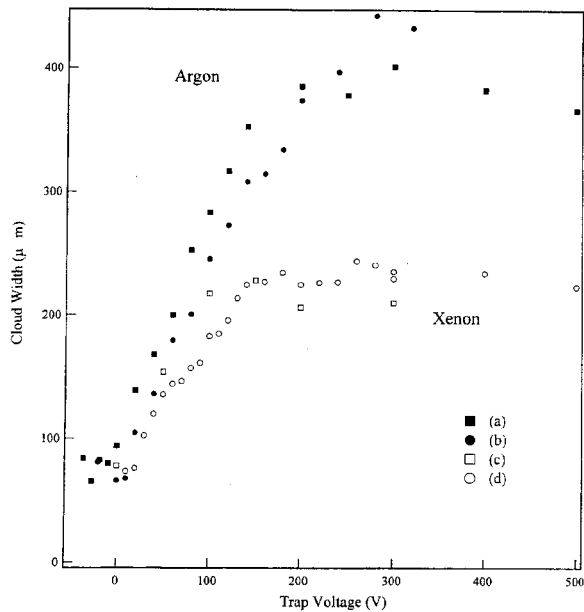


FIG. 6. The width of the ion cloud image as a function of static trapping voltage V_z . The EBIT parameters for the different data labeled as shown are given in Table II.

B. Static ion cloud widths

In order to quantify the thermal expansion of the cloud, for each image we calculated a width for the imaged distribution. Given the shape of the distributions, which are not well described by Gaussian or Lorentzian functions under all conditions, the full width at half maximum is not very indicative of the average width of the cloud. We therefore calculated the weighted average width by integrating over the image

$$x_{\text{rms}}^2 = \frac{\int I(x)x^2 dx}{\int I(x) dx}. \quad (6)$$

Here, $I(x)$ is the intensity of the image at a given position, and x is measured from the position of peak intensity. (The largest integration range is limited by the slits in the end cap electrodes, which mask the image at $\pm 1200 \mu\text{m}$.) The resulting widths as a function of end cap trapping voltage are shown in Fig. 6 for four different measurements. The different electrostatic trapping conditions in each of the measurements are given in Table II.

We expect the ion cloud's dependence on V_z to separate into three regimes corresponding to (i) an open trap at negative V_z ($\Delta V_z < 0$), (ii) a closed trap at intermediate V_z which is dominated by axial losses ($0 < \Delta V_z < \Delta V_\rho$), and (iii) an axially closed trap at large V_z which has saturated due to the increased prominence of radial losses at the inner surface of the electrodes ($\Delta V_z > \Delta V_\rho$). Based on the preceding discussions it seems appropriate to scale all trapping potentials by $V_0 = \lambda/4\pi\epsilon_0$; and the widths of the ion clouds plotted against the scaled trap voltage is shown in Fig. 7. The cross-over from the axial loss dominated to the radial loss dominated trap can be seen at $\approx 11V_0$ for both the argon and xenon measurements.

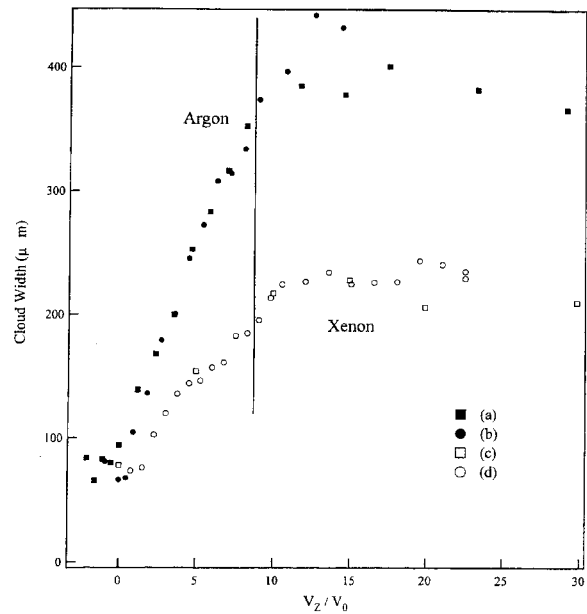


FIG. 7. The widths from Fig. 6, but plotted as a function of the scaled trapping voltage, V_z/V_0 . The vertical line indicates the total radial depth of the trap in the low ion density limit, $V_z - V_{\text{im}} = 9.6V_0$.

The axial trap depth $\Delta V_z = V_z + V_{\text{im}}$ is equal to the radial trap depth when $V_z = \Delta V_\rho - V_{\text{im}}$. Equation (4) gives $\Delta V_\rho = V(R) \approx 11V_0$. Without substantial trap neutralization the transition from V_z -dependent to V_z -independent behavior should occur roughly at $V_z = 11V_0 - 2.4V_0 = 9.6V_0$. The data in Fig. 7 become independent of the axial potential at a reasonably well defined value of V_z which is somewhat above this value. A direct comparison between ΔV_ρ and ΔV_z can provide information about the trap neutralization, and the relative sharpness of the transition indicates that it might be possible to use ion images to roughly measure the neutralization of the beam. In particular, for the xenon measurements where the beam neutralization would be largest the transition occurs at the same large value of V_z/V_0 as for argon. Since neutralization of the radial potential should lower the saturation point, this indicates that the beam is not very neutralized. This analysis is complicated by the fact that hot ion clouds are not effective at neutralizing the radial potential, as discussed above and shown in Fig. 5. The technique should be more effective for ions that are cooled by simultaneous injection of lower charged ions. This simple argument also ignores the possible differences in radial and axial escape rates, which are determined by the different velocity diffusion rates in the two directions due to the presence of the magnetic field. One might expect that a substantial difference in diffusion rates would smear out the transition to the radial loss regime, but a detailed description of the diffusive behavior is needed to fully interpret the images.

The transition to the open trap regime when $\Delta V_z = 0$ is difficult to observe using the ion cloud widths because the signal vanishes as the trap is made shallower. The time scale for highly charged ion production is much larger than a single axial transit time, and ions leave the open trap before

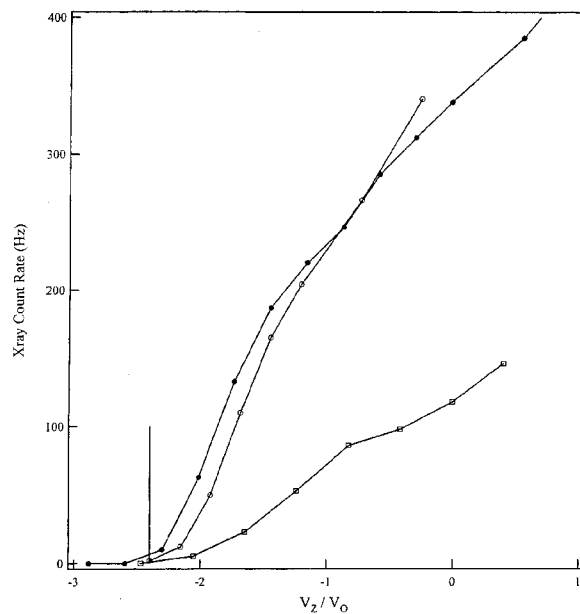


FIG. 8. The x-ray count rate from neon-like xenon (Xe^{44+}) as a function of the scaled end cap voltage V_z/V_0 . The vertical line marks the calculated values of V_z/V_0 for an open trap, $V_{\text{im}}/V_0 = -2.4$. The data were taken at electron beam currents of 120 mA (open circles), 100 mA (filled circles), and 70 mA (squares). The beam energy was 8 keV.

they can be sequentially ionized to high charge state. We can, however, use the vanishing of the total collected light as a function of V_z to measure the point $V_z = -V_{\text{im}}$ at which the trap is "open." Since we are measuring the intensity and not the actual spatial distribution of ions, the measurement can be made using any fluorescence proportional to the number of ions in the trap, e.g., x-ray fluorescence. (X-ray lines are easier to measure because most of the emission of highly charged ions occurs in the x-ray regime, and x-ray count rates are typically much larger than visible or UV rates.) As an example we show in Fig. 8 the total x-ray fluorescence of the neon-like lines in Xe^{44+} as a function of V_z/V_0 . The x-rays were collected in the 3–5 keV range with a solid state detector. Since the ion density is necessarily small when the trap is nearly emptied, we can safely use Eq. (5). The three data sets were taken at conditions where V_0 differed by a factor of 1.7, but they clearly indicate that the trap empties at $V_z \approx -2.4V_0$, in agreement with the simple calculation of Eq. (5).

In the intermediate regime, where the cloud width is approximately linear in V_z , the cloud size can be used as a temperature diagnostic. Since the ion cloud shape is determined by the ratio of the trap depth to the temperature, it is useful to scale the temperature by $Q_i V_0$. In the absence of interactions between different charge states, the scaled temperature would be roughly the same for all charge states at a given V_z/V_0 . This is because without cooling from lower charge states of the ion the temperature would increase until the ion cloud filled the trap. Highly charged ions would see a much deeper potential, but the temperature would be proportionally higher, leaving the spatial distribution approximately the same. Interactions among the different charge states tend

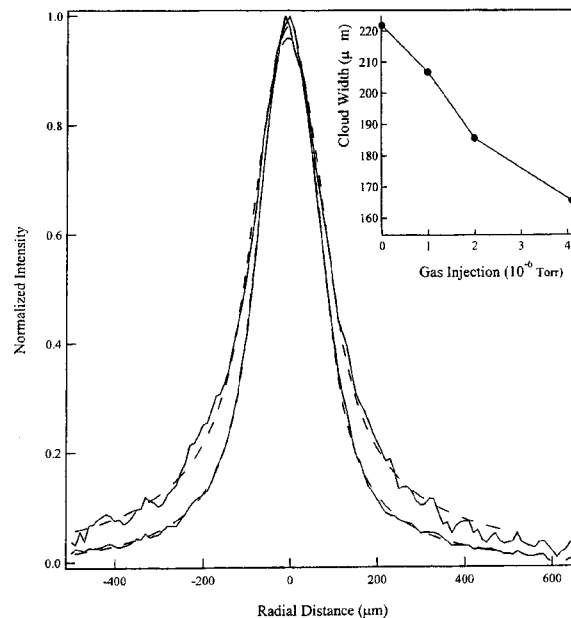


FIG. 9. A plot showing the effect of low charged nitrogen cooling ions on the spatial distribution of Xe^{32+} ions. The narrower image was taken with 4.1×10^{-6} Torr of nitrogen in the gas injection chamber, while no nitrogen was added for the wider image. All other trap conditions were identical. The pressure of xenon gas in the injection chamber was 2.7×10^{-7} Torr and the end cap voltages were set to 300 V. The dashed lines are fits to a truncated Boltzmann distribution, with temperatures of $0.77Q_i V_0$ and $0.9Q_i V_0$. The inset shows the width of Xe^{32+} ion cloud as a function of nitrogen gas pressure in the injection chamber.

to drive the ions toward equilibrium, so that ions of higher charge Q_i have a smaller spatial distribution and smaller scaled temperature $kT/Q_i V_0$ than ions of lower charge state. This can clearly be seen in Fig. 7. The slope of width versus V_z/V_0 for xenon ions ($Q = 32e$) is roughly half that for the argon ions ($Q = 16e$) under similar scaled trap conditions.

Using a separate low charged cooling gas, we can see the effects of reduced temperature directly on a single charge state without having to compare different ions. Figure 9 shows two Xe^{32+} images taken with and without the simultaneous injection of nitrogen, which acts as a cooling gas. The intensity from the cooled ion cloud was a factor of 3 larger than from the uncooled cloud, so the data have been scaled in order to compare the shapes. The cloud width as a function of injection gas pressure is plotted in the inset of the figure. Clearly the cloud width provides a qualitative measure of the ion cloud temperature.

In order to determine more quantitative measures of the temperature, more detailed modeling of the distribution is required. The simplest estimate assumes a thermal distribution in the low ion density limit. For a classical distribution in the static thermal limit, the effects of the magnetic field can be ignored,¹³ so $V(\rho)$ should represent only the electrostatic potential. The logarithmic potential in Eq. (4) results in a Boltzmann distribution $\exp(-(Q_i V(\rho)/kT))$ that has a power law dependence on ρ . A fit to this distribution is shown as the dashed lines in Figs. 3, 4, and 9. Despite the reasonable agreement with the data, the temperature determined from

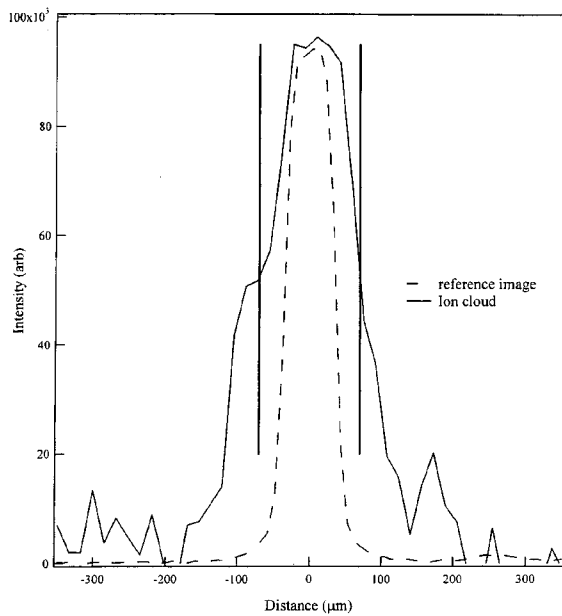


FIG. 10. A representative ion cloud image at low trapping voltage V_z . The ion is Xe^{31+} at $V_z=0$ V, which corresponds to a scaled trap depth of roughly $2.4V_0$. The vertical lines represent the maximum possible radial extent of ions with less than this energy. The dashed line is an image of a $75 \mu\text{m}$ pinhole taken with the imaging system.

such a fit must be interpreted with care. One limitation of the model is the finite lifetime of the visible lines we observe. Despite being longer than any of the dynamical scales for individual ions, fluorescence from an ion requires that the ion has been excited within the last few milliseconds. The predominant source of excitation is the electron beam, and for very hot distributions there are likely to be some ions whose trajectories are completely outside the beam and will remain dark. (Excitation rates from collisional processes including charge exchange with background gas are expected to be much lower.¹⁴) The effect this has on the *shape* of the visible distribution must be determined from more complicated distribution modeling.

Another interesting limitation of the simple Boltzmann distribution is that it is not normalizable at temperatures $kT \geq kT_{\text{max}} = Q_i V_0$. A logarithmic potential is simply too weak to support a bound, high temperature ion cloud and very energetic ion clouds are necessarily nonthermal. In the EBIT the Boltzmann distribution is necessarily truncated at $\rho = R$. At low temperature this does not significantly alter the distribution. At high temperature, however, the cooling rate increases as T approaches T_{max} from below, since the truncation of the distribution at R cuts out an increasing fraction of the ions. The increased flux of ions from small to large ρ implies that the role of the magnetic field must be considered in determining the shape of the distribution. In addition, the ion temperature (to the extent that it can be defined) is not expected to be much larger than T_{max} . The temperatures determined from the fits behave qualitatively similar to the widths shown in Fig. 6. Using the truncated Boltzmann distribution, the largest fit temperatures kT_{fit} were less than $\approx 1.0QV_0$. The fits were relatively poor at large radius for

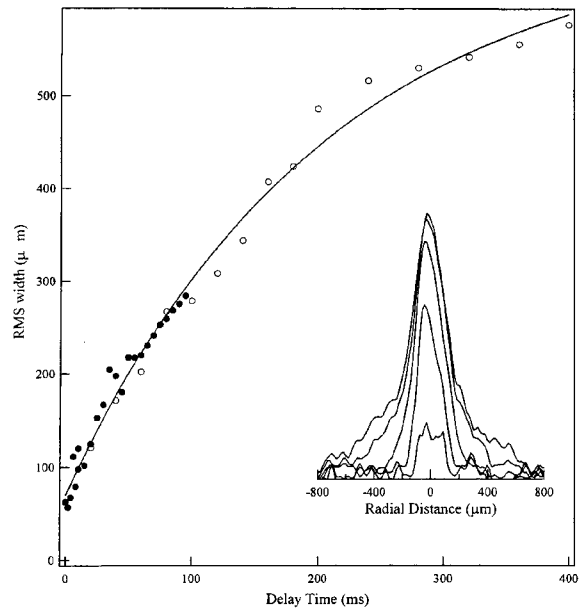


FIG. 11. The width of Ar^{13+} ion clouds as a function of time after raising the end cap voltage to 300 V. The widths were determined from images like those shown in the inset. (The images shown were collected in a 5-ms-wide time window at increasing delay times of 0, 4, 20, 60, and 95 ms, in order of increasing width.) The different symbols represent data taken under similar conditions but on separate occasions several months apart. The electron beam energy and current was 7.25 kV and 89 mA, respectively. The solid line is a fit to a simple exponential, which gives a time constant of 210 ms.

the high temperature argon data, as can be seen in Fig. 3.

Understanding the conditions for nonthermal distributions is important for determining the ion cloud distribution in a given experiment. A nonthermal ion cloud could be manifest as a nonthermal form for the distribution in the ρ , z , v_ρ , and v_z components, or as an inequilibrium between different phase space directions ρ - z and v_ρ - v_z . Directly imaging the ions' radial distribution can help provide information about the ρ and v_ρ dependence. These effects should be largest at low density, where the ion-ion collision rate is too low relative to the escape rate to establish equilibrium. The cylindrical symmetry implies that the radial and axial motions are not well mixed without collisions. We can look for indications of nonthermal distributions at low trap depths where the ion density is necessarily small.

In all weakly trapped ion clouds we've observed, the width of the cloud appeared larger than expected based on estimates^{15,16} of the cloud temperature under equilibrium conditions. For example, Fig. 10 shows a Xe^{32+} ion cloud at $V_z=0$ V, which corresponds to a trap depth of about $2.4V_0$. Given reasonable estimates of the ion cloud temperature¹⁶ under equilibrium conditions, the cloud width should not substantially exceed that of electron beam. In fact, the *maximum* energy possible for any ion in a roughly thermalized cloud (i.e., a truncated Boltzmann distribution) would be $Q_i \Delta V_z$. The radius at which the radial potential equals this energy, $V(\rho_{\text{max}}) = \Delta V_z$, is only about $70 \mu\text{m}$. The ion cloud appears considerably wider than even this maximum width. This could indicate a nonequilibrium distribution and a smaller than thermal overlap with the electron beam. An-

other possible explanation could arise from instabilities in the electron beam that time average to give a wider electron distribution. Given the significant implication of this finding for numerous EBIT experiments, we carefully tested the camera imaging system to determine its resolution in order to rule out instrumental sources for the excess widths. The dashed line in Fig. 10 is a reference image of an illuminated $75\ \mu\text{m}$ pinhole taken with exactly the same imaging arrangement as the EBIT images. The pinhole is roughly the diameter of the electron beam, and indicates a total instrument resolution of about $25\ \mu\text{m}$.

C. Dynamic ion cloud widths

The speed at which the intensified CCD can be gated provides us with the possibility of measuring ion cloud dynamics. As an example, we quickly raised the end cap voltages on an originally empty trap and watched the ion cloud develop toward equilibrium. This process requires first the production of ions and then the subsequent heating and diffusion of the ions to their steady state distribution. Several images taken while viewing the Ar^{13+} line are shown in the inset of Fig. 11. The images were created by repeatedly dumping the trap, then raising the end caps to 300 V at $t=0$. The signal was summed in a delayed, 5-ms-wide time window. The widths as a function of the time after raising the end cap voltages are shown in Fig. 11, and the total integrated intensity is shown in Fig. 12. The intensity of the line was also monitored simultaneously with a time resolved spectrometer whose input and output slits were opened to 1 mm, and the spectrometer signal is included in the inset to Fig. 12 for comparison. The experiment was performed at a beam energy of 7.25 kV, which is much larger than the ion-

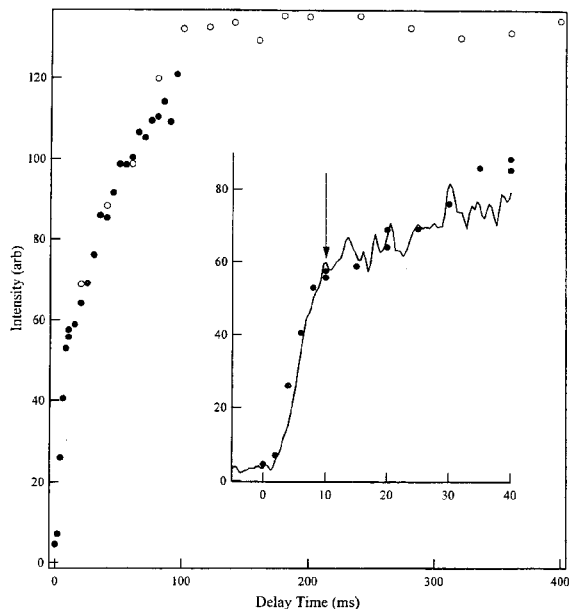


FIG. 12. The total intensity of Ar^{13+} ion cloud image as a function of time for the conditions described in Fig. 11. The inset shows an expanded view of the early times. The solid line of the inset is simultaneous data taken with a spectrometer observing the same line in Ar^{13+} .

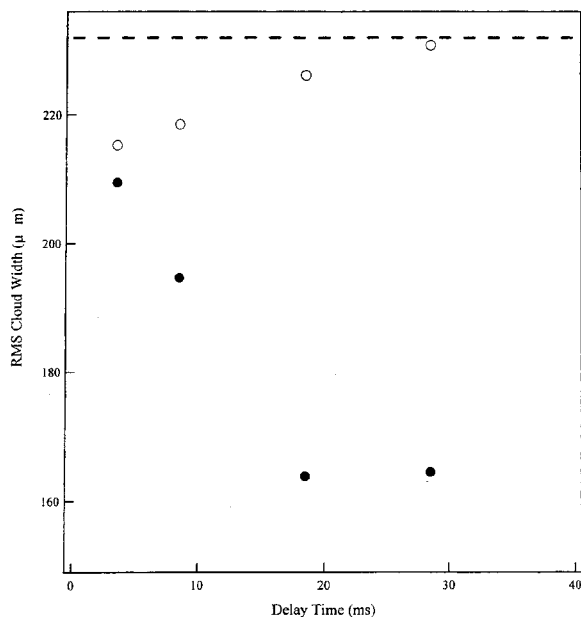


FIG. 13. The width of Xe^{32+} ion clouds as a function of time after quickly lowering the trapping voltage from 300 to 230 V at $t=0$. The dashed line represents the static equilibrium cloud width established for times $t<0$. For the solid circles, the end caps were held at 230 V. For the open circles, the end caps were subsequently raised back to 300 V after 2.5 ms.

ization potential for Ar^{13+} ($\approx 750\ \text{eV}$). In this case, at very early times when the ions have not been substantially heated, the production and loss rates of a given charge state are determined largely by electron impact ionization.¹⁷ In this particular measurement, it turns out that the time scale for ion production is sufficiently smaller than the time scale for ion heating that the two time scales can be distinguished, as indicated by the arrow in Fig. 12. Clearly, a large fraction of the Ar^{13+} ions are produced within 10 ms, a time scale determined by electron impact ionization cross sections. As the ion cloud heats up, other charge changing and loss processes become important (e.g., charge exchange and ion evaporation) and the net rate of ion production slows down.

The initial production time scale is consistent with estimates made from the electron current density and the ionization cross sections for argon. The characteristic time to produce ions depends on the sum of the characteristic times of all the lower charge states, $\tau = \sum \tau_i$, where the individual times depend on the current density and the electron impact ionization cross section σ_i^{EI} , $\tau_i = eI(J\sigma_i^{\text{EI}})$. This is dominated by the cross sections of the last few charge states, which are on the order of 10^{-20} – $10^{-19}\ \text{cm}^2$ for Ar^{13+} through Ar^{9+} .¹⁸ With a current density of $J \sim 2000\ \text{A cm}^{-2}$ ($J/e \approx 12 \times 10^{21}\ \text{s}^{-1}\ \text{cm}^{-2}$) the estimated time for Ar^{13+} production is approximately 5–10 ms. The slower evolution associated with the increase of ion cloud widths occurs on a time scale in excess of 200 ms. Systematic studies of the time scale dependence on the ion charge state, ion density, electron energy, and electron density should allow an experimental determination of heating rates.

As another example of the usefulness of the dynamic imaging, we performed preliminary measurements designed

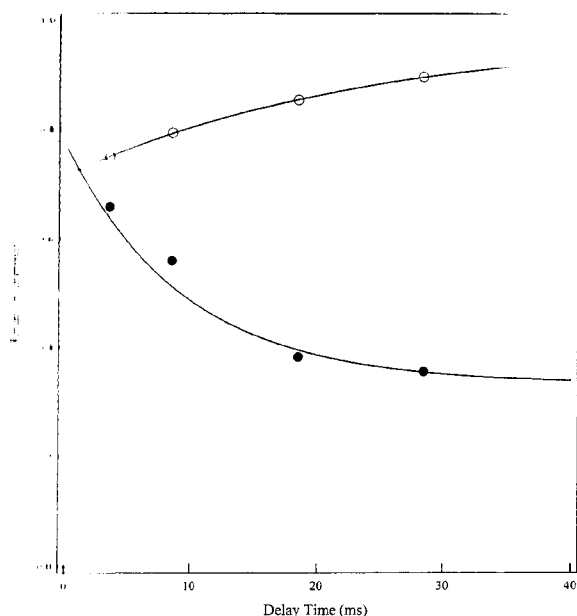


FIG. 14. The intensity of Xe^{32+} ion clouds as a function of time for the same conditions described in Fig. 13. The intensities have been scaled by the static equilibrium intensity. The solid lines are fits to simple exponential

to observe velocity diffusion. When the axial trap depth is rapidly lowered, ions with axial velocity v_z large enough to exit the trap will leave within one axial transit time, which for hot ions is less than $10 \mu\text{s}$. Ions which have enough total energy to leave the trap but which have large radial and azimuthal velocities v_ρ and v_ϕ and small v_z will not leave the trap until the velocity components have been partially mixed. Velocity mixing can occur via collisions or trap imperfections. We can use the camera to watch the mixing process. We performed two similar experiments while viewing the Xe^{32+} line. A nearly steady state ion cloud was prepared by leaving the end cap voltages at 300 V for 300 ms. In the first measurement, we lowered the end cap voltages to 230 V at $t=0$ for 2.5 ms, and then raised the end caps back to 300 V. The rise and fall times for the end cap switching were ≈ 0.7 ms. We followed the ion cloud evolution by taking 5-ms-long images at different delay times after the trap depth was lowered. In the second measurement, we simply lowered the end cap voltages to 230 V without raising them again. The widths and intensity of the resulting cloud dynamics are shown in Figs. 13 and 14. The images show a drop in intensity of about 25% at $t=0$, corresponding to the loss of ions with large axial velocities. The relaxation of the

remaining ions occurs on a time scale of approximately 10–20 ms after the $t=0$ trap switch. This technique clearly shows potential for studying collisional dynamics which are extremely difficult to observe using other techniques, and the dynamic capabilities of the imaging system can provide information about the heating, cooling, and collision rates within the ion cloud.

ACKNOWLEDGMENTS

The authors would like to thank D. J. Alderson for technical assistance in the lab, E. Takács and M. Laming for helpful discussions, and E. Träbert for helping initiate this experiment. I. K. acknowledges support from the Swedish Foundation for International Cooperation in Research and Higher Education (STINT).

- ¹J. D. Gillaspay, *Phys. Scr.*, T **T65**, 168 (1996).
- ²P. Beiersdorfer, G. V. Brown, J. C. LopezUrrutia, V. Decaux, S. R. Elliott, D. W. Savin, A. J. Smith, G. S. Stefanelli, K. Widmann, and K. L. Wong, *Hyperfine Interact.* **99**, 203 (1996).
- ³D. Schneider, *Phys. Scr.*, T **T59**, 189 (1995).
- ⁴S. B. Utter, P. Beiersdorfer, J. C. Lopez-Urrutia, and K. Widmann, *Nucl. Instrum. Methods Phys. Res. A* **428**, 276 (1999).
- ⁵C. A. Morgan, F. G. Serpa, E. Takács, E. S. Meyer, J. D. Gillaspay, J. Sugar, J. R. Roberts, C. M. Brown, and U. Feldman, *Phys. Rev. Lett.* **74**, 1716 (1995).
- ⁶D. Schneider, D. Dewitt, M. W. Clark, R. Schuch, C. L. Cocke, R. Schmieder, K. J. Reed, M. H. Chen, R. E. Marrs, M. Levine, and R. Fortner, *Phys. Rev. A* **42**, 3889 (1990).
- ⁷L. P. Ratliff, E. W. Bell, D. C. Parks, A. I. Pikin, and J. D. Gillaspay, *Rev. Sci. Instrum.* **68**, 1998 (1997).
- ⁸F. G. Serpa, J. D. Gillaspay, and E. Traebert, *J. Phys. B* **31**, 3345 (1998).
- ⁹E. Traebert, P. Beiersdorfer, G. V. Brown, A. J. Smith, S. B. Utter, M. F. Gu, and D. W. Savin, *Phys. Rev. A* **60**, 2034 (1999).
- ¹⁰D. A. Church, *Phys. Scr.*, T **T59**, 216 (1995).
- ¹¹J. D. Gillaspay, *Phys. Scr.*, T **T71**, 99 (1997).
- ¹²C. A. Morgan, F. G. Serpa, E. Takács, E. S. Meyer, J. D. Gillaspay, J. Sugar, J. R. Roberts, C. M. Brown, and U. Feldman, *Phys. Rev. Lett.* **74**, 1716 (1995).
- ¹³R. P. Feynman, R. B. Leighton, and M. Sands, *Lectures on Physics* (Addison-Wesley, Reading, MA, 1966).
- ¹⁴P. Beiersdorfer, L. Schweikhard, J. C. LopezUrrutia, and K. Widmann, *Rev. Sci. Instrum.* **67**, 3818 (1996).
- ¹⁵B. M. Penetrante, J. N. Bardsley, D. DeWitt, M. Clark, and D. Schneider, *Phys. Rev. A* **43**, 4861 (1991).
- ¹⁶P. Beiersdorfer, A. L. Osterheld, V. Decaux, and K. Widmann, *Phys. Rev. Lett.* **77**, 5353 (1996).
- ¹⁷E. Sokell, F. J. Currell, H. Shimizu, and S. Ohtani, *Phys. Scr.*, T **T80B**, 289 (1999).
- ¹⁸M. A. Lennon, K. L. Bell, H. B. Gilbody, J. G. Hughes, A. E. Kingston, M. J. Murray, and F. J. Smith, *J. Phys. Chem. Ref. Data* **17**, 1285 (1988).
- ¹⁹B. Edlen, *Mon. Not. R. Astron. Soc.* **114**, 700 (1954).
- ²⁰F. G. Serpa, J. D. Gillaspay, and E. Traebert, *J. Phys. B* **31**, 3345 (1998).
- ²¹C. A. Morgan, F. G. Serpa, E. Takács, E. S. Meyer, J. D. Gillaspay, J. Sugar, J. R. Roberts, C. M. Brown, and U. Feldman, *Phys. Rev. Lett.* **74**, 1716 (1995).
- ²²Calculated using the relativistic Cowan code.
- ²³F. G. Serpa, C. A. Morgan, E. S. Meyer, J. D. Gillaspay, E. Traebert, D. A. Church, and E. Takács, *Phys. Rev. A* **55**, 4196 (1997).

X-ray radiation

Polarization measurements on a magnetic quadrupole line in Ne-like barium

E. Takács,* E. S. Meyer, J. D. Gillaspy, and J. R. Roberts

Atomic Physics Division, National Institute of Standards and Technology, Gaithersburg, Maryland 20899

C. T. Chantler,† L. T. Hudson, and R. D. Deslattes

Quantum Metrology Division, National Institute of Standards and Technology, Gaithersburg, Maryland 20899

C. M. Brown and J. M. Laming‡

E. O. Hulburt Center for Space Research, Naval Research Laboratory, Washington, D.C. 20375

J. Dubau

Observatoire de Paris, CNRS UPR No. 176, 92195 Meudon Cedex, France

M. K. Inal

Institut des Sciences Exactes, Departement de Physique, Boite Postale 119, 13000 Tlemcen, Algeria

(Received 12 December 1995)

We have measured the absolute polarization of the $2p^6\ ^1S_0 - 2p^5(^2P_{3/2}^o)3s[3/2]_2^o$ magnetic quadrupole transition in Ne-like barium, excited in an electron-beam ion trap at a variety of energies. We find strong evidence for the existence of resonant excitation processes that are not explained by our collisional-radiative calculations even when the polarization arising from impact excitation is included. At energies well away from where the resonances occur, the agreement between experiment and theory is good. [S1050-2947(96)06208-7]

PACS number(s): 32.10.-f, 32.30.Rj, 34.80.Kw

I. INTRODUCTION

In the absence of strong external electric or magnetic fields, atomic states differing in magnetic quantum number, but otherwise having identical principal and angular momentum quantum numbers, are degenerate in energy. Since the magnetic quantum numbers describe the spatial orientation of the atom's electron charge cloud, there may still be observable differences between such degenerate states if some type of spatial asymmetry is present. For example, if collisional excitation occurs by impact in a preferred direction, the magnetic sublevels of the excited state can be populated with nonstatistical probabilities. When the state decays, the emitted electromagnetic radiation will be spatially anisotropic and partially polarized [1].

Anisotropic excitation mechanisms are quite common in astrophysical plasmas and are readily reproduced in a laboratory environment. In solar flares, ions and atoms can be excited by electrons moving along fixed magnetic field lines, which give rise to a preferred direction in space [2]. A similar situation occurs in supernova shock waves [3] and also in polar aurorae and possibly in jets in active galactic nuclei. On earth, there have been many crossed-beam or beam-foil studies whereby atoms and ions are excited in a spatially asymmetric way [4].

In the experiment described in this paper, we study the

polarization of radiation emitted from ions that have been excited by impact with a unidirectional monoenergetic electron beam inside an electron-beam ion trap (EBIT). The EBIT is a powerful tool for creating very highly charged ions for atomic structure and electron-ion interaction studies. Techniques for measuring electron-impact ionization [5], excitation [6], and recombination [7] cross sections using an EBIT have been demonstrated; however, these measurements have all been adjusted to take into account polarization effects.

Inside an EBIT, the ions interact with a narrow (about 60- μm -diam) beam of electrons. This well-collimated electron beam acts as a quantization axis, creating a cylindrically symmetric environment for the ions. Care must be taken then in interpreting emission line intensities when they are used for obtaining electron-ion interaction cross sections. Polarization of the emitted radiation is especially important when measurements are made with spectrometers in which the energy disperser is polarization selective (e.g., Bragg crystal x-ray spectrometers). Even when a polarization-insensitive energy detector is used [e.g., solid-state Si(Li) detector], polarization is important because the detector is generally positioned normal to the electron beam rather than at the "magic angle" of 55° (i.e., the angle θ at which polarization for dipole radiation disappears, given by $\cos^2\theta=1/3$). Depending upon the experiment, however, polarization can be a tool rather than a complication in the analysis. The measurement of the polarization or the angular distribution of photon emission gives information about the magnetic sublevels involved in electron-ion collisions that would normally remain hidden in a simple energy dispersive measurement. As we will illustrate below, polarization-sensitive measurements may also be used to detect resonance processes that would

*Also at Experimental Physics Department, Kossuth University, Debrecen, Bem t. 18/a., Hungary.

†Present address: School of Physics, University of Melbourne, Parkville, Victoria 3052, Australia.

‡Also at SFA Inc., Landover, MD 20785.

otherwise be too weak to be observed directly. In what follows, the polarization P is defined as

$$P = \frac{I_{\parallel}(90^{\circ}) - I_{\perp}(90^{\circ})}{I_{\parallel}(90^{\circ}) + I_{\perp}(90^{\circ})}, \quad (1)$$

where $I_{\parallel}(90^{\circ})$ and $I_{\perp}(90^{\circ})$ are the intensities of the parallel and perpendicularly polarized radiation measured at 90° with respect to the axis of symmetry (the electron-beam direction in our experiment).

II. OBSERVED Ne-LIKE $M2$ TRANSITION

In the standard spectroscopic notation for $J_1 l$ (pair) coupling [8] used for noble-gas spectra, the spectral line we report on in this paper arises from the $2p^6 \ ^1S_0 - 2p^5 \ (^2P_{3/2}^o) 3s \ [3/2]_2^o$ magnetic quadrupole transition in Ne-like barium (hereinafter referred to as the $M2$ transition or the $M2$ line). This transition was originally observed in Ne-like iron created in the solar corona [9]. It has since been observed in several other Ne-like systems in a laboratory Tokamak source [10], as well as in an EBIT [11]. In barium, the energy of this transition is calculated to be 4.563 keV, corresponding to a wavelength of 2.717 Å. The upper level is the lowest-energy excited state of the Ne-like systems. Because of its high angular momentum, many of the high angular momentum excited states preferentially decay to it. This results in a complicated cascade feeding scheme.

Because the transition is magnetic quadrupole, it has a relatively small Einstein-A coefficient for an x-ray transition: about $3.0 \times 10^8 \text{ s}^{-1}$ in Ne-like barium [13]. However, in low-density plasmas such as that in an EBIT, the relative intensity of the line is comparable to that of the large Einstein-A coefficient lines. This is because of the strong cascade feeding and the fact that the number of decays per unit time is bottlenecked by the electron-impact excitation rates, rather than the decay rates.

In previous EBIT work, the $M2$ line was studied by Beiersdorfer *et al.* [11] using a flat crystal spectrometer. The electron-beam energy dependence of the intensity relative to a reference line made it possible to separately measure the effects of different indirect line formation mechanisms. These included resonance excitation of the line, dielectronic recombination onto F-like barium, and inner-shell ionization of Na-like barium. As the authors pointed out in their paper, their diffractive crystal was oriented to preferably reflect x rays with polarization vector parallel to the electron beam direction. They could not orient it for x rays of complementary polarization and therefore had to use theoretical estimates of the polarization to compare their observed line intensities with predictions based on the various line formation mechanisms (both direct and indirect). They estimated the polarization P , defined in Eq. (1) above, to be -0.05 ± 0.10 over the entire range of electron-beam energies used. That is, they assumed that the polarization had no dependence upon electron-beam energy and justified this assumption with calculations of the impact energy dependence (or, rather, relative independence) of the polarization of the $2p^6 \ ^1S_0 - 2p^5 \ (^2P_{3/2}^o) 3d \ [5/2]_1^o$ electric-dipole line [11] using the method of Zhang, Sampson, and Clark [12]. However, as

we remarked above, the formation of the upper level of the $M2$ line is dominated by cascade decays from high angular momentum states. The relative contribution of the different cascade paths dramatically changes with electron-beam energy. Some of the paths are completely excluded once the energy of the electron beam falls below the excitation threshold for the root state of the path (i.e., the highest-energy state in the path). In turn, the feeding of the different magnetic sublevels of the $M2$ line also changes with the electron-beam energy. Thus, even if the direct electron-impact excitation cross sections for the magnetic sublevels do not change relative to one another with impact energy, there may still be a significant change in the polarization because of the (energy-dependent) cascade feeding process. Studying the importance of this effect on the energy dependence of the polarization was the primary motivation for the present work.

III. CALCULATIONS

To gain a better understanding of the cascade feeding of the upper level of the $M2$ line we carried out calculations with a collisional-radiative model. An analysis using the HULLAC computer code [13] was done at a number of electron-impact energies between 5.2 and 7.8 keV, which coincided with the energy range in our experiment. The output of the code gives the relative populations of the levels, the decay rates, electron-impact excitation rates, and energies for the different transitions involved. The calculation included all of the $n=3$ and $n=4$ energy levels of Ne-like barium. Because the excitation threshold energies vary a great deal over the $n=3$ and $n=4$ levels, the number of levels involved in the cascade process increases quickly with electron-beam energy. At 5.2 keV, only 23 levels can be excited, whereas at 7.8 keV, all 89 $n=3$ and $n=4$ levels can play some role. If we consider that the population transfer between the different magnetic sublevels strongly depends on the angular momentum values of the upper and lower levels of the cascading transition, it is clear that the change in the relative population of the magnetic sublevels of the $M2$ line can be significant. Figure 1 shows the Grotrian diagram of the levels involved in the population of the upper level of the $M2$ line at 7.8 keV beam energy. It can be seen from this figure that the upper level is preferentially populated from upper states with total angular momentum different from zero. The various excitation and cascade fractions were calculated using the HULLAC code.

The cross section and collisional-radiative programs in the HULLAC code do not treat sublevels of different M for a given J . In order to model the polarization expected following cascades through a number of levels, we wrote a collisional-radiative program that explicitly considers each M sublevel. In order to simplify the problem somewhat, we only considered collisional excitations and deexcitations between the ground state and the various excited levels, since x-ray radiative transitions are much faster than collisional transitions in the EBIT. Using angular momentum relationships, the Einstein-A coefficient between magnetic sublevels in terms of the M averaged A coefficient $A(J_i \rightarrow J_j)$ is [14]

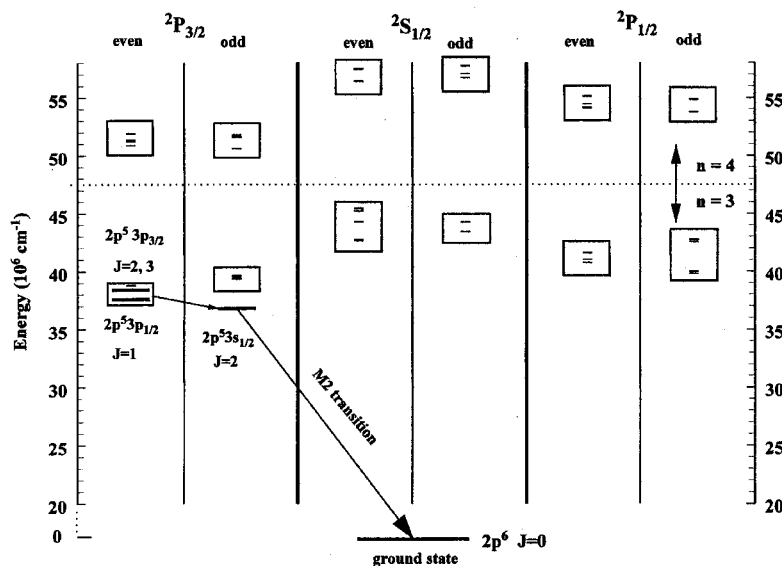


FIG. 1. Partial Grotrian diagram showing all the levels involved in the cascade feeding of the upper level of the $M2$ transition at 7.81 keV beam energy. The dominant levels are shown with long bars and connected with arrows, while the levels that individually contribute less than a few percent to the population are shown by short bars.

$$A(J_i, M_i \rightarrow J_j, M_j) = \left| \begin{pmatrix} J_j & q & J_i \\ -M_j & m & M_i \end{pmatrix} \right|^2 \times (2J_i + 1) A(J_i \rightarrow J_j), \quad (2)$$

where the quantity $\begin{pmatrix} J_j & q & J_i \\ -M_j & m & M_i \end{pmatrix}$ is the usual Wigner 3- j symbol. In this symbol, q is the multipolarity of the transition and $m = M_j - M_i$, by the properties of the 3- j symbol. In our modeling, we take the decay rates $A(J_i \rightarrow J_j)$ from the previously described HULLAC runs. We take collisional excitation cross sections from the same source, but split these up into the M -dependent quantities according to a variety of approximations. The collisional-radiative matrix inversion is run to establish the populations of each M sublevel. Following this, the polarization in each emission line is calculated according to Eq. (19) of Inal and Dubau [15].

As an initial estimate for the polarization fraction of each level, we took the limits given by Percival and Seaton [1]. We assumed that only the orbital angular momentum sublevel $M_l=0$ is populated in the electron impact and then coupled the orbital angular momentum with the electron spins to form J . As such, this approximation assumes exact LS coupling and therefore a polarization fraction that can only be realized for impact excitation of neutral atoms at threshold. This approximation turns out to overestimate the measured polarization by a large factor, but the dependence on electron-beam energy is qualitatively correct. A similar jj coupling approximation (i.e., assuming sublevels with $M_l=0$ only are populated) gives an even larger polarization (leading to a larger discrepancy). jj coupling might be expected to be a better approximation for Ne-like barium, so it is probable that the cause of the discrepancy is our neglect of the depolarization that occurs when the incident electron scatters through a large angle in the Coulomb field of the target ion. The direction of the scattered electron sets the quantization axis for the excited ion, so the stronger the interaction (and thus the larger the scattering angle), the greater the depolarization will be.

Accordingly, we decided to perform detailed calculations of the impact-excitation cross sections from the ground state to the magnetic sublevels of each of the participating excited levels at an impact energy of 410 Ry (5.578 keV). These were undertaken by two of us (J.D. and M.K.I.) essentially following the formalism in Inal and Dubau [15]. The important simplifications are that the collisions are treated nonrelativistically and that we have only one energy point at which the polarization is calculated. Note that the total cross sections we use still retain their energy dependence (which is actually quite weak over the energy range we consider) since these are taken from our earlier HULLAC computations. Eventually a total of 37 levels were included in the calculation, allowing us to employ the cascade model for electron-beam energies up to 5.98 keV; above this, higher excited states are involved for which we have no polarization fraction calculations. Putting these results into our modified collisional-radiative model gives the polarizations that are shown in Table I. These results are about a factor of 4 smaller than those predicted by the simple model described in the preceding paragraph.

We should emphasize that only excitation by direct electron impact followed by radiative decay has been included in our model. Since the polarization fractions were calculated at one impact energy only, we are implicitly assuming that the polarization fractions for a given excited state do not change substantially with beam energy over the range of interest. Energy scaling is included for the total cross sections, but not for the fractions going to each M sublevel. Overall, the only substantial omission in our calculation is that resonant processes appearing at energies near 5.2 and 5.8 keV have been neglected. We believe that the effect of resonance excitation is quite evident in the data presented below and can explain the regions in which there is a significant discrepancy between our calculations and our experiment.

IV. INSTRUMENTS

Descriptions of the history and operating principle of the EBIT have been published elsewhere [16,17]. Our machine

TABLE I. Polarizations of the $M2$ and $E1$ lines. Polarizations of the $M2$ and $E1$ lines are calculated using the collisional-radiative model and realistic starting polarization fractions. From left to right the columns are beam energy in keV, $M2$ line polarization, $E1$ line polarization, and the number of levels included in the calculation.

Energy (keV)	$M2$ (%)	$E1$ (%)	No. of levels
5.04	-12.5	4.77	19
5.10	-12.5	4.77	19
5.20	-12.2	3.77	21
5.27	-12.0	3.71	23
5.40	-12.1	3.57	25
5.50	-12.4	2.63	33
5.58	-12.4	2.63	33
5.70	-12.4	2.63	33
5.80	-14.8	2.64	37
5.90	-15.0	3.07	37
5.98	-15.0	3.07	37

[18] is similar in design to the Lawrence Livermore National Laboratory EBIT, which is described in detail in Ref. [19]. The highly charged ions are created, excited, and trapped radially by a 60- μm -diam, 3500-A cm^{-2} electron beam. A series of three cylindrical drift tubes—two end cap tubes biased at 250 V positive with respect to a center drift tube—provide axial trapping for the ions. The voltage applied to the center drift tube V_0 determines the electron-beam energy (5.0–8.0 keV in our experiment). The electron-beam energy is not precisely equal to eV_0 , however, because the space charge of the electron beam itself depresses the on-axis potential. We corrected for this effect using a simple calculation based on Gauss's law. Our electron-beam energy scale has perhaps a ± 50 -eV absolute uncertainty due to the space-charge correction; the relative uncertainty is on the order of only a few eV, though. Observation of x rays emitted by ions in the trap is made at 90° with respect to the electron-beam direction through a series of two beryllium windows that have a total thickness of 0.175 mm. Since barium, which is a dopant in the electron gun cathode, boils off of the cathode and fills the trap automatically, it is one of the easiest elements to study in an EBIT. Just by turning on the electron beam and tuning to an energy above the 3.3-keV ionization potential of Na-like barium, an abundant sample of Ne-like barium is created. About 81% of naturally occurring barium has zero nuclear spin, so that the effect of the hyperfine interaction on line polarizations is negligible [20].

The measurement was carried out using two identical Johann-type, bent crystal x-ray spectrometers operating simultaneously. A description of the spectrometers and detectors can be found in Ref. [21]. For the wavelength range studied (approximately 2.72 Å), we used a Ge(220) ($2d=4.00$ Å) crystal. During the polarization measurement, the two spectrometers were installed so that their respective reflection planes were perpendicular to each other and at 90° to the electron-beam direction. The Bragg angle is near 45° (42.8°), so the spectrometers function as near-perfect x-ray polarizers. The polarization of the emitted radiation is obtained by inserting the observed normalized intensities in Eq. (1) and then dividing the result by a correction factor

Q [22], where $Q=1-Y1-Y2$, with Y 's representing the amount of parallel-polarized radiation that leaks through into the perpendicular-polarized measurement (and vice versa). The Q factor depends on crystal quality, curvature, alignment, and angle and is very close to unity for high-quality crystals and a Bragg angle close to 45° . A very thin perfect crystal (or a thick or thin mosaic crystal) would have $Y=X/(1+X)$, where $X=\cos^2(2\theta)$ or about 0.6% for the exact angle used in our experiment. For the case of a thick perfect crystal, the exponent on the cosine would be 1 and the value of X would be 7.7%. Our crystal has been previously quantified and is intermediate in thickness between the limiting forms, leading to Y values that are about 1.9% and an overall value of $Q=0.963(5)$.

V. DETERMINATION OF THE ABSOLUTE POLARIZATION

In order to determine the absolute line polarization, the orthogonal spectrometers had to be intensity cross calibrated. This can be done by observing an unpolarized line if one can be found near the same energy as the line under study. This method of intensity calibration takes account of the different geometrical and detector efficiency factors at the same time. The ideal candidate isotropic line is one that has a $J=0$ upper level, since in that case there is only one magnetic sublevel and therefore $P=0$. For intensity cross calibration, we used the $2p^6\ ^1S_0-2p^5(^2P_{3/2}^o)3s[3/2]_1^o$ electric dipole transition in Ne-like barium (hereinafter referred to as the $E1$ transition or the $E1$ line). This line appears at 4.568 keV, which is much closer to the $M2$ line than a similar electric dipole transition that was used for the same purpose by Beiersdorfer *et al.* [11]. The proximity of our $E1$ line to the $M2$ line allowed us to simultaneously observe them in high resolution with our spectrometers.

Calculations using the collisional-radiative model and the HULLAC code (including all $n=3$ and $n=4$ states) predict that at an electron-beam energy of 7.8 keV, the upper level of the $E1$ line is primarily ($>80\%$) populated by cascades from states with $J=0$ angular momentum. As a consequence, even though the upper level of the $E1$ line has non-zero angular momentum, it is mostly unpolarized and isotropic. Figure 2 shows the partial Grotrian diagram of the levels involved in the population of the upper level of the $E1$ line, which we constructed from the output of the HULLAC code. Using the HULLAC data, we estimate that the absolute value of the polarization for the $E1$ line is less than 3% over the entire range of beam energies in our experiment. For calibration purposes, we assumed complete isotropy for the $E1$ line and took account of the small polarization due to $J\neq 0$ cascades in the error bars on our final results for the $M2$ line polarization.

It is interesting to compare the ratio of the efficiencies of the two spectrometers based upon observation of the mostly unpolarized $E1$ line with a sophisticated computer model. The two spectrometers are very nearly identical, but because the x-ray source is in the shape of a thin cylinder (only ions within the 60 μm diameter of the electron beam and within the 2 cm length of the center drift tube can be excited within the EBIT), there is a rather large geometrical effect; that is, their relative efficiencies depend strongly upon their orienta-

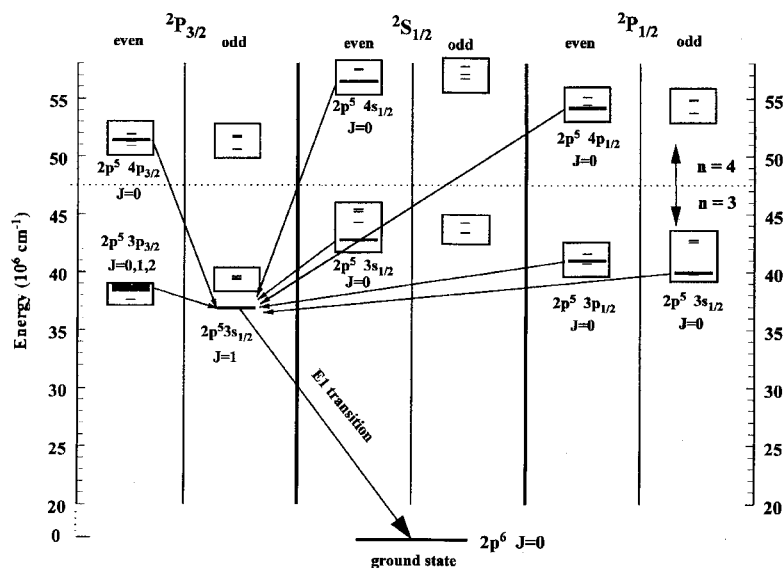


FIG. 2. Partial Grotrian diagram showing all the levels involved in the calculation of the cascade feeding of the upper level of the $E1$ transition for electron-beam energy 7.81 keV. The notation is explained in the caption to Fig. 1.

tion. The computer model [23] predicts that the spectrometer perpendicular to the electron beam has a factor of 1.9 ± 0.20 greater efficiency than the one oriented parallel to the electron beam. Using the unpolarized $E1$ line as a reference, we observe experimentally an efficiency factor of 1.83.

VI. DATA ACQUISITION AND EVALUATION

Data were taken at 15 different electron impact energies between 4.97 and 7.81 keV. The energies were chosen to fall below the excitation thresholds of certain $n=4$ and $n=3$ levels so as to exclude them completely from the cascade feeding routes to the upper level of the $E1$ line. Each data point represents between 6 and 12 h of collection time. Longer times were required for the lowest energies because fewer levels are excited that can potentially feed the $M2$ or $E1$ lines, thus making the lines appear weaker. Figure 3 shows typical spectra at a beam energy of 6.00 keV for each spectrometer. The $M2$ and $E1$ lines are clearly resolved and no other strong features are present in the spectrum. For all of the data points, electron-beam currents ranged between 135 and 150 mA, depending on the energy we had set. The current and energy were held fixed during the entire collection time and a small amount of N_2 was injected to improve evaporative cooling of the trapped barium ions [24]. After the data were taken, the six best spectra from each spectrometer were summed to generate two spectra with the highest signal-to-noise ratio. These were used to determine the line centers as accurately as possible and to extract the individual spectrometer response functions. The line centers and response functions were then held fixed in subsequent fits used to extract the polarization-dependent line intensities. The data evaluation was done using a spectrum fitting program [25]. Initially, peaks were fit to Voigt line shapes, but it was quickly discovered that the peaks had a predominantly Gaussian shape. Accordingly, fits to Gaussian line shapes with linear background subtraction were performed for all of the spectra. From fits to each of the 15 different spectra (representing 15 different electron-beam energies), the intensity of both lines ($J=2$ and $J=1$) was determined. Compar-

ing the intensity ratio of the two lines for each spectrometer gave a measure of the absolute polarization in accordance with Eq. (1).

VII. SYSTEMATIC ERRORS

We have already mentioned some minor corrections that must be applied to the measured polarization, arising from a small polarization dependence in the crystal reflectivity, as well as a small deviation in the Bragg angle from 45° . Ac-

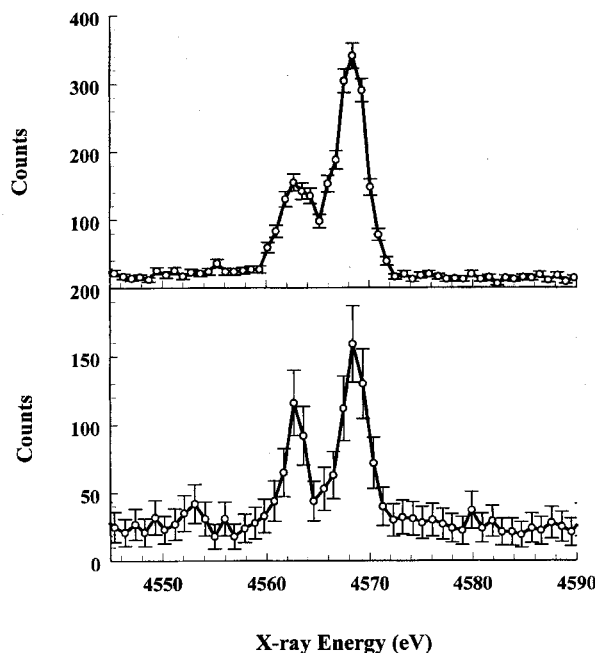


FIG. 3. Simultaneous data from the spectrometers that measure perpendicular (top) and parallel (bottom) polarization. The beam energy was 6.00 keV. The $M2$ and $E1$ lines are clearly resolved in both spectra. X-ray energy increases to the right, so that the $M2$ line lies to the left (lower energy) of the $E1$ line.

according to our model calculations [23] of the crystal reflectivity (accurate to 1–2%), the corresponding correction to the polarization is no more than 1.6%, with a far smaller uncertainty. These model calculations also allow us to apply a theoretical normalization to the two spectrometers so we can experimentally confirm that the reference line is indeed unpolarized, $P=0.0(1)$. In addition, the model calculations imply that the x-ray signal emerging from our EBIT forms an effective source height of 13(7) mm.

Another correction and accompanying source of error arises from the transverse motion of electrons in the beam. The presence of the strong magnetic field B_0 in the EBIT allows rigid-rotor motion of the electron beam at a maximum angular frequency approximately equal to the electron cyclotron frequency $\omega_{ce} = eB_0/m_e$ [26]. This rotation can develop when the beam moves through a magnetic-field gradient. In the EBIT, the electrons move from a region of near-zero magnetic field at the cathode to a region of 3-T magnetic field in the center of the trap [27]. The incident electron velocity vectors therefore lie on the surface of an inverted cone and this leads to some depolarization from the case of a perfectly aligned beam.

The total velocity of the electron beam is determined by the potential V_0 applied to the center drift tube. We estimate the transverse component of this total velocity using several independent methods. First, we note that under our conditions of 3-T field, the angular frequency is 5×10^{11} Hz, which means a maximum transverse kinetic energy of 700 eV for electron orbits inside a 60- μ m-diam beam. This transverse energy is consistent with the fact that we have been unable to operate our EBIT below 700 eV total beam energy without picking up significant stray currents in the electrodes (such as the electron gun anode) that surround the electron beam at various points along its trajectory. The maximum possible rotation velocity estimated in this way gives an angle of incidence with respect to normal (“pitch angle”) ranging from 21° to 17° for total beam energies ranging from 5.0 to 7.8 keV, respectively. The final angular velocity of the beam could be less than the maximum, however. It is essentially determined by the magnetic field at the cathode since v_{\perp}^2/B is an adiabatic invariant for a charged particle traveling through a fixed magnetic field. Thus we make our second estimate as follows. We note that at the cathode, v_{\perp}^2 is of order $2kT_c/m_e$, where $T_c = 1500$ K is the temperature of the cathode. The cathode magnetic field B_c is not known, but it is believed to be of order a few hundred microtesla (a few gauss) since that is the level of control that the EBIT bucking coil (which is used to null out the field at the cathode) gives. As discussed in the Appendix, a theoretical estimate of the cathode magnetic field gives values $B_c = 240\text{--}210 \mu\text{T}$ (2.4–2.1 G), which give pitch angles of 24°–20° for beam energies in the range 5.0–7.8 keV, respectively. This second estimate should be considered as a rough estimate for the “typical” pitch angles, but since it is somewhat larger than the more rigorously obtained pitch angles obtained in the first estimate, we use the first estimate for analysis of our data.

With the incident electron velocity vectors lying on the surface of an inverted cone, there are two geometric effects that will cause some depolarization. The first is that the angle of observation with respect to the incident electron velocity

vector will deviate from 90°. The second and more serious problem is that for electron velocity vectors with nonzero components lying in the plane normal to the observation direction, the axes for the polarization measurement will be rotated. The first case was accounted for by running polarization calculations as described above, but for an average angular deviation from observation at right angles. The cosine of this angle is given by

$$\langle \cos\beta \rangle = (2/\pi) \int_0^{\pi/2} \sin(\phi_p) \cos(\theta) d\theta = 2 \sin(\phi_p) / \pi \approx 0.2, \quad (3)$$

where ϕ_p is the typical electron pitch angle to the beam axis, given by $\arctan(v_{\perp}/v_{\parallel})$, taken here to be about 17°. In the limit of small angles, the observed polarization is reduced by a factor $1 - \langle \cos\beta \rangle^2$ [15], or about 0.96.

The second effect reduces the observed polarization by a factor

$$\begin{aligned} \langle \cos(2\phi) \rangle &= (2/\pi) \int_0^{\pi/2} \frac{1 - \tan^2(\phi_p) \sin^2(\theta)}{1 + \tan^2(\phi_p) \sin^2(\theta)} d\theta \\ &= 1 - \tan^2(\phi_p) \\ &\approx 0.90. \end{aligned} \quad (4)$$

This expression is easily obtained from the general form of Eq. (1) rotated through an angle ϕ rather than evaluated at 90°.

The combined result of the two geometric effects is the product of the two, so the measured polarization is approximately 87% of the true value. This percentage will change slightly (about 5%) with beam energy in the range we consider, but not sufficiently to alter the energy dependence of our observed polarization.

We do not have direct measurements of the magnitude of the transverse kinetic energy of electrons in the EBIT or of the cathode magnetic field (from which the final transverse kinetic energy can be estimated). We note, however, that a polarization measurement of a suitable line might in fact be a good way of measuring this. A strong line with a large polarization could be monitored as the cathode magnetic field B_c is changed through tuning of the bucking coil current.

Another potential source of systematic error arises from anisotropy in the emitted radiation from the $E1$ line used for normalization. In the analysis, we determined the cascade feeding scheme with the HULLAC code as in the case of the $M2$ line. Our estimate for the polarization of the $E1$ line, which is probably an overestimate for energies well above the excitation threshold, is $P = -1.6\%$ at high energies. Over the entire range of our energies, the $E1$ polarization is estimated to remain below 3% and the effect on the polarization of the $M2$ line, in turn, is less than 0.01. Note that in estimating the polarization of the $E1$ line we have neglected the effect of resonances, but these should further drive the polarization towards the assumed value of zero, just as they do for the $M2$ line.

Finally, there is an uncertainty in the absolute beam energy. As discussed above, there is a depression of the energy due to the negative space charge of the electron beam, which tends to reduce the on-axis potential with respect to the drift

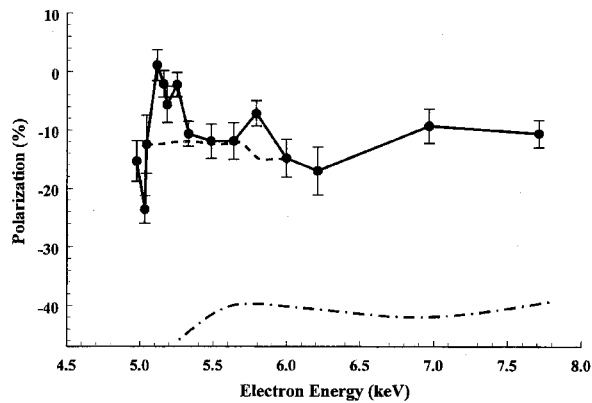


FIG. 4. Polarization P of the $M2$ line as a function of beam energy. The 15 beam energies were chosen to fall below the excitation thresholds of certain cascading levels, thus completely excluding those levels from the cascade scheme. Both the simple theory (which neglects levels with a nonzero orbital angular momentum, as appropriate near the excitation threshold) and the best presently available theoretical estimate (which includes collisional radiative effects but not resonant excitation processes) are also shown with a dash-dotted line and a dashed line, respectively.

tube electrode voltage V_0 . This space-charge correction can be calculated; however, there is an additional complication because trapped positive ions (both barium ions and background gas ions) partially neutralize the electron-beam space charge. This neutralization is difficult to determine theoretically, but it is possible to estimate it experimentally by observing the wavelength of a radiative recombination line (which changes with electron-beam energy) or by observing the change in intensity of a dielectronic recombination resonance line with beam energy. We determined that the overall space-charge correction in our situation was 250 eV, with an uncertainty of ± 50 eV. The uncertainty, however, represents an unknown but constant offset that must be applied to all of the data; the relative beam energies are known to within ± 5 eV. Thus, in the results that follow, the energy scale has an offset uncertainty of about ± 50 eV, but the shape of the curve of polarization versus energy is certain within the one-standard-uncertainty error bars shown.

VIII. RESULTS

Our measurements are shown in Fig. 4 as a plot of the polarization P of the $M2$ line as a function of electron-impact energy. The beam energies were chosen to exclude certain levels from the cascade scheme, thereby simplifying the theoretical calculations and maximizing the significance of each data point. For example, all $n=4$ levels were excluded in the measurements below 6.3 keV. Also, at these electron-impact energies, neither the resonance excitation to the F-like charge state nor the inner-shell ionization of the Na-like charge state can play a role since both are energetically excluded.

The theoretical estimates are also shown in Fig. 4. The dash-dotted line corresponds to an approximation where only the sublevels with zero orbital angular momentum are populated. This is a very crude approximation and supposed to be

valid only near the excitation threshold.

The fairly strong decrease in the absolute value of the polarization around 5.5 keV beam energy coincides with the intensity increase seen by Beiersdorfer *et al.* [11] in the parallel polarized component of the $M2$ line. This intensity increase was interpreted by Beiersdorfer *et al.* [11] to be the result of a resonance excitation of the upper level of the $M2$ line. In this two-step process, a dielectronic resonance transition to one of the autoionizing Na-like levels takes place. The dielectronic process is followed by an autoionization, whereby the final state includes the upper level of the $M2$ line. If the interpretation is correct, the 25% decrease in the line polarization could be accounted for by the resonance excitation process itself. However, since polarization calculations already show a similar tendency, we have to conclude that at least part of the polarization change is due to the change in the cascade feeding scheme for the upper level of the $M2$ line. The assumption made by Beiersdorfer *et al.* in Ref. [11] of a $-5 \pm 10\%$ polarization that is independent of electron-impact energy holds over a good part of the energy range of our measurement, but not in those places where resonances can occur. In our case, we measured a negative line polarization with an average value of $-0.12 \pm 0.10\%$. The absolute value of the polarization increases close to the direct excitation threshold energy and decreases strongly near 5.2 and 5.8 keV, where LNO and LOO dielectronic resonance (DR) excitations are allowed (in Auger notation, LOO denotes an L -shell electron promoted to the O shell while an incident unbound electron is captured in the O shell). These results do not change the basic conclusions of Ref. [11] and we believe that these deviations of the polarization from its average value are in fact due to the indirect processes reported by Beiersdorfer *et al.* [11]. In fact, we attribute the region of strong deviation near 5.8 keV to an LOO resonance process that was not observed in Ref. [11].

It appears that the resonant excitation process (DR followed by autoionization) creates unpolarized radiation. In a simple picture, this might be expected, since even if the initial DR process populates the m sublevels of the doubly excited intermediate state nonuniformly, the subsequent electron emission in the autoionization process will scramble the quantization axis of the final-state singly excited ion.

IX. CONCLUSION

We have measured the absolute polarization of the $2p^6 1S_0 - 2p^5 ({}^2P_{3/2}^o) 3s [3/2]_2^o$ magnetic quadrupole transition in Ne-like barium. We find that for electron-impact excitation in the energy range from 5.0 to 7.8 keV, this line shows a strong negative polarization. The polarization typically falls between -4% and -18% , but changes sharply near 5.0 keV, as well as near 5.1–5.3 and 5.8 keV.

We have also found a steady decrease in the polarization between 5.5 and 6.0 keV, which should be due at least in part to the change in the cascade feeding routes. It appears that the quantitative agreement between models and experiment is greatly improved when realistically calculated polarization fractions are included. The precise degree of agreement at certain energies is probably fortuitous, however, since important resonant processes have not been included. In fact, it seems that polarization measurement may represent a sensi-

tive method for confirming the presence of such resonant excitation processes. In our data, for example, a decrease in the absolute value of the polarization is quite prominent near 5.8 keV, which we interpret as being due to an *LOO* dielectronic resonance excitation. This resonance is difficult to isolate in a plot of total line intensity versus beam energy and was not observable in Ref. [11].

Finally, we note that polarization measurements might also be used to determine the magnitude of rigid-rotor motion in the electron beam of an EBIT. This rotation might be controlled through tuning of the cathode magnetic field, and it would be interesting to see if such effects are indeed important in EBIT.

ACKNOWLEDGMENTS

We thank E. Bell and F.G. Serpa for assistance during the course of this experiment and V. Jacobs for helpful discussions. One of the authors (E.T.) acknowledges the Foundation for Hungarian Higher Education and Research for support.

APPENDIX

Here we discuss the intensity of the magnetic field at the EBIT cathode B_c . While the minimum electron-beam radius is obtained for zero field at the cathode, under this condition the electrons cannot enter the trap. By maximizing an expression for the current density in the ion trap j ,

$$j = n_e q v_{\parallel} = \frac{N_e}{\pi R^2} q (v^2 - v_{\perp t}^2)^{1/2} \quad (\text{A1})$$

in the trap with respect to B_c , where $v_{\perp t}$ is the perpendicular velocity in the trap (as opposed to at the cathode, denoted by $v_{\perp c}$), n_e is the electron density, and N_e is the number of electrons per unit length in the beam (assumed constant), we

can derive a theoretical estimate for the optimum cathode magnetic field. The beam radius R is given by Herrmann's theory [28]

$$R = r_b \left\{ \frac{1}{2} + \frac{1}{2} \left[1 + 4 \left(\frac{8kT_c}{m_e} \frac{r_c^2}{\eta^2 B_t^2 r_b^4} + \frac{B_c^2 r_c^4}{B_t^2 r_b^4} \right) \right]^{1/2} \right\}^{1/2}, \quad (\text{A2})$$

where r_b is the Brillouin radius, r_c is the cathode radius, B_t is the trap magnetic field, T_c is the cathode temperature, m_e is the electron mass, and η is the charge to mass ratio q/m_e of the electron. A consideration of adiabatic invariant quantities leads to the following expression for the perpendicular velocity in the trap:

$$v_{\perp t} = v_{\perp c} \left(\frac{B}{B_c} \right)^{1/2}. \quad (\text{A3})$$

Substituting Eqs. (A2) and (A3) into (A1), differentiating with respect to B_c , setting the result equal to zero, and rearranging gives

$$B_c^3 = B_t^3 \frac{v_{\perp c}^2}{v^2 - v_{\perp c}^2 B_t/B_c} \frac{R^4 - R^2 r_b^2/2}{2r_c^4}, \quad (\text{A4})$$

which can be simplified for $v \gg v_{\perp t}$ and $R \approx r_b$ to give

$$B_c \approx B_t \left(\frac{v_{\perp c}^2 R^4}{4v^2 r_c^4} \right)^{1/3}. \quad (\text{A5})$$

Taking $T_c = 1500$ K, which gives $v_{\perp c} \approx 1.5 \times 10^5$ ms⁻¹, $R = 3 \times 10^{-5}$ m, $r_c = 1.5 \times 10^{-3}$ m, and $B_t = 3$ T, gives a value for B_c of $(2.1 - 2.4) \times 10^{-4}$ T for electron-beam energies of 5.0–7.8 keV, in reasonable agreement with (and completely independent from) the value inferred from the sensitivity of the electron beam to the bucking coil current.

-
- [1] I. C. Percival and M. J. Seaton, *Philos. Trans. R. Soc. London Ser. A* **251**, 113 (1958).
- [2] See, e.g., J. M. Laming, *Astrophys. J.* **357**, 275 (1990).
- [3] J. M. Laming, *Astrophys. J.* **362**, 219 (1990).
- [4] J. M. Laming, *Nucl. Instrum. Methods Phys. Res. Sect. B* **43**, 359 (1989).
- [5] D. Vogel, P. Beiersdorfer, R. Marrs, K. Wong, and R. Zasadzinski, *Z. Phys. D* **21**, S193 (1991); K. L. Wong, P. Beiersdorfer, D. Vogel, R. Marrs, and M. Levine, *ibid.* **21**, S197 (1991).
- [6] R. E. Marrs, M. A. Levine, D. A. Knapp, and J. R. Henderson, *Phys. Rev. Lett.* **60**, 1715 (1988); C. M. Brown, U. Feldman, G. A. Doschek, J. F. Seely, R. E. LaVilla, V. L. Jacobs, J. R. Henderson, D. A. Knapp, R. E. Marrs, P. Beiersdorfer, and M. A. Levine, *Phys. Rev. A* **40**, 4089 (1989).
- [7] D. A. Knapp, R. E. Marrs, M. A. Levine, C. L. Bennett, M. H. Chen, J. R. Henderson, M. B. Schneider, and J. H. Scofield, *Phys. Rev. Lett.* **62**, 2104 (1989); D. A. Knapp, *Z. Phys. D* **21**, S143 (1991).
- [8] W. C. Martin, R. Zalubas, and L. Hagan, *Atomic Energy Levels—The Rare-Earth Elements*, Natl. Bur. Stand. (U.S.) Circ. No. 60 (U.S. GPO, Washington, DC, 1978).
- [9] M. Loulergue and H. Nussbaumer, *Astron. Astrophys.* **24**, 209 (1973); J. H. Parkinson, *ibid.* **24**, 215 (1973).
- [10] M. Klapisch *et al.*, *Phys. Lett.* **69A**, 34 (1978).
- [11] P. Beiersdorfer, A. L. Osterheld, M. H. Chen, J. R. Henderson, D. A. Knapp, M. A. Levine, R. E. Marrs, K. J. Reed, M. B. Schneider, and D. A. Vogel, *Phys. Rev. Lett.* **65**, 1995 (1990).
- [12] H. L. Zhang, D. H. Sampson, and R. E. H. Clark, *Phys. Rev. A* **41**, 198 (1990).
- [13] M. Klapisch, A. Bar Shalom, W. H. Goldstein, E. Meroz, A. Chon, and M. Cohen, HULLAC code for atomic physics, 1988 (unpublished).
- [14] This is derived from the Wigner-Eckart theorem and properties of the 3- j symbols.
- [15] M. K. Inal and J. Dubau, *J. Phys. B* **20**, 4221 (1987); **22**, 3329 (1989) (this paper corrects some typographical errors in the relevant equation).
- [16] R. E. Marrs, P. Beiersdorfer, and D. Schneider, *Phys. Today* **47** (10), 27 (1994).
- [17] J. D. Gillaspay, *Proceedings of the Sixth International Sympo-*

- sium on Electron Beam Ion Sources [Phys. Scr. (to be published)].
- [18] J. D. Gillaspay, J. R. Roberts, C. M. Brown, and U. Feldman, in *VIIth International Conference on the Physics of Highly Charged Ions*, edited by P. Richard, M. Stöckli, C. L. Cocke, and C. D. Lin, AIP Conf. Proc. No. 274 (AIP, New York, 1993), p. 682.
- [19] M. A. Levine, R. E. Marrs, J. R. Henderson, D. A. Knapp, and M. B. Schneider, Phys. Scr. **T22**, 157 (1988).
- [20] J. R. Henderson, P. Beiersdorfer, C. L. Bennett, S. Chantrenne, D. A. Knapp, R. E. Marrs, M. B. Schneider, K. L. Wong, G. A. Doschek, J. F. Seely, C. M. Brown, R. E. LaVilla, J. Dubau, and M. A. Levine, Phys. Rev. Lett. **65**, 705 (1990).
- [21] B. P. Duval, J. Barth, R. D. Deslattes, A. Henins, and G. G. Luther, Nucl. Instrum. Methods **222**, 274 (1984); A. Henins, Rev. Sci. Instrum. **58**, 1173 (1987).
- [22] B. Cleff, Acta Phys. Pol. A **61**, 285 (1982).
- [23] C. T. Chantler (private communication) [using the computer code described in C. T. Chantler, Ph.D. thesis, Oxford University, 1990 (unpublished)]; J. Appl. Crystallogr. **25**, 674 (1992); **25**, 694 (1992)].
- [24] B. M. Penetrante, J. N. Bardsley, M. A. Levine, D. A. Knapp, and R. E. Marrs, Phys. Rev. A **43**, 4873 (1991).
- [25] J. Végh, Candidate's thesis, Institute of Nuclear Research of the Hungarian Academy of Sciences (ATOMKI), 1991 (unpublished).
- [26] R. C. Davidson, *Theory of Nonneutral Plasmas* (Benjamin, New York, 1974).
- [27] J. D. Jackson, *Classical Electrodynamics* (Wiley, New York, 1975).
- [28] G. Herrmann, J. Appl. Phys. **29**, 127 (1958).

Radiative and inner-shell dielectronic recombination in a highly charged barium ion

D. J. McLaughlin

Department of Physics, University of Hartford, West Hartford, Connecticut 06117

Y. Hahn

Department of Physics, University of Connecticut, Storrs, Connecticut 06269

E. Takács, E. S. Meyer, and J. D. Gillaspay

Physics Laboratory, National Institute of Standards and Technology, Gaithersburg, Maryland 20899

(Received 28 September 1995)

The direct radiative recombination (RR) to $n=3, 4$, and 5 levels and the resonant dielectronic recombination (DR) cross section involving $2p \rightarrow 3d$ excitation of Sc-like barium Ba^{35+} and Ti-like barium Ba^{34+} are calculated and compared with a recent electron beam ion trap experiment at the National Institute of Standards and Technology. Assuming a fractional population of Ba^{35+} in the trap of about 30%, we obtain good agreement between theory and experiment for the cross section ratio $\sigma(DR)/\sigma(RR)(n=4)$, as well as for $\sigma(RR)(n=5)/\sigma(RR)(n=4)$. The result confirms again that the simple angular momentum averaged procedure can be effective in treating DR for heavy open-shell ions when the energy resolution is not high. A large, broad peak below 2 keV in the x-ray spectrum is being theoretically examined. [S1050-2947(96)04008-5]

PACS number(s): 34.80.Kw, 32.80.Hd

I. INTRODUCTION

The availability of the electron beam ion trap (EBIT) at Lawrence Livermore National Laboratory (LLNL), Oxford, and the National Institute of Standards and Technology (NIST) has opened up a rich field of experiments with highly charged ions at low velocities. There have been several recent measurements of x-ray spectra emitted by highly charged ions produced by EBIT [1,2] and merged beams [3] that involve electron capture with inner-shell excitations.

In a recent investigation carried out with the EBIT at NIST, scandiumlike barium $Ba^{35+}([Ar]3d^3)$ and titaniumlike barium $Ba^{34+}([Ar]3d^4)$ ions were created, trapped, and excited using an electron beam of approximately 2.3 keV energy. A strong x-ray emission peak was observed at 4.6 keV, and several smaller peaks were measured at lower energies, down to approximately 2 keV where the spectrum is gradually cut off due to detector limitations (Fig. 1). This experiment is particularly interesting because x-ray peaks arising from both dielectronic recombination (DR), labeled *a* in Fig. 1, and radiative recombination (RR), labeled *b* in Fig. 1, can be studied simultaneously. Since the binding energy of the $3d$ orbital is about 2.3 keV and noting the energy difference between the $2p$ and $3d$ orbitals is 4.6 keV, we attributed the principal x-ray peak to a DR process in which a continuum electron collisionally excites a $2p$ electron in the trapped ion and is in turn captured into the $3d$ orbital. One of the M -shell electrons ($3d$) of the recombined ion subsequently decays radiatively to the $2p$ vacancy, thereby emitting a 4.6 keV x-ray, i.e., an x ray of energy twice the incident kinetic energy of the projectile electron. The peak due to this DR process is denoted in Fig. 1 as *ab* because it also contains contributions from RR corresponding to radiative capture into states with principal quantum number $n=3$. The smaller DR peak labeled *a'* at 4.0 keV corresponds to radiative decay of an M -shell $3s$ electron into the $2p$ vacancy. The x ray

peaks at 3.7 keV (*b4*) and at 3.3 keV (*b5*) and 3.4 keV (*b4*) correspond to direct radiative capture into states with $n=4$ and 5, respectively, while the broad peak (*b*) at 2.9 keV corresponds to RR into states with $n \geq 6$. Finally, a very large and broad bump (*c*) was observed, stretching over the energy range 1–2 keV. This peak is not treated here. The dependence of this spectrum on electron-beam energy was studied by varying the beam energy by as much as 100 eV on both sides of the DR resonance. These spectra are shown in Fig. 2. We note that as the kinetic energy of the electron beam moves away from the DR resonance energy the RR peak in *ab* shifts to higher energy while the resonances, *a* and *a'*, gradually disappear. Peaks *b4* and *b5* (as well as bump *c*) remain more or less the same in magnitude but

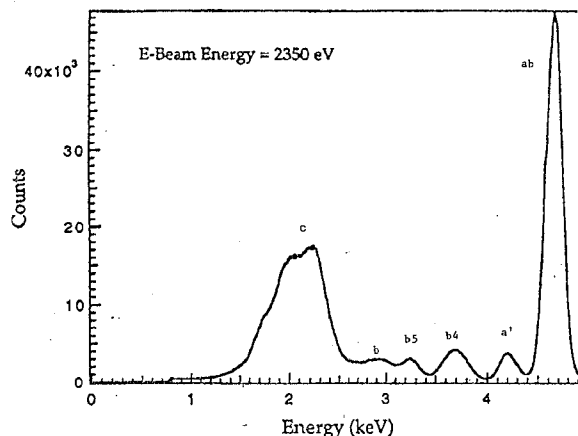


FIG. 1. Sc-like barium spectrum at an electron-beam energy of approximately 2350 eV and a beam current of 65 mA. The detector resolution is about 200 eV, and the spread in electron-beam energy is about 30 eV. The spectrum was acquired over six hours.

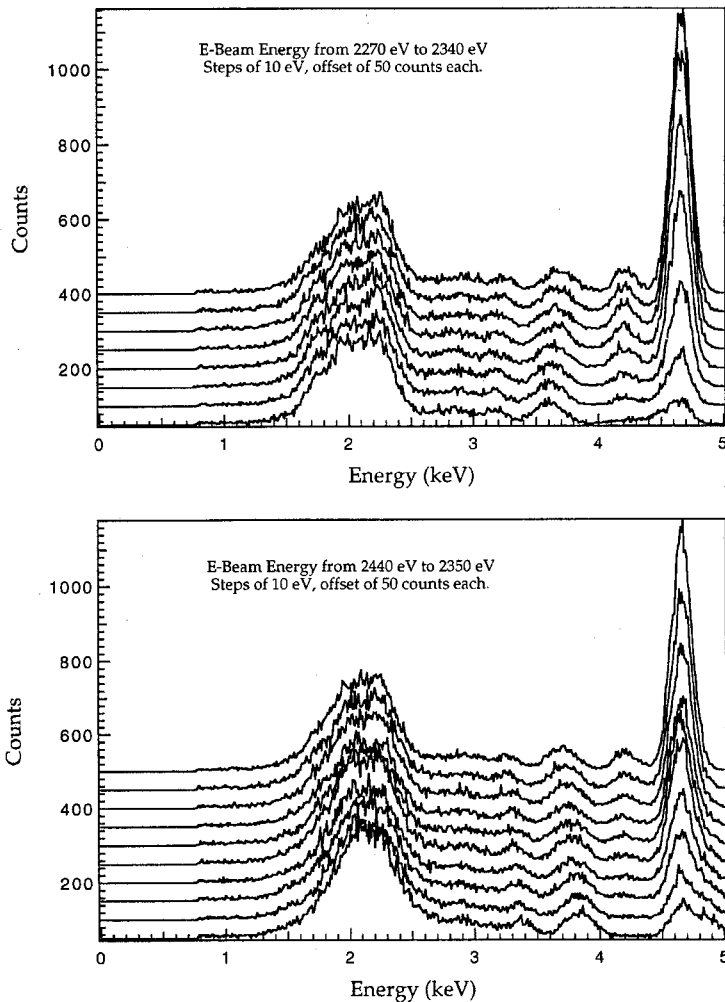


FIG. 2. Sc-like barium spectra taken at electron-beam energies ranging from 2270 eV to 2440 eV in steps of 10 eV. The top graph shows the spectra for energies above the main DR resonance, with the beam energy decreasing with offset from the x axis. The bottom graph shows the spectra for energies below the main DR resonance, with the beam energy increasing with offset from the x axis.

slowly shift to higher energies with increasing electron energy. The main peak ab is reduced in size off resonance, but there is a small recognizable peak which persists at about 4.6 keV. This important information, together with approximate energy levels of the ground and excited states of Ba^{35+} calculated by Kim [4], is sufficient to assign tentatively the peaks $b4$ and $b5$ and the residual peak in ab to RR processes, and the main portion of the peak ab and a' to DR processes.

We present here the experimental data of DR and RR for the Ba^{34+} and Ba^{35+} target ions and details of an estimation of their cross sections. Our calculations indicate that the 4.6 keV peak ab and the peak a' at 4 keV do indeed arise from DR and estimates of the relative magnitude of the accompanying RR cross sections are found to be in favorable agreement with the data.

II. EXPERIMENTAL DISCUSSION

The operation of the EBIT has been described in several reviews [5]. Briefly, the EBIT consists of a 10–150 mA electron beam focused to less than 100 μm diameter by a strong magnetic field. The electron beam is accelerated to between 1 keV and 30 keV by a series of positively biased cylindrical electrodes or drift tubes. Atoms and low-charged ions that

are injected into the center of the drift tubes are stripped to higher-charge states by the electron beam and trapped radially by the space charge of the electron beam as well as the action of the magnetic field. The trap along the electron beam is formed by a collection of three drift tubes, a center drift tube and two end caps. The end caps are biased 100–500 V above the center one to provide axial trapping for the ions. The electron-ion interaction energy is controlled by the absolute voltage applied to the center drift tube.

Barium is perhaps the easiest element to study in the EBIT because it is a primary dopant in the electron gun cathode, and sufficient barium evaporates from the heated cathode to provide an abundant source for the trap. To make a specific charge state, the electron-beam energy must be tuned appropriately (to an energy above the ionization potential of the next lowest-charge state, but slightly below the ionization potential of the desired charge state). The energy of the electron beam is controlled by the voltage V_0 applied to the center drift tube, but it is not exactly equal to eV_0 . The space charge of the electron beam depresses the on-axis potential somewhat, and therefore lowers the electron-beam energy below this. It is a simple matter to calculate the effect of the electron space charge on the energy [6], but inside the EBIT there is a complication due to the partial neutralization

of the negative electron space charge by the positive charge of trapped ions. It is difficult to determine the total number of trapped ions of all charge states (including those of any background gas trapped), but through a combination of calculation and measurement of the position of certain radiative recombination (RR) lines, it is possible to get a good estimate. We estimate that the overall space-charge correction to the energy is 150 eV, with an uncertainty of ± 50 eV. In order to produce Ba^{35+} , it is necessary for the electron-beam energy to be greater than the ionization potential of Ti-like barium (2.259 keV). In order to prevent the conversion of Ba^{35+} into Ba^{36+} , it is necessary to tune the beam energy to just below the ionization potential of the Ba^{35+} state itself (about 2.355 keV). We adjusted the drift tube potential so as to give a space-charge corrected value of the beam energy of about 2.35 keV. We confirmed that the beam energy was in the correct place by monitoring a previously observed [7] visible line in Ti-like barium using a monochromator and phototube. By maximizing the strength of this line and then increasing the center drift tube voltage by 100 V, we could be confident that the beam was optimized for producing Sc-like barium.

The EBIT was designed with several side ports at 90° to the electron beam which look directly into the ion trap. Certain ports are covered by thin (0.125 mm) beryllium windows, so as to hold the vacuum without appreciably attenuating x rays of energy greater than 2.5 keV. We took a number of Sc-like barium spectra using a solid-state Si(Li) detector. The spectrum shown in Fig. 1 was integrated over six hours at an estimated beam energy of 2.35 keV and a beam current of 56 mA. Although the monochromaticity of the electron beam has not been measured directly, we expect that the energy spread in the beam is less than 50 eV and probably less than 30 eV full width at half maximum (FWHM). The detector has an energy resolution of approximately 200 eV, and the combined detector-window system has about 45% efficiency at 2.5 keV, which increases to about 75% at 3.5 keV and 90% at 4.5 keV.

Using a computer simulation of the evolution of the charge state balance within the trap [8], which neglects the effect of DR, we estimate that over 90% of the trapped barium ions are either in the Ba^{34+} or Ba^{35+} states, with a ratio of 1:1.4 between them at 2.35 keV electron-beam energy. Including the effect of the expected DR process in the calculation, the ratio of Ba^{35+} to Ba^{34+} may be reduced significantly. In the analysis that follows, we account for this reduction by allowing P , the ratio of Ba^{35+} ion density to the sum of the Ba^{35+} and Ba^{34+} ion densities, to be reduced by a factor of β ($0 < \beta < 1$) which we track throughout the analysis to insure that the final comparison with theory is not circular. To confirm the line identifications described above, we measured spectra at a number of different beam energies in 10 eV steps. The precision with which we can change the center electron-beam energy is better than 2 eV, although the spread in electron-beam energy might be several tens of eV. The spectra taken at steps in beam energy are shown in Fig. 2. The main peak (ab) is reduced in magnitude as the beam energy is varied and at the same time its centroid shifts with energy. This is because the peak (ab) is composed of one DR peak and one RR peak. The resonant DR peak does not move, but its intensity is reduced when the RR peak moves.

Therefore the overall shift is more apparent off resonance. The radiative recombination (RR) lines all shift in the direction of change in the beam energy.

III. DR CROSS SECTION

The DR process proceeds as

$$e^- + A^{Z+}(i) \rightarrow A^{(Z-1)+**}(d) \rightarrow A^{(Z-1)+*}(f) + \hbar\omega. \quad (1)$$

The initial capture is a resonant process with conservation of energy and momentum leading to a doubly excited autoionizing resonance state A^{**} . As this state relaxes by x-ray emission ($d \rightarrow f$), the x-ray energies $\hbar\omega = E_d - E_f$ provide the distinct signature of the process. The DR cross section $\sigma^{\text{DR}}(i \rightarrow d \rightarrow f)$ calculated in the distorted-wave-projection operator method [9] and in the isolated resonance approximation, is given explicitly by

$$\sigma^{\text{DR}}(i, e_c \rightarrow d \rightarrow f) = \frac{4\pi}{(k_c a_0)^2} \tau_0 V_a(d \rightarrow i, e_c) \omega(d \rightarrow f) \times \tilde{\delta}(E_d \rightarrow E_i + e_c) (\pi a_0^2), \quad (2)$$

where k_c is the wave number of the continuum electron, a_0 is the Bohr radius, and τ_0 is the atomic unit of time. $V_a(i \rightarrow d)$ is the inverse of the autoionization rate $A_a(d \rightarrow i)$ of the intermediate state, and they are related by $V_a = g_d / (2g_i) A_a$, where g_d and g_i are the statistical weights of the intermediate and initial states, respectively. Also introduced in (2) is the fluorescence yield

$$\omega(d) = \frac{\Gamma_r(d)}{\Gamma_r(d) + \Gamma_a(d)} = \frac{\Gamma_r(d)}{\Gamma(d)} = \sum_f \omega(d \rightarrow f), \quad (3)$$

where $\Gamma_r(d) = \sum_f A_r(d \rightarrow f)$ and $\Gamma_a(d) = \sum_{i'} A_a(d \rightarrow i')$ are the total radiative and autoionization widths, respectively, of the d state of full width $\Gamma(d) = \Gamma_r(d) + \Gamma_a(d)$. The Lorentzian factor is defined as

$$\tilde{\delta}(E_d \rightarrow E_i + e_c) \equiv \frac{\Gamma(d)}{2\pi \left[(E_i + e_c - E_d)^2 - \frac{\Gamma(d)^2}{4} \right]},$$

with $\int \tilde{\delta} d e_c = 1. \quad (4)$

All possible states i that are connected to d , and which are allowed by energy conservation and angular momentum and parity rules, are summed over in $\Gamma_a(d)$.

The bound-state orbitals used in the calculation of $A_a(d \rightarrow i)$ and the radiative decay rate $A_r(d \rightarrow f)$ are computed numerically with the nonrelativistic, single-configuration Hartree-Fock code [10]. The continuum-wave function is calculated with the Hartree-Fock direct and explicit nonlocal exchange potentials. Because of the strong configuration mixing required for the ions of interest here, and the large number of angular momentum coupled states involved in the intermediate states (d), A_a and A_r may be conveniently evaluated in an angular momentum average (AMA) scheme in which all the couplings are averaged. This scheme only requires specification of the orbitals directly

involved and their statistical factors [11]. Spectator electrons play no direct role in AMA, except to screen the active electrons (thereby altering the radial wave functions) and to modify some of the statistical factors. An additional justification for the choice of the AMA is that the experimental width of the electron beam is $\Delta B_{\text{exp}} \sim 30$ to 50 eV, which averages out contributions from many term levels. Our past experience shows that the AMA and the resulting $\bar{\sigma}^{\text{DR}}$ are quite reasonable, particularly when dominant states d are involved, as is the case here [12]. [For a given d -state configuration there is only one AMA state but, in general, many LS terms, so the calculation of DR cross sections is conveniently done in the AMA scheme. In fact, in the limit that $\Gamma_r \gg \Gamma_a$, $\omega(d) \sim 1$, and the total DR cross sections obtained in different coupling schemes are identical to that of the AMA because of the sum over all terms involved.] The AMA scheme tends to overestimate the cross section by roughly 20%~40%, however.

Since the full width $\Gamma(d)$ of the DR peak described by $\tilde{\delta}$ is very narrow, on the order of ~ 0.1 eV or less, it is convenient for comparison with experiment to define an energy averaged cross section [11]

$$\begin{aligned} \bar{\sigma}^{\text{DR}}(i, e_c \rightarrow d \rightarrow f) &= \frac{1}{\Delta e_c} \int \sigma^{\text{DR}}(i, e_c \rightarrow d \rightarrow f) de'_c \\ &\equiv \frac{S^{\text{DR}}}{\Delta e_c}, \end{aligned} \quad (5)$$

where e_c is the kinetic energy of the recombining electron. Obviously, $\bar{\sigma}^{\text{DR}}$ depends on the choice of Δe_c , while $S^{\text{DR}} = \Delta e_c \bar{\sigma}^{\text{DR}}$ for the area under the DR peak is independent of Δe_c . The energy-averaged form is especially useful when experimental energy resolution of the electron beam is much larger than $\Gamma(d)$, and/or in describing many resonances which are present in a small energy interval. The choice for the energy bin Δe_c is completely arbitrary, so long as $\Delta e_c \gg \Gamma(d)$. Two convenient choices are $\Delta e_c = W =$ the detector-window resolution, or $\Delta e_c = \Delta B =$ the electron-beam width. We choose in this paper

$$\Delta e_c = W, \quad (6)$$

because the DR data are presented with the width W . As will become clear below, however, the final comparison is independent of this choice, especially when $W > \Delta B$.

IV. RR CROSS SECTION

We estimate the direct radiative recombination cross section σ^{RR} for the processes

$$e^- + [\text{Ar}]3d^n \rightarrow [\text{Ar}]3d^{n+1} + \hbar\omega, \quad (7)$$

$$e^- + [\text{Ar}]3d^n \rightarrow [\text{Ar}]3d^n 4l + \hbar\omega, \quad (8)$$

where $n=4$ for the Ba^{34+} ion and $n=3$ for the Ba^{35+} ion. The direct recombination cross section defined for capture (8) into a completely empty subshell nl is given by [13,14]

$$\begin{aligned} \sigma_{nl}^{(0)\text{RR}} &= \frac{16}{3\sqrt{2}\alpha^2} \left(\frac{\hbar\omega}{mc^2} \right)^3 \left(\frac{mc^2}{e_c} \right)^{1/2} [l(R_{nl}^{e_c, l-1})^2 + (l+1) \\ &\quad \times (R_{nl}^{e_c, l+1})^2] (\pi a_0^2), \end{aligned} \quad (9)$$

where $\alpha = e^2/\hbar c$ and e_c is the energy of the continuum electron. The radial integrals in (9) are defined as $R_{nl}^{e_c, l'} = \int_0^\infty R_{e_c, l'} R_{nl} r^3 dr$, where R_{nl} and $R_{e_c, l'}$ are the bound state and continuum radial wave functions, respectively, and $R_{e_c, l'}$ is here momentum normalized [13]. For capture (7) into a partially filled shell, the RR cross section is reduced simply as

$$\sigma_{nl}^{\text{RR}} = \frac{h_f}{2(2l_f+1)} \sigma_{nl}^{(0)\text{RR}}, \quad (10)$$

where h_f is the number of holes in the subshell nl_f before the radiative recombination transition and l_f is the orbital angular momentum quantum number. The bound-state and continuum-wave functions are calculated as in the DR case described above. Alternatively, we may also obtain the σ_{nl}^{RR} using the scaled Coulomb formula given in Ref. [9], with $Z_{\text{eff}} = (Z_C + Z_I)/2 \sim 45$, where Z_C is the nuclear core charge of the target ion and Z_I is the degree of ionization of the target ion before capture. For sufficiently large n , the RR cross-section scales as $1/n^3$, as can be seen from Kramer's formula [15],

$$\sigma_n^{\text{Kramer}}(\pi a_0^2) = \frac{8\pi}{3\sqrt{3}} \frac{\alpha^3}{\bar{\nu}^3} \frac{Z_{\text{eff}}^4}{e_c \left(e_c + \frac{Z_{\text{eff}}^2}{2\bar{\nu}^2} \right)}, \quad (11)$$

where $\bar{\nu}$ is the average effective principal quantum number given by $\bar{\nu} = n - \mu$, and μ is the quantum defect. In general, the relativistic and multipole contributions are known [13] to approximately cancel each other, so that the simple nonrelativistic dipole approximation (9) seems to provide a reliable estimate.

While the DR cross section described above is peaked at a particular resonance energy, the nonresonant RR cross section is continuous and slowly varying with the beam energy. Therefore for comparison with experiment the RR cross section is integrated over an energy bin width equal to the width of the experimental electron-beam ΔB as

$$S^{\text{RR}} = \int_{\Delta B} \sigma^{\text{RR}} de_c \approx \Delta B \bar{\sigma}^{\text{RR}}, \quad (12)$$

where it is assumed that $\Delta B < W$. In the opposite case of $W < \Delta B$, the ΔB in (12) is to be replaced by W .

V. RESULTS

The spectrum shown in Fig. 1 contains all the x rays emitted by both the RR and DR processes for an electron-beam energy of 2.35 keV (with strong attenuation below 2 keV due to absorption in the beryllium windows). Since the absolute x ray intensities depend on, among other factors, the trapped ion density and the overlap between the electron beam and the ions, which are not known, we focus on only

TABLE I. The autoionization and radiative rates for the resonance state $1s^2 2s^2 2p^5 3s^2 3p^6 3d^5$ of the Ba^{35+} ion are presented in units of (1/sec) in the AMA coupling scheme. Brackets indicate powers of 10.

i	$e_c(\text{Ry})$	l_c	$A_a(d \rightarrow i, l_c)$	f	$A_r(d \rightarrow f)$	$\hbar\omega(\text{Ry})$
[Ar] $3d^3$	172	1	0.310[+14]	[Ar] $3d^4$	0.259[+15]	340
		3	0.418[+15]	[Ar] $3s3d^5$	0.136[+14]	315
		5	0.567[+13]			
[Ne] $3p^6 3d^5$	131	1	0.547[+13]			
[Ne] $3s3p^5 3d^5$	141	0	0.126[+15]			
		2	0.341[+13]			
[Ne] $3s3p^6 3d^4$	156	1	0.146[+13]			
		3	0.126[+14]			
[Ne] $3s^2 3p^4 3d^5$	151	1	0.528[+15]			
		3	0.127[+14]			
[Ne] $3s^2 3p^5 3d^4$	166	0	0.468[+14]			
		2	0.493[+15]			
		4	0.401[+14]			

their relative magnitudes. In this case, we are comparing resonant and nonresonant total cross sections, each with a unique energy dependence. Therefore S^{DR} of (5) and S^{RR} of (12) are the basic theoretical quantities for comparison with experiment, since these are the quantities that the experimentalist directly measures. (It is also assumed that the x-ray detector for the RR and DR at 90° does not affect the relative ratios.)

A. Theoretical result

The results of the calculation are presented in Tables I and II. The autoionization and radiative rates calculated in the AMA scheme are presented in units of 1/sec. Reemphasizing that the choice of the energy averaging bin size Δe_c is completely arbitrary [i.e., for $\Delta e_c \gg \Gamma(d)$], the DR cross section is averaged over a bin size equal to the resolution of the x-ray detector W where $\Delta e_c = W = (15 \pm 3)$ Ry. This dependence will drop out in the cross-section ratios. The AMA procedure generally overestimates σ^{DR} by approximately 20%–40%, so that the corrected theoretical ratio should be reduced [11,12] by a factor of 1.3. Although the AMA theory

is relatively simple, the adjustment factor in fact contains the details of state coupling; it is the result of many detailed calculations performed previously.

For the Ba^{35+} system, we find that the autoionization width of the resonance state $d = 1s^2 2s^2 2p^5 3s^2 3p^6 3d^5$ is $\Gamma_a(d) = 0.172 \times 10^{16} \text{ sec}^{-1}$, the radiative width is $\Gamma_r(d) = 0.273 \times 10^{15} \text{ sec}^{-1}$, and thus the fluorescence yield is $\omega(d) = 0.137$. The energy averaged total DR cross section for the $2p \rightarrow 3d$ excitation capture is then

$$\bar{\sigma}_{Ba^{35+}}^{\text{DR}} = 2.7 \times 10^{-21} \text{ cm}^2 / 1.3 = 2.1 \times 10^{-21} \text{ cm}^2, \quad (13)$$

where both the $3d \rightarrow 2p$ and $3s \rightarrow 2p$ radiative decay contributions are included. For the Ba^{34+} case with $d = 1s^2 2s^2 2p^5 3s^2 3p^6 3d^6$ we find that $\Gamma_a = 0.203 \times 10^{16} \text{ sec}^{-1}$, $\Gamma_r = 0.318 \times 10^{15} \text{ sec}^{-1}$, $\omega = 0.136$, yielding

$$\bar{\sigma}_{Ba^{34+}}^{\text{DR}} = 1.9 \times 10^{-21} \text{ cm}^2 / 1.3 = 1.4 \times 10^{-21} \text{ cm}^2. \quad (14)$$

The $2P_{1/2} - 2P_{3/2}$ splitting is on the order of 500 eV, so only the $2P_{3/2}$ excitations satisfy the resonance condition. This is

TABLE II. The autoionization and radiative rates for the resonance state $1s^2 2s^2 2p^5 3s^2 3p^6 3d^6$ of the Ba^{34+} ion are presented in units of (1/sec) in the AMA coupling scheme. Brackets indicate powers of 10.

i	$e_c(\text{Ry})$	l_c	$A_a(d \rightarrow i, l_c)$	f	$A_r(d \rightarrow f)$	$\hbar\omega(\text{Ry})$
[Ar] $3d^4$	178	1	0.454[+14]	[Ar] $3d^5$	0.305[+15]	339.0
		3	0.615[+15]	[Ar] $3s3d^6$	0.133[+14]	312.0
		5	0.821[+13]			
[Ne] $3p^6 3d^6$	135	1	0.538[+13]			
[Ne] $3s3p^5 3d^6$	145	0	0.126[+15]			
		2	0.325[+13]			
[Ne] $3s3p^6 3d^5$	161	1	0.177[+13]			
		3	0.147[+14]			
[Ne] $3s^2 3p^4 3d^6$	155	1	0.517[+15]			
		3	0.126[+14]			
[Ne] $3s^2 3p^5 3d^5$	172	0	0.542[+14]			
		2	0.576[+15]			
		4	0.471[+14]			

TABLE III. The direct radiative capture cross section σ^{RR} is given for capture into states $[\text{Ar}]3d^3nl$ for the cases $n=3, 4$, and 5 for the Ba^{35+} ion in (cm^2) corresponding to the experimental electron beam energy $e_c=173$ Ry. Brackets indicate powers of 10.

f	$\hbar\omega(\text{Ry})$	$\sigma^{\text{RR}} (\text{cm}^2)$
$[\text{Ar}]3d^4$	333.0	1.62[-22]
$[\text{Ar}]3d^34s$	263.0	3.37[-23]
$[\text{Ar}]3d^34p$	259.0	1.05[-22]
$[\text{Ar}]3d^34d$	253.0	1.04[-22]
$[\text{Ar}]3d^34f$	247.0	2.68[-23]
$[\text{Ar}]3d^35s$	226.0	1.63[-23]
$[\text{Ar}]3d^35p$	224.0	5.10[-23]
$[\text{Ar}]3d^35d$	221.0	5.58[-23]
$[\text{Ar}]3d^35f$	218.0	2.03[-23]
$[\text{Ar}]3d^35g$	215.0	2.03[-24]

accounted for by further reducing the DR cross sections obtained in the AMA scheme by a factor of 1/1.5, as has been done above.

Tables III and IV show the direct radiative recombination (RR) cross sections along with the photon energies corresponding to the electron-beam energy of 172 Ry=2.35 keV. Since the energy of the emitted x ray is the same in both cases, we first note that the peak ab is a combination of DR ($2p+l_c \rightarrow 3d3d \rightarrow 2p3d + \gamma$) and RR ($n=3$). From Tables I-IV, the theoretical cross-section ratios for the two ions are

$$\frac{\bar{\sigma}_{\text{Ba}^{35+}}^{\text{DR}}}{\bar{\sigma}_{\text{Ba}^{35+}}^{\text{RR}}(n=3)} \sim 13, \quad (15)$$

and

$$\frac{\bar{\sigma}_{\text{Ba}^{34+}}^{\text{DR}}}{\bar{\sigma}_{\text{Ba}^{34+}}^{\text{RR}}(n=3)} \sim 11.$$

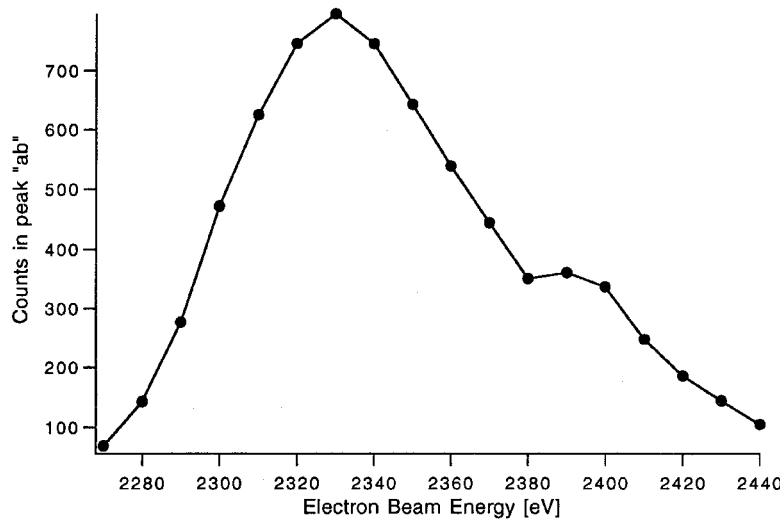


FIG. 3. Sc-like barium spectra of the DR peak ab taken at electron-beam energies ranging from 2270 eV to 2440 eV in steps of 10 eV. The graph clearly shows the Ba^{35+} - Ba^{34+} DR separation.

TABLE IV. The direct radiative capture cross section σ^{RR} is given for capture into states $[\text{Ar}]3d^4nl$ for the cases $n=3$ and 4 for the Ba^{34+} ion in (cm^2) corresponding to the experimental electron beam energy $e_c=173$ Ry. Brackets indicate powers of 10.

f	$\hbar\omega(\text{Ry})$	$\sigma^{\text{RR}} (\text{cm}^2)$
$[\text{Ar}]3d^5$	326.0	1.40[-22]
$[\text{Ar}]3d^44s$	259.0	3.24[-23]
$[\text{Ar}]3d^44p$	255.0	1.01[-22]
$[\text{Ar}]3d^44d$	249.0	1.02[-22]
$[\text{Ar}]3d^44f$	243.0	2.55[-23]

Therefore the contribution of about 8% to the ab peak from direct radiative recombination to the $n=3$ level, (RR, $n=3$), must be subtracted before comparing with the theory.

Next, we examine the relative size of the two DR peaks ab and a' . They arise from the initial radiationless capture $2p+l_c \rightarrow 3d3d$ followed by radiative decays; either $3d \rightarrow 2p$ (with a photon energy 4.6 keV for Ba^{35+}); or $3s \rightarrow 2p$ (with a photon energy 4 keV for Ba^{35+}). Similar decays occur for the Ba^{34+} ion. From Tables I and II, the relative probability for these two branches is

$$A_r(3d \rightarrow 2p)/A_r(3s \rightarrow 2p) \approx 19. \quad (16)$$

This is consistent with the ratio seen in Fig. 1, where the two DR peaks, $a \equiv ab - b3$ and a' , have an intensity ratio of about 16.

In order to compare the resonant DR process with the nonresonant RR process, we adopt the energy integrated cross-section S . For the DR case, we have

$$S^{\text{DR}} \equiv \bar{\sigma}^{\text{DR}} W, \quad (17)$$

which is independent of W , the detector resolution. For the RR case, assuming $W > \Delta B$,

$$S^{\text{RR}} \equiv \bar{\sigma}^{\text{RR}} \Delta B. \quad (18)$$

TABLE V. The ratio of the DR and RR cross sections η are given corresponding to capture into $4l$ levels for the Ba^{35+} and Ba^{34+} systems.

Ba^{35+}	
$\eta_{\text{theory}}^{\text{AMA}}(3d \rightarrow 2p)$	14
$\eta_{\text{theory}}^{\text{AMA}}(3s \rightarrow 2p)$	0.7
$\eta_{\text{theory}}^{\text{corrected}}(3d \rightarrow 2p)$	7 ± 1
$\eta_{\text{theory}}^{\text{corrected}}(3s \rightarrow 2p)$	0.4 ± 0.1
Ba^{34+}	
$\eta_{\text{theory}}^{\text{AMA}}(3d \rightarrow 2p)$	11
$\eta_{\text{theory}}^{\text{AMA}}(3s \rightarrow 2p)$	0.6
$\eta_{\text{theory}}^{\text{corrected}}(3d \rightarrow 2p)$	6 ± 1
$\eta_{\text{theory}}^{\text{corrected}}(3s \rightarrow 2p)$	0.3 ± 0.1

As noted earlier, $\bar{\sigma}^{\text{RR}}$ is nearly independent of ΔB , so that S^{RR} is proportional to ΔB . For the present experiment, we take $\Delta B \approx (4 \pm 1)$ Ry. (See Sec. V D and Fig. 3.)

To facilitate comparison of the DR and RR cross sections we use the $n=4$ RR capture cross section to normalize the data. This is necessary partly because of the difficulty of determining absolute ion densities and ion-electron spatial overlap inside the EBIT. The cross-section ratios are independent of these parameters, such as the ion and electron densities. For convenience, we thus define $\eta \equiv \bar{\sigma}^{\text{DR}}(\Delta e_c) / \bar{\sigma}_4^{\text{RR}}$, with Δe_c given by (6). Treating the Ba^{35+} system first, we find, for the full participation of 6 $2p$ electrons,

$$\eta_{\text{theory}}^{\text{AMA}}(3d \rightarrow 2p) = \frac{\bar{\sigma}^{\text{DR}}(3d \rightarrow 2p)}{\bar{\sigma}_4^{\text{RR}}} = \frac{3.9 \times 10^{-21} \text{ cm}^2}{2.7 \times 10^{-22} \text{ cm}^2} \sim 14, \quad (19)$$

and

$$\eta_{\text{theory}}^{\text{AMA}}(3s \rightarrow 2p) = \frac{\bar{\sigma}^{\text{DR}}(3s \rightarrow 2p)}{\bar{\sigma}_4^{\text{RR}}} = \frac{2.0 \times 10^{-22} \text{ cm}^2}{2.7 \times 10^{-22} \text{ cm}^2} \sim 0.7.$$

The theory must contain the AMA correction factor of 1/1.3 and the $p_{3/2}$ correction of 1/1.5. Thus for the Ba^{35+} case we finally have the theoretical result

$$\eta_{\text{theory}}^{\text{corrected}}(3d \rightarrow 2p) \sim \eta_{\text{theory}}^{\text{AMA}}(3d \rightarrow 2p) \frac{1}{1.3} \frac{1}{1.5} \sim 7 \pm 1$$

$$\eta_{\text{theory}}^{\text{corrected}}(3s \rightarrow 2p) \sim \eta_{\text{theory}}^{\text{AMA}}(3s \rightarrow 2p) \frac{1}{1.3} \frac{1}{1.5} \sim 0.4 \pm 0.1. \quad (20)$$

Applying the same procedure to the Ba^{34+} system we obtain the result summarized in Table V. For this case we find $\eta_{\text{theory}}^{\text{AMA}}(3d \rightarrow 2p) = 11$, $\eta_{\text{theory}}^{\text{AMA}}(3s \rightarrow 2p) = 0.5$, $\eta_{\text{theory}}^{\text{corrected}}(3d \rightarrow 2p) = 6 \pm 1$, and $\eta_{\text{theory}}^{\text{corrected}}(3s \rightarrow 2p) = 0.3 \pm 0.1$.

B. Experimental result

Since experimentally $W > \Delta B$, the RR cross section is effectively measured in terms of ΔB . Therefore, following (12), it is more convenient for comparison with experiment to define

$$\eta' \equiv \frac{S^{\text{DR}}}{S^{\text{RR}}} \approx \frac{S^{\text{DR}}}{\Delta B \bar{\sigma}^{\text{RR}}} \approx \frac{\bar{\sigma}^{\text{DR}}(W)}{\bar{\sigma}^{\text{RR}}} \frac{W}{\Delta B} \approx \eta \frac{W}{\Delta B}. \quad (21)$$

Obviously, the W dependence of η drops out in η' , since $\bar{\sigma}^{\text{DR}}(W) W$ is independent of W .

We should make two further points before the comparison is made. First, for Ba^{34+} and Ba^{35+} , the RR x rays are only separated in energy by about 80 eV, which is well within W , so that x rays from both Ba^{34+} and Ba^{35+} are collected. Second, the experimentally derived DR cross sections are very much dependent on the relative abundances of the Ba^{35+} and Ba^{34+} . The DR resonance energy difference for the two charge states is also ~ 80 eV, which is outside the electron beam width ΔB . Therefore, when e_c is fixed at the DR resonance for the Ba^{35+} ion, no DR is allowed for the Ba^{34+} target ion (see Sec. V D.) The theoretical η' should be further multiplied by P , the ratio of the Ba^{35+} ion density to the sum of the Ba^{34+} and Ba^{35+} ion densities before comparing with experiment. Thus

$$\eta' = \frac{\bar{\sigma}^{\text{DR}}(W)}{\bar{\sigma}^{\text{RR}}} \left(\frac{W}{\Delta B} P \right). \quad (22)$$

For $P \approx 1/3$, obtained by combining the results of the numerical simulation [8] for the charge state distribution and an intermediate value of $\beta = 0.6$, we have

$$\frac{W}{\Delta B} P \approx \frac{200 \text{ eV}}{45 \text{ eV}} \times 1/3 \approx 1.5 \pm 0.4, \quad (23)$$

and thus $\eta' \approx \eta$ in the present experiment. (For comments on the 45 eV beam width see Sec. V D.) As our assumption for β varies over the full range of physically allowed values, corresponding to the DR cross sections varying from the extremes of zero to infinity, the value listed in (23) remains between 2.6 and 0, respectively. Our estimates of uncertainty on (23) reflect a more reasonable range of allowance for the DR correction.

The experimental DR ($3d \rightarrow 2p$) cross section is extracted from the data by first subtracting the RR ($n=3$) contribution. To eliminate the dependence on the ionic and electronic densities in this subtraction, we set

$$\begin{aligned} \sigma_{\text{exp}}^{\text{DR,adjusted}}(3d \rightarrow 2p) \\ \approx \sigma_{\text{exp}}^{\text{DR}}(3d \rightarrow 2p) - \frac{\sigma_{\text{exp}}^{\text{RR}}(n=4)}{\sigma_{\text{theory}}^{\text{RR}}(n=4)} \sigma_{\text{theory}}^{\text{RR}}(n=3). \end{aligned} \quad (24)$$

The $3s \rightarrow 2p$ transition corresponding to peak a' need not be adjusted. From the fit of the experimental data, we can directly obtain only η' . The relative magnitudes of the DR and RR peaks (ab and $b4$) and (a' and $b4$) are then given by

$$\eta'_{\text{exp}}(3d \rightarrow 2p) \approx 11 \pm 3,$$

$$\eta'_{\text{exp}}(3s \rightarrow 2p) \approx 0.8 \pm 0.2. \quad (25)$$

Hence, to compare with (20) the quantities in (25) are converted to η using (21) as

$$\eta_{\text{exp}} = \eta' \times \left(\frac{\Delta B}{WP} \right). \quad (26)$$

Comparing (26) with (20) we find for the Ba^{35+} case

$$\eta_{\text{exp}}(3d \rightarrow 2p) = 7 \pm 3,$$

$$\eta_{\text{exp}}(3s \rightarrow 2p) = 0.5 \pm 2 \quad (27)$$

and the theoretical peak ratios are found to be in excellent agreement with the experimentally observed values.

C. RR ratios

We also compare the relative magnitudes of the RR peaks ξ . The theory predicts (see Table III) for Ba^{35+}

$$\xi(4,5)_{\text{theory}} = \frac{\sigma_5^{\text{RR}}}{\sigma_4^{\text{RR}}} = 0.54 \quad (0.51), \quad (28)$$

$$\xi(4,6)_{\text{theory}} = \frac{\sigma_6^{\text{RR}}}{\sigma_4^{\text{RR}}} = 0.31 \quad (0.30),$$

and

$$\xi(5,6)_{\text{theory}} = \frac{\sigma_6^{\text{RR}}}{\sigma_5^{\text{RR}}} = 0.58 \quad (0.58),$$

where the numbers in parentheses are the ratios expected from the n^{-3} scaling behavior of $\sigma^{\text{RR}}(n)$. The ξ 's for Ba^{34+} (from Table IV) are similar to the above, (28). Clearly, the calculated ratios (which were done in the distorted-wave approximation) are consistent with the n^{-3} scaling. This is also the case in (11) when $e_c \gg (Z_{\text{eff}}^2/2\bar{v}^2)$. The experiment gives

$$\xi(4,5)_{\text{exp}} \sim 0.56 \quad (29)$$

which is quite close to the theoretical value of 0.52 obtained from (26), after averaging the weighted contributions from the two charge states.

D. Electron energy dependence of the DR peak

The DR part of peak *ab* [which contains both the DR and RR ($n=3$) contributions] may further be analyzed by varying the electron beam energy. Figure 3 shows two peaks corresponding to the DR contribution from Ba^{35+} and Ba^{34+} , respectively. The RR ($n=3$) contribution should be an approximately constant background on the order of 1/20 of the large peak value, as shown in (15). Thus, in Fig. 3, the RR count should be on the order of 35. The figure shows an upper bound on the electron-beam width of $\Delta B \approx 5 \text{ Ry} \approx 65 \text{ eV}$ (FWHM). The total width of the line is made up by the fine-structure splitting of the $3d$ level into $j=3/2$ and $j=5/2$ levels and the electron-beam energy width. The $3d$ fine-structure splitting can be calculated to be around 20 eV

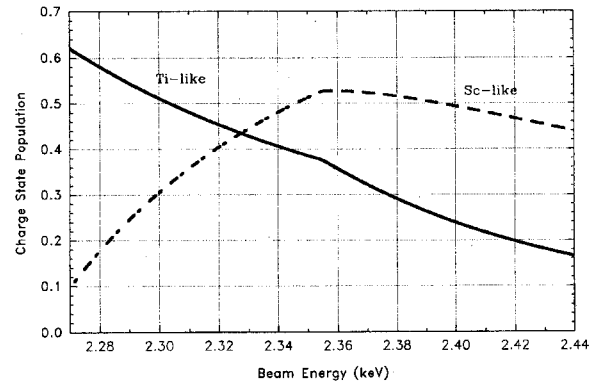


FIG. 4. Relative charge state populations of scandiumlike Ba^{35+} and titaniumlike Ba^{34+} ions in the EBIT as a function of the kinetic energy of the electron beam.

which gives a value of about 45 eV for the beam energy width. This is in accordance with our earlier estimate for the width to be between 30 eV and 50 eV. We used the above determined 45 eV beam energy width throughout our analysis. The large peak in Fig. 3 centered around $e_c \approx 2330 \text{ eV}$ corresponds to the DR process for the Ba^{35+} target ion, while the small peak around 2400 eV should be the contribution from Ba^{34+} . The reason for the reduced count rate for the second peak is the change of the charge state balance by changing the beam energy. Figure 4 shows the dependence of the Ba^{35+} and Ba^{34+} charge state populations on the electron-beam energy using the results of our model calculations (Ref. [8]). To be able to compare the experimental DR ratios with theory, one has to normalize the peak intensities to the same number of ions in the particular charge state the resonance corresponds to. This can be done using the populations of the corresponding charge states as shown in Fig. 4. The ratio of the relative population of the Ba^{35+} ions at 2.33 keV and the Ba^{34+} ions at 2.39 keV is $44\%/26\% = 1.69$. Since this ratio does not include the effect of DR itself on the charge state balance the value given here may be biased by the fact that the DR process removes ions from the particular charge state in which they are resonant. Multiplying the theoretical DR cross-section ratio with this number our estimate for the intensity ratio is

$$\frac{\bar{\sigma}^{\text{DR}}(35+)}{\bar{\sigma}^{\text{DR}}(34+)} 1.69 = 1.3 \times 1.69 = 2.2. \quad (30)$$

This is very good agreement with the experimentally observed peak intensities shown on Fig. 3. We note that the changing charge state balance complicates the analysis of the results in all the cases when the experiment requires the change of the electron-beam energy. This is the situation, e.g., when one studies resonant processes just as in our case. Since DR removes ions from the charge state in which they are resonant, there are fewer ions in the appropriate charge state at the peak centroid than in the tails. Thus, the estimate of the DR cross section obtained by using the integral of the peak is biased low, and the estimate of the width is biased high. These biases are not as important in obtaining the ratios of the two DR resonances, however. To resolve this problem in future experiments we plan to apply a transient operation

technique. In this method one optimizes for a certain charge state balance at a given beam energy then transiently changes the beam energy to a different value where the observation is made. By choosing the off-steady-state time sufficiently short one can make sure that the number of ions in a given charge state is always the same independently of the transient energy. Alternatively, rather than the beam flipping procedure described above, the beam ramping technique may also be used.

VI. DISCUSSION

We have presented recent experimental data on RR and DR processes in Ba^{35+} and Ba^{34+} ions obtained with the EBIT at NIST, as well as a theoretical analysis. The x-ray peak (ab), corresponding to the DR $2p \rightarrow 3d$ excitation followed by the $3d \rightarrow 2p$ radiative decay, has been compared to the $n=4$ RR x-ray peak $b4$. Note that the energy of the DR x-ray is twice that of the incident electron kinetic energy. In addition, the smaller peak a' at 4 keV has been shown to be consistent with the ab peak and with $b4$. In all cases, good agreement is obtained to within $\pm 20\%$, after slight but justifiable adjustments are made to both the theoretical and experimental values. The present analysis confirms our earlier experience with the AMA procedure that, for complex open-shell ions such as Ba^{35+} , and for W and ΔB large, the method works well in describing the dominant transitions. As the experimental resolution improves, more refined treatment should be necessary. Comparisons of the RR peaks relative to each other was not possible for $n > 5$ due to the uncertainty in isolating their contributions from the data. However, the plateau around 2.6 keV is probably due to the RR contribution from $n > 5$. Thus all the significant features of the x-ray spectrum above 2.4 keV have been satisfactorily explained.

The x-ray energies for the DR processes differ by $\sim 20\text{--}30$ eV for the Ba^{35+} and Ba^{34+} target ions, while e_c for the two ions differ roughly by 80 eV. Therefore, within the resolution of the electron beam energy $\Delta B \leq 50$ eV, it is impossible for both ions to be involved in the DR process at the same time. On the other hand, the RR peaks can have contributions from both charge states, as the detector resolution is $W \approx 200$ eV, much larger than the 80 eV difference in the x-rays from two different ions, for each n . Therefore part of the broadening of the peaks may be due to the presence of two or more charge states in the neighborhood of Ba^{35+} . We emphasize that under the experimental conditions $W > \Delta B \gg \Gamma(d)$ the RR x-ray counts were detected from both ions Ba^{35+} , Ba^{34+} with a band width of ΔB , while the DR counts were from the Ba^{35+} only. Therefore, we expect the

spectral shapes to change as W and ΔB , and their ratio, are altered.

The final broad peak at the x-ray energies $\hbar\omega < 2$ keV is currently being examined theoretically [16]. This peak is produced mainly by collisional excitation fluorescence along with the cascade contribution from the primary RR process discussed above, and by Bremsstrahlung. In addition, the DR processes contribute which involve the M -shell electron excitations to high Rydberg levels ($n > 6$) accompanied by capture to these levels. Preliminary estimates indicate that the individual cross sections for such M -shell DR processes are roughly 100 times smaller than the $2p$ excitation DR considered above. This is to be expected from the approximate n^{-6} scaling. There are very many available intermediate resonance states to be included, however, with the angular momenta of the levels extending to large values $l \leq 10$. The explicit calculation of the M -shell DR is difficult and time consuming, even in the AMA procedure. A direct attempt is being made [16], employing the same procedure as in the L -shell DR, while a simpler alternate theoretical procedure is being developed. We also conjecture that at least some part of this low-energy x-ray peak is the result of a recombination effect [Radiative DR (RDR)] proposed recently [17], in which the excitation capture takes place simultaneously with an x-ray emission. Such a process is DR-like, but nonresonant, and should be important when DR is weak or forbidden. Previous estimates suggest that the RDR contribution can be a few tens of a percent of DR, and can compete with RR processes as well.

Further experimental study of the DR lines in Ba^{34+} and Ba^{35+} is being planned, employing a transient technique which prevents the DR resonance from altering the charge state balance. By repeatedly switching the electron-beam energy on to resonance for approximately 10 ms and then off resonance for approximately 50 ms, the charge balance may remain approximately steady at its off-resonance value. This would increase the Ba^{35+} ion fraction P decrease its uncertainty, and simplify the analysis.

This relatively simple EBIT experiment has yielded a surprisingly diverse amount of information, as demonstrated in this report. In addition, it would be very interesting to extend the x-ray measurement below the 2 keV limit, where a rich variety of physical processes are expected.

ACKNOWLEDGMENTS

The theoretical part of the work reported here was supported in part by a DOE Grant.

-
- [1] D. DeWitt, D. Schneider, M. H. Chen, M. B. Schneider, D. Church, G. Weinberg, and M. Sakurai, *Phys. Rev. A* **47**, R1597 (1993).
- [2] D. Knapp, P. Beiersdorfer, M. H. Chen, J. Scofield, and D. Schneider, *Phys. Rev. Lett.* **74**, 54 (1995).
- [3] G. Kilgus, D. Habs, D. Schwalm, A. Wolf, N. R. Badnell, and A. Müller, *Phys. Rev. A* **46**, 5730 (1992); and J. Linkemann, J. Kenntner, A. Müller, A. Wolf, D. Habs, D. Schwalm, W. Spies, A. Frank, A. Liedtke, G. Hoffmann, E. Salzborn, N. R. Badnell, and M. S. Pindzola, *Nucl. Instrum. Methods Phys. Res. B* **98**, 154 (1995).
- [4] Y.-K. Kim (private communication).
- [5] A. Levine, R. E. Marrs, J. R. Henderson, D. A. Knapp, and M. Schneider, *Phys. Scr.* **T22**, 157 (1988); R. E. Marrs, C. Bennet, M. H. Chen, T. Cowan, D. Dietrich, J. R. Henderson, D. A. Knapp, M. A. Levine, K. J. Reed, M. B. Schneider, and J. H.

- Scofield, *J. Phys. (Paris)* **50**, C1-445 (1989); R. E. Marrs, *Comments At. Mol. Phys.* **27**, 57 (1991); J. D. Gillaspy, J. R. Roberts, C. M. Brown, and U. Feldman, in *VIIth International Conference on the Physics of Highly Charged Ions*, edited by P. Richard, M. Stockli, C. L. Cocke, and C. D. Lin (AIP, New York, 1993), p. 682.
- [6] Assuming a uniform charge density within the beam and then applying Gauss's law gives the correct answer to within 5%.
- [7] C. A. Morgan, F. G. Serpa, E. Takács, E. S. Meyer, J. D. Gillaspy, J. Sugar, J. R. Roberts, C. M. Brown, and U. Feldman, *Phys. Rev. Lett.* **74**, 1716 (1995).
- [8] B. M. Penetrante, J. N. Bardsley, D. deWitt, M. W. Clark, and D. Schneider, *Phys. Rev. A* **43**, 4861 (1991); We thank H. Margolis for an improved C language version of B. M. Penetrante's original Fortran code, and D. Knapp for a similar but simpler independently written code.
- [9] J. Gau and Y. Hahn, *J. Quant. Spectrosc. Radiat. Transfer* **23**, 121 (1980); Y. Hahn, *Phys. Rev. A* **12**, 895 (1975).
- [10] C. Froese-Fisher, *The Hartree-Fock Method for Atoms* (Wiley, New York, 1977).
- [11] Y. Hahn, *Advances in Atomic and Molecular Physics*, Vol. 21, edited by D. R. Bates and B. Bederson (Academic, New York, 1985), p. 123; Y. Hahn and K. J. LaGattuta, *Phys. Rep.* **166**(4), 195 (1988), particularly p. 212.
- [12] D. J. McLaughlin and Y. Hahn, *J. Quant. Spectrosc. Radiat. Transfer* **28**, 343 (1982).
- [13] Y. Hahn and D. W. Rule, *J. Phys. B* **10**, 2689 (1977).
- [14] D. J. McLaughlin and Y. Hahn, *Phys. Rev. A* **43**, 1313 (1991).
- [15] H. A. Kramer, *Philos. Mag.* **46**, 836 (1923).
- [16] D. McLaughlin and Y. Hahn (unpublished).
- [17] Y. Hahn, *Z. Phys. D* **33**, 247 (1995).

The use of a Spherically Curved Crystal Spectrometer for X-ray Measurements on Electron Beam Ion Trap

Y. Aglitskiy,^{1*} F. G. Serpa,^{1†} E. S. Meyer,¹ J. D. Gillaspay,¹ C. M. Brown,² A. Ya. Faenov³ and T. A. Pikuz³

¹ National Institute of Standards and Technology Gaithersburg, MD 20899, USA

² Naval Research Laboratory, Washington D. C. 20375, USA

³ Multicharged Ions Spectra Data Center of VNIIFTRI, Mendeleevo, Moscow region, 141570, Russia

Received March 3, 1997; accepted in revised form December 22, 1997

PACS Ref: 61.10–i, 61.50Ah, 52.25Nz

Abstract

Spherically curved crystal spectrometers are demonstrated for use on an Electron Beam Ion Trap (EBIT) for the first time. Such spectrometers are characterized by high light collection efficiency and relative insensitivity to source position, simultaneously, giving them an advantage that no X-ray spectrometer previously used on an EBIT has had. One of the spectrometer crystals tested is composed of mica, giving it the additional advantage that it can be used with reasonable efficiency up to very high order, allowing spectra to span a broad wavelength range from 0.5 Ångströms to 20 Ångströms. Spectra from Ne-like barium and He-like argon are presented.

1. Introduction

The Electron Beam Ion Trap (EBIT) is well known as a unique source for high precision measurements of multicharged ion spectra [1–8]. When compared to the commonly used high temperature and often high density plasmas, the EBIT plasma line shapes are not distorted by Doppler and Stark broadenings and shifts. The inevitable presence of dielectronic satellites in the vicinity of almost every line of multicharged ions mimics the line shift in conventional ion sources. In the case of EBIT the right choice of an electron beam energy can significantly diminish this complication. The spatial stability and the very small diameter of the ion trap make it possible to use slitless spectrometers throughout wide wavelength regions. Even a simple flat crystal spectrometer can provide quite high resolution in this case.

Von Hamos X-ray crystal spectrometers with focusing in the direction perpendicular to the dispersion plane were successfully used for spectral recording of highly ionized atoms excited in the Lawrence Livermore National Laboratory EBIT [3]. Since this method is spectroscopically equivalent to the flat crystal scheme, it limits the possible reference lines to internal ones. The use of spectrographs with focusing in the dispersive plane (Johann or Johansson type) [4–7] is insensitive to source position which gives one the possibility to use reference lines from an external source i.e. a conventional X-ray tube. The somewhat low EBIT count rates and resultant collecting times require the use of low-noise detectors with high quantum efficiency. Position sensitive proportional counters (PSPC) meet these requirements

but they have relatively poor spatial resolution (200 μm to 300 μm). Therefore, if the goal is to have high spectral resolution, one has to increase the size of the crystal spectrometer i.e. the radius of the focusing crystal. This leads in turn to lower intensity and makes the detector noise requirements even more difficult. The total number of ions in the trap has been estimated to be close to 10^5 [2]. This number is sufficient for some observations but it is worthwhile to use more efficient and sophisticated techniques of spectral recording to reduce the time required to collect statistically good data.

It has already been shown that the use of spherically curved crystals can significantly improve the efficiency of X-ray spectrometers [9–18]. The most spectacular results were obtained for point source devices such as laser produced plasmas and low inductance vacuum discharges of different types. Actually such crystals can produce an image of an X-ray source [19–27]. In this work we present the first application of spherically curved crystals of mica and quartz for recording X-ray spectra of multicharged ions excited in an EBIT.

The quartz crystal with the 10 $\bar{1}1$ orientation has high resolution and high reflectivity in the wavelength region below 6.67 Å and is very useful for recording weak spectra from the EBIT. A spherically curved mica crystal spectrometer has several useful properties. The first available order of reflection from mica corresponds to the lattice spacing $2d \approx 19.9$ Å. It can record X-ray spectra with a low energy limit of about 700 eV. The EBIT has demonstrated the ability to produce the most highly ionized atoms in the laboratory, and spectra with very short wavelengths. It is also opportune to seek new and worthwhile objectives at lower energies and lower stages of ionization as well. More efficient spectrometers will allow studies that formerly had to be bypassed because of the low brightness of the EBIT. For instance in the trade-off between the magnitude of the Lamb-shift, which increases with Z , and the accuracy with which it can be measured, the optimum does not necessarily fall in the region of extremely high energy transitions. There are also many other interesting spectra in the soft X-ray region to study. For example, sodium-like as well as other ions with open M-shells belonging to elements in the middle of the periodic table, have their resonance lines in this soft X-ray spectral region. Also transitions without change of principal quantum number ($\Delta n = 0$) of extremely heavy multicharged ions are found in this region as well. $\Delta n = 1$ transitions in multicharged ions of rare earth elements with

* Science Applications International Corporation, McLean, Virginia, 22102, USA.

† Physics Department, University of Notre Dame, Notre Dame, IN 46556, USA.

an open 3d shell are also found in this region. Thus developing sensitive spectrometers for soft X-ray spectra could be quite fruitful when applied to EBIT sources.

In the case of mica, it is possible to use more than one order of reflection. In fact one can use orders $n = 1, 2, 3, 4, 5, 7, 8, 10, 11, 12$ and 13 with quite reasonable efficiency [9–18, 21–29]. This means that while maintaining optimal geometric conditions, we can apply mica as a high resolution X-ray analyzer from 0.5 \AA to almost 20 \AA . The possibility of having spectra recorded in multiple orders of reflections is also useful for some applications of X-ray spectroscopy to high precision atomic physics.

A differential measurement of the ground state Lamb-shift in H-like ions is an example of such techniques [30]. This idea of the measurement is based on the approximate 4:1 ratio in the wavelengths of Balmer β and Lyman α lines of all H-like ions. That means these transitions can be observed at the same Bragg angle simultaneously for mica crystals in the first and fourth, second and eighth, or third and twelfth orders of reflection, respectively.

The Balmer β transitions ($n = 4 \rightarrow n = 2$) are much less sensitive to the quantum electrodynamics effects than the Lyman α ($n = 2 \rightarrow n = 1$). This means that precisely calculated Balmer β lines can be used as the reference for the Lyman α wavelength measurements, and hence for the extraction of the ground state Lamb shift. In the case of an EBIT, the intensity of Balmer β transitions could be optimized by choosing the appropriate energy of the electron beam. This idea is attractive for EBIT measurements since it does not require an external calibration source. (Spherically curved crystals in principle allow the use of an external source of reference lines because they have the advantages of the X-ray optical schemes with vertical and horizontal focusing).

It should be noted that using any crystal for high precision measurements with reference lines, and having the lines under investigation appear in different orders, requires information on refraction in the crystal. This effectively changes the Bragg angle and should be taken into account as a small difference in the $2d$ spacing between the different orders. Quite reliable calculations of refraction are available for many crystals [31]. As for mica, independent experimental work must be performed since its properties vary slightly for samples of different origin.

2. The geometry of a spherically curved crystal X-ray spectrometer

The main properties of a spherically bent crystal can be explained using two independent mutually perpendicular planes: the *horizontal* or *meridional* or *dispersive* plane and the *vertical* or *sagittal* or *focusing* plane. Since the sphere itself does not have any specific geometrically determined planes, the first plane can be defined by the position of the source, detector and vertex of the crystal. The second plane is perpendicular to the first.

Let us consider the rays in the meridional plane shown in Fig. 1, where a is the distance from the source to the crystal vertex, b is the distance from the crystal vertex to the image, H is the length of the crystal in the meridional plane and R is the crystal bending radius. The glancing angle Θ of the radiation at the crystal vertex is related to the wavelength λ

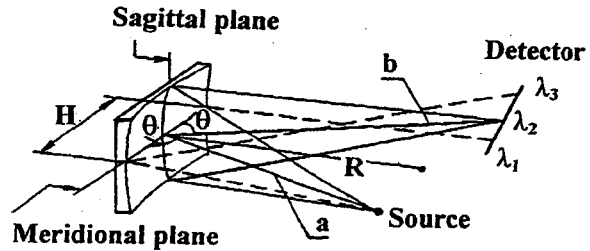


Fig. 1. Optical scheme of the formation of spectra spatially resolved in one dimension with a spherically curved crystal.

by the Bragg condition:

$$2d_n \sin \Theta = n\lambda, \quad (1)$$

where n is the reflection order and d_n is the interplanar distance for the n -th reflection order.

After reflection from the crystal, spectrally selected beams are formed in the meridional plane. Due to astigmatism, these beams focus at different points in the meridional and sagittal planes. For the positions of these foci, we have in the sagittal plane

$$1/a + 1/b_s = 2 \sin \Theta / R \quad (2)$$

and in the meridional plane

$$1/a + 1/b_m = 2/R \sin \Theta, \quad (3)$$

where b_s and b_m are the distances from the crystal vertex to the sagittal and meridional foci.

To achieve the best possible spectral resolution and the greatest intensity in the image, we must place the detector at the distance b_s from the crystal. For example, if distance $a = R \sin \Theta$ (a source on the Rowland circle), then

$$b = b_s = R \sin \Theta / (2 \sin^2 \Theta - 1). \quad (4)$$

In such a scheme the linear magnification in the sagittal plane is

$$b_s/a = [\sin \Theta (2 \sin^2 \Theta - 1)]^{-1}. \quad (5)$$

The best spatial resolution achieved thus far is about $2 \mu\text{m}$ to $4 \mu\text{m}$ [22, 24, 27].

3. Experimental set up

Observations have been performed with spherically curved crystals manufactured by the National Institute for the Physical, Technical and Radiotechnical Measurements (Russia). Mica ($2d = 19.9 \text{ \AA}$) and quartz ($10\bar{1}1$, $2d = 6.67 \text{ \AA}$) are available with radii of curvature of 100, 186, 250 and 443 mm. We have used both mica and quartz crystals with a radius of 250 mm since that best fits the dimensions of our EBIT vacuum chamber.

For the present study, the spherical crystal was mounted in the vacuum chamber of the tunable Naval Research Laboratory X-ray spectrometer [19] which is attached to an EBIT viewport at NIST. This vacuum chamber has a variable angle between the entrance and exit arms (see Fig. 2). The actual range of the available Bragg angles was 23° to 67° . The spectrometer is normally tuned by varying the crystal radius while the lengths of the arms are constant. The use of this chamber is not optimal since we are unable to change the distance between the crystal and the detector

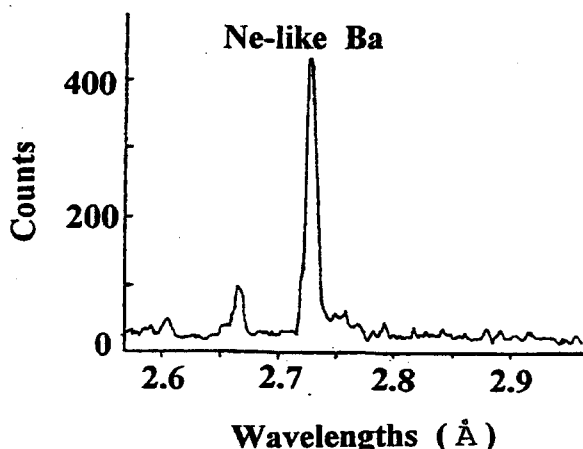


Fig. 5. Spectrum of Ne-like Ba recorded with a quartz 1011 spherically bent crystal in the first order of reflection.

the most intense line in the Ba Ne-like spectra appeared at the very edge of the wavelength region available for this specific crystal and was not properly recorded.

He-like Ar spectrum (see Fig. 6) is interesting for our purpose because of its proximity to H-like Ar, which is a good candidate for differential Lamb-shift measurements. There are several He-like transitions including resonance, intercombination and satellite lines detected in the present experimental spectrum. The intensity ratio of the recorded lines, however, can not be attributed to a single electron energy since the energy of the electron beam was changed during the collection time.

There is a practical difference between using the spectrometer with (two dimensional) photographic detection when compared to one dimensional position sensitive detection. To take full advantage of the spherically curved crystal in the case of a point source, we have to put all elements in the right place according to Bragg's law and the lens formulas (2) and (3). If we are not concerned about the spatial resolution of the X-ray image in the vertical direction, we are less restricted concerning the source being at the exact distance given by the formulas. In our EBIT case, we have a long but very narrow vertical X-ray source, so defocusing of a spectral line in the vertical direction does not change the flux density in the image plane very much. We can still take advantage of the reflected beam compression in the vertical direction, especially if our detector is one-dimensional. All

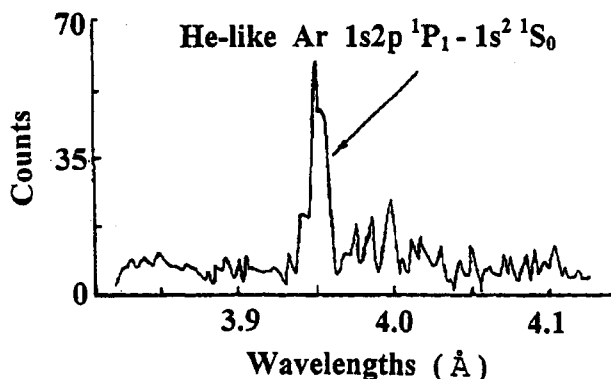


Fig. 6. Spectrum of He-like Ar recorded with a spherically bent crystal of quartz 1011 in the first order of reflection.

we require is for the radiation reflected from the crystal to fall completely in the input window of the detector. Also, we are no longer limited by the minimum Bragg angle, since we do not require the best vertical focus to be exactly in the position of best spectral focusing i.e. on the Rowland circle.

5. Conclusion and future developments

The EBIT port available for X-ray spectroscopy and the PSPC detector were not equipped yet with a window transparent to the lowest energy X-rays. A direct test in the wavelength region longer than 6 Å (limit presently set by the 160 μm Be windows on the EBIT and detector) is in the plan for future development.

Two improvements are foreseen that could increase the efficiency of the X-ray spectral detection on EBIT. The first is to use a detector with higher spatial resolution. This step will permit us to decrease the crystal radius to a more reasonable value and consequently increase the count rate. The second, demonstrated here, is using efficient spectrometers with spherically bent crystals. That also improves the count rate and makes the signal to noise ratio more acceptable for X-ray detection.

Technical parameters of contemporary CCD detectors are quite close to those needed for the successful registration of relatively weak EBIT spectra. Combining spherically curved crystals and CCD detectors can provide a powerful high resolution device for X-ray spectroscopy in a wide wavelength range.

References

- Levine, M. A., Marrs, R. E., Henderson, J. R., Knapp, D. A. and Schneider, M. B., *Physica Scripta* T22, 157 (1988).
- Gillaspay, J. D. *et al.*, *Physica Scripta* T59, 392 (1995).
- Beiersdorfer, P. *et al.*, *Rev. Sci. Instrum.* 61, 2338 (1990).
- Marrs, R. E. *et al.*, *J. Physique*, Coll. Cl, suppl. 1, 50, C1-455 (1989).
- Brown, C. M. *et al.*, *Phys. Rev.* A40, 4089 (1989).
- Takacs, E. *et al.*, *Phys. Rev.* A54, 1342 (1996).
- Marrs, R. E., *Exp. Meth. Phys. Sciences* 29A, 391 (1995).
- Serpa, F. G. *et al.*, *Phys. Rev.* 53, 2220 (1996).
- Faenov, A. Ya. *et al.*, *Physica Scripta* 50, 333 (1994).
- Nilsen, J. *et al.*, *Phys. Rev.* A50, 2143 (1994).
- Pikuz, T. A. *et al.*, *J. X-ray Science Tech.* 5, 323 (1995).
- Pikuz, S. A. *et al.*, *Physica Scripta* 51, 517 (1995).
- Faenov, A. Ya. *et al.*, *Phys. Rev.* A51, 3529 (1995).
- Faenov, A. *et al.*, *Phys. Rev.* A52, 2644 (1995).
- Skobelev, I. Yu. *et al.*, *J. Exp. Theor. Phys.* 81, 692 (1995).
- Magunov, A. I. *et al.*, *J. Exp. Theor. Phys.* 83, 267 (1996).
- Osterheld, A. L. *et al.*, *Phys. Rev.* A54, 3971 (1996).
- Skobelev, I. Yu. *et al.*, *Phys. Rev. E.* (1997).
- Brennan, S. *et al.*, *Rev. Sci. Instrum.* 60, 2243 (1989).
- Boiko, V. A. *et al.*, *J. Sov. Laser Res.* 6, 85 (1985).
- Bryunetkin, B. A. *et al.*, *Quant. Electron.* 24 356 (1994).
- Pikuz, S. A. *et al.*, *J. Exp. Theor. Phys.* 61, 638 (1995).
- Faenov, A. Ya. *et al.*, *Physica Scripta* 53, 591 (1996).
- Pikuz, S. A. *et al.*, *Rev. Sci. Instrum.* 68, 740 (1997).
- Dyakin, V. M. *et al.*, *Quant. Electron.* 26, 75 (1997).
- Aglitskiy, Y. *et al.*, *Phys. Plasmas* 3, 3438 (1996).
- Brown, C. *et al.*, *Phys. Plasmas* 4, 1397 (1997).
- Pikuz, S. A. *et al.*, *Kvantovaya Elektronika* 22, 21 (1995).
- Pikuz, T. A. *et al.*, "Measurements and Calculations of Flat and Spherically Bent Mica Crystals Reflectivity and Using Them for Different Applications in the Spectral Range 1–19 Å." Proceedings of SPIE-95, San Diego 9–11 July (1995), vol. 2515, p. 468–486.
- Silver, J. D. *et al.*, *Phys. Rev.* A36, 1515 (1987).
- Brennan, S. and Cowan, P. L., *Rev. Sci. Instrum.* 63, 850 (1992).
- Duval, B. P. *et al.*, *Nucl. Instrum. Meth.* 222, 274 (1984).

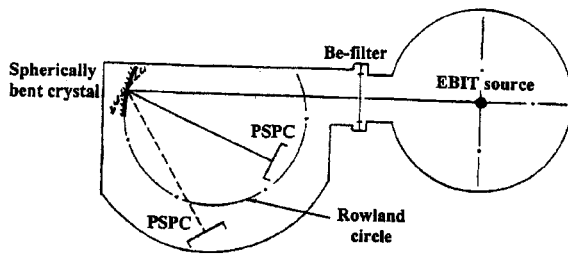
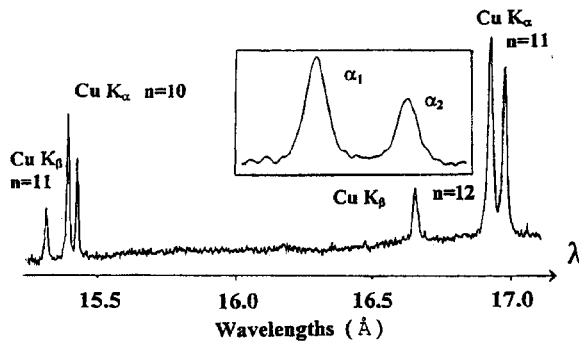
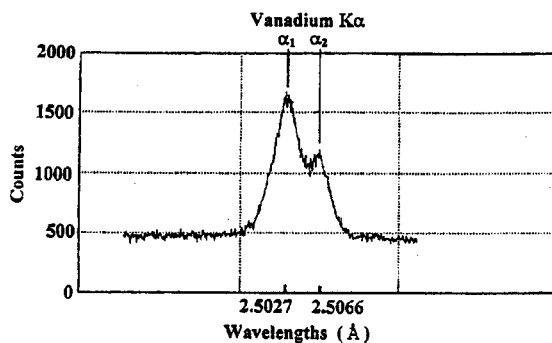


Fig. 2. Schematic of the experimental apparatus set up. The spherically curved crystal spectrometer was in a vacuum chamber with independent pumping. A beryllium filter between the two vacuum chambers limited the wavelength available for registration to $\lambda < 6 \text{ \AA}$. A position sensitive proportional counter was attached directly to the spectrometer vacuum chamber at a fixed distance of the crystal.

to accommodate the fixed radius of the crystal. In the horizontal direction, however, a spherically curved crystal spectrometer is quite similar to a conventional Johann type spectrometer. This means that the depth of focus depends on the size of crystal illuminated by X-rays of a given wavelength. The EBIT source is about $70 \mu\text{m}$ in diameter and is located about 200 mm to 300 mm outside the Rowland circle (depending on the Bragg angle). In this position we are able to obtain good spectral resolution ($\lambda/\Delta\lambda$ about 1000 to 2000 depending on the crystal and Bragg angle) even though we could not put the detector at exactly the right position (i.e. on the Rowland circle).



(a)



(b)

Fig. 3. (a) The densitometer tracing of Cu K_α and K_β spectrum recorded in several orders of reflection on X-ray film with a mica ($R = 10 \text{ cm}$) crystal. The inset shows the high degree of resolution achieved in the 11th order of reflection. (b) The spectrum of V K_α doublet recorded with a PSPC detector.

Physica Scripta 58

A backgammon type position sensitive proportional counter has been used as a detector [32]. The spatial resolution of this detector (about $200 \mu\text{m}$ to $300 \mu\text{m}$) is sufficient for the large radius cylindrically curved crystal spectrometer with high spectral dispersion, but seriously limits the resolution that could be achieved with our spherical crystals. The spectral resolution in all experiments presented here was limited by the spatial resolution of the detector.

Before being coupled with the EBIT as an X-ray source, the 100 mm mica X-ray spectrometer underwent a test with a conventional X-ray tube. X-ray film was used as a detector. This gave us information about the inherent spectral resolution of the spectrometer in the correct geometry independent of the limiting properties and location of our position sensitive detector. A typical densitometer trace is presented in Fig. 3(a), where we resolve the Cu K_α doublet in the 11th order of reflection. This result demonstrates the good optical quality of the crystal bending. It also illustrates the convenient technique of tuning a mica spectrometer for the soft X-ray region by using relatively hard X-ray radiation outside the vacuum chamber. Of course, the actual resolutions for different wavelength regions reflected at the same Bragg angle in different orders would be different. The spectrum of the V K_α doublet was recorded in the seventh order of reflection from the mica crystal ($R = 250 \text{ mm}$), see Fig. 3(b). A position sensitive proportional counter was used as a detector. This picture demonstrates the good resolution obtained in a geometry similar to the main EBIT experiment.

4. Test results and discussion

Spectra of Ne-like Ba and He-like Ar have been chosen for study in our experiment. The identifications of the spectral lines have been made on the basis of similarity of the recorded spectra to the well known previously studied ones. Precise measurements of the wavelengths and relative intensities were not among the main goals of the experiment described. Two regions of the Ne-like Ba spectrum were recorded. The first was recorded with the $R = 250 \text{ mm}$ mica crystal in the seventh order of reflection and shows three spectral lines (see fig. 4). The second was recorded with the $R = 250 \text{ mm}$ quartz crystal (first order of reflection) in the wavelength region close to the $2p^6-2p^53s$ transition in $\text{Ba } 46^+$ as is shown in Fig. 5. With the present vacuum chamber we cannot set the Bragg angle smaller than 23° , so

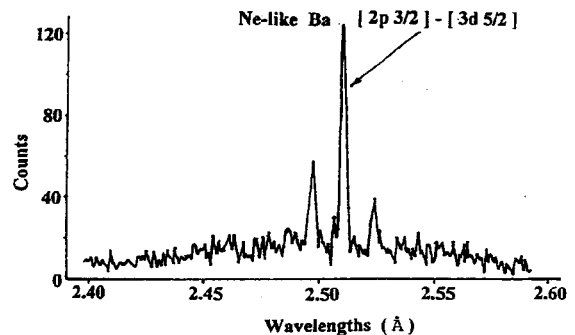


Fig. 4. Spectrum of Ne-like Ba recorded with a mica spherically bent crystal in the 7th order of reflection.

Progress Towards Absolute X-ray Spectroscopy on the NIST Electron-Beam Ion Trap: Current Status and Results

C. T. Chantler,¹ D. Paterson,¹ L. T. Hudson,² F. G. Serpa,² J. D. Gillaspay² and R. D. Deslattes²

¹ School of Physics, University of Melbourne, Parkville, Victoria 3052, Australia

² Atomic Physics Division, NIST, Gaithersburg, MD20899, USA

Received September 23, 1996; accepted in revised form March 21, 1997

Abstract

Recent observation of Hydrogen-like ions of Vanadium at the NIST Electron-Beam Ion Trap and measurements of Helium-like resonance line are presented. One particular feature of the current series of experiments is the possibility of absolute calibration in a near Doppler-free environment. The current approach to the possible measurement of QED effects in such a system is reviewed. There is great potential for precision measurements in the near future.

1. Introduction

The development of EBIT devices around the world since the first EBIT at Livermore [1] is symptomatic of their interest and utility for investigating questions of fundamental and applied significance. The NIST [2] and Oxford EBIT's began operational status at similar times and hence rank as equal third operational devices in this short history. In this context the contributions to this issue from the Oxford EBIT [3], the Tokyo EBIT [4] and the Berlin EBIT [5] indicate the development of tools and techniques to address important problems.

The NIST EBIT has had several priorities including the development of a tool for precision X-ray spectroscopy and QED (Quantum Electro-Dynamics) measurement with minimal Doppler broadening and Doppler shifts that have characterized fast-beam experiments and limited their overall precision [6]. All EBIT facilities share this advantage with regard to Doppler shifts; and all share the difficulty of relatively low fluxes. The latter difficulty can be addressed by compromising the data collection technique to generate data quickly, or by slow and careful development of techniques appropriate for EBIT investigations and allowing absolute measurements of significant quantities. We propose the latter approach as being more likely to produce important and meaningful new results.

2. Absolute polarization measurements

The X-ray investigations at NIST have recently reported successful and precision measurements of absolute polarization of a magnetic quadrupole line in Ne-like barium [7]. The polarization is not measured simply relative to surrounding lines or an assumed unpolarized structure (although this is an important tool for confirming polarizations). Instead, a polarization-sensitive method of detection is used in two configurations, with calibration of the detection in both an experimental and theoretical sense at the required (0.1%–1%) level.

This provided an absolute calibration, rather than a relative measure of degree of polarization. This minimises

uncertainty in the results, and (in these complex systems) allows detailed analysis of theory in the application to the systems involved. Complex multi-level cascades and population mechanisms are responsible for the final polarizations observed, and without an absolute calibration this is difficult to analyse. Our results, with an accurate absolute calibration, observed and investigated dramatic variation of cascade-feeding contributions to polarization across a wide range of electron-beam energy.

This general approach provides more accurate and probing results than alternate techniques.

3. X-ray measurements

This general principle can be applied to the spectroscopic measurement of energy. In brief, any series of spectral lines should be interpretable in terms of absolute energy and absolute intensity. The two issues are sometimes incompatible in a system of low flux like the EBIT, or for particular high-efficiency but low resolution detectors (e.g. proportional counters). The two requirements are that an appropriate absolute energy calibration sequence be used in investigations, and that this be able to be confirmed by theory. In particular, the use of reference lines of unknown wavelength and unknown systematics to “calibrate” secondary lines is able to provide useful observations, but other results may be questionable. An exception to this is the Lyman α -Balmer β intercomparison technique used in accelerator observations, for reasons which are explained in several places [8].

In the context of high-resolution X-ray measurements, the standard approach is to use diffracting crystals, so that dynamical diffraction theory will be the theoretical basis for the confirmation of calibration and results. This is made more difficult by the low-flux regime, so that curved crystals are a necessary tool to provide adequate statistics. Further details and progress on this issue are provided in another paper of this issue [9].

Our programme in this direction has pursued precision measurements of neon-like barium in the NIST EBIT, in part as a testing ground for the techniques and approaches used, since barium is ubiquitous in EBITs and neon-like levels are convenient and accessible. It is also important in its own right, as a study of closed shell spectra and possible astrophysical and laboratory population mechanisms as indicated earlier [6].

Figure 1 presents data taken from a single run on neon-like barium, taken with a precision high-resolution spectrometer. This data was collected over 6.2 h of EBIT operation, with simultaneous observation by a Si(Li) detector which

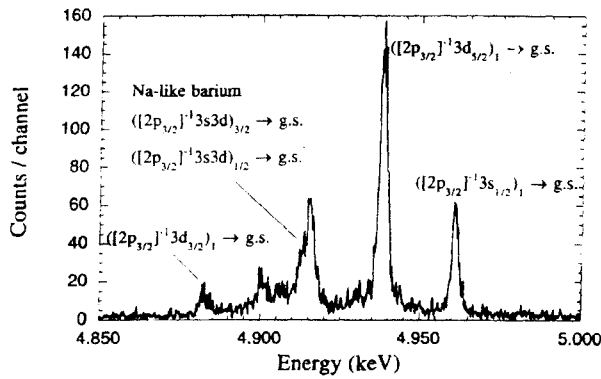


Fig. 1. Spectrum of Neon-like Barium recorded over 6.2h on the NIST EBIT with a high-precision curved crystal spectrometer. Statistics are clear and contributions from Na-like barium charge states in this run are indicated. The spectrum has been truncated as adjacent regions show no spectral features.

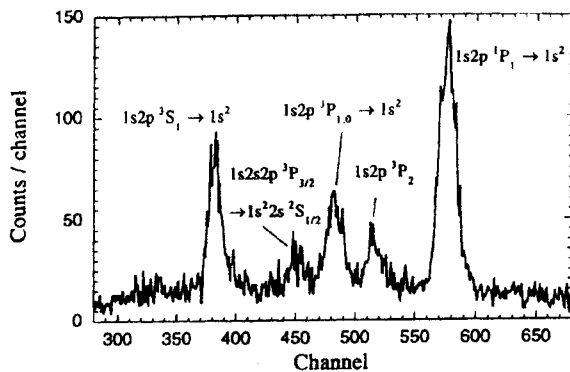


Fig. 2. Spectrum of Helium-like resonance lines of Vanadium taken on the NIST EBIT. The x-axis is channel number, and linear in energy (see text). Lithium-like contamination is present but unlikely to impair the final measurement, given the data quality and resolution obtained.

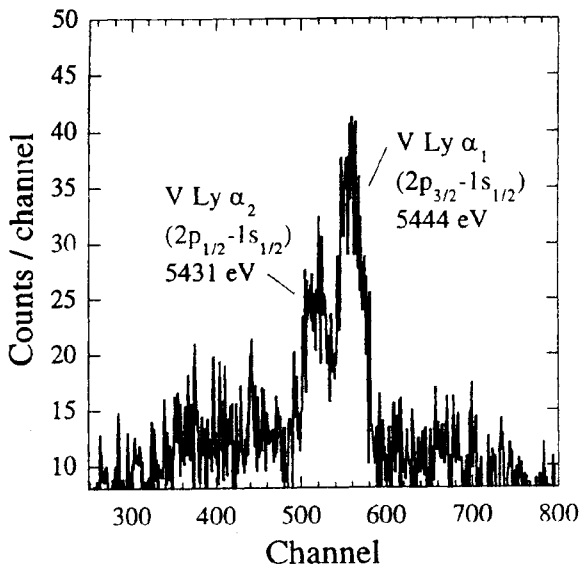


Fig. 3. Observation of Hydrogen-like Vanadium Ly α_1 ($2p_{3/2}^{-1}1s$) and Ly α_2 ($2p_{1/2}^{-1}1s$). Statistics are limited but the peaks are clear and resolved. The channel number indicates the integrated and peak counts for a given transition.

Physica Scripta T73

aids identification of charge state and species contamination. Absolute calibration is aided by the overlap in energy of this spectrum with the robust calibration line of Ti $K\beta_{1,3}$. This observation does not overlap with the polarization measurement referred to earlier, but reveals details of a similar interest and complexity. This work is proceeding.

4. QED measurements

Some of the most fundamental questions can be addressed by investigating few-electron systems. In particular QED and electron correlation in systems of high effective coupling strengths may be tested effectively in hydrogenic and helium-like levels [10, 11]. For the medium- Z regime, Lyman α wavelength precision of 30 ppm or so is required to contribute usefully to the current comparison of theory and experiment.

There has been significant interest in helium-like transitions in the region $Z = 19$ to $Z = 26$ given recent speculation of errors in theory at the 40 ppm level [12]. Helium-like Vanadium is therefore ideally situated to investigate such concerns. Our investigations of the resonance lines are proceeding, with the quality of the data and statistics indicated in Fig. 2. This represents data collected over 24 h. Possible drifts between individual scans are allowed for by use of clinometry readings [9]. Na-like barium contamination is present but clearly separated. The energy calibration must be further refined before a serious estimate of imprecision can be made. The necessary involvement of theory to confirm experimental calibration is discussed in [9] and is the basis of the principle of research which we are pursuing.

Recently, the first observations of hydrogen-like Vanadium have been made at the NIST EBIT in a lower resolution geometry. The 13 eV separation between V Ly α_1 and V Ly α_2 is clearly resolved despite the lower resolution (higher flux) arrangement. A current spectrum from a single run is given in Fig. 3. Currently statistics is quite limited.

The ionization and recombination balance in EBITs makes hydrogenic systems more challenging than closed shell systems, and in particular leads to much lower fluxes. The population and emission rates also vary greatly between systems and spectral components. In each of these systems, operating conditions on the MEVVA source and EBIT have been optimised. Nonetheless, our results confirm that for individual spectral lines the Ne-like barium spectra obtained fluxes of 4 times the He-like Vanadium flux and 13 times the hydrogenic ion flux.

This reveals the operational status of the MEVVA injector, demonstrates one of the specifications of the NIST EBIT, and highlights the potential for precision measurement. Currently statistics is limited for high-resolution spectra and hydrogenic systems – but it appears that further analysis will allow a QED measurement at the significant level.

5. Summary

The NIST EBIT is fully operational, and has successfully acquired high-resolution data with a curved crystal spectrometer suited to EBIT conditions. We have collected data pertaining to three important physical systems: neon-like

barium, helium-like vanadium and hydrogenic vanadium. Further work will pursue application of these principles to few-electron nickel and other systems. Analysis of systematic shifts and hence of the absolute calibration of the spectra is proceeding. They are expected to produce robust and reliable estimates of energies of these lines soon, and may be compared to alternate observations which reference secondary calibration lines of low intrinsic accuracy.

References

1. Levine, M. A., Marrs, R. E., Henderson, J. R., Knapp, D. A. and Schneider, M. B., *Physica Scripta* **T22**, 157 (1988).
2. Gillaspy, J. D., Roberts, J. R., Brown, C. M. and Feldman, U., "The NIST EBIT: A Progress Report", Proc. VIth International Conference on the Physics of Highly Charged Ions (Edited by P. Richard, M. Stockli and C. D. Lin) **274**, 682 (AIP press, New York 1993).
3. Margolis, H. S., Groves, P. D., Oxley, P. K., Silver, J. D. and Varney, A. J., *Physica Scripta*, this issue.
4. Asada, J. *et al.*, *Physica Scripta*, this issue.
5. Biedermann, C., Förster, A., Fußmann, G. and Radtke, R., *Physica Scripta*, this issue.
6. Gillaspy, J. D. *et al.*, *Physica Scripta* **T59**, 392 (1995).
7. Takács, E. *et al.*, *Phys. Rev.* **A54**, 1342 (1996).
8. Laming, J. M. *et al.*, *Nucl. Instr. Meth.* **B31**, 21 (1988).
9. Paterson, D. *et al.*, *Physica Scripta*, this issue.
10. Brodsky, S. J. and Mohr, P. J., "Quantum Electrodynamics of high-Z few-electron atoms", in: "Physics of Highly-ionized Atoms" (Edited by R. Marrus) NATO ASI Series **B201** (Plenum, New York 1989) 111.
11. Deslattes, R. D., *Physica Scripta* **T46**, 9 (1993).
12. Beiersdorfer, P., Bitter, M., von Goeler, S. and Hill, K. W., *Phys. Rev.* **A40**, 150 (1989).

Precision X-ray Spectroscopy at the NIST Electron-Beam Ion Trap: Resolution of Major Systematic Error

C. T. Chantler,¹ D. Paterson,¹ L. T. Hudson,² F. G. Serpa,² J. D. Gillaspay² and E. Takács³

¹School of Physics, University of Melbourne, Parkville, Victoria 3052, Australia

²Atomic Physics Division, NIST, Gaithersburg, MD20899, USA

³Experimental Physics Dept., Kossuth University, Debrecen, Bem t. 18/a., Hungary H-4026 and Institute of Nuclear Research of the Hungarian Academy of Sciences (ATOMKI), Debrecen, Bem ter 18/c, Hungary

Received September 14, 1998; revised November 30, 1998; accepted December 3, 1998

PACS ref: 32.30.Rj, 34.80.Kw, 31.30.Jv

Abstract

Some of the most critical tests of the QED Lamb shifts are currently being pursued in the X-ray regime by investigating the core levels of medium Z atoms such as vanadium. The current approach to the measurement of the Lamb shift in such a system is outlined. We present major progress in understanding and reducing the systematic errors within our system. The error budget has been reduced to a level where critical tests of QED can be performed. Recent observations of Lyman α in hydrogenic vanadium at the NIST Electron-Beam Ion Trap are presented.

1. Introduction

One of the goals of much current research is to test Quantum Electro-Dynamics (QED) critically in new and important regimes. Parallel investigations include muonium [1], positronium [2] and $g-2$ experiments in different systems. Most effort has been directed to Lamb shift measurements in hydrogenic and helium-like systems.

In our current research we target medium Z hydrogenic and helium-like ions where transition energies are in the X-ray region. To critically test current theory a precision of 10–30 ppm is required. In such measurements absolute calibration is essential. Using methods outlined below we have achieved calibration at the desired precision. This work continues the efforts towards precision spectroscopy on an Electron-Beam Ion Trap [3] and the progress made earlier with respect to calibration and systematics for X-ray energies [4].

2. X-ray spectroscopy and QED measurement

Investigation of pure QED effects (rather than correlation) often involves the hydrogenic Lyman α transitions. These have been best studied in the X-ray regime, because they look directly at the full $1s$ Lamb shift and are resonant transitions. These experiments have usually been performed at accelerators. Some of the best measurements have reached 30–40 ppm, depending on Z [5].

Diffracting crystals are used in these medium Z investigations of $1s-2p$ transitions. However, systematic effects relating to diffraction including refractive index corrections, differential depth penetration and focussing, and source size or geometric effects are often simplified or neglected. This is particularly true for curved crystal geometries, which are often used to obtain increased signal and lower statistical error. These critical issues led to the development of the first theory to combine curvature and mosaicity in a dynamical diffraction theory [6].

3. QED measurements on the Electron-Beam Ion Trap (EBIT)

An EBIT involves an electron beam, focussed by superconducting electromagnets, which attract and ionise positive ions. By selecting the beam potential you can select the charge state of the positive ions, so it is a sensitive probe for high Z ionised atoms [7]. EBITs avoid the concern with Doppler broadening, shifts and limiting uncertainties that dominate in conventional accelerator experiments. EBIT experimental approaches are complementary with accelerator approaches: two experiments using different techniques and with different limiting systematics are a sensitive probe of the validity of experimental results. EBIT experiments hold promise for a significant improvement in QED measurement.

There are only two major issues with EBIT-based QED measurements:

- 1) Flux and statistics, and
- 2) Calibration and systematics

In our first experiment helium-like vanadium was studied and the uncalibrated spectra have been published previously [8]. The spectra are clean, resolution is good, and the statistics after a long accumulation of data are adequate. Hence the helium-like vanadium measurement is competitive on the first issue with other sources and other QED measurements. However, the optimised population of hydrogenic vanadium in the same experimental run was much poorer, and produced inadequate statistics for a 30 ppm QED measurement.

We have made a number of improvements in Melbourne and at NIST, which has led to higher resolution spectra, increased fluxes, and good statistics for a QED measurement in hydrogenic vanadium (see Lyman α spectra, Fig. 1). At this stage calibration and systematics are the limiting errors.

4. Resolution of systematics in EBIT measurement

Investigation of the systematic issue has encouraged us in our current experimental plan. Often, results have emphasised a high-flux collection mode with *relative* calibration to less well-defined lines. We have concentrated on *absolute* calibration of lines by direct reference to standard sources used as the second link in an X-ray metrological programme. The wavelength of calibration lines are determined by correcting Bearden's values [9,10,11]. Recent work in this area has reduced the errors on Bearden's values, in general by

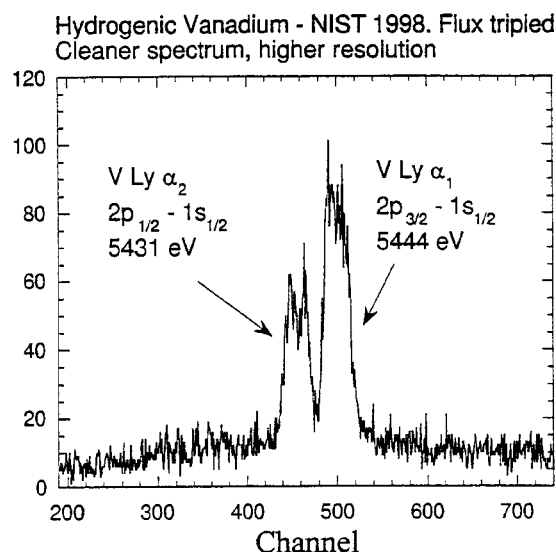


Fig. 1. New hydrogenic vanadium spectrum showing good statistics.

25%–30% [12] from 12 ppm to 8–10 ppm. We also do not rely on a single absolute calibration energy, but require a series to calibrate the dispersion function of the spectrometer.

Our curved-crystal spectrometer is not immune to systematics, but their effect is at a much lower order than other techniques. Our observations two years ago were loosely limited at 100 ppm (or a rather weak QED measurement) as a consequence of these systematics. It was clear then that the problem was due to an inadequate application of diffraction theory and the computation of effective refractive index centroid shifts. Other researchers have ignored this problem, which compromises results at around the 100 ppm level.

A critical insight related to the effect of the Seemann wedge. The “wedge” is a knife-edge limiting the region of the crystal across which effective diffraction can proceed to an image on the detector. The location “out” means that the full crystal surface may be used; “in” will restrict the diffraction to regions near the optimum axis of the crystal spectrometer. Both approaches give common results when the spectrometer is tuned to give a focused profile on the Rowland circle (i.e. when the detector is centered on the Rowland circle). As we go further from this region, the two results for wedge “in” and “out” follow quite different trends and systematics as illustrated in Fig. 2. This is a plot of experimental calibration data across the entire range of calibration lines measured. The discrepancy angle is the difference between the fitted dispersion function of the spectrometer (for wedge “in” data only) and the data. Several data points are shown for each individual calibration line and wedge position. The difference between measured experimental values and the predicted theoretical position shows the magnitude of shifts associated with wedge position (as indicated by the two arrows diverging with decreasing diffraction angle). The spread of values at a given angle indicates other sources of experimental error, such as detector alignment.

We have proven that the wedge “in-out” discrepancy is due to asymmetric partial focusing on the detector plate. Extrapolated shifts at the Rowland circle do not agree with shifts at our flat, extended detector, and must be corrected. The conse-

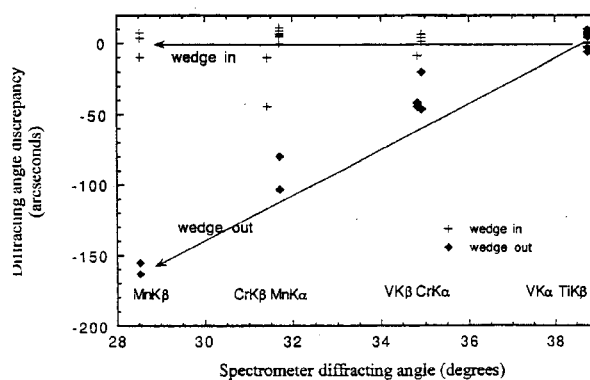


Fig. 2. Experimental results for wedge position, uncorrected for the plate function. Several data points are plotted for each calibration line and wedge position and the variation between these points indicates the shifts due to other experimental parameters such as detector position and source size. Discrepancies due to wedge position can exceed 150 arcseconds.

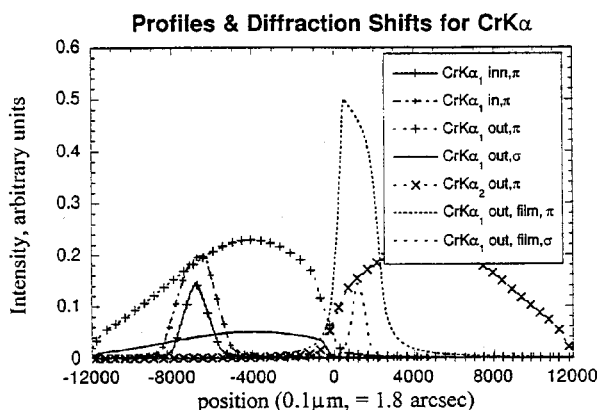


Fig. 3. Theoretical modelling of diffraction profiles for various wedge positions and detector types. Profiles labeled “film” are those imaged by a detector that always lies along the Rowland circle. The polarisation of the incident X-rays are labeled as “ π ” or “ σ ”, denoting electric field vector perpendicular or parallel to plane of incident radiation, respectively. The qualitative effects of changing the wedge position from ‘out’ to ‘in’ are dramatic.

quence is illustrated in Fig. 3 which shows theoretically calculated diffraction profiles for the chromium $K\alpha$ calibration line. Plotted are two sets of calculations for our experimental situation with various wedge positions. The first set of profiles, labeled “film”, are for a detector which always remains on the Rowland circle (traditionally photographic film is used). The second set is for a flat detector located at a fixed distance from the crystal. The profiles change to a more complex shape with significant offsets of the centroid when the detector is flat and not located on the Rowland circle. These profiles are calculated using dynamical theory of diffraction for curved crystals, observed at either a curved detector on the Rowland circle or a defocused location on a flat plate. The profiles cannot be predicted from flat crystal profiles and include significant additional broadening and asymmetry.

Figure 4 illustrates how the theoretical modelling accurately predicts the real systematics as shown in Fig. 2 and as a result we have resolved this major systematic error. The variation with diffracting angle is highly non-linear with

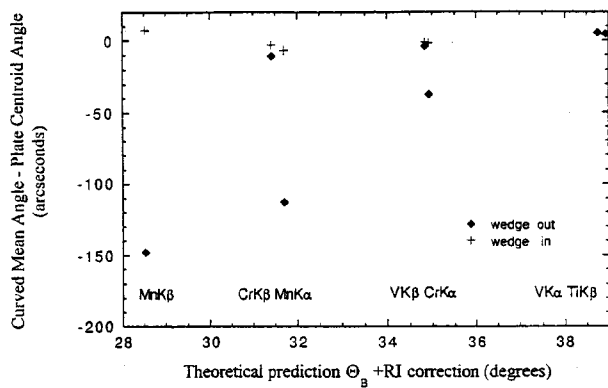


Fig. 4. Theoretical modelling of shifts due to wedge position for one set of experimental parameters (source size and detector position). There is very good qualitative and quantitative agreement between experimental results (see Fig. 2) and the theoretical modelling.

wavelength. With the inclusion of the plate function systematic shift the dispersion function of the spectrometer can now be determined with errors of less than one arcsecond. This corresponds to a precision of 7–8 ppm, with the final error on a measured transition being further reduced. Hence the systematics in the calibration has now dropped by about a factor of 5–10, or down to circa 10–20 ppm, and no longer limit the measurement.

So the error budget has dramatically reduced to the following:

Spectrometer Systematics (dispersion function uncertainties which were 100+ppm in 1996 for any curved crystal EBIT investigation) reduced to	10–20 ppm
EBIT Statistics (100 ppm for H-like V in 1996); now	15–20 ppm
Bearden (reference wavelengths)	10–12 ppm
Calibration profile fitting, Temperature, Doppler shifts	< 5ppm
Total:	20ppm – 30ppm

This represents a 3% – 5% Lamb shift measurement, which is comparable to the results obtained using accelerator and other techniques. The main sources of uncertainty are all accessible to further investigation, and the error could certainly halve under appropriate conditions. The hardest limit in the above list is the statistics, but several approaches are being pursued which could halve this in subsequent investigations.

5. Conclusion

Measurement of the Lamb shift in hydrogenic medium Z atoms such as vanadium remains one of the most critical tests of QED. Major progress in understanding and developing absolute X-ray spectroscopy for an EBIT source has been outlined. We are pursuing developments to further increase the precision of current approaches in the X-ray regime.

References

1. Chu, S. *et al.*, Phys. Rev. Lett. **60**, 101 (1998); Maas, F. E. *et al.*, Phys. Lett. **A187**, 247 (1994).
2. Chu, S., Mills Jr., A. P. and Hall, J. L., Phys. Rev. Lett. **52**, 1689 (1984); Fee, M. S. *et al.*, Phys. Rev. Lett. **70**, 1397 (1993).
3. Gillaspay, J. D., *et al.*, Physica Scripta **T59**, 392 (1995).
4. Paterson, D., *et al.*, Physica Scripta **T73**, 400 (1997).
5. Deslattes, R. D., Physica Scripta **T46**, 9 (1993).
6. Chantler, C. T., J. Appl. Cryst. **25**, 674 (1992); Chantler, C. T., J. Appl. Cryst. **35**, 694 (1992).
7. Gillaspay, J. D., *et al.*, Physica Scripta **T59**, 392 (1995).
8. Chantler, C. T., *et al.*, Physica Scripta **T73**, 87 (1997).
9. Bearden, J. A., Rev. Mod. Phys. **39**, 78 (1976).
10. Kessler, E. G. *et al.*, Phys. Rev. **A26**, 2696 (1982).
11. Schweppe, J., Deslattes, R. D., Mooney, I. and Powell, C. J., J. Electron Spectrosc. Relat. Phenom. **67**, 463 (1994).
12. Deslattes, R. D., Kessler, E. G., Indelicato, P. and Lindroth, E., section 4.2.2 Int. Tables for Crystallography, (Kluwer Academic Press, Stockholm, 1999).

Absolute measurement of the resonance lines in heliumlike vanadium on an electron-beam ion trap

C. T. Chantler,¹ D. Paterson,¹ L. T. Hudson,² F. G. Serpa,² J. D. Gillaspay,² and E. Takács^{2,*}¹*School of Physics, University of Melbourne, 3010, Australia*²*National Institute of Standards and Technology, Gaithersburg, Maryland 20899*

(Received 14 February 2000; published 11 September 2000)

Absolute measurements of the energies of resonance lines in heliumlike vanadium on an electron-beam ion trap are reported. The $1s2p\ ^1P_1 \rightarrow 1s^2$, $1s2p\ ^3P_2 \rightarrow 1s^2$ ($1s2p\ ^3P_1 \rightarrow 1s^2$ and $1s2p\ ^3P_0 \rightarrow 1s^2$) blend and $1s2s\ ^3S_1 \rightarrow 1s^2$ transitions are 5205.10 ± 0.14 eV, 5189.12 ± 0.21 eV, 5180.22 ± 0.17 eV, and 5153.82 ± 0.14 eV, respectively. This agrees with recent theoretical calculations and the experimental precision lies at the same level as the current uncertainty in theory (0.1 eV). These measurements represent a 5.7–8% determination of the QED contribution to the transition energies and are the most precise measurements of heliumlike resonance lines in the $Z=19$ –31 range. The measurement of the $1s2s\ ^3S_1 \rightarrow 1s^2$ transition is also sensitive to the $1s2s\ ^3S_1$ QED contribution at the 40% level. The intensity of the strong $1s2p\ ^3P_1 \rightarrow 1s^2$ component of the blend compared to the total blend intensity is $94\% \pm 12\%$. This is in accord with current theoretical predictions but disagrees with an earlier reported ratio.

PACS number(s): 31.30.Jv, 32.30.Rj, 12.20.Fv, 34.80.Kw

I. INTRODUCTION AND BACKGROUND

The calculation of two-electron ion energy levels has been a topic of much research since the discovery of quantum mechanics. The contribution of relativistic and quantum electrodynamic (QED) effects has been intensely studied in the last three decades [1,2]. Two-electron systems provide a test bed for not only quantum electrodynamics and relativistic effects calculations, but also for many-body formalisms [3].

Theoretical calculations of energy levels in heliumlike ions using variational techniques, relativistic corrections, and a $Z\alpha$ expansion in the unified approach were pioneered by Drake in 1979 and 1988 [4,5]. Since then there has been active research in the calculation of energy levels in heliumlike ions using new techniques. Major progress in theoretical calculations of QED contributions has occurred in the last decade, particularly in developments avoiding the $Z\alpha$ expansion by using all-orders techniques [6–9]. Plante *et al.* [6] provide a recent review of calculations of the $n=1$ and $n=2$ states of heliumlike ions and present relativistic all-order many-body calculations.

To critically test QED contributions at the 10% or better level in medium Z ions requires an experimental precision of 10–30 ppm. In many cases experiments of sufficient precision have not been performed which could resolve the differences between theories [6,9,10]. Repeated claims in the literature have suggested that across the $Z=19$ –32 range experimental determinations of the $1s2p\ ^1P_1 \rightarrow 1s^2$ transition energy are greater than theory [11–13]. We have directed our research at an absolute precision measurement of heliumlike resonance lines in vanadium ($Z=23$) to investigate these claims in the center of the region of interest (heliumlike resonance lines refer to $n=2$ to $n=1$ transitions in two-electron ions where one electron remains in the ground ($1s$) state as illustrated in Fig. 1). No prior high precision

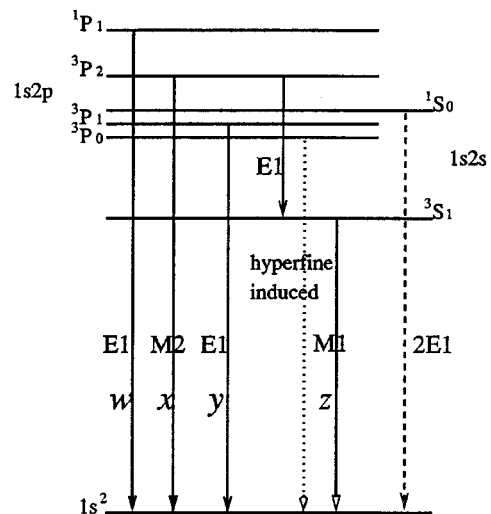


FIG. 1. Radiative decay scheme of medium Z heliumlike ions, indicating the nature of decay: $E1$ electric dipole, $M1$ magnetic dipole, $M2$ magnetic quadrupole radiation, and $2E1$ two-photon $E1$ process. The hyperfine-induced $1s2p\ ^3P_0 \rightarrow 1s^2$ transition is only allowed if the nuclear magnetic moment is finite (vanadium $7/2\ \hbar$). The notation of Gabriel [14] is indicated for each resonance line.

absolute measurements in vanadium have been performed, which was an additional motivation. For the $1s2p\ ^1P_1 \rightarrow 1s^2$ transition (w line, notation of Gabriel [14]) it has been claimed that the heliumlike resonance line calculated by Drake is too large by about 60 ppm [12] based upon a series of measurements of the w line ($Z=19$ –26) [11]. The QED contributions to the heliumlike resonance lines in vanadium are 480–550 ppm of the transition energies [5] and therefore precise measurements (better than 30 ppm) of these transitions are sensitive to, and can test, calculations of the QED component.

The uncertainty of theoretical determinations of energy states in two-electron ions has been a focus of recent attention [10]. Earlier theoretical work [5] claimed an uncertainty

*Permanent address: Institute of Experimental Physics, University of Debrecen, Debrecen, Bemter 18/a, H-4026 Hungary.

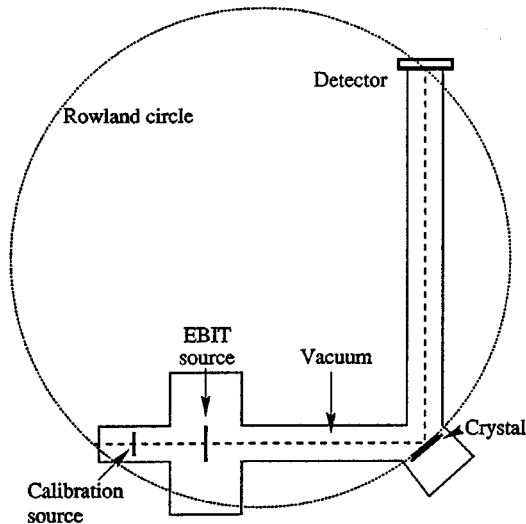


FIG. 2. Spectrometer configuration at the NIST EBIT; note that the EBIT source is located well inside the Rowland circle. The spectrometer is oriented such that the axis of the spectrometer is perpendicular to the long axis of the EBIT source and the detector arm moves vertically with changes in diffraction angle.

of 1 ppm due to uncalculated higher-order terms. However, the discrepancy between current theories approaches 30 ppm in the $Z=23$ region. Recent work of Persson *et al.* [10] estimates missing correlation effects in QED terms to be 20 ppm in the $Z=23$ region (absolute value of order 0.1 eV across medium and high- Z elements). Precise experimental determination of the heliumlike resonance lines can probe these discrepancies and uncertainties.

Most precision spectroscopy of medium- Z ions has been conducted at accelerators or tokamak plasmas. The recent development of the electron-beam ion trap (EBIT) has offered another spectroscopic source to experimenters. Our experimental method takes advantage of the Doppler-free and relatively clean spectra produced by an EBIT coupled to an external calibration source to allow absolute measurements on highly charged ions. We have made absolute measurements of the heliumlike resonance lines in vanadium with an uncertainty of 27 ppm for the $1s2p\ ^1P_1 \rightarrow 1s^2$ transition. Our results for vanadium do not support evidence of a systematic discrepancy between theory and experiment [11–13]. These are the first precision x-ray measurements conducted at the NIST EBIT facility.

II. EXPERIMENT

The experimental configuration is shown in Fig. 2. Other experiments have been conducted on the NIST EBIT using this spectrometer including polarization studies by Takács *et al.* [15].

The EBIT uses an intense and monoenergetic electron beam which is magnetically confined to trap and ionize charged ions [16,17]. Metal ion species such as vanadium are created by a metal vapor vacuum arc (MEVVA) ion source and are sequentially ionized as they enter the trap region of the electron beam. The electron-beam energy distribution of

the EBIT is narrow and the energy can be tuned. The heliumlike vanadium resonance lines are excited by setting the electron-beam energy to 6.9 keV (including space-charge correction), 1.75 keV above the direct electron-impact excitation energy. The electron-beam current was typically 140 mA.

We employ a Johann spectrometer with a Ge(220) crystal ($2d=4.0007\text{ \AA}$) which has a useful wavelength range between 1.9 and 2.8 \AA in first order. The radius of crystal curvature is 1.846 m and the resolving power ($\lambda/\Delta\lambda$) of the spectrometer in the wavelength region of investigation is 2000–2500. The spectrometer has a Seemann wedge that can be lowered towards the crystal pole, reducing the diffracting crystal area used and the x-ray throughput but improving the resolution [18]. The detector is a two-dimensional position-sensitive proportional counter that employs capacitive charge division from a backgammon design cathode to determine position [19]. The spectrometer has a fixed crystal radius so the detector does not always remain on the Rowland circle. This has substantial systematic effects on measurements [20,21].

The spectrometer is aligned with respect to the EBIT so that the plane of crystal dispersion is parallel to the electron beam axis (see Fig. 2). The range of Bragg diffraction angles accessible with the spectrometer is 25.0–60.9° and the heliumlike resonance lines of vanadium are observed at approximately 39°. The crystal acts as a polarizer at Bragg angles near 45° and therefore radiation polarized perpendicular to the electron beam axis is the dominant diffracted component. The detector has a window wider than the full heliumlike vanadium spectrum of the EBIT. Hence several detector angles centering on various features of the spectrum were able to characterize detector linearity.

Our work is concerned with the measurement of heliumlike resonance lines. Dielectronic satellites can affect the precision of the measurements. By tuning the electron-beam energy well above the dielectronic resonance energies they are not excited, resulting in a spectrum clean of dielectronic satellite lines. Transitions from the lithiumlike states of vanadium of type $1s2l2l'$ lie very close to the lines of interest. Efforts must be made to minimize or eliminate these satellites from the spectra observed. The lithiumlike resonance lines that directly concern this research—due to their close location to the heliumlike resonance lines and their relatively large electron-impact cross section for inner-shell excitation—are the q and r [14] or $1s2s2p\ ^2P_{3/2} \rightarrow 1s^22s\ ^2S_{1/2}$ and $1s2s2p\ ^2P_{1/2} \rightarrow 1s^22s\ ^2S_{1/2}$ transitions. Our treatment of the lithiumlike resonance lines is discussed in detail in Sec. IV.

A. Calibration

Calibration is a detailed and extensive procedure because we map the dispersion function of the spectrometer across a broad range of wavelengths around the region of interest. Using a large number of calibration lines ensures the dispersion function is well determined and a wide range of wavelengths ensures that any higher-order wavelength-dependent effects are included. We also systematically investigate the

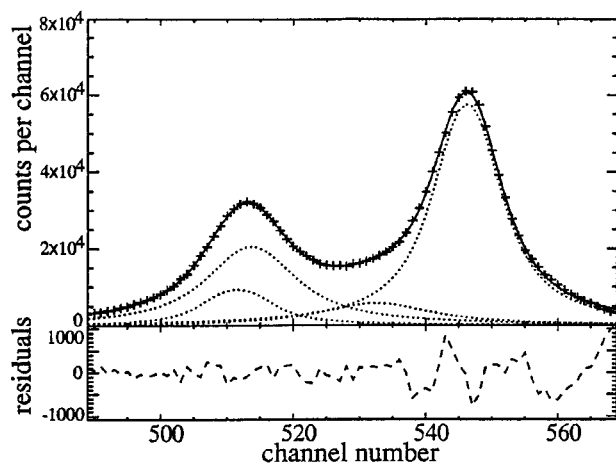


FIG. 3. Curve fitting to vanadium $K\alpha$ calibration lines. The fitted functions are Lorentzian convolved with a slit function. Four individual profiles are fitted (see text) and indicated by dotted lines. + represents data points and the solid line indicates the sum of fitted components. Residuals to the fit are shown by a dashed line underneath the main plot.

effects of variations of source size and the Seemann wedge position during calibration. Thus calibration is a time consuming but necessary procedure for an absolute precision measurement.

The calibration source consists of a 20-keV electron gun and a series of metal targets (Mn, Cr, V, Ti) located on the opposite port of the EBIT to the spectrometer as indicated in Fig. 2. We locate the calibration source and the EBIT source inside the Rowland circle by design to increase flux, reduce systematic uncertainties, and increase the spectral band pass to the point that the entire vanadium spectrum can be acquired in parallel [21]. Calibration spectra are collected for a range of $K\alpha$ and $K\beta$ characteristic wavelengths (1.9–2.8 Å) about the heliumlike resonance lines of vanadium. Bragg diffraction angles of calibration lines are in the range 29° – 45° while the heliumlike resonance lines of vanadium are observed at approximately 39° . $K\alpha_1$ and $K\alpha_2$ are well resolved in our system and so the $K\alpha$ doublet provides two reference wavelengths at one detector location [20,21]. This is useful for absolute calibration of the detector channel number in micrometers. A typical vanadium $K\alpha$ calibration spectrum is shown in Fig. 3. Approximately 100 individual calibration measurements were made with some 20 independent integrated observations of heliumlike resonance lines in vanadium.

B. Energy dispersive measurement

A solid-state Si(Li) detector is used when optimizing the EBIT conditions to maximize the flux of heliumlike vanadium transitions and to minimize contamination from other charge states and dielectronic recombination transitions. An example of a typical Si(Li) spectrum is shown in Fig. 4. The resolution is sufficient to identify hydrogenic and heliumlike vanadium as well as various barium charge states (barium, emanating from the electron gun, is common in EBIT spec-

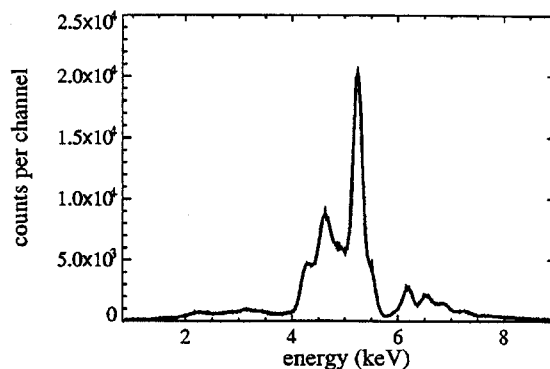


FIG. 4. General features of the Si(Li) spectrum observed on the NIST EBIT: The highest peak at 5.2 keV is composed of a blend of the heliumlike vanadium resonance lines, and the broad peak between 4.6–4.9 keV is predominantly neonlike barium and other barium charge states.

tra). A small amount of pure nitrogen gas is leaked into the trap to increase the proportion of higher charge states via evaporative cooling.

In the EBIT an axial trapping potential is created by a series of three drift tubes. The voltage applied to the middle drift tube determines the energy of the electron beam and sets the position of the trap with respect to the ground potential. The drift tube voltages can be switched rapidly in a time sequence. This is necessary in order to catch the ions injected from the MEVVA ion source and to empty the trap after a certain amount of time to avoid the accumulation of unwanted long lifetime charge states and background barium ions. The time sequencing was optimized using the signal from the Si(Li) detector.

Once the optimum EBIT operating conditions are chosen, crystal spectrometer data are collected while continuing to monitor the performance with the Si(Li) detector. A single spectrum is collected and saved for each period, approximately 2 h, between liquid nitrogen fills of the outer cryogenic jacket of the EBIT. Spectra are collected continuously for several days with a 24-hour-a-day EBIT operation. Spectra collected under the same conditions are then summed during the analysis of data. Figure 5 shows a heliumlike vanadium spectrum from 24 h of observation with the crystal spectrometer. The position and relative intensity of the q lithiumlike resonance line is also indicated in Fig. 5. Contamination from the r line is negligible.

C. Clinometry

During the relatively long data acquisition periods, care must be taken to monitor and minimize any shifts in the diffraction angle or detector position. Clinometers continually monitor the detector and crystal angles with arcsecond resolution and can be used to determine any changes in angular position during EBIT observations. The clinometers also record certain large amplitude vibrations of the detector arm and crystal mount. Such vibrations may be caused by faults in vacuum pumps or rapid surging of liquid nitrogen through the feed lines to the EBIT. Data obtained displaying these vibrations are rejected because the diffraction profiles

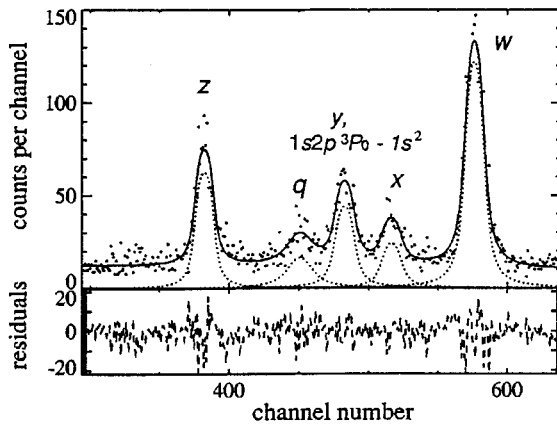


FIG. 5. Heliumlike vanadium spectra observed at the NIST EBIT. Resonance lines and lithiumlike satellite lines are labeled according to Gabriel's scheme. Summed observations represent some 24 of observation. The $q(1s2s2p^2P_{3/2} \rightarrow 1s^22s^2S_{1/2})$ lithiumlike satellite contamination is at a level which does not impair the final measurement. Spectra are fitted with a Lorentzian convolved with a slit profile and a background. The dotted lines are the fitted profiles to each resonance line; the solid line is the sum of all fitted profiles and background.

will be broadened, compromising resolution and precision. Rejected data comprised a small subset of the total measurements. Most observations were made with the Seemann wedge removed to maximize flux.

A post-measurement calibration was conducted to insure that no changes in the spectroscopy system had occurred during the measurement process. The post-run calibration, when subsequently analyzed in conjunction with prerun calibration data, was used to ensure against physical shifts and changes in alignment.

III. CURVED CRYSTAL THEORY AND SYSTEMATIC SHIFTS

Curved crystal geometries are often used in precision x-ray spectroscopy to obtain increased signal and lower statistical error, or to focus an extended source. All systematic shifts down to the level of 10–30 ppm must be accounted for to perform useful tests of QED in medium Z highly charged ions. Dynamical x-ray diffraction plays a crucial role in any wavelength dispersive spectroscopy such as ours. A systematic shift which is commonly accounted for in x-ray diffraction is the refractive index (RI) correction which is due to the mean change in refractive index in the crystal changing the angle of incidence relative to the air or vacuum. The angle of diffraction θ_B is shifted causing Bragg's law of diffraction

$$n\lambda = 2d \sin \theta_B \quad (1)$$

to become

$$n\lambda = 2d \sin \theta_B \left(1 - \frac{1-RI}{\sin^2 \theta_B} \right), \quad (2)$$

where RI is the index of refraction (specific to λ and the crystal). The magnitude of the refractive index correction is 100–300 ppm [22,23], depending upon the wavelength, crystal, and geometry, and so must be determined to a few percent.

Most curved and flat crystal spectroscopy QED investigations have addressed systematic corrections based upon ray-tracing methods, incorporating the simple refractive index correction [24–26]. Some of these QED measurements were calibrated using wavelengths observed in different orders of diffraction [11]. These measurements, however, did not use a full dynamical diffraction theory to calculate systematic shifts and therefore did not consider significant effects relating to depth penetration, lateral shifts, source size, and detector location. Any of these effects can cause systematic shifts comparable to the refractive index correction.

A. Depth penetration

Depth penetration refers to the mean depth that x-rays penetrate into the crystal and the effect that this penetration has upon the observed diffraction angle. For curved crystals depth penetration at angles other than normal to the surface will result in a variation of the angle of incidence in successively deeper crystal layers. The depth penetration of x-rays into a crystal can have effects larger than refractive index shifts [23]. It is therefore the dominant systematic in many curved crystal measurements, and is independent of refractive index and ray-tracing (geometrical) corrections. The magnitude of the depth penetration is dependent upon diffraction order and angle of incidence. The resulting shift in angle for curved crystals (radius $2R_z$ where R_z is the Rowland circle radius) can be estimated using

$$\Delta \theta_{in/out} \approx \arccos \left[\left(1 + \frac{\bar{d}}{2R_z} \right) \cos(\theta_B \pm \alpha_p) \right] - (\theta_B \pm \alpha_p), \quad (3)$$

where \bar{d} is the mean depth of penetration and α_p is the mean angle of diffracting planes to the crystal surface [23]. Simple estimates of \bar{d} can be made but a rigorous calculation with 1% precision requires the dynamical diffraction theory. The strong dependence upon diffraction order, due to the dependence of attenuation (μ) upon energy, implies that any x-ray QED measurement employing diffraction in different orders should address this effect explicitly.

B. Lateral shifts

Lateral shifts are also due to depth penetration and refer to a shift in the exit location of an x-ray at the crystal surface. For flat crystals this results in a transverse shift at the detector and is dependent on μ and extinction. For curved crystals the lateral shift causes a shift at the detector (if positioned on the Rowland circle) of

$$\Delta Y_{lateral}(A, B) \approx R_z \arccos[\Phi] - 2R_z B, \quad (4)$$

where

$$\Phi = [(2 \cos B - \cos A) \cos A - \sqrt{\sin^2 A (\sin^2 A + \cos^2 B - \cos B \cos A)}] \quad (5)$$

and $B = \theta_B + \alpha_p$, $A = B + \theta_A$, and $\theta_A = \Delta \theta_{in} + \Delta \theta_{out}$ as given by Eq. (3). Simpler, less precise estimates can be formulated for specific situations but ultimately any calculation relies on a precise determination of depth penetration. For low angle and low order diffraction, lateral shifts will be 10–100 % of the refractive index corrections [23]. Equation (4) will determine the lateral shift on the Rowland circle but not the shift at a detector located off the Rowland circle.

C. Source and detector shape and position

Geometrical effects such as source size and position can cause shifts of a similar magnitude to refraction [23]. While ray tracing can adequately describe these situations outside the crystal, the effect of dynamical diffraction, associated depth penetration, and lateral shifts modifies these estimates.

Estimates of shifts or errors presented in curved crystal geometries are often calculated for an ideal detector located on the Rowland circle. However, the detection surface is usually flat and therefore does not conform to the Rowland circle. Detectors located on a fixed length detector arm will also travel off the Rowland circle with a variation in the detection angle unless the crystal curvature is also varied precisely.

Mosaicity and crystal curvature effects are also often disregarded but these effects must be considered for the precision which has been the aim of this research. These issues led to the development of the theory that combines curvature and mosaicity in a dynamical diffraction theory by Chantler [27,28]. One systematic shift is caused by the calibration source not being in the same location as the EBIT source. Theoretical modeling determines the shifts associated with this mislocation and the correction is 3–5 ppm depending upon wavelength.

Detailed theoretical modeling of our spectroscopy system has revealed a wavelength-dependent systematic error associated with detector shape and location due to asymmetric partial focusing on the detector plate. Conventional shifts calculated for detection on the Rowland circle do not agree with shifts computed for flat extended detectors. This systematic error can be 100–200 ppm and would be present in any Johann curved crystal spectrometer with fixed length detector arm and flat detection surface.

In later work [20,21] this theory was expanded to incorporate flat surface detectors located off the Rowland circle. We have therefore developed the computational techniques to deal with all of the above-mentioned systematics in a rigorous and integrated manner.

IV. DATA ANALYSIS AND ERROR SOURCES

Calibration and EBIT spectra are fitted with Lorentzian line shapes convolved with slit profiles. The width of the Lorentzian and common slit components are free parameters in the fit. The background is negligible and is not fitted. For calibration lines, two components are fitted to each line fol-

lowing Deutsch *et al.* [29] and Hartwig *et al.* [30] to reproduce the asymmetry of real profiles (see Fig. 3). The helium-like resonance lines and satellite contamination are fitted by a single component with a Lorentzian convolved with a slit profile in addition to a quadratic background. Figure 5 shows the result of profile fitting to a heliumlike vanadium spectrum.

The location of the calibration lines with two fitted components is determined from the peak position of the sum of the two components. Peak values are used to correspond to the reference values of Bearden [22] (this point is discussed further in Sec. IV B). For the heliumlike resonance lines the centroid position and peak position correspond since the line shapes are symmetrical and only one component is fitted to each line.

A. Dispersion function determination

Bearden's tabulation of characteristic x-ray lines [22], although published in 1967, is the most comprehensive data set available. Reference wavelengths for calibration lines are corrected from Bearden's values using the recent CODATA determination of lattice spacings [31]. The adjustment required is relatively constant at –15 ppm across the wavelengths we use for calibration. The dispersion function is fitted to the 10 calibration wavelengths: Ti $K\beta_{1,3}$, V $K\alpha_1$, V $K\alpha_2$, V $K\beta_{1,3}$, Cr $K\alpha_1$, Cr $K\alpha_2$, Cr $K\beta_{1,3}$, Mn $K\alpha_1$, Mn $K\alpha_2$, and Mn $K\beta_{1,3}$. Prerun and postrun calibration data can be compared for consistency and systematic shifts. The dispersion function relates the wavelength of a spectral feature located at the detector center to the angle of diffraction which is measured by clinometers attached to crystal and detector arms of the spectrometer.

Clinometer values for the crystal and detector are continually recorded with any spectrum and the centroid of each clinometer distribution is the measure of the angle for crystal (θ_B) and the detector ($2\theta_B$). The dispersion function is determined by a bivariate nonlinear least-squares fit to the function

$$\Theta = \arcsin\left[\frac{DC - A(1)}{A(2)}\right] - \arcsin\left[\frac{CC - A(3)}{A(4)}\right] + A(0), \quad (6)$$

where DC is the centroid of the detector clinometer, CC the centroid of the crystal clinometer, Θ the reference wavelength of the calibration line (adjusted for refractive index correction and other systematic shifts), and $A(0)$ – $A(4)$ the parameters of the fit relating to offsets and scaling of the clinometer response function, which has been demonstrated to be highly linear in $\sin \theta$.

We observe all the resonance lines of heliumlike vanadium at one spectrometer setting. Thus the position-sensitive detector scale (in channels/ μm or channels/arcsecond) is an important input into the dispersion function.

Any systematic shifts must be accounted for when determining the dispersion function. As described in the preceding section, we account for refractive index corrections, depth penetration of x rays in the crystal, shifts associated with source size and location, and shifts due to detector

TABLE I. Error budget for heliumlike vanadium measurement.

Error source	Magnitude of error (ppm)			
	Resonance line			
	<i>w</i>	<i>x</i>	<i>y</i>	<i>z</i>
Statistical uncertainty of centroid position	9.5	31.0	22.3	12.9
Reference wavelengths (Bearden [22])			12	
Adjustment of Bearden wavelengths			<0.5	
Diffraction theory ^a			6	
Dispersion function determination ^a			20	
Temperature and diffraction crystal $2d$ spacing variation			<5	
Doppler shifts			<4	
Total excluding statistics ^b			24.9	
Total	26.7	39.8	33.4	28.1

^aSummation of related uncertainties (see text).

^bTotal excluding statistics: Sum of all errors except statistical uncertainty of heliumlike vanadium observations.

shape and location. The dispersion function is not a simple relationship between angle and wavelength but a complex (but smooth) function of reference wavelengths, clinometer values, detector scale, and systematic shifts.

B. Error budget

The error budget is laid out in Table I. The statistical uncertainty varies between 9.5 ppm ($w, 1s2p \rightarrow 1s^2$) and 31.0 ppm ($x, 1s2p \rightarrow 3P_2 \rightarrow 1s^2$) with the relatively low flux of the EBIT prohibiting trivial improvement. The uncertainty is determined from the curve fitting routine and is the standard deviation of the centroid position for each resonance. This corresponds to a determination varying between 1/27 and 1/77 of the widths.

Recent work by Deslattes *et al.* [32] on reference wavelengths has resulted in lower estimates of uncertainties than those on Bearden's values. Bearden's uncertainties in general have been reduced by 25–30% from 12 ppm to 8–10 ppm. In most cases, including all the wavelengths used in our investigations, the further refinement yielded the same value for the wavelengths within uncertainties. Our values (adjusted from Bearden) and those of Deslattes *et al.* have a small discrepancy of 0.5 ppm. This discrepancy is insignificant compared to the uncertainty of the wavelengths and does not compromise our final result.

The peak locations in the spectra and the derived centroid determinations for $V K\alpha_1$, $V K\alpha_2$ differ by 50–80 ppm. The choice of peak and centroid values in our calibration system is an important systematic effect. We have found that the shift does not create an error in first order if theory and experimental results are computed consistently for peak or centroid values. Peak values for single-vacancy spectra remain the preferred measure for reporting or determining characteristic energies despite advanced methods for determining centroids [33]. In the final analysis peak values are therefore used and determined from curve fitting to experimental profiles as discussed in Sec. IV.

Diffraction theory uncertainty refers to the diffraction calculations that are used to determine systematic shifts. The

reliability and self-consistency of these calculations when compared to calibration lines resulted in a variance of less than 6 ppm. The magnitude of each of the component shifts are of order 100 ppm (and vary quite dramatically for the range of angles and energies of interest), but the uncertainty on the net result is 6 ppm. We emphasize that 6 ppm is not the net shift which varies for our experiment from about 70 to 300 ppm. The uncertainty is low for the total calculated shift because of relative insensitivity of the result to experimental uncertainties in source location, source size, and detector location. To detail one example, the shift associated with the mislocation of the calibration and EBIT sources results in a small shift (3–5 ppm); the separation of these sources is 0.25 m. It follows that uncertainty in the longitudinal position of the sources at the millimeter level is not critical.

The uncertainty of the dispersion function determination shown in Table I is currently the dominant systematic correction. The determination of the dispersion function involves interrelated variables, and the absolute uncertainties of these input variables do not add linearly to the final uncertainty of the function. For example, the calibration source size uncertainty is 10% but in the Johann geometry this contributes less than 5 ppm to wavelength determination. Longitudinal source location is very uncertain (± 1 mm) but in our geometry this has a negligible effect on the final accuracy. The overall contribution of calibration source size and alignment uncertainty is 5 ppm. The statistical error associated with the calibration lines is 2–3 ppm and the error associated with the calibration profile fitting is 3–4 ppm.

The major contribution to the dispersion function uncertainty is the detector scale uncertainty. This uncertainty relates to the absolute calibration of the detector position scale in channels per micrometer and the linearity of that scale. The heliumlike resonance lines are widely spaced on our detector (“*w*”–“*z*” separation ≈ 190 channels or ≈ 8.5 mm) and therefore any uncertainty in the detector scale is critical. The absolute detector scale is determined at less than 0.5% which results in an average contribution to the dispersion

TABLE II. Energies of heliumlike resonance lines in vanadium, comparison to theory.

Notation	Transition	Theory ^a Energy (eV)	QED cont. ^b (ppm)	NIST EBIT and Univ. Melbourne (this work)		
				Energy (eV)	ΔE^c (ppm)	Expt. test of QED (%)
<i>w</i>	$1s2p\ ^1P_1 \rightarrow 1s^2\ ^1S_0$	5205.15	471.1	5205.10(14)	-10(27)	5.7%
<i>x</i>	$1s2p\ ^3P_2 \rightarrow 1s^2\ ^1S_0$	5188.72	478.1	5189.12(21)	80(40)	8.4%
<i>y</i>	$1s2p\ ^3P_1 \rightarrow 1s^2\ ^1S_0$	5180.31	482.5	5180.22(17) ^d	-19(33)	6.9%
<i>z</i>	$1s2s\ ^3S_1 \rightarrow 1s^2\ ^1S_0$	5153.88	415.5	5153.82(14)	-11(28)	6.7%

^aDrake (Ref. [5])^bQED cont.: QED contribution to transition energy using QED definitions of Drake [5].^c ΔE : Energy (expt.-theory)/theory.^dBlend of *y* and $1s2p\ ^3P_0 \rightarrow 1s^2$ transitions.

function imprecision of 15 ppm.

The contribution of satellite lines has also been included in the dispersion function uncertainty. The $q(1s2s2p\ ^2P_{3/2} \rightarrow 1s^22s\ ^2S_{1/2})$ lithiumlike satellite is explicitly fitted (see Fig. 5) and has a peak intensity of 13% of the *w* intensity. Any dielectronic satellites will be at least an order of magnitude less intense than the lithiumlike satellites or less than 1% of the intensity of the heliumlike resonance lines [with full widths at half maximums (FWHMs) corresponding to 600–800 ppm of the resonance energy]. Thus any unresolved satellite, even located at a half-width from the centroid of a heliumlike resonance line, will cause a shift of no more than 3–4 ppm.

Dispersion function uncertainty has been reduced to 20 ppm through the careful determination of systematic shifts. This has been a major achievement of this work. We have done explicit analysis to determine the error associated with the omission of the systematic shift caused by a flat detector shape and location off the Rowland circle. This revealed a poor determination of the dispersion function and errors of 100 ppm, which was corrected for as described above. Further improvement with future experiments is expected.

Doppler shifts due to the low thermal velocities of the highly charged ions in the EBIT are not significant sources of uncertainty. On average the Doppler shifts will be zero as there is no preferred direction of motion. Doppler broadening is 1.8 eV for 1 keV ions and we allow for a possible 1% asymmetry of velocity distribution resulting in a maximum Doppler shift of less than 0.02 eV or less than 4 ppm. Temperature effects, particularly on the diffraction crystal 2d spacing, are also insignificant sources of uncertainty. The linear expansion coefficient of the germanium crystal we use is $5.95 \times 10^{-6} \text{ K}^{-1}$ [34] and the crystal is in moderate vacuum (10^{-6} Torr) with monitored external temperature variations of $\approx 2^\circ\text{C}$. Also any direct lattice spacing errors have only a second-order effect on the measurement accuracy (because of the calibration) so that the effect on wavelength determination will be less than 5 ppm.

Summing all systematics errors in quadrature results in a 24.9 ppm systematic uncertainty and a total uncertainty for the resonance lines of 27–40 ppm. The main sources of uncertainty are therefore statistical, reference wavelengths, and dispersion function determination. All may be regarded as

soft limits at present (subject to improvement with additional work in the future). Methods of reducing statistical uncertainty by improving spectrometer efficiency are being investigated and improved flux from the NIST EBIT has been achieved in subsequent studies. Reference wavelength uncertainty is limited at present to Bearden's values but some of the metals we employ for calibration have been measured with improved precision recently [35]. Future measurements of the characteristic wavelengths on, for example, a vacuum double-crystal spectrometer are very likely to reduce uncertainty.

V. RESULTS AND DISCUSSION

Our results are the first absolute measurements of all the resonance lines in heliumlike vanadium using an EBIT. We do not rely on a single calibration energy, but require a series of calibration lines to determine the dispersion function of the spectrometer. These measurements represent a 27–40 ppm determination of the heliumlike resonance lines in vanadium. Results are summarized in Table II and the notation of Gabriel [14] for each transition is indicated.

A. Comparison to Theory

Our results for all of the heliumlike vanadium resonance lines are compared to the theory of Drake [5] in Table II. The values for the $w(1s2s\ ^1P_1 \rightarrow 1s^2)$ and $z(1s2s\ ^3S_1 \rightarrow 1s^2)$ transitions lie just below theory but well within experimental uncertainty. The $x(1s2p\ ^3P_2 \rightarrow 1s^2)$ transition is the least intense of the heliumlike resonance lines, so the statistical uncertainty is larger. However, the result for the *x* line is less than 2σ from theory [5] which is within reasonable statistical variation. The comparison of the *y* ($1s2p\ ^3P_1 \rightarrow 1s^2$) and $1s2p\ ^3P_0 \rightarrow 1s^2$ blend to theory is discussed in detail in Sec. V F.

The uncertainty of theoretical calculations including the estimation of missing or uncalculated terms has been receiving increasing scrutiny as techniques have advanced. One of the most recent two-electron Lamb shift calculations by Persson *et al.* [10] estimates missing correlation effects in QED contributions at 0.1 eV for all elements or 20 ppm of transition energies in medium *Z* ions. In earlier work, Drake [5]

TABLE III. Selected $w(1s2p\ ^1P_1 \rightarrow 1s^2)$ transition energies (eV) for vanadium and surrounding medium Z ions.

Z	Experiment	Ref.	Theoretical transition energies				ΔTh^a (ppm)	QED ^b (eV)	$2e$ QED ^c (eV)
			Unified [5]	AO [6]	CI [7]	MCDF [9]			
18	3139.553(38)	[47]	3139.577	3139.582	3139.617	3139.65	23	1.055	0.09
22	4749.74(17)	[11]	4749.63	4749.64	4749.71		17		
23	5205.10(14)	[^d]	5205.15	5205.16				2.474	0.16
24	5682.32(40)	[11]	5682.05	5682.06	5682.15		18		
26	6700.08(24)	[27]	6700.40	6700.43	6700.54	6700.60	30		
32	10280.70(22)	[13]	10280.14	10280.19	10280.39		24	7.674	0.40

^a ΔTh : Maximum discrepancy between theories.

^bQED: QED contribution to the ground state ($1s^2\ ^1S_0$) [5].

^c $2e$ QED: Two-electron QED contribution extrapolated (see text) [10].

^dThis work.

claimed uncertainty for $Z=23$ was less than 0.005 eV or 1 ppm of heliumlike resonance lines due to uncalculated higher-order terms. Some of the latest theoretical calculations for the w transition in medium Z ions are summarized in Table III. The discrepancy between theories is indicated and the maximum discrepancy ranges from 23 to 30 ppm for $Z=18$ –26 and differences are consistent. Our measurements are at this level of uncertainty.

Table II also shows the QED contributions to heliumlike resonance lines in vanadium as determined by Drake. The QED contributions are also expressed as a proportion of the relevant transition in ppm. The level at which our measurements test these contributions is between 5.7% and 8%. The theoretical QED contributions include mass polarization and nuclear size effects but these contribute less than 1% to the total. If the QED contributions to the $2l$ states are assumed to be correct, then the $1s$ QED contribution is measured to 6%.

Our result for the w line in vanadium is within our experimental uncertainty of the theory of Drake [5] and Plante *et al.* [6]. We therefore find no evidence of the earlier reported trend that experimental values are greater than theory [11]. Figure 6 shows our result for the w transition compared to theory [5] and other measurements for heliumlike vanadium and surrounding medium Z heliumlike ions. Our measurements are compared with other experiments in the context of medium Z x-ray measurements in the following discussion.

B. Two-electron Lamb shifts

The two-electron Lamb shift has been a topic of considerable interest recently following significant variation in the recent calculations of two-electron contributions to the ground state of medium and high Z heliumlike ions [10,6,5]. The “two-electron Lamb shift” can be defined as the difference between the hydrogenic $1s_{1/2}$ Lamb shift and the QED contributions to the heliumlike ground state ($1s^2\ ^1S_0$). The two-electron Lamb shift relates to the two-electron radiative QED Feynman diagrams (vacuum polarization and self-energy) due to interactions between the electrons [10]. Non-radiative two-electron QED (ladder and crossed-photon diagrams) are negligible for $Z \leq 32$. We have calculated the two-electron Lamb shift by subtracting the results of Johnson and

Soff [37] for the hydrogenic $1s_{1/2}$ Lamb shift from the QED contributions to the heliumlike ground state from Drake [5]. For $Z=32$ (germanium) we obtain 0.31 eV which can be directly compared to the 0.4 eV result of Persson *et al.* [10]. For vanadium, the two-electron Lamb shift calculated in this manner is 0.15 eV or 29 ppm of the $1s2s\ ^1P_1 \rightarrow 1s^2$ transition energy. Two-electron QED calculations for $Z < 32$ are not available from Persson *et al.*, so no direct comparison can be made with Drake’s calculation of vanadium.

As a simple alternative calculation, we have estimated the two-electron Lamb shift for heliumlike ions of Z less than 32 by extrapolating the results of Persson *et al.* for $Z=32$ –92 using a power-law fit ($2e\ \text{QED} = aZ^b$). The Z power dependence is interestingly found to be $b \approx 2.5$. Derived results for $Z=18$ and 23 are tabulated with Persson’s result for $Z=32$ in Table III. Theory might expect a power-law dependence of $b=3$ as the two-electron contributions scale as Z^3 . The result ($b \approx 2.5$) from the power-law fit to the sum of all computed contributions is in reasonable agreement with the expected theoretical value. For vanadium the two-electron Lamb shift is 0.16 eV or 31 ppm, slightly larger than the

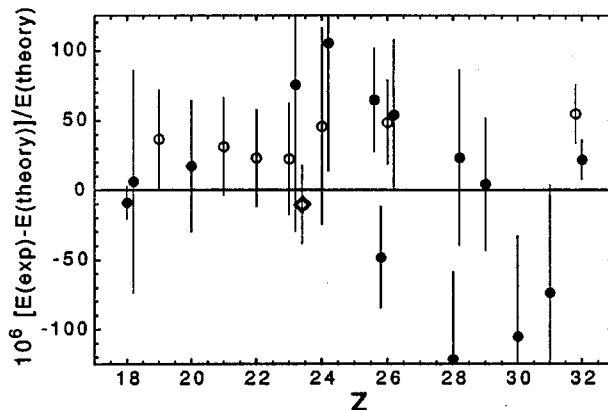


FIG. 6. Measurements of the $w(1s2p\ ^1P_1 \rightarrow 1s^2)$ transition in medium Z ions: comparison to theoretical work of Drake [5]. $E(\text{exp})$: experimental transition energy; $E(\text{theory})$: theoretical transition energy. \diamond , this work; \circ , Beiersdorfer *et al.* (1989), Ref. [11], $Z=32$, MacLaren *et al.* (1992), Ref. [13]; \bullet , other sources (see Table III references).

TABLE IV. Experimentally determined energies (eV) of heliumlike vanadium $1s2l \rightarrow 1s^2$ resonance lines. The source of highly charged ions is indicated.

Key	Transition	PLT tokamak Ref. [11]	LIVS plasma Ref. [39]	Energy	LLNL EBIT [12]		TFR tokamak [38]	
					$E_w - E^a$	dE^b	$E_w - E$	dE
w	$1s2p \ ^1P_1 \rightarrow 1s^2$	5205.27(21)	5205.58(55)	5205.33 ^c				
x	$1s2p \ ^3P_2 \rightarrow 1s^2$			5188.86(22)	16.47	0.04	17.0	0.56
y	$1s2p \ ^3P_1 \rightarrow 1s^2$			5180.30(22)	25.03	0.19	25.7	0.82
3P_0	$1s2p \ ^3P_0 \rightarrow 1s^2$			5180.30(22)	25.03	-1.28	25.7	-0.65
z	$1s2s \ ^3S_1 \rightarrow 1s^2$			5153.90(30)	51.43	0.16	51.9	0.66

^a $E_w - E$: difference between energy of w transition and energy of relevant transition.

^b $dE = (E_w - E)_{\text{theory}} - (E_w - E)_{\text{expt}}$.

^cReference line set to semiempirical value of 5205.33 eV.

experimental uncertainty of 0.14 eV of our measurements. The agreement between this result obtained from extrapolation of the results of Persson *et al.* and the value obtained by direct calculation from Johnson and Soff and Drake is excellent (0.01 eV difference). For $Z=32$, where the comparison can be made directly without extrapolation, the difference is 0.09 eV, remarkably consistent with the uncertainty estimate (0.1 eV) of Persson *et al.* for contributions from missing correlation effects in QED. As was the case with the experiment of Marrs *et al.* [36], a significant improvement in experimental precision would provide a critical test of two-electron QED.

In terms of basic physical effects included, the calculations of Drake and of Persson *et al.* are equivalent up to all terms of order α^3 (assuming that the many-body perturbation theory expansion has converged sufficiently well), and also terms of order $\alpha^4 Z^6$ and $\alpha^4 Z^5$. Any difference between the two calculations should therefore scale as $\alpha^4 Z^4$, at least through the intermediate range of Z .

Persson *et al.* states that the missing correlation effects in their two-electron QED calculations is estimated to be of the order of 0.1 eV for all elements. Formally this should only be applied to the range of elements $32 < Z < 92$. The associated uncertainties for $Z < 32$ are unknown, but could be expected to increase in this regime. In the calculations of Drake, the uncertainty due to relativistic correlation effects in QED scales as $\alpha^4 Z^4$. The sources of the uncertainty are quite different in the calculations of Drake and of Persson *et al.* The lowest-order Lamb shift is of order $\alpha^3 Z^4$, and so the leading two-electron correction is of order $\alpha^3 Z^3$, i.e., smaller by a factor of $1/Z$. Higher-order correlation effects contribute further terms of order $\alpha^3 Z^2, \alpha^3 Z, \dots$. In the calculations of Persson *et al.*, it is the uncertainty in these correlation corrections to the lowest-order (in α) Lamb shift that accounts for their estimate of 0.1 eV for all elements. In contrast, the calculation of Drake accurately sums this entire series of terms, but there are relativistic correlation corrections to the QED shift of order $\alpha^4 Z^4, \alpha^4 Z^3, \dots$, not included in this calculation. This accounts for Drake's error estimate of $1.2(Z/10)^4 \text{ cm}^{-1}$ [5], scaling as Z^4 . It has been suggested that Drake's error estimate should be multiplied by 8 for the ground state, to take into account a $1/n^3$ scaling.

In summary, the calculation of Drake accurately treats the $1/Z$ expansion of the nonrelativistic two-electron QED shift, but not the αZ expansion of relativistic and correlation corrections. The calculation of Persson *et al.* is improved for the αZ expansion, but not the $1/Z$ expansion of the nonrelativistic correlation terms. For larger Z the calculations of Persson *et al.* may be preferred, and for smaller Z the calculations of Drake may be preferable.

C. Excited-state QED

Measuring the heliumlike $n=2$ to $n=1$ transitions can be sensitive to the excited-state QED contributions if the precision is sufficient. The QED contribution to the $1s2s \ ^3S_1$ is 0.333 eV from Drake [5] or 65 ppm of the transition energy. Our measurement of the z ($1s2s \ ^3S_1 \rightarrow 1s^2$) transition is sensitive to the $1s2s \ ^3S_1$ QED contribution at the 40% level. Most previous experiments in the medium Z region have only measured the w transition, while others have only measured the w and close-lying x and y lines. Ours is one of the most precise measurements of the z transition in medium Z ions.

Of course, the result is a direct measure of the $1s2s \ ^3S_1 \rightarrow 1s^2$ QED contribution. Most such measurements are insensitive to the excited-state ($2s$ or $2p$) QED contribution. However, our measurement is indeed sensitive to the excited-state QED contribution at the 40% level. Our result is comparable to the 51-ppm measurement for $Z=32$ [13] which tests the $1s2s \ ^3S_1$ QED contribution at the 48% level.

D. Previous heliumlike vanadium observations

Four other observations of heliumlike vanadium spectra have been reported (see Table IV). Two of these [38,12] were relative measurements to the w line and, as such, cannot be compared to absolute measurements of the w line. These relative observations include a study of heliumlike vanadium at an EBIT [12] and are the only prior observations of the heliumlike resonance lines other than the w line (the x , y , and z lines).

Two measurements [39,11] were conducted at a low-inductance vacuum spark plasma and a tokamak plasma, respectively. In both cases only the w line was reported. The first study by Aglitsky *et al.* [39] in 1988 was part of a broad survey of resonance transitions in heliumlike ions ($Z = 16-39$). A double Johann spectrograph was used to record spectra. Characteristic K lines were used for calibration based upon reference wavelengths of Cauchois [40]. The precision reported for the w transition in vanadium was 105 ppm.

The second study by Beiersdorfer and co-workers [11] was part of a survey of medium Z elements in the heliumlike isoelectronic sequence in tokamak plasmas at the Princeton Large Torus (PLT). The uncertainty reported for vanadium was 40 ppm. Close-lying Lyman series lines were used for calibration. Shorter-wavelength calibration lines and heliumlike resonance lines were observed in second-order diffraction. As discussed in Sec. III, significant systematic shifts can occur in measurements that utilize several diffraction orders unless properly accounted for. The theoretical values of Mohr [41] were used in that analysis for the hydrogenic transitions and therefore QED theory was assumed to be correct [11]. A review of hydrogenic medium Z measurements demonstrates that the experimental evidence is incomplete in this region of Z .

While several high precision absolute measurements of hydrogenic transitions have been reported for argon ($Z = 18$, e.g., Marmar *et al.* [42] and Beyer *et al.* [43]) and iron ($Z=26$, Chantler [27]), the elements with $Z=19$ to $Z=25$ have not been measured precisely and absolutely and in some cases have not been measured at all. For example, the Lyman α transitions in vanadium have only been investigated recently [44]. The practice of using internal reference lines based upon QED theory, while having spectroscopic advantages, cannot reliably be used to infer conclusions about QED contributions in two-electron systems.

Dielectronic satellite lines are often associated with heliumlike transitions particularly in plasmas where a wide range of electron energies are present. Satellite contamination in hot plasmas is often the major limiting uncertainty on the precision of energy measurements [45]. Bulk motions within the plasma can also be very fast and vary between charge states [46]. This may be contrasted to the situation in an EBIT where very low satellite contamination can be achieved and Doppler shifts are negligible.

The measurements of the w resonance line in heliumlike vanadium [39,11] are shown in Table IV and plotted in Fig. 6 where they can be compared to current theory and other experiments including this work. The results of Aglitsky *et al.* [39] lie higher in energy than theory but within experimental error. The measurements of Beiersdorfer *et al.* [11] across the range of Z observed were consistently higher than theoretical energies but most, including vanadium, were individually within experimental errors of theory. It was claimed that the comparison shows that there are systematic differences between data and predictions, which indicate a need to include additional corrections in the calculations [11]. The implication of this series of measurements was that there was a systematic offset between theory and experiment,

and that the uncertainty in the offset was smaller by roughly a factor of \sqrt{N} than that of the individual measurements [more precisely, the mean offset of the six measurements is 34(15) ppm]. Our result for the w line in vanadium indicates there is no systematic offset from theory; our value for the offset, $-10(27)$ ppm, differs from that inferred from the measurements of Beiersdorfer *et al.* by 44(27) ppm.

E. Other absolute medium Z measurements

A survey of experimental measurements across medium Z heliumlike resonance lines is shown in Table III and Fig. 6 and compared with recent theory. The most precise absolute measurement of medium Z heliumlike ions is attributed to Deslattes and co-workers [47] with a 12 ppm measurement of the w transition in argon. The x and y transitions were also measured in this work to similar accuracy, but the z transition was not observed. Our methodology is similar to that of Deslattes *et al.* in the use of an external x-ray calibration standard lying close to the wavelength of interest. The recoil experimental method used therein also eliminates the need for Doppler corrections and uncertainties in that work as opposed to other experiments but is comparable to our work on the EBIT. A novel experimental arrangement produced Ar^{16+} by collisions of MeV U^{66+} ions with an argon-gas target [43]. A Johann curved crystal spectrometer was employed with a position-sensitive proportional counter of the backgammon type (both the spectrometer and detector are similar to those used in this research). This spectroscopy method may have systematic errors associated with the geometry and detector type and position as discussed above (Sec. III). Three-electron satellite contamination in these observations was considerably reduced by adjusting the gas target pressure. The contribution of the residual satellite contamination to the overall precision of wavelength determination was estimated to be 3 ppm. However, as with all spectra with strong satellites, the limiting uncertainty is difficult to quantify. Argon is at the lower end of the medium Z elements where QED effects are smaller relative to the transition energies. This very precise measurement of argon [47] is within experimental uncertainty of the unified [5] and all orders (AO) [6] calculations, but excludes the configuration-interaction (CI) [7] and multiconfiguration Dirac-Fock (MCDF) [9] calculations, as shown in Table III.

F. Intensities of $1s2p\ ^3P_1 \rightarrow 1s^2$ and $1s2p\ ^3P_0 \rightarrow 1s^2$ transitions

The probability of the $1s2p\ ^3P_0 \rightarrow 1s^2$ transition reveals information about the dominant processes in an electron-beam ion trap. In helium, the $1s2p\ ^3P_0$ level can only decay to the ground state by two or three photon processes, $E1M1$ or $3E1$, respectively, but the probability is very low for all Z [48]. Vanadium has a finite nuclear moment ($7/2\hbar$ [49]), so the transition from the $1s2p\ ^3P_0$ state to the ground state ($1s2\ ^1S_0$) can also occur via the hyperfine interaction [50]. Mohr has calculated the $1s2p\ ^3P_0 \rightarrow 1s^2$ transition rate to be $10.5 \times 10^9\ \text{s}^{-1}$ in vanadium [50].

TABLE V. Experimental determinations of the relative intensity of the strong $y(1s2p\ ^3P_1 \rightarrow 1s^2)$ component compared to the total intensity of the blend (y and $1s2p\ ^3P_0 \rightarrow 1s^2$), using theoretical energies of Drake, Ref. [5].

y % of total blend intensity	TFR tokamak [38]	LLNL EBIT [12]	NIST EBIT ^a
Normalized to experimental w line		$99\% \pm 15\%$	$94\% \pm 12\%$
Normalized to theoretical w line	44% ^b	$87\% \pm 15\%$	$97\% \pm 12\%$

^aNIST EBIT: This work.

^bRelative measurement, no errors were published.

For vanadium, earlier theoretical work has claimed a ratio of 4:1 for the intensity of the $y(1s2p\ ^3P_1 \rightarrow 1s^2)$ transition relative to the $1s2p\ ^3P_0 \rightarrow 1s^2$ transition based upon electron-impact excitation cross-section calculations [12]. The calculation of Mohr combined with the y transition rate ($1.638 \times 10^{13} \text{ s}^{-1}$) of Drake [51], and assuming equal initial-state populations, results in a ratio of 1560:1. The competing $1s2p\ ^3P_0 \rightarrow 1s2s\ ^3S_1$ rate is only 2% of the $1s2p\ ^3P_0 \rightarrow 1s^2$ transition rate so it does not influence the result.

The hyperfine-induced decay of the 3P_0 level in vanadium cannot be resolved from the $y(^3P_1)$ transition in any available experimental method [12,38]. The relative intensities of the 3P_0 and y transitions therefore shift the observed centroid. The energy separation between 3P_0 and y lines is 1.47 eV in vanadium which is equivalent to 290 ppm of the energy of these transitions.

We determine the relative intensity of the y component compared to the blend to be $94 \pm 12\%$ (and consequently the 3P_0 component is $6 \pm 12\%$) based on the theoretical energies of Drake [5] and the experimentally determined centroid position of the blend. The width of each component is also consistent: $w = 3.82(29) \text{ eV}$, $x = 4.3(9) \text{ eV}$, $y - ^3P_0 = 4.1(7) \text{ eV}$, and $z = 3.27(38) \text{ eV}$. There is no direct evidence for individual high- n or recombination satellite contamination. The width of the $y - ^3P_0$ blend is within 1σ of that of the other resonances and narrower than the (weak) x line. This is consistent with our findings for the ratio of intensities based upon the centroid position and suggests an almost complete absence of the 3P_0 transition. The results for position and width of the $y - ^3P_0$ blend from a second study of vanadium at the NIST EBIT agree with those of the first study, although the statistical uncertainties are larger.

Our absolute experimental determination of the relative intensity of the y component is compared to relative measurements [12,38] of the heliumlike resonance lines in vanadium in Table V. Achard *et al.* [38] results are substantially different from recent theory (see dE values in Table IV) and were conducted at a tokamak plasma where satellite contamination was intense.

A comparison between EBIT experiments and their respective measurements is more revealing. The results from the Livermore EBIT [12] for the relative intensity of the y component compared to the total blend intensity are presented in Table V. We have presented the relative intensity, firstly, based upon the absolute experimental results compared with theory and secondly based upon relative differences from the w line and compared with differences as calculated in theory (results are normalized to the theoretical

position of the w line). Relative intensities of the y component derived from the EBIT measurements range from 87% to 99% (with 15% uncertainty) for the Livermore EBIT and from 94% to 97% for the NIST EBIT, depending upon normalization.

Drake [51] has suggested that differences between EBIT results for the ratio may be due to pressure differences because low-pressures and steady-state conditions could lead to a build up of the 3P_0 population relative to the 3P_1 state. The experimental evidence from both EBIT studies supports an almost complete absence of the 3P_0 transition and the results from the NIST EBIT are within experimental uncertainty of Drake's prediction (1560:1) [51] but exclude the earlier theoretical calculation of 4:1 [12]. The differences between EBIT results are within experimental errors. We conclude that the differences in EBIT experimental conditions have had a negligible effect on wavelength determination. This supports the value of absolute measurements from an EBIT source for precision QED investigations.

VI. CONCLUSIONS

The use of well-determined reference wavelengths has been crucial to this research, and has led to the first absolute determination of heliumlike resonance lines in vanadium using an EBIT. The uncertainties of the $w(1s2p\ ^1P_1 \rightarrow 1s^2)$ and $z(1s2s\ ^3S_1 \rightarrow 1s^2)$ lines are 27 and 28 ppm, respectively, and the measurements of all the transitions are a 5.7–8% test of QED contributions. The results are in accord with, but do not discriminate between, current theories of Drake [5] and Plante *et al.* [6] which differ by 0.01 eV. The measurement of the $z(1s2s\ ^3S_1 \rightarrow 1s^2)$ transition is sensitive to the $1s2s\ ^3S_1$ QED contribution at the 40% level.

The absolute calibration is achieved by using a spread of characteristic wavelengths ($K\alpha$ and $K\beta$) to map out and rigorously determine the dispersion function of the spectrometer. We have developed the dynamical diffraction theory necessary to evaluate systematic shifts at the precision level required to test QED. Systematic shifts associated with the shape and location of the detector used in the Johann geometry have been evaluated and reduced to a level that is comparable to the uncertainty of the reference wavelengths used for calibration.

Our measurement of the w line in vanadium is not in accord with previous measurements of medium- Z heliumlike ions (Beiersdorfer *et al.* [11]) conducted at a tokamak plasma

and the EBIT at LLNL [13] which reported a trend of experimental energies above theory. The location and width of the $\gamma-^3P_0$ blend implies a relative intensity of the γ component of 94% compared to the total blend intensity. This is in accord with recent predictions based upon transition rates but in disagreement with an earlier claim.

The unique spectroscopic advantages of the EBIT have been crucial in the success of these QED investigations, allowing Doppler-free and low-satellite contamination spectra to be measured. The benefits of absolute calibration com-

bined with rigorous diffraction theory in precision tests of QED have been demonstrated.

ACKNOWLEDGMENTS

We would like to acknowledge the assistance of A. Henins, R. D. Deslattes, and L. Ratliff during the experiments at NIST. We thank G. W. Drake for helpful discussions and comments. This research was supported by the Australian Research Council.

-
- [1] G. W. Series, *The Spectrum of Atomic Hydrogen: Advances* (Utopia, Singapore, 1988).
- [2] P. J. Mohr, in *Atomic, Molecular, & Optical Physics Handbook* (AIP, Woodbury, NY, 1996), Chap. 28.
- [3] R. Marrus *Physics of Highly-Ionized Atoms* (Plenum, New York, 1989).
- [4] G. W. F. Drake, *Phys. Rev. A* **19**, 1387 (1979).
- [5] G. W. Drake, *Can. J. Phys.* **66**, 586 (1988).
- [6] D. R. Plante, W. R. Johnson, and J. Sapirstein, *Phys. Rev. A* **49**, 3519 (1994).
- [7] K. T. Cheng, M. H. Chen, W. R. Johnson, and J. Sapirstein, *Phys. Rev. A* **50**, 247 (1994).
- [8] M. H. Chen, K. T. Cheng, and W. R. Johnson, *Phys. Rev. A* **47**, 3692 (1993).
- [9] P. Indelicato, F. Parente, and R. Marrus, *Phys. Rev. A* **40**, 3505 (1989); P. Indelicato, *Nucl. Instrum. Methods Phys. Res. B* **31**, 14 (1988); P. Indelicato, O. Gorceix, and J. P. Desclaux, *J. Phys. B* **20**, 651 (1987).
- [10] H. Persson, S. Salomonson, P. Sunnergren, and I. Lindgren, *Phys. Rev. Lett.* **76**, 204 (1996).
- [11] P. Beiersdorfer, M. Bitter, S. von Goeler, and K. W. Hill, *Phys. Rev. A* **40**, 150 (1989).
- [12] P. Beiersdorfer, M. H. Chen, R. E. Marrs, M. B. Schneider, and R. S. Walling, *Phys. Rev. A* **44**, 396 (1991).
- [13] S. MacLaren, P. Beiersdorfer, D. A. Vogel, D. Knapp, R. E. Marrs, K. Wong, and R. Zasadzinski, *Phys. Rev. A* **45**, 329 (1992).
- [14] A. H. Gabriel, *Mon. Not. R. Astron. Soc.* **160**, 99 (1972).
- [15] E. Takács, E. S. Meyer, J. D. Gillaspay, J. R. Roberts, C. T. Chantler, L. T. Hudson, R. D. Deslattes, C. M. Brown, J. M. Laming, J. Dubau, and M. K. Inal, *Phys. Rev. A* **54**, 1342 (1996).
- [16] J. D. Gillaspay, *et al.*, *Phys. Scr.* **T59**, 392 (1995).
- [17] J. D. Gillaspay, *Phys. Scr.* **T65**, 168 (1996).
- [18] A. Henins, *Rev. Sci. Instrum.* **58**, 1173 (1987).
- [19] B. P. Duval, J. Barth, R. D. Deslattes, A. Henins, and G. G. Luther, *Nucl. Instrum. Methods Phys. Res. A* **222**, 274 (1984).
- [20] D. J. Paterson, C. T. Chantler, C. Tran, L. T. Hudson, F. G. Serpa, and R. D. Deslattes, *Phys. Scr.* **T73**, 400 (1997).
- [21] C. T. Chantler, D. J. Paterson, L. T. Hudson, F. G. Serpa, J. D. Gillaspay, and E. Takács, *Phys. Scr.* **T80**, 440 (1999).
- [22] J. A. Bearden, *Rev. Mod. Phys.* **39**, 78 (1967).
- [23] C. T. Chantler and R. D. Deslattes, *Rev. Sci. Instrum.* **66**, 5123 (1995).
- [24] J. P. Briand, M. Tavernier, R. Marrus, and J. P. Desclaux, *Phys. Rev. A* **29**, 3143 (1984).
- [25] H. F. Beyer and D. Liesen, *Nucl. Instrum. Methods Phys. Res. A* **272**, 895 (1988).
- [26] P. Beiersdorfer, R. E. Marrs, J. R. Henderson, D. A. Knapp, M. A. Levine, D. B. Platt, M. B. Schneider, D. A. Vogel, and K. L. Wong, *Rev. Sci. Instrum.* **61**, 2338 (1990).
- [27] C. T. Chantler, D. Phil. thesis, Oxford University, 1990 (unpublished).
- [28] C. T. Chantler, *J. Appl. Crystallogr.* **25**, 674 (1992); **25**, 698 (1992).
- [29] M. Deutsch and M. Hart, *Phys. Rev. B* **26**, 5558 (1982).
- [30] J. Härtwig, G. Hölzer, J. Wolf, and E. Förster, *J. Appl. Crystallogr.* **26**, 539 (1993).
- [31] J. Schweppe, R. D. Deslattes, T. Mooney, and C. J. Powell, *J. Electron Spectrosc. Relat. Phenom.* **67**, 463 (1994).
- [32] R. D. Deslattes, E. G. Kessler, P. Indelicato, and E. Lindroth, *International Tables for Crystallography* (Kluwer Academic Press, Stockholm, 1999), Vol. C, Sec. 4.2.2.
- [33] R. D. Deslattes, *Phys. Scr.* **T46**, (1993).
- [34] R. D. Deslattes, E. G. Kessler, W. C. Sauder, and A. Henins, *Ann. Phys. (N.Y.)* **129**, 378 (1980).
- [35] G. Hölzer, M. Fritsch, M. Deutsch, J. Härtwig, and E. Förster, *Phys. Rev. A* **56**, 4554 (1997).
- [36] R. E. Marrs, S. R. Elliot, and T. Stöhlker, *Phys. Rev. A* **52**, 3577 (1995).
- [37] W. R. Johnson and G. Soff, *At. Data Nucl. Data Tables* **33**, 405 (1985); P. J. Mohr, *Phys. Rev. A* **46**, 4421 (1992).
- [38] M. H. Achard *et al.*, M. Cornille, J. Dubau, and M. Loulergue TFR Group, *Phys. Rev. A* **32**, 3000 (1985).
- [39] E. V. Aglitsky, P. S. Antsiferov, S. L. Mandelstam, A. M. Panin, U. I. Safronova, S. A. Ulitin, and L. A. Vainshtein, *Phys. Scr.* **38**, 136 (1988).
- [40] Y. Cauclous and C. Senemaud, *Wavelength of X-ray Emission Lines and Absorption Edges* (Pergamon, London, 1988).
- [41] P. J. Mohr, *At. Data Nucl. Data Tables* **29**, 454 (1983).
- [42] E. S. Marmar, J. E. Rice, E. Källne, J. Källne, and R. E. LaVilla, *Phys. Rev. A* **33**, 774 (1986).
- [43] H. F. Beyer, R. D. Deslattes, F. Folkmann, and R. E. La Villa, *J. Phys. B* **18**, 207 (1985).
- [44] D. J. Paterson, Ph.D. thesis, University of Melbourne, 1999 (unpublished).
- [45] E. Träbert, *The Spectrum of Atomic Hydrogen: Advances* (Utopia, Singapore, 1988), Chap. 6.

- [46] E. Källne, J. Källne, P. Richard, and M. Stöckli, *J. Phys. B* **17**, L115 (1984).
- [47] R. D. Deslattes, H. F. Beyer, and F. Folkmann, *J. Phys. B* **17**, L687 (1984).
- [48] H. F. Beyer, H. J. Kluge, and V. P. Shevelko, *X-Ray Radiation of Highly Charged Ions* (Springer, Berlin, 1997).
- [49] R. C. Weast, *Handbook of Physics and Chemistry* (CRC Press, Boca Raton, FL, 1985).
- [50] P. J. Mohr, in *Beam-Foil Spectroscopy*, edited by I. A. Sellin and D. J. Pegg (Plenum, New York, 1976).
- [51] G. W. Drake (personal communication).



ELSEVIER

Nuclear Instruments and Methods in Physics Research A 444 (2000) 156–160

**NUCLEAR
INSTRUMENTS
& METHODS
IN PHYSICS
RESEARCH**
Section A

www.elsevier.nl/locate/nima

Laboratory astrophysics and microanalysis with NTD-germanium-based X-ray microcalorimeters

E. Silver^{a,*}, H. Schnopper^a, S. Bandler^a, S. Murray^a, N. Madden^b, D. Landis^b, J. Beeman^b, E. Haller^b, M. Barbera^c, G. Tucker^d, J. Gillaspie^e, E. Takacs^e, J. Porto^e

^aHarvard-Smithsonian Centre For Astrophysics, 60 Garden Street, Cambridge, MA 02138, USA

^bLawrence Berkeley National Laboratory, 1 Cyclotron Road, Berkeley, CA 94720, USA

^cBrown University, Providence, Box 1843, RI 02912, USA

^dOsservatorio Astronomico di Palermo, Palermo, Italy

^eNational Institute of Standards and Technology, 100 Bureau Drive, Gaithersburg, MD, USA

Abstract

With the ability to create cosmic plasma conditions in the laboratory it is possible to investigate the dependencies of key diagnostic X-ray lines on density, temperature, and excitation conditions that exist in astrophysical sources with X-ray optics and a high-resolution X-ray microcalorimeter. The same instrumentation can be coupled to scanning electron microscopes or X-ray fluorescence probes to analyze the elemental and chemical composition of electronic, biological, geological and particulate materials. We describe how our microcalorimeter and X-ray optics provide significantly improved capabilities for laboratory astrophysics and microanalysis. © 2000 Elsevier Science B.V. All rights reserved.

1. Introduction

High resolving power, quantum efficiency approaching 100% and a bandwidth that spans the X-ray energies from 0.1–10 keV are properties of the microcalorimeter that make it the ideal spectrometer for laboratory astrophysics and microanalysis studies. An X-ray optic [1,2] was used to couple an X-ray microcalorimeter [3,4] to an Electron Beam Ion Trap (EBIT) at NIST [5]. Broad-band X-ray spectra from astrophysically relevant ionic species were obtained with an energy resolution approaching that of a Bragg crystal. The

unique plasma conditions in the EBIT allow these microcalorimeter experiments to demonstrate the limitless potential to acquire a database of atomic structure and cross sections in the isolated-ion limit (atomic energy levels, oscillator strengths and transition cross-sections). The microcalorimeter can obtain significant quantities of astrophysically relevant spectral data in relatively short times. Examples of newly obtained spectral data are presented in Section 3.

The same X-ray optic has been incorporated into a microcalorimeter-based X-ray microanalysis system that can be attached to a scanning electron microscope (SEM) or an X-ray fluorescence probe. The microcalorimeter allows X-ray microanalysis at low SEM beam energies. This

* Corresponding author.

improves significantly its spatial resolution, sensitivity to minor elemental constituents, and ability to unambiguously identify X-ray signatures from a mixture of light and heavy elements. Microcalorimeters have made it possible to distinguish K lines of low Z elements from L lines of transition elements or the M lines of very high Z materials. Representative measurements are shown in Section 4 and those from other investigators may be found in the literature [6,7].

2. The microcalorimeter and X-ray optic

A 2×2 array of NTD germanium-based microcalorimeters [8] views the laboratory plasma or the X-ray microanalysis sample through an X-ray optic developed at SAO. The X-ray optic [1,2] is a cylindrical spiral that focuses X-rays in a point-to-point geometry. The design can satisfy an extremely wide variety of focal lengths and energy ranges.

For SEM-based microanalysis, the eventual goal is to replace the liquid helium in the microcalorimeter cryostat with a mechanical cryocooler. Estimates of the vibrational and acoustical effects of a cryocooler operating in close proximity to an SEM show a need to decouple the microcalorimeter-cryocooler combination from the SEM. An X-ray optic was designed to focus X-rays on a detector located 1.5 m from the SEM. The solid angle for X-ray collection is equivalent to that expected without the X-ray optic when the same detector is located 3–5 cm away from the sample.

For laboratory plasma experiments on the EBIT, it is extremely difficult to locate the microcalorimeter in close proximity to the source volume. Access to a viewing port at this distance is restricted by magnet coils, cryogenic lines and other instruments. One meter is the nominal distance of closest approach for a microcalorimeter cryostat. This limits the solid angle to $\sim 2 \times 10^{-7}$ sr and makes the measurements extremely time consuming.

For our measurements at the NIST EBIT, the optic was equidistant (762 mm) from the source and detector. Fig. 1 shows the performance of the optic for this geometry as a function of X-ray energy when viewed by a 1 mm^2 detector 1.5 m from the

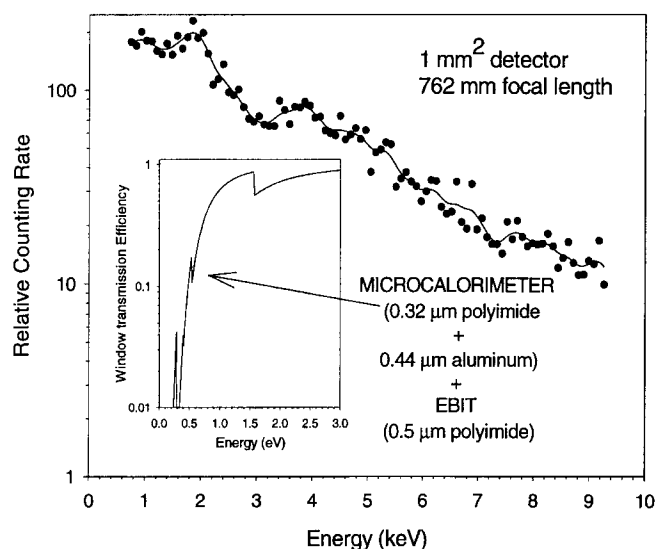


Fig. 1. Relative counting rate with and without the X-ray optic for a 1 mm^2 detector 1524 mm from the X-ray source. The inset shows the transmission efficiency of the detector and EBIT windows.

source. The data (dark circles) are the ratios of the counting rates obtained with the X-ray optic to the rates measured without the X-ray optic. The solid curve is a spline fit to the data. The figure inset shows the calculated transmission efficiency of the detector and EBIT windows. The relative counting rate should be interpreted differently depending upon whether the application is laboratory astrophysics or microanalysis. In the plasma experiments where the distance of closest approach is limited, the X-ray optic can increase the X-ray intensity by as much as 250. If decoupling the microcalorimeter and cryocooler from the SEM is the objective, then the optic provides the same solid angle with the microcalorimeter 15 times further away from the SEM than it would be for a closely coupled detector.

3. Laboratory astrophysics

The EBIT is a device to produce and study hot laboratory plasmas in an experimentally well-controlled environment. Details of its operation can be found in the literature [5].

Previous EBIT-based laboratory astrophysics programs made use of crystal spectrometers. These

experiments are complex and require, for example, a large number of runs to establish the parametric dependences in collisional excitation dominated and recombination dominated regimes. The analysis of the data requires high-resolution spectra of the He and H-like lines and the recombination continua. An additional complication is the polarization dependence induced by the strong anisotropy of the EBIT electron beam. The effect of polarization needs to be accounted for in the evaluation of intensities for lines excited by dielectronic electron capture and by electron impact. Precise values for crystal reflectivities as a function of polarization are required to correct the raw data.

The microcalorimeter is the ideal spectrometer for the EBIT-type plasma. The efficiency of the microcalorimeter shortens the measurement time by several orders of magnitude when compared with that needed by crystal spectrometers. The microcalorimeter obtains data simultaneously over the entire energy range of interest for all of the astrophysically relevant spectral components. In addition, the microcalorimeter is insensitive to the polarization of the EBIT plasma X-ray emission.

Fig. 2 is the first measurement of helium-like FeXXV with a microcalorimeter and was obtained without the aid of an X-ray optic. About three hours were needed to acquire the ~ 100 counts shown. Figs. 3 and 4 are representative of the significant results that can be obtained with much greater efficiency using the X-ray optic. For

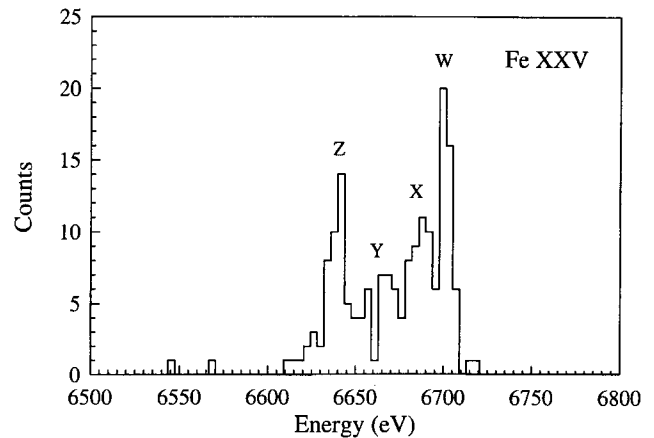


Fig. 2. The first laboratory plasma spectrum of helium-like FeXXV made with a microcalorimeter on the LLNL EBIT [4].

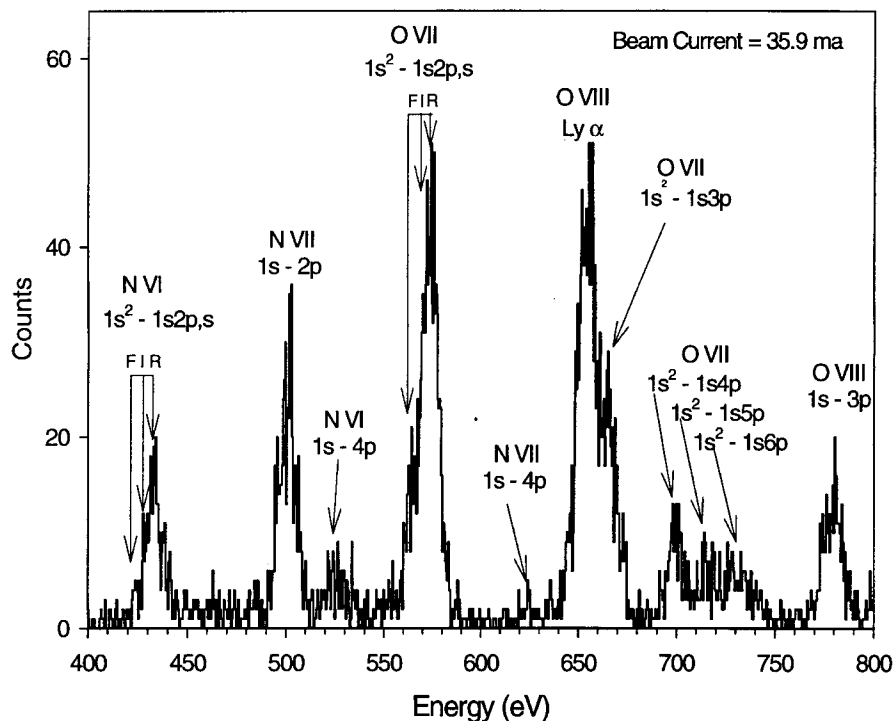


Fig. 3. Microcalorimeter X-ray spectra of ionized nitrogen and oxygen from the NIST EBIT. The collection time was ~ 20 mins.

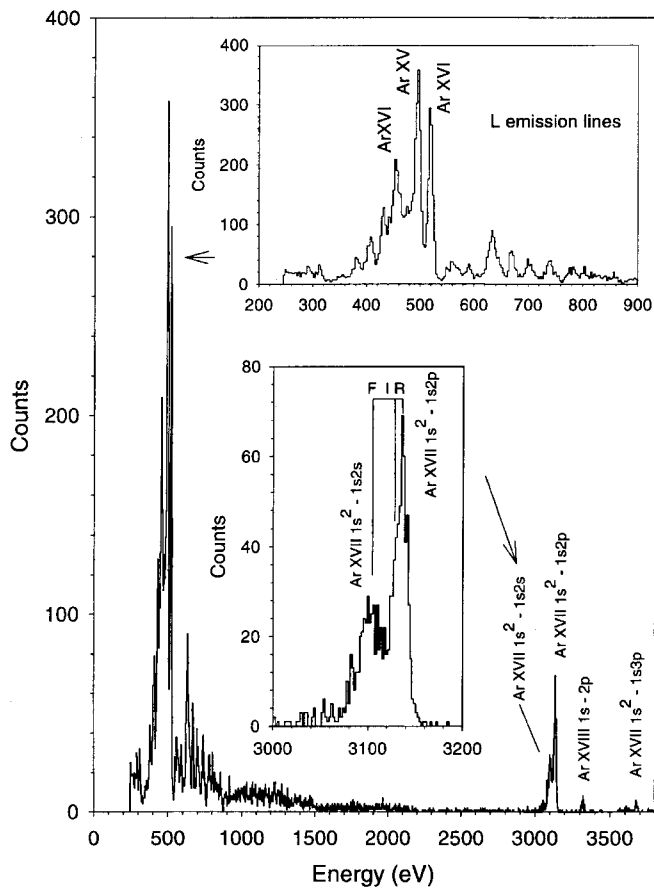


Fig. 4. Microcalorimeter X-ray spectra of ionized argon from the NIST EBIT. The collection time was ~ 20 mins.

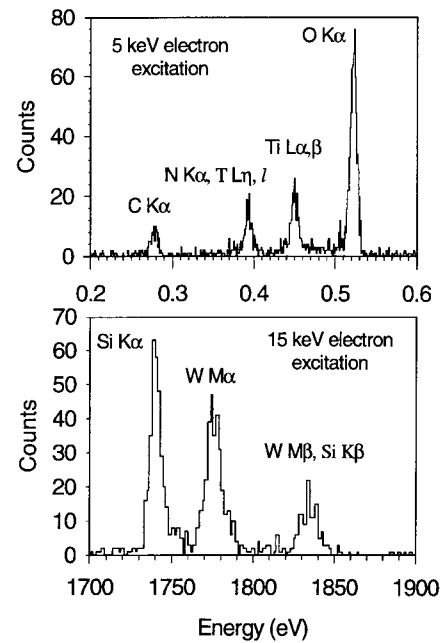


Fig. 6. Top: X-ray spectrum obtained from titanium target. Bottom: Si K and W M lines from SEM microanalysis of a W-coated silicon wafer. Energy is 6 eV without accounting for the natural line widths.

example, it took about 20 mins to acquire the ~12000 counts from argon X-rays shown in Fig. 4.

4. SEM-based microanalysis

A spectrum from a multielement sample in an SEM demonstrating the broad energy band of the microcalorimeter-optic combination is shown in Fig. 5. The counting rate was 25 Hz. An expanded view of the low energy part of the spectrum is shown in the inset. Fig. 6 shows a spectrum obtained when silicon (Si) coated with > 3000 Å of tungsten (W) is irradiated by electrons in an SEM. The W Mα emission is shown resolved from Si Kα. Fig. 6 also shows the O K line well resolved from the Ti L emission for a sample of TiO.

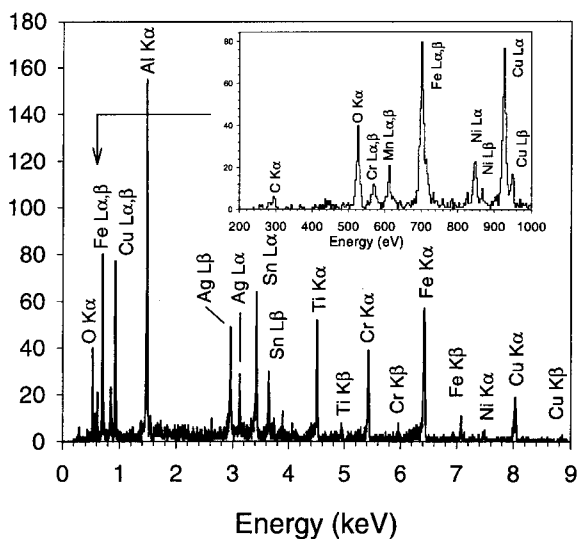


Fig. 5. Broad band spectrum from a multielement sample.

References

[1] E. Silver et al., US Patent application, Serial No. 09064476, 1998.

- [2] H. Schnopper et al., SPIE 3766 (1999).
- [3] E. Silver et al., manuscript in preparation, 1999.
- [4] E. Silver et al., unpublished data, 1995.
- [5] J. Gillaspay et al., Physica Scripta T59 (1995) 392.
- [6] D. Wollman et al., Nucl. Instr. and Meth. A 444 (2000) 145.
These Proceedings.
- [7] S. Friedrich et al., Nucl. Instr. and Meth. A 444 (2000) 151.
These Proceedings.
- [8] S. Bandler et al., Nucl. Instr. and Meth. A 444 (2000) 273.
These Proceedings.

LABORATORY ASTROPHYSICS SURVEY OF KEY X-RAY DIAGNOSTIC LINES USING A MICROCALORIMETER ON AN ELECTRON BEAM ION TRAP

E. SILVER, H. SCHNOPPER, S. BANDLER, N. BRICKHOUSE AND S. MURRAY
Harvard-Smithsonian Center For Astrophysics, 60 Garden Street, Cambridge, MA 02138

M. BARBERA

Osservatorio Astronomico G.S. Vaiana, Piazza del Parlamento 1, 90134 Palermo, Italy

E. TAKACS¹

Massachusetts Institute of Technology, 77 Massachusetts Avenue, 26-239, Cambridge, MA 02139-4307

J. D. GILLASPY, J. V. PORTO, AND I. KINK

National Institute of Standards and Technology, 100 Bureau Drive, Gaithersburg, MD 20899

J. M. LAMING

Naval Research Laboratory, Code 7674L, Washington, DC 20375

AND

N. MADDEN, D. LANDIS, J. BEEMAN, AND E. E. HALLER

Lawrence Berkeley National Laboratory, 1 Cyclotron Road, Berkeley, CA 94720

2000 February 9; 2000 April 25

ABSTRACT

Cosmic plasma conditions created in an electron beam ion trap (EBIT) make it possible to simulate the dependencies of key diagnostic X-ray lines on density, temperature, and excitation conditions that exist in astrophysical sources. We used a microcalorimeter for such laboratory astrophysics studies because it has a resolving power ≈ 1000 , quantum efficiency approaching 100%, and a bandwidth that spans the X-ray energies from 0.2 keV to 10 keV. Our microcalorimeter, coupled with an X-ray optic to increase the effective solid angle, provides a significant new capability for laboratory astrophysics measurements. Broadband spectra obtained from the National Institute of Standards and Technology EBIT with an energy resolution approaching that of a Bragg crystal spectrometer are presented for nitrogen, oxygen, neon, argon, and krypton in various stages of ionization. We have compared the measured line intensities to theoretical predictions for an EBIT plasma.

Subject headings: atomic data — atomic processes — line: identification — methods: laboratory — plasmas — X-rays: general

1. INTRODUCTION

X-ray spectroscopic measurements are used to determine the temperature distribution, density, ionization state, and elemental composition of hot cosmic plasmas. Knowledge of these basic parameters provides an understanding of physical processes in the hot universe such as atmospheric heating, transport, shock waves, and accretion. Plasmas of special interest are found in the magnetically heated coronae of late-type stars, the accretion disks surrounding collapsed stellar objects, the bubbles of gas heated by supernovae and the tunnels throughout interstellar space they create, the halos of elliptical galaxies, the nuclei of active galaxies, and the vast regions in galaxy clusters. The determination of the physical parameters that define the plasma relies on complex models of the continuum and line emissions. Experimental data are unavailable, except in rare cases, and the atomic data that are needed for these models are largely derived from theoretical work.

The current understanding of the fundamental processes occurring in highly ionized plasmas is not commensurate with the quality of data that will be obtained by the new X-ray telescopes and spectrometers flown on *ASCA*, *Chandra*, and *XMM*. With a nominal goal of a 1% calibration, the *Chandra X-ray Observatory*, launched in 1999 July, had a 6 month ground-based calibration effort, which was followed by a comprehensive set of in-flight measure-

ments. By contrast, few individual atomic rates are known with an accuracy less than 20%, and emission lines that depend on many processes (e.g., both direct excitation and cascades from recombination) are less accurately known. Dielectronic recombination rate coefficients and uncertain ionization state fractions derived from different ionization balance calculations may differ by factors of 2 or more.

To achieve the best scientific interpretation of the data from *Chandra*, *XMM*, and *ASCA*, theoretical calculations must be verified or modified by the results obtained from spectroscopic measurements in the laboratory. An excellent way to study the behavior of highly charged plasma ions is to confine them in an electron beam ion trap (EBIT). The EBIT produces customized, well-characterized, homogeneous plasmas well suited to a wide variety of precision measurements. The manipulation of the plasma conditions in the EBIT will generate a comprehensive database for comparison with theoretical atomic physics calculations. The EBIT is also uniquely capable of simulating specific slices through astrophysical plasma conditions (ions at rest, electrons with nearly constant energy) to allow the systematic examination of how the atomic structure and dynamics of plasma ions influence the energy release in cosmic X-ray sources. The literature contains numerous examples of EBIT applications (Gillaspy 1996; Beiersdorfer et al. 1996). Measurements of impact excitation rates, excited state lifetimes, ionization cross sections, resonant excitation and dielectronic recombination cross sections, and of course,

¹ Permanent address: Kossuth University, Debrecen, Hungary.

precision wavelength measurements providing tests of quantum electrodynamics have all been demonstrated.

High-resolution X-ray crystal spectrometers and broadband semiconductor ionization detectors have been the traditional tools for these investigations. Although they have yielded many excellent results (Beiersdorfer et al. 1992; Brown et al. 1998), these instruments are limited either by a poor energy resolution (solid state detector) or by low efficiency caused by a narrow bandwidth (crystal spectrometer). An additional complication is the polarization dependence induced by the strong anisotropy of the EBIT electron beam (Henderson et al. 1990; Takacs et al. 1996). The effect of polarization must be included in the analysis of crystal spectrometer-derived intensities for lines excited by dielectronic electron capture and by electron impact.

In the experiments discussed here and in subsequent papers related to this work, the solid state ionization detector and the crystal spectrometer are replaced with a cryogenic X-ray microcalorimeter. The microcalorimeter combines the broadband capability of the semiconductor ionization detector with the high resolving power of a Bragg crystal. X-ray photons absorbed in the microcalorimeter are converted into heat, causing a temperature rise proportional to the X-ray energy. It is the ideal instrument for EBIT plasma studies and this was first demonstrated in a pilot experiment we carried out in 1995 (Silver et al. 1999). During the intervening time, an X-ray optic has been developed to increase the solid angle subtended by the microcalorimeter. This paper describes the first application of the microcalorimeter/optic combination to the spectroscopic study of astrophysically relevant plasma ions in an EBIT at the National Institute of Standards and Technology (NIST).

In § 2 we review the operation of the EBIT. Section 3 is a description of the experimental setup and the adaptation of the microcalorimeter and X-ray optic to the EBIT. In § 4 we present the X-ray spectra of highly ionized nitrogen, oxygen, neon, argon, and krypton. In § 5 we compare the measured intensities of the helium-like lines to the theoretical predictions for the EBIT plasma.

2. THE ELECTRON BEAM ION TRAP (EBIT)

In traditional laboratory plasma X-ray sources such as tokamaks, mirror machines, and those produced with lasers, the physical processes responsible for X-ray line formation cannot be isolated easily. The interpretation of the spectra obtained from these sources requires modeling of the charge balance together with a mix of line formation physics. In 1988 a new plasma source was developed jointly at the Lawrence Berkeley National Laboratory (LBNL) and Lawrence Livermore National Laboratory (LLNL), called the Electron Beam Ion Trap (EBIT) (Levine et al. 1988). This source operates at electron densities of $\approx 10^{12}$ cm⁻³. It simplifies the plasma diagnostics by eliminating the transport issues and line-of-sight integrations that make tokamak spectra difficult to interpret. The only other US EBIT facility is located at NIST (Gillaspy 1996). In an EBIT, the plasma is eliminated as the perturbing medium and is replaced by a narrow, well-defined, electron beam. At NIST, an energy-tunable, 0–150 mA, electron beam can be accelerated to moderate energies (700 eV to 30 keV) by a series of cylindrical electrodes (drift tubes). The beam is focused to a small diameter (70 μ m) by a superconducting,

Helmholtz pair magnet that provides a maximum axial field of 3 T. Atoms or slightly charged ions are introduced into the center of the middle drift tube, where the electron beam has its highest kinetic energy and tightest focus, are stripped of their outer electrons by impact ionization, and reach successively higher charge states. The limiting charge state is determined by the voltage applied to the center drift tube. It is reached when the ionization potential of the ion is greater than the energy of the colliding electrons. An axial trap for the ions in the center is formed by applying a small positive bias (30–500 V) on the end cap drift tubes located on either side of the center drift tube. Radial trapping is provided by the space charge of the electron beam itself, and also by the axial magnetic field which restricts the motion of the ions to modified cyclotron orbits. In addition to creating the highly charged ions and trapping them, the electron beam plays a third important role; it creates excited states that can decay by photon emission.

When compared with a conventional plasma that has a broader electron distribution, i.e., a Maxwell-Boltzmann distribution, the electron beam is nearly monoenergetic. It is precisely tunable and rapidly switchable in energy (at rates of several keV ms⁻¹). A wide range of species to be studied can be loaded into the trap either as gases or metal ions. A gas at room temperature, or a volatile liquid or solid, can be introduced as neutral atoms through a series of collimating holes through a side port. Metals can be loaded vertically (along the magnetic field lines) as slightly charged ions (+1 to +4) using a metal vapor vacuum arc (MEVVA) ion source.

The NIST EBIT is equipped with an “event mode” data acquisition system that is used to measure transient processes and atomic lifetimes. This system is capable of switching EBIT operating parameters (beam energy, beam current, trapping voltage, etc.) at high speed and data can be time stamped to correlate it with the EBIT configuration.

3. EBIT SPECTROSCOPY WITH A MICROCALORIMETER AND X-RAY OPTIC

Operating at 65 mK, our microcalorimeters combine excellent energy resolution with relatively high count rate performance. The spectrometer has 95% quantum efficiency at 6 keV and a large collecting area in the 0.2–10 keV energy band. In the calorimeter, X-ray photons are absorbed in a foil of superconducting tin. The temperature rise is proportional to the X-ray energy and is measured with a neutron transmutation-doped (NTD) germanium thermistor that is attached to the underside of the absorber (Haller 1997). The small heat capacity of the composite calorimeter produces a relatively large temperature change (≈ 5 mK). The NTD thermistor is impedance-matched to a junction field effect transistor negative voltage feedback circuit (Silver et al. 1989). The detector used at NIST has an energy resolution of 5.9 eV at 1.5 keV and 7 eV at 6 keV. The microcalorimeter eliminates the need for multiple, inefficient crystal spectrometers to measure X-ray emission lines that span the 0.2–10 keV band. Consequently, the microcalorimeter shortens the total measurement time by several orders of magnitude. It is also insensitive to the polarization of X-ray emission.

The minimum distance from the plasma center to the vacuum wall is 110 mm in the NIST EBIT. The close proximity of other ongoing experiments mounted on adjacent viewing ports of the EBIT, however, made it difficult to

locate the microcalorimeter closer than 1 meter. This would have limited the solid angle to 2×10^{-7} sr, comparable to that of a crystal spectrometer, and would have made measurements extremely time consuming. A greater solid angle was obtained by viewing the EBIT plasma through an X-ray optic made from thin gold coated plastic foil (Silver, Schnopper, & Ingram 1998; Schnopper et al. 1999). The design can satisfy a wide variety of focal lengths and energy ranges. The focused image has a half-power diameter that is ≤ 1 mm (Schnopper et al. 1999). For the EBIT plasma experiments, where the distance of closest approach is limited, the optic was placed equidistant (762 mm) from the source and detector. Since the EBIT creates a plasma in the shape of a narrow line, the X-ray optic can increase the X-ray intensity by at least 30 times, helping to compensate for the X-ray absorption of the microcalorimeter windows at low energies (Silver et al. 1999).

4. LABORATORY ASTROPHYSICS MEASUREMENTS

The capability to selectively study ions of individual species is one of the major strengths of the EBIT/microcalorimeter combination. In the real case of a cosmic plasma, temperature, and density variations exist that lead to severe line blending. An accurate diagnosis will be very difficult without having access to a database that can be established with measurements of the kind we describe here. We have surveyed the *K* X-ray emission from various charge states of nitrogen, oxygen, and neon; *L* and *K* emission from argon; and *L* emission from krypton. For nitrogen, oxygen, neon and argon, in particular, the He-like resonance (*w*) $1s^2 1S-1s2p \ ^1P$, intercombination (*x*, *y*) $1s^2 1S-1s2p \ ^3P$, and forbidden (*z*) $1s^2 1S-1s2s \ ^3S$ transitions are observable. The relative strengths of these are useful as density and temperature diagnostics (Gabriel & Jordan 1969). For the measurements presented here, we have determined the density dependent ratio, $R = Z/(X + Y)$ and the temperature dependent ratio $G = (X + Y + Z)/W$ for nitrogen, oxygen, neon, and argon and compare these values to those predicted for a model of the non-Maxwellian EBIT plasma.

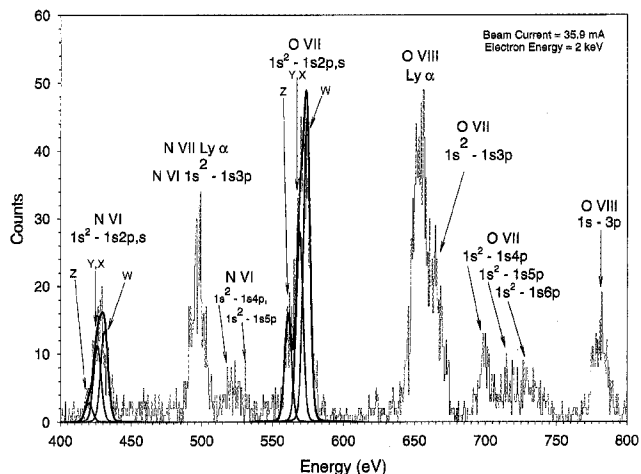


FIG. 1.—Microcalorimeter X-ray spectra from collisionally excited ions of nitrogen and oxygen from the NIST EBIT. The contributions to He-like nitrogen (N vi) and He-like oxygen (O vii) from the forbidden line (*Z*; dark blue line), intercombination line (*Y*, *X*; red line) and resonance line (*W*; dark green line) are shown. The collection time was ~ 30 minutes.

4.1. Nitrogen and Oxygen

Oxygen and nitrogen were injected into the EBIT and for an electron beam current of 35.9 mA the spectrum in Figure 1 was obtained in 30 minutes. The He-like and H-like (Lyman α) transitions, of nitrogen (N vi and N vii) and oxygen (O vii and O viii) are shown along with some higher transitions ($1s^2-1snp$; $n > 2$). The relative contributions of the resonance (*W*; dark green), intercombination (*X*, *Y*; red) and forbidden (*Z*; dark blue) lines to the He-like emission of nitrogen and oxygen are determined from a least-squares fit (solid black line) to the data (blue histogram) and for a nominal detector energy resolution of 6 eV. The values for *R* are listed in Table 1 for both nitrogen and oxygen.

4.2. Neon

Neon was injected into the EBIT and X-ray spectra were obtained for various electron beam energies, electron beam currents, and trap confinement (or “dumping”) times. A spectral survey of three different machine conditions is presented in Figure 2. Each spectrum was obtained in 20 minutes. A higher resolution spectrum follows in Figure 3 that shows the line structure more clearly.

The first and second panels in Figure 2 show mixtures of H-like and He-like neon species. The data in the second panel were obtained at a higher electron beam energy, but the same electron beam current as for the data in the first panel. Since different electron beam velocities compress or stretch out the electrons along a line for the same beam

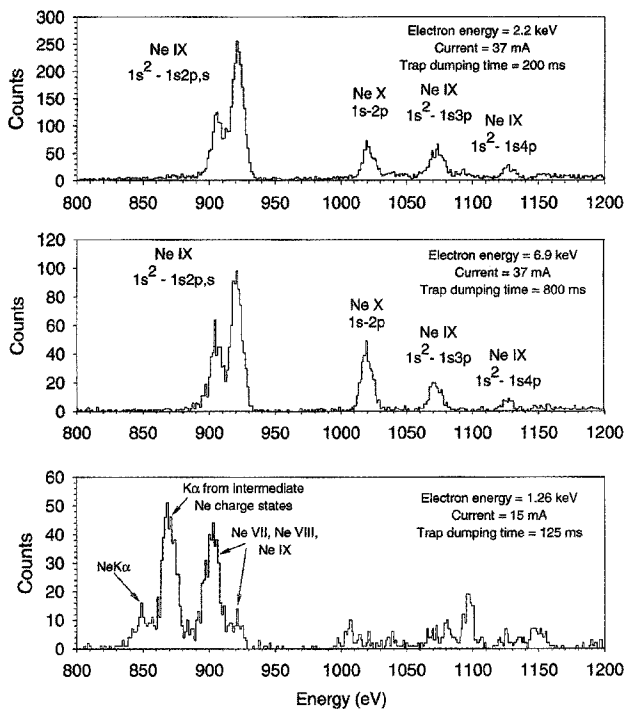


FIG. 2.—First two panels are spectra of H- and He-like spectra of neon (Ne x and Ne ix). The data in the second panel were obtained at the same electron beam current but higher beam energy. The intensity of the H-like $1s \rightarrow 2p$ line increases relative to the He-like lines. Within the He-like structure, the contribution from the intercombination line decreases at lower densities and higher beam energies (see text). The beam current and beam energy in the third panel are lower than in the second. Fewer H- and He-like ions and more ions of lower charge states (Li-like (Ne viii) and Be-like (Ne vii)) are produced. The spectrum in each panel was obtained in 20 minutes.

TABLE 1

MEASURED VALUES FOR R AND G AND INFERRED ELECTRON DENSITY			
Element	R_{measured} $Z/(X+Y)$	Electron Density (cm^{-3})	G_{measured} $(X+Y+Z)/W$
N VI.....	0.25 ± 0.11	$+3.5 \times 10^{11}$ 4.5×10^{11} -1.5×10^{11}	1.05 ± 0.17
O VII.....	0.55 ± 0.11	$+1.7 \times 10^{11}$ 6.0×10^{11} -1.1×10^{11}	0.97 ± 0.10
Ne IX.....	1.6 ± 0.2	$+4.0 \times 10^{11}$ 1.3×10^{12} -3.0×10^{11}	0.95 ± 0.06
Ar XVII.....	1.1 ± 0.3	2×10^{12a}	0.86 ± 0.12

NOTE.— Uncertainties shown represent one combined standard deviation

^a From the machine parameters plus an estimate of the beam radius.

current, the electron density is inversely proportional to the square root of the electron beam energy. Therefore, the electron density in the second panel is approximately one half of that in the first panel. By increasing the electron beam energy and keeping the ions in the trap longer (greater trap dumping time), the probability of reaching higher charge states improves. Thus, the intensity of the H-like (Ne x) $1s \rightarrow 2p$ transition increases relative to the He-like transition. Within the He-like structure, the contribution from the intercombination lines decreases at lower densities and higher electron excitation energies as expected. As the density decreases, the collisional transfer to the 3P_1 upper state from the metastable 3S_1 level decreases. Also, the cross section for excitation from the 3S_1 level to the 3P_1 decreases with increasing electron energy. This is evident by the deeper valley between the peaks in the second panel. In the third panel, the electron density is the same as in the second

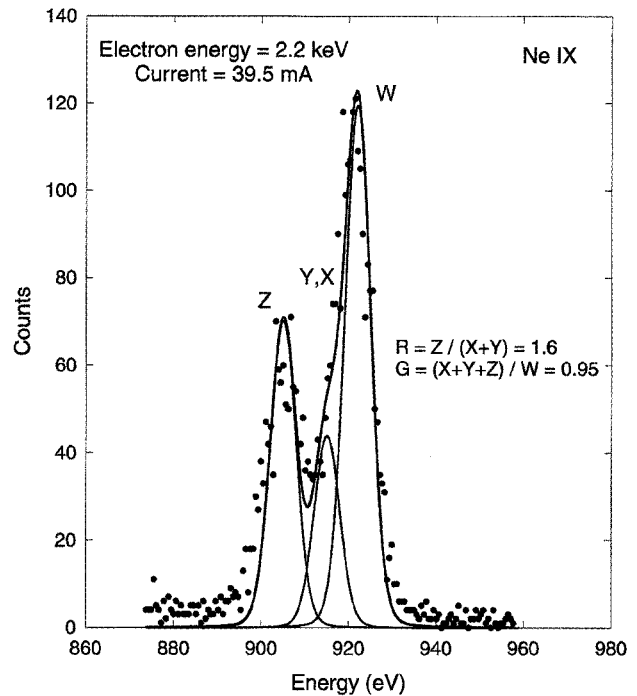


FIG. 3.—Fit to the resonance (W ; blue line), intercombination (X, Y ; red line) and forbidden (Z ; dark green line) lines yields a line ratio $R = Z / (X + Y) = 1.6$ and $G = (X + Y + Z) / W = 0.95$. The collection time was 29 minutes.

panel but the electron beam energy is only slightly above the He-like ionization potential (1.12 keV). In addition, the frequency of dumping the ions from the trap is 6.4 times higher than in the previous panel. Consequently, fewer H- and He-like ions are created. We have used the HULLAC

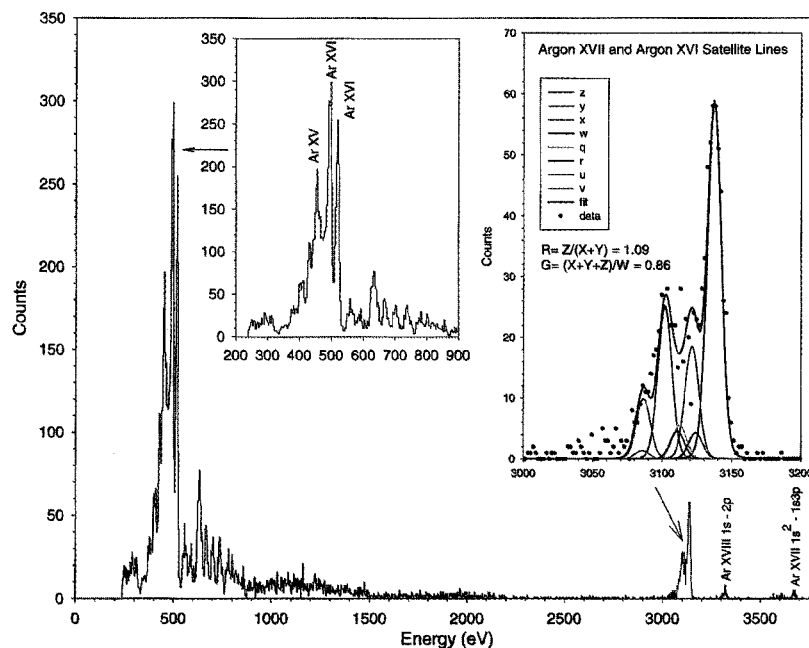


FIG. 4.—Simultaneously observed K and L spectra from Argon. The inset at the upper left shows the richness of the L emission features from argon (blue line). The inset at the right is an expanded view of the He-like complex of Ar XVII (red line) and the additional contributions of the Ar XVI satellite lines. The collection time was 40 minutes.

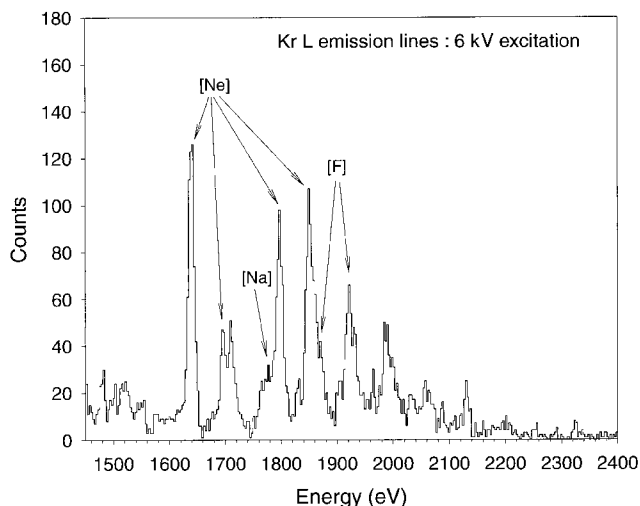


FIG. 5.—*L* emission lines of highly charged krypton ions measured at 6 keV electron beam energy. Energies of the marked lines ([Ne] means Ne-like Kr, etc.) are taken from Burkhalter et al. (1979).

(Klapisch et al. 1988; Goldstein et al. 1988) suite of codes to identify the lines between 891 and 933 eV as Ne VIII (Li-like) lines of the type $1s2s2p$, $1s2s^2$, $1s2p^2$ to $1s^22s$ or $1s^22p$. The next peak down in energy at ≈ 870 eV is due to similar transitions in Be-like Ne VII, and the smallest peak at ≈ 850 eV is neutral neon plus any low charge state of neon that drifts into the trap from the plasma edge.

In another series of measurements the gain of the pulse-height analysis system was increased to provide higher precision in the measurement of the helium-like complex in Ne IX. The data are shown in Figure 3, where the contributions from the resonance, intercombination and forbidden lines are clearly seen. The values for R and G are shown and listed Table 1.

4.3. Argon

A broadband spectrum of argon that includes the *L* emission lines between 400 and 700 eV and the *K* emission lines at approximately 3100 eV is shown in Figure 4. Simultaneous high-resolution measurements of the *L* and *K* emission from the same portion of the plasma are not possible with any X-ray spectrometer other than a microcalorimeter. The argon *L* emission spectrum is very rich, but has received comparatively little theoretical work. Consequently a definitive identification of these lines will have to await further analysis. The argon *K* spectrum, on the other hand, has been studied more carefully and the *K* spectrum is fitted with the known contributions from the Ar XVII He-like lines and the satellite lines from inner shell excitation in Li-like Ar XVI whose transitions have the form $1s^2nl-1s2pnl$ with $n \geq 2$. (Phillips et al. 1993). The values for R and G are shown and also listed in Table 1.

4.4. Krypton

Krypton gas was introduced into the EBIT and X-ray spectra were obtained for different gas pressures and electron excitation energies. A sample spectrum obtained for an electron beam energy of 6 keV is displayed in Figure 5. The lines include contributions from Li-like to Mg-like ions and will be discussed in detail in a separate paper (Kink et al. 2000).

5. DISCUSSION

The broad bandwidth capability of the microcalorimeter, coupled to an EBIT with an X-ray optic, made it possible to measure simultaneously spectra from highly ionized elements of astrophysical importance. The high resolving power of the detector allowed a determination of the relative contributions to the helium-like complex from the resonance, intercombination and forbidden lines. In principle, their relative intensities provide information about the density and temperature of the non-Maxwellian EBIT plasma. These values are compared to the predictions of a model for the EBIT plasma. Levels are excited by electron impacts, and de-excited either by radiative decay or by electron impact. The energy levels, radiative decay rates and electron impact excitation cross sections are calculated using the HULLAC suite of codes. They compute bound state energy levels and wave functions using a parametric potential method, and excitation cross sections in the distorted wave approximation. Since these techniques omit resonances in excitation cross sections we were free to choose EBIT beam energies that avoid such complications and to isolate particular processes of interest.

Theoretical values for $R = Z/(X + Y)$ for N VI, O VII, Ne IX and Ar XVII are shown in Figure 6. The observed ratios for R and the densities inferred for these ratios are shown by the open data points with error bars and are also given in Table 1. Nitrogen and oxygen were in the EBIT trap at the same time and the measured R -values for the He-like emission lines predict the same electron density for them to within the 1σ errors. The inferred electron density of $5.8 \times 10^{11} \text{ cm}^{-3}$, together with the electron beam energy of 2 keV and beam current of 35.9 mA, provides a measure of the electron beam radius of $69 \mu\text{m}$. This is consistent with the expectation that the radius of the electron beam ($35 \mu\text{m}$ at 6 keV) will increase as the beam energy is reduced. (Takacs et al. 1996; Levine et al. 1988) The neon measure-

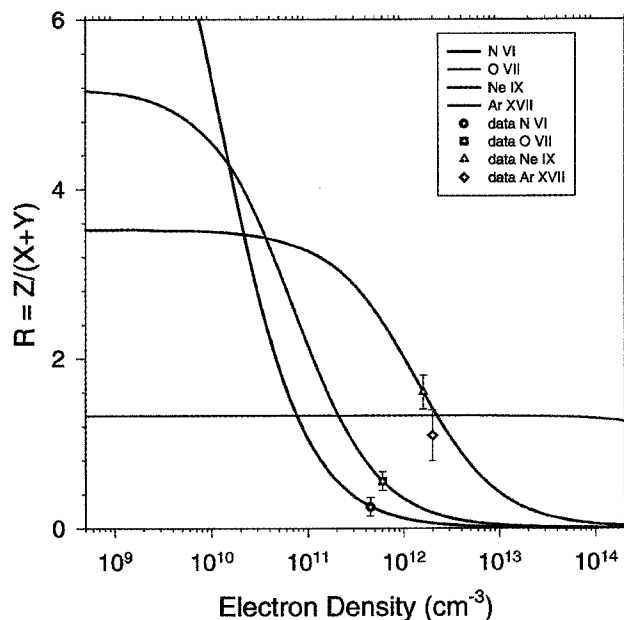


FIG. 6.—Calculated values for $R = Z/(X + Y)$ for N VI (black), O VII (blue line), Ne IX (red line) and Ar XVII (green line). The measured values and their 1σ uncertainties are shown by the open data points.

ments were made under similar machine conditions and the R -values for Ne IX are consistent with those for N VI and O VII. These results may also be affected by the gyration of the ions in and out of the electron beam. The inferred density would be lower than the actual value. The R -value for the Ar XVII spectrum, obtained with a beam energy of 6.7 keV is consistent at the 1σ level with density estimates of $\approx 10^9 \text{ cm}^{-3}$ to 10^{12} cm^{-3} . However, the theory shows that the R -value for Ar XVII is not a sensitive indicator of the density for such high electron energies. The measured value is therefore plotted in Figure 6 at the nominal electron density that can be estimated from the beam current and beam energy.

The observed ratios for G do not agree well with our theory; all experimental values indicate too much population in the 2^3S and 2^3P states compared with 2^1P . (The predicted G -value is 50 times larger than the experimental values for N VI, 30 times for O VII, 10 times for Ne IX, and it is 4 times larger for Ar XVII). This is most likely the result of charge exchange into excited states of the He-like ion from the H-like ion. The ionization balance for these observations is determined mainly by the electron impact ionization caused by the EBIT beam (whose energy is much greater than the ionization potential for the H-like ions of N, O, and Ne) and by charge exchange recombination when highly charged ions in the trap collide with the neutral atoms that provide the gas loading. Unlike radiative recombination, where the primary electron capture is in the ground state of the recombining ion, charge exchange mainly populates excited states. These subsequently decay by a radiative cascade. The relative excitation rates to the levels of the 2^3S and 2^3P terms are determined by the statistical weights of the levels, and, therefore, are very similar to the electron impact excitation rates for N VI, O VII, and Ne IX. In principle, the R ratio should be essentially unchanged while the G ratio will be altered. Since the G ratio involves the 2^3P intensity, it behaves quite differently under charge exchange than under impact excitation. The charge exchange process is not pursued further in this paper. Note, however, that the EBIT offers the potential to

measure charge exchange rates into excited states. This may be important for interpreting cometary X-ray spectra or perhaps spectra from other plasmas where neutrals can coexist with highly charged ions, such as in the shock wave of supernova remnants.

6. SUMMARY

A microcalorimeter coupled to an EBIT with an X-ray optic provides a significant new capability for laboratory astrophysics measurements. In this pilot survey, broadband spectra obtained with an energy resolution approaching that of a Bragg crystal spectrometer have been obtained for nitrogen, oxygen, neon, argon, and krypton in various stages of ionization. The relative intensities of the He-like emission lines, in particular, were measured and compared to a theoretical model of the non-Maxwellian EBIT plasma. The electron densities that are inferred from the ratio of forbidden to intercombination lines of nitrogen, oxygen, and neon spectra agree well with theory. Charge exchange in the EBIT appears to influence the intensity of the He-like resonance line relative to the forbidden and intercombination lines. Further measurements are necessary to model properly the effects of charge exchange.

E. Silver, H. Schnopper, and S. Bandler acknowledge support in part by NASA grant NAG 5-5104, I. Kink acknowledges the Swedish Foundation for Cooperation in Research and Higher Education (STINT), and M. Laming acknowledges support from NASA contract W19539 (Applied Information Systems Research Program) and by the NRL/ONR Solar Magnetism and the Earth's Environment 6.1 Research Option. The authors wish to thank Richard Deslattes for helpful discussions and for encouraging them to make these measurements, John Raymond for suggesting measurement objectives with important implications for astrophysical spectral observations, Kate Kirby for critically reviewing the manuscript, and Frank DeFreze and Douglas J. Alderson for their excellent technical support.

REFERENCES

- Beiersdorfer P., et al. 1996, *Hyperfine Interactions*, 99, 203
 Beiersdorfer P., Phillips, T. W., Wong, K. L., Marrs, R. E., & Vogel, D. A. 1992, *Phys. Rev. A*, 46, 3812
 Brown, G. V., Beiersdorfer, P., Liedahl, D. A., Widman, K., & Kahn, S. M. 1998, *ApJ*, 502, 1015
 Burkhalter, P. G., Shiloh, J., Fisher, A., & Cowan, R. D. 1979, *J. Appl. Phys.*, 50, 4532
 Gabriel, A., & Jordan, C. 1969, *MNRAS*, 145, 241
 Gillaspay, J. D. 1996, *Phys. Scr.*, T65, 168
 Goldstein, W. H., Oreg, J., Zigler, A., Bar-Shalom, A., & Klapisch, M. 1988, *Phys. Rev. A*, 38, 1797
 Haller, E. E. 1997, *Proc. Fourth International Symposium on Low Temperature Electronics and High Temperature Superconductors*, ed. C. L. Claeys, S. I. Raider, M. J. Deen, W. D. Brown, & R. K. Kirschman (Pennington: Electrochemical Society), 298
 Henderson, J. R., et al. 1990, *Phys. Rev. Lett.*, 65, 705
 Kink, I., et al. 2000, in preparation
 Klapisch, M., Bar-Shalom, A., Goldstein, W. H., Meroz, E., Chon, A., & Cohen, M. 1988, *HULLAC Code for Atomic Physics*, unpublished
 Levine, M. A., Marrs, R. E., Henderson, J. R., Knapp, D. A., & Schneider, M. B. 1988, *Phys. Scr.*, 22, 157
 Phillips, K. J. H., Harra, L. K., Keenan, F. P., Zarro, D. M., & Wilson, M. 1993, *ApJ*, 419, 426
 Schnopper, H. W., et al. 1999, *Proc. SPIE*, 3766, 350
 Silver, E., Schnopper, H., & Ingram, R. 1998, *US Patent Application*, Serial No. 09064476
 Silver, E., et al. 1999, in *Proc. Eighth International Workshop on Low Temperature Detectors*, ed. P. de Korte & T. Peacock (Amsterdam: Elsevier), 2000
 ———. 1989, *Proc. SPIE*, 1159, 423
 Takacs, E., et al. 1996, *Phys. Rev. A*, 54, 1342

Analysis of broadband x-ray spectra of highly charged krypton from a microcalorimeter detector of an electron-beam ion trap

I. Kink,¹ J. M. Laming,² E. Takács,³ J. V. Porto,¹ J. D. Gillaspay,¹ E. Silver,⁴ H. Schnopper,⁴ S. R. Bandler,⁴ M. Barbera,⁵ N. Brickhouse,⁴ S. Murray,⁴ N. Madden,⁶ D. Landis,⁶ J. Beeman,⁶ and E. E. Haller⁶

¹National Institute of Standards and Technology, Gaithersburg, Maryland 20899

²Naval Research Laboratory, Code 7674L, Washington, DC 20375

³Massachusetts Institute of Technology, Cambridge, Massachusetts 02139

⁴Harvard-Smithsonian Center for Astrophysics, Cambridge, Massachusetts 02138

⁵Osservatorio Astronomico G. S. Vaiana, Palermo, Italy

⁶Lawrence Berkeley National Laboratory, Berkeley, California 94720

(Received 13 June 2000; published 28 March 2001)

Spectra of highly charged Kr ions, produced in an electron-beam ion trap (EBIT), have been recorded in a broad x-ray energy band (0.3 keV to 4 keV) with a microcalorimeter detector. Most of the spectral lines have been identified as transitions of B- to Al-like Kr. The transition energies have been determined with 0.2% uncertainty. A semi-empirical EBIT plasma model has been created to calculate a synthetic spectrum of highly charged Kr and to determine a charge state distribution of Kr ions inside the EBIT.

DOI: 10.1103/PhysRevE.63.046409

PACS number(s): 52.70.-m, 32.30.Rj, 34.50.Fa, 34.80.Dp

I. INTRODUCTION

Laboratory plasmas produced from high Z gases have attracted interest in a number of applications. Laser-irradiated gaseous targets are routinely used for producing calibrated x-ray sources. The gas target remains below the critical density of the laser, improving the efficiency with which laser light is absorbed, and converts much more of this energy to radiation, losing less to kinetic energy and conduction as in the cases with solid targets [1,2]. They also have advantages compared to solid targets in some potential technological applications (e.g., x-ray lithography [3]). High-Z gases are also useful as “radiating divertors” in tokamaks. These create a buffer between the hot tokamak plasma and the tokamak chamber, thereby reducing particle fluxes and heat losses to the chamber walls (c.f. Ref. [4]). The investigation and application of plasma diagnostic potential of many of these applicable elements have largely been focused on K-shell emission (e.g., see Refs. [5,1]). However in principle the L shells of these elements offer significant additional diagnostic potential [6]. In this paper we investigate line energies and relative intensities in ions of Kr between B- and Al-like.

Electron-beam ion traps (EBIT's) have proven to be versatile tools for investigating properties of very highly charged ions (see e.g., Ref. [7]). These properties are important for testing different theoretical atomic models as well as in a number of applications where high-temperature plasmas are involved. It is typical for these ions that a large fraction of the photon emission occurs in the x-ray spectral region because of the fact that electron excitation energy increases with nuclear charge Z [8]. Therefore spectroscopic investigations in the x-ray region are important for determining the properties of highly charged ions. The majority of the experimental spectroscopic data in the x-ray region have so far been obtained with various types of crystal spectrometers. Although these instruments can provide the best resolving

power necessary for precision studies, there are several limitations in their application for investigations of highly ionized plasmas. Their low transmission efficiency, which typically decreases with increasing spectral resolution, limits the resolving power typically to around thousands to tens of thousands. The narrow x-ray energy range that can be covered with one particular crystal sets limits to the studies where different parts of the spectra have to be compared, a situation that often occurs in the analysis of complex spectra of laboratory and astrophysical heavy ion plasmas, where lines from different charge states may overlap. Semiconductor detectors [Si(Li), Ge, etc.] that can detect x rays in a broad energy band, on the other hand, have low-energy resolution (several hundred eV), which is usually not sufficient for detailed spectroscopic investigations of highly charged ions.

An x-ray microcalorimeter [9,10] is a recently developed type of x-ray detector that has several unique properties that significantly improve spectroscopic measurements involving x-ray photon detection. These instruments can cover a broad energy range (0.1 to 10 keV) with relatively high-energy resolution (about 6 eV) and close to 100% quantum efficiency. These properties make data acquisition more efficient and can provide information that is difficult or sometimes impossible to obtain by conventional methods. For example, since the spectra contain accurate line intensity information recorded over a broad spectral range, the comparison with a synthetic spectrum provided by plasma modeling calculations can yield information about various atomic and plasma parameters, e.g., excitation cross sections, electron and ion densities, etc. In this paper we demonstrate the microcalorimeter-EBIT combination in an investigation of highly ionized Kr.

Until now, the experimental spectroscopic data in the x-ray region for highly charged Kr ($q \geq 23+$) ions have remained rather limited. In addition to pure atomic physics interest, these transitions have applications in radiative cooling experiments with tokamak plasmas by puffer gases

[11,12]. The $\Delta n=0$ transitions within $n=2$ and $n=3$ configurations that occur in the extreme ultraviolet (EUV) regions have been studied by many groups with different techniques (e.g., Ref. [13–15]). However, the x-ray transitions from the $n=3$ levels to the ground state have been observed only by Burkhalter *et al.* [16] and Gordon *et al.* [17] who studied these transitions in the F-, Ne- and Na-like Kr ions produced in a z-pinch plasma. We determine line energies in the ions Kr_{xxiv}–xxxii, and identify some line ratios that have applications as electron density diagnostics for tokamak (10^{12} – 10^{14} cm⁻³) or laser-plasma (10^{19} – 10^{21} cm⁻³) sources.

In the following paragraphs details of the instrumentation, the plasma ionization balance modeling and spectral analysis will be summarized. The results of the line identifications of the observed x-ray lines of B- to Al-like Kr as well as the charge state distribution of the krypton plasma will be presented, and finally some discussion of the electron-density sensitivity some of these lines are expected to exhibit is given.

II. EXPERIMENTAL SETUP

The experimental setup is thoroughly described in Refs. [18–20]. Here only a general outline is given. The Kr ions are radially confined inside the EBIT trap region by the combination of an electric field due to an intense beam of electrons and a homogeneous strong magnetic field parallel to the electron beam. Axially the ions are trapped by an electric field created by a set of cylindrical drift tube electrodes. The electron beam is compressed by a 3 T magnetic field that is generated with a superconducting coil to achieve maximum current density. In our measurements the beam current was typically 115 mA with an estimated radius of 35 μ m (current density ≈ 3 kA/cm²). The beam energy (typically in the few keV range) was one of the adjustable experimental parameters. The krypton gas was let into the trap using a gas injection system attached to the EBIT [21]. By varying the neutral gas pressure inside the EBIT the charge state distribution and dynamics can be manipulated [22] due to shifts in the balance between ionization and recombination processes.

The trap was dumped every 1.35 s to prevent a slow buildup of contaminating heavy ions, small amounts of which are present inside the EBIT despite the ultrahigh vacuum conditions (typically $\approx 10^{-7}$ Pa).

Collisions of Kr atoms and ions with beam electrons lead to gradual ionization and excitation of the Kr ions. The x rays emitted in the region of 0.3 keV to 10 keV were collected with a focusing x-ray optic [23,24] and detected by a neutron transmutation-doped germanium-based microcalorimeter [10,20], where the increase of the temperature of the detector, that is proportional to the energy of the absorbed photon, is recorded. The x-ray optic and detector were separated from the EBIT with a thin (20 nm) mylar window to prevent contamination of the vacuum inside the EBIT. The transmission characteristics of the x-ray optic and a description of the detector can be found in Ref. [20]. Over the spectral region where the analyzed Kr lines appear, the combination of the total transmission of the optical components and

TABLE I. Experimental conditions for Kr spectra.

Set	Beam energy (keV)	Gas injection pressure ^a ($\times 10^{-4}$ Pa)
I	5.77	1.33
II	12.44	1.33
III	6.06	11.7
IV	6.06	0.5

^aMeasured in the gas injection chamber outside the EBIT before expansion into the low-pressure region at the trap center [21].

the efficiency of the microcalorimeter is a smooth and flat function of the photon energy, and therefore no corrections to the line intensities have been made. Four recordings with Kr gas were taken (Table I), varying the gas pressure and electron-beam energy. The data acquisition time for each spectrum was about 20 min. Spectra of highly charged N, Ar, and O were also recorded under identical experimental conditions for detector energy calibration purposes.

III. DATA ANALYSIS

Experimental spectra were calibrated using He-like N [25,26] and Ar [27], H-like N and O [28], and Ne- and F-like Kr [16] lines. Altogether, 15 reference lines were used that spread over the large energy interval of 300 eV to 4000 eV. Three groups of lines are well distinguished in the spectra: N and O lines at the low-energy side, Kr lines in the center, and Ar lines at the high-energy side. Polynomial functions were used for energy calibration and the best fit was achieved with a third degree polynomial. The weighted average scattering of reference lines was 1.4 eV, where inverse squares of the uncertainties of the reference lines (mainly due to statistical uncertainty in the line positions) were used as the weights.

The spectral lines were first fitted with a sum of Gaussian profiles to get accurate line positions using the computer code GFIT [29]. The typical full width at half maximum was 2.5 data channels, corresponding to approximately 6 eV. The statistical uncertainty (one standard deviation) of the line position was typically 0.5 eV to 1.0 eV which, taking into account the accuracy of the calibration, gives an uncertainty of 1.7 eV for identified single lines. Since most of the lines are blended with close-lying lines we quote 3.5 eV as an estimate of the combined standard uncertainty of transition energies. This value includes the statistical uncertainty (uniform distribution) in the line position of 3.2 eV and the calibration uncertainty of 1.4 eV. The final energies that are presented in Table II are the averages from the four different measurements. The quoted uncertainty agrees well with the statistical deviation of transition energies from four different measurements (average ≈ 2.5 eV) indicating that there are no significant systematic deviations between different measurements. In Fig. 1, the part of the spectrum where the Kr lines appear is shown. This spectral structure contains lines of Al- to Be-like Kr ions. Most of the strong lines come from the $\Delta n=1$ transitions between $n=2$ and $n=3$ configurations (L transitions). The electronic structure of ions with many elec-

TABLE II. Measured and calculated energies of $E1$, $E2$, and $M1$ transitions in B-like to Al-like Kr Ions.

I_{exp}^a	$E_{exp}(\text{eV})^b$	I_{th}^c	$E_{th}(\text{eV})^d$	Lower level		Upper level		Leading eigenfunction contribution ^e
B-like ($2s^22p^2\ ^2P^{\circ}_{1/2}$)								
7	2230.3	1.9	2231.9	2p	$^2P^{\circ}_{1/2}$	2s2p3p	(1,3/2) _{3/2}	89%
		1.1	2229.5				(1,3/2) _{1/2}	90%
1	2223.9	0.7	2217.9				(0,3/2) _{3/2}	93%
22	2183.7	7.1	2187.8			3d	$^2D_{3/2}$	100%
1	2126.1	0.5	2127.7	2s2p ²	$^4P_{3/2}$	2s2p3d	(0,5/2) ^o _{5/2}	45%
		1.1	2126.6	2p	$^2P^{\circ}_{3/2}$	3d	$^2D_{3/2}$	100%
30	2089.1	2.4	2090.1	2s2p ²	$^2D_{3/2}$	2s2p3d	(1,5/2) ^o _{5/2}	72%
		1.4	2079.2		$^2P_{1/2}$	2s2p3d	(1,5/2) ^o _{3/2}	49%
18	2010.7	1.5	2010.1		$^2D_{3/2}$	2s2p3s	(1,1/2) ^o _{1/2}	81%
31	1995.7	0.8	2001.0		$^2P_{1/2}$			
C-like ($2s^22p^2\ ^3P_0$)								
53	2113.6	12.5	2118.6	2p ²	3P_0	2p3d	(1/2,3/2) ^o ₁	99%
10	2060.1	0.8	2058.5		1D_2		(1/2,5/2) ^o ₃	98%
18	2010.7	0.6	2010.4			2p3p	(1/2,1/2) ₀	99%
22	1875.6	0.8	1879.9	2s2p ³	$^3D^{\circ}_1$			
N-like ($2s^22p^3\ ^4S^{\circ}_{3/2}$)								
10	2060.1	2.7	2055.1	2p ³	$^4S^{\circ}_{3/2}$	2p ² (3P)3d	(2,3/2) _{1/2}	48%
44	2047.8	4.2	2053.0			2p ² (1D)3d	(2,3/2) _{3/2}	43%
		2.9	2051.3			2p ² (3P)3d	(2,3/2) _{5/2}	26%
1	2035.8	1.1	2033.8				(1,3/2) _{5/2}	66%
		0.7	2031.8				(1,3/2) _{3/2}	94%
18	2010.7	1.3	2012.0		$^2D^{\circ}_{3/2}$	2p ² (1D)3d	(2,5/2) _{5/2}	34%
31	1995.7	1.3	1995.2			2p ² (3P)3d	(1,5/2) _{5/2}	81%
		4.6	1994.9		$^4S^{\circ}_{3/2}$		(0,5/2) _{5/2}	75%
		0.6	1992.0		$^2D^{\circ}_{5/2}$	2p ² (1D)3d	(2,3/2) _{3/2}	43%
1	1986.4	1.6	1990.1			2p ² (3P)3d	(2,3/2) _{5/2}	26%
		0.8	1985.6		$^4S^{\circ}_{3/2}$		(0,3/2) _{3/2}	79%
1	1941.1	0.5	1942.7			2p ² (1D)3s	(2,1/2) _{5/2}	51%
17	1788.2	0.8	1790.3	2s2p ⁴	$^4P_{3/2}$	2p ² (3P)3p	(2,1/2) ^o _{3/2}	30%
O-like ($2s^22p^4\ ^3P_2$)								
31	1995.7	0.7	1992.0	2p ⁴	3P_2	2p ³ ($^2D^{\circ}$)3d	$^3S^{\circ}_1$	63%
		2.8	1991.0		3P_0	2p ³ ($^2P^{\circ}$)3d	$^3D^{\circ}_1$	47%
1	1986.4	0.9	1987.2		3P_2	2p ³ ($^2D^{\circ}$)3d	$^3P^{\circ}_1$	50%
		2.9	1987.2				$^3D^{\circ}_2$	59%
		0.7	1986.6		1D_2	2p ³ ($^2P^{\circ}$)3d	$^3D^{\circ}_3$	44%
		0.7	1985.6				$^1F^{\circ}_3$	49%
46	1981.5	7.5	1984.0		3P_2	2p ³ ($^2D^{\circ}$)3d	$^3D^{\circ}_3$	50%
		0.6	1979.3				$^3P^{\circ}_2$	30%
1	1973.5	1.4	1968.6				$^3G^{\circ}_3$	42%
12	1961.9	1.0	1966.1				$^3F^{\circ}_3$	44%
		1.1	1964.5				$^3F^{\circ}_2$	41%
1	1941.1	0.7	1939.9		1D_2	2p ³ ($^2P^{\circ}$)3d	$^3F^{\circ}_3$	51%
32	1932.4	0.7	1935.4		3P_1	2p ³ ($^2D^{\circ}$)3d	$^3P^{\circ}_1$	50%
		0.9	1935.4				$^3D^{\circ}_2$	59%
		6.7	1934.2		3P_2	2p ³ ($^4S^{\circ}$)3d	$^3D^{\circ}_3$	26%

TABLE II. (Continued).

I_{exp}^a	$E_{exp}(\text{eV})^b$	I_{th}^c	$E_{th}(\text{eV})^d$	Lower level	Upper level	Leading eigenfunction contribution ^e		
38	1925.2	1.2	1930.6	1D_2	$2p^3(^2D^o)3d$	$^1F^o_3$	63%	
		1.1	1927.3	3P_1		$^3P^o_2$	30%	
		0.8	1926.7	1D_2		$^3S^o_1$	63%	
		2.2	1924.9	3P_2	$2p^3(^4S^o)3d$	$^5D^o_2$	24%	
		0.9	1924.3		$2p^3(^2D^o)3p$	3F_4	100%	
42	1917.5	0.5	1918.3		$2p^3(^4S^o)3d$	$^5D^o_1$	51%	
		0.8	1917.1			$^5D^o_3$	39%	
		2.2	1917.1	3P_0		$^3D^o_1$	45%	
		0.6	1877.9	3P_1	$2p^3(^2P^o)3s$	$^3P^o_2$	59%	
24	1861.5	2.7	1864.4	3P_2	$2p^3(^2D^o)3s$	$^3D^o_3$	100%	
		0.6	1864.4	1D_2	$2p^3(^2P^o)3s$	$^3P^o_2$	59%	
44	1854.1	1.3	1851.0	3P_2	$2p^3(^4S^o)3s$	$^5S^o_2$	40%	
		1.3	1809.7			$^3S^o_1$	40%	
50	1803.9	2.1	1803.9			$^5S^o_2$	48%	
		0.6	1802.8	3P_1	$2p^3(^2D^o)3s$	$^3D^o_1$	51%	
		1.1	1802.6	1D_2		$^1D^o_2$	66%	
36	1797.0	0.6	1799.2			$^3D^o_3$	100%	
F-like ($2s^22p^5\ ^2P^o_{3/2}$)								
20	2025.3	0.7	2020.2	$2s^22p^5$	$^2P^o_{3/2}$	$2s2p^53p$	$(1,3/2)_{5/2}$	82%
18 ^f	2010.7	0.6	2009.8				$(2,3/2)_{1/2}$	50%
		0.6	2007.5				$(1,1/2)_{3/2}$	74%
31	1995.7	0.8	1999.7				$(2,3/2)_{5/2}$	99%
		0.6	1996.8				$(2,3/2)_{3/2}$	82%
46 ^f	1981.5	0.6	1983.4				$(2,1/2)_{5/2}$	99%
42 ^f	1917.5	10.0	1919.5			$2s^22p^4(^1D)3d$	$(2,3/2)_{5/2}$	64%
		5.6	1918.0				$(2,3/2)_{3/2}$	36%
		0.6	1914.8				$(2,5/2)_{5/2}$	80%
		2.8	1914.8				$(2,3/2)_{1/2}$	60%
1 ^f	1900.7	2.1	1903.6			$2s^22p^4(^3P)3d$	$(1,5/2)_{5/2}$	77%
		2.3	1901.9				$(1,3/2)_{5/2}$	63%
22 ^f	1875.6	0.6	1876.2		$^2P^o_{1/2}$	$2s^22p^4(^1D)3d$	$(2,5/2)_{1/2}$	51%
		1.4	1873.4				$(2,3/2)_{3/2}$	30%
		4.2	1873.1		$^2P^o_{3/2}$	$2s^22p^4(^3P)3d$	$(0,5/2)_{5/2}$	47%
33 ^f	1869.7	2.1	1869.4				$(0,3/2)_{3/2}$	41%
24 ^f	1861.5	0.9	1863.0		$^2P^o_{1/2}$	$2s^22p^4(^1D)3d$	$(2,3/2)_{3/2}$	36%
		6.8	1861.9		$^2P^o_{3/2}$	$2s^22p^4(^3P)3d$	$(2,5/2)_{5/2}$	68%
		3.4	1858.2				$(2,5/2)_{3/2}$	57%
44 ^f	1854.1	1.4	1853.8				$(2,5/2)_{1/2}$	56%
56 ^f	1847.0	0.7	1842.0	$2s2p^6$	$^2S_{1/2}$	$2s2p^53d$	$(1,3/2)^o_{3/2}$	51%
16 ^f	1783.1	1.7	1785.5	$2s^22p^5$	$^2P^o_{3/2}$	$2s^22p^4(^1D)3s$	$(2,1/2)_{5/2}$	78%
12 ^f	1771.5	1.0	1771.4			$2s^22p^4(^3P)3s$	$(1,1/2)_{3/2}$	99%
		0.9	1769.9			$2s^22p^4(^3P)3p$	$(2,1/2)^o_{5/2}$	76%
1 ^f	1735.6	0.6	1742.3			$2s^22p^4(^3P)3s$	$(0,1/2)_{1/2}$	51%
		0.5	1732.1		$^2P^o_{1/2}$	$2s^22p^4(^1D)3s$	$(2,1/2)_{3/2}$	74%
21 ^f	1722.6	2.1	1724.1		$^2P^o_{3/2}$	$2s^22p^4(^3P)3s$	$(2,1/2)_{3/2}$	75%
		3.0	1719.1				$(2,1/2)_{5/2}$	79%
17 ^f	1716.1	1.3	1718.9	$2s2p^6$	$^2S_{1/2}$	$2s2p^53s$	$(1,1/2)^o_{3/2}$	75%
		1.2	1699.3				$(2,1/2)^o_{3/2}$	93%
7	1615.8	2.7	1611.2			$2s^22p^4(^1D)3p$	$(2,1/2)^o_{3/2}$	32%

TABLE II. (Continued).

I_{exp}^a	$E_{exp}(\text{eV})^b$	I_{th}^c	$E_{th}(\text{eV})^d$	Lower level		Upper level		Leading eigenfunction contribution ^e
Ne-like ($2s^22p^6\ ^1S_0$)								
1	2035.8	1.4	2034.8	$2p^6$	1S_0	$2s2p^63d$	1D_2	97%
12 ^f	1961.9	3.1	1960.5			$2s2p^63p$	$^1P^o_1$	76%
1 ^f	1941.1	1.1	1945.4				$^3P^o_1$	76%
44 ^f	1854.1	28.0	1852.7			$2p^53d$	$^1P^o_1$	53%
50 ^f	1803.9	23.0	1803.4				$^3D^o_1$	46%
12	1771.5	0.7	1772.7			$2p^53p$	3D_2	47%
21	1722.6	0.7	1720.1				3P_2	67%
31 ^f	1705.5	6.7	1705.9			$2p^53s$	$^3P^o_1$	63%
		1.3	1703.7			$2p^53p$	3D_2	53%
44 ^f	1651.5	11.8	1652.4			$2p^53s$	$^1P^o_1$	63%
		5.9	1649.1				$^3P^o_2$	100%
Na-like ($2s^22p^63s\ ^2S_{1/2}$)								
56	1847.0	14.4	1841.1	$2p^63s$	$^2S_{1/2}$	$2p^53s3d$	$(1,3/2)^o_{3/2}$	43%
13 ^f	1834.0	9.6	1836.8				$(1,3/2)^o_{1/2}$	95%
17	1788.2	15.0	1790.3				$(2,5/2)^o_{3/2}$	47%
		7.3	1789.1				$(2,5/2)^o_{1/2}$	88%
Mg-like ($2s^22p^63s^2\ ^1S_0$)								
1	1822.5	25.0	1827.6	$2p^63s^2$	1S_0	$2p^53s^23d$	$(1/2,3/2)^o_1$	97%
16	1783.1	21.4	1778.5				$(3/2,5/2)^o_1$	80%
Al-like ($2s^22p^63s^23p\ ^2P^o_{1/2}$)								
50	1803.9	6.8	1802.8	$3s^23p$	$^2P^o_{1/2}$	$2p^53s^23p3d$	$(1,3/2)_{3/2}$	90%

^aTaken from data set IV (see Table I) in arbitrary units proportional to the number of photons.

^bAverage of data sets I–IV (see Table I). Estimated combined standard uncertainty is 3.5 eV.

^cCalculated with model (Sec. IV) for data set II. Intensities are in arbitrary units proportional to the number of photons/s.

^dCalculated with relativistic parametric potential method (HULLAC code).

^eCalculated with superposition-of-configurations method (COWAN code).

^fIdentified first by Burkhalter [16] or Gordon [17].

trons in an open $2p$ shell is relatively complicated and results in numerous closely spaced lines that we were not able to resolve experimentally. Because of the EBIT excitation mechanism, lines that have a strong electric dipole ($E1$) transition probability to the ground state dominate the spectrum. However, in the low-density environment (negligible collisional deexcitation) inside the EBIT $E2$ (electric quadrupole) and $M1$ (magnetic dipole) transitions are also observable. The complexity of the spectra (for example, a spectrum of B-like Kr consists of more than one hundred $2p^6$ - $2p^53l$ lines that are calculated to be stronger than 1/200 of the strongest line) demands additional tools for correct line identifications. We used two different theoretical calculations as an additional aid. The transition energies were calculated using the superposition-of-configurations method developed by R. D. Cowan [30]. For energy-level structure calculations we included all $n=2$ and $n=3$ configurations except the configurations with an open $1s$ subshell, and

$n=4$ configurations excluding all innershell excited configurations. The electrostatic and configuration interaction parameters were scaled to 90% of their *ab initio* values whereas spin-orbit parameters were kept at 95% of their *ab initio* values. It has been shown previously [30] that these estimates predict level energies closer to the experimental ones. Line intensities were calculated using a plasma model (see next section) that is based on a relativistic parametric potential calculation using the HULLAC code [31,32]. The qualitative behavior of the spectral lines under different experimental conditions was used to support the identifications.

IV. KR IONIZATION BALANCE

A. Basic Procedures

The ionization fraction f_q of the Kr ions with charge q is given by

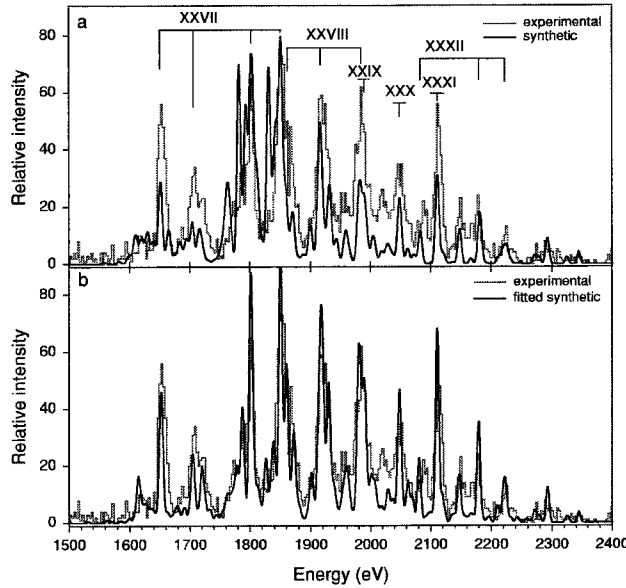


FIG. 1. Comparison of the experimental (set I, Table I) and fitted synthetic spectra of Kr calculated with the model described in Sec. IV. (a) equal charge state distribution. (b) nonequal charge state distribution including charge-exchange processes. Roman numerals mark lines belonging to the corresponding Kr spectrum (e.g., XXVII marks Ne-like Kr etc.)

$$\frac{df_q}{dt} = n_e(I_{q-1}f_{q-1} - I_q f_q) + n_e[(R_{q+1} + D_{q+1})f_{q+1} - (R_q + D_q)f_q] + n_{Kr}(X_{q+1}f_{q+1} - X_q f_q), \quad (1)$$

where I_q , R_q , D_q , and X_q are the rates for electron-impact ionization, radiative recombination, dielectronic recombination, and charge-exchange recombination, respectively, for the charge state q , n_e is the electron density and n_{Kr} is the density of neutral Kr atoms in the trap. The calculation of the various rates is discussed in more detail below. Equation 1 neglects charge exchange between ions and three-body recombination, the inverse of electron collisional ionization. The latter would scale as n_e^2 and, although insignificant for the EBIT beam, becomes important as the electron density increases.

The EBIT trap was emptied every 1.35 s. As we will describe below, the relevant ionization and recombination rates are $\approx 100 \text{ s}^{-1}$, allowing us to considerably simplify our model by assuming a steady-state ionization balance, i.e., putting the time derivatives in Eq. (1) equal to zero. Another important simplification comes from the observation that the ion-ion collision time in the trap, given by Ref. [33], is

$$\tau_i = \frac{3}{4\sqrt{\pi}} \frac{\sqrt{m_i}(kT_i)^{3/2}(4\pi\epsilon_0)^2}{n_i q^4 e^4 \log\Lambda} \sim 10^{-3} \text{ s} \quad (2)$$

for an ion density $n_i \approx 6 \times 10^{14} \text{ m}^{-3}$ (this is about 2% of the ion density required to fully compensate the space charge of the electron beam), where m_i , T_i , and n_i are the ion mass, temperature, and density, e is the elementary charge, and

$\Lambda = (4\pi/3)n_e\lambda_D^3$ with $\lambda_D = \sqrt{kT_e\epsilon_0/n_e q^2 e^2}$ being the Debye length for electron temperature T_e and density n_e . For typical conditions inside the EBIT, $\log\Lambda \approx 18$. This collision time is about an order of magnitude less than the ionization and recombination times, allowing us to put all ion temperatures at the same value. Note that when a light gas (e.g., oxygen) with significantly lower charge q is introduced to provide evaporative cooling [22], this inequality is not met. The coolant gas may then have a different temperature than the trapped ions, as indeed it must have in order to cool the trap.

A relevant objection to the foregoing is that the Debye length is approximately an order of magnitude larger than the EBIT electron-beam radius, and the plasma parameter should more realistically be given by $\Lambda = (4\pi/3)n_e\lambda_D r_b^2$. The value of $\log\Lambda$ is then ≈ 14 , and our conclusions still hold.

B. Ionization, Recombination, and Loss Rates

Cross sections for electron-impact ionization are taken from Ref. [34] for levels up to the $n=3$. The cross sections are essentially identical to those coming from the Lotz formula (see e.g., Ref. [35]). For the monoenergetic EBIT beam the rates are formed by simply multiplying the cross section by the electron velocity. Radiative recombination cross sections are taken in the Kramers' approximation (see e.g., Ref. [36]). We sum the radiative recombination cross section to each of the $n=2$ and $n=3$ configurations to arrive at the total cross section. Other workers [35] have used a formula due to [37] that sums the radiative recombination to $n=\infty$. This sum, however, includes only recombination to s states.

In our model we neglect the dielectronic recombination because for the beam energies at which our spectra were taken (around 6 keV and 12 keV), it is unlikely that any dielectronic resonances will exist in ions with ionization potentials in the range 1 keV to 4 keV.

Charge-exchange recombination with neutral Kr atoms inside the trap are treated in a simple level crossing model. The potential of the ion-neutral system is written (in atomic units, where $e=m_e=\hbar=1$) as $V = -I_q + (q-1)/r = -I_0$, where I_q and I_0 are the ionization potentials of the ion (after the charge-exchange process) and neutral (before charge exchange), respectively, and r is the ion-neutral distance. Hence at a pseudocrossing $r_{cx} = (q-1)/(I_q - I_0)$, and the cross section is given by $\sigma_{cx} = \pi r_{cx}^2$, subject to the constraint that $r_{cx} \leq (2q^{1/2} + 1)/I_0$ (see Ref. [38] for details). During the EBIT runs described in this paper, it was not possible to get an accurate measurement of the neutral Kr density near the trapped ions (assuming that the charge exchange occurs between highly charged trapped ions and neighboring Kr neutrals) and so the above formulas were used to model the relative charge-exchange rates for the various Kr ions, with the absolute normalization left as a free parameter to vary when optimizing the model prediction to the observations.

The rates for ion reactions with electrons (impact ionization, radiative recombination) need to be modified to account for the time that the ions spend outside the electron beam in radial excursions. We neglect the azimuthal drift imposed on the ion orbits by the magnetic field. The potential in which the ions move is given by the solution to Laplace's equation

in cylindrical symmetry, subject to the boundary condition that at a radius equal to the drift tube radius (r_{dt}), the potential is 300 V (the voltage applied to form the electrostatic trap). Then the fraction of time that an ion spends inside the beam is given by

$$f = \int_0^{r_b} \frac{dr}{v} \left\{ \int_0^{r_b} \frac{dr}{v} + \int_{r_b}^{r_m} \frac{dr}{v} \right\}, \quad (3)$$

where r_b and r_m are the electron-beam radius and maximum ion radius, and $v = v(r)$ is the ion velocity given by $m_i v^2/2 = 3kT_i/2 - qeV$. Evaluating the integrals (using $r - r_b \ll r_b$ in the second) we arrive at the following expression for f :

$$f = \frac{\arcsin \sqrt{\eta}}{\arcsin \sqrt{\eta} + \sinh^{-1} \left(\frac{r_m/r_b - 1}{\sqrt{4 + 1\eta}} \right)}, \quad (4)$$

where $\eta = (qe|Q/l|)/6\pi\epsilon_0 kT_i$ and $r_m = r_b \exp[3kT_i \pi \epsilon_0 / \times (qe|Q/l|) - \frac{1}{2}]$ with Q/l being the charge per unit length of the electron beam. This fraction is implemented in our model neglecting the compensation of the trapped positive ions, consistent with an ion density of $6 \times 10^{14} \text{ m}^{-3}$ assumed above.

The remaining process to be considered is that of ion escape from the trap. We follow the treatment of Ref. [35], assuming only radial escape to be important. They give an expression for the ion loss rate

$$\frac{dN_q}{dt} = v_{\text{escape}} \Delta N_q, \quad (5)$$

where N_q is the number of ions of charge q and ΔN_q is the fraction of them with energy $E > qeV_b$, and V_b is the trapping potential, i.e., the number of ions energetically allowed to escape from the trap. The escape rate v_{escape} is given by

$$v_{\text{escape}} = \frac{2}{r_b(r_{dt} - r_b)} \frac{kT_i \tau_i / m_i}{1 + (\tau_i qeB / m_i)^2} \approx 10^3 \text{ s}^{-1}, \quad (6)$$

which is derived from standard results for cross-field diffusion. For ions of charge q from 26 to 32, $\Delta N_q / N_q < 10^{-2}$ giving a maximum loss rate of order 10 s^{-1} . This is an order

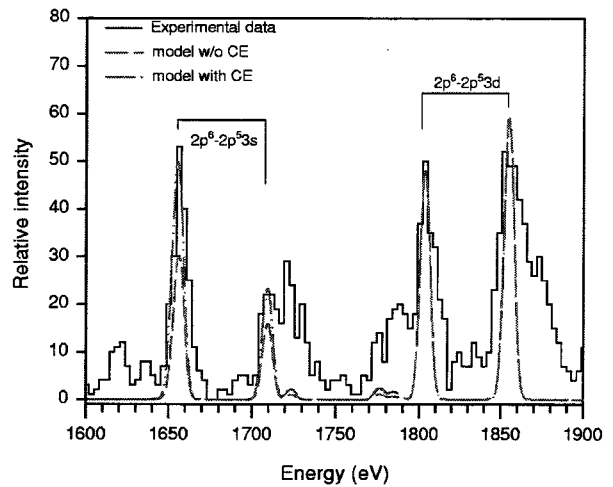


FIG. 2. Comparison of Ne-like Kr $2p^6-2p^5 3s$ and $2p^6-2p^5 3d$ lines (set IV, Table I). Charge exchange. Synthetic spectra are normalized using $2p^6-2p^5 3d$ lines.

of magnitude lower than the collisional ionization and recombination rates and is neglected.

C. Modeling and Fitting of Charge State Distributions

A charge state distribution was fitted to the experimental data by the following procedure. Model spectra for each Kr ionization state (Al- to Be-like) were computed for the relevant EBIT beam parameters using the HULLAC suite of codes (Table III). These calculate the energy levels and radiative decay rates using a parametric potential, and the electron impact excitation cross sections in the distorted-wave approximation. The total synthetic spectrum is a sum of spectra of the ten (Al- to Be-like) different Kr ions where individual spectra are scaled with the relative charge state fraction. This total spectrum was fitted to the data using the charge state fractions as the fitting parameters on the assumption that electron-impact excitation was the sole excitation process, and a charge state distribution was obtained. Generally the agreement between experimental and fitted synthetic spectra was not satisfactory [Fig. 1(a)]. In particular, we noted a large discrepancy for the Ne-like and F-like

TABLE III. Configurations included for Kr ions in HULLAC calculations.

Ion	Configurations
Li-	$2s 2p 3s 3p 3d$
Be-	$2s^2 2s2p 2p^2 2s3s 2s3p 2s3d$
B-	$2s^2 2p 2s2p^2 2p^3 2s^2 3s 2s^2 3p 2s^2 3d 2s2p3s 2s2p3p 2s2p3d$
C-	$2s^2 2p^2 2s2p^3 2p^4 2s^2 2p3s 2s^2 2p3p 2s^2 2p3d$
N-	$2s^2 2p^3 2s2p^4 2p^5 2s^2 2p^3 3s 2s^2 2p^3 3p 2s^2 2p^3 3d$
O-	$2s^2 2p^4 2s2p^5 2p^6 2s^2 2p^3 3s 2s^2 2p^3 3p 2s^2 2p^3 3d$
F-	$2s^2 2p^5 2s2p^6 2s^2 2p^4 3s 2s^2 2p^4 3p 2s^2 2p^4 3d 2s2p^5 3s 2s2p^5 3p$
Ne-	$2s^2 2p^6 2s^2 2p^5 3s 2s^2 2p^5 3p 2s^2 2p^5 3d 2s2p^6 3s 2s2p^6 3p 2s2p^6 3d$
Na-	$2s^2 2p^6 3s 2s^2 2p^6 3p 2s^2 2p^6 3d 2s^2 2p^5 3s^2 2s^2 2p^5 3s 3p 2s^2 2p^6 3s^2 2s2p^6 3s 3p 2s2p^6 3s 3d$
Mg-	$2s^2 2p^6 3s^2 2s^2 2p^6 3s 3p 2s^2 2p^6 3s 3d 2s^2 2p^6 3p^2 2s^2 2p^6 3p 3d 2s^2 2p^6 3d^2 2s^2 2p^5 3s^2 3p 2s^2 2p^5 3s^2 3d$

TABLE IV. $3s/3d$ intensity ratios for some transitions in the Ne- and F-like Kr.

Ion	Level ^a	Model w/o CE ^b	Model with CE ^b	Exp. ^c
Ne-like	$3s\ ^3P^o_2$	0.11	0.38	0.5
	$3s\ ^1P^o_1$	0.44	0.60	0.9
	$3s\ ^3P^o_1$	0.24	0.34	0.4
F-like	$2p^4(^1D)3s\ (2,1/2)_{5/2}$	0.11	0.25	0.3
	$2p^4(^3P)3s\ (2,1/2)_{5/2}$	0.12	0.43	0.4
	$2p^4(^1D)3s\ (2,1/2)_{3/2}$	0.18	0.26	0.3

^aIntensity ratios have been calculated for transitions from these levels to the ground level relative to $3d^1P_1 \rightarrow$ ground level and $2p^4(^1D)3d\ (2,3/2)_{5/2} \rightarrow$ ground level transitions in Ne- and F-like Kr, respectively.

^bCharge exchange (CE), see discussion in text.

^cBoth experimental and theoretical data have been taken for 6 keV, low pressure (set IV, Table I) conditions.

Other spectra showed qualitatively similar behavior.

charge states, where substantially more intensity was observed in the $3s \rightarrow 2p$ lines relative to the $3d \rightarrow 2p$ lines of these ions (Fig. 2). The observation that these intensity ratios deviated more from the theory for the 6 keV Kr spectrum at high pressure than for the low pressure led us to suspect that charge exchange might play a role in exciting these lines.

The fitted ionization balance was then matched with a model with suitable choices for the normalization of the charge exchange recombination rates and the ion temperature in the trap. The emission spectrum from each ion was recalculated now including the effects of charge exchange, approximated by assuming that each level considered in the target ion was populated according to its statistical weight, followed by radiative cascading down. In this way the $3s$ population in Ne- and F-like ions is boosted, since significant extra population cascades through these levels. In Fig. 2 the strongest $3s$ and $3d$ lines are shown together with the calculated spectra; the numerical values are presented in Table IV.

The spectra from each ion iterated in this way were refitted to the data treating the charge exchange rates and the

temperature as additional fitting parameters. The final fitted charge state distribution is presented in Table V.

V. DISCUSSION

From Figs. 1 and 2 it can be seen that our modeling approach gives a satisfactory account of the relative line intensities, at least for the strong well detected lines, over a wide range of charge states. We draw particular attention to the relative intensities in the Ne-like charge state Kr XXVII. From Fig. 2 it can be seen that irrespective of the inclusion of charge exchange in our model, the intensity ratio between the $2p^6\ ^1S_0 - 2p^53d^3D_1$ and the $2p^6\ ^1S_0 - 2p^53d\ ^1P_1$ lines agrees with our calculations. This is quite different from the isoelectronic system Fe XVII, where discrepancies between theory and observations are well documented in the solar physics literature [39–44], and are becoming apparent in x-ray observations of stellar coronae as well ([45] and references therein). The ratios of $2p^6 - 2p^53s$ lines to those from the $2p^6 - 2p^53d$ configurations, which are also prob-

TABLE V. Fitted and modeled charge state distributions.

Ion	12 keV		6 keV (low pressure)		6 keV (high pressure)	
	Fit ^a	Model ^b	Fit	Model	Fit	Model
Li-	0.010	0.021	0.024	0.011	0.003	0.0009
Be-	0.097	0.070	0.10	0.051	0.060	0.008
B-	0.17	0.14	0.16	0.13	0.091	0.032
C-	0.19	0.20	0.17	0.21	0.096	0.085
N-	0.16	0.20	0.13	0.23	0.14	0.15
O-	0.14	0.16	0.14	0.18	0.11	0.20
F-	0.087	0.010	0.10	0.11	0.17	0.21
Ne-	0.066	0.060	0.085	0.055	0.17	0.17
Na-	0.026	0.025	0.040	0.018	0.081	0.093
Mg-	0.019	0.008	0.022	0.004	0.044	0.037

^aFitted ionization balances are determined by least-squares fits to experimental data, using theoretical line intensities for each ion, iterated as described in the text to include the charge-exchange contribution.

^bModel ionization balances are calculated by using the ionization and recombination rates described in the text, with the magnitude of the charge-exchange rates adjusted to give the best match to the “fitted” ionization balance.

lematic in solar and astrophysical spectra, are harder for us to check experimentally because of the problems of charge exchange in our experiment enhancing the $2p^6-2p^53s$ intensities.

These effects of charge exchange may however allow the measurement of state selective charge-exchange cross sections, relative to those for electron-impact excitation or ionization. As well as applications of neutral beam heating in tokamaks, we expect such data to be very useful in interpretation of cometary x-ray spectra [46–48]. Here, neutral material outgassing from the comet nucleus encounters highly charged ions in the solar wind. The ensuing charge-exchange collisions populate highly excited states of the solar wind ions, followed by x-ray emission as these states radiatively decay. An astrophysically relevant experiment would require trapped ions of C, N, O, or Ne, and the admission to the EBIT chamber of the appropriate neutral gas, i.e., H_2O , CO_2 , etc.

Among our line identifications are several lines with potential for electron-density diagnostics. The density sensitivity arises because the relative populations among the different levels of the ground configurations varies with density. If this results in higher population accumulating in a level of higher angular momentum (i.e., the $2s^22p^2P_{3/2}$ in Kr XXXII, the $2s^22p^2^3P_2$ in Kr XXXI, or the $2s^22p^3^2D_{5/2}$ in Kr XXX) than the ground level, then excitations to levels among the $n=3$ configurations with higher angular momentum than are possible from the ground state alone, result. Hence new lines from these high angular momentum level states become visible at higher densities.

In Fig. 3(a) we show two line intensity ratios in Kr XXXII that vary as a result of $n=3$, $j=5/2$ levels becoming excited, calculated for an electron temperature of 2×10^7 K. The electron densities over which this ratio varies is $10^{19} - 10^{21} \text{ cm}^{-3}$, which is the relevant density range for high Z underdense plasma radiators. This should be very useful, since the density diagnostic available in the Kr K -shell spectrum, the ratio of the $1s^2^1S_0-1s2p^3P_2$ to either of the $1s^2^1S_0-1s2p^1^3P_1$ lines only becomes sensitive at densities greater than 10^{21} cm^{-3} , i.e., higher than is usually achieved in such experiments. One solution to this is to suspend pellets of material of slightly lower Z in the Xe filled enclosure, so that the corresponding He-like transitions are sensitive in the right range. This would be most appropriate in the hottest regions of the Xe enclosure, since Kr and similar ions will be ionized beyond the B-like charge state, but elsewhere the B-like density diagnostic we discuss might be preferable. We note that previously discussed L shell diagnostics in Xe [6,49] for the electron temperature are still dependent on the electron density, due to the density sensitivity of the dielectronic recombination process and the ionization balance itself in such experiments. The density diagnostic we identify is much less dependent on the electron temperature, and would go some way towards resolving such ambiguities.

Further density sensitive line ratios at the same electron temperature in Kr XXXI and Kr XXX are plotted in Fig. 3(b), which may have applications to tokamak plasmas with density in the range $10^{12} - 10^{14} \text{ cm}^{-3}$.

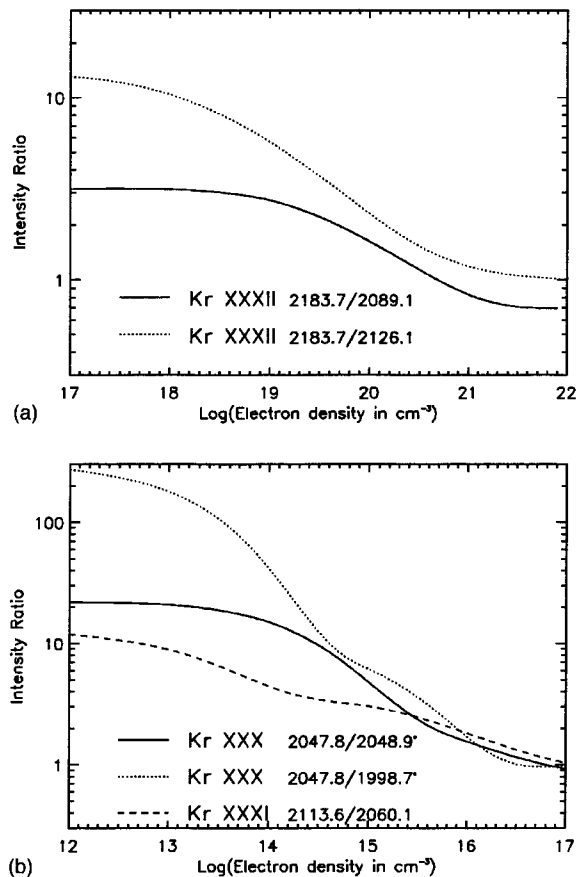


FIG. 3. Electron-density ($\log_{10} n_e$) dependence of line intensity ratios at electron temperature $T_e = 2 \times 10^7$ K calculated with a model described in Sec. IV for selected transitions in Kr XXX–XXXII (identified in Table II).

VI. CONCLUSION

We have demonstrated the value of using an EBIT plasma model for the analysis of complex and only partially resolved x-ray spectra obtained with a broadband high-resolution x-ray detector. This approach can be applied in the determination of numerous physical characteristics of the EBIT plasma, such as measurements of important reaction rates and the validation of diagnostic line ratios. In this paper we have identified many new lines in the spectra of L -shell Kr ions, some with diagnostic potential applicable in other fields of plasma physics, and have made progress towards understanding conditions in the EBIT trap itself.

ACKNOWLEDGMENTS

The authors thank D. J. Alderson for his technical support. I.K. acknowledges support from the Swedish Foundation for Cooperation in Research and Higher Education (STINT). J.M.L. was supported by NASA Contract W 19353 (Applied Information Systems Research Program) and ONR/NRL 6.1 Research Option ‘‘Solar Magnetism and the Earth’s Environment.’’

- [1] J. M. Laming, C. A. Back, C. D. Decker, J. Grun, U. Feldman, J. F. Seely, and J. F. Davis, *Phys. Rev. E* (to be published).
- [2] C. A. Back, J. Grun, C. Decker, L. J. Suter, J. Davis, O. L. Landen, R. Wallace, W. W. Hsing, J. M. Laming, U. Feldman, M. Miller, and C. Wuest, *Phys. Rev. Lett.* (to be published).
- [3] H. Fiedorowicz, A. Bartnik, P. Parys, and Z. Patron, *Inst. Phys. Conf. Ser.* **130**, 515 (1992).
- [4] M. J. May, M. Finkenthal, V. Soukhanovskii, D. Stutman, H. W. Moos, D. Pacella, G. Mazzitelli, K. Fournier, W. H. Goldstein, and B. Gregory, *Rev. Sci. Instrum.* **70**, 375 (1999).
- [5] M. Bitter, H. Hsuan, K. W. Hill, and M. Zarnstorff, *Phys. Scr.* **T47**, 87 (1993).
- [6] C. J. Keane, B. A. Hammel, A. L. Osterheld, and D. R. Kania, *Phys. Rev. Lett.* **72**, 3029 (1994).
- [7] J. D. Gillaspy, *Phys. Scr.* **T65**, 168 (1996).
- [8] B. Edlén, in *Handbuch der Physik*, edited by S. Flügge (Springer-Verlag, Berlin, 1964), p. 148.
- [9] S. Bandler, E. Silver, H. Schnopper, S. Murray, M. Barbera, N. Madden, D. Landis, J. Beeman, E. Haller, and G. Tucker, *Nucl. Instrum. Methods Phys. Res. A* **444**, 273 (2000).
- [10] E. Silver, H. Schnopper, S. Bandler, S. Murray, N. Madden, D. Landis, J. Beeman, E. Haller, M. Barbera, G. Tucker, J. Gillaspy, E. Takacs, and J. Porto, *Nucl. Instrum. Methods Phys. Res.* (to be published).
- [11] M. J. May, M. Finkenthal, V. Soukhanovskii, D. Stutman, H. W. Moos, D. Pacella, G. Mazzitelli, K. Fournier, W. Goldstein, and B. Gregory, *Rev. Sci. Instrum.* **70**, 375 (1999).
- [12] M. J. May, K. B. Fournier, D. Pacella, H. Kroegler, J. E. Rice, B. Gregory, M. Finkenthal, H. W. Moos, G. Mazzitelli, and W. H. Goldstein, *Phys. Rev. E* **61**, 3042 (2000).
- [13] J. P. Buchet, M. C. Buchet-Poulizac, A. Denis, J. Desesquelles, M. Druetta, S. Martin, D. Lecer, E. Luc-Koenig, and J. F. Wyart, *Nucl. Instrum. Methods Phys. Res. B* **31**, 177 (1988).
- [14] E. Hinnov, *Phys. Rev. A* **14**, 1533 (1976).
- [15] J. F. Wyart and TFR Group, *Phys. Scr.* **31**, 539 (1985).
- [16] P. G. Burkhalter, J. Shiloh, A. Fisher, and R. D. Cowan, *J. Appl. Phys.* **50**, 4532 (1979).
- [17] H. Gordon, M. G. Hobby, N. J. Peacock, and R. D. Cowan, *J. Phys. B* **12**, 881 (1979).
- [18] J. D. Gillaspy, J. R. Roberts, C. M. Brown, and U. Feldman, in *Proceedings of the VIth International Conference on the Physics of Highly Charged Ions*, edited by P. Richard, M. Stockli, C. L. Cocke, and C. D. Lin (AIP press, New York, 1993), Vol. 274, p. 682.
- [19] J. D. Gillaspy, *Phys. Scr.* **T71**, 99 (1997).
- [20] E. Silver, H. Schnopper, S. Bandler, N. Brickhouse, S. Murray, M. Barbera, E. Takacs, J. Gillaspy, J. Porto, I. Kink, N. Madden, D. Landis, J. Beeman, and E. Haller, *Astrophys. J.* (to be published).
- [21] F. G. Serpa, E. W. Bell, E. S. Meyer, J. D. Gillaspy, and J. R. Roberts, *Phys. Rev. A* **55**, 1832 (1997).
- [22] B. M. Penetrante, J. N. Bardsley, M. A. Levine, D. A. Knapp, and R. E. Marrs, *Phys. Rev. A* **43**, 4873 (1991).
- [23] E. Silver, H. Schnopper, and R. Ingram, US Patent Application No. 09064476, 1998.
- [24] H. Schnopper, E. Silver, R. Ingram, F. Christensen, A. Hus-sain, M. Barbera, S. Romaine, A. Collura, A. Kenter, S. Bandler, and S. Murray, *Proc. SPIE* **3766**, 350 (1999).
- [25] B. Edlén, *Rep. Prog. Phys.* **26**, 181 (1963).
- [26] F. Tyrén, *Nova Acta Regiae Soc. Sci. Ups.* **12**, 7 (1940).
- [27] N. J. Peacock, R. J. Speer, and M. G. Hobby, *J. Phys. B* **2**, 798 (1969).
- [28] J. D. Garcia and J. E. Mack, *J. Opt. Soc. Am.* **55**, 654 (1965).
- [29] L. Engström, *Lund Reports on Atomic Physics*, LRAP-232, University of Lund, 1998.
- [30] R. D. Cowan, *The Theory of Atomic Structure and Spectra* (University of California, Berkeley, 1981).
- [31] A. Bar-Shalom and M. Klapisch, *Comput. Phys. Commun.* **50**, 375 (1988).
- [32] A. Bar-Shalom, M. Klapisch, and J. Oreg, *Phys. Rev. A* **38**, 1773 (1988).
- [33] D. B. Melrose, *Instabilities in Space and Laboratory Plasmas* (Cambridge University, Cambridge, 1986).
- [34] D. L. Moores, L. B. Golden, and D. H. Sampson, *J. Phys. B* **13**, 385 (1980).
- [35] I. V. Kalagin, D. Kuchler, V. P. Ovsyannikov, and G. Zschornack, *Plasma Sources Sci. Technol.* **7**, 441 (1998).
- [36] H. A. Bethe and E. E. Salpeter, *Quantum Mechanics of One- and Two- Electron Atoms* (Springer-Verlag, Berlin, 1957).
- [37] Y. S. Kim and R. H. Pratt, *Phys. Rev. A* **27**, 2913 (1983).
- [38] R. Mann, F. Folkmann, and H. F. Beyer, *J. Phys. B* **14**, 1161 (1981).
- [39] A. K. Bhatia and G. A. Doschek, *At. Data Nucl. Data Tables* **52**, 1 (1992).
- [40] K. J. H. Phillips, C. J. Greer, A. K. Bhatia, and F. P. Keenan, *Astrophys. J.* **469**, L57 (1996).
- [41] J. L. R. Saba, J. T. Schmelz, A. K. Bhatia, and K. T. Strong, *Astrophys. J.* **510**, 1064 (1999).
- [42] A. K. Bhatia and S. O. Kastner, *Astrophys. J.* **516**, 482 (1999).
- [43] G. V. Brown, P. Beiersdorfer, D. A. Liedahl, K. Widman, and S. M. Kahn, *Astrophys. J.* **502**, 1015 (1998).
- [44] L. W. Acton, M. E. Bruner, W. A. Brown, B. C. Fawcett, W. Schweizer, and R. J. Speer, *Astrophys. J.* **291**, 865 (1985).
- [45] J. M. Laming, I. Kink, E. Takacs, J. V. Porto, J. D. Gillaspy, E. H. Silver, H. W. Schnopper, S. R. Bandler, N. S. Brickhouse, S. S. Murray, M. Barbera, A. K. Bhatia, G. A. Doschek, N. Madden, D. Landis, J. Beeman, and E. E. Haller, *Astrophys. J. Lett.* (to be published).
- [46] V. Kharchenko and A. Dalgarno, *J. Geophys. Res.* **105**, 18 351 (2000).
- [47] J. B. Greenwood, I. D. Williams, S. J. Smith, and A. Chutjian, *Astrophys. J. Lett.* **533**, L175 (2000).
- [48] T. E. Cravens, *Geophys. Res. Lett.* **24**, 105 (1997).
- [49] B. H. Failor, J. C. Fernandez, B. H. Wilde, A. L. Osterheld, J. A. Cobble, and P. L. Gobby, *Phys. Rev. E* **59**, 6053 (1999).

EMISSION-LINE INTENSITY RATIOS IN Fe XVII OBSERVED WITH A MICROCALORIMETER
ON AN ELECTRON BEAM ION TRAP

J. M. LAMING¹ I. KINK,² E. TAKACS,³ J. V. PORTO,² J. D. GILLASPY,² E. H. SILVER,⁴ H. W. SCHNOPPER,⁴ S. R. BANDLER,⁴
N. S. BRICKHOUSE,⁴ S. S. MURRAY,⁴ M. BARBERA,⁵ A. K. BHATIA,⁶ G. A. DOSCHEK,¹ N. MADDEN,⁷
D. LANDIS,⁷ J. BEEMAN,⁷ AND E. E. HALLER⁷

Received 2000 June 16; accepted 2000 October 11; published 2000 December 6

ABSTRACT

We report new observations of emission line intensity ratios of Fe XVII under controlled experimental conditions, using the National Institute of Standards and Technology electron beam ion trap (EBIT) with a microcalorimeter detector. We compare our observations with collisional-radiative models using atomic data computed in distorted wave and *R*-matrix approximations, which follow the transfer of the polarization of level populations through radiative cascades. Our results for the intensity ratio of the $2p^6\ ^1S_0-2p^53d\ ^1P_1$ 15.014 Å line to the $2p^6\ ^1S_0-2p^53d\ ^3D_1$ 15.265 Å line are 2.94 ± 0.18 and 2.50 ± 0.13 at beam energies of 900 and 1250 eV, respectively. These results are not consistent with collisional-radiative models and support conclusions from earlier EBIT work at the Lawrence Livermore National Laboratory that the degree of resonance scattering in the solar 15.014 Å line has been overestimated in previous analyses. Further observations assess the intensity ratio of the three lines between the $2p^6-2p^53s$ configurations to the three lines between the $2p^6-2p^53d$ configurations. Both *R*-matrix and distorted wave approximations agree with each other and our experimental results much better than most solar and stellar observations, suggesting that other processes not present in our experiment must play a role in forming the Fe XVII spectrum in solar and astrophysical plasmas.

Subject headings: atomic data — methods: laboratory — stars: individual (Capella) — Sun: corona — techniques: spectroscopic — X-rays: general

The high elemental abundance of Fe and the closed shell structure of Ne-like ions cause Fe⁺¹⁶ to be one of the dominant ions in forming emission-line spectra from plasmas with temperatures $\sim 5 \times 10^6$ K. Fe XVII lines will be the dominant lines in most spectra obtained by gratings on *Chandra* and *XMM-Newton* from a wide variety of objects. For example, in the Capella spectra acquired by *Chandra* (Brinkman et al. 2000; Canizares et al. 2000), Fe XVII contributes four or five of the six strongest lines observed. In conditions of ionization equilibrium, Fe XVII is unique in providing an electron temperature diagnostic between two sets of these strong lines (Raymond & Smith 1986). Solar flare observations have long pointed to discrepancies between the observed intensity ratios among the strong emission lines of Fe XVII in the 15–17 Å region. The Capella spectra referred to above hint that similar problems may exist for astrophysical sources as well. Among the six strong lines arising from transitions between the ground state $2p^6\ ^1S_0$ and the excited states $2p^53s\ ^1P_1$, 3P_1 , 3P_2 , and $2p^53d\ ^1P_1$, 3D_1 , and 3P_1 , the strongest line from $2p^53d\ ^1P_1$ at 15.014 Å often appears diminished in intensity relative to other features. This has led to suggestions that it may be affected by resonance scattering that removes photons pre-

dominantly from the line of sight in this transition (Schmelz, Saba, & Strong 1992; Phillips et al. 1996, 1997; Bhatia & Kastner 1999; Saba et al. 1999). Furthermore, the overall intensity of the lines from the $2p^53s$ configuration often appears enhanced relative to the intensity theory would predict when compared with the lines from the $2p^53d$ configuration. This has led some authors (U. Feldman 2000, private communication; see Sampson & Zhang 1987) to suggest that an inner shell ionization of a $2p$ electron from the Na-like Fe ion plays a role in forming the spectrum, producing Ne-like Fe in the excited configuration $2p^53s$. Other explanations suggest that strong dielectric recombination occurs (Liedahl et al. 1990) or simply that the theoretical atomic models do not include a sufficient number of excited levels to adequately treat all the radiative cascades. In this Letter we describe initial results of experiments designed to test some of these ideas.

In a study of tokamak spectra of Fe XVII, Phillips et al. (1997) found good agreement between observations and synthetic spectra calculated from models including the lowest 37 fine-structure levels of Fe XVII (i.e., all configurations up to $2s2p^63d$), including dielectronic and inner shell satellites of Fe XVI. The collisional data used in Phillips et al. (1997) are similar to some of those used here. They are computed in the distorted wave approximation and tabulated in Bhatia & Doschek (1992). Tokamak plasma sources do not allow the individual atomic processes to be experimentally isolated and studied in detail. More control is possible with the use of an electron beam ion trap (EBIT). Positive ions are trapped in the space charge of an essentially monoenergetic electron beam that also ionizes and excites the ions. The ion charge state is selected by tuning the electron beam energy. In the case of Ne-like ions, almost complete selectivity is possible. Taking advantage of this, Brown et al. (1998) made detailed observations of Fe XVII at beam energies of 850, 1150, and 1300 eV. They observed lines originating from levels with principal quantum number n up to 11. Their mea-

¹ E. O. Hulburt Center for Space Research, US Naval Research Laboratory, Washington, DC 20375.

² National Institute of Standards and Technology, 100 Bureau Drive, Gaithersburg, MD 20899.

³ Massachusetts Institute of Technology, 77 Massachusetts Avenue, 26-239, Cambridge, MA 02139-4307; and University of Debrecen, Debrecen, Bem ter 18/A, H-4026, Hungary.

⁴ Harvard-Smithsonian Center for Astrophysics, 60 Garden Street, Cambridge, MA 02138.

⁵ Osservatorio Astronomico G. S. Vaiana, Piazza del Parlamento 1, 90134 Palermo, Italy.

⁶ Laboratory for Astronomy and Solar Physics, NASA Goddard Space Flight Center, Greenbelt, MD 20771.

⁷ Lawrence Berkeley National Laboratory, 1 Cyclotron Road, Berkeley, CA 94720.

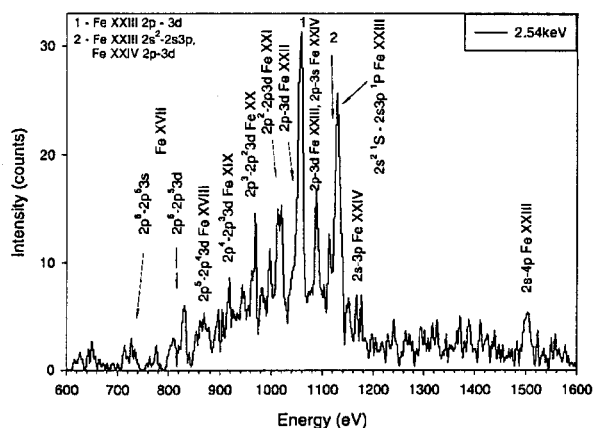


FIG. 1.—Section of a microcalorimeter spectrum of Fe L shell lines recorded at an EBIT beam energy of 2.54 keV. Lines from Fe XVII to Fe XXIII are prominent.

surement of the intensity ratio of the strongest 15.014 Å line to the 15.265 Å line originating from the $2p^5 3d^3 D_1$ level was 3.04 ± 0.12 , which is in between theoretical values (generally closer to 4) and ratios observed in solar and stellar coronae (usually in the range 2–2.5). Table 2 of Brown et al. (1998) gives a useful summary of the various calculations and observations of this intensity ratio. However, Brown et al. (1998) in their paper report no results for the intensities of the $3s-3p$ transitions.

Our experimental technique couples the National Institute of Standards and Technology (NIST) EBIT with a microcalorimeter detector and is discussed in detail in Silver et al. (2000). This offers a combination of high throughput, wide bandpass, and sufficient spectral resolution to allow most lines to be resolved (see Kelley et al. 2000; Silver et al. 2000). One modification from previous experimental runs was to move the microcalorimeter to a new observation port on the EBIT, which allowed much closer access to the trapped ions in the electron beam. This further improved the high-energy bandpass and allowed us to dispense with the X-ray optic. Another important feature is that the microcalorimeter when used in this configuration is polarization blind. Thus, the only correction required for this effect is for the degree of spatial anisotropy in the emission of polarized light; the measured intensity will depend on the degree of polarization through this anisotropy, which is different for lines of different polarization. As we discuss below, such effects are rather small and can be adequately modeled. A part of a spectrum taken at a beam energy of 2500 eV is shown in Figure 1 to illustrate the capabilities of the detector. These data were collected in only 15 minutes. The complete spectrum extends to much higher energies and would include the Fe K line complex if the beam energy was sufficiently high. Of course, in this case the Fe L spectrum would not be so strong, and it is these lines, and specifically Fe XVII, that are the main focus of this Letter.

We observed Fe XVII transitions at a variety of electron beam energies between 900 and 4000 eV. Comparing spectra at beam energies of 900 and 1250 eV allows us to study what effect (if any) enhanced radiative cascades at the higher energy might have. At 900 eV, we are also well below the thresholds for excitation by inner shell ionization of Fe XVI (Sampson & Zhang 1987) should any be present in our trap (see below). For these two beam energies, experimental intensity ratios were obtained by fitting a sum of Gaussian functions to the experimental data,

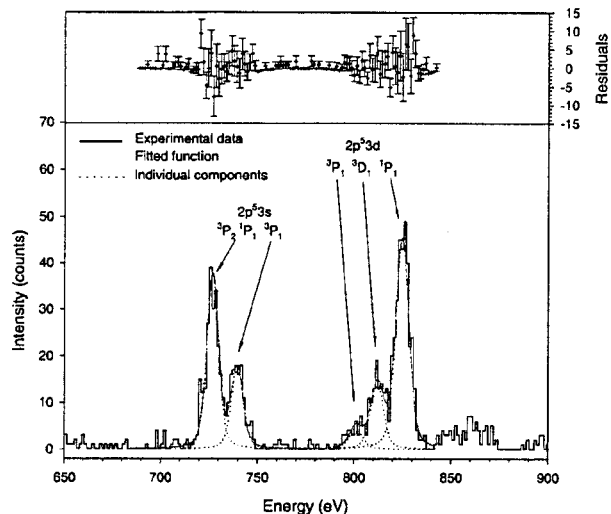


FIG. 2.—Fit to the six strong Fe XVII lines recorded at an electron beam energy of 900 eV. The line wavelengths are 15.014, 15.265, 15.456, 16.780, 17.055, and 17.100 Å. The last two transitions are blended together at the resolution of the microcalorimeter and are fitted as a single component. The upper panel gives the residuals from the fit.

and the area underneath a particular Gaussian was treated as a line intensity. The Gaussian functions slightly underestimate the “wing” of the spectral lines, and better resemblance is achieved with Voigt functions. However, the results from these different fits remained well within quoted error bars, determined from the statistical quality of the fit (dominant uncertainty) and systematic uncertainties (much smaller contributions) due to the detector/window efficiency, and therefore the results from Gaussian fits are presented. The data, fit, and residuals for the 900 eV beam energy spectrum are shown in Figure 2. At these beam energies, there is no evidence of inner shell transitions in Fe XVI. The strongest of these lines, the $2s^2 2p^6 3s^2 S_{1/2} - 2s^2 2p^5 3s^2 P_{3/2}$, calculated to be at a wavelength between 17.29 and 17.31 Å (Phillips et al. 1997; Bautista 2000), would be easily visible in our spectra, resolved from the Fe XVII 17.055 and 17.100 Å lines. Using higher resolution crystal spectrometers observing one of the Lawrence Livermore National Laboratory EBITs under similar conditions, Brown et al. (1998) also saw no evidence for these transitions.

The spectra were corrected for the transmission efficiencies of the microcalorimeter windows. (The quantum efficiency of the detector is 100% for energies below 5 keV.) The window transmission has been well defined for the entire microcalorimeter bandpass of 0.1–10 keV. The three windows are made of polyimide (800 Å) and aluminum (1100 Å), and their thicknesses have been measured to an accuracy of 0.5% (Powell et al. 1997). The efficiency curve is smooth and featureless in the energy band that includes the Fe L emission. We have taken great care to minimize potential contamination of these windows, but over long periods of time (days) it is possible that minute amounts of hydrocarbons could collect on the outer window (the most susceptible since it views the vacuum connection to the EBIT). Our calculations show that only several monolayers of nitrogen or oxygen would freeze out on the window given the cleanliness of the EBIT vacuum connection and the extremely low pressures at the initiation of the cooling cycle. Since the Fe XVII lines were measured over a period of

TABLE 1
OBSERVATIONAL AND THEORETICAL Fe XVII INTENSITIES RELATIVE TO THE 15.014 Å LINE

LINE WAVELENGTH (Å)	LINE ENERGY (eV)	UPPER LEVEL	DATA (0.9 keV)	THEORETICAL (0.9 keV) ^a		DATA (1.25 keV)	THEORETICAL (1.25 keV) ^a	
				Distorted Wave	R-Matrix		Distorted Wave	R-Matrix
15.265	812.5	$2p^5 3d^3 D_1$	0.34 ± 0.02^b	0.25	0.25	0.40 ± 0.02	0.26	0.26
15.456	802.5	$2p^5 3d^3 P_1$	0.10 ± 0.01	0.047–0.036	0.059–0.046	0.09 ± 0.01	0.035–0.027	0.034–0.027
16.780	739.1	$2p^5 3s^3 P_1^c$	0.45 ± 0.04	0.46–0.41	0.47–0.41	0.40 ± 0.02	0.51–0.44	0.47–0.42
17.055	727.1	$2p^5 3s^3 P_1^c$		0.54–0.47	0.60–0.53		0.58–0.50	0.55–0.47
17.100	725.0	$2p^5 3s^3 P_2$		0.34–0.30	0.43–0.38		0.41–0.35	0.39–0.33
17.055+17.100 ^d			0.88 ± 0.09	0.88–0.77	1.03–0.91	0.92 ± 0.12	0.99–0.85	0.94–0.80

^a Theoretical range goes from unpolarized to maximum polarization case. *R*-matrix cross sections are from Mohan et al. 1997 substituted for first 26 excited levels.

^b Uncertainties correspond to 1 σ .

^c Some authors swap the *LS* coupling notation for these levels, with 16.780 Å originating from 1P_1 and 17.100 Å from 3P_1 .

^d Experimental result is for the sum of 17.055 and 17.100 intensities; theoretical results are for each line separately and their sum.

1 hr (as opposed to several days), the chances of a contamination buildup occurring is unlikely. Furthermore, we point out that the Fe XVII line ratios measured by our instrument are relatively insensitive to even a large amount of contamination. For example, 3000 Å of nitrogen or oxygen ice formed on the outer cryostat window could reduce transmission by 25% but only alter the ratios for the $3s/3d$ lines by 9%; the $2p-3d$ line ratios would remain unchanged. This scenario is highly unlikely since 3000 Å of N or O ice is 2 times thicker than the window itself and would undoubtedly break it.

We compare our observations with theoretical results computed using a model Fe XVII ion comprising the configurations up to $2s2p^6 4d$, i.e., 73 levels, with extra configurations $2s^2 2p^5 ns$, $2s^2 2p^5 nd$, and $2s2p^6 np$ for $n = 5$ and 6 included for their radiative cascades. This brings the total up to 113 levels. Excitation rates are calculated for monoenergetic electron beams between 0.9 and 4.0 keV energy, including only those levels that are energetically accessible in each case. The calculations use impact excitation cross sections computed in a distorted wave approximation as described in Bhatia & Doschek (1992) for all transitions among the lowest 73 levels. As an alternative, *R*-matrix cross sections from the ground state to the configurations up to $2p^5 3d$ (i.e., the first 26 excited levels) can be substituted from Mohan, Sharma, & Eissner (1997). Energy levels and radiative decay rates are taken from the distorted wave target calculation, supplemented with those for higher lying configurations taken from a computation with the HULLAC (Hebrew University Lawrence Livermore) Code for Atomic Physics (M. Klapisch, A. Bar Shalom, W. H. Goldstein, E. Meroz, A. Chon, & M. Cohen 1988, unpublished; Goldstein et al. 1988). Collisional excitation rates to these higher levels are scaled from those for the lower lying ones.

For the purposes of modeling emission from the EBIT, we follow the analysis in Takacs et al. (1996) and expand our 113-level model to the 457 magnetic sublevels present. This is done in order to account for the polarization arising from the excitation by the electron beam. For the upper levels of the strongest transitions (i.e., those with $j = 1$), excitation cross sections to individual magnetic sublevels are given in the relativistic distorted wave approximation by Zhang, Sampson, & Clark (1990). For transitions where a nonrelativistic approach is valid, these data are supplemented with simple results from a Coulomb-Bethe approximation.

All levels with $j \geq 3$ are assumed to be unpolarized. More accurate m_j dependent cross sections will be substituted as they become available, but the current procedure should model the transmission of polarization through radiative cascades suffi-

ciently accurately to allow us to evaluate the anisotropy of the emission from the EBIT. More precise work would be necessary with crystal spectrometers.

In Table 1 we compare our experimental Fe XVII line intensity ratios with those calculated by the methods outlined above for beam energies of 0.9 and 1.25 keV. The theoretical results come from the distorted wave cross sections calculated herein and from the same distorted wave results but with the cross sections for excitation from the ground state to the first 26 excited levels replaced by the *R*-matrix results of Mohan et al. (1997). The range of theoretical ratios extends from results calculated in the limit of zero polarization to those in the limit of maximum polarization. The finite distribution of pitch angles in the electron beam causes the true theoretical result to lie somewhere between these two limits. This depolarization can be estimated from results given in Gu, Savin, & Beiersdorfer (1999). Even in the limit of no depolarization, the polarization correction required for the microcalorimeter is rather small, less than would be the case for a crystal spectrometer, but remains the dominant systematic uncertainty in our experiment at these two beam energies.

Brown et al. (1998) measured intensity ratios for the 15.014/15.265 Å lines of 2.93 ± 0.16 , 3.15 ± 0.17 , 2.77 ± 0.19 , and 3.00 ± 0.20 from observations at beam energies of 1150, 1150, 850, and 1300 eV, respectively. They then average these values to give a mean result of 3.04 ± 0.12 , compared with theoretical predictions of around 4. Explicit in this argument is an assumption that the polarizations of these two lines are the same, since the observations were made with crystal spectrometers at Bragg angles where they are polarization sensitive. Such an assumption is supported by theory (Zhang et al. 1990). However, the result obtained using this assumption demonstrates that this same theory gives an intensity ratio between these two lines inconsistent with experiment. While it is quite possible that the calculations get the polarizations right and the intensity ratio wrong, it is certainly not guaranteed. The microcalorimeter employed in the present work is not polarization sensitive, and our experimental values for the intensity ratio— 2.94 ± 0.18 at 0.9 keV and 2.50 ± 0.13 at 1.25 keV—are more robust, being sensitive only to the possible difference in the anisotropy of the emitted radiation. The first value is consistent with the average result of Brown et al. (1998), while the second is slightly lower. These results support the suggestion of Brown et al. (1998) that the effect of resonance scattering in the 15.014 Å resonance line in solar spectra has hitherto been overestimated.

Intensity ratios from our data for the three lines originating from $2p^5 3s$ to those from $2p^5 3d$ are shown in Figure 3. For energies greater than 1.25 keV, they are obtained by summing

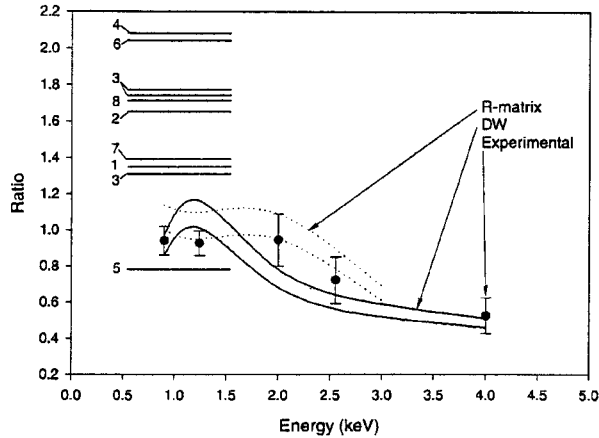


FIG. 3.—Variation of the intensity ratio $(I_{16.780} + I_{17.055} + I_{17.100}) / (I_{15.014} + I_{15.265} + I_{15.456})$ with electron beam energy. The first three lines originate in the $2p^33s$ configuration and the second three in the $2p^53d$. For comparison, results from model calculations using the distorted wave results (see Bhatia & Doschek 1992) are shown, and where appropriate the *R*-matrix results of Mohan et al. (1997) are overlaid. The range given for each calculation corresponds to the limits of unpolarized (upper curve) and completely polarized (lower curve) emission. The observational ratios from various solar and stellar observations are shown for reference on the same plot. For these, the energy scale on the *x*-axis should be disregarded. Fe XVII is generally formed in plasmas at a temperature of 5×10^6 K, and electrons with energies close to threshold, i.e., less than 1 keV, dominate the excitation rate. The references are (1) Blake et al. (1965); (2) Parkinson (1975); (3) Hutcheon, Pye, & Evans (1976); (4) McKenzie et al. (1980); (5) Phillips et al. (1982); (6) Acton et al. (1985); (7) Brinkman et al. (2000); and (8) Canizares et al. (2000).

the number of detected photons over the spectral regions where the $2p^6-2p^53s$ and $2p^6-2p^53d$ lines appear, respectively, correcting for the presence of the Fe XIX lines at 15.114 and 15.210 Å (820 and 815 eV, respectively), by measuring the strong Fe XIX $2p^4-2p^33d$ lines at 13.465, 13.507, and 13.521 Å (920 eV) and subtracting off the appropriate ratio determined from calculations with HULLAC. Since Fe XIX has a 3P_2 ground-state, polarization corrections are negligible. The calculated ratios, in the range 0.25–0.33 for beam energies 2–4 keV, also agree well with higher resolution observations of solar active regions (recently reassessed by Phillips et al. 1999). The error bars are estimated from the Poisson counting statistics and uncertainties arising from background subtraction (i.e., the Fe XIX lines) and

in the detector/window quantum efficiency but are dominated by a $\pm 20\%$ error in the measured intensity of the Fe XIX blend at 920 eV. Also shown in Figure 3 are observational ratios of the three $3s$ lines to the three $3d$ lines taken from various solar and stellar observations.

The experimental ratios for the electron beam energy of 0.9 keV suggest that the models including the *R*-matrix cross sections are less preferable than those using only distorted wave cross sections. The former cross sections appear to overestimate slightly the emission in the 17.055 and 17.100 Å lines. Elsewhere we have a small preference for the *R*-matrix results, although we caution here that a small contribution to the Fe XVII emission may arise by recombination from Fe⁺¹⁷ into excited states of Fe XVII, and until this effect is adequately modeled firm conclusions might be premature. Our experience with similar spectra of Kr XXVII (Kink et al. 2000) suggests that the inclusion of recombination would increase the theoretical $3s/3d$ ratios. More importantly, the difference between the two theoretical approaches and our experiment is significantly smaller at all energies than the discrepancies between the solar and astrophysical observations summarized in Figure 3 (with the exception of Phillips et al. 1982) and either theory. The basic electron impact excitation theory for these lines in Fe XVII appears to be correct, in contrast with that for the 15.265/15.014 ratio (see Table 1), and one must look to other processes to model the solar and astrophysical observations satisfactorily. These may invalidate the electron temperature diagnostic of Raymond & Smith (1986).

These measurements are a subset of a larger survey of spectroscopy experiments performed with the microcalorimeter on the NIST EBIT. Future work will concentrate on acquiring spectra with significantly higher statistical quality, simply by increasing the integration time at each beam energy. This might also allow the simultaneous observation of radiative recombination features from the EBIT.

A. K. B., G. A. D., and J. M. L. were supported by NASA contract W19539 (Applied Information Systems Research Program); G. A. D. and J. M. L. were also supported by the NRL/ONR Solar Magnetism and the Earth's Environment 6.1 Research Option. E. H. S., H. W. S., and S. R. B. acknowledge support in part by NASA grant NAG5-5104, and I. K. acknowledges support from the Swedish Foundation for Cooperation in Research and Higher Education (STINT). We also acknowledge the comments of an anonymous referee, particularly in regard to the Fe XIX lines.

REFERENCES

- Acton, L. W., et al. 1985, *ApJ*, 291, 865
 Bautista, M. A. 2000, *J. Phys. B*, 33, 71 (erratum 33, 2833)
 Bhatia, A. K., & Doschek, G. A. 1992, *At. Data Nucl. Data Tables*, 52, 1
 Bhatia, A. K., & Kastner, S. O. 1999, *ApJ*, 516, 482
 Blake, R. L., Chubb, T. A., Friedman, H., & Unizicker, A. E. 1965, *ApJ*, 142, 1
 Brinkman, A. C., et al. 2000, *ApJ*, 530, L111
 Brown, G. V., Beiersdorfer, P., Liedahl, D. A., Widman, K., & Kahn, S. M. 1998, *ApJ*, 502, 1015 (erratum 532, 1245 [2000])
 Canizares, C. R., et al. 2000, *ApJ*, 539, L41
 Goldstein, W. H., Oreg, J., Zigler, A., Bar Shalom, A., & Klapisch, M. 1988, *Phys. Rev. A*, 38, 1797
 Gu, M. F., Savin, D. W., & Beiersdorfer, P. 1999, *J. Phys. B*, 32, 5371
 Hutcheon, R. H., Pye, J. P., & Evans, K. D. 1976, *MNRAS*, 175, 489
 Kelley, R. L., et al. 2000, *Nucl. Instrum. Methods Phys. Res.*, 444, 170
 Kink, I., et al. 2000, *Phys. Rev. E*, submitted
 Liedahl, D. A., Kahn, S. M., Osterheld, A. L., & Goldstein, W. H. 1990, *ApJ*, 350, L37
 McKenzie, D. L., Landecker, P. B., Broussard, R. M., Ruge, H. R., Young, R. M., Feldman, U., & Doschek, G. A. 1980, *ApJ*, 241, 409
 Mohan, M., Sharma, R., & Eissner, W. 1997, *ApJS*, 108, 389
 Parkinson, J. H. 1975, *Sol. Phys.*, 42, 183
 Phillips, K. J. H., et al. 1982, *ApJ*, 256, 774
 Phillips, K. J. H., Greer, C. J., Bhatia, A. K., Coffey, I. H., & Keenan, F. P. 1997, *A&A*, 324, 381
 Phillips, K. J. H., Greer, C. J., Bhatia, A. K., & Keenan, F. P. 1996, *ApJ*, 469, L57
 Phillips, K. J. H., Mewe, R., Harra-Murnion, L. K., Kaastra, J. S., Beiersdorfer, P., Brown, G. V., & Liedahl, D. A. 1999, *A&AS*, 138, 381
 Powell, F. R., et al. 1997, *Proc. SPIE*, 3113, 432
 Raymond, J. C., & Smith, B. W. 1986, *ApJ*, 306, 762
 Saba, J. L. R., Schmelz, J. T., Bhatia, A. K., & Strong, K. T. 1999, *ApJ*, 510, 1064
 Sampson, D. H., & Zhang, H.-L. 1987, *Phys. Rev. A*, 36, 3590
 Schmelz, J. T., Saba, J. L. R., & Strong, K. T. 1992, *ApJ*, 398, L115
 Silver, E., et al. 2000, *ApJ*, 541, 495
 Takacs, E., et al. 1996, *Phys. Rev. A*, 54, 1342
 Zhang, H. L., Sampson, D. H., & Clark, R. E. H. 1990, *Phys. Rev. A*, 41, 198

Microcalorimeter/EBIT Measurements of X-ray Spectra of Highly Charged Ions

I. Kink¹, J. M. Laming², E. Takács³, J. V. Porto¹, J. D. Gillaspay¹, E. Silver⁴, H. Schnopper⁴, S. R. Bandler⁴, M. Barbera⁵, N. Brickhouse⁴, S. Murray⁴, N. Madden⁶, D. Landis⁶, J. Beeman⁶ and E. E. Haller⁶

¹National Institute of Standards and Technology, Gaithersburg, MD 20899, USA

²Naval Research Laboratory, Code 7674L, Washington, DC 20375, USA

³Massachusetts Institute of Technology, Cambridge, MA 20139, USA

⁴Harvard-Smithsonian Center for Astrophysics, Cambridge, MA 02138, USA

⁵Osservatorio Astronomico G. S. Vaiana, Palermo, Italy

⁶Lawrence Berkeley National Laboratory, Berkeley, CA 94720, USA

Received July 31, 2000; accepted October 18, 2000

PACS Ref: 32.30.Rj, 34.50.Fa, 34.80.Dp, 32.70.Fw

Abstract

Spectra of highly charged Ar, Kr, Xe and Fe ions, produced in an Electron Beam Ion Trap (EBIT), have been recorded in a broad X-ray energy band (0.2 keV to 10 keV) with a microcalorimeter detector. The first analysis of the Kr spectra has been completed and most of the spectral lines have been identified as transitions of B- to Al-like Kr. Line intensity ratios of Fe XVII have been measured and compared with theoretical models.

1. Introduction and experimental setup

Electron Beam Ion Traps (EBITs) have successfully been used for investigating properties of very highly charged ions for more than a decade (e.g. [1]). They have several advantages over traditional laboratory high temperature plasma sources such as tokamaks, mirror machines and those produced with lasers, where the physical processes responsible for X-ray line formation cannot be isolated easily. In an EBIT, the plasma is eliminated and replaced by a narrow, well-defined, electron beam. At the National Institute of Standards and Technology, USA (NIST), an energy-tunable electron beam of up to 150 mA can be accelerated to moderate energies (700 eV to 30 keV) by a series of cylindrical electrodes (drift tubes). The beam is compressed to a small (70 μm) diameter by a superconducting Helmholtz pair magnet that provides a maximum axial magnetic field of 3 T. Atoms or singly charged ions are introduced into the center of the middle drift tube where the electron beam has its highest kinetic energy and tightest focus, and are stripped of their outer electrons by impact ionization. Nearly every charge state of every stable element can be produced and their properties investigated [1], providing important tests of different theoretical atomic models, as well as data for a number of applications where high temperature plasmas are involved. Typically, a large fraction of the photon emission from these ions occurs in the X-ray spectral region.

The experimental high resolution spectroscopic data in the X-ray region have up to now been obtained largely with various types of crystal spectrometers. Although these instruments can provide the best resolving power necessary for precision studies, there are several limitations in their application for investigations of highly ionized plasmas. They have low efficiency, which typically decreases with increasing spectral resolution, and a particular crystal cover a narrow

energy range, which makes comparisons of different spectral regions difficult. Semiconductor detectors (Si(Li), Ge, etc.) that can detect X-rays in a broad energy band, on the other hand, have low energy resolution (several hundred eV), which is usually not sufficient for detailed spectroscopic investigations of highly charged ions. The microcalorimeter used in this experiment combines high energy resolution, very broad bandwidth, and close to 100% quantum efficiency [2]. In the calorimeter, single X-ray photons are absorbed in a foil of superconducting tin that is kept at 65 mK. The temperature rise of the absorber is proportional to the X-ray energy and is measured with a neutron transmutation-doped (NTD) germanium thermistor which is attached to the underside of the absorber. The NTD thermistor is impedance-matched to a JFET negative-voltage feedback circuit [3]. The detector used in the present experiment has an energy resolution of 5.9 eV at 1.5 keV and 7 eV at 6 keV [2]. The observed X-ray emission lines span from 0.2 keV to 10 keV. A special X-ray lens [2] can be placed between the EBIT and microcalorimeter to focus the X-rays onto the detector.

2. Results

Spectra of Ar, Kr, Xe and Fe have been recorded from 200 eV to 10 keV under different conditions (electron beam energy and current, ion/atom density, trap dumping time). Examples of the spectra are presented in Figures 1–4. Observed lines are mainly due to $n = 2$ to $n = 3$ transitions in Li-like to Mg-like ions except, for Xe where most of the lines are due to $n = 3$ to $n = 4$ transitions in Ni-like and neighboring ions. The first analysis of the Kr spectra is completed [4]. Most of the spectral lines have been identified with 0.2% transition energy uncertainty as transitions of B- to Al-like Kr. Synthetic spectra for each Kr ionization state (Al- to Be-like) were created using a model that includes collisional radiative calculations implemented in the HULLAC suite of codes [5,6] and charge-exchange processes. The latter plays an important role since the experimental intensity ratios deviate from the theory more at high gas injection pressures than for the low pressure. The intensities of the synthetic spectral lines were fitted to experimental ones using the charge state fractions, temperature, and relative charge exchange rates as fitting

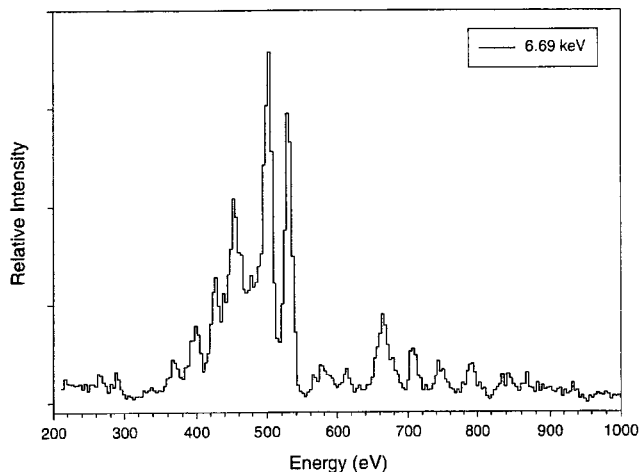


Fig. 1. Spectrum of highly charged Ar at electron beam energy $E_b = 6.69$ keV, beam current $I_b = 120$ mA, trap dumping time $t_d = 200$ ms, gas pressure $p_g = 1.33 \times 10^{-4}$ Pa [4]. Most of the lines are due to $n = 3$ to $n = 2$ transitions in Be-like and neighboring Ar ions.

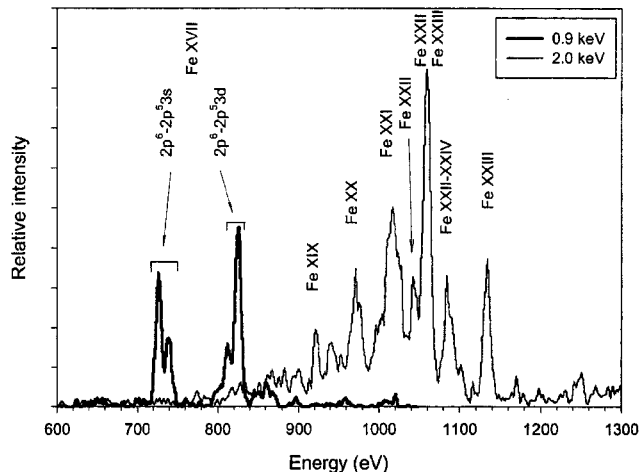


Fig. 4. Spectrum of highly charged Fe at $E_b = 0.9$ keV, $I_b = 14.2$ mA, and $E_b = 2.0$ keV, $I_b = 33.0$ mA; $t_d = 1.0$ s.

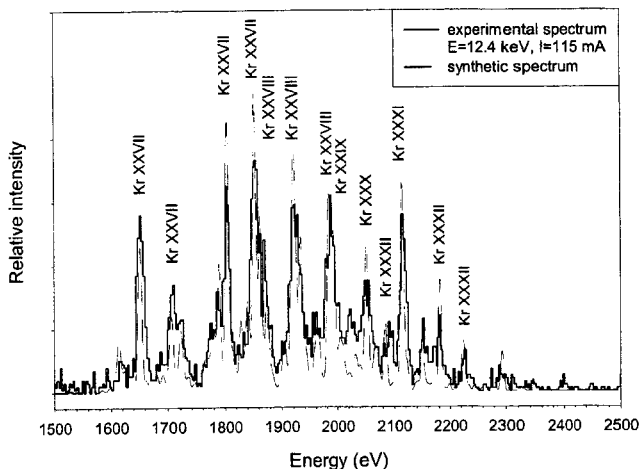


Fig. 2. Spectrum of highly charged Kr at $E_b = 12.4$ keV, $I_b = 115$ mA, $t_d = 1.35$ s, $p_g = 1.33 \times 10^{-4}$ Pa [4]. Synthetic spectrum is calculated and fitted using a model thoroughly described in Ref. [4].

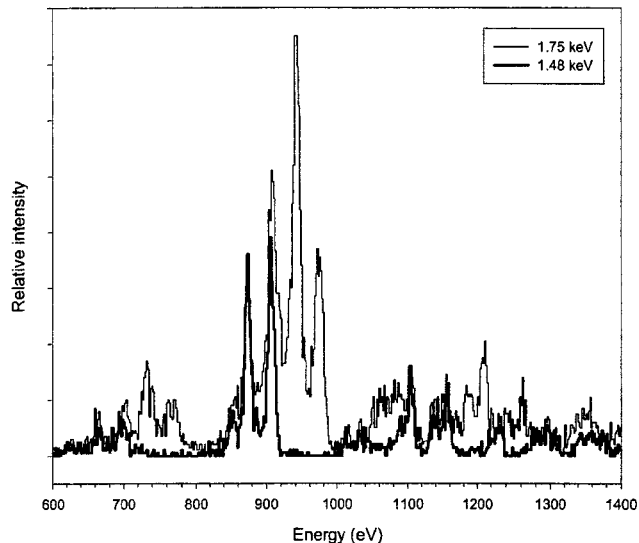


Fig. 3. Spectrum of highly charged Xe at $E_b = 1.48$ keV, $I_b = 42$ mA, and $E_b = 1.75$ keV, $I_b = 51.6$ mA. No trap dumping, $p_g = 1.25 \times 10^{-4}$ Pa [4]. Most of the lines are due to $n = 4$ to $n = 3$ transitions in Ni-like and neighboring Xe ions.

parameters and thus establishing semi-experimental ionization balance inside the trap. Details of the model, fitting procedure, and results can be found in Ref. [4].

Due to the high elemental abundance of Fe and the closed shell structure of Ne-like ions, Fe^{16+} is one of the dominant emitter of line spectra from astrophysical plasmas with temperatures around 5×10^6 K. However, among the six strong lines between the $2p^6 \ ^1S_0$ ground state and the excited states $2p^5 3s \ ^1P_1, \ ^3P_1, \ ^3P_2$ and $2p^5 3d \ ^1P_1, \ ^3D_1, \ ^3P_1$, the strongest line at 15.012 \AA from the $2p^5 3d \ ^1P_1$, often appears diminished in intensity relative to other spectral features [7]. One suggested explanation is that it may be affected by resonance scattering, predominantly removing photons from the line of sight in this transition (e.g. [8,9]). Furthermore, the overall intensity of the lines from the $2p^5 3s$ configuration often appears enhanced relative to what theory would predict when compared to the lines from the $2p^5 3d$ configuration. This has been explained by inner shell ionization of a 2p electron of the Na-like Fe ion [10], strong dielectric recombination [11], and also by incomplete theoretical atomic models that do not include a sufficient number of excited levels to adequately treat all the radiative cascades. We compared our observations with theoretical results computed including up to 113 levels (457 magnetic sublevels for the polarization correction) using both distorted wave [12] and R -matrix [13] excitation cross sections (Figs 5,6). Our values for the intensity ratio of the $15.260/15.012 \text{ \AA}$ lines are consistent with those of [14], supporting the suggestion that the effect of resonance scattering in the 15.012 \AA resonance line in solar spectra has hitherto been overestimated.

Acknowledgements

The authors thank D. J. Alderson for his technical support. IK acknowledges support from the Swedish Foundation for Cooperation in Research and Higher Education (STINT). JML was supported by NASA Contract W 19539 (Applied Information Systems Research Program) and by the NRL/ONR Solar Magnetism and the Earth's Environment 6.1 Research Option. ES, HS, and SB acknowledge support in part by NASA Grant NAG5-5104.

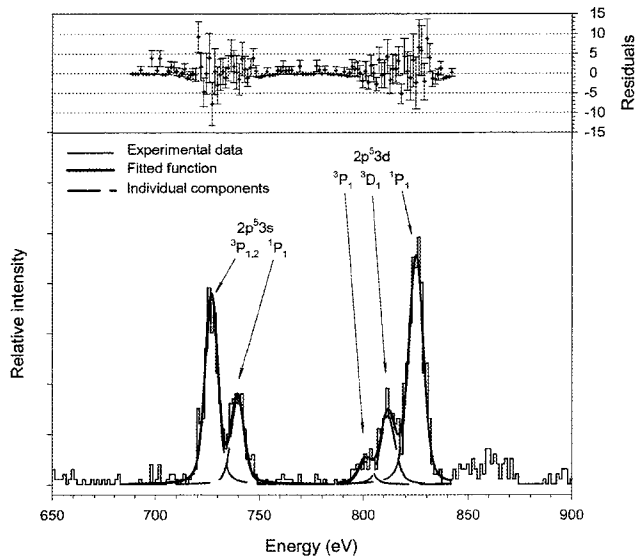


Fig. 5. Fit to the six strong Fe XVII lines recorded at $E_b = 900$ eV. The line wavelengths are 15.012 Å, 15.260 Å, 15.449 Å, 16.776 Å, 17.051 Å, and 17.100 Å. The last two transitions are blended together at the resolution of the microcalorimeter, and are fitted as a single component. The upper panel gives the residuals from the fit. Error bars come from Poisson statistics.

References

- Gillaspy, J. D., *Physica Scripta* **T65**, 168 (1996).
- Silver, E. *et al.*, *Nucl. Instr. Meth. Phys. Research A* **444**, 156 (2000).
- Bandler, S. *et al.*, *Nucl. Instr. Meth. Phys. Research A* **444**, 273 (2000).
- Kink, I. *et al.*, *Phys. Rev. E* (submitted, 2000).
- Bar-Shalom, A. and Klapisch, M., *Computer Phys. Comm.* **50**, 375 (1988).
- Bar-Shalom, A., Klapisch, J. D. and Oreg, J., *Phys. Rev. A* **38**, 1773 (1988).
- Laming, J. M. *et al.*, *Astrophys. J. Lett.* (accepted, 2000).

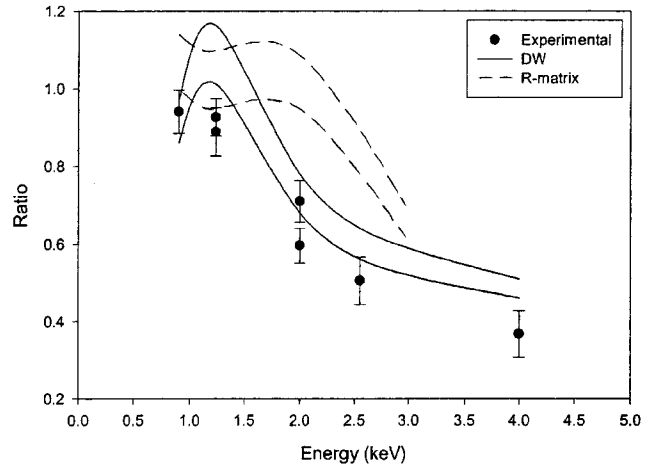


Fig. 6. The variation of the intensity ratio $(I_{16.776} + I_{17.051} + I_{17.100}) / (I_{15.012} + I_{15.260} + I_{15.449})$ with electron beam energy. The first three lines originate in the $2p^5 3s$ configuration and the second three in the $2p^5 3d$. For comparison, results from model calculations using the DW (distorted wave) results [12] and, where appropriate, the R -matrix results [13] are overlaid. The range given for each calculation corresponds to the limits of unpolarized and completely polarized emission. The experimental error bars correspond to Poisson statistics.

- Phillips, K. J. H. *et al.*, *Astron. Astrophys.* **324**, 381 (1997).
- Bhatia, A. K. and Kastner, S. O., *Astrophys. J.* **516**, 482 (1999).
- Feldman, U., private communication.
- Liedahl, D. A. *et al.*, *Astrophys. J.* **350**, L37 (1990).
- Bhatia, A. K. and Doschek, G. A., *At. Data Nucl. Data Tables* **52**, 1 (1992).
- Mohan, M., Sharma, R. and Eissner, W., *Astrophys. J. Suppl.* **108**, 389 (1997).
- Brown, G. V., Beiersdorfer, P., Liedahl, D. A., Widman, K. and Kahn, S. M., *Astrophys. J.* **502**, 1015 (1998).

| on-surface interactions

A beam line for highly charged ions

A. I. Pikin,^{a)} C. A. Morgan,^{b)} E. W. Bell,^{c)} L. P. Ratliff, D. A. Church,^{b)} and J. D. Gillaspay
*Atomic Physics Division, National Institute of Standards and Technology, Gaithersburg, Maryland
20899*

(Received 13 March 1996; accepted for publication 8 April 1996)

The design and operation of a beam line for transporting and charge-to-mass selecting highly charged ions extracted from the National Institute of Standards and Technology electron beam ion trap (EBIT) are described. This beam line greatly extends the range of experiments possible at this facility. Using the transport system, pure beams of low-energy, highly charged ions up to Xe^{44+} have been produced with substantially higher fluxes than previously reported from an EBIT source. Design choices and computer modeling for the various components of the beam line are explained in detail. © 1996 American Institute of Physics. [S0034-6748(96)03907-X]

I. INTRODUCTION

Many areas of science, including controlled nuclear magnetic fusion research, x-ray lasers, and astrophysics, have driven the need to study plasmas of highly charged ions as well as plasma-surface interactions. The description and modeling of natural and manmade plasmas require detailed information on the processes occurring within the plasma. In recent years, the growing need for atomic physics data for highly charged ions has fostered innovation in the ways that such data are gathered. The advent of the electron beam ion trap (EBIT) at Lawrence Livermore National Laboratory (LLNL) in 1986¹ provided a versatile new instrument for the study of trapped highly charged ions. A successor to the electron beam ion source,² the EBIT is a smaller device whose performance in producing the highest charged ions (up to $q=92+$)³ has greatly exceeded its predecessor.

The original EBIT design is well suited for experiments that study processes that can be measured *in situ*. Data for experiments in electron-ion collisions that are readily measurable by this device include cross sections for dielectronic recombination,⁴ electron-impact excitation,³ and ionization.⁵ A great number of other experiments, however, require the ions to be extracted from the trap. One such class of experiments is the study of ion-surface interactions, including the investigation of surface damage, electron emission, and x-ray emission.^{6,7} Ion-gas interactions such as charge exchange and recoil-ion experiments may be studied as well.⁸ Another important class of experiments involves recapturing ions into secondary ion traps for atomic physics experiments, which cannot be done in the presence of the EBIT electron beam (long excited-state lifetime measurements,⁹ cold ion dynamics studies,^{8,10} and precision mass measurements,¹¹ for example). For many of these types of experiments, data for highly charged ions are very sparse or nonexistent. Finally, extracted ions may also be used to reveal important information about the conditions inside the EBIT¹² and, therefore, provide complementary information for spectroscopic stud-

ies being performed on ions trapped in the EBIT. Clearly, a system to extract and transport ions created in an EBIT broadens the scope of the work that can be done with the device.

The first EBIT ion beam line was constructed and demonstrated at LLNL over five years ago,¹³ however, the published descriptions of this system are not sufficiently detailed to allow it to be reproduced. The EBIT beam line at the National Institute of Standards and Technology (NIST) is the second such system to come into operation worldwide, and the present article describes it in full detail. The design of the system described here was based on extensive computer modeling and therefore embodies different design details for the individual ion-optical elements, as well as a different overall layout of the positions of the components with respect to each other. The main general requirements were to charge-to-mass select the ion beam and to maximize the amount of the beam transported to the experimental chamber while keeping distortions in the beam to a minimum. The resulting beam line is highly efficient and transports essentially all the ions extracted from the EBIT either continuously or in a pulsed mode, over a wide range of pulse lengths.

Detailed descriptions of the operating principles of our EBIT have been provided elsewhere,¹⁴ so only a brief overview as it relates to operation as an ion source is presented here. The EBIT operates by trapping and ionizing any species of atomic ion in the space charge of an intense electron beam and a high magnetic field. The operating parameters of the EBIT can be tuned to maximize the number of trapped ions in any desired charge state or range of charge states. Ions can be extracted from the trap into the beam line continuously or in pulses, typically 50 μs to 100 ms wide. Extracted ions with kinetic energies in the range 3 to 12 kV per charge have been studied, but both limits can be extended.

II. BEAM LINE

A. Overview

A schematic of the beam line for the NIST EBIT is depicted in Fig. 1 and some of the typical operating parameters for the various elements are listed in Table I. Figure 2 shows the configuration of the ion-optical elements in the beam line. Constrained by the geometry of the EBIT and the

^{a)}Permanent address: University of Maryland, College Park, MD 20742.

^{b)}Permanent address: Physics Department, Texas A&M University, College Station, TX 77843-4242.

^{c)}Permanent address: JILA, University of Colorado and National Institute of Standards and Technology, Boulder, CO 80309-0440.

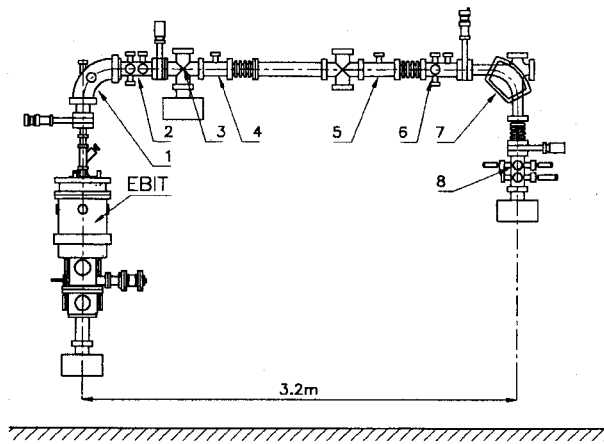


FIG. 1. Schematic view of the exterior of the beam line. Locations of ion optical elements are indicated by numbers (see Table I).

layout of the laboratory, the beam line extends up to the ceiling, across the laboratory, and back down into a second experimental area 3.2 m from the EBIT. The ions emerge vertically from the EBIT near the ceiling of the laboratory, so the first element in the beam line is a 90° electrostatic bender. Two pairs of electrostatic deflectors used for steering and alignment of the beam are located just after the electrostatic bender. Two einzel lenses are employed both to prevent the beam from diverging as it travels across the room to the experimental area and to focus the beam at the object plane of the charge-to-mass analyzing magnet. At this focus, a four-jaw slit defines the entrance of the magnet. A second four-jaw slit is placed at the image plane of the magnet, defining the exit of the analyzer. Two Faraday cups mounted on motion feedthroughs are used to monitor the beam current

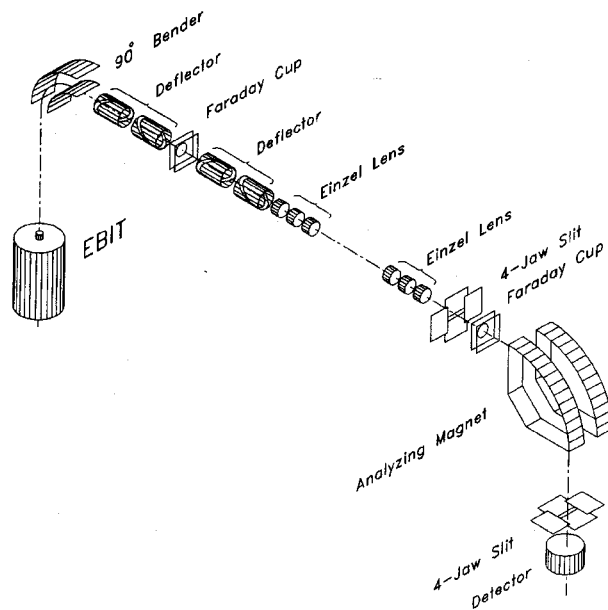


FIG. 2. Schematic view of the interior of the beam line.

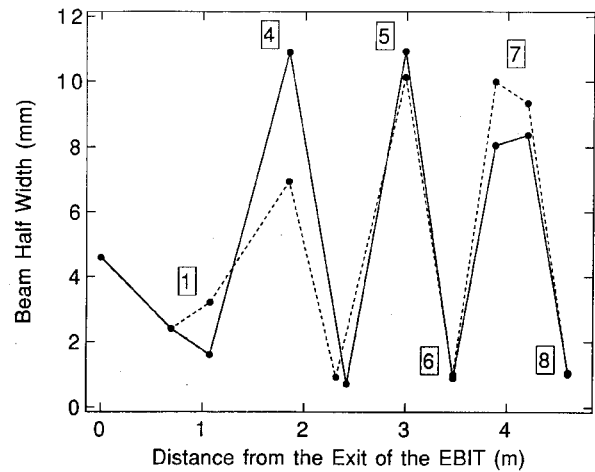


FIG. 3. Example of TRANSPORT modeling showing the radius of the beam as a function of distance from the exit of the EBIT (computed widths are indicated by points). The solid line connecting the points represents the beam half width in the vertical direction and the dashed line represents the beam half width in the horizontal direction. Locations of ion optical elements are indicated by numbers (see Table I).

at positions after the first electrostatic deflector and after the magnet entrance slit.

The entire system is fabricated from ultrahigh vacuum compatible materials. Vacuum pumps maintain a pressure in the beam line of about 10^{-6} Pa (10^{-8} Torr) or better, after baking the system to 100 °C. This level of vacuum is sufficient to prevent significant losses to the ion beam from charge-exchange collisions with residual gas in the beam line.

B. Computer modeling

The beam line was designed with the aid of two computer modeling programs. TRANSPORT¹⁵ is a program that uses matrix multiplication to determine the size and divergence of an ion beam as it travels through various drift spaces and ion-optical elements in the beam line. It is useful for studying the beam line as a whole, but does not take aberrations such as fringing fields into account. The rough positioning of the elements was determined with TRANSPORT. Figure 3 shows the results of a calculation for the beam line design. The points represent the calculated radius of the ion beam in the two transverse directions taken at several positions along the beam line (the boxed numbers in the figure correspond to the positions of the optical elements listed in Table I). The points are connected by a solid line for the radius of the beam in the vertical direction and by a dashed line for the radius in the horizontal direction. The lines represent interpolated (not calculated) beam radii. This particular example predicts a beam with a spot size approximately 2 mm in diameter at the exit slit of the magnet.

The second modeling program, SIMION,¹⁶ is a commonly used ray tracing program that allows the description of individual elements in either cylindrically symmetric or planar geometries. The electrodes are user defined on a grid, the potentials are calculated using numerical relaxation methods,

TABLE I. Typical operating parameters for the beam line for 7.6 keV per charge Xe⁴⁴⁺. The position of each element in Fig. 1 is indicated in the first column.

Element No.	Description	Typical value
1	Electrostatic bender	1.3 kV
2	First electrostatic deflector	-100 to +100 V
3	Second electrostatic deflector	-100 to +100 V
4	First einzel lens	1.9 kV
5	Second einzel lens	2.4 kV
6	Magnet entrance slit	2 mm
7	Analyzing magnet	0.11 T
8	Magnet exit slit	3 mm

and voltage contours and ion trajectories are computed. Because each element is defined by the user in detail, the full effect of distortions introduced in the ion beam by the electrodes is taken into account. SIMION is a two dimensional program, so it is capable of modeling elements that do not contain a mixture of planar and cylindrical geometries, such as the einzel lenses and the electrostatic bender. However, the electrostatic deflectors cannot be described using such simple geometries, thus, they cannot be modeled adequately by SIMION. Using SIMION to model the entire beam line would be impractical; however, it was extremely useful for the optimization of the design for individual elements.

C. Beam line elements

1. Electrostatic bender

The electrostatic bender is used to deflect the ion beam through 90° and cannot be used for charge-to-mass selection in the present beam line. The bender is shown in Fig. 4 and consists simply of two parallel plates that are bent through 90° and operated at equal and opposite voltages. Located just above the EBIT, the bender employs relatively large electrodes to increase the acceptance of ions from the EBIT. The plates are 10 cm wide and have radii of curvature of 22 cm for the inner electrode and 26 cm for the outer electrode. This bender, which is housed in an elbow with an inner diameter (i.d.) of 15 cm, is the only element of the beam line that is not in a 10-cm-i.d. chamber. A 1.3-cm-diam aperture in the outer electrode allows direct transmission of ions when the bender is held at ground potential. This aperture is covered by a 90% transmission mesh to obviate dis-

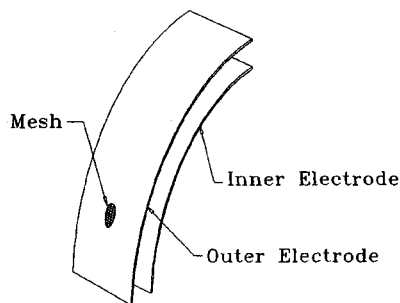


FIG. 4. Schematic view of the 90° electrostatic bender.

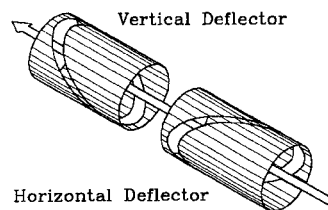


FIG. 5. Schematic view of one of the electrostatic deflectors. The deflector consists of two pairs of electrodes that steer the beam in the vertical and horizontal directions.

tortions in the electric field of the bender caused by the break in the electrode. The outer electrode can also be used as a Faraday cup to monitor the ion flux from the EBIT.

2. Electrostatic deflectors

For small-angle steering of the beam, electrostatic deflectors made from pairs of obliquely cut cylindrical electrodes are used. Figure 5 demonstrates the general design of one such deflector. Each electrostatic deflector consists of two pairs of electrodes rotated in the azimuthal direction by 90° with respect to each other, in order to provide steering of the ion beam in the horizontal and vertical directions. In each electrostatic deflector, the horizontal and vertical deflectors are separated by about 5 mm, but this is not a critical dimension. The cut-electrode pairs are each 8.1 cm long, have an inner diameter of 3.8 cm, and are cut at a 32° angle. In each pair, the electrodes are separated by approximately 2 mm and are operated with voltages of opposite polarities. Each electrode is operated with an independent power supply. In the beam line, two deflectors (eight electrodes total) are placed in series in order to provide the capability for arbitrary offset of the ion beam in both position and angle.

Electrodes of this basic design are widely used for measuring the transverse shift of beams in accelerators and beam lines.¹⁷ To our knowledge, the reversed application described here (in which the electrodes are used for precise and relatively distortion-free deflection of the ion beam) is not widely known or reported in the literature, although it has been used for beam line control at least once before.¹⁸ The most significant advantage of this design over deflectors with planar symmetry is the minimization of the effects of fringing fields on the ion beam, so the ion beam is not adversely affected by traveling through the deflector. Furthermore, the cylindrical nature of the design uses most of the internal volume of vacuum chamber, allowing the largest possible inner diameter for the electrodes. A deflector of this design can also be used as a focusing element by applying a voltage offset to both elements.

3. Einzel lenses

To aid in the focusing and transport of the ions, two identical einzel lenses are situated along the beam line. The design of these lenses was determined by a compromise between minimizing distortion to the ion beam as it passes through the lens (this would demand a large inner diameter of the lens) and a requirement that the voltage on the central

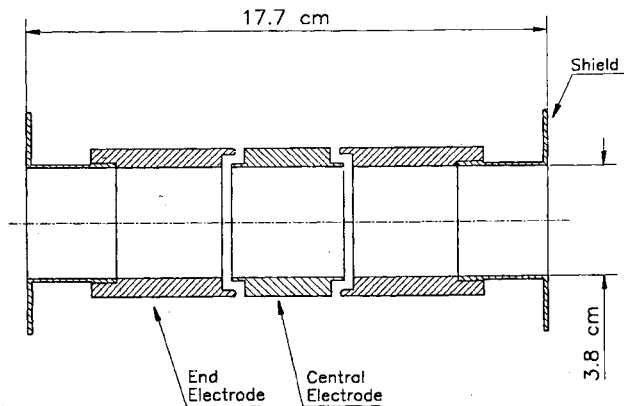


FIG. 6. Schematic view of one of the einzel lenses.

electrode not exceed 5 kV for the desired focusing properties (this would favor a lens with a small inner diameter). Figure 6 shows the geometry of the lenses. Each of these lenses consists of three cylindrical elements with inner diameters of 3.8 cm and central electrodes 3.8 cm long. There are shields on the ends of the outer electrodes that prevent the insulating material used to mount the lenses from charging due to stray ions. The shields are also used as Faraday cups during the initial tuning of the ion beam.

Each einzel lens is operated with positive voltage on the central electrode and the end electrodes grounded. Negative voltage will also focus the ion beam, but to get the same focusing, the voltage must be significantly higher.¹⁹

4. Analyzing magnet

Before the analyzing magnet, the beam line transports an ion beam containing all charge states of all ions extracted from the EBIT. The analyzing magnet is used to separate out ions with the desired charge-to-mass ratio and transport them to the experimental chamber. The magnet is used as the second 90° bend in the beam line, rather than the first, so that the beam can be properly aligned and focused for optimal performance of the magnet. The magnet for the present beam line is of a double focusing dipole design²⁰ with a nominal bending radius of 20.3 cm. It accepts a beam that is focused to a point by the einzel lens before the magnet (the object plane) and then focuses it in two dimensions to a point after the magnet (the image plane). Under typical operating conditions, for example, 7.8 kV per charge Xe^{44+} , a current of 55 A is used, yielding a magnetic field of 0.11 T. At the maximum current of our power supply, 240 A, the magnetic field in the gap of the magnet is 0.32 T, which is enough to deflect U^{8+} ions with 8.0 kV per charge of kinetic energy through 90°. In the magnet, the vacuum chamber has a gap of 3 cm in the direction parallel to the field lines. The magnet is operated under computer control and can be used to measure a charge-to-mass spectrum by recording the count rate from a detector, which is located after the image plane, as the field is ramped. The magnetic field can be fixed at a single peak of such a spectrum for experiments involving a single charge-to-mass selected state.

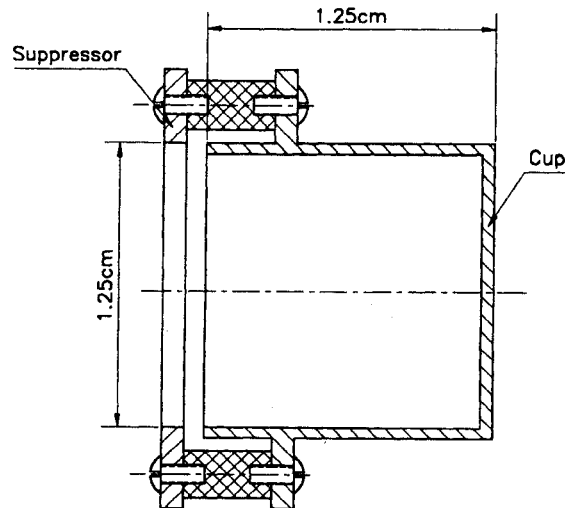


FIG. 7. Schematic view of one of the Faraday cups and suppressor electrode.

At the object and image planes of the magnet are four-jaw slits, adjustable apertures that consist of four knife-edged copper plates that can be independently adjusted with linear motion feedthroughs. This configuration allows the definition of a rectangular aperture with arbitrary dimensions and position. Typically, the entrance slit is set to about 2 mm in the direction perpendicular to the field lines of the analyzing magnet. With proper tuning of the ion beam, this width is sufficient to allow over 90% of the incident ion beam through the slit.

5. Ion detectors

There are two identical Faraday cups in the horizontal part of the beam line, shown schematically in Fig. 7. The first is located after the first electrostatic 90° bend, between the two sets of electrostatic deflectors, and the other is located in the object plane of the magnet after the four-jaw slit. The Faraday cups have apertures 1.25 cm in diameter and have electrodes that suppress secondary electrons created during ion collection. A -30 V bias applied to these electrodes is sufficient to suppress the secondary electrons. Both Faraday cups are mounted on linear motion feedthroughs and can be inserted and removed from the ion path. Analog signals from the Faraday cups are observed using an oscilloscope after amplifying the signal with a current amplifier using a typical gain of 10^7 V/A. These Faraday cups are mainly used for rough alignment of the ion beam, but they are also very useful for diagnosing the ion extraction and transport efficiency.

After the exit slit of the analyzing magnet, an electron multiplier detector²¹ with a 2-cm-diam active area is mounted on a linear motion feedthrough. The detector is usually operated in pulse counting mode, but it can also be used as a Faraday cup to monitor the ion current under high flux conditions. A pulse height distribution from the multiplier for a beam of Xe^{44+} ions is presented in Fig. 8. The inset in the figure shows the shape of a single pulse from the detec-

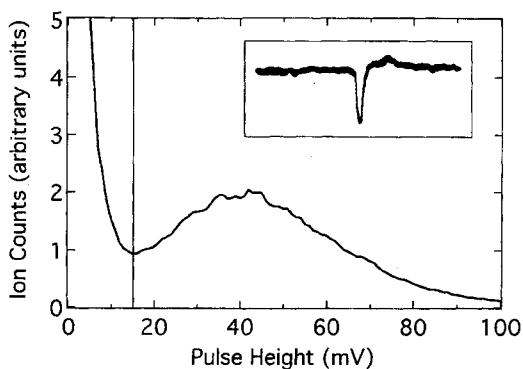


FIG. 8. Example of a pulse height distribution of signal pulses from the electron multiplier used to characterize the beam line performance. The discriminator setting for the detector was 15 mV (shown by the solid line). The inset shows the shape of a single pulse from the detector.

tor. By setting the discriminator level to 15 mV (shown by the vertical line in the figure), most of the background is cut off while most of the signal is retained.

D. Ion beam tuning and voltage scaling

When ions are extracted from their trapped position inside the core of the EBIT (which is held at a potential U), they gain a kinetic energy qU . The velocity of any ion extracted into a field-free region will, therefore, be proportional to the square root of the charge-to-mass ratio (q/m) and the square root of U , resulting in a beam of several different velocities corresponding to the various q/m values. Electrostatic elements will transmit all of these ions because the effect of the increased force on more highly-charged ions will be balanced by the effect of the higher velocities of these ions. Thus, ions with differing velocities will follow the same trajectories through electrostatic elements. Changing the value of U requires linear scaling of all electrostatic elements. These properties are illustrated by the equation determining the potentials $\pm V$ that must be applied to the electrostatic bender plates in order to deflect an ion by 90° , $V = U(s/R)$, where s is the plate separation and R is the radius of curvature of the trajectories.

The situation for an ion in a magnetic field is different. The magnetic field required to deflect an ion by 90° is $B = (l/R)\sqrt{2Um/q}$. Thus, for constant U , all values of q/m will be separated by a magnetic field. Furthermore, if an ion experiences a charge-changing collision with background gas in the horizontal section of the beam line, the ion will be transported through the magnet at a different magnetic field and will not contaminate the parent line in the mass spectrum. When changing the accelerating potential, the magnetic field must be scaled by the square root of U .

III. BEAM LINE PERFORMANCE

Ion beams of several highly charged ion species have been transported through the beam line and into the experimental chamber after the analyzing magnet. Measurements

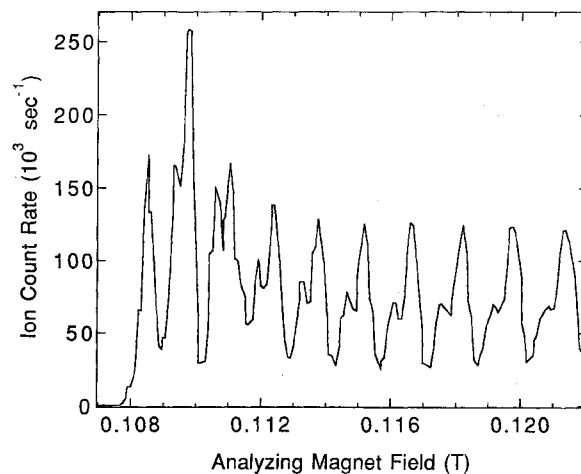


FIG. 9. Mass spectrum of xenon ions with a magnet entrance slit of 2 mm.

comparing the signal detected at the two Faraday cups and on the electrostatic bender indicate that essentially the entire beam is transported to the analyzing magnet.

Figure 9 shows a charge-to-mass scan for 7.8 kV per charge Xe ions with the EBIT operated in a continuous-extraction mode. The entrance slit for this scan was 2 mm and the spot size on the detector was about 3 mm in diameter. The number of ions in the peak with the most counts is about 250 000 ions per second, assuming a detector efficiency of 100%. The total integrated ion flux for the 19 charge-to-mass peaks in the spectrum is 2 500 000 ions per second. For ions extracted under the same conditions except in pulsed mode with a repetition rate of 3 Hz and a pulse length of 10 ms, the largest peak has about 70 000 counts per pulse, corresponding to a peak flux of over 200 000 ions per second of a single charge-to-mass selected value. We observe, therefore, high and approximately equal time-averaged extraction fluxes in both pulsed and continuous modes of operation, in contrast to the behavior reported by LLNL¹³ in which the continuous mode of operation was observed to be ten times less efficient than the pulsed mode. We note also that our overall flux values are substantially higher than reported in the earlier studies,^{6,13} even when we assume a detection efficiency of 100% rather than the 50%–60% assumed in the previous studies.¹³

Note that while most of the different charge states are separated in Fig. 9, the signal from several isotopes of the same charge state is not resolved. Xenon has several stable isotopes (three of which have natural abundances greater than 20%) and, since we use xenon with a natural abundance of isotopes, the spectrum is a convolution of a range of charge states and all the stable isotopes. The highest peak in Fig. 9 actually results from a mixture of two ions, $^{132}\text{Xe}^{44+}$ and $^{129}\text{Xe}^{43+}$. The highest continuous count rate for a pure peak ($^{129}\text{Xe}^{44+}$) is about 180 000 per second.

Figure 10 displays part of another charge-to-mass scan for 7.8 kV per charge Xe ions taken with similar operating conditions. For this scan, the entrance slit was reduced to 0.5 mm in order to improve the resolution. There is a small shift in the positions of the peaks compared with Fig. 9 because of

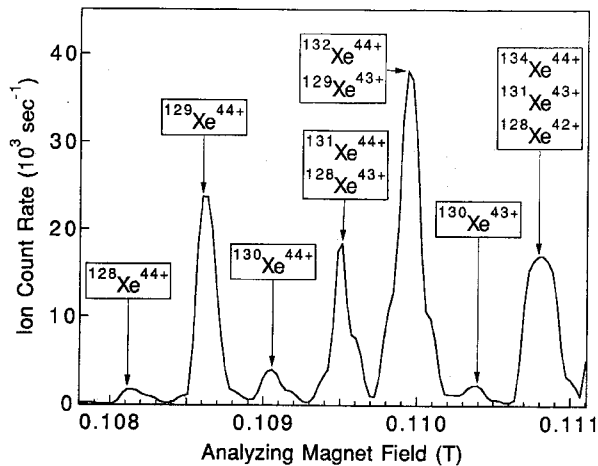


FIG. 10. Mass spectrum of Xe ions with a magnet entrance slit of 0.5 mm.

slightly different beam tuning. In Fig. 10 many isotopes are clearly separated, even for the highest charge states. The signals from some isotopes of ions are still overlapping, however. For example, $^{132}\text{Xe}^{44+}$ and $^{129}\text{Xe}^{43+}$ have virtually the same charge-to-mass ratio ($q/m \approx 1/3$), and, thus, cannot be resolved with a conventional mass-analyzer. Clearly, in the case of xenon, it would be advantageous to use isotopically enriched gas for the production of the ion beam. This would increase the signal for a particular line and greatly simplify the structure of the mass spectrum.

IV. CONCLUSION

An efficient beam line for the transport and mass selection of highly charged ions from the NIST EBIT has been constructed and is now in use. This addition greatly increases the range of experiments now possible at the NIST EBIT facility. The beam line incorporates design features never before used with an EBIT, in order to transport ions virtually without loss to an analyzing magnet that is capable of resolving isotopes of most ions and charge states. The beam line can presently deliver into a spot 3 mm in diameter a continuous beam of over 200 000 charge-to-mass selected highly charged ions (Xe^{44+}) per second, a value that exceeds previously reported continuous values^{6,13} by several orders of magnitude. The system has also been operated with pulsed beams (70 000 ions per pulse, 10 ms pulse length, 3 Hz repetition rates) to boost the instantaneous flux by another factor of 35 while maintaining a similar time-averaged value.

ACKNOWLEDGMENTS

The authors would like to thank Professor Robert Tribble for assisting us with the TRANSPORT code. We also thank D. Alderson for his technical assistance.

- ¹M. A. Levine, R. E. Marrs, J. R. Henderson, D. A. Knapp, and M. B. Schneider, *Phys. Scr. T* **22**, 157 (1988).
- ²E. D. Donets, V. I. Ilyuschenko, and V. A. Alpert, Preprint, Joint Institute for Nuclear Research, R7-4124, Dubna (1968); E. D. Donets, *Phys. Scr. T* **3**, 11 (1983).
- ³R. E. Marrs, S. R. Elliot, and D. A. Knapp, *Phys. Rev. Lett.* **72**, 4082 (1994).
- ⁴P. Beiersdorfer, T. W. Phillips, K. L. Wong, R. E. Marrs, and D. A. Vogel, *Phys. Rev. A* **46**, 3812 (1992).
- ⁵S. Chantrenne, P. Beiersdorfer, R. Cauble, and M. B. Schneider, *Phys. Rev. Lett.* **69**, 265 (1992).
- ⁶D. H. Schneider, M. A. Briere, J. McDonald, and J. Biersack, *Radiat. Eff. Defects Solids* **127**, 113 (1993).
- ⁷D. C. Parks, R. Bastasz, R. W. Schmieder, and M. Stöckli, *J. Vac. Sci. Technol. B* **13**, 941 (1995).
- ⁸D. A. Church, *Nucl. Instrum. Methods B* **53**, 504 (1991).
- ⁹D. A. Church, *Phys. Rep.* **228**, 253 (1993).
- ¹⁰Joseph N. Tan, J. J. Bollinger, B. Jelenkovic, and D. J. Wineland, *Phys. Rev. Lett.* (in press).
- ¹¹C. Carlberg, I. Bergström, G. Bollen, H. Borgenstrand, R. Jertz, H.-J. Kluge, G. Rouleau, R. Schuch, T. Schwartz, L. Schweikhard, P. Senne, and F. Söderberg, *IEEE Trans. Instrum. Meas.* **44**, 553 (1995).
- ¹²D. R. DeWitt, D. Schneider, M. W. Clark, M. H. Chen, and D. Church, *Phys. Rev. A* **44**, 7185 (1991).
- ¹³D. Schneider, D. DeWitt, M. W. Clark, R. Schuch, C. L. Cocke, R. Schmieder, K. J. Reed, M. H. Chen, R. E. Marrs, M. Levine, and R. Fortner, *Phys. Rev. A* **42**, 3889 (1990).
- ¹⁴J. D. Gillaspay, Proceedings of the 6th International Symposium on Electron Beam Ion Sources and Their Applications, Stockholm, 1994 [*Phys. Scr.* (submitted)].
- ¹⁵K. L. Brown, F. Rothacker, D. C. Carey, and Ch. Iselin, "TRANSPORT—A Computer Program for Designing Charged Particle Beam Transport Systems" (CERN 80-04, European Organization for Nuclear Research, Geneva, 1980); D. C. Carey "New Features in TRANSPORT" (Fermilab, TM-1064, Batavia, IL 1981).
- ¹⁶D. A. Dahl and J. E. Delmore, EGG Publication No. EGG-CS-7233, Rev. 2, April 1988, Idaho National Engineering Laboratory, EG&G Idaho, P.O. Box 1625, Idaho Falls, ID 83415.
- ¹⁷L. L. Gol'din and A. A. Kuz'min, *Instrum. Exp. Tech. (USSR)* **10**, 251 (1967).
- ¹⁸K. K. Onosovskiy (private communication).
- ¹⁹For a discussion of the focusing properties of einzel lenses, see E. Harting and F. H. Read, *Electrostatic Lenses* (Elsevier, New York, 1976).
- ²⁰R. W. Schmieder (private communication).
- ²¹Hamamatsu Model R2362 electron multiplier. Certain commercial equipment, instruments, or materials are identified in this article in order to specify the experimental procedure adequately. Such identification is not intended to imply recommendation or endorsement by the National Institute of Standards and Technology, nor is it intended to imply that the materials or equipment identified are necessarily the best available for the purpose.

Continuous highly charged ion beams from the National Institute of Standards and Technology electron-beam ion trap

L. P. Ratliff, E. W. Bell,^{a)} D. C. Parks, A. I. Pikin,^{b)} and J. D. Gillaspay
Atomic Physics Division, National Institute of Standards and Technology, Gaithersburg, Maryland 20899

(Received 17 December 1996; accepted for publication 20 January 1997)

We describe our newly modified beam line and present its performance in conjunction with the National Institute of Standards and Technology electron-beam ion trap. We find that, contrary to previously reported results from similar ion sources, the highest intensity time-averaged ion fluxes are achieved by letting the ions boil out of the trap in a continuous stream rather than periodically dumping the trap to produce a pulsed beam. We produced continuous beams of $3.0(6) \times 10^6$ Xe⁴⁴⁺ ions per second and lower flux beams of charge states up to Xe⁴⁹⁺. Also, in pulsed mode, we created beams with very high peak flux, over 10^{10} Xe⁴⁴⁺ ions per second. [S0034-6748(97)01005-8]

I. INTRODUCTION

The electron-beam ion trap (EBIT)¹ is a versatile device that has transformed the study of highly charged ions. Initially, most EBIT experiments involved detecting photons (visible and x ray) emitted from excited, highly charged trapped ions.^{2,3} More recently, the EBIT device has also proven to be useful as a source of highly charged ion beams for use in experiments that study collisions between ions and external solid targets^{4,5} and those that study ions in external traps.⁶

The EBIT and its predecessor, the electron-beam ion source (EBIS),⁷ have been used primarily to produce pulsed beams of very highly charged ions. For some collision experiments, however, the ions in a pulse can arrive undesirably close together. For instance, in a coincidence experiment where two collision products are to be detected and related to a single event, the events must be temporally separated to avoid confusion about which products resulted from a particular event. For such applications, extraction of the ions in a continuous stream is ideal, allowing both the maximum signal and the maximum separation between events. Several groups in the EBIT/EBIS community have made continuous beams of multiply charged light ions: Becker, Kleinod, and Klein⁸ have made continuous beams of Ne⁸⁺ with a flux of 10^6 ions per second and of Ne¹⁰⁺ with a flux of 3000 ions per second. Other groups have seen low current continuous beams of higher charge states: Tawara *et al.*⁹ have made continuous beams of I⁴¹⁺ with a flux of 10^3 ions per second and Schneider *et al.*⁴ have made a continuous beams of Ar¹⁷⁺ and Xe⁴⁴⁺ with a flux of $\sim 2 \times 10^3$ ions/s. Stockli¹⁰ has made quasicontinuous beams of 3×10^6 Ar¹⁷⁺ ions per second (time averaged count rate) with a 50% duty cycle. In this article we report the first demonstration of high continuous fluxes of very highly charged ions using an EBIT/EBIS type source (3×10^6 ions/s of Xe⁴⁴⁺). In addition to the high flux offered by the continuous mode of op-

eration, we also find that this mode is simpler to optimize and more stable than the pulsed mode.

Other experiments require fast pulses of ions that are microseconds long. A prominent example is an experiment in which the ions are produced in an EBIT and then transferred into a secondary penning ion trap specially designed to carry out more detailed studies.⁶ As the pulse length of the ions extracted from the EBIT is decreased, the energy spread of the extracted ions can be expected to increase, thereby making the transported beam more sensitive to chromatic (energy) aberrations in the ion optics and increasing losses. When our system is operated in pulsed mode, however, we find that the losses are significantly less than previously reported.⁶

II. THE ELECTRON BEAM ION TRAP

The details of the National Institute Standards and Technology (NIST) EBIT can be found elsewhere.^{11,12} The trap consists essentially of three cylindrical drift tubes through which a monoenergetic, magnetically confined electron beam travels. The electron beam ionizes gas atoms (xenon in the present work) which are injected into the drift tubes. These ions are then trapped in the radial direction by the space charge of the electron beam and by the magnetic field. To trap the ions in the axial direction, the upper and lower drift tubes are held at a higher potential than the center drift tube, forming an electrostatic well. The base pressure is 10^{-8} Pa (10^{-10} Torr). Highly charged ions are created by successive electron impact of the lower charged ions. The charge state distribution in the trap can be adjusted by changing the injected gas flow, the electron-beam energy, and other voltages and magnetic fields that control the EBIT.

The electron beam is created by a commercial three element electron gun located 16 cm below the center of the trap. The gun has a barium oxide cathode, and focus and anode electrodes whose potentials are adjusted to optimize the performance of the EBIT. The electron beam leaves the gun, travels through a transition electrode, through the drift tubes, and is stopped inside an electron collector electrode. The transition electrode helps to guide the electron beam through a small hole in the grounded liquid-nitrogen shield.

^{a)}Permanent address: Diamond Semiconductor Group, Gloucester, MA 01930.

^{b)}Permanent address: Brookhaven National Laboratory, Upton, NY 11973.

TABLE I. Typical operating parameters for the NIST EBIT optimized for the production of continuous Xe^{44+} ion beams.

Parameter	Value
Electron-beam current	135 mA
Center drift tube voltage	7.8 keV
Upper drift tube voltage	7.925 kV
Lower drift tube voltage	7.935 kV
Transition voltage	6.20 kV
Suppressor voltage	580 V
Extractor voltage	3.0 kV
Collector voltage	1.40 kV
Bucking magnet current (and field)	17.9 A (12.5 mT)
Focus voltage of electron gun	6 V
Count rate of Xe^{44+}	3×10^6 counts/s

The combination of a positive potential on the electron collector electrode and a magnetic field that cancels the fringing field from the primary trap magnet forces essentially all of the electron beam to hit the collector. A suppressor electrode is located just below the collector to prevent secondary electrons in the collector from traveling back toward the electron gun. Inside the collector, a negatively biased cone called the extractor helps to guide the ions out of the EBIT, while preventing secondary electrons from leaving the collector region. The ions leaving the extractor are focused by an einzel lens before leaving the EBIT. Table I shows the typical EBIT parameters for maximizing the extraction of Xe^{44+} ions.

Upon escape over the upper drift tube of the trap, the ions are accelerated to a kinetic energy of qV_o , where q is the ion charge and V_o is the potential on the upper drift tube. They then travel through a beam line consisting of electrostatic elements that focus and align the beam and a magnet used for charge-to-mass analysis of the beam. The beam line was described in detail in Ref. 13, but has since been modified (see Fig. 1); we have installed three more einzel lenses, a third set of deflectors, and a second electrostatic bender in the vertical part of the beam line (after the analyzing magnet's exit slit). The lenses are of a different design from those reported earlier.¹³ The edges between adjacent elements in the new einzel lenses are rounded (0.8 cm radius of curvature) to minimize spherical aberrations to the beam. In all three lenses, the end electrodes are 1.4 cm long and the center electrode is 2.5 cm long. The lens located below the second electrostatic bender has an inner diameter of 2.5 cm, and the other two lenses have inner diameters of 3.8 cm. The deflectors are identical to those described in Ref. 13. The bender is the same as that described in Ref. 13 except that the radii of the inner and outer plates are 11.5 and 14 cm, respectively, and the plates are 6.1 cm wide. The outer bender plate has a mesh covered hole to allow ion passage when the bender is off, allowing us to switch the beam between two different beam lines. In passing through this mesh, the beam is calculated to be attenuated by approximately 15%. Directly below the bender is a target chamber which is used for ion-surface interaction studies. The data presented here were taken with an electron multiplier located in that chamber after some focusing elements, and with a Faraday cup that can be inserted into the beam directly above

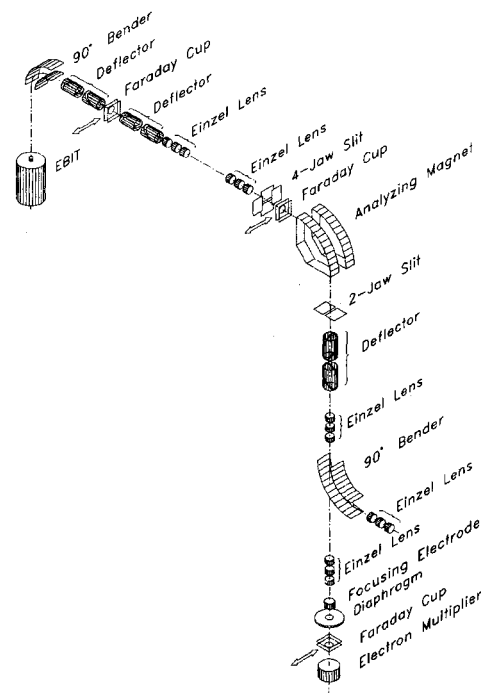


FIG. 1. Schematic of the ion-beam line.

the multiplier. By comparing the electron multiplier to the Faraday cup we determine the multiplier's efficiency to be 50% for Xe^{44+} ions. The composition (charge-to-mass ratio) of the beam is measured by ramping the analyzing magnet and observing the transported ion signal on the electron multiplier. Once the beam line voltages are optimized, they typically require very little adjustment when changing the ion species or charge state. The voltages on the ion optical elements must be scaled with the ion energy, however, when the EBIT is readjusted to emit ions with a different velocity.¹³

Small external magnetic field coils located near the center drift tube of the trap (perpendicular to the primary magnet coils) are used to deflect the electron beam slightly. The electrodes inside the EBIT were aligned during assembly to be coaxial to an accuracy of approximately $50 \mu\text{m}$, except for the extractor which may be off axis by several times that amount. The steering coils might make it possible to partially compensate for the misalignment in the extractor. It is observed that adjusting the steering coils does greatly increase the transmitted ion-beam current.

Another parameter that is important is the magnetic field produced by the bucking coil that surrounds the electron gun. This field is used to adjust the residual magnetic field near the electron gun, so that the electron beam is formed at the optimum field, believed to be a few hundred μT (a few G).¹⁴ Very small changes in this field ($<0.5\%$) can cause a change in the transported beam flux of a factor of 10 or more.

III. PULSED EXTRACTION

The standard way to extract beams from EBIT and EBIS devices is a pulsed mode, whereby all of the ions in the trap

TABLE II. Pulse widths, peaks currents, and time-averaged currents for pulses extracted with different ramp times.

Ion	Ramp time (μ s)	FWHM ^a (μ s)	Peak current (nA)	Time-averaged current (pA)
Ar ¹⁷⁺	5	12	15	0.26
Ar ¹⁷⁺	20	13	26	0.7
Ar ¹⁷⁺	120	20	16	0.6
Ar ¹⁷⁺	5000	1000	1.1	2.2
Ar ¹⁷⁺	20 000	4000	0.3	2.4
Xe ⁴⁴⁺	11	12	75	1.8
Xe ⁴⁴⁺	22	18	130	4.6
Xe ⁴⁴⁺	120	28	92	5.2
Xe ⁴⁴⁺	10 000	2800	1.7	9.6

^aFull width at half-maximum.

are periodically released into the beam line by raising the potential of the center drift tube above that of the upper drift tube. This causes the ions to be ejected from the trap axially into the beam line. The upper drift tube is held at a lower potential than the lower drift tube, so that all of the ions escape over the upper drift tube into the beam line. After the trap is dumped and the center drift tube is lowered, the charge state distribution is rebuilt. For maximum current, the center drift tube is ramped to its maximum voltage in about 20 ms and the ions are ejected in a pulse a few milliseconds wide. For xenon extraction, the trap is usually dumped every 0.3 s to optimize the time-averaged current of the higher charge states.

In experiments where the ions are retrapped into a secondary trap, a fast ramp time (on the order of microseconds) is essential for efficient loading the secondary trap. In practice, the efficiency of the ion-beam extraction and transport are reduced as the pulse length is reduced, perhaps due to an increased energy spread in the extracted ions causing increased aberrations in the ion optics. Table II gives the pulse widths, peak currents and time averaged currents for pulses extracted with different ramp times. These data were taken by first adjusting the beam line and EBIT parameters to optimize the current in continuous mode, then changing to pulsed mode without adjusting anything except the time for ramping the center drift tube to its maximum value. The ion current on the Faraday cup is displayed on an oscilloscope after being amplified with a gain of 10^6 to 10^9 V/A. The amplifier's minimum rise time is 10 μ s which increases the measured width of the shortest pulses, making the measured peak current less than the actual value. Even with this problem, we observe less than a factor of 10 loss in our beam current when the ramp time is reduced from 4 ms to 10 μ s. This is compared to a loss of a factor of 100 when decreasing the extraction time from 400 to 5 μ s in a similar ion source.⁶ Combining our high overall flux with our efficient transport at short extraction times, we have achieved peak currents of over 100 nA of Xe⁴⁴⁺ for 10 μ s ramp times.

We consider the ion trap to be full when the sum of all of the positive ion charges is equal to the negative charge of the electron beam in the trap region. With our operating conditions, there are approximately 5×10^8 electrons in the trap. Comparing the ion current on a Faraday cup before the ana-

lyzing magnet to the current in the Xe⁴⁴⁺ peak after the magnet, and assuming no loss of Xe⁴⁴⁺ in between, we determine that 6% of the charge is in the Xe⁴⁴⁺ peak. This implies that if the ion trap is full, we should observe 10^6 Xe⁴⁴⁺ ions per pulse, which is identical to that obtained from our Faraday cup measurement of 5 pC (10^6 Xe⁴⁴⁺ ions) per pulse. This agreement is somewhat surprising because the calculation is quite crude, however, it illustrates the fact that the pulsed mode has a practical limit in total ion flux per pulse and that, based on trap capacity, we might be near that limit now. In a previous spectroscopic study of the trapped ions in the NIST EBIT,¹⁵ it was determined that the electron beam was approximately 50% space-charge neutralized.

IV. CONTINUOUS EXTRACTION

In the continuous mode of operation, also referred to as leaky mode^{4,10} or dc mode,^{8,16} ions escape the trap by gaining enough energy to pass over the electrostatic barrier at the upper drift tube which is held at a constant potential. The ions gain the required energy through collisions with electrons. Extracted ions are replaced continuously by injected gas atoms.

We have observed a higher time-averaged current of ions in continuous extraction mode than in pulsed mode, even for charge states as high as Xe⁴⁴⁺. The highest single isotope count rate that we have measured is $3.0(6) \times 10^6$ (¹³⁶Xe⁴⁴⁺) ions/s which corresponds to a current of over 20 pA. The uncertainty in these measurements is limited by the accuracy of the Faraday cup. The beam is considerably easier to tune when extracting ions using the continuous mode, because the count rate is more stable than in the pulsed mode. In fact, to get the maximum flux in pulsed mode, we optimize the beam for continuous mode and then switch to pulsed mode without adjusting any of the electrodes.

For some experiments the trap must be dumped periodically, even during continuous extraction, to avoid the buildup of heavy ions in the trap which tend to displace the lighter atoms. The source of the heavy ions can be residual gas atoms, or barium atoms which are continuously given off by the electron gun. This is not important for xenon, but can be significant for lighter atoms, such as neon or argon.

V. MASS SCANS

A mass scan showing the number of transported ions versus the field of the analyzing magnet for continuously extracted ¹³⁶Xe ions with an accelerating potential of 7.8 kV is shown in Fig. 2. The electron-beam current in the EBIT for this scan was 135 mA. The highest peak in the scan is ¹³⁶Xe⁴⁴⁺ at 1130 G.

There appear to be very few low-charge contaminant ions in our beam compared with other beams from similar sources.^{4,10} This may be because our detector efficiency drops from 50% for Xe⁴⁴⁺ to 1% for N⁶⁺. Figure 3 shows a higher-resolution scan for xenon ions obtained by narrowing the slits before and after the analyzing magnet. The double peaks in the scan arise from the 10% ¹³⁴Xe present in the isotopically enriched ¹³⁶Xe seed gas.

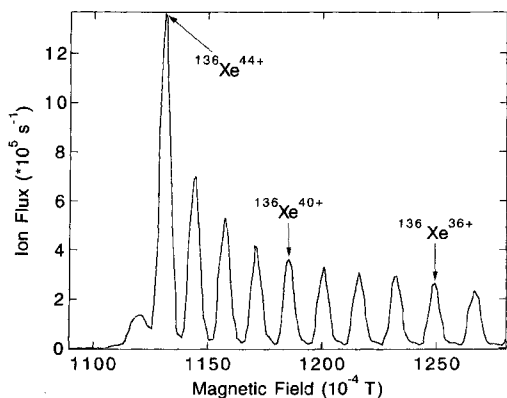


FIG. 2. Mass scan of ^{136}Xe ions from a continuous beam.

There is very little difference in the distribution of charge states in pulsed and continuous operation. This is somewhat surprising because the dynamics of the charge state build up and ion extraction are quite different in the two modes. With the electron-beam energy at approximately 8 keV, the spectrum is peaked at $Q=44$. In contrast to our results, other groups observed a large preference toward lower-charge states in continuous extraction.⁴ In the case of light ions (neon and argon), this preference might be due to a buildup a heavy ions in the EBIT/EBIS suppressing the formation of highly charged lighter ions. This does not explain, however why this effect is seen in the case of heavy ions such as xenon and iodine. In a simple picture, the lower-charge-state ions see a lower potential barrier and are expected to boil out more readily than those with higher charge states.^{10,17} Another factor is the upper drift tube potential that we use in continuous mode, >100 V, is much higher than that (~ 20 V) used by some of the other workers.^{16,17} While the optimal upper drift tube potential must depend on the details of the trapping and extraction dynamics of each machine, the deeper axial well should allow our ions to remain in the trap, interacting with the electron beam, for a longer time.

By increasing the EBIT drift tube potential, charge states

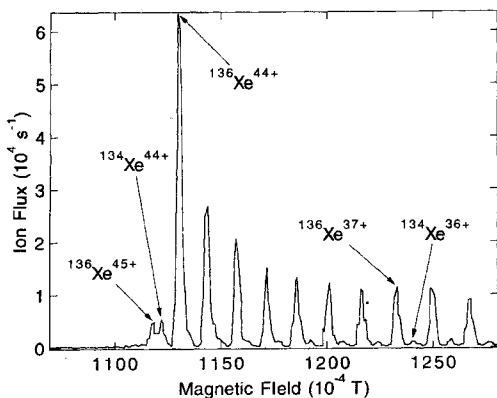


FIG. 3. High-resolution scan of xenon ions. The resolution was increased over that in Fig. 2 by narrowing the analyzing magnet's entrance and exit slits. The small peaks are due to the $\sim 10\%$ ^{134}Xe in our enriched ^{136}Xe sample.

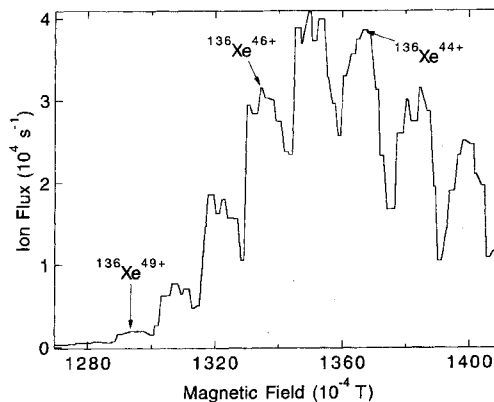


FIG. 4. Mass scan of xenon ions at an electron energy of 11.6 keV. The largest peak is $^{136}\text{Xe}^{45+}$, and charge states up to $Q=49$ can now be seen.

up to Xe^{49+} have been produced in significant quantities. Figure 4 shows a mass scan of xenon ions extracted continuously from the EBIT at 11.5 keV/ q (the drift tube voltage is 11.5 kV). The Xe^{44+} peak is still nearly the largest, but we now measure almost 10 000 counts per second of Xe^{48+} . Presumably, we could increase our production of higher charge states by increasing the drift tube voltage, but we would have to lower it just before extraction since some of the power supplies on our beam line are at their present limits with an 11.5 keV/ q beam.

VI. DISCUSSION

We have demonstrated that it is possible to maximize the production of highly charged ion beams from an EBIT source using a continuous extraction technique. In this way, we have created the highest-flux Xe^{44+} beam reported from this type of ion source. Contrary to previous results and predictions, our continuous extraction mode produces a similar distribution of charge states to that produced in pulsed mode. Finally, we have shown that we can extract the ions in fast pulses without the heavy losses previously seen by other groups. The improved performance of our system compared to other systems was verified with an independent set of ion detectors and electronics in a collaborative experiment carried out with scientists from the Livermore EBIT group.¹⁸ We attribute the performance of our system to ion optics that are less subject to aberrations than those in use elsewhere.

¹M. A. Levine, R. E. Marrs, J. R. Henderson, D. A. Knapp, and M. B. Schneider, Phys. Scr. **T22**, 157 (1988).

²P. Beirsdorfer, G. V. Brown, J. Crespo López-Urrutia, V. Decaux, S. R. Elliott, D. W. Savin, A. J. Smith, G. S. Stefanelli, K. Widmann, and K. L. Wong, Hyperfine Interact. **99**, 203 (1996).

³J. D. Gillaspay, Phys. Scr. **T65**, 168 (1996).

⁴D. Schneider, D. Dewitt, M. W. Clark, R. Schuch, C. L. Cocke, R. Schmieder, K. J. Reed, M. H. Chen, R. E. Marrs, M. Levine, and R. Fortner, Phys. Rev. A **42**, 3889 (1990).

⁵D. H. G. Schneider and M. A. Briere, Phys. Scr. **53**, 228 (1996).

⁶D. Schneider, D. A. Church, G. Weinberg, J. Steiger, B. Beck, J. McDonald, E. Magee, and D. Knapp, Rev. Sci. Instrum. **65**, 3472 (1994).

⁷E. D. Donets, in *The Physics and Technology of Ion Sources*, edited by I. G. Brown (Wiley, New York, 1989), p. 245.

⁸R. Becker, M. Kleinod, and H. Klein, Nucl. Instrum. Methods Phys. Res. **B 24/25**, 838 (1987).

⁹H. Tarawa, T. Iwai, Y. Kaneko, M. Kimura, N. Kobayashi, A. Matsumoto,

- S. Ohtani, K. Okuno, S. Takagi, and S. Tsurubuchi, *J. Phys. B* **18**, 337 (1985).
- ¹⁰M. P. Stockli, *Rev. Sci. Instrum.* **67**, 892 (1996).
- ¹¹J. D. Gillaspay, J. R. Roberts, C. M. Brown, and U. Feldman, in *VIIth International Conference on the Physics of Highly Charged Ions*, AIP Conf. Proc. 274, edited by P. Richard, M. Stockli, C. L. Cocke, and C. D. Lin (AIP, New York, 1993), p. 682.
- ¹²J. D. Gillaspay, *Phys. Scr.* (to be published).
- ¹³A. I. Pikin, C. A. Morgan, E. W. Bell, L. P. Ratliff, D. A. Church, and J. D. Gillaspay, *Rev. Sci. Instrum.* **67**, 2528 (1996).
- ¹⁴E. Takács, E. S. Meyer, J. D. Gillaspay, J. R. Roberts, C. T. Chantler, L. T. Hudson, R. D. Deslattes, C. M. Brown, J. M. Laming, J. Dubau, and M. K. Inal, *Phys. Rev. A* **54**, 1342 (1996).
- ¹⁵C. A. Morgan, F. G. Serpa, E. Takács, E. S. Meyer, J. D. Gillaspay, J. Sugar, J. R. Roberts, C. M. Brown, and U. Feldman, *Phys. Rev. Lett.* **74**, 1716 (1996). The electron beam energy shown in Fig. 4 of this reference includes a 70 eV space-charge shift at 2.026 keV beam energy, obtained by assuming a 50% neutralization of the full space-charge correction predicted by a simple model. This shift is required in order to make the peak positions agree with accurate calculations of the atomic ionization energies.
- ¹⁶M. Kleinod, R. Becker, J. Dietrich, G. Isaia, H. Klein, A. Lakatos, B. Pfisterer, and H. Thomae, in *Proceedings of the 5th International Symposium on Electron Beam Ion Sources and their Applications*, edited by E. Donets and I. P. Yudin (Joint Institute for Nuclear Research, Dubna, Russia, 1992), p. 64.
- ¹⁷R. W. Schmieder, in *Physics of Highly Ionized Atoms*, edited by Richard Marrus (Plenum, New York, 1989).
- ¹⁸J. McDonald and J. Steiger (unpublished).



ELSEVIER

X-ray emission for 3–137 keV Ar¹⁷⁺ impacting SiO₂

E. Takács^{a,*}, Z. Ónodi-Szűcs^a, L.P. Ratliff^b, J.D. Gillaspay^b, J. Pálinkás^a^a Experimental Physics Department, Kossuth University, Bem tér 18 / a, Debrecen, Hungary^b Atomic Physics Division, National Institute of Standards and Technology, Gaithersburg, MD 20899, USA

Abstract

We report X-ray spectra from Ar¹⁷⁺ impacting a SiO₂ surface at 30° from normal incidence, for projectile energies ranging from 3 to 137 keV. At the highest energy we see only X-rays from the filling of the argon K shell. As the projectile energy is reduced, these argon X-rays are gradually reduced to zero while a silicon K_α peak appears. We interpret these data to be the result of the onset of a direct transfer of a silicon K-shell electron to the K-shell vacancy in the argon projectile. We suggest that this transfer occurs through an argon–silicon Auger process which takes place during a close collision in the solid. The velocity dependence of this process is not yet fully understood.

1. Introduction

The interaction of slow, highly-charged ions with solid surfaces has become a subject of intense research in recent years. The studies are facilitated by the availability of powerful, compact sources of highly-charged ions: the Electron Cyclotron Resonance Ion Source (ECRIS) [1], the Electron Beam Ion Source (EBIS) [2], and the Electron Beam Ion Trap (EBIT) [3]. The study of these interactions is important for understanding basic collision processes, plasma–wall interaction phenomena, and novel methods of modifying surfaces at nanometer length scales.

Despite considerable progress in characterizing and modeling the interaction of highly charged ions with surfaces during the past few years, there are still a number of critical issues under debate, and the overall understanding is still rather incomplete. Several recent reviews give extensive accounts of the present understanding [4–8]. Although the surfaces and projectiles differ from one experiment to another, the following picture is believed to be quite general. While the ion approaches the surface, still at a large distance (several, or even tens of nanometers, depending on the charge), electrons are transferred from the surface to the high lying levels of the ion until the ion is completely neutralized (“hollow atom” formation). The highly excited states of the projectile relax by various mechanisms such as Auger processes, radiative decay, and perhaps even surface plasmon formation. The stage of relaxation in which the projectile reaches the surface depends not only on its speed and impact angle but also on

the random statistics of the various decay mechanisms. It is widely accepted, however, that even at the lowest impact velocities achievable in the laboratory, the potential energy stored in the ion has not yet been fully transferred onto the surface prior to impact. Specifically, if the projectile originally had inner shell (K, L) vacancies, most of these vacancies are usually carried into the surface. Note that there is a lower limit for the impact velocity due to the interaction of the projectile with its image charge in the case of metals [9]. The situation for insulators is not so clear. In the case of an idealized insulator with no electron flow, localized charging of the surface from a single incident ion can be sufficient to slow down and repel the ion backwards [10]. In an experiment where a normally insulating LiF target was heated to prevent charging, the results were interpreted as evidence that the dielectric response of an insulator can accelerate ions into the surface [11], as in the case of metals. When the ion reaches the surface, the electrons which orbit the nucleus of the projectile at distances larger than the screening length of the solid peel off and are replaced by electrons which, due to the proximity of the surface, can now be captured directly into lower lying energy levels. There are several studies however, which show that even with this process available, the inner shell vacancies of the ions can be preserved in this phase (e.g. Refs. [12–20]). The filling of the L- and K-shell vacancies usually happens at the time of interaction of the ion with the bulk or in some cases after the ion has reflected from the bulk and leaves the solid [20]. It was also pointed out earlier [20] that the slow ion does not penetrate deep into the solid. There is a shallow region below the surface in which the ion can suffer one or more large angle deflections in close encounters with the atoms of the solid and scatter out of the target. In these

* Corresponding author. Fax +36 52 416 181, e-mail etakacs@tigris.klte.hu.

close collisions, electrons can transfer from the tighter bound levels of the target to the unfilled core of the projectile. In a follow-up work Stolterfoht et al. [27] presented a multiple-cascade model for a more complete theoretical analysis of the filling process.

The hydrogen-like argon ion has played an important role in these studies. It was used, for example, in the first experiment where hollow atom formation was shown [12]. Several other milestone experiments used the same ion to shed light on the basic interactions and processes in ion–solid collisions [12–18]. Ar^{17+} ions have a K inner shell vacancy which energetically lies well below the empty L shell (by more than 3 keV) and therefore possesses a large amount of potential energy. If the K hole is filled by a radiative transition from a higher-lying level, a characteristic X-ray is observed. In earlier studies, the mean energy and the structure of the K_α line were investigated to determine the dynamics of the filling of the K, L, and M shells [12–18].

Most of the experiments so far have been carried out with projectile charge states below $Q = 20$, leaving the very highly charged regime ($Q > 30 +$) relatively unexplored [7]. Also, as pointed out recently by Winecki et al. [21], most previous experiments have been done with heavy solid targets and light ion projectiles ($Z_{\text{ion}} < Z_{\text{solid}}$), a situation which may favor certain processes over others. A complete understanding will undoubtedly need to be guided and tested by a variety of experiments carried out for different projectiles, charge states, substrates, energies, and angles. In the present work, we present data from a new study which helps fill out the full range of possible regimes. We present X-ray data for highly charged but relatively light ions (Ar^{17+}) impinging on a substrate containing lighter (Si and O) atoms. Unlike the experiment of Winecki et al. [21], however, we use a substrate containing atoms which are not *too* light to be able to produce inner shell X-rays that can be readily detected through conventional window materials. This allows us to directly monitor X-rays produced by the substrate as well as those produced by the projectile. We also vary the total impact velocity directly, at a fixed angle, rather than using the method widely employed previously of varying only the incident angle to adjust the normal component of velocity.

2. Experiment

The experiments were carried out at the EBIT facility at the National Institute of Standards and Technology (Gaithersburg) [22]. Ar^{17+} ions were created in the trap and extracted into a continuous beam which was subsequently charge-to-mass analyzed and transferred to our experimental chamber by a new, highly efficient beam line [23]. The vacuum in the beam line and experimental chamber was approximately 10^{-6} Pa (10^{-8} Torr), so the chance of charge exchange collisions with background gas

was insignificant. Upon extraction from the EBIT, the ions were accelerated to the energy of the upper drift tube of the EBIT. The collision velocity was adjusted by changing a voltage applied simultaneously to the sample and to an aperture located just above the sample. A modification of the energy due to the space charge of the electron beam in the EBIT was taken into account. Image charge acceleration, which is important for very low velocity and for metal targets, was not accounted for here.

We used a 50 nm thick SiO_2 sample (prepared on a silicon substrate) as a target. Because we had no in situ surface cleaning capabilities, we expect that there was a thin layer of hydrocarbons on the surface of the target. As in related studies by others, however, (Refs. [17,20], etc.) we believe that the presence of this layer did not prevent us from extracting some general conclusions which are of considerable significance. In fact, we speculate that the very large internal energies stored in the highly charged ions may make experiments with them less sensitive to surface contamination than corresponding experiments carried out with low charge ions.

The ion beam hit the target at 30° with respect to the normal to the target surface. The X-rays were detected at 90° with respect to the ion beam by a Peltier-cooled silicon PIN diode detector. The detector has an instrumental width of 250 eV at 5.9 keV X-ray energy. Since we detected X-rays with energy below 2 keV, we had to correct for the transmission through the 25 μm thick beryllium window in front of the detector. The solid angle of detection was 4×10^{-4} sr. With the present setup, our typical X-ray count rate is 5 to 10 counts per s. A typical spectrum took approximately 40 min to collect. The energy calibration of the detector was done with the K_α and K_β lines of Sc, Ti, and Ca from a commercial calibration source.

3. Analysis

In general, the spectra had three main components: two characteristic X-ray peaks and a broad background (see Fig. 1). The two peaks, at about 1.75 and 3.1 keV are identified as K_α X-ray emission lines of Si and Ar respectively (to differentiate between the energy levels and transitions in silicon and argon, we will use the superscripts $\text{K}_\alpha^{\text{Si}}$, $\text{K}_\alpha^{\text{Ar}}$, $\text{K}_\alpha^{\text{Si}}$, $\text{K}_\alpha^{\text{Ar}}$). Note that while we can readily detect K_α X-rays from the silicon, the use of a much lower mass substrate (carbon) by Winecki et al. [21] positioned the C K_α X-rays well below 1 keV, into the range at which conventional X-ray windows are opaque.

We attribute the broad background structure in our data to an instrumental effect consisting of a combination of window transmission and X-rays not coming from the target (possibly, bremsstrahlung radiation from charged particles accelerating into the ion deceleration plate). This background is present even when the target is removed and changes with the deceleration voltage. A fourth-order re-

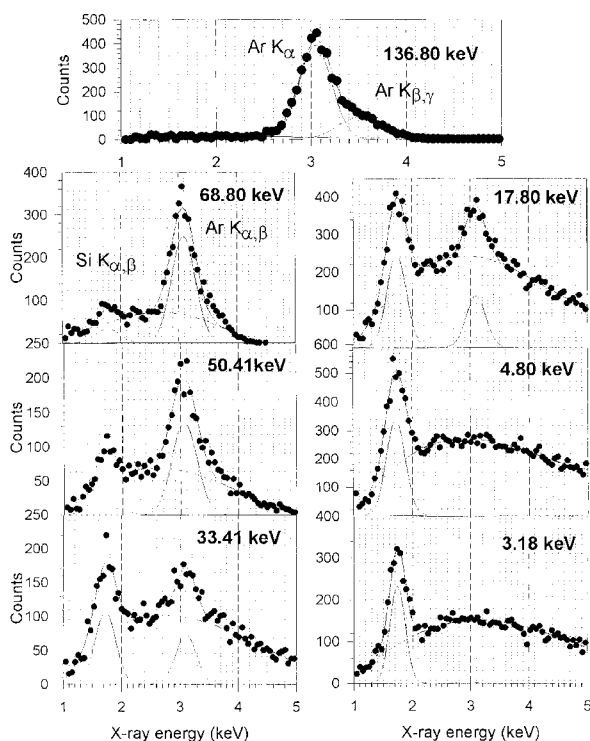


Fig. 1. X-ray spectra at various projectile energies. The spectra are fitted with a broad background and characteristic X-ray peaks. The top graph shows the Ar K lines at the highest beam energy. It exhibits the same structure as in earlier observations [12–17].

gression was used to fit the broad structure, excluding the regions of the two sharper peaks. Improved modeling and correction for the broad structure might improve the accuracy of the final results, but for the present level of analysis, the simple correction we have made appears to be sufficient (as evidenced by the quality of the fit described below).

The two K_{α} X-ray lines are fit using a Gaussian function. As seen in the raw data shown in Fig. 1, the relative intensities of the two K_{α} X-ray lines vary with projectile velocity. In particular, the K_{α}^{Si} line is the strongest at low velocity while the K_{α}^{Ar} line is the strongest at high velocity.

4. Interpretation of the silicon and argon X-ray lines

The energy of the K_{α}^{Si} line indicates that the X-rays originate from neutral or low-charge-state silicon. A simple interpretation of the data is that at low energies, where highly charged ions are known to be most efficient in removing electrons from surfaces [7], a locally charged region of the surface builds up and then explodes under its own Coulomb repulsion, producing a high temperature microplasma which emits X-ray radiation. Although the 10 keV internal potential energy stored in the sum of the

Ar¹⁷⁺ vacancies is more than enough energy to produce the observed X-rays, large scale molecular dynamics simulations of such Coulomb explosions in silicon [24] show that even in an idealized situation, the temperature inside the exploding region falls about 100× short of that required to produce the observed silicon K_{α} X-rays. Furthermore, the simultaneous decrease in intensity of the Ar K_{α} X-ray peak observed in our data suggests that a more likely interpretation of our spectra is that a silicon K-shell electron is being directly transferred to the Ar projectile in a close collision at or beneath the surface.

The possibility that this electron transfer from the silicon K shell to the argon K shell occurs via a radiative coupling can be ruled out empirically by the lack of observed X-rays at the requisite energy of 2.2 keV. We attribute the appearance of the silicon K vacancy, therefore, to an interatomic Auger decay involving the transfer of a K-shell electron from the silicon to the K shell of the argon, ejecting a second electron in the process. This process happens in a close encounter of the argon projectile with a silicon atom in the solid. Since the Born–Oppenheimer approximation is satisfied for inner shell electrons (the ion moves slower than the bound electron) a transient, quasi-molecule is formed between the projectile ions and the target atom of the solid. In this complex, a vacancy transfer can take place in which the K^{Ar} inner shell vacancy is filled by a K^{Si} electron and a second electron is ejected.

The most likely candidate for the second electron in the Auger process would seem to be the other remaining K-shell electron in the silicon, since this electron would be highly correlated with the first (in the same shell). Since the energy required to transfer a K-shell electron from neutral silicon to the K shell of hydrogenic argon is sufficient (barely) to remove the remaining K-shell electron in silicon, it is possible to create this double-vacancy silicon ion. In this case, however, half of the silicon X-rays should be emitted with energies that are shifted, due to missing screening from the second K-shell electron, by approximately 140 eV [25] from the value that we measure. Higher integrity experimental data, with improved counting statistics for example, would be useful to definitively rule out this possibility.

In the absence of evidence for the Auger process with two final vacancies in the K shell, the next likely candidates (those with the next highest electron–electron correlation with the K shell) involve the ejection of an L-shell electron from either the silicon or the argon. Since intra-atomic Auger rates decrease significantly with increasing energy of the emitted electrons, the alternative with the most deeply bound L-shell electron is favored. We hypothesize, therefore, that the process we observe is dominated by a ($K^{\text{Ar}} K^{\text{Si}} L^{\text{Ar}}$) Auger decay.

The observation of the emitted $K^{\text{Ar}} K^{\text{Si}} L^{\text{Ar}}$ Auger electron would be the direct evidence for the process, but, in the present experiment, we did not have the capability for

such a measurement. If such a vacancy transfer takes place with a fairly large cross section it is a competitive way of filling the inner shell vacancies as pointed out by Briand et al. in a different context [15]. They considered the quasi-molecule Auger transition as a way of filling the M-, N-, and O-shell vacancies to form hollow atoms within the solid. Stolterfoht in Ref. [26] provided evidence for autoexcitation producing inner shell vacancies in slow Ar⁺ on SiH₄ collisions. The author pointed out that the process dominates at very low collision energies. This fact also supports the interpretation of our present findings.

5. Summary

X-ray observations of highly charged Ar¹⁷⁺ impinging on SiO₂ at total energies of 137 keV and below show that a large signal from the silicon appears when the ion velocity is decreased, rather than increased. This is interpreted as a potential energy effect, namely, a K^{Ar}K^{Si}L^{Ar} Auger transfer which leads to the subsequent emission of a hard Si K_α X-ray. Due to the deep binding energy of the silicon K shell, one can infer that this process must take place during close collisions (at or beneath the surface). This direct filling of the vacancy proceeds fast enough to quench the radiative processes which would otherwise allow the projectile to decay by emitting its own characteristic K_α radiation. More work is needed in order to understand the velocity dependence in the context of presently available models of the interaction of highly charged ions with solids, and to extend these measurements to higher charge state projectiles where the situation may be qualitatively different [7].

Acknowledgements

We thank Dr. Yong-Ki Kim for helpful discussions and calculations. Part of the work was done with the support of the Hungarian Science Foundation (OTKA, contract number: F 019344). One of the authors (E.T.) acknowledges the Foundation for the Hungarian Higher Education and Research for the support.

References

- [1] M. Delaunay, S. Dousson, R. Geller, B. Jaquot, D. Hitz, P. Ludwig, P. Sortais and S. Bliman, Nucl. Instr. and Meth. B 23 (1987) 177.
- [2] M. Stöckli, C.L. Cocke and P. Richard, Rev. Sci. Instr. 61 (1990) 242.
- [3] D.H. Schneider, M. Clark, B.M. Penetrante, J. McDonald, D. DeWitt and J.N. Bradsley, Phys. Rev. A 44 (1991) 1653.
- [4] F. Auymar and H.P. Winter, Comm. At. Mol. Phys. 29 (1994) 275.
- [5] P. Varga, Comm. At. Mol. Phys. 23 (1989) 11.
- [6] J. Burgdörfer, C. Reinhold, L. Hagg and F. Meyer, Aust. J. Phys. 49 (1996) 527.
- [7] D.H.G. Schneider and M.A. Briere, Physica Scripta 53 228 (1996).
- [8] H.J. Andra, in: Atomic Physics of Highly Charged Ions, ed. R. Marrus (Plenum, New York, 1989).
- [9] F. Auymar, H. Kurz, D. Schneider, M.A. Briere, J.W. McDonald, C.E. Cunningham and H.P. Winter, Phys. Rev. Lett. 71 (1993) 1943.
- [10] O. Pankratov, private communication on computer simulation, Livermore, 1996.
- [11] C. Auth, T. Hecht, T. Iget and H. Winter, Phys. Rev. Lett. 74 (1995) 5244.
- [12] J.P. Briand, L. de Billy, P. Charles, S. Essabaa, P. Briand, R. Geller, J.P. Desclaux, S. Bliman and C. Ristori, Phys. Rev. Lett. 65 (1990) 159.
- [13] J.P. Briand, L. de Billy, P. Charles, J.P. Desclaux, P. Briand, R. Geller, S. Bliman and C. Ristori, Z. Phys. D 21 (1991) S123.
- [14] B. d'Etat, J.P. Briand, G. Ban, L. de Billy, J.P. Desclaux and P. Briand, Phys. Rev. A 48 (1993) 1098.
- [15] J.P. Briand, B. d'Etat, D. Schneider, M. Clark and V. Decaux, Nucl. Instr. and Meth. B 79 (1994) 138.
- [16] M. LeGros, E. Silver, D. Schneider, J. McDonald, S. Bardina, R. Schuch, N. Madden and J. Beeman, Nucl. Instr. and Meth. A 357 (1995) 110.
- [17] M. Schulz, C.L. Cocke, S. Hagmann, M. Stöckli and H. Schmidt-Böcking, Phys. Rev. A 44 (1991) 1653.
- [18] S. Adriaonje, H.J. Andra, A. Brenac, G. Lambole, T. Amy, A. Simonivici, M. Bonnefoy, J.J. Bonnet, M. Chassevent and A. Fleury, Nucl. Instr. and Meth. B 79 (1993) 381.
- [19] R. Morgenstern and J. Das, Physica Scripta T46 (1993) 231.
- [20] R. Köhrbrück, K. Sommer, J.P. Biersack, J. Bleck Neuhaus, S. Schippers, P. Roncin, D. Lecler, F. Fremont and N. Stolterfoht, Phys. Rev. A 45 (1992) 4653.
- [21] S. Winecki, C.L. Cocke, D. Fry and M.P. Stöckli, Phys. Rev. A 53 (1996) 4228.
- [22] J.D. Gillaspay, Y. Aglitskiy, E.W. Bell, C.M. Brown, C.T. Chantler, R.D. Deslattes, U. Feldman, L.T. Hudson, J.M. Laming, E.S. Meyer, C.A. Morgan, A.I. Pikin, J.R. Roberts, L.P. Ratliff, F.G. Serpa, J. Sugar and E. Takács, Physica Scripta T59 (1995) 392.
- [23] A.I. Pikin, C.A. Morgan, E.W. Bell, L.P. Ratliff, D.A. Church and J.D. Gillaspay, Rev. Sci. Instr. 67 (1996) 2528.
- [24] H.-P. Cheng and J.D. Gillaspay, Phys. Rev. B 55 (1997) 2628.
- [25] Y.-K. Kim, private communication on calculation, 1996.
- [26] N. Stolterfoht, Phys. Rev. A 47 (1993) R763.
- [27] N. Stolterfoht, A. Arnaud, M. Grether, R. Köhrbrück, A. Spieler, R. Page, A. Saal, J. Tomaschewski and J. Bleck-Neuhaus, Phys. Rev. A 52 (1995) 445.

Nanoscale modification of silicon surfaces via Coulomb explosion

Hai-Ping Cheng

Department of Physics & QTP, University of Florida, Gainesville, Florida 32611

J. D. Gillaspay

Physics Laboratory, National Institute of Standards and Technology, Gaithersburg, Maryland 20899

(Received 12 March 1996)

Coulomb explosions on silicon surfaces are studied using large-scale molecular-dynamics simulations. Processes under investigation begin by embedding a region consisting of 265–365 singly charged Si^+ ions on a Si [111] surface. The repulsive electrostatic energy, initially stored in the charged region, leads to a local state with ultrahigh pressure and stress. During the relaxation process, part of the potential energy propagates into the surrounding region while the remainder is converted to kinetic energy, resulting in a Coulomb explosion. Within less than 1.0 ps, a nanometer-sized hole on the surface is formed. A full analysis of the density, temperature, pressure, and energy distribution as functions of time reveals the time evolution of physical properties of the systems related to the violent explosive event. A shock wave that propagates in the substrate is formed during the first stage of the explosion, $0 < t < 100$ fs. The speed of the shock wave is twice the average speed of sound. After the initial shock the extreme nonequilibrium conditions leads to ultrarapid evaporation of Si atoms from the surface. Qualitatively similar features are observed on a smaller scale when the number of initial surface charges is reduced to 100. Our simulations demonstrate the details of a process that can lead to permanent structure on a semiconductor surface at the nanoscale level. The work reported here provides physical insights for experimental investigations of the effects of slow, highly charged ions ($Q > 40$, e.g.) on semiconductor materials. [S0163-1829(97)02104-8]

I. INTRODUCTION

Fabricating structures at the nanometer length scale has become an increasingly active area for physical, chemical, and material sciences.^{1,6} Various experimental techniques, from the assembly of nanosized clusters and chemical etching to ion beam lithography and surface sputtering, have been developed to construct nanostructured materials.^{7–14} These and other advances in nanotechnology have created opportunities for contemporary scientific investigations of the physical properties of novel materials and the transient states and processes of physical systems. Many physical phenomena that occur in the nanometer regime and femtosecond to picosecond time domain exist under extreme physical conditions. Much research effort has been focused on the physical mechanisms underlying material properties and nanomachining.^{15–19} Understanding the physical origins of the observed phenomena, the time evolution of thermodynamical properties of systems far away from equilibrium, and the relationships among physical properties, intermediate states in the physical processes, and the ultrafine structure of materials is of basic and technological importance.

Accompanying the technological achievements, scientists have been seeking new theories to explain the results observed in nanoscale experiments. Much attention has been given to the development of new methodology for theoretical studies. The necessity for new methods arises for several reasons. First, traditional condensed matter approaches can not be applied directly to nanostructured systems because of surface or boundary effects. Second, traditional statistical theories are not suited for solving problems associated with states far from equilibrium. Third, traditional atomic and mo-

lecular theories fail to predict the behavior of nanoscale systems due to the large number of degrees of freedom in these systems.

Advances in computer science and technology have exerted a significant influence on scientific research in the area of nanoscale science. Large-scale computer simulations are becoming powerful tools for investigations of complex physical and chemical processes.^{20–23} By deriving physical quantities such as kinetic energy, potential energy, pressure, and temperature from the trajectories of atoms in phase space, simulations can correlate microscopic pictures with macroscopic phenomena. Time-dependent simulations of molecular dynamics allow studies of physical and chemical properties as functions of time. Results from the simulations can often be compared directly to the experimental measurements, and can also be used as input for analytical theoretical modeling.¹⁵ Consequently, innovative ideas such as directing chemical reaction pathways,^{24,25} controlling cluster-surface collision outcomes,¹⁵ preparing, size selecting, and identifying nanocrystals⁷ become well understood realities in the laboratory after iterations in the cycle of simulation, modeling, and experimentation.

II. EXPERIMENTAL BACKGROUND

The goals of our investigations are to search for new methods for nanofabricating of semiconductor surfaces and to study characteristic features of the phenomena involved in these processes. We are especially encouraged by the recent progress in the electron beam ion trap^{14,26–30} (EBIT) experiments. In these experiments, the projectile atoms are highly ionized ($Q > 40+$ typically), and impinge on the target sur-

face with low kinetic energy. Unlike high kinetic energy particle-surface sputtering experiments, the key issue in the EBIT experiments is the internal electrostatic potential energy of the ions. This internal energy can be over 750 keV, five orders of magnitude higher than that for a conventional (singly charged) ion. When a single such highly charged ion neutralizes itself by impacting a solid, it can create a surface structure of order 10 nm in dimension. The size of the structure can be varied by adjusting the charge of the incident ion,^{26,31} and the efficiency of the feature formation is essentially 100% (one feature for each incident ion). Speculations emerging from experimental evidence suggest that there may be technological applications of the highly charged ions as a new method for modifying or etching semiconductor or insulator surfaces.^{26,30–36} However, there is very little information about the Coulomb explosion process, which is proposed to be the main cause for surface damage.^{26,37} In fact, it is only recently that clear evidence for the existence of surface Coulomb explosions induced by slow highly charged ions has been obtained.^{38,27} In this paper, we report the results of computer simulations of Coulomb explosions on silicon surfaces. These simulations are performed in conjunction with ongoing experimental studies of highly charged high Z ion-surface bombardment at NIST.³⁰

III. MODELING AND SIMULATIONS

The basic physical picture leading to a Coulomb explosion in a surface is as follows. As a highly charged ion approaches a surface, its intense Coulomb field is sufficient to rapidly pull electrons from the solid, even when the ion is still many atomic diameters away from the surface (e.g., up to 540 Bohr radii, in one model³⁹). Electrons are captured into high-lying Rydberg levels, producing a superexcited “hollow atom,” which may be fully neutralized.^{40–43,35} The atom can decay (collapse) towards its ground state via Auger cascade, ejecting electrons in the process,^{26,34} or by other mechanisms such as radiative decay or surface plasmon formation.⁴⁵ Only if electrons are ejected fast enough and the ion approaches the surface slowly enough can electrons continue to be removed from the solid during the ion’s approach. A fully stripped incident ion of atomic number Z can therefore remove at least Z electrons, perhaps quite a few more, during its approach. If the ion is not fully neutralized and collapsed prior to impact, more electrons can be removed during and after the collision with the surface. Observations exist for incident charges up to Th^{75+} ($Z=90$) where approximately 300 ejected (free) electrons per ion were detected,^{26,44} not including the additional $Q=75$ electrons that were removed simply to neutralize the incident ion. Theories predict that by increasing the charge of the incident ion even further it should be possible to remove over 1000 electrons per ion.⁴⁶ Earlier scaling-law extrapolations from low-charge data had indicated that this number might be several times larger still.⁴⁶ If even a fraction of these electrons are removed sufficiently fast that the solid cannot replenish them, a localized region of the surface will become charged. Data on GaAs indeed show that the replenishment of electrons from the surrounding solid to the locally charged region does not proceed fast enough to circumvent the effect that we discuss here.³⁶ As we will show, the localized

charged region overcomes the cohesive forces that hold the solid together, and the region explodes under its mutual electrostatic repulsion. Subsequent shock waves and thermal processes ensue, leaving a crater-like feature in the surface. To our knowledge, the work reported here is the first full-scale three-dimensional molecular dynamics calculation for the Coulomb explosion of a surface. Earlier work on the problem was restricted to two dimensions, and carried out for 50 times fewer atoms than we consider here.⁴

The simulations begin by preparing a Si [111] surface in its ground state. The sample consists of 34 560 atoms distributed over 24 layers. Thus, the thickness of the surface is approximately 40 Å (70 a.u.), and the width and length are about 140 Å. Periodic boundary conditions are applied only to the substrate in the x and y directions but not to the ions. This ensures that there are no artificial long-range Coulomb interactions existing between neighboring unit cells. Our results are checked for artifacts by performing additional simulations with different sample sizes. In order to stabilize the surface, 6 layers of static atoms are placed at the bottom. The remaining 18 layers, above the static layers, are dynamical. Temperature control is applied only to the deepest dynamical layer. This method of applying temperature control leads to a realistic simulation of atomic motion during a dynamic event. At the same time, it allows energy exchange between the system and a constant temperature heat bath.

At $t=0$, 265–365 atoms in a hemispherical region in the center of the surface are singly charged. This initial condition is chosen to imitate the consequences of bringing a slow, high-charged ion, such as Xe^{+44} or U^{+92} into the neighborhood of a nonmetal surface. Such an initial condition has been put forth by a number of researchers active in this field,^{33,35,38,36} but to our knowledge this is the first time that the subsequent Coulomb explosion has been investigated at the atomic level by detailed simulations and calculations rather than simply depicted as an artist’s conception. Since there is some evidence that the time scale for the electron emission from a surface can be very short,^{26,34,40,48,44} we separate the dynamics of the surface explosion from the process of multielectron capture and Auger cascade, which leads to the initial conditions assumed here. This simplified model is supported by the evidence of fast Coster-Kronig transitions in ion-silicon surface interactions.³⁴ Here, we focus on the dynamics of the surface atoms after a huge amount of repulsive electrostatic energy is suddenly deposited. The number of ions is chosen to be either 365 or 265. This is consistent with experimental results,²⁶ in which the number of electrons removed from the surface is found to be more than 4 times the charge number of the slow (v_i is of order 10^3 m/s) incoming ion.

Each silicon atom interacts with the other atoms via a three-body Tersoff potential function,⁴⁹ which has been tested for both crystalline and amorphous silicon. The Si^+ ions interact simply via pairwise Coulomb repulsion. In order to describe interactions between Si and Si^+ , we combine information from experimental measurements and first-principles calculations⁵⁰ on Si-Si and Si- Si^+ dimers. These data are then fitted to a function,

$$V(r_{ij}) = \epsilon \left[\left(\frac{\sigma}{r_{ij}} \right)^{12} - \left(\frac{\sigma}{r_{ij}} \right)^4 \right]. \quad (1)$$

The term $1/r^4$ is chosen due to the interaction of the charge (on Si^+) and the induced dipole (on Si). The parameters σ and ϵ are chosen to be $3.69 a_0$ and 9.17 eV , respectively. It should be pointed out that the Si-Si^+ and Si^+-Si^+ potentials used in our simulations are not extensively optimized. However, for the events of interest here, they capture the basic physical features of the important atomic interactions, and provide sufficient numerical accuracy as well.

The equations of motion for each particle in the dynamical substrate are then integrated using Gear's predictor-corrector algorithm.⁵¹ The time step of $\Delta t = 0.4 \text{ fs}$ is chosen to maintain energy conservation. The temperature of the bottom dynamical layer is controlled to be 300 K . The systems evolve in time according to classical Newtonian dynamics. Positions, velocities, and accelerations of all the atoms and ions are obtained via numerical solution of the classical equations of motion at each time step.

IV. RESULTS

Figure 1 shows several snapshots of a system with 365 ions, at $t = 0.0, 40.0, 80.0,$ and 360.0 fs . We see that the region filled with ions expands significantly at $t = 40 \text{ fs}$, and a hole is formed by 80 fs . At this point, the size of the hole is similar to the size of the initially charged region. The last snapshot displays a much larger hole with many Si atoms, as well as Si^+ ions, exploding from the surface. More atoms and ions leave the surface as the simulation continues. We separate the process into two stages. First is the initial, extremely violent explosive stage, which ends at $80\text{--}100 \text{ fs}$. This is followed by a period of rapid, high-temperature evaporation. The detailed dynamics of these stages can be analyzed by studying various physical properties, such as pressure, energy, density, and temperature.

Figure 2 depicts the temperature of several subdivisions in the substrate as a function of time. These subdivisions are three-dimensional concentric shells that coincide with the center of the hemispherical charged region. The thickness of each shell is chosen to be 2.6 \AA (5 a.u.). The innermost shell is just outside the initially charged region. Panel (a) shows the results for a 365-ion system: the temperature of each shell increases sharply at a rate of over 10^{18} K/s , peaks at over 10^5 K , and then begins to relax back towards ambient temperature. Two striking phenomena can be observed in this picture. First is the time delay for two adjacent shells to undergo the sudden temperature jump. This is a signature of shock-wave propagation. The speed of the wave is estimated to be $2.0 \times 10^4 \text{ m/s}$, or a little more than 2 times the average speed of sound in silicon.⁵² The rapid dissipation of the shock wave at about $80\text{--}100 \text{ fs}$ coincides with the time required for the charged region to expand significantly and lose its geometric symmetry. Second, we note that the rate of temperature increase observed here is extremely fast. Compared with other methods used for rapid heating, for example, by laser heating^{53,54} or cluster-surface collision,¹⁵ 10^{18} K/s is several orders of magnitude faster. Even if we factor out the initial impact of the shock wave, the temperature at 100 fs is above 6000 K , corresponding to an average rate of about 10^{17} K/s . After 100 fs the temperature begins to decrease, as Si atoms are ejected from the surface. Panel (b) shows the same quantities for a system starting with 265

ions. Again, we observe a pattern very similar to that in panel (a). The time for the shock wave to collapse also coincides with that in (a). The only noticeable difference is the temperature. The order of the magnitude of the heating rate, however, remains the same.

The initial energy in the charged region is calculated to be 87.3 keV ($3.21 \times 10^3 \text{ a.u.}$) due to the Coulomb repulsive interaction of 365 ions. For 265 ions, the initial energy is 50.8 keV ($1.87 \times 10^3 \text{ a.u.}$). Figure 3 shows the three curves representing the kinetic energy (solid line), potential energy (dashed line), and energy propagating to the substrate (dotted line). For $t < 100 \text{ fs}$, the amount of potential energy converted to the kinetic energy of the ions is greater than the energy transfer to the substrate. The two curves cross each other at 95 fs in both panels (a) and (b). At the crossing point, the total kinetic energy of the ions is slightly less than 10^3 a.u. for 365 ions, and 580 a.u. for 265 ions. We estimate that these numbers correspond to 31% of the initial potential energy. After 100 fs the rate of increase of the kinetic energy of the ions slows significantly. The crossing time of the two energy curves coincides with the ending of the propagation of the shock wave. Somewhat later, at $110\text{--}120 \text{ fs}$, the potential energy drops below the other two energy curves.

In Fig. 4, snapshots of the pressure and potential energy distributions (for 365 ions) at several times are shown. At $t = 0$, the large amount of repulsive Coulomb energy stored in the charged region causes an extremely high pressure in the hemispherical region. The highest pressure in the system corresponds to $1.4 \times 10^3 \text{ GPa}$ of pressure. However, the value of highest pressure quickly drops to $4.3 \times 10^2 \text{ GPa}$ at $t = 40 \text{ fs}$, and then to $1.8 \times 10^2 \text{ GPa}$ at $t = 80 \text{ fs}$. At $t = 360 \text{ fs}$, the pressure is still very high, about 9.2 GPa , even though it is much smaller than its initial value. The potential energy distribution undergoes a similar evolution, where the highest-energy value for $t = 0, 8, 16, 40,$ and 80 fs is $11.0, 10.7, 9.9, 7.3,$ and 5.2 a.u. , respectively. This value further decreases to 1.5 a.u. at 360 fs . Note that the pressure decreases faster than the energy during the expansion, due to the relation $P \propto (\partial E / \partial V)$.

Density distributions (for the 365 ions system) at different time instants are displayed in Fig. 5. At $t = 0$, the distribution is uniform throughout the substrate as expected (not shown). The density of the charged region decreases rapidly, in contrast with the formation of a high density ring near the center region. The highest density found in the explosion, which occurs between 40 and 55 fs , reaches more than 50% of the initial density, thus indicating an extremely nonequilibrium environment. A hole of 35.3 \AA in diameter and 13.8 \AA in depth is quickly formed at the center of the surface. This initial phase (at $t < 100 \text{ fs}$) of the hole formation is mainly due to Coulomb explosion. A total number of 141 particles, including 115 ions and 26 atoms, are ejected from the surface. At $t < 100 \text{ fs}$, the large amount of energy that is delivered into the substrate melts the silicon crystal. Eventually, atoms with sufficient kinetic energy evaporate from the surface. At $t = 360 \text{ fs}$, the size of the hole is about 62.5 \AA in diameter and 19.6 \AA in depth. A total number of 768 particles, including 598 atoms and 170 ions, have left the surface. The diameter of the hole further increases to more than 10 nm at about 600 fs .

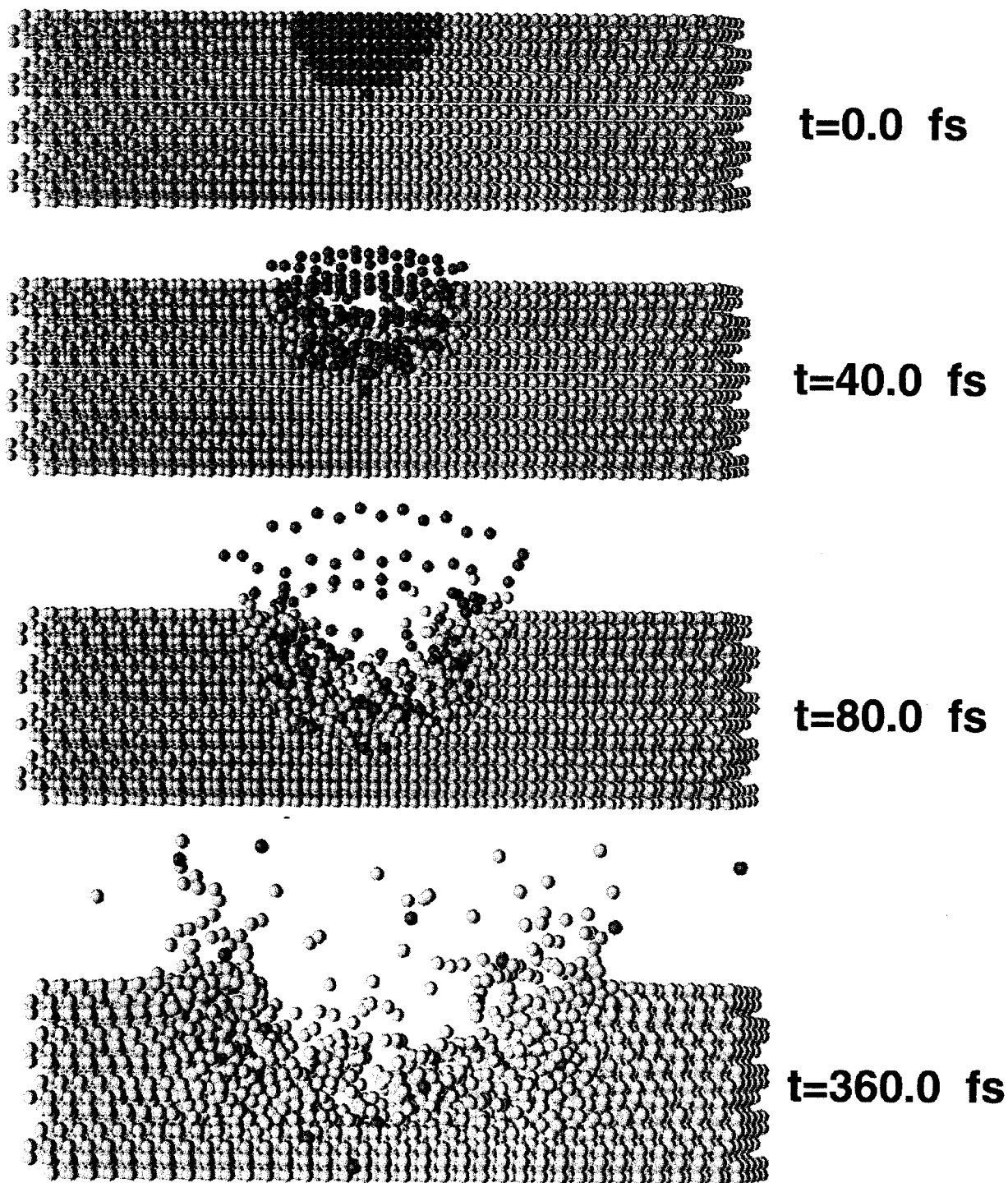


FIG. 1. (Color) Snapshot of the time evolution of the Coulomb explosion process. Red and green spheres are used to indicate Si⁺ ions and Si atoms, respectively. This particular system consists of 365 ions. The initial Coulomb repulsive energy stored in the hemispherical region is about 87.3 keV. Between $t=0$ and 40 fs, the charged region expands significantly. At $t=80$ fs, over 100 ions are ejected from the surface, forming a pronounced hole. By 360 fs, the hole is much larger, and about 800 atoms and ions are driven from the surface.

Figure 5 also shows the temperature distributions at several times. The temperature of hottest spot in the system is 7.1×10^4 , 2.5×10^5 , 9.2×10^5 , and 1.6×10^6 K for $t=8$, 16, 40, and 80 fs, respectively. We note that the temperature is derived from the total kinetic energy of the ions. As can be

seen in the figures, the system is far from equilibrium. Even after the initial shock wave passes, the temperature gradient is very large in the substrate. This extremely nonequilibrium situation is directly responsible for the rapid evaporation of the atoms.

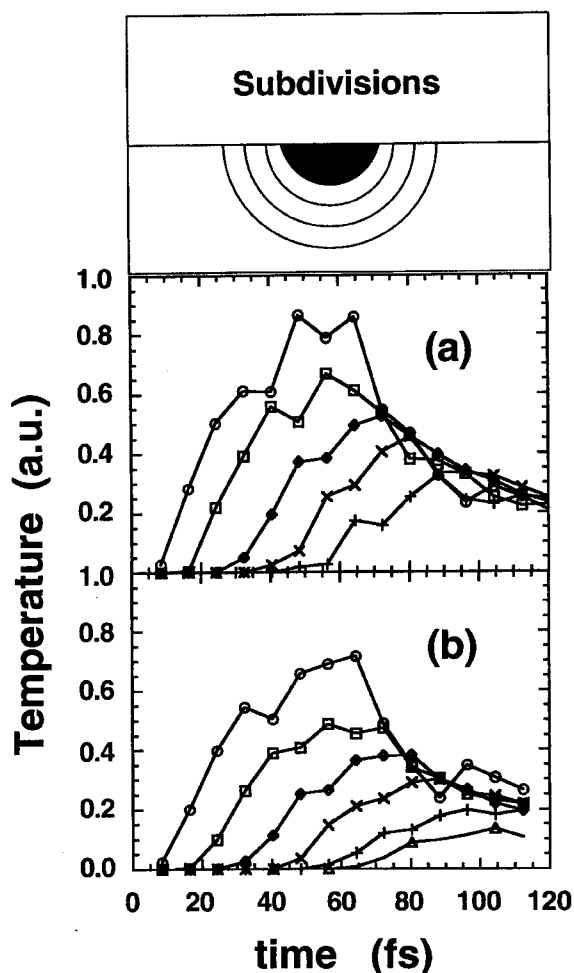


FIG. 2. Temperature of subregions of the substrate as functions of time. Panel (a) is the plot of a system consisting initially of 365 Si^+ ions, and panel (b) is for 265 Si^+ ions. The subregions correspond to several concentric shells with a thickness of 5 a.u. The jumps in temperature seen in each shell indicate a shock wave propagating through the substrate. The patterns in panels (a) and (b) are very similar. After 100 fs, the temperatures in different shells converge to the same value. Numbers are given in a.u. where 9.5×10^{-4} a.u. = 300 K.

V. DISCUSSION

The results of our simulations are in rough agreement with experiments. The fact that the crater does not preserve the hemispherical shape of the initial conditions but instead becomes more oblate may be partly an artifact due to the finite number of layers used in the simulation. Results from simulations with only 100 ions in the initially charged region show crater formation of a similar type, but with a more spherical shape. If the crater shape shown in Fig. 5 is convolved with a typical atomic force microscope (AFM) tip radius of 30 nm the *apparent* (measured) depth would be only 0.4 nm for a 10-nm-diameter crater. A more spherical crater of the same diameter would appear to have roughly the same apparent depth, so the distinction between actual depths would not show up in existing experiments. Craters in mica have been observed to have apparent depths of 0.3 nm

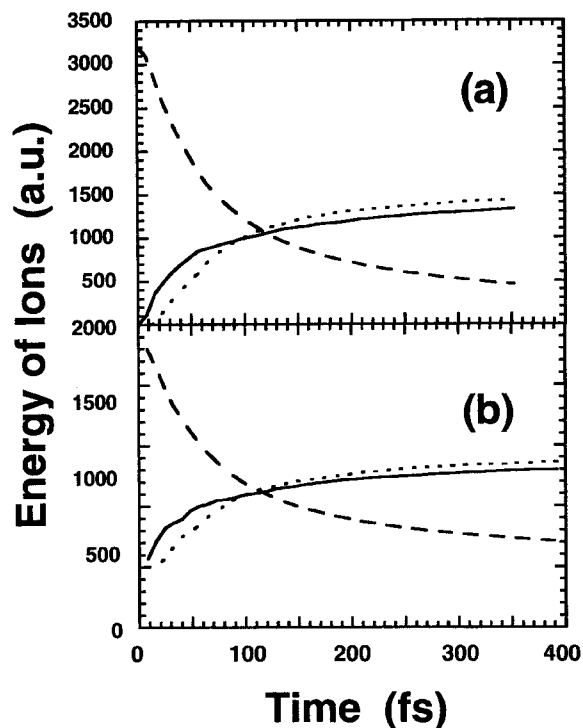


FIG. 3. Kinetic energy (solid line) and potential energy (dashed line) of the ions during the Coulomb explosion. The dotted line is the energy transferred from the ions to the substrate. Panel (a) is for the 365-ion system and panel (b) the 265-ion system. Notice that after the initial shock, which ends at 80–100 fs, most of the energy originally stored in the ions is transferred to the substrate. After this time, the potential energy decreases more slowly than at the beginning. At the same time, the gain in kinetic energy of the ions slows down significantly compared to that during the initial 80 fs. Panels (a) and (b) display similar patterns. The energies are plotted in a.u. where 1 a.u. = 27.2 eV.

and diameters of 7 nm,⁵⁵ both of which scale up with increasing charge of incident the ion.^{26,33} As of yet, there are no published data showing crater topography in silicon under the influence of highly charged ion bombardment. Such data would be of great theoretical and practical interest. The question of whether there is a critical range of electrical conductivity above which Coulomb explosions are quenched by the ability of free carriers to flow quickly into the region being charged by the incident ion might be addressed by varying the initial temperature and doping of the silicon. By using cryogenic temperatures and highly doped silicon, the full range of possibilities from perfect insulator to semimetals can be probed in one system.

We emphasized that this simulation does not address the question of whether or not surface Coulomb explosions exist (or can be made to) in the laboratory. It only helps elucidate how the process would unfold and what the aftereffects would be if the assumed initial condition could be realized. Together with the explosion time scales determined in this work, a number of atomic physics and materials time scales must also be considered in order to predict what conditions need to be achieved in the laboratory in order to produce the Coulomb explosion.^{56–60,43,36} This will be the topic of a more

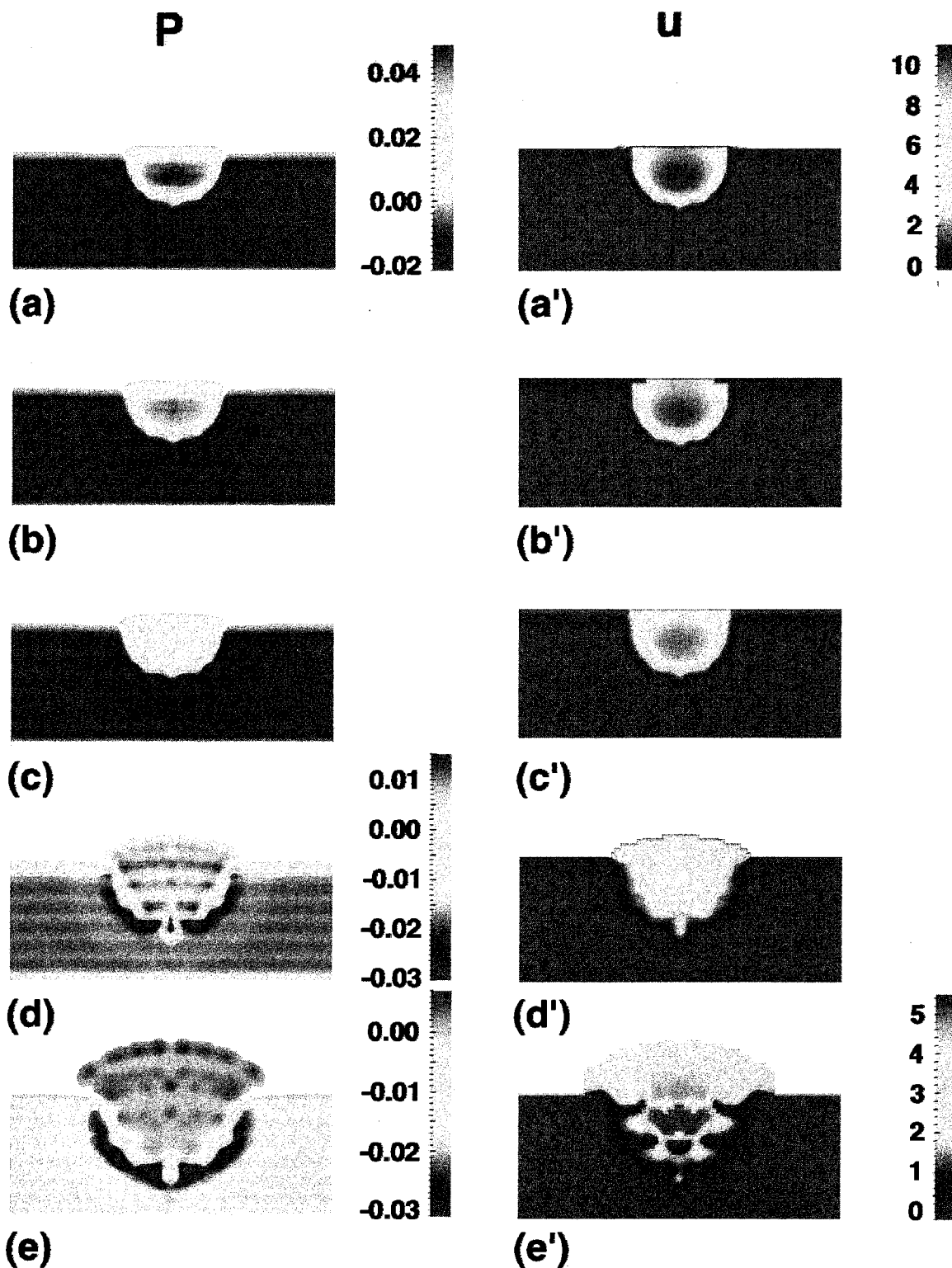


FIG. 4. (Color) Spatial distributions of pressures (left column) and potential energy (right column) for the system with 365 ions, at several time instants. The times represented in panels (a)–(e) and (a')–(e') are 0, 8, 16, 40, and 80 fs, respectively. All units are in a.u., where 1 a.u. = 2.94×10^{13} Pa or 2.94×10^4 GPa in pressure. The same color scales are used in (a)–(c) and (a')–(d') to demonstrate the dissipation between 0 and 16 fs. Different color scales for (d), (e), and (e') are used to focus on the detail of the patterns in the plots.

complete analysis once both upper and lower bounds on all the relevant time scales become better known. Recent experiments have yielded evidence that the necessary conditions may already have been achieved in two instances.^{26,36}

We would also like to stress the fact that we consider this simulation to be only a first step towards a more detailed understanding of the Coulomb explosion process. The present simulations focus mainly on effects derived from

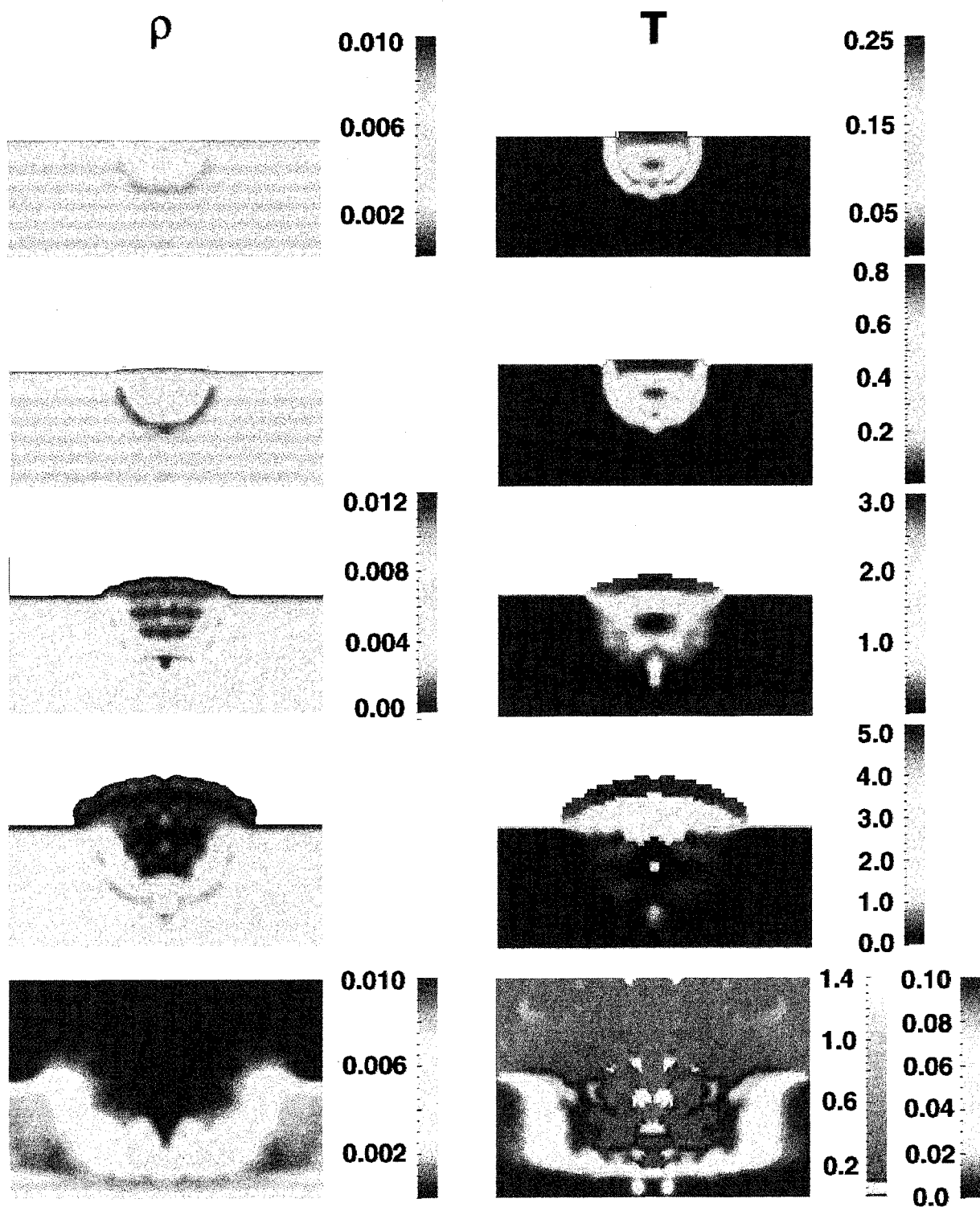


FIG. 5. (Color) Spatial distributions density (left column) and temperature (right column) for the system with 365 ions, shown at several time instants. The times represented in panels (a)–(e) and (a')–(e') are 8, 16, 40, 80, and 360 fs. All units are in a.u., where 1 a.u. = $6.75 \times 10^{30} \text{ m}^{-3}$ or $6.75 \times 10^{24} \text{ cm}^{-3}$ in density. The same color scales are used in (a) and (b) and (c) and (d) to demonstrate the density changes between 8 and 40 fs. A different color scale is used for (e) to display the hole on the surface at 360 fs. For the right column, each picture has a different color scale due to the rapid changes in kinetic energy. Panels (a')–(d') show the hot leading edge of the ions during the explosion. For (e') two color scales are used to show both the extremely hot region and the details of the temperature distribution in the substrate. Deep blue to deep red describes $0 < T < 0.1$ a.u. (or, $0 < T < 3 \times 10^4$ K), and deep red-pink-white describes $0.1 < T < 1.4$ a.u., where 1.4 a.u. = 4.4×10^6 K.

stored potential energy. In the case of ion-surface bombardments in which the kinetic energy of the incident ion is comparable to or greater than the potential energy, the effects of the ion colliding on the surface should be considered. Experimental evidence with highly charged ions on mica, however, shows that crater topography is essentially independent of the kinetic-energy-potential-energy ratio (R) for $R = 0.08-18$ (kinetic energy from 4.4–440 keV).⁵⁵ Studies on GaAs with singly charged ions having kinetic energy comparable to that of the slowest highly charged ions have shown craters that consist of only one or a few ejected atoms.⁶ These craters are so small that they have only been observed with UHV-STM (ultrahigh vacuum scanning tunneling microscope) techniques, and they would therefore be invisible in all of the highly charged ion studies referenced in this paper. It is reasonable, therefore, to neglect the kinetic energy effects as a first-order approximation, as we have done in this paper. We note, however, that material-dependent variations (either in the solid or the projectile) may be important. Molecular dynamics simulations of the impact of a single neutral argon atom with a kinetic energy of 1 keV have shown that hundreds of atoms may be dislodged from volatile (weakly bound) surfaces consisting of a cryogenically condensed gas.⁶² Simulations of experiments with massive energetic projectiles such as bucky balls⁶³ impinging on silicon, or multiply charged fast proteins⁶⁴ impinging on biomolecular surfaces can also cause massive disruptions. Very recent studies of mica surfaces suggest that very high kinetic energy (80 meV) low-charge ions may pro-

duce surface craters similar to those observed with slow, very highly charged ions.⁶⁵

Another aspect of the ion-surface interaction that can influence the degree to which our assumed initial conditions are realistic is the fraction of the ion's internal energy that is neutralized (a) during its approach to the surface, (b) during impact, and (c) subsequent to impact. Much work is still required to fully understand each of these three phases and, in particular, the relevant time scales that govern processes within each of them.

In addition to the limitations mentioned above, this work does not include heat conduction due to the electronic degree of freedom. We consider the amount of energy (heat) carried by the electrons as secondary compared to the overall energy redistribution. Also, the charge transfer between Si and Si⁺ has not been considered because the time scale for charge transfer in semiconductors is much greater than the time scale of the explosion. More complete simulations of the ion-surfaced interactions are in progress.

ACKNOWLEDGMENTS

The authors acknowledge valuable discussions with Dr. E. Meyer, as well as his efforts of stimulating collaborations between theoretical and experimental work. The simulations are performed using computer facilities at Quantum Theory Project, University of Florida and at the NIST computing center.

- ¹See *Materials-Fabrication and Patterning at the Nanoscale*, edited by F. Cerrina and C. R. K. Marrinan, MRS Symposia Proceedings No. 380 (Materials Research Society, Pittsburgh, 1995).
- ²See review by H. Gleiter, *Nanostruct. Mater.* **1**, 1 (1992), and references therein.
- ³See *Physics and Chemistry of Finite Systems: From Clusters to Crystals*, edited by P. Jena, S. N. Khanna, and B. K. Rao, Vol. 374 of *NATO Advanced Studies Institute Series C: Mathematical and Physical Sciences* (Kluwer, Dordrecht, 1992).
- ⁴R. T. Bate, *Nanotechnology* **1**, 1 (1990).
- ⁵H. I. Smith and H. G. Craighead, *Phys. Today* **43**(2), 24 (1990).
- ⁶J. I. Brauman *et al.*, *Science* **254**, 1277 (1991), special issue on Cluster.
- ⁷R. L. Whetten, J. T. Houry, M. M. Alvarez, S. Murphy, I. Vesmar, Z. L. Wang, C. Cleveland, W. D. Luedtke, and Uzi Landman, *Adv. Mater.* **8**, 428 (1996).
- ⁸S. T. DeZwart, T. Fried, D. O. Boerma, R. Hoekstra, A. G. Drentje, and A. L. Boers, *Surf. Sci.* **177**, L939 (1986).
- ⁹T. Ogawa and T. Abe, *J. Mat. Sci.* **26**, 1903 (1991).
- ¹⁰D. Schneider, M. A. Briere, M. W. Clark, J. McDonald, J. Bier-sack, and W. Siekhaus, *Surf. Sci.* **294**, 403 (1993).
- ¹¹Proceedings of the 29th International Conference on Electron, Ion, and Photon Beam Technology and Nanofabrication [*J. Vac. Sci. Technol. B* **13**, No. 6 (1995)].
- ¹²Proceedings of the 8th International MicroProcess Conference [*Jpn. J. Appl. Phys.* **34**, No. 12B, (1995)].
- ¹³Micro- and Nano-Engineering 95 [*Microelectronic Engineering* **30**, No. 1–4 (1996)].
- ¹⁴R. W. Schmieder and R. Bastasz, Proceedings of the VIth International Conference on the Physics of Highly Charged Ions, AIP Conf. Proc. No. 274 (AIP, New York, 1992), p. 690.
- ¹⁵H.-P. Cheng and Uzi Landman, *Science* **260**, 1304 (1993).
- ¹⁶R. N. Barnett, H.-P. Cheng, H. Hakkinen, and Uzi Landman, *J. Phys. Chem.* **99**, 7731 (1995).
- ¹⁷J. I. Pascual, J. Mendez, J. Gomez-Herrero, A. M. Baro, N. Garcia, Uzi Landman, W. D. Luedtke, E. N. Bogachev, and H.-P. Cheng, *Science* **267**, 1793 (1995).
- ¹⁸R. S. Berry, T. L. Beck, H. L. Davis, and J. Jellinek, in *Evolution of Size Effects in Chemical Dynamics, Part 2*, edited by I. Prigogine and S. A. Rise [*Adv. Chem. Phys.* **70**, 75 (1988)].
- ¹⁹See review by U. Landman and W. D. Luedtke, *Appl. Surf. Sci.* **60/61**, 1 (1992). See *Clusters and Fullerenes*, edited by E. Tosatti, V. J. Kumar, and T. P. Martin (World Scientific, London, 1992).
- ²⁰See review by F. F. Abraham, *Adv. Phys.* **35**, 1 (1986); see also *Melting, Localization and Chaos*, edited by R. K. Kalia and P. Vashishta (Elsevier Science, Amsterdam, 1982).
- ²¹See *Computations for the Nanoscale*, edited by P. E. Blochl, A. J. Fisher, and C. Joachim (Kluwer, Dordrecht, 1993).
- ²²R. Car and M. Parrinello, *Phys. Rev. Lett.* **60**, 204 (1988).
- ²³H.-P. Cheng, R. N. Barnett, and Uzi Landman, *Chem. Phys. Lett.* **237**, 161 (1995).
- ²⁴W. S. Warren, H. Rabitz, and M. Dahled, *Science* **259**, 1581 (1993).
- ²⁵B. Kohler, J. L. Krause, F. Raksi, K. R. Wilson, V. Y. Yakovlev,

- R. M. Whitmell, and Y. Yan, *Accts. Chem. Res.* **28**, 133 (1995).
- ²⁶D. H. Schneider, M. A. Briere, J. McDonald, and J. Biersack, *Radiat. Eff. Def. Solids* **127**, 113 (1993).
- ²⁷D. H. G. Schneider and M. A. Briere, *Phys. Scr.* **53**, 228 (1996).
- ²⁸D. Schneider, M. W. Clark, B. M. Penetrante, J. McDonald, D. Dewitt, and J. N. Bardsley, *Phys. Rev. A* **44**, 3119 (1991).
- ²⁹D. Schneider, D. DeWitt, M. W. Clark, R. Schuch, C. L. Cocke, R. Schmieder, K. J. Reed, M. H. Chen, R. E. Marrs, M. Levine, and R. Fortner, *Phys. Rev. A* **42**, 3889 (1990).
- ³⁰J. D. Gillaspay, Y. Agilitkiy, E. W. Bell, C. M. Brown, C. T. Chantler, R. D. Daslettes, U. Feldman, L. T. Hudson, J. M. Laming, E. S. Meyer, C. A. Morgan, A. L. Pikin, J. R. Roberts, L. P. Ratliff, F. G. Serpa, J. Sarga, and E. Takas, *Phys. Scr.* **T59**, 392 (1995).
- ³¹R. W. Schmieder and R. J. Bastasz (unpublished).
- ³²R. W. Schmieder and R. J. Bastasz, in *Proceedings of the VIth International Conference on the Physics Highly Charged Ions* (Ref. 14), p. 675.
- ³³R. Morgenstern and J. Das, *Europhys. News* **25**, 3 (1994).
- ³⁴J. Limburg, J. Das, S. Schippers, R. Hoekstra, and R. Morgenstern, *Phys. Rev. Lett.* **73**, 786 (1994).
- ³⁵I. Hughes, *Physics World* **8**, 43 (1995).
- ³⁶N. Itabashi, K. Mochiji, H. Shimizu, S. Ohtani, Y. Kato, H. Tanuma, N. Kobayashi, *Jpn. J. Appl. Phys.* **34**, 6861 (1995).
- ³⁷I. S. Bitenski, M. N. Murakhmetov, and E. S. Parilis *Zh. Tekh. Fiz.* **49**, 1044 (1979) [*Sov. Phys. Tech. Phys.* **24**, 618 (1979)].
- ³⁸M. A. Briere, T. Schnekel, and D. Schneider (unpublished).
- ³⁹P. Apell, *Nucl. Instrum. Methods B* **23**, 242 (1987).
- ⁴⁰J. P. Briand, L. de Billy, P. Charles, S. Essabaa, P. Briand, R. Geller, J. P. Desclaux, S. Bliman, and C. Ristori, *Phys. Rev. Lett.* **65**, 159 (1990).
- ⁴¹J. P. Briand, B. d'Etat, D. Schneider, M. Clark, and V. Decaux, *Nucl. Instrum. Methods B* **87**, 138 (1994).
- ⁴²B. d'Etat, J. P. Briand, G. Ban, L. de Billy, J. P. Desclaux, and P. Briand, *Phys. Rev. A* **48**, 1098 (1993).
- ⁴³J.-P. Briand, B. d'Etat-Ban, D. Schneider, M. A. Briere, V. Decaux, J. W. McDonald, and S. Bardin, *Phys. Rev. A* **53**, 2194 (1996).
- ⁴⁴F. Aumayr, H. Kurz, D. Schneider, M. A. Briere, J. W. McDonald, C. E. Cunningham, and H. P. Winter, *Phys. Rev. Lett.* **71**, 1943 (1993).
- ⁴⁵P. Apell, *J. Phys. B* **21**, 2665 (1988).
- ⁴⁶J. N. Bardsley and B. M. Penetrante, *Comments At. Mol. Phys.* **27**, 43 (1991).
- ⁴⁷E. Y. Wu, R. J. Friauf, and T. P. Armstrong, *Surf. Sci.* **249**, 350 (1991).
- ⁴⁸N. Vaeck and J. E. Hansen, *J. Phys. B* **28**, 3523 (1995).
- ⁴⁹J. Tersoff, *Phys. Rev. B* **39**, 5566 (1988).
- ⁵⁰S. Wei (private communication).
- ⁵¹M. P. Allen and D. J. Tildesley, *Computer Simulations of Liquids* (Clarendon, Oxford, United Kingdom, 1987).
- ⁵²K. Y. Kim, W. Sachse, and A. G. Every, *J. Acoust. Soc. Am.* **93**, 1393 (1993).
- ⁵³K. M. Yoo, X. M. Zhao, M. Siddique, R. R. Alfano, D. P. Osterman, M. Radparvat, and J. Cunniff, in *Chemical Physics*, edited by C. B. Harris, E. P. Ippen, G. A. Morou, and A. H. Zewail (Springer-Verlag, 1990), Vol. 53, p. 357.
- ⁵⁴P. B. Allen, *Phys. Rev. Lett.* **59**, 1460 (1987); S. D. Broson, J. G. Fujimoto, and E. P. Ippen, *Phys. Rev. Lett.* **59**, 1962 (1987).
- ⁵⁵D. C. Parks, R. Bastasz, R. W. Schmieder, and M. Stockli, *J. Vac. Sci. Technol. B* **13**, 941 (1995).
- ⁵⁶J. Burgodorfer, C. Reinhold, L. Hagg, and F. Meyer, *Aust. J. Phys.* **49**, 527 (1996).
- ⁵⁷L. Folkerts, S. Schippers, D. M. Zehner, and F. W. Meyer, *Phys. Rev. Lett.* **74**, 2204 (1995).
- ⁵⁸P. Barga, *Comments At. Mol. Phys.* **23**, 111 (1989).
- ⁵⁹N. Stolterfoht, A. Arnau, M. Grether, R. Kohrbruck, A. Spieler, R. Page, A. Saal, J. Thomaschewski, and J. Bleck-Neuhaus, *Phys. Rev. A* **52**, 445 (1995).
- ⁶⁰S. Schippers, S. Hustedt, W. Heiland, R. Kohrbruck, J. Bleck-Neuhaus, J. Kemmler, D. Leeler, N. Stolterfoht, *Nucl. Instrum. Methods B* **78**, 106 (1993).
- ⁶¹X.-S. Wang, R. J. Pechman, and J. H. Weaver, *J. Vac. Sci. Technol. B* **13**, 2031 (1995).
- ⁶²H. Urbassek and K. T. Waldeer, *Phys. Rev. Lett.* **67**, 105 (1991).
- ⁶³R. Smith, K. Beardmore, and A. Gras-Marti, *Vacuum* **46**, 1195 (1995).
- ⁶⁴C. T. Reimann, A. P. Quist, J. Kopniczky, B. U. R. Sundqvist, R. Erlandsson, and P. Tengvall, *Nucl. Instrum. Methods B* **88**, 29 (1994).
- ⁶⁵D. D. N. Barlo Daya, A. Hallen, P. Hakansson, B. U. R. Sundqvist, and C. T. Reimann, *Nucl. Instrum. Methods B* **103**, 454 (1995).

Large Scale Molecular Dynamics Simulation of a Surface Coulomb Explosion.

Hai-Ping Cheng

*Department of Physics & QTP
University of Florida
Gainesville Fl 32611*

and

J. D. Gillaspay

*Physics Laboratory
National Institute of Standards and Technology
Gaithersburg, MD 20899*

Highly charged ions colliding with a solid have been predicted to produce localized Coulomb explosions on the surface. We have modeled the explosion using a large scale molecular dynamics simulation. Our results show the temporal evolution of three different types of craters which are formed when an incident highly charged ion produces 100 singly-charged Si atoms in various initial distributions on the surface. The total number of ejected particles ranges from 245 to 317 and appears to be determined by the initial shape of the ionized region rather than simply by the initial repulsive energy restored in the charged region. Contrary to intuition, a long and thin cylindrical distribution is the most efficient pattern for ejecting particles. In all three cases, the number of ejected neutral particles is much greater than the number of ejected ions (6-10 times as many atoms as ions). The angular distribution of ejected particles is also analyzed.

INTRODUCTION

Recent developments in highly charged ion-surface bombardment experiments (reviewed in [1]) have generated a major need for theoretical modeling and understanding at the atomic level. In some of the experiments, when a slow, highly charged ion (HCI) collides with a non-metallic surface, a hillock or crater of nanometer-size can be generated and directly imaged with atomic force microscopy [1-2]. Several groups have speculated that research with HCIs may lead to important practical applications in the fabrication of nanostructures on surfaces[1-7].

The experimental investigations have shown that the creation of surface features is sustained down to very low kinetic energies, at which point most of the energy is deposited in the form of internal potential energy of the ion [2]. A Coulomb explosion was postulated as a mechanism for the formation of such craters as early as 1979 [8]. Since then, considerable effort by a number of groups [1-15] has been put into studying the electronic transitions and ionization processes during HCI-surface bombardment.

Explicit descriptions and depictions of the surface Coulomb explosion dynamics [4, 5, 7, 9, 15] have been largely phenomenological in character, however. Since the lattice dynamics governs the

formation of craters, understanding the Coulomb explosion at the atomic level is a first step towards a more complete and fundamental understanding of the overall process.

Our previous paper [16], involving approximately 300 surface charges, was the first that provided a microscopic description of Coulomb explosion based on a large-scale molecular dynamics simulation. We demonstrated the explosion process on a silicon surface with specified model initial conditions. Shockwave propagation, ultra-rapid evaporation of surface atoms, and the formation of craters were analyzed in detail, and atomic-scale visualizations of the explosion process were presented.

In this work, we carry out additional simulations involving fewer initial surface charges and we focus on a comparative study of the influence of the initial shapes of the charged region on the final crater shape, as well as on the angular distribution of emitted particles.

SIMULATIONS

Numerical solutions of the Newtonian equations of motion are obtained via Gear's predict-corrector algorithm [17] for an N particle system. Each

of the 34560 particles interacts with each of the other particles. We use the Tersoff potential [18] for Si-Si interactions, $1/r$ Coulomb potential for Si^+-Si^+ interactions and a 12-4 potential of the following form for Si-Si⁺ interactions:

$$V(r_{ij}) = \varepsilon \left[\left(\frac{\sigma}{r_{ij}} \right)^{12} - \left(\frac{\sigma}{r_{ij}} \right)^4 \right] \quad (1)$$

The parameters ε and σ are obtained as described previously [16] by combining first-principle calculations and experimental data.

The substrate is represented by a slab that is periodically repeated in x and y directions. In the positive z direction, we use free boundary condition for the surface. We use a few static layers at the bottom of the substrate to stabilize the systems. By controlling the temperature of the layer(s) between dynamical layer and static layers, we simulate a infinite substrate in $-z$ direction. To properly treat the system we are interested in, the periodic boundary conditions in x , y directions are not applied to ions.

At $t=0$, 100 Si ions are embedded in the Si surface. The shape of the three initial charge distributions we choose to study are hemispherical, flat disc, and long thin cylindrical. The initial temperature of the substrate in all three cases is very low, about 10 K. The temperature of the static layers is fixed during the explosion processes to provide a heat bath for the dynamical layers above. We use time interval, $\Delta t = 0.4$ fs, to achieve energy conservation during the processes. The simulations are carried out for 1.6 ps.

RESULTS

Three initial shapes of the charged region is shown in figure 1. The positions of the atoms and ions at 160 fsec after the initial condition is illustrated in figure 2. At 1.6 ps, we collect particles that are more than 0.6 nm (12 a.u.) above the surface layer for each of the three simulations. The total numbers of ejected particles are 245, 245, and 317 for (a) hemisphere, (b) flat disc, and (c) long cylinder. The number of ejected ions of these three situations are 31, 35, and 24 respectively. At a first glance, the relative numbers of ejected ions is intuitive. Since (b) has the most ions on the surface layer, it is relatively easier for the ions to be pushed out. For the same reason, case (c) has the least number of ejected ions. Nevertheless, the total numbers of ejected particles are not what we would expect since they do not increase or decrease monotonically as a function of total initial energies. The repulsive Coulomb energies stored in the charged region for the three shapes (a)-(c) at $t=0$ are, 9.61 keV, 8.95 keV and 9.33 keV respectively. By summing up the

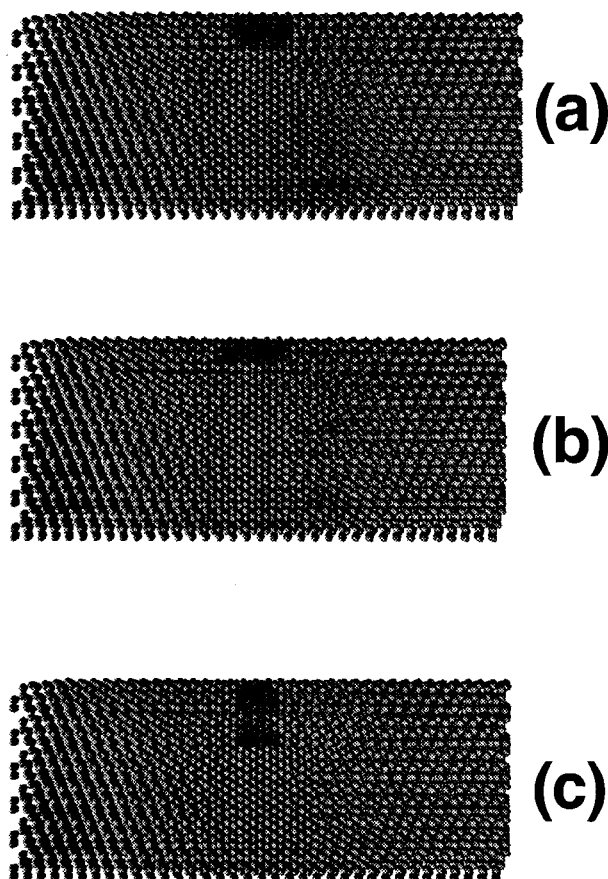


FIGURE 1. Molecular dynamics simulation of a Coulomb explosion in silicon at $t=0.0$ for initial charged region shaped as (a) hemisphere, (b) disc, and (c) cylinder. Ions are indicated with a darker shade than the atoms.

amount of energy dissipated into the substrate, we find that case (c) is higher than the other two cases. The higher efficiency of this geometry for depositing energy into the lattice explains the increased evaporation of surrounding lattice atoms.

From the simulation data, angular distribution of the total ejected particles can be obtained. Fig.3 displays the distribution of azimuthal angles of three simulations. All of the three histograms have a similar broad distribution over 0-100 degrees. On the other hand, the distribution patterns in the ejected ions of the three situations are quite different from each other (see Fig.4). The cylindrical shape has a relatively uniform distribution.

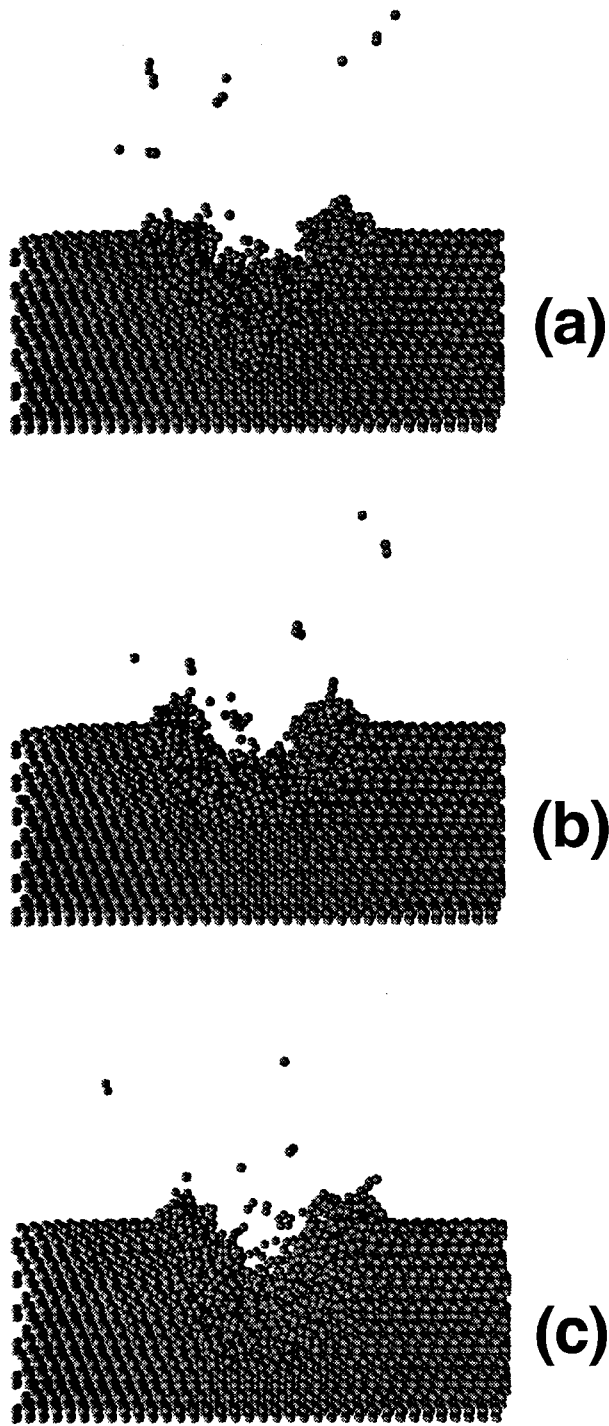


FIGURE 2. Molecular dynamics simulation of a Coulomb explosion in silicon at $t=0.160$ for initial charged region shaped as (a) hemisphere, (b) disc, and (c) cylinder.

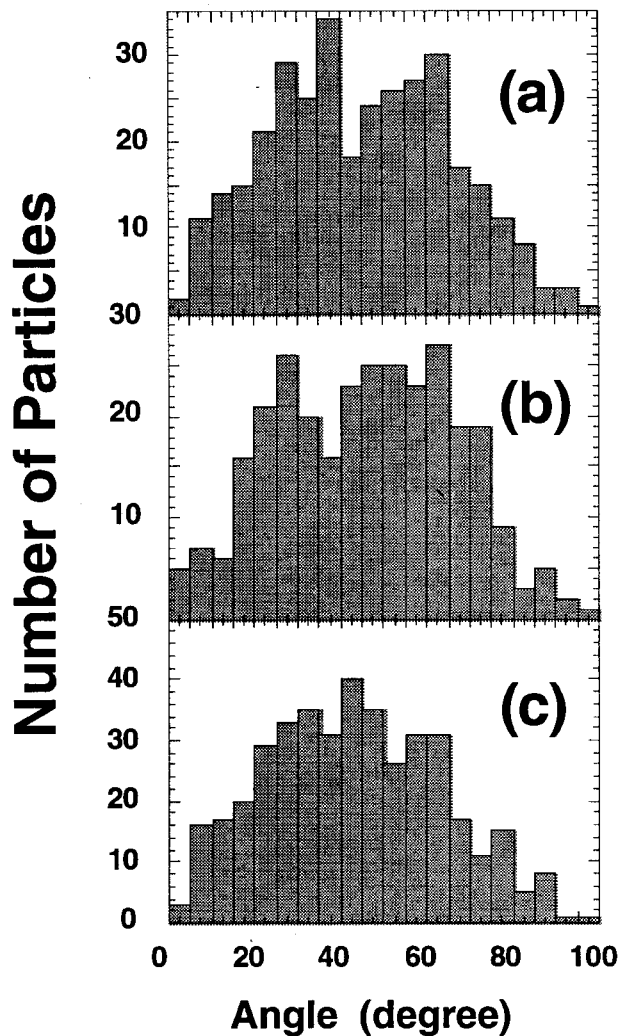


FIGURE 3. Distribution of azimuthal angle of all the particles (Si^+ and Si) ejected from the surface. Panel (a)-(c) represent a 100 ion system with a initial charge distribution of hemisphere, flat disc, and cylinder respectively.

CONCLUSIONS

Our simulation of Coulomb explosions on a Si surface suggest that $t \approx 100$ fs is an important time scale. In comparing this work to our previous work, we find that for all the systems under investigation, such as systems with 100, 265, and 365 ions, 10^2 fs is the time for shockwaves to collapse and for potential energies to drop to about e^{-1} of their initial values. The numbers of ejected particles depend on the energy that is dissipated into the substrate. This is the mechanism for the initial

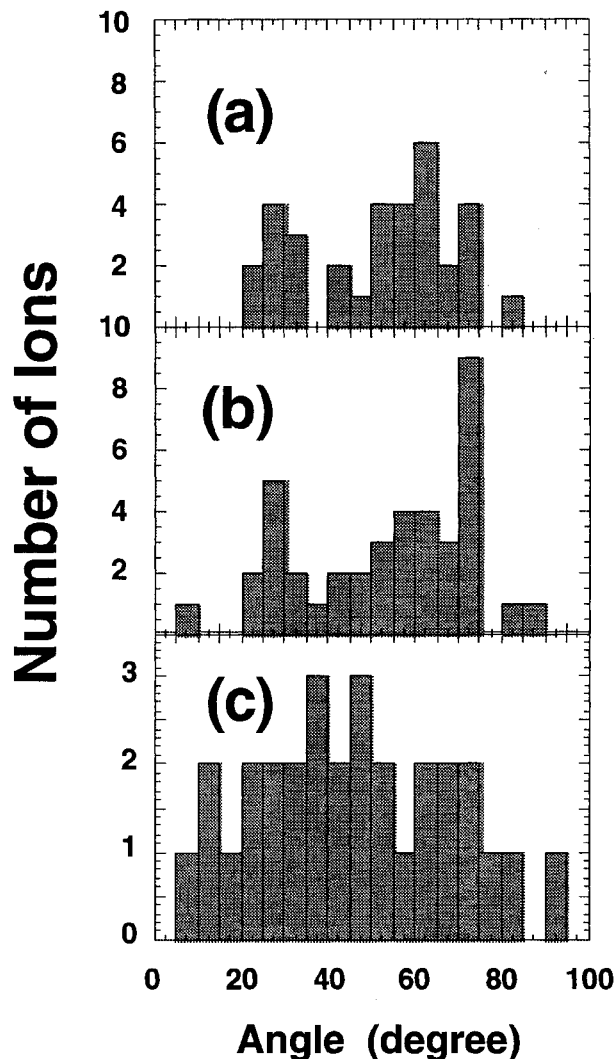


FIGURE 4. Distribution of azimuthal angle of all the ions (Si^+ only) ejected from the surface. Panel (a)-(c) represent a 100 ion system with a initial charge distribution of hemisphere, flat disc, and cylinder respectively. Notice the stronger shape dependence in fig.4 than in fig.3

shape dependence of the total ejected particles. Finally, we conclude that the fraction of energy that goes into the substrate decreases as the number of ions increases from 100 to 365.

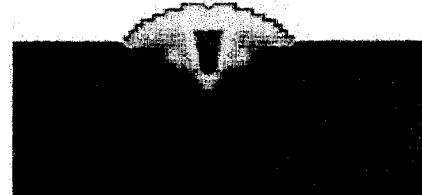
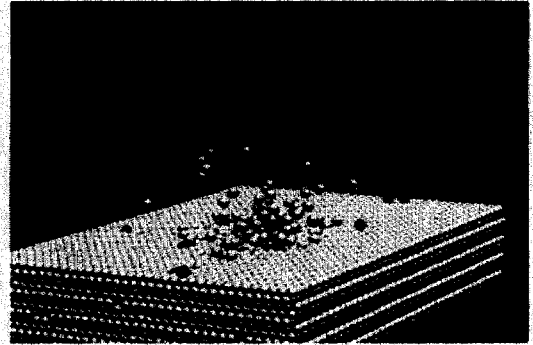
REFERENCES

1. D.H. Schneider, M.A. Briere, *Physica Scripta*, **53**, 228 (1996).
2. D.C. Parks, R. Bastasz, R.W. Schmieder, and M. Stöckli, *J. Vac. Sci. Technology*. **B13**, 941(1995).

3. R.W. Schmieder and R.J. Bastasz, *Proc. Vllth Intl. Conf. Physics Highly Charged Ions*, AIP Conf. Proc. **274**, 675 (1992).
4. Itabashi, 1995: N. Itabashi, K. Mochiji, H. Shimizu, S. Ohtani, Y. Kato, H. Tanuma, N. Kobayashi, *Jpn. J. Appl. Phys.*, **34**, 6861 (1995).
5. 11. R. Morgenstern and J. Das, *Europhysics News*, **25**, no. 1, 3 (1994)
6. J.D. Gillaspy, Y. Agilitskiy, E.W. Bell, C.M. Brown, C.T. Chantler, R.D. Daslettes, U. Feldman, L.T. Hudson, J.M. Laming, E.S. Meyer, C.A. Morgan, A.L. Pikin, J.R. Roberts, L.P. Ratliff, F.G. Serpa, J. Surga, and E. Takas, *Physica Scripta*, **T59**, 392 (1995).
7. I. Hughes, *Physics World*, **8**, no. 4, 43 (1995);
8. I.S. Bitenskii, M.N. Murakhmetov and E.S. Parilis, *Sov. Phys. Tech. Phys.* **24**, 618(1979).
9. D. Schneider, M.A. Briere, T. Schenkle, EBIT, N-Division, Livermore annual report (1994).
- 10.P. Apell, *J. Phys. B*, **21**, 2665 (1988); N. Vaeck and J. E. Hansen, *J. Phys. B*, **28**, 3523 (1995);
11. F. Aumayr, H. Kurz, D. Schneider, M.A. Briere, J.W. McDonald, C.E. Cunningham, and H.P. Winter, *Phys. Rev. Lett.*, **71**, 1943 (1993); P. Varga, *Comments At. Mol. Phys.*, **23**, 111 (1989).
12. J.P. Briand, B. d'Etat-Ban, D. Schneider, M.A. Briere, V. Decaux, J.W. McDonald, and S. Bardin, *Phys. Rev. A*, **53**, 2194 (1996).
13. J. Burgdorfer, C. Reinhold, and F. Meyer, *Nucl. Instrum. and Methods in Phys. Res.*, **B**, **98**, 415 (1995).
- 14 M. Grether, A. Spielder, R. Kohnbruck, and N. Stolterfoht, *Phys. Rev. A*, **52**, 426 (1995).
15. E. Parilis, Caltech preprint.
16. Hai-Ping Cheng and J.D. Gillaspy, *Phys. Rev. B*, Jan. 15 (1996).
17. M.P. Allen and D.J. Tildesley, *Computer Simulations of Liquids* (Clarendon, Oxford, United Kingdom, 1987).
18. J. Tersoff, *Phys. Rev. B* **39**, 5566 (1988).

VOLUME 9, Nos. 3-4
JANUARY 1998
COMMAT 9 (3-4) 285-434 (1998)
<http://www.elsevier.nl>

COMPUTATIONAL MATERIALS SCIENCE



Editors:
U. LANDMAN and
R. NIEMINEN

LAST ISSUE OF THIS VOLUME

ELSEVIER

ISSN 0927-0256

NIST-259

Copyright © 1998 Elsevier Science B.V. All rights reserved.

This journal and the individual contributions contained in it are protected by the copyright of Elsevier Science B.V., and the following terms and conditions apply to their use:

Photocopying

Single photocopies of single articles may be made for personal use as allowed by national copyright laws. Permission of the publisher and payment of a fee is required for all other photocopying, including multiple or systematic copying, copying for advertising or promotional purposes, resale, and all forms of document delivery. Special rates are available for educational institutions that wish to make photocopies for non-profit educational classroom use.

In the USA, users may clear permissions and make payment through the Copyright Clearance Center, Inc., 222 Rosewood Drive, Danvers, MA 01923, USA, tel.: (508) 750-8400, fax: (508) 750-4744. In the UK, users may clear permissions and make payment through the Copyright Licensing Agency Rapid Clearance Service (CLARCS), 90 Tottenham Court Road, London W1P 0LP, UK, tel.: (171) 4365931; fax: (171) 4363986. In other countries where a local copyright clearance centre exists, please contact it for information on required permissions and payments.

Derivative works

Subscribers may reproduce tables of contents or prepare lists of articles including abstracts for internal circulation within their institutions. Permission of the publisher is required for resale or distribution outside the institution.

Permission of the publisher is required for all other derivative works, including compilations and translations.

Electronic storage

Permission of the publisher is required to store electronically any material contained in this journal, including any article or part of an article. Contact the publisher at the address indicated.

Except as outlined above, no part of this publication may be reproduced, stored in a retrieval system or transmitted in any form or by any means, electronic, mechanical, photocopying, recording or otherwise, without prior written permission of the publisher.

No responsibility is assumed by the Publisher for any injury and/or damage to persons or property as a matter of products liability, negligence or otherwise, or from any use or operation of any methods, products, instructions or ideas contained in the material herein.

☉ The paper used in this publication meets the requirements of ANSI/NISO Z39.48-1992 (Permanence of Paper).

Printed in The Netherlands

Cover: Distributions of particle, velocity and temperature during Colomb explosion. For more details see the paper by H.-P. Cheng and J.D. Gillaspay on page 285 of this issue.

Surface Coulomb explosions: The influence of initial charge distributions

Hai-Ping Cheng ^{a,*}, J.D. Gillaspay ^b

^a *Department of Physics and QTP, University of Florida, Gainesville, FL 32611, USA*

^b *Physics Laboratory, National Institute of Standards and Technology, Gaithersburg, MD 20899, USA*

Received 14 March 1997; accepted 10 May 1997

Abstract

Using molecular dynamics simulations, we have studied the Coulomb explosion processes on silicon surfaces. Three different initial shapes of ion distributions are used to model the possible localized charge distributions generated in highly charged ion (HCI)-surface impact. The three distinct distributions include a hemispherical, a flat disk, and a long and thin cylindrical geometrical. At $t = 0$, 100 singly-charged Si ions are embedded in the Si(111) surfaces. In about 100 fs, the strong repulsive electrostatic forces in these three systems cause Coulomb explosions and thus create three different shapes of craters on the surfaces. All simulations are carried to 1.6 ps, at which point the size and shape of the craters are nearly stabilized. The detailed analysis of the ejected ions, atoms, and the substrates reveals the dynamical consequences of the different initial conditions. For these 100 ions, the differences in the total number of the ejected particles, ranging from 245 to 317 particles, appear to be determined by the initial shape of the ionized region and not by the initial repulsive energy restored in the charged region. Contrary to intuition, a long and thin cylindrical distribution is the most efficient pattern for ejecting particles. The underlying mechanism is that ions with this initial configuration transfer more energy to the surrounding atoms. In all three cases, the number of ejected neutral particles are much greater than the number of ions (6–10 times as many atoms as ions). Among the ejected particles, a small percent of particles are found to return the surface at a later time. The angular distribution of ejected particles are also analyzed. While the differences in the distributions of polar angle of the Si atoms of the three configurations is small, the differences in distributions of the ions portray a strong shape dependence in the polar angle. © 1998 Published by Elsevier Science B.V.

1. Introduction

Recent developments in highly charged ion–surface bombardment experiments [1–5] have generated a major need for theoretical modeling and understanding of the HCI–surface interactions and the

dynamical consequences of the interactions at the atomic level. The basic physical picture of HCIs interacting with a surface is as follows (Fig. 1): when a HCI approaches a surface, its intense Coulomb field rapidly pulls electrons from the solid, even when the ion is many atomic diameters away from the surface (up to 80 bohr radii or more in some models [6,7]). Some of the emitted electrons are captured into high-lying Rydberg levels of the ion, producing a super-excited ‘hollow atom’ [8–10],

* Corresponding author. Tel.: +1-352-3921597; fax: +1-352-3928722; e-mail: cheng@qtp.ufl.edu.

while others simply escape. The hollow atom can rapidly decay (collapse) via Auger cascade, ejecting electrons in the process [11,12]. The ion can then continue to remove electrons from the solid, eventually removing many more electrons than would be required for a simple neutralization of the ion. Furthermore, highly excited surface atoms can also undergo processes that contribute to the massive electron emission. Emissions of up to approximately 300 electrons per ion have been observed [11,12], and some theories predict that by further increasing the charge of the incident ion it should be possible to remove over 1000 electrons per ion [6].

In insulators or semiconductors, experiments on multiply charged ion (MCI)–LiF [13], MCI–GaAs [14,15], HCI–SiO₂, and HCI–mica surface bombardment have shown that at a given kinetic energy, the sputtering yield and/or secondary ion yield and/or size of induced surface defect increases as the charge of the projectile ions increases. The effects are much larger for HCI bombardment compared with conventional ion–surface bombardment. Nanometer size surface features have been observed via atomic force microscopy (AFM) in some cases. We note that ordinary surface sputtering relies on direct contact between the projectile ion and the surface and is dominated by the kinetic energy. The experimental investigations have also shown that the creation of surface features is sustained down to very low kinetic energies at which point most of the energy is deposited in the form of internal potential energy of the ion [2]. This phenomenon suggests the potential application of HCI beams in the fabrication of shallow nano-structures on surfaces.

A Coulomb explosion was postulated as the mechanism of the formation of the craters in the

HCI–surface interactions in the early 70's [16]. Since then numerous efforts have been made in studying the electronic transitions and ionization processes during the HCI–surface bombardment [17–24]. Most of the descriptions of the surface dynamics have remained primarily phenomenological until very recently, when we published the first full-scale molecular dynamics simulations [25] that provide a microscopic description of Coulomb explosions on Si [111] surfaces. In our previous paper, we have demonstrated the explosion processes with simple model initial conditions. Shockwave propagation, ultra-rapid evaporation of surface atoms, and the formation of craters were analyzed in detail and the first atomic-scale visualizations of the explosion process were presented. Previous depictions of surface Coulomb explosions have been essentially artist's conceptions [3,26–31].

Since the lattice dynamics govern the formation of craters, continuing of our investigations of the Coulomb explosion at the atomic level is necessary and an important step towards a more complete and fundamental understanding of the overall process. Our previous study is based on a simplified theoretical model that assumes an instant ionization of atoms in a hemispherical region in the surface. Reality, however, can be more complicated. The detailed dynamics of charge transfer from the surface to the incoming ion and the charge flow from the substrate to the surface remains unknown. While our initial results capture the fundamental physical picture, there are still many dimensions in the parameter space which can be explored. A modification of the simple model will allow the investigation of the effects of the initial density distribution of the charged region. This focus will allow for the possibility of multiply-charged surface ions, ions spreading over a larger area with neutral atoms in between, and a variety of geometrical shapes. A large range of physical situations, including a partially quenched Coulomb explosion, can then be modeled. To date, very little experimental information is available on the exact distribution of the positive charge. Investigations of the correlation between the initial density distribution and/or geometry of the charged region and the topology of the craters will provide valuable input for theoretical modeling of electron emission and the resulting crater topography. Further improvement of

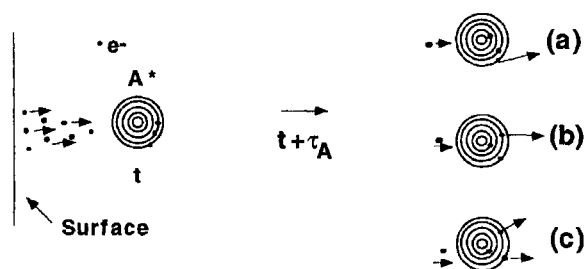


Fig. 1. Schematic picture of HCI–surface interactions. (a)–(c) illustrate three of the possible Auger cascade processes after $t + \tau_A$, the lifetime of a particular excited state A^* of the projectile ion.

the model will include the rate of electron hopping from substrate to the surface ions, the initial kinetic energy of the incident HCl, the time duration needed for a complete neutralization of the HCl, and differences among different surface materials. All of these processes are involved in crater formation. It is necessary to isolate and test the importance of each individual factor.

In this work, simulations were performed with a focus on the comparative study of the influence of the initial shapes of charged region on the final crater shape, as well as on angular distribution of

emitted particles. We investigated the Coulomb explosion on Si(111) surfaces caused by the repulsive interactions among the 100 ions. From the simulation results, we analyzed the differences in the physical properties such as number of ejected atoms and ions, angular distributions, and energetics as consequence of the different shapes of the initial charged region. Dynamics of substrate atoms were studied via a detailed analysis of their phase-space trajectories. This work has demonstrated the dynamic properties of the surface for a longer time period than our previous work, and along all directions of Si(111)

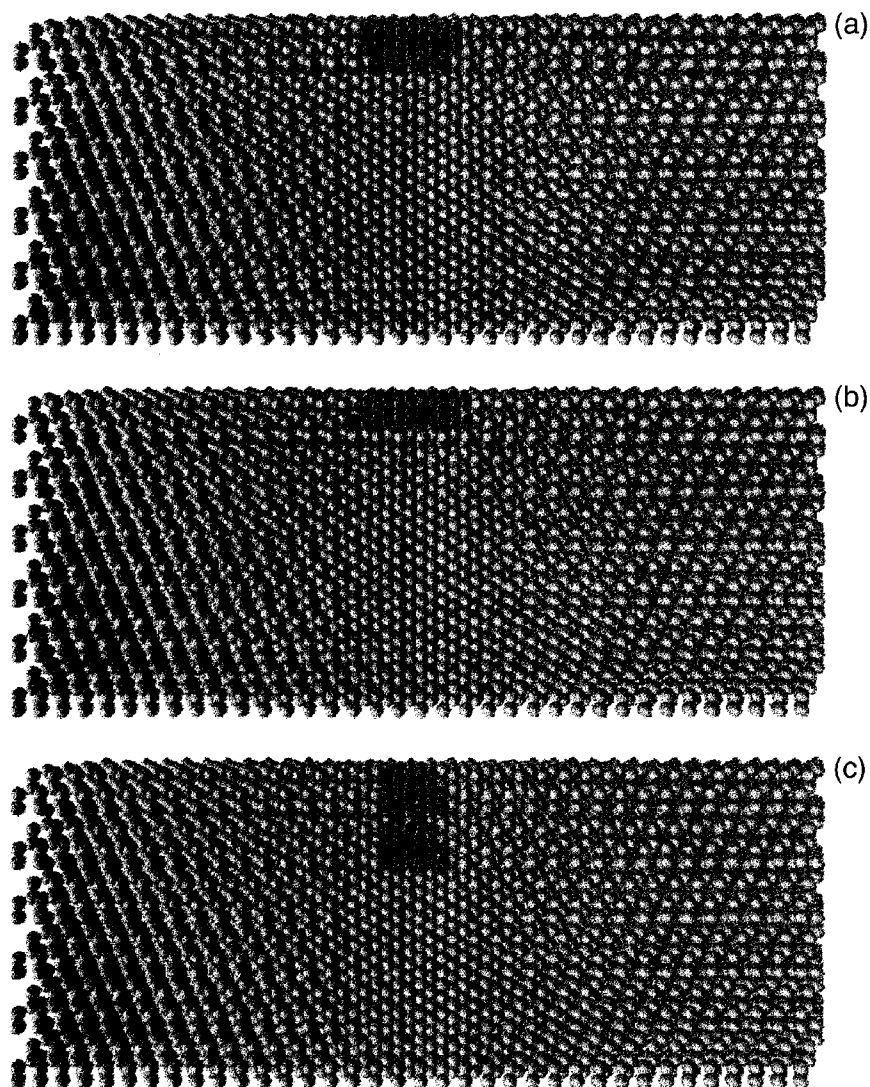


Fig. 2. Molecular dynamics simulation of a Coulomb explosion in silicon at $t = 0.0$ for the initial charged region shaped as (a) hemisphere, (b) disc, and (c) cylinder. Ions are indicated with a red sphere and atoms are in green.

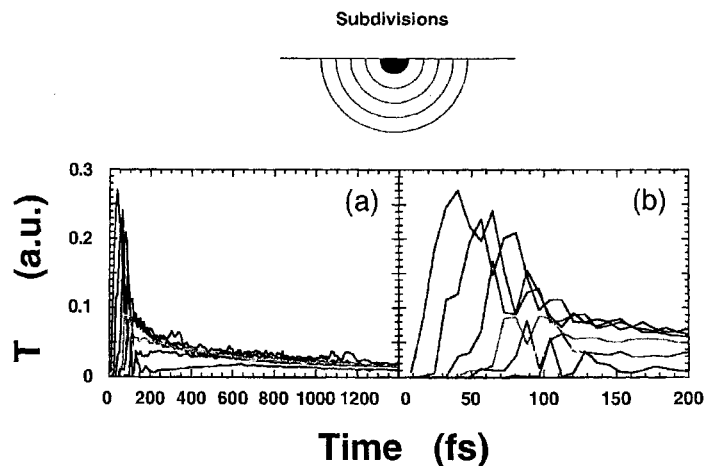


Fig. 3. Temperature of sub-regions of the substrate as a function of time. The subregions correspond to several concentric shells with a thickness of 0.255 nm (5 a.u.). The jumps in temperature seen in each shell indicate a shock wave propagating through the substrate. After 120 fs, the temperatures in different shells converge to the same value. Numbers are given in a.u. where 9.50×10^{-4} a.u. = 300 K.

surface crystalline. Shockwave propagation and dissipation are demonstrated using visualization. Preliminary results from part of this work were presented earlier in a short conference paper [32].

2. Simulations

Classical MD simulations based on parameterized interatomic potentials are used to study Coulomb explosion processes. The classical equation of motion

$$m_i \frac{d^2 \mathbf{R}_i}{dt^2} = -\nabla U(\mathbf{R}_1, \mathbf{R}_2, \dots, \mathbf{R}_n), \quad (1)$$

for each atom (ion) in the dynamical substrate is integrated using Gear's predictor–corrector algorithm [33]. Positions, velocities, and accelerations of all the atoms and ions are obtained via numerical solution of the classical equations of motion at each time step, and stored for later analysis. From the

phase–space trajectories, physical properties such as distributions of temperature, pressure, stress, and potential energy are derived [25,34,35].

The model interaction potential functions are chosen to properly describe the material properties and the dynamical processes. In our simulations we use Tersoff potential [36] for Si–Si interactions, $1/r$ Coulomb potential for $\text{Si}^+ - \text{Si}^+$ interactions and a 12–4 potential for Si– Si^+ interactions. The 12–4 potential has the following form:

$$V(r_{ij}) = \varepsilon \left[\left(\frac{\sigma}{r_{ij}} \right)^{12} - \left(\frac{\sigma}{r_{ij}} \right)^4 \right]. \quad (2)$$

The parameters ε and σ are obtained as described previously [25] by combining first-principle calculations and experimental data. It should be pointed out that the Si– Si^+ and $\text{Si}^+ - \text{Si}^+$ potentials have not been optimized extensively. However, for the events of interest in this study, this potential captures the basic physical features of the important atomic interactions.

Fig. 4. Top view of a Si surface initially with a (a) hemispherical, (b) flat disc, and (c) long cylindrical charged region. The snapshots are taken at $t = 400$ fs. The colors indicate the value of the square root of the speed of the atoms. The numbers are given in a.u. where 1.95×10^{-2} a.u. = 1.0 km/s. Hexagonal shockwave fronts for all three cases can be observed.

Fig. 5. Top view of a Si surface initially with a long cylindrical charged region. The snapshots are taken at (a) $t = 500$ fs and (b) 600 fs. Panel (c) is a top view of 1.02 nm ($20 a_0$) under the surface at 400 fs. The colors indicate the value of the square root of the speed of the atoms. The numbers are given in the same units as defined in Fig. 4. The shockwave fronts are again visible with a hexagonal geometry in panels (a)–(c).

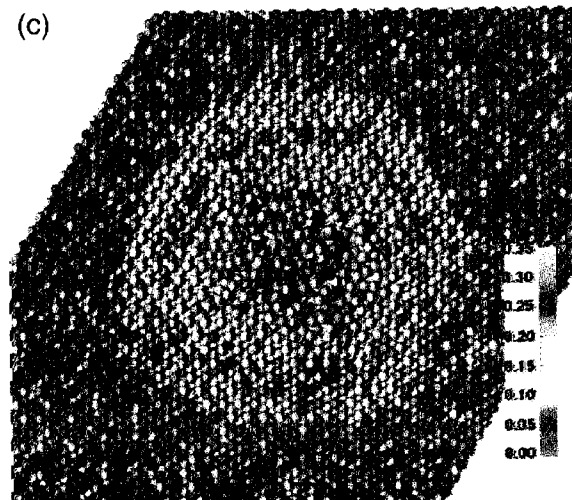
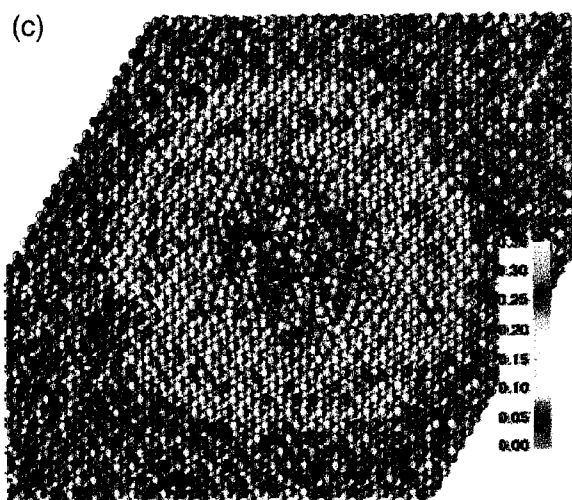
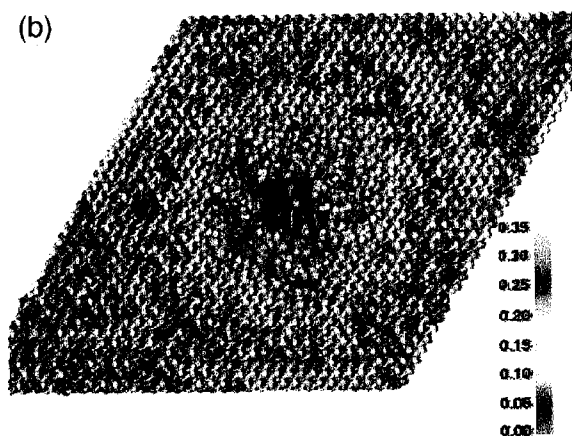
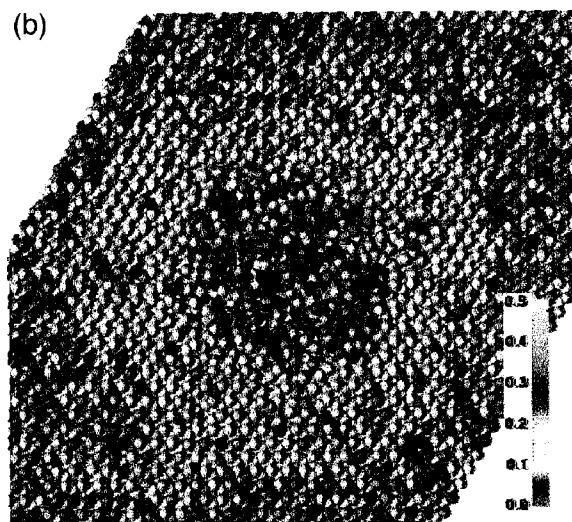
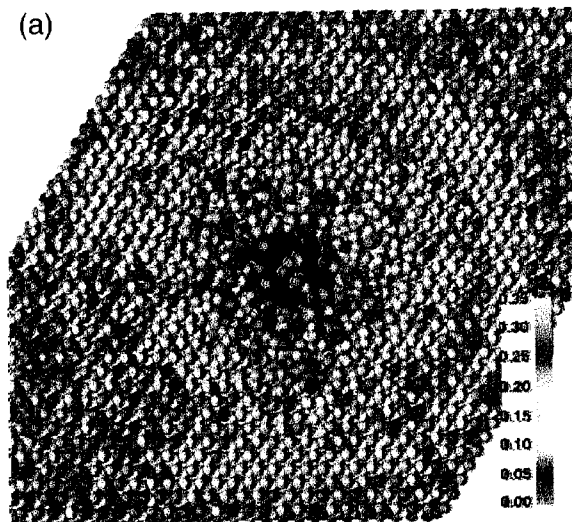
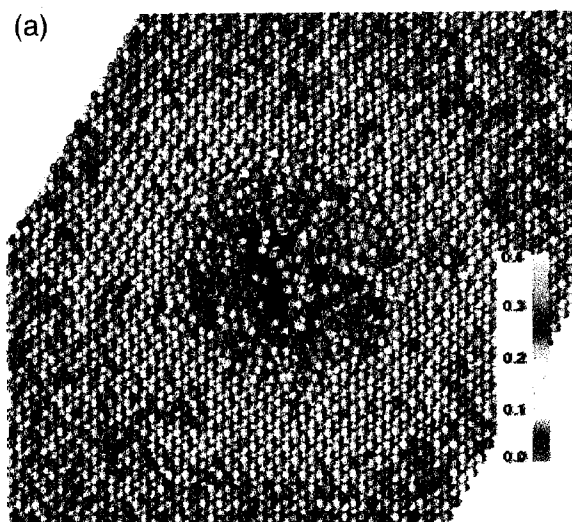


Fig. 4

Fig. 5

The substrate is represented by a slab that is periodically repeated in xy directions. The total number of atoms (ions) in the unit cell is chosen to be 45,360. The size of the slab is about $13 \times 13 \times 5.6$ nm³. The direction of the (111) surface is chosen along positive z , in which a free boundary condition is applied. The total number of surface layers is 17, out of which three layers at the bottom of the substrate are held static to stabilize the systems. During the explosion, the temperature control is applied to a layer right above the three static layers to allow heat exchange between the system and a heat bath. This arrangement allows simulations of a substrate which is infinite in negative z direction. To properly treat the system for our dynamic studies, the periodic boundary conditions in x , y directions are not applied to ions.

As we already introduced in the previous paper [25], a simple model is used to describe the initial conditions. In this simple model, the ionization of a local region in the surface occurs much rapidly compared to lattice motion. This simplification is made to simulate the consequences of bringing a slow, highly-charged ion, such as Xe⁴⁴⁺ or U⁹²⁺ to the vicinity of a non-metallic surface. Based on the simple model, at $t = 0$, 100 Si ions are embedded in the Si surface. The shape of the three initial charge distributions we choose to study are: (a) hemispherical, (b) flat disc, and (c) long thin cylindrical. The initial temperature of the substrate in all three cases is sufficiently low, about 10 K, so that it is a very poor electrical conductor under equilibrium conditions.

The temperature control to the deepest dynamical layer is applied during the explosion processes. Initially, we used a time interval, $\Delta t = 0.4$ fs, to achieve energy conservation during the processes. After about 1.0 ps, the time interval is increased to 0.8 fs to maximize efficiency. All three simulations are carried out for 1.6 ps.

3. Results

The positions of the atoms and ions at $t = 0$ and 1.6 ps are illustrated in Fig. 2 (cross sections). The radius of the hemisphere is 0.92 nm ($18 a_0$). The height and radius of the flat disc is 0.37 nm ($7.3 a_0$),

and 0.97 nm ($19 a_0$), respectively. For the cylindrical shape, the height and radius are 1.53 nm ($30 a_0$), and 0.577 nm ($11.3 a_0$), respectively.

The temperature analysis in the subdivisions adjacent to the explosion center indicates strong shock wave propagation in the substrates for the first 100 fs (Fig. 3). This phenomenon has been described in our previous paper for systems with 265–365 ions. The speed of the shockwave in case (a) is 15 km/s. This is slightly lower than the value in the systems with more ions [25] since the energy that causes the shockwave is lower in the 100 ion case compared to the 265 or 365 ion cases. Further analysis on the kinetic energy reveals that the shock waves can last much longer than 100 fs, which is the time scale for extremely strong shock we presented in our previous paper.

In Fig. 4 we illustrate the distribution of kinetic energy of each individual particle in a system. The color bar is calibrated according to the square root of speed of the atoms in order to increase the contrast of the wave front. At 400 fs, we can see the shock wave moving away from the center of the explosion. All three simulations display a hexagonal shape of the wave front which reflects the symmetry of surface crystalline structure.

The cylindrical shape, case (c), at 400 fs displays the most clear picture of shock wave propagation. The hexagonal patterns are similar to the one in Fig. 4 upon viewing the lower surface layers (Fig. 5). The patterns are blurred at later times (Fig. 5), indicating further dissipation of the shock. At 600 fs, the wave fronts reach the boundary of the system, and our simulation with the chosen unit box size cannot properly follow the propagation any further.

The disc shape, case (b), shows a different picture. It does not have a clear shock wave ring as seen in case (c). On the other hand, in some directions, the energy propagation is faster than most of the other directions. The colors indicate that some particles ahead of the hexagonal wave front carry higher kinetic energy than particles at the hexagonal shock wave front. This fast-modes propagation is quasi-one dimensional as shown in Fig. 4. The characteristic pattern quickly diminishes as the depth into the surface layer increases.

The hemispherical shape, case (a), falls in between (b) and (c). It should be mentioned that the

‘square root of velocity’ color scale makes the shockwaves considerably more easy to visualize. Although this choice is still somewhat ad hoc, it suggests a way to detect shockwave fronts in a complicated system. Further development is under-way to process the images.

At 1.6 ps, we collect particles that are more than 12 a.u. above the surface layer for each of the three simulations. The total numbers of ejected particles are 245, 245, and 317 for (a) hemisphere, (b) flat disc, and (c) long cylinder. The numbers of ejected ions corresponding to the three situations are 31, 35, and 24, respectively. At first glance, the relative numbers of ejected ions is intuitive. Since (b) has the most ions on the surface layer, it is relatively easier for ions to be pushed out. For the same reason, case (c) has the least number of ejected ions. Nevertheless, the total numbers of ejected particles are not what we would expect since they do not increase or decrease monotonically as a function of total initial energies. The repulsive Coulomb energies stored in

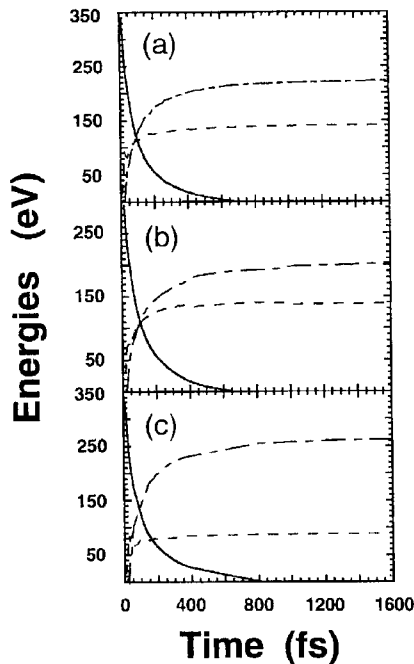


Fig. 6. Energies as a function of time. The solid line is the potential energy of the ions, the dashed line is the kinetic energy of the ions, and the dotted–dashed line is the energy dissipated into the substrate. Panels (a)–(c) represent a 100 ion system with an initial charge distribution of hemisphere, flat disc, and cylinder, respectively. Notice the curve crossing at 100 fs.

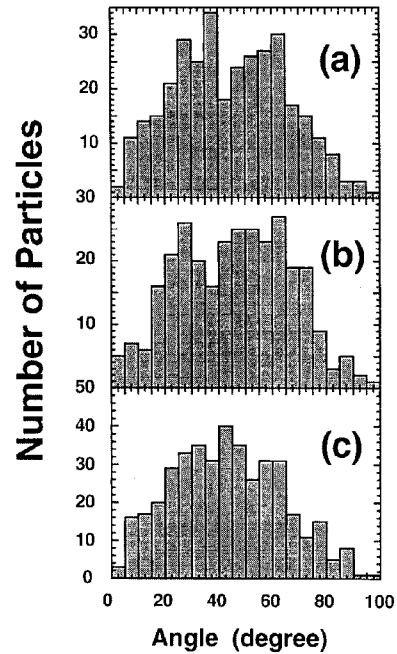


Fig. 7. Distribution of the polar angle of all the particles (Si^+ and Si) ejected from the surface. Panels (a)–(c) represent a 100 ion system with a initial charge distribution of hemisphere, flat disc, and cylinder, respectively.

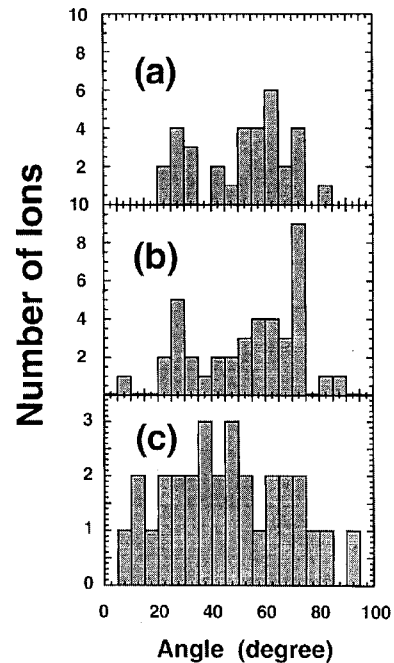


Fig. 8. Distribution of the polar angle of all the ions (Si^+ only) ejected from the surface. Panels (a)–(c) represent a 100 ion system with a initial charge distribution of hemisphere, flat disc, and cylinder, respectively. Notice the stronger shape dependence in Fig. 3 than in Fig. 2.

the charged region for the three shapes (a)–(c) at $t = 0$ are 9.61, 8.95 and 9.33 keV, respectively.

To explain this phenomenon, we study the partitioning of energy during the explosions. Fig. 6 dis-

plays the time dependence of three energies: the potential energy of the ions, the kinetic energy of the ions, and the energy dissipated into the substrate. It is immediately seen that for case (c) the third energy

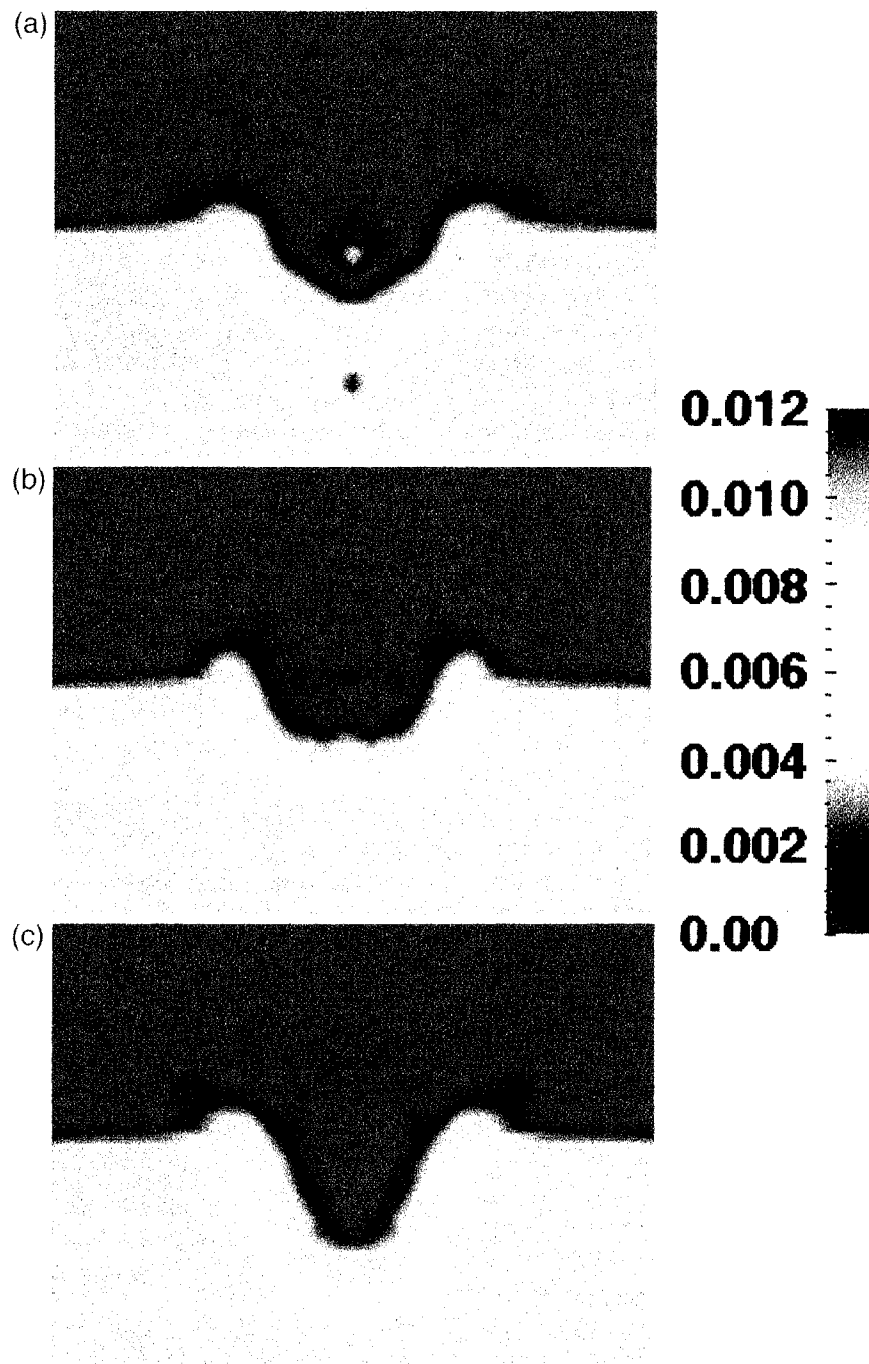


Fig. 9. Density plots of the three systems at 1.6 ps. Panels (a)–(c) are results from simulations with hemispherical, flat disc and thin cylindrical shape initial charged regions, respectively.

(energy dissipated into the substrate) is higher than the other two. The total increase of kinetic energy of the ions are, on the other hand, lower than in case (a) and (b). This explains why case (c) has only 24 ions ejected from the surface while the total number of ejected particles is the highest among the three. The higher efficiency of the geometry of case (c) for depositing energy into the lattice also explains the clear shock wave pattern at 400 fs as we discussed earlier.

There is another interesting feature seen in Fig. 6. At $t \approx 100$ fs, the three curves cross over for (a) and (b). For (c) two of the three curves cross each other while the third energy does not increase enough to meet the other two. From our previous paper, 100 fs is the time duration for the shock wave to collapse (or weaken its strength substantially). The energy curves demonstrate the same crossover pattern for 345 ions and 256 ions (both have hemispherical initial configurations).

We also notice that systems with fewer numbers of ions deliver energy more efficiently to the substrate compared to systems with higher numbers of ions. At $t = 400$ fs, the electrostatic energy that is transferred to the substrate in systems (a)–(c) is 58%, 65% and 70%, respectively. Meanwhile, only 49% of energy is transferred in a system with 265 ions and 46% in a system with 365 ions. Here, a direct comparison gives a ratio of 58%:49%:46% for the systems with 100, 265, and 365 ions which are initially distributed in a hemisphere.

From the simulation data, angular distributions of the total number of ejected particles are obtained from the direction of the velocity of the particles. Fig. 7 displays the computed distributions of polar angles, i.e. the angles between the velocity of i th atom and z coordinate, from three simulations. All of the three histograms have a similar broad distribution over 0–100 degree. Note that there is finite population between 90–100° that indicates a small percentage of particles may eventually return to the surface. On the other hand, the distribution patterns of the same angle in the ejected ions calculated from the three situations are quite different from each other (see Fig. 8). The cylindrical shape has a relatively uniform distribution compared to the other two cases.

Finally, the shapes of the craters generated by the

three initial charge configurations is depicted in Fig. 9. The number densities of atoms (ions) in the substrate are obtained by averaging over the azimuthal angles. The distributions are then displayed in a two dimensional plane. The hemispherical geometry is preserved after the explosion in case (a). In case (b), the crater has the shape of frustum of a cone, and in case (c), a cone-shape crater (with a blunted tip) is formed after the explosions. These shapes suggest that the shapes of the initially charged region, which have been shown from our studies to be important in energy partitioning, may be traced back from the topology of the final shape of the craters.

4. Conclusions

Our studies of Coulomb explosion on a Si surface suggest that $t \approx 100$ fs is a characteristic time-scale. For all the systems under investigation, such as systems with 100, 265 and 365 ions, 100 fs is the time for ultra strong shockwaves to dissipate dramatically and for potential energies to drop to about e^{-1} of their initial values. At a later time, a few hundred femtoseconds, shockwaves continue to propagate. The wave fronts preserve approximately the surface symmetry, i.e. hexagonal shape. The intensities and speeds of the waves decrease as they propagate away from the explosion centers. In addition to the normal shockwave modes, we have also observed a special one dimensional shockwave mode which propagates at a much faster speed than the two dimensional waves.

The total number of ejected particles depends on the energy that is dissipated into the substrate rather than the total initial potential energy of the ions. This is the mechanism for the initial shape dependence of the total ejected particles. From the energy analysis we also conclude that the fraction of energy that goes into the substrate decreases as the number of ions increases from 100 to 365. This fact suggest that there will be saturation of the yields as a function of the initial charge number in potential energy driven sputtering processes.

Contrary to the simple picture in which a surface Coulomb explosion is presumed to eject primarily ions, our simulation predicts that 90% or more of the

ejected material may be neutral. Previously, a qualitative application of the simple picture to experimental data (which showed that most of the ejected material is neutral) led some investigators [37] to conclude that the Coulomb explosion is a subdominant process. Our results indicate that even a simple model of the Coulomb explosion can lead to the same qualitative results, and therefore a more quantitative analysis is required before forming conclusions about the dominance of various mechanisms. We believe that the simulations should be refined further and the experiments extended to higher charge states (where the Coulomb explosion model may be more applicable) before such a comparison is made, however. A model that includes change of the electronic states of the substrate atoms (ions) would allow the investigations of effects of electronic excitation and charge transfer processes in the substrates during the explosion, for example. We are presently working to achieve this goal by implementing the electronic–atomic hybrid molecular dynamics method. Meanwhile, the simple model presented here has already yielded significant insights into the basic nature of the surface Coulomb explosion scenario.

Acknowledgement

Acknowledgement is made by the authors to the Department of Energy for partial support of this work, and to the NIST supercomputer center and QTP computer center.

References

- [1] D. Schneider, *Hyperf. Interact.* 99 (1996) 47.
- [2] D.C. Park, R. Bastasz, R.W. Schmieder, M. Stöckli, *J. Vac. Sci. Technol. B* 13 (1995) 941.
- [3] I. Bitsensky, E. Parilis, S. Della-Negra, Y.L. Beyec, *Nucl. Instrum. Methods B* 72 (1992) 380, and references therein.
- [4] C.A. Morgan, F.G. Serpa, E.S. Meyer, J.D. Gillaspay, J.R. Sugar, C.M. Brown, U. Feldman, *Phys. Rev. Lett.* 74 (1995) 1717.
- [5] D. Schneider, D. DeWitt, M.W. Clark, R. Schuch, C.L. Cocke, R. Schmieder, K.J. Reed, M.H. Chen, R.E. Marrs, M. Levine, R. Fortner, *Phys. Rev. A* 42 (1990) 3889.
- [6] J.N. Bardsley, B.M. Penetrante, *Comments At. Mol. Phys.* 27 (1991) 43.
- [7] A. Barany, C.J. Setterlind, *Heavy Ion Phys.* 1 (1995) 115.
- [8] J.-P. Briand, S. Thuriiez, G. Giardino, G. Borsoni, M. Froment, M. Eddrief, C. Sebénne, *Phys. Rev. Lett.* 77 (1996) 1452.
- [9] I. Hughes, *Phys. World* 8 (1995) 43.
- [10] J.P. Briand, *Phys. Rev. Lett.* 65 (1990) 159.
- [11] D.H. Schneider, M.A. Briere, J. McDonald, J. Biersack, *Radiat. Eff. Def. Solids* 127 (1993) 113.
- [12] F. Aumayr, H. Kurz, D. Schneider, M.A. Briere, J.W. McDonald, C.E. Cunningham, H.P. Winter, *Phys. Rev. Lett.* 71 (1993) 1943.
- [13] T. Neidhart, F. Pichler, F. Aumayr, H.P. Winter, M. Schmid, P. Varga, *Phys. Rev. Lett.* 74 (1995) 5280.
- [14] N. Itabashi, K. Mochiji, H. Shimizu, S. Ohtani, Y. Kato, H. Tanuma, N. Kobayashi, *Jpn. J. Appl. Phys.* 34 (1995) 6861.
- [15] K. Mochiji, N. Itabashi, S. Yamamoto, I. Ochiai, K. Okuno, *Jpn. J. Appl. Phys.* 33 (1994) 7108.
- [16] I.S. Bitsenskii, M.N. Murakhmetov, E.S. Parilis, *Sov. Phys. Tech. Phys.* 24 (1979) 618.
- [17] P. Apell, *J. Phys. B* 21 (1988) 2665.
- [18] N. Vaeck, J.E. Hansen, *J. Phys. B* 28 (1995) 3523.
- [19] D. Schneider, M.A. Briere, M.W. Clark, J. McDonald, J. Biersack, W. Siekhaus, *Surf. Sci.* 294 (1993) 403.
- [20] F. Aumayr, H. Kurz, D. Schneider, M.A. Briere, J.W. McDonald, C.E. Cunningham, H.P. Winter, *Phys. Rev. Lett.* 71 (1993) 1943.
- [21] J.P. Briand, B. d'Etat, D. Schneider, M. Clark, V. Decaux, *Nucl. Instrum. Methods B* 87 (1994) 138.
- [22] J.P. Briand, B. d'Etat-Ban, D. Schneider, M.A. Briere, V. Decaux, J.W. McDonald, S. Bardin, *Phys. Rev. A* 53 (1996) 2194.
- [23] J.P. Briand, L. de Billy, P. Charles, S. Essabaa, P. Briand, R. Geller, J.P. Desclaux, S. Bliman, C. Ristori, *Phys. Rev. Lett.* 65 (1990) 159.
- [24] B. d'Etat, J.P. Briand, G. Ban, L. de Billy, J.P. Desclaux, P. Briand, *Phys. Rev. A* 48 (1993) 1098.
- [25] H.-P. Cheng, J.D. Gillaspay, *Phys. Rev. B* 55 (1997) 2628.
- [26] R. Morgenstern, J. Das, *Europhys. News* 25 (1) (1994) 3.
- [27] R. Morgenstern, J. Das, in: J.W. Rabalais (Ed.), *Low Energy Ion-Surface Interactions*, Wiley, Chichester, 1994, p. 190.
- [28] D. Schneider, M.A. Briere, T. Schenkle, EBIT, N-Division, Livermore Annual Report, 1994.
- [29] I. Hughes, *Phys. World* 8 (4) (1995) 43.
- [30] E. Parilis, Caltech preprint.
- [31] K. Mochiji, N. Itabashi, S. Yamamoto, H. Shimizu, S. Ohtani, Y. Kakto, H. Tanuma, K. Okuno, N. Kobayashi, *Surf. Sci.* 357–358 (1996) 673.
- [32] H.-P. Cheng, J.D. Gillaspay, *Proc. of the Fourteenth Int. Conf. on the Application of Accelerators In Research and Industry*, Denton, TX, 1997, in press.
- [33] M.P. Allen, D.J. Tildesley, *Computer Simulations of Liquids*, Clarendon, Oxford, United Kingdom, 1987.
- [34] H.-P. Cheng, U. Landman, *Science* 260 (1993) 1304.
- [35] U. Landman, W.D. Luedtke, M.W. Ribarsky, R.N. Barnett, C.L. Cleveland, *Phys. Rev. B* 37 (1988) 4637.
- [36] J. Tersoff, *Phys. Rev. B* 39 (1988) 5566.
- [37] J. Burgdorfer, Y. Yamazaki, *Phys. Rev. A* 54 (1996) 4140.



Non-kinetic damage on insulating materials by highly charged ion bombardment

D.C. Parks^{a,b,*}, M.P. Stöckli^b, E.W. Bell^c, L.P. Ratliff^a, R.W. Schmieder^d,
F.G. Serpa^{a,1}, J.D. Gillaspay^a

^a Atomic Physics Division, National Institute of Standards and Technology, Gaithersburg, MD 20899, USA

^b J.R. Macdonald Laboratory, Department of Physics, Kansas State University, Manhattan, KS 66506-2604, USA

^c Diamond Semiconductor Group, Gloucester, MA 01930, USA

^d Sandia National Laboratories, Livermore, CA 94551, USA

Received 19 May 1997; received in revised form 26 August 1997

Abstract

We have measured the damage caused by the impact of low velocity, highly charged ions on insulating surfaces. Atomic force microscopy allows us to observe directly the surface topography with nanometer resolution. Using constant velocity (100 keV) Xe^{q+} ions ($25 \leq q \leq 50$) impinging on mica, we observe damage caused by single ion impacts. Impact sites typically are circular hillocks. Within the range and accuracy of the data, the height and volume of the damaged regions are well approximated by a linear function of ion potential energy. © 1998 Elsevier Science B.V.

PACS: 34.50.Dy; 61.16.Ch; 61.72.Qq; 61.80.Jh

Keywords: Highly charged ion; Surface damage; AFM; Coulomb explosion; EBIT; EBIS

1. Introduction

While the effects of ion bombardment on solid materials due to the kinetic energy carried by ions is well known, the role of the potential energy carried by the ions is much less understood. Using highly charged ions of a single atomic species and holding the velocity at a low constant value,

it is possible to observe ion-surface interactions and surface damage where the potential energy is the independent variable.

The interaction of ions and solids is understood in the context of deposition of ionic kinetic energy and the associated lattice damage [1]. Slow ions ($E < 100$ keV for Xe on Si targets) interact principally by means of a few direct collisions with target atoms (nuclear stopping). Relatively few atoms are sputtered or displaced. Somewhat swifter ions (100 keV $< E < 10$ MeV for Xe on Si targets) are initially slowed mainly through interaction with target electrons (electronic stopping). Several

* Corresponding author. Tel.: 301 975 3131; fax: 301 975 3038; e-mail: daniel.parks@nist.gov.

¹ Permanent address: Department of Physics, University of Notre Dame, Notre Dame, IN 46556, USA.

atoms may be displaced or sputtered. Ions with even higher velocities ($E > 10$ MeV for Xe on Si targets) can create extensive tracks of displaced atoms including additional lattice damage along the tracks of secondary showers. In this regime many atoms and ions may be sputtered.

The interaction of highly charged ions with solids involves some very different additional mechanisms for energy deposition and lattice damage formation. The potential energy carried by highly charged ions is released upon their neutralization and decay to the ground state. If this neutralization can be effected very quickly, as it probably is in the case of a highly charged ion impacting on a solid surface, the potential energy carried by the ion will be deposited into a relatively small volume of the target material. The amount of potential energy available is enough to cause lattice damage and particle sputtering. In comparison to the much studied kinetic processes, the processes for damage formation and ionic neutralization that involve highly charged ions are much less well understood.

Ion sources capable of delivering sufficient quantities of the required slow, but highly charged ions in a well-collimated beam have become available only recently. The Electron Beam Ion Source (EBIS) and the related Electron Beam Ion Trap (EBIT) are now capable of providing slow beams of ions with charge states previously obtainable only by means of passing high velocity ions through stripper foils. The EBIS/EBIT sources can provide beams of ions whose potential energies are comparable to or greater than their kinetic energies.

In the present experiments, we measure the physical damage on insulating solid surfaces after irradiation by a beam of relatively slow, but highly charged ions. While the mechanisms for conversion of internal energy into solid material damage have yet to be elucidated, the experimental results do show unambiguously that the amount of near surface damage increases nearly linearly with the amount of potential energy carried by the ions.

Neutralization of highly charged ions in solid materials is a topic of much recent discussion and study [2–13]. Here we postulate a model for interactions between highly charged ions and solid surfaces. As a highly charged ion approaches a solid surface, the surface potential is eventually low-

ered enough that electrons may traverse the gap to the ion (classical over-the-barrier model) [8,14]. Such electrons are principally extracted from the valence states of the surface and end in high lying Rydberg states of the approaching ion [15]. A so-called “hollow atom” [16] configuration results. Auger and radiative processes within the atom begin filling the inner vacancies. These cascades release potential energy in the form of energetic free electrons and photons. Electrons are continuously extracted from the surface until the ion is neutralized or enters the solid material. After impact it becomes possible for electrons to transfer directly from core states of the target atoms to low core states in the projectile [17]. The ion quickly comes to a charge equilibrium determined by its velocity and the particulars of the target material.

During the neutralization process, electrons required for neutralizing the ion are, of course, extracted from the surrounding material. This local depletion of target electrons could result in a “coulomb explosion” [18]. Briefly, a coulomb explosion can be described as follows. The neutralization of the highly charged ion principally removes electrons from a relatively small volume near the point of entry into the solid. If the electronic relaxation times within the target material are slow compared to the ionic neutralization time, there is formed a volume with a net positive charge near the surface. The remaining positively charged constituent ions are then mutually repulsed. The subsequent dynamics result in ejection of ions and neutrals as well as significant lattice damage due to atomic displacement. It is not yet clear if this coulomb explosion process is responsible for the material damage reported here.

2. Experiment

We irradiated freshly cleaved single crystals of mica (ruby mica, Goodfellow²) at normal inci-

² Certain commercial materials or products are identified in this paper to foster understanding. Such identification does not imply recommendation or endorsement by the National Institute of Standards and Technology, nor does it imply that the materials or products identified are necessarily the best available for the purpose.

dence. Mica was chosen for a variety of beneficial characteristics. It is known to be an extremely good insulator that can also easily be prepared to give a pristine, very flat surface. Furthermore, mica is a commonly imaged substrate for Atomic Force Microscopy (AFM) studies and is known to be stable under contact mode microscopy. AFM imaging of mica shows that atomically flat terraces up to 10 μm in width are commonly observed.

Two different ion sources were used; the Kansas State University Cryogenic Electron Beam Ion Source (KSU-CryEBIS) and the NIST EBIT. Because of limitations of the electron beam energy, the highest charge state for which we achieved sufficient ion flux in the KSU-CryEBIS was $q=47$. At the NIST EBIT we were able to push the upper limit to $q=50$. Samples were irradiated by $q=44$ ions from both sources with quantitatively similar results.

The principle of operation of the two ion sources is similar. Since it is well described in the literature [19], only a short description of the EBIT will be given here. An electron beam is launched axially along the bore of a superconducting magnet. The electron beam is squeezed to a very small diameter ($\sim 100 \mu\text{m}$) by the magnetic field ($B=3 \text{ T}$). The electrons are accelerated to energies sufficient to ionize tightly bound electrons by applying a large positive voltage to a series of drift tubes coaxial with the electron beam. Background gas atoms ionized by electron impact become radially trapped by the magnetic field and by the space charge of the electron beam. Ions are trapped axially by voltages applied to the drift tubes. This is accomplished by setting the end drift tube segments at positive potentials slightly higher than the central drift tube sections. The drift tube potentials and the space charge of the electrons and ions inside the trap determine the energy of extracted ion beams.

The highest charge state for which a sufficient population is attained is limited primarily by the electron beam energy and the time spent inside the trap. Ions are stepwise ionized by successive collisions with high velocity electrons. Since the cross section for ionization by electron impact vanishes at threshold, the electron beam energy is

commonly set to be several kV above threshold for the desired charge state. Lifetime of ions inside the trap is limited by the escape of fast moving ions and charge exchanging collisions with lower charge ions or background gas atoms.

Ions are extracted from the trap either in a pulsed mode or in a continuous mode. In the pulsed mode the center drift tube potential is periodically ramped up to the level of the end drift tube, expelling the ions into the beam line. The end drift tube voltage in the desired extraction direction is set slightly lower than the opposite end drift tube voltage. In continuous mode, ions continuously spill over the end drift tube, when they have gained sufficient energy from collisional heating with electrons or other ions. Ion beam currents typically were 0.5–10 pA in each charge state delivered to the target.

Charge state selection of ions is accomplished by means of a 90° bending magnet. The magnet is capable of resolving adjacent charge states even for Xe^{50+} . To enhance the yield and to reduce beam contamination from other charge states composed of differing isotopes, we used 92% (NIST) and 99% (KSU) isotopically enriched ^{136}Xe . In the worst case of $^{136}\text{Xe}^{50+}$, contamination from $^{134}\text{Xe}^{49+}$ is estimated to be less than 10%. There is less than 3% $^{134}\text{Xe}^{(q-1)+}$ in the $^{136}\text{Xe}^{q+}$ beam for q in the range $45 \leq q \leq 47$. All other charge states have contamination less than 1%.

The ion beam was decelerated and focused on the target by means of an electrostatic lens assembly. The potential at the target was adjusted to set the final ion beam kinetic energy to 100 keV for each charge state. Mica targets were exposed through a mask with a 3 mm diameter circular aperture. The masked region provided an easily referenced control region for each irradiated surface. The beam current was measured with a suppressed Faraday cup immediately downstream from the target position.

Adjusting the potential energy carried by the ions was accomplished by varying the charge q in the range $25 \leq q \leq 50$. In this way we could isolate those effects due to Coulomb potential energy from those due to kinetic and chemical processes. To avoid contamination of the beam by other atomic species we did not use Xe charge states with

charge to mass ratios the same as those derivable from background gases (i.e., ^4He , ^{12}C , ^{14}N and ^{16}O). All irradiations were done at room temperature in UHV with typical background pressures approximately 1×10^{-6} Pa.

The ion bombarded surfaces were imaged in air using contact mode AFM (Nanoscope II²). Considering previously noted mixing of lateral forces into topographic signals [20], care was taken to minimize this effect. We used pyramidal Si_3N_4 tips with a nominal cantilever stiffness of 0.58 N/m. These relatively short, stiff cantilevers are also torsionally rigid, reducing the lateral force component mixed into the topographic signal. All images were taken with the scan size set to $1 \mu\text{m} \times 1 \mu\text{m}$.

Optimally, all samples would be imaged on the same day with the same probe. The relatively short mean time of probe use before becoming contaminated and thus changing its imaging and adhesion characteristics make this goal unattainable. Instead, samples were imaged using several probes. For all images, the force between tip and sample was reduced to the minimum stable value to minimize torsional bending of the cantilever and to reduce scanning damage to the features of interest. The adhesion between tip and sample as estimated from pull-off forces was 10^{-8} N. Most of this adhesion is due to surface tension on the water film that is ubiquitous in ambient conditions. However, not knowing the microscopic radius of the imaging section of the probe prevents calculation of the more important parameter, the local pressure exerted by the probe.

As previously reported [20], the damage created by single ions in mica is susceptible to modification by contact mode AFM imaging. Almost universally, the observed topography was erased by repeated scanning over any given region. This process was usually completed in fewer than 10 scans. We did not, however, observe a peeling open of the blisters as was noted by other researchers [21]. This may be due to our effort to keep contact forces low, as the transformation of blisters into pits may be a result of repeated scanning at high forces. To reduce the effect of scanning induced modification of the features of interest, data were only collected from the initial scan over any region.

3. Results

AFM images show the irradiated sections of the mica surfaces to be randomly marked with circular hillocks (Fig. 1). They are best described as right circular cones, with height to width aspect ratios of about 1 : 20. Typical dimensions of the hillocks are 10–20 nm diameter and 0.5–1 nm height. These hillocks occur only in the irradiated regions. The areal density of hillocks corresponds well to the expected ion density as calculated from the irradiated area, measured ion flux and exposure time. Typically the ion fluence was 10–50 ions per square micron. The calculations are consistent with the identification of the observed hillocks as damage caused by individual ion impacts.

The measured peak height and the integrated volume of the hillocks are shown in Figs. 2 and 3. In Fig. 2 the data is plotted as a function of ion charge q . Fig. 3 shows the same data plotted as a function of ion potential energy. One anomalous point at $q = 48$ ($v = 40 \text{ nm}^3$, $h = 0.43 \text{ nm}$) which may have been contaminated by a defective AFM tip is not shown in the plot. (All other samples were imaged using multiple probes ensuring against this problem.) The error bars represent the standard deviation of all individual hillock

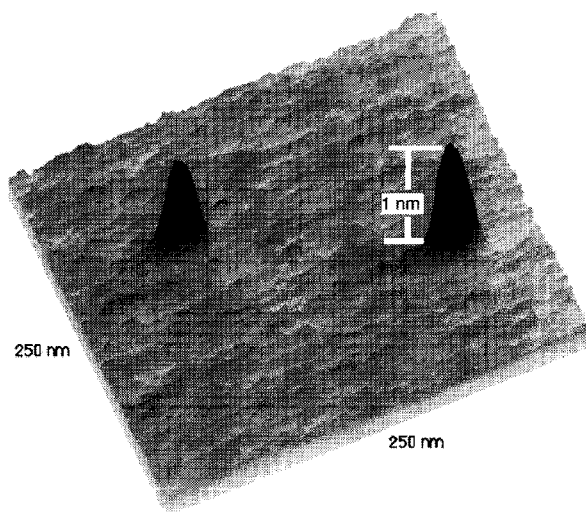


Fig. 1. Atomic force microscope image of two Xe^{50+} ion impact sites on mica. Damage is seen as conical hillocks that are typically 20 nm in diameter and 1 nm high. (Note exaggerated vertical scale.)

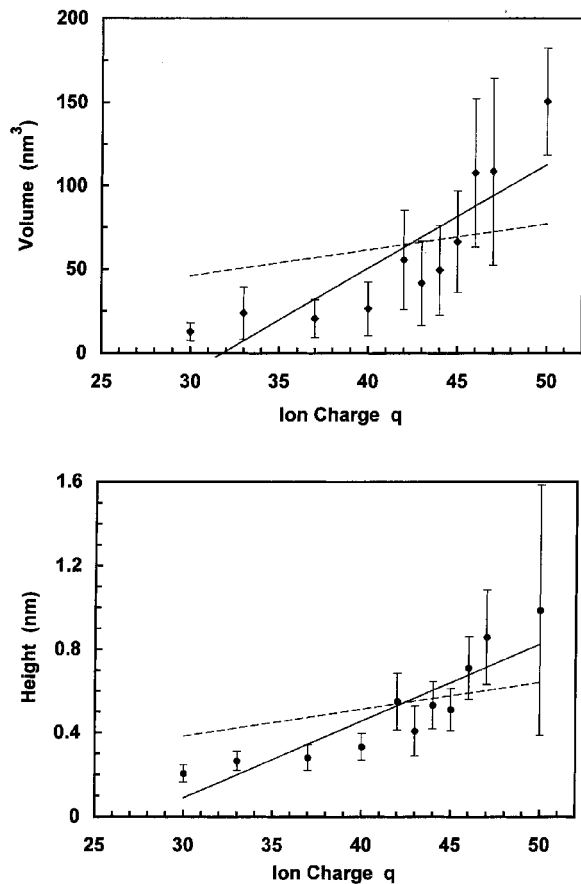


Fig. 2. (a) Volume of damage hillocks on mica as measured by AFM as a function of ion charge for 100 keV Xe^{q+} ions. The solid line is a linear fit to the data. The broken line is a linear fit constrained to pass through the origin. Error bars represent the standard deviation of the measurements. (b) AFM measurement of peak height of damage hillocks on mica as a function of ion charge. The solid line is a linear fit to the data. The broken line is a linear fit constrained to pass through the origin. All linear fits are unweighted.

measurements for samples irradiated with like charged ions. We observe the height, volume, and area to all increase with increasing q . A lower threshold for observable damage is noted at $q \approx 30$. The average of 0.15 nm height of the hillocks measured for $q = 30$ is only slightly greater than the noise in the surrounding background. We do not observe damage by 100 keV Xe ions for $q < 30$.

The observational threshold value we observe is roughly consistent with that found by other researchers [22]. We do observe damage for 100

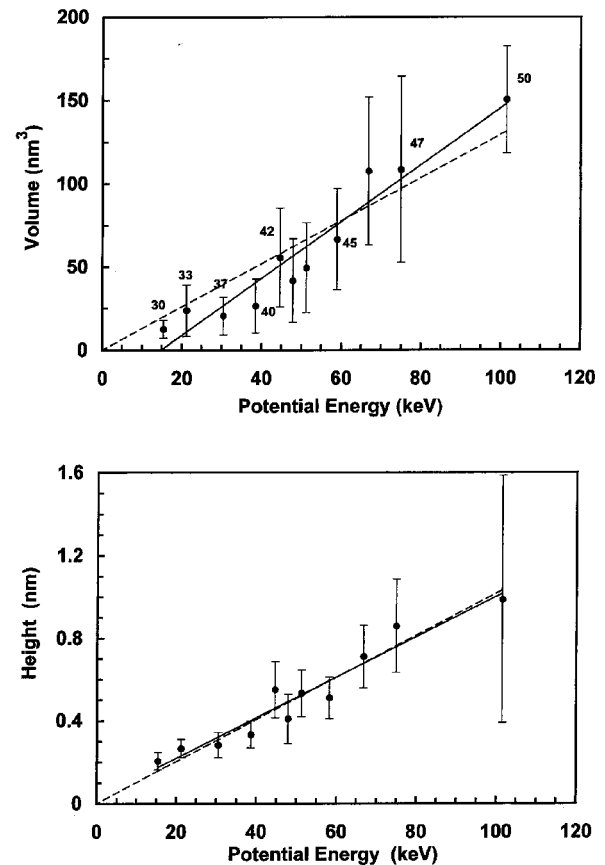


Fig. 3. The same data as shown in Fig. 2, but plotted as a function of potential energy instead of ion charge. (a) Volume of damage hillocks on mica as measured by AFM for 100 keV Xe^{q+} ions. The solid line is a linear fit to the data. The broken line is a linear fit constrained to pass through the origin. Error bars represent the standard deviation of the measurements. Data points are labeled with the ion charge. (b) AFM measurement of peak height of damage hillocks on mica. The solid line is a linear fit to the data. The broken line is a linear fit constrained to pass through the origin. Assignment of ion charge is the same as in (a).

keV Xe^{q+} ions for $q < 35$, which is somewhat less than the threshold estimated in [22]. Although not specified, the kinetic energy for those ions is stated to be between 200 and 500 keV.

4. Discussion

As seen in the graphs, the measured damage increases proportional to the potential energy carried by the ions. This agrees with the increase in

the sputtering rate as a function of potential energy observed with Ar^{q+} ions on GaAs targets [23]. Much of the damage increase is observed to occur above $q = 44$. This agrees well with the greater increases in the potential energy per electron with removal of L shell electrons. The calculated ionization energy per electron for L shell electrons is approximately twice the value calculated for M shell electrons.

Previously we have measured the damage caused on mica by irradiation with Xe^{44+} (potential energy = 50 keV) ions at several different kinetic energies. Those measurements do not show any significant change in hillock dimensions for kinetic energies in the range 20–800 keV [20]. While it is true that 100 keV ions are expected to do some lattice damage, that damage is distributed along the ion path ($\sim 1 \mu\text{m}$). This is in contrast to the damage from the deposition of ion potential energy that we expect to be deposited within a small volume near the surface. So even though the ions have 100 keV kinetic energy, only a small amount of that energy is transferred to the lattice in the near surface region.

Although we do not see damage from lower charge ions, some undetected kinetically derived damage is surely present. High velocity ions in mica are shown to leave tracks that are detectable by AFM as mechanically softer regions [24]. High velocity ions are also known to produce hillock type defects in mica [25] and in the organic crystal L-valine [26].

The physical processes by which hillocks are created instead of the perhaps more expected craters are not understood. We speculate that the effect is closely related to the layered structure of mica. This structure may make it especially sensitive to damage by highly charged ion impact. Mica consists of charged alumino–silicate sheets weakly bonded by counter ions. Coulomb repulsion as the result of local removal of electrons may easily force adjacent sheets apart at the relatively weakly bonded ionic layers. Locally this may be seen as a raised hillock at the surface. Raised surface regions may be generated by a large inter-layer rupture immediately below the surface, forming a void. Alternatively, the collective effect of small expansions between each of

several layers might also result in a measurable protrusion at the surface.

5. Conclusions

We observe damage features on insulating surfaces that are not kinetically derived. We have previously seen [20] that Xe^{44+} ions (potential energy = 50 keV) even at slow velocities (kinetic energy = 20 keV) cause measurable damage on mica surfaces. In this study using constant velocity ions (kinetic energy = 100 keV) and varying the ion charge we see the damage to be a function of the potential energy. At $q = 25$, a Xe ion carries 8 keV potential energy. We do not observe damage on mica using these ions. However, at $q = 30$, the 15 keV potential energy carried by a Xe ion is enough to cause observable damage. We observe the height and volume of the damage to increase with increasing potential energy through our maximum value of $q = 50$ where the potential energy is 100 keV.

Acknowledgements

Those sections of this research done at the J.R. Macdonald Laboratory were supported by the Division of Chemical Sciences, Office of Basic Energy Sciences, Office of Energy Research, US Dept. of Energy.

References

- [1] J.F. Ziegler, J.P. Biersack, U. Littmark, *The Stopping And Range of Ions In Solids*, Pergamon Press, New York, 1985.
- [2] S. Winecki, C.L. Cocke, D. Fry, M.P. Stöckli, *Phys. Rev. A* 53 (1996) 4228.
- [3] H. Winter, *Z. Phys. D* 21 (1991) S129.
- [4] D. Schneider, M.A. Briere, M.W. Clark, J. McDonald, J. Biersack, W. Siekhaus, *Surf. Sci.* 294 (1993) 403.
- [5] J.P. Biersack, *Nucl. Instr. and Meth. B* 80/81 (1993) 12.
- [6] D.H. Schneider, M.A. Briere, J. McDonald, J. Biersack, *Radiat. Eff. and Defects in Solids* 127 (1993) 113.
- [7] H. Kurz, K. Töglhofer, HP. Winter, F. Aumayr, *Phys. Rev. Lett.* 69 (1992) 1140.

- [8] J. Burgdörfer, P. Lerner, F.W. Meyer, Phys. Rev. A 44 (1991) 5674.
- [9] F. Aumayr, H. Kurz, D. Schneider, M.A. Briere, J.W. McDonald, C.E. Cunningham, HP. Winter, Phys. Rev. Lett. 71 (1993) 1943.
- [10] J.W. McDonald, D. Schneider, M.W. Clark, D. DeWitt, Phys. Rev. Lett. 68 (1992) 2297.
- [11] R.W. Schmieder, R.J. Bastasz, Nucl. Instr. and Meth. B 43 (1989) 318.
- [12] G. Schiwietz, D. Schneider, M. Clark, B. Skogvall, D. DeWitt, J. McDonald, Radiat. Eff. and Defects in Solids 127 (1993) 11.
- [13] I. Bitensky, E. Parilis, S. Della-Negra, Y. Le Beyec, Nucl. Instr. and Meth. B 72 (1992) 380.
- [14] J. Burgdörfer, P. Lerner, F.W. Meyer, Phys. Rev. A 44 (1991) 5674.
- [15] H. Kurz, K. Töglhofer, HP. Winter, F. Aumayr, Phys. Rev. Lett. 69 (1992) 1140.
- [16] E.D. Donets, Nucl. Instr. and Meth. B 9 (1985) 522.
- [17] P. Varga, Comments At. Mol. Phys. 23 (1989) 111.
- [18] D.H.G. Schneider, M.A. Briere, Phys. Scripta 53 (1996) 228.
- [19] E.D. Donets, in: I.G. Brown (Ed.), Electron Beam Ion Sources in The Physics and Technology of Ion Sources, Wiley, New York, 1989, p. 245.
- [20] D.C. Parks, R. Bastasz, R.W. Schmieder, M. Stöckli, J. Vac. Sci. Technol. B 13 (1995) 941.
- [21] M.A. Briere, D. Schneider, J. McDonald, M. Reaves, C. Rühlicke, G. Weinberg, D. Knapp, Nucl. Instr. and Meth. B 90 (1994) 231.
- [22] C. Rühlicke, M.A. Briere, D. Schneider, Nucl. Instr. and Meth. B 99 (1995) 528.
- [23] K. Mochiji, N. Itabashi, S. Yamamoto, H. Shimizu, S. Ohtani, Y. Kato, H. Tanuma, K. Okuno, N. Kobayashi, Surf. Sci. 357/358 (1996) 673.
- [24] F. Thibaudau, J. Cousty, E. Balanzat, S. Bouffard, Phys. Rev. Lett. 67 (1991) 1582.
- [25] D.D.N. Barlo Daya, A. Hallén, J. Eriksson, J. Kopniczky, R. Papaléo, C.T. Reimann, P. Håkansson, B.U.R. Sundqvist, A. Brunelle, S. Della-Negra, Y. Le Beyec, Nucl. Instr. and Meth. B 106 (1995) 43.
- [26] J. Kopniczky, A. Hallén, N. Keskitalo, C.T. Reimann, B.U.R. Sundqvist, Radiat. Meas. 25 (1995) 47.

Masked ion beam lithography with highly charged ions

J. D. Gillaspay,^{a)} D. C. Parks, and L. P. Ratliff

National Institute of Standards and Technology, Gaithersburg, Maryland 20899

(Received 29 May 1998; accepted 16 September 1998)

Masked ion beam lithography using highly charged ions is demonstrated for the first time by producing an array of hundreds of ordered micrometer wide dots using Xe^{44+} on poly(methylmethacrylate) resist. At low dose, exposure of the resist is incomplete and isolated single-ion impact sites can be seen within the exposed areas. Atomic force microscope images of the single-ion impact sites show craters with a width of 24 nm. At high dose, the exposure is complete and the dot morphology is consistent with limitations from the mask. Scanning electron microscope images indicate that the sidewall slope is steeper than four. © 1998 American Vacuum Society. [S0734-211X(98)13006-8]

I. INTRODUCTION

Recent technical advances have made it possible to produce beams of very highly charged ions ($q > 30+$ per ion) using compact laboratory sources based on electron beam ion traps (EBITs).^{1,2} This has led to a number of studies which explore the fundamental interaction of ions with surfaces in an unusual regime in which the potential energy, rather than kinetic energy, plays the dominant role. The amount of potential energy that a single highly charged ion releases during neutralization at a surface can be over 750 000 eV.³ Using an EBIT source, such ions can be produced and easily formed into beams with accelerating potentials of $V = 0.1 - 10$ kV, resulting in ions with kinetic energies, $\text{KE} = qV$, in the range of 1 keV to 1 MeV. The amount of continuous beam current that can be produced from such ion sources has increased by more than a factor of 1000 during the past few years,^{2,4} and further increases of many orders of magnitude are expected soon. Presently, it is possible to produce a 100–200 pA continuous beam of xenon with charge states in the range of 25+ to 44+.^{2,4} In such a beam, the $q = 44+$ component alone can be optimized to be over 20 pA. These currents already exceed those reported in useful focused ion beam lithography systems.⁵ The next generation of highly charged ion sources which are under development should have a brightness over four orders of magnitude higher than that of present EBITs, and should yield 2×10^{10} ions $\text{mm}^{-2} \text{mrad}^{-2} \text{s}^{-1}$ in a single charge state.⁶

Fueled by these advances in instrumentation, a number of studies involving the interaction of highly charged ions with surfaces have already been carried out in the two EBIT laboratories in the U.S.^{1,2} Complementary work has been carried out at other facilities in the U.S.^{7,8} and abroad^{9–12} where more moderately charged ion beams can be produced with higher intensity. These studies have already produced a number of intriguing results, such as potential energy mediated formation of nanoscale surface features on mica,^{1,13} and dramatic enhancements in the yield of secondary ions^{1,14} and neutral particles.^{10,14} These results have led to proposals of possible applications in the area of nanotechnology,^{3,10,15–21} some of which are discussed in more detail below. Highly

charged ions are already being used in practice as a surface analysis tool in at least one laboratory.¹⁴

In most of the work done so far, however, emphasis has been on understanding the basic (and relatively uncharted) phenomenology of how these exotic ion beams interact with surfaces. In all of this work, the highly charged ions were formed into relatively large diameter beams (of order 1 mm) with no microscopic pattern encoding. Microscopic imaging of surfaces has shown only a random spatial distribution of features. Although there are applications in which random distributions of features can be exploited for the manufacture of useful devices,^{22,23} a much wider variety of applications can be envisioned if micropatterning can be achieved. This article demonstrates that highly charged ions can be used to produce a regular array of dots in a commercial lithographic resist using a standard stencil mask technique.

II. EXPERIMENT

The ion beam was produced at the NIST EBIT ion-surface interaction facility.⁴ A charge/mass selection magnet was used to purify the beam into a single isotopic charge state, $^{136}\text{Xe}^{44+}$. The beam current, 11 pA through a 3-mm-diam aperture, was measured with a suppressed Faraday cup.⁴ The exposure was made for 15 min, for an integrated ion dose of $2.0 \times 10^{10} \text{ cm}^{-2}$. The target surface was a section of a silicon wafer, coated with 400 nm of poly(methylmethacrylate) (PMMA) resist (4.5% solution spun on at 3000 rpm for 40 s and baked at 82 °C for 30 min). This target was screened from above with a commercial nickel stencil mask composed of a two dimensional square array of nominally 1 μm square openings arranged on a grid with a 12.5 μm pitch. Target exposure was carried out under a vacuum of approximately 10^{-6} Pa (10^{-8} Torr). After exposure, the targets were removed from the vacuum and submerged in an equal parts mixture of standard PMMA developer chemicals (isopropyl alcohol and methyl isobutyl ketone) at room temperature. After 30–45 s in the developer, the targets were rinsed in isopropyl alcohol and dried with nitrogen gas. Imaging was subsequently carried out with an optical microscope, a scanning electron microscope (SEM), and a contact mode atomic force microscope (AFM).

^{a)}Electronic mail: John.Gillaspay@NIST.gov

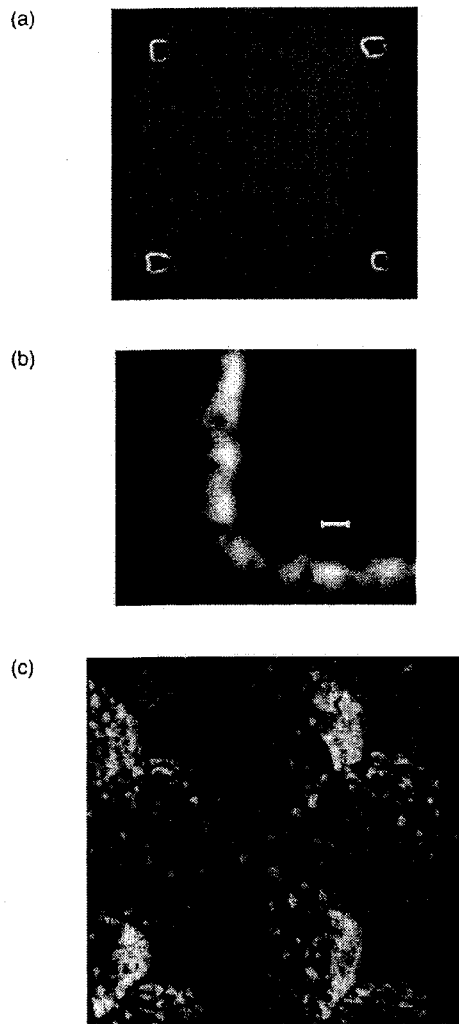


FIG. 1. (a) SEM image showing four adjacent dots fabricated in PMMA with highly charged ions. The separation between the dots is approximately $10\ \mu\text{m}$. The figure shown is a small portion of a larger array of over 250 such dots. Each dot is the result of multiple ion impacts. (b) Closeup SEM image of a corner of a single dot. The scale is given by the $100\ \text{nm}$ white horizontal bar. (c) SEM image of a portion of a stencil mask of the type used to produce (a).

When observed with the optical microscope, over 250 regularly spaced dots filled the field of view, but were incompletely resolved. The dots were well resolved by the SEM [Fig. 1(a)]. A closeup of the corner of a single dot [Fig. 1(b)] indicates an edge roughness of less than $100\ \text{nm}$. Some cracking of the substrate is evident and may have been caused by overheating the sample in the SEM (operated at energies up to $20\ \text{keV}$). The images were taken with the electron beam energy at $10\ \text{kV}$ [Fig. 1(a)] and $15\ \text{keV}$ [Fig. 1(b)]. A portion of a typical mask of the type used in this work is shown in Fig. 1(c). The openings in the masks were highly nonuniform and evidently the actual region used to produce Fig. 1(a) contained significantly smaller openings than those shown in Fig. 1(c). Figure 1 suggests that the quality of the dot shape in this study was limited by the mask.

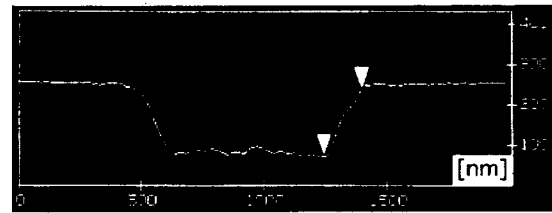


FIG. 2. Depth profile of a dot like those shown in Fig. 1(a), measured with an atomic force microscope.

The kinetic energy of the ion beam (discussed below) was determined by the difference in the potential between the target and the ion source, $4.8\ \text{kV}$ in this case. The mask was pressed in contact with the PMMA surface at the edges, but the extreme flexibility of the mask prevented us from being certain that the mask was in contact with the surface over the entire exposed area.

An AFM was used to determine the depth of the dots (Fig. 2). The indicated horizontal distance between the two triangular markers on the right hand sidewall of Fig. 2 is $160\ \text{nm}$ and the vertical distance is $172\ \text{nm}$. The slope on the sidewalls is limited by the profile of the AFM probe. To actually determine the sidewall slope with the AFM would require a more sophisticated measuring instrument and technique, such as that used by Griffith *et al.*²⁴ If experimental data for ordinary ions on PMMA²⁵ is extrapolated to Xe and linearly scaled with energy, a range of $172\ \text{nm}$ is predicted—in excellent agreement with our observed depth. We note that a surface roughness which is substantial on the nanometer length scale appears along the bottom of the dot.

When a target was exposed to a low dose of ions and developed, no macroscopic removal of PMMA was observed, but single-ion impact sites could be imaged directly, as shown in Fig. 3. The apparent width of the impact sites is $24\ \text{nm}$. The AFM could only probe the impact sites up to a depth of $3\ \text{nm}$, limited by the AFM probe tip. This low-dose target was bombarded using an ion accelerating voltage of $8.0\ \text{kV}$.

On several occasions we searched for dots before developing the PMMA to see if evidence for direct ablation of material could be obtained. Although no such evidence was found, the possibility that the ablation craters are smaller than the developed craters, and the limited amount of effort spent on this attempt, make it impossible to rule out the existence of direct ablation. Other groups have recently measured how the direct ablation of various materials increases with ion charge,^{10,14} but no work of this sort has been done on PMMA. Very recent work by the Livermore EBIT group has shown that a single highly charged ion can directly ablate as many as 1400 particles from GaAs substrates.²⁶

III. DISCUSSION

The minimum dose required to expose PMMA with a conventional Ga^{1+} ion beam at $100\ \text{keV}$ is $6 \times 10^{11}\ \text{cm}^{-2}$, 30 times higher than our integrated dose.⁵ Interpolation of results from a previous study²⁷ of the species dependence for

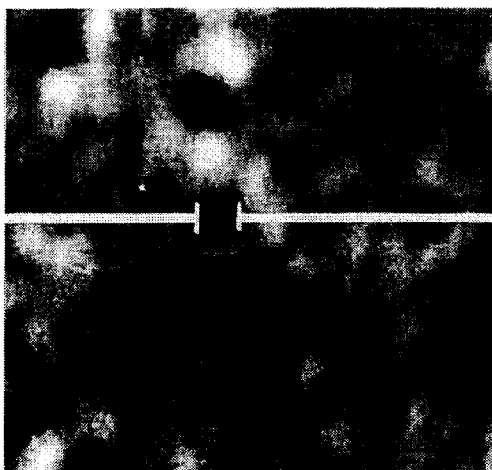


FIG. 3. Atomic force micrograph of nanoscale dots fabricated in PMMA with highly charged ions. Each dot is formed by exposure to a single Xe^{44+} ion. The apparent width of the dot which is bracketed by the horizontal white indicator is 24 nm.

singly charged ions indicates that Xe^{1+} should be only about 50% more efficient in exposing PMMA than Ga^{1+} . We caution that no definitive conclusion concerning the relative dose efficiency for Xe^{44+} should be made at this time, however, because our beam homogeneity was not particularly well characterized and the local dose may have varied substantially from the integrated value. A beam viewing system is presently being designed which will allow us to microscopically characterize the beam profile and to more precisely determine the local dose. The emphasis in this article, therefore, is primarily on the topography of the surface features.

An enhanced surface sensitivity to ions that are very highly charged is not unlikely, however, particularly for chemical and physical processes that are based on electron rearrangement. If the number of electrons/ion removed from the target is equal to the charge of the ion, then a Xe^{44+} ion dose of $2.4 \times 10^{10} \text{ cm}^{-2}$ results in an electron removal of over $1 \times 10^{12} \text{ cm}^{-2}$. The actual number of electrons/ion removed, however, might be much larger. On other surfaces, for example, it has been shown by direct measurement that a single highly charged ion can pump as many as 300 electrons away from the surface¹ in addition to the number of electrons that are required to neutralize the ion itself. Explanations for this electron pumping mechanism can be found in such processes as Auger reionization during collapse of highly excited "hollow atom" states formed during neutralization of the ion.⁹ Another contribution to the collapse of hollow atoms,¹¹ and the interaction of highly charged ions with surfaces in general,^{1,28-30} involves the emission of x rays. It is possible that this x-ray emission contributes to an increased sensitivity of PMMA to these ions (in fact, a patented sub-micron lithography process has been proposed based on the use of x rays generated locally on a surface by the neutralization of multiply charged ions).³¹

There is little other experimental data involving the imag-

ing of ion tracks at the surface of PMMA which can be directly compared to our results. Melngailis⁵ has pointed out that conventional ions are often visualized as producing columnar defects (tracks) of approximately 10 nm diameter in PMMA. Kubena³² has used a focused Ga^+ ion beam to produce dots in PMMA with a width as small as 6 to 7 nm when observed with a SEM. In Kubena's study the average dot width was 25 nm when exposed with an average of 82 ions/dot, and 15 nm when the exposure was lowered to 23 ions/dot; extrapolating these data by the square root of the exposure to 1 ion/dot yields an estimated single ion track width of 6 nm. Döbeli *et al.*³³ have used an AFM to image PMMA after exposure to ions produced by a particle accelerator. They found that the craters produced by low charge and high velocity monatomic ions decreased in width as the ion energy was lowered, and that craters as large as the ones we observed were not found unless the kinetic energy was much higher ($>10\times$) than that used in the present work. This, together with the energy deposition considerations discussed in the next paragraph, suggests that the extreme potential energy carried by our ions is dominating the interaction near the surface.

From the work completed thus far it is not possible to fully sort out the interplay between kinetic and potential energy in the formation of the surface features in our experiment, but a number of aspects are already quite clear. Other experiments on thin carbon foils have shown that ions of similar charge and kinetic energy are fully neutralized within $0.01 \mu\text{m}$ of surface penetration.³⁴ Electronic binding energies in atoms can be accurately calculated, so it is known that the total potential energy transferred during neutralization of a single Xe^{44+} ion is about 50 000 eV. The energy loss rate at the surface which results from combining these two numbers is $5000 \text{ keV}/\mu\text{m}$, substantially more than that of ordinary ions.²⁵ It is clear, therefore, that highly charged ions should be capable of strongly modifying the surface of materials even when the kinetic energy is reduced towards zero. This has been confirmed experimentally in considerable detail in the studies of Parks *et al.*^{7,13} on mica. In that work, a xenon ion beam of similar charge state and kinetic energy was shown to induce surface features of similar lateral dimension to those observed here. Furthermore, the surface topography was shown to scale in dimension with ion charge but remain unchanged when the kinetic energy was varied over a range which extended nearly two orders of magnitude below the energies used here.

The ability of highly charged ions to strongly modify surfaces, even in the limit of low velocities when the range should only be of order 1 nm, has motivated the speculation that exotic ion beams of this sort might be used as a new tool for shallow-junction and thin-film semiconductor processing, where the ability to limit unwanted damage deep in the substrate is desirable.^{12,20} Other potential applications have been suggested as well, such as using highly charged ions as a potent tool for "soft" (low velocity) sputter cleaning and probing of surfaces.^{10,21} The enhanced x-ray yield which can accompany the interaction of highly charged ions with

surfaces²⁸ might be considered for possible exploitation in the development of improved forms of particle induced x-ray emission (PIXE) diagnostic tools. As mentioned above, highly charged ions are already being used in a prototype SIMS diagnostic tool at Livermore;¹⁴ similar work is underway at Kansas State University,³⁵ in collaboration with scientists from Japan. In all of these applications, the determination of the spatial zone of the surface interaction is relevant, and thus our work at NIST has focused on atomic scale imaging of surface topography. Although rapidly growing, the field is still in its infancy, and a great deal more remains to be learned about the fundamental processes involved in the interaction of highly charged ions with surfaces before the feasibility of developing any of these proposed applications can be ascertained.

IV. CONCLUSION

We have demonstrated that beams of highly charged ions can be used to pattern a lithographic resist on the micrometer length scale. We have explored the surface topography with atomic force microscopy and scanning electron microscopy, and have presented the first direct surface images of single-ion tracks in PMMA. The fundamental transverse length scale, at the potential and kinetic energies used in this work, appears to be several tens of nanometers, suggesting that the method demonstrated here can be extended deep into the submicrometer range.

ACKNOWLEDGMENTS

The authors thank Alexander Shapiro and James Kelly for the SEM imaging, and Kris Helmersen for the optical imaging. We thank John Melngailis, Jon Orloff, Skip Berry, Stacy Mogren, and Walt Finkelstein (and numerous members of the Advanced Lithography Group consortium under his direction) for their encouragement, advice, and other assistance in this and our ongoing related work with highly charged ions.

¹D. H. G. Schneider and M. A. Briere, *Phys. Scr.* **53**, 228 (1996).

²L. P. Ratliff, E. W. Bell, D. C. Parks, A. I. Pikin, and J. D. Gillaspay, *Rev. Sci. Instrum.* **68**, 1998 (1997).

³H.-P. Cheng and J. D. Gillaspay, *Phys. Rev. B* **55**, 2628 (1997).

⁴A. I. Pikin, C. A. Morgan, E. W. Bell, L. P. Ratliff, D. A. Church, and J. D. Gillaspay, *Rev. Sci. Instrum.* **67**, 2528 (1996).

⁵J. Melngailis, *Nucl. Instrum. Methods Phys. Res. B* **80**, 1271 (1993).

⁶R. E. Marrs, *Nucl. Instrum. Methods Phys. Res. B* (to be published).

⁷D. C. Parks, R. Bastasz, R. W. Schmieder, and M. Stockli, *J. Vac. Sci. Technol. B* **13**, 941 (1995).

⁸L. Folkerts, S. Schippers, D. M. Zehner, and F. W. Meyer, *Phys. Rev. Lett.* **74**, 2204 (1995).

⁹A. Arnau, F. Aumayr, P. M. Echenique, M. Grether, W. Heiland, J. Limburg, R. Morgenstern, P. Roncin, S. Schippers, R. Schuch, N. Stolterfoht, P. Varga, T. J. M. Zouros, and H. P. Winter, *Surf. Sci. Rep.* **27**, 113 (1997).

¹⁰M. Sporn, G. Libiseller, T. Neidhard, M. Schmid, F. Aumayr, H. P. Winter, P. Varga, M. Grether, D. Niemann, and N. Stolterfoht, *Phys. Rev. Lett.* **79**, 945 (1997).

¹¹J.-P. Briand, S. Thuriez, G. Giardino, G. Borsoni, M. Froment, M. Ed-drief, and C. Sebenne, *Phys. Rev. Lett.* **77**, 1452 (1996).

¹²N. Itabashi, K. Mochiji, H. Shimizu, S. Ohtani, Y. Kato, H. Tanuma, and N. Kobayashi, *Jpn. J. Appl. Phys., Part 1* **34**, 6861 (1995).

¹³D. C. Parks, M. P. Stockli, E. W. Bell, L. P. Ratliff, R. W. Schmieder, F. G. Serpa, and J. D. Gillaspay, *Nucl. Instrum. Methods Phys. Res. B* **134**, 46 (1998).

¹⁴T. Schenkel, A. V. Barnes, A. V. Hamza, D. H. Schneider, J. C. Banks, and B. L. Doyle, *Phys. Rev. Lett.* **80**, 4325 (1998).

¹⁵R. W. Schmieder and R. J. Bastasz, in *VIIth International Conference on the Physics of Highly Charged Ions, Manhattan, Kansas, 1992*, edited by P. Richard, M. Stöckli, C. L. Cocke, and C. D. Lin, AIP Conf. Proc. No. 274 (AIP, New York, 1993), p. 675.

¹⁶D. H. Schneider, M. A. Briere, J. McDonald, and J. Biersack, *Radiat. Eff. Defects Solids* **127**, 113 (1993).

¹⁷J. Limburg, J. Das, S. Schippers, R. Hoekstra, and R. Morgenstern, *Phys. Rev. Lett.* **73**, 786 (1994).

¹⁸R. Morgenstern and J. Das, *Europhys. News* **25**, 3 (1994).

¹⁹I. Hughes, *Phys. World* **8**, 43 (1995).

²⁰J. D. Gillaspay, Y. Aglitskiy, E. W. Bell, C. M. Brown, C. T. Chantler, R. D. Deslattes, U. Feldman, L. T. Hudson, J. M. Laming, E. S. Meyer, C. A. Morgan, A. I. Pikin, J. R. Roberts, L. P. Ratliff, F. G. Serpa, J. Sugar, and E. Takacs, *Phys. Scr.* **T59**, 392 (1995).

²¹N. Kakutani, T. Azuma, Y. Yamazaki, K. Komaki, and K. Kuroki, *Nucl. Instrum. Methods Phys. Res. B* **96**, 541 (1995).

²²C. R. Musil, D. Jeggle, H. W. Lehmann, L. Scandella, J. Gobrecht, and M. Doebeli, *J. Vac. Sci. Technol. B* **13**, 2781 (1995).

²³H. W. Deckman and J. H. Dunsmuir, *J. Vac. Sci. Technol. B* **1**, 1109 (1983).

²⁴J. E. Griffith, L. C. Hopkins, C. E. Bryson, A. Berghaus, E. J. Snyder, J. J. Plombon, L. A. Vasilyev, M. Hecht, and J. B. Bindell, *J. Vac. Sci. Technol. B* **15**, 2189 (1997).

²⁵R. G. Wilson, *J. Appl. Phys.* **73**, 2215 (1993).

²⁶T. Schenkel, A. V. Hamza, A. V. Barnes, D. H. Schneider, J. C. Banks, and B. L. Doyle, *Phys. Rev. Lett.* **81**, 2590 (1998).

²⁷S. Matsui, K. Mori, T. Shiokawa, K. Toyoda, and S. Namba, *J. Vac. Sci. Technol. B* **5**, 853 (1987).

²⁸R. Schuch, D. Schneider, D. A. Knapp, D. DeWitt, J. McDonald, M. H. Chen, M. W. Clark, and R. E. Marrs, *Phys. Rev. Lett.* **70**, 1073 (1993).

²⁹E. Takacs, Z. Onodi-Szucs, L. P. Ratliff, J. D. Gillaspay, and J. Palinkas, *Nucl. Instrum. Methods Phys. Res. B* **124**, 431 (1997).

³⁰S. Winecki, C. L. Cocke, D. Fry, and M. P. Stockli, *Phys. Rev. A* **53**, 4228 (1996).

³¹K. S. Golovanivsky and E. M. Omeljanovsky, U.S. Patent No. 5,327,475 (Ruxam, Inc.) (1994).

³²R. L. Kubena, J. W. Ward, F. P. Stratton, R. J. Joyce, and G. M. Atkinson, *J. Vac. Sci. Technol. B* **9**, 3079 (1991).

³³M. Döbeli, F. Ames, C. R. Musil, L. Scandella, M. Suter, and H. A. Synal, *Nucl. Instrum. Methods Phys. Res. B* **143**, 503 (1998).

³⁴T. Schenkel, M. A. Briere, H. Schmidt-Bocking, K. Bethge, and D. H. Schneider, *Phys. Rev. Lett.* **78**, 2481 (1997).

³⁵M. Stockli (private communication).

Exposure of self-assembled monolayers to highly charged ions and metastable atoms

L. P. Ratliff, R. Minniti, A. Bard, E. W. Bell,^{a)} J. D. Gillaspay,^{b)c)} and D. Parks
Atomic Physics Division, National Institute of Standards and Technology, Gaithersburg, Maryland 20899

A. J. Black and G. M. Whitesides^{b)}
Department of Chemistry and Chemical Biology, Harvard University, Cambridge, Massachusetts 02138

(Received 18 February 1999; accepted for publication 2 June 1999)

The doses of neutral metastable argon atoms (Ar^*) and highly charged xenon ions (HCIs) required to damage self-assembled monolayers (SAMs) of alkanethiolates on gold are compared in a set of experiments carried out concurrently. The extent of damage to the SAM is determined by developing the samples in a gold etching solution, then measuring the decrease in reflectivity of the gold; $\approx 10^5$ Ar^* are required to cause the same amount of damage as 1 HCI, as measured by this assay. We have also demonstrated HCI micropatterning of a surface using a physical mask, suggesting the application of this system in lithography. © 1999 American Institute of Physics. [S0003-6951(99)03330-6]

Efforts to improve the techniques of micropatterning surfaces have involved the use of alternative resists or unconventional exposure methods. In this letter we do both simultaneously, using a beam of highly charged ions (HCIs) and a beam of neutral metastable atoms to expose an ultrathin self-assembled monolayer (SAM) resist. Besides providing one of the first demonstrations of lithographic patterning using HCIs, the results allow us to compare and contrast the relative efficiencies of ion and atom exposure quantitatively.

The internal energy (defined as the energy released in bringing an atom or ion to its neutral ground state) of metastable helium and argon atoms has been used previously to damage SAMs of dodecanethiol (DDT) on gold.¹⁻³ By using a mask to pattern the exposure, followed by etching, one can form patterns in gold and then in silicon.

The highly charged ions used in this work, Xe^{44+} , have a much greater potential energy (51.3 keV) than the atoms used previously, but they also have greater kinetic energy (350 keV for ions vs <0.1 eV for atoms). The ions neutralize rapidly (typically in less than ≈ 20 fs⁴), however, depositing the potential energy into a small volume localized in the first few nanometers of the surface.⁴⁻⁶ Because the kinetic energy is deposited in the solid over a region hundreds of nanometers deep, the energy *density* deposited on the surface is dominated by the contribution from the potential energy. Previous studies on mica have confirmed that the amount of damage to the surface caused by ions correlates with changes in internal potential energy (related to the charge of the ion) and not kinetic energy.^{7,8}

Figure 1 summarizes the process used to expose SAMs to the beams. The procedure for exposing the substrates to the beam of Ar^* is described in detail elsewhere.² The flux of Ar^* was $1.7 \times 10^4 \mu\text{m}^{-2} \text{s}^{-1}$ in a collimated beam ≈ 7.5 mm in diameter. The ion beam was a continuous stream of $\approx 11.0 \times 10^6 \text{Xe}^{44+}$ ions/s from an electron beam ion trap

(EBIT),⁹ the ion beam was passed through an aperture 3 mm in diameter, 5 mm above the sample.

Gold (40 nm thick) was evaporated onto silicon wafers using titanium (2 nm thick) as an adhesion promoter. The wafers, coated with gold, were stored under ambient conditions prior to the formation of SAMs. SAMs were prepared by immersing the gold films into a solution of dodecanethiol (DDT) in absolute ethanol (0.01 mol) for at least 16 h. Samples were then rinsed with ethanol, and blown dry in a stream of nitrogen gas before being loaded into the vacuum system.

In order to compare directly the doses of atoms and ions required to damage SAMs, we exposed samples to each of the two beams, concurrently, keeping the samples in each chamber under vacuum for the same total time. The pressure in the chamber in the case of the atom exposure experiment was approximately 1 mPa ($\approx 10^{-5}$ Torr) while in the case of the ion exposure the pressure was approximately 1 μPa ($\approx 10^{-8}$ Torr). We performed 12 exposures of HCIs of ≈ 90 min each on 6 separate samples of SAMs of DDT (Table I). The dose given in Table I is calculated from the average of

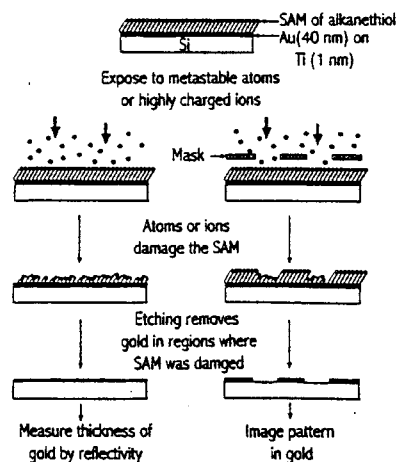


FIG. 1. Schematic of the experimental procedure.

^{a)}Present address: Diamond Semiconductor Group, Gloucester, MA 01930.

^{b)}Authors to whom correspondence should be addressed.

^{c)}Electronic mail: john.gillaspay@nist.gov

TABLE I. Exposure time, dose, and loss of reflectance measured when SAMs of DDT are exposed to HCIs and etched.

Time (s)	Dose ($\times 10^{11} \text{ cm}^{-2}$)	Loss of Reflectance	Time (sec)	Dose ($\times 10^{11} \text{ cm}^{-2}$)	Loss of reflectance
5400	1.35	22%	5100	1.35	48%
5400	1.24	12%	5040	1.30	41%
4380	1.33	8%	4980	1.39	42%
4380	1.29	7%	4800	1.36	41%
4500	1.34	16%	4620	1.29	41%
4620	1.34	14%	4860	1.27	35%
Average			1.32(04)		27(15)%

the flux before and after the exposure (the flux of ions can vary by up to 10% during the exposure). We determine the flux of ions with an electron multiplier in pulse counting mode; the ion detection efficiency is 0.50 with an uncertainty of less than 0.25.⁹

After exposure to the ion or atom beam, the samples were removed from the vacuum chamber and immediately etched in an aqueous ferricyanide solution (1 mol/l potassium hydroxide (KOH), 0.1 mol/l potassium thiosulfate (K_2SO_4), 0.01 mol/l potassium ferricyanide [$\text{K}_3\text{Fe}(\text{CN})_6$], and 0.001 mol/l potassium ferrocyanide [$\text{K}_4\text{Fe}(\text{CN})_6$] for ≈ 20 min). After etching, the samples were rinsed with distilled water and blown dry. The exposed regions were visible as darker areas corresponding in size to the widths of the beams.

The degree of etching of the exposed regions relative to the unexposed regions was quantified as a decrease in reflectivity of the surface.² A HeNe laser ($\lambda = 632 \text{ nm}$) was focused onto the sample at normal incidence and the reflected beam was separated from the incident beam with a polarizing beam splitter cube. The beam waist was calculated to be $\approx 15 \mu\text{m}$, but the resolution was limited by the point spacing in our scans to $70 \mu\text{m}$. The intensity of the reflected beam was monitored with a photodiode as the sample was stepped through the laser beam. The reflectivity was measured at points along several horizontal scans across the surface, each scan separated vertically by $\approx 0.5 \text{ mm}$, and then averaged. The fractional loss in reflectivity is defined as the unexposed value (average signal outside of the exposed region for that particular sample) minus the average signal from the exposed region divided by the unexposed value.

In the case of HCI exposure through a mask, some of the parameters discussed above were changed slightly. Chromium rather than titanium were used as an adhesion layer, and SAMs of hexadecanethiol (HDT) rather than DDT were used.

After etching, the regions of the surfaces that were exposed to HCIs show a decrease in reflectivity relative to that of unexposed gold. The maximum possible decrease in reflectivity gives a value that corresponds to that of bare silicon; none of the samples showed this maximum. By averaging the reflectivity across the exposed region for each sample, the analysis accounts for the fact that the distribution of ions across the beam (unlike the beam of atoms) is non-uniform. The average loss in reflectivity is 0.27(15) caused by an average dose of ions of $1.32(4) \times 10^{11} \text{ ions/cm}^2$. The uncertainty that we quote is the standard deviation of the 12

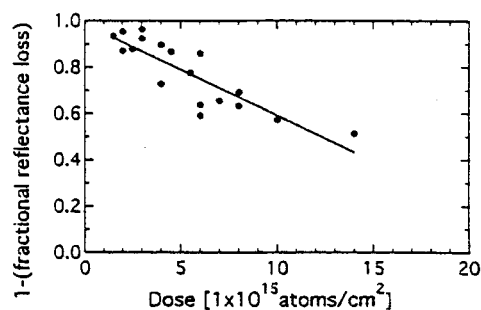


FIG. 2. Reflectance of gold vs dose for exposures of SAMs of DDT to Ar*.

individual data points. Since there may be a systematic component this deviation, we have used this conservative estimate of the uncertainty and not reduced it by the square root of the number of data points. Given that there are 4×10^{14} alkanethiol molecules/ cm^2 , we infer that each ion—and the subsequent etching process—generates a crater in the gold approximately 35 nm in diameter and encompassing ≈ 3000 alkanethiol molecules in the SAM. This is in reasonable agreement with the directly imaged results for randomly dispersed single ion impact craters obtained subsequently to our work by the Livermore group (50–63 nm diameter),¹⁰ given the fact that the SAMs used were different, and that the direct images do not appear to be corrected for imaging probing tip effects (tip radii approximately 70 nm). These craters are comparable in size to those formed in a more standard resist, poly (methylmethacrylate), which was exposed to Xe^{44} [after etching, single ion impact craters 25 nm in diameter were observed with atomic force microscopy (AFM)].¹¹

In order to compare exposure with HCIs to that with Ar*, we chose various doses of Ar* to bracket the exposure obtained with HCIs and interpolated to the dose which gives an equivalent exposure as measured by the reflectivity. The results of our reflectivity measurements for exposures of SAMs of DDT to metastable argon atoms is plotted in Fig. 2. The slope of the solid line is $4.1(12) \times 10^{-17} \text{ cm}^2/\text{atom}$, in reasonable agreement ($< 2\sigma$) of the previously determined value.² The statistical contribution to the overall (combined standard) uncertainty of the present result is $0.6 \times 10^{-17} \text{ cm}^2/\text{atom}$. The overall uncertainty is limited by the detection efficiency (ϵ) of the metastable atoms, as described previously.²

A loss of reflectivity of 27% (the average loss obtained with HCIs) thus corresponds to a dose of $6.6 \times 10^{15} \text{ atoms/cm}^2$. This value implies that multiple impacts (~ 16) of Ar* are required to damage a point on the surface such that etching will remove the underlying gold. Therefore, $\sim 10^{15}$ Ar* are required to cause (after etching) the same amount of damage as one Xe^{44+} ion, as compared to the ratio of potential energy, 4400. That is, the HCI is much more efficient at converting its potential energy to surface damage than is the metastable atom. This nonlinear energy dependence is not surprising because a similar effect has been seen in a comparison of damage to SAMs using Ar* (P.E.=12 eV) and He* (P.E.=21 eV) projectiles.² In that case, an increase in the potential energy per atom of less than a factor of 2 resulted in a decrease in the required dose of

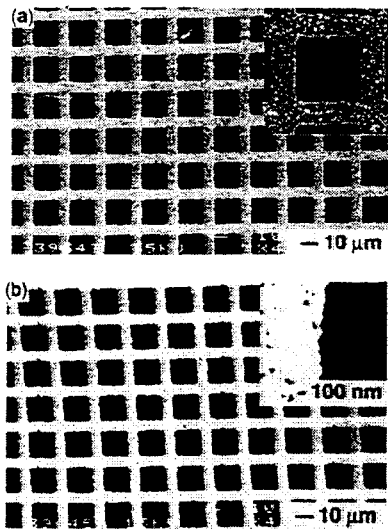


FIG. 3. SEM of (a) the TEM grid and (b) the gold patterns made by exposing SAMs of HDT to HCIs. The insets show that the edge roughness of the features in gold is comparable to that of the TEM grid.

more than an order of magnitude. It was speculated that the damage was caused by secondary electrons, and comparison of the metastable atom dose (assuming one secondary electron per Ar^*) with the dose used in experiments where electron beams were used to expose SAMs, gave reasonable agreement. Perhaps the increased efficiency of the He^* comes from the decrease in inelastic mean free path¹² as the electron energy goes from 12 to 20 eV, which allows the electron to undergo a higher density of collisions within the SAM. The mean free path increases above 20 eV, but this increase might not be relevant as the damage mechanisms might be quite different for the two projectiles as their potential energies differ by over three orders of magnitude. Because the HCI deposits a large parcel of potential energy into a small volume of the surface in a short time, the excitation is concentrated and collective effects might be important. Two models predict cratering of surfaces due to the large energy density deposited by a single HCI. One model asserts that the HCI will extract many electrons from the surface leading to a charge buildup which will Coulomb explode,¹³ ejecting ions from the surface and causing a shock wave that ejects neutral material as well.¹⁴ A second model predicts that the HCI impact excites many surface electrons from bonding states to antibonding states, rendering the material structurally unstable.¹⁵ The result is the displacement of a large number of surface atoms.

In order to demonstrate the ability of HCIs to pattern SAMs, we exposed SAMs of HDT to the ion beam through a physical mask—a nickel transmission electron microscopy (TEM) grid (Fig. 1). Figure 3 shows SEM images of gold patterned by exposing SAMs on gold to a beam of HCIs through a mask for ≈ 2 h: the flux was measured prior to exposing the samples, and the dose calculated to give a 50% loss in reflectivity of the gold after etching. Samples were etched in an aqueous ferricyanide solution to reveal the pattern in gold. The edge roughness of the features in gold (≈ 100 nm) is comparable to that of the TEM grid (Fig. 3 inserts).

In summary, we have demonstrated that Xe^{44+} damages SAMs in doses five orders of magnitude lower than doses of Ar^* . Using currently available high flux sources of HCIs,^{9,16–18} the overall exposure time can be shorter than that used in previous studies involving metastable atoms. Furthermore, since the production of HCI beams is an area of research still in its infancy and appears to be progressing rapidly, there is much room for future improvements. The next generation of EBIT devices, for example, will have a greatly increased intensity and brightness; the brightness, a figure of merit that combines intensity and emittance (ability to focus to a small spot), is expected to be improved by four orders of magnitude.¹⁸

We have also used HCIs to pattern gold films by exposing SAMs of HDT on gold to ions through a stencil mask, and then etching the gold from the exposed regions. Because this process is significantly more efficient than patterning with metastable atoms, it may be suited to lithography. Furthermore, because of the high energy density the HCIs deposit on the surface, thicker SAMs can be used, leading to a more robust process with greater contrast.

This work is supported by ONR/DARPA and NSF Grant No. PHY 9312572. This study made use of the MRSEC Shared Facilities supported by the NSF under Award No. DMR-9400396. A.B. was supported by the Humboldt Foundation. We gratefully acknowledge Doug Alderson's technical assistance with the EBIT.

¹K. K. Berggren, A. Bard, J. L. Wilbur, J. D. Gillaspay, A. G. Helg, J. J. McClelland, S. L. Rolston, W. D. Phillips, M. Prentiss, and G. M. Whitesides, *Science* **269**, 1255 (1995).

²A. Bard, K. K. Berggren, J. L. Wilbur, J. D. Gillaspay, S. L. Rolston, J. J. McClelland, W. D. Phillips, M. Prentiss, and G. M. Whitesides, *J. Vac. Sci. Technol. B* **15**, 1805 (1997).

³S. Nowak, T. Pfau, and J. Mlynek, *Appl. Phys. B: Lasers Opt.* **63**, 203 (1996).

⁴T. Schenkel, M. A. Briere, A. V. Barnes, A. V. Hamza, H. Schmidt-Böcking, K. Bethge, and D. H. Schneider, *Phys. Rev. Lett.* **78**, 2481 (1997).

⁵T. Schenkel, M. A. Briere, A. V. Barnes, A. V. Hamza, H. Schmidt-Böcking, K. Bethge, and D. H. Schneider, *Phys. Rev. Lett.* **79**, 2030 (1997).

⁶T. Schenkel, A. V. Hamza, A. V. Barnes, and D. H. Schneider, *Phys. Rev. A* **56**, R1701 (1997).

⁷D. C. Parks, M. P. Stöckli, E. W. Bell, L. P. Ratliff, R. W. Schmieder, F. G. Serpa, and J. D. Gillaspay, *Nucl. Instrum. Methods Phys. Res. B* **134**, 46 (1998).

⁸D. C. Parks, R. Bastasz, R. W. Schmieder, and M. P. Stockli, *J. Vac. Sci. Technol. B* **13**, 941 (1995).

⁹L. P. Ratliff, E. W. Bell, D. C. Parks, A. I. Pikin, and J. D. Gillaspay, *Rev. Sci. Instrum.* **68**, 998 (1997).

¹⁰T. Schenkel, M. Schneider, M. Hattass, M. W. Newman, A. V. Barnes, A. V. Hamza, D. H. Schneider, R. L. Cicero, and C. E. D. Chidsey, *J. Vac. Sci. Technol. B* **16**, 3298 (1998).

¹¹J. D. Gillaspay, D. C. Parks, and L. P. Ratliff, *J. Vac. Sci. Technol. B* **16**, 3294 (1998).

¹²M. P. Seah and W. A. Dench, *Surf. Interface Anal.* **1**, 2 (1979).

¹³I. S. Bitenski, M. N. Murakhmetov, and E. S. Parilis, *Sov. Phys. Tech. Phys.* **24**, (1979).

¹⁴H.-P. Cheng and J. D. Gillaspay, *Phys. Rev. B* **55**, 2628 (1997).

¹⁵T. Schenkel, A. V. Hamza, A. V. Barnes, D. H. Schneider, J. C. Banks, and B. L. Doyle, *Phys. Rev. Lett.* **81**, 2590 (1998).

¹⁶E. D. Donets, *Rev. Sci. Instrum.* **69**, 614 (1998).

¹⁷Z. Q. Xie, *Rev. Sci. Instrum.* **69**, 625 (1998).

¹⁸R. E. Marrs, *Nucl. Instrum. Methods Phys. Res. B* **149**, 182 (1999).

Separation of inner-shell vacancy transfer mechanisms in collisions of slow Ar^{17+} ions with SiO_2

E Takács^{1,2}, Z Berényi², J D Gillaspay¹, L P Ratliff¹, R Minniti¹,
J Pedulla¹, R D Deslattes¹ and N Stolterfoht³

¹ National Institute of Standards and Technology, Gaithersburg, MD 20899, USA

² University of Debrecen, Institute of Experimental Physics, ATOMKI, Bem ter 18, Debrecen H-4026, Hungary

³ Hahn Meitner Institut, Glienikerstrasse 100, D-14109 Berlin, Germany

Received 30 November 2000

Abstract

We have studied the spectrum of x-rays emitted when 130 and 200 keV kinetic energy hydrogen-like argon ions impact silicon dioxide surfaces. Specifically, we were interested in the mechanism for creation of K-shell holes in the silicon target atoms, which can be filled with the release of a 1.75 keV x-ray. Two mechanisms have been hypothesized for the vacancy transfer between the K-shells of silicon and argon atoms: ‘direct vacancy transfer’ and ‘projectile-decay-product-mediated vacancy transfer’. To separate these mechanisms, we used a target with a metallic coating (preventing close collisions between Si and Ar but allowing x-ray transmission) and a target without such a coating. We found that x-ray photoionization is the dominant mechanism in both cases and measured an upper limit for the contribution from the ‘direct mechanism’ on the uncoated sample. Furthermore, we measured the relative strengths of the $K\alpha$, $K\beta$ and $K\gamma$ lines of the argon projectile as a function of kinetic energy and found satisfactory agreement with charge exchange and cascade model calculations.

1. Introduction

Collisions of ions with surfaces have been studied for many years and the results have been successfully applied to various technologies including ion implantation [1], secondary ion mass spectroscopy (SIMS) [2], ion etching [1], focused ion beams for lithographic mask repair [3] and surface polishing [4]. Although the understanding of these processes is continually evolving, successful models that describe them have existed for many years [5–7]. These models allow engineers to vary parameters associated with the ion, such as its speed and mass, in order to optimize a particular process for a particular surface. One potentially important parameter that has been largely ignored in this optimization is the ion’s charge. With the recent development of compact sources of highly charged ions (HCIs), there is a great potential for further innovation in ion-related technologies. With this new generation of sources, ions of a

wide variety of masses and a wide variety of charge states can be formed with kinetic energies comparable to their potential energies, which can be tens or even hundreds of keV. Experiments with these HCIs have revealed, for instance, that the sputtering yields and secondary ion yields are quite high due to the localized deposition of the ion's large potential energy, and nanoscale surface features attributable to individual HCI impacts can be seen on various surfaces [8–10].

Using a crystal microbalance, Sporn *et al* [11] recently showed that highly charged argon ions produce strong potential sputtering in SiO₂. This result supports the assertion that an efficient potential energy transfer takes place on the surface. Furthermore, sputtering with argon ions was found to be less effective than sputtering with xenon ions possessing about the same amount of potential energy [11]. The authors attribute this effect to the fact that, in argon, the energy is available in larger quanta because inner-shell vacancies provide most of its potential energy. This study emphasizes the need to understand the details of how the potential energy carried by inner-shell vacancies of the projectile is transferred to the solid.

The basic understanding of the HCI–surface interaction is based on the classical over-the-barrier model [12]. That is, the ion begins to extract electrons from the surface even before impact. These electrons become bound in high-lying states of the projectile while the core states remain vacant, forming a ‘hollow atom’. Upon impact, electrons in high-lying states are ‘peeled off’ and are soon replaced by electrons that become bound in intermediate states, forming a second, smaller ‘hollow atom’. The projectile relaxes further as it travels through the solid. Although at the kinetic energies typically used in these experiments (a few eV to a few hundred keV) the ions may penetrate hundreds of nanometres into the solid, the potential energy is released within a few nanometres of the surface [13].

In this way, the potential energy of the projectile can be deposited into a very small volume (nanometre sized) in a very short time (femtoseconds). Therefore, the projectile and the solid are both far from equilibrium and the interaction cannot be treated as a small perturbation to either the projectile or the surface. This situation makes the theoretical treatment of this interaction quite complicated. A deeper understanding of the effects that come into play at moderate and high charge states could enable one to tailor the projectile ion, including its charge state, to various applications. In this way, one might improve techniques currently in use and find new applications. In order to deepen the current understanding of the effects that are important in HCI–surface interactions, experiments must be designed that probe specific aspects of the collisions as well as models to explain these phenomena. Such a study is presented in this paper.

Among the key issues in the field today are (1) the mechanism and timescale of the hollow atom formation and decay, and (2) the mechanism, the time evolution and the spatial distribution of the deposition of the HCI's potential energy into the substrate. These two issues are intimately related because it is in the process of neutralization and decay that the projectile deposits its potential energy into the surface. To resolve these questions, the dynamics of the interaction must be investigated. One fruitful approach is to study the secondary particles such as electrons [14–17], x-rays [18, 19], atoms, ions and clusters [20, 21] that are emitted from the projectile and from the surface. Investigations where emission from both the target and the projectile can be observed at the same time are particularly useful because the relative intensities of the various emission products carry information about the effectiveness of the energy transfer mechanisms.

X-ray spectroscopy experiments that involve the interaction of one-electron Ar¹⁷⁺ ions with solids are among the workhorses of the field. Many important details about the time scale and mechanism of the hollow atom formation and decay have been revealed in the investigation of such systems ([19, 22] and references therein). Our group pointed out that in the interaction of slow Ar¹⁷⁺ ions with SiO₂ surfaces, x-rays emitted by the *target*, in addition to those emitted

by the projectile, can be observed [23]. These x-rays were interpreted differently in previous investigations (e.g. [24]). The observation of even a weak silicon K x-ray peak (relative to the argon projectile K peak) is important because the silicon fluorescence yield (5.0% [25]) is at least two or three times smaller than that of the argon L shell (depending on the electron configuration in the argon hollow atom at the time of the K x-ray emission). This means that the fraction of argon ions creating inner-shell vacancies in Si is at least two or three times higher than the observed target to projectile K line intensity ratio. In our previous study [23], we also took spectra at several different projectile energies, but the presence of instrumental artifacts in our data and uncertainties about the normalization of the beam flux hitting the target led us to avoid making quantitative conclusions about the velocity dependence of the intensity ratios of the target and projectile K x-ray lines. Lehnert *et al* [26] measured the velocity dependence in a later experiment and argued that photoionization of target atoms by K x-rays from the argon projectile could explain their observed line intensity ratios. In the current paper, we directly separate the various possible mechanisms for the creation of K vacancies in silicon by Ar¹⁷⁺ impact.

The potential energy of the K-shell vacancy in Ar¹⁷⁺ ions is 4.12 keV (the binding energy of a single K-shell electron). While there are different mechanisms through which this energy can be transferred to the surface, the largest energy quantum that the surface can absorb in a single step (neglecting less probable higher-order processes) is 1.84 keV, the binding energy of a Si K-shell electron. This process can occur via a ‘direct vacancy transfer’ from the argon to the silicon in a close collision. Because of the large mismatch between the silicon and argon K energy levels, the probability of a one-electron process is relatively low. However, it was suggested that the process can take place via a dielectronic mechanism, where the excess energy is taken away by an electron from either the target or the projectile itself [23].

A second type of vacancy-transfer mechanism, ‘decay-product-mediated vacancy transfer’, is a multi-step process. In the first step, the projectile fills its K-vacancy by emitting a high-energy x-ray or electron. In the second step (or in several further steps), the decay product (x-ray or electron) deposits its energy into the solid. We argue in the next section that the electron-mediated mechanism is not important in our experiment. This leaves the direct transfer mechanism and x-ray-mediated mechanism to be separated experimentally.

In addition to studying the vacancy transfer that results in silicon K emission, we also look at the structure of the argon K peak. Specifically, we look at the relative intensities of the K α , K β and K γ peaks, which are determined by the populations of the L, M and N shells, respectively, at the time of emission. The ratios of these peaks, which are quite different from the case of a ground state atom with a single K-vacancy, give information about the cascade of transitions that fills in the hollow atom. These ratios are compared with those calculated by the charge exchange and cascade model [27].

In the following paragraphs we will describe our method for separating the direct and the ‘x-ray-mediated’ vacancy-transfer mechanisms by using two different target samples. First we will present our assumptions and their justifications. This will be followed by the experimental and data analysis details. Next we will present our results on the Si and Ar K intensity ratio and its consequences. After that we will discuss our results on the ratios of the different components of the argon K peak. We will close our paper with a conclusion.

2. Separation of the vacancy transfer mechanisms

In the present experiment, we isolate the ‘x-ray-mediated vacancy-transfer mechanism’ from the other mechanisms, ‘electron-mediated vacancy transfer’ and ‘direct vacancy transfer’, by covering a silicon sample with a thin metallic layer. This layer prevents the ions from

penetrating into the silicon before their K vacancies have been filled while allowing high-energy x-rays to penetrate largely unimpeded. The rate of 'x-ray-mediated vacancy transfer', as measured using the coated sample, is compared to the total rate of vacancy transfer, as measured with a sample that is not metallized, to determine the relative importance of the mechanisms. This technique relies on two key assumptions:

Assumption 1. The K-vacancy in the argon ion is filled within the metallic layer.

This assumption is well established by both theory and experiment. In studies where HCIs are sent through 10 nm foils with kinetic energies comparable to those used in the present experiment, they were found to emerge from the foil in their equilibrium charge states and in their ground states [13]. According to calculations, the K-shell of an Ar^{17+} ion with a kinetic energy of 170 keV is filled in the first 10 nm of a solid [27]. Silicon K-shell vacancies, therefore, can be created by the 'direct-vacancy-transfer' mechanism (which requires a close collision) only if the Si atom is located within 10 nm of the surface. Furthermore, there is experimental evidence [28] that the filling can take place at much shorter distances in certain situations. It was shown that a single monolayer of LiF molecules on Au(111) completely shields the interaction of hydrogen-like oxygen projectiles with the gold substrate with respect to neutralization [28].

Assumption 2. The contribution to silicon K-shell vacancy production from energetic electrons is negligible.

Among the decay products of the argon hollow atom, the only two that are energetic enough to create Si K vacancies are K x-rays (3.4 keV) and K Auger electrons (KLL: 2.5 keV and KLM: 2.9 keV). The ratio of the number of x-rays emitted per projectile ion to the number of electrons emitted per projectile ion can be extracted from the K-shell fluorescence yield of the argon hollow atoms. The relevant fluorescence yield in this dynamic system is an average of the fluorescence yields of the individual hollow atom electron configurations that exist at the time of the decay of the K-vacancy. A conservative lower limit is 11.8%, which is the fluorescence yield in neutral argon [25]. This yield means that up to ten times more K Auger electrons than K x-rays could be produced when hydrogen-like argon ions collide with a surface. Therefore, it is important to consider the effect of electrons on the K-vacancy creation in silicon. From the electron spectrum of [29], where the same collision system was investigated, we can estimate that about 2/3 of the electrons are KLL and 1/3 are KLM Auger electrons.

Although there may be more electrons than x-rays emitted when the argon K-shells decay, we will show that their effect on the silicon K-shell ionization is negligible. As they penetrate the surface, electrons quickly lose energy in collisions with the electrons in the solid. From the energy distribution of the electrons receding from a collision event, we estimate that within about five collision steps, more than 99% of the argon KLL and KLM Auger electrons would be below the ionization threshold for the silicon K-shell. Comparing the cross section for the removal of a valence electron in SiO_2 (which is the dominant process) to the ionization cross section of the silicon K-shell [30], it turns out that only about 10^{-4} of the argon K Auger electrons create K vacancies in silicon.

To compare the silicon K-vacancy production from electron impact to that from x-ray absorption, we need to look at the efficiency of the latter process. Because the energy of the argon x-rays lies just above the K absorption edge of silicon (1.84 keV), the x-ray absorption is dominated by K-shell ionization. We estimate the effect of other contributing processes to be about 10% [31]. Assuming that the angular distribution of x-rays emitted from the projectile

is isotropic, approximately half of the emitted x-rays penetrate the solid, and most of these x-rays create K-shell vacancies in silicon.

Combining the estimates above (the small fraction of fast electrons that create inner-shell holes and the large fraction of x-rays that create inner-shell holes), we conclude that, although the fluorescence yield may be small, the contribution from fast electrons to the creation of silicon K vacancies is about 10^3 times less than that from x-rays. This result justifies our second assumption.

We would like to note here that, although fast Auger electrons do not efficiently contribute to inner-shell vacancy creation, they play an important role in transferring the ion's potential energy to the substrate. Fast electrons quickly distribute their kinetic energy into a shower of slow electrons, which come mainly from the valence band of the crystal. It is still to be investigated whether either the electronic defects created in this way or the positive charge surplus has enough density to induce a local modification of the crystal structure. Understanding the details of the processes caused by secondary electrons is important in determining whether the ion impact can create the necessary conditions for a structural instability [32] or a Coulomb explosion [33–35] to occur in the solid.

The attenuation length in silicon for 3 keV x-rays is $4\ \mu\text{m}$ [31]; therefore, most of the vacancies that are created by the x-ray-mediated mechanism are located well below the surface. Because the energy of the silicon K x-rays lies below the K absorption edge of silicon (1.84 keV), their attenuation on the way out of the solid is small.

Apart from the above, in the comparison of the different samples we made an implicit assumption that our method is independent of the electronic structure of the target. This assumption is made because we compare relative intensities of projectile and target x-rays rather than absolute yields.

3. Experimental arrangement

The experiments were performed at the NIST electron beam ion trap (EBIT) facility. Hydrogen-like argon ions created inside the EBIT were transported to the sample by a highly efficient ion extraction and transport system [36]. The sample was kept at ground potential, so the energy of the ions was determined by the voltage applied to drift tubes in the region where the ions were created. We made measurements at 8 and 12 kV drift tube voltages: The projectile energies were roughly equal to the charge state times the potential difference between the central drift tube of the EBIT and the target sample. There is a small correction to the energy of the ions due to the space charge of the electrons inside the EBIT; this was taken into account in the analysis.

Our experiments were performed with two targets. The first target was a special multilayer structure of silicon, molybdenum and carbon. The second target consisted of a 100 nm SiO₂ layer on a silicon substrate.

In order to observe silicon target x-rays originating purely from the 'x-ray-mediated mechanism' we made a special multilayer structure. On top of a silicon substrate, we prepared a molybdenum layer and a carbon layer using low-pressure ion beam sputtering combined with simultaneous ion beam polishing. The thicknesses of the layers were measured by high-resolution diffractometry. The method of production and characterization is fully described in [37]. The molybdenum film thickness varied from 24.3 to 25.4 nm across the length of the sample and the interface between the molybdenum and silicon was about 0.6 nm thick. The thickness of the carbon layer was 5 nm with an uncertainty similar to that of the molybdenum.

The thick molybdenum film completely prevented the ions from penetrating into the silicon before their K vacancies were filled. (The molybdenum layer also prevents the penetration of

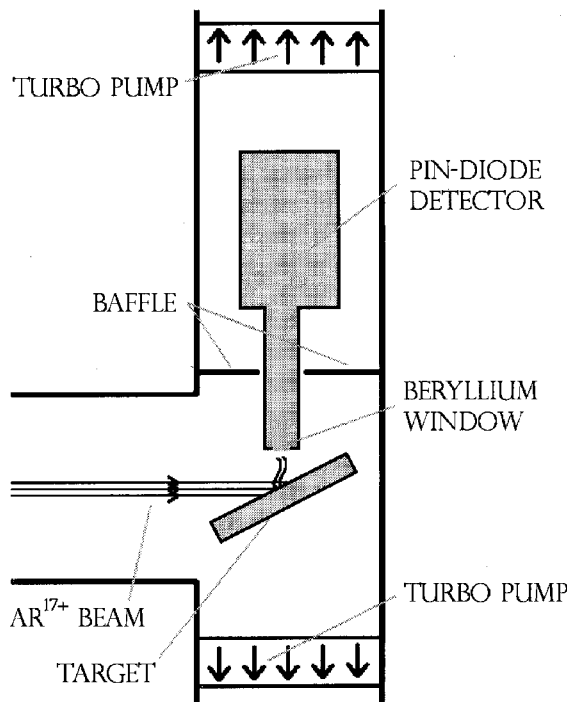


Figure 1. Experimental arrangement. X-rays from the projectile and the sample were detected by a Si PIN diode detector at 90° to the direction of the incoming beam.

energetic electrons although, as we have shown above, their effect is already negligible even without the coating.) The carbon on the top served as a passivation layer that ensured that there was no unknown heavy element contamination on the top of our sample. The penetration of the x-rays through the top layers was more than 80% and was accounted for in the analysis.

The x-ray data were taken with a PIN-diode x-ray detector with a $12.5 \mu\text{m}$ thick beryllium window in front of the sensitive area. The detector was energy calibrated and its resolution measured using the $K\alpha$ and $K\beta$ lines of Sc, Ti and Ca from a commercial x-ray source. The 250 eV resolution allowed us to separate the target and projectile x-rays, but was not enough to resolve the different components of the projectile K peak. The detector was placed at 90° with respect to the ion beam and 30° with respect to the surface normal as shown in figure 1.

In our earlier experiment [23], we used an ion deceleration system and placed the target at a biased potential in order to study collisions at very low energy (typically a few hundred eV). As we pointed out in that work, however, an observed broad bremsstrahlung background probably signalled the existence of secondary charged particles. Our present bremsstrahlung-free measurements confirm this hypothesis and indicate that most of the previously observed silicon signal was due to impact ionization by spurious background electrons. To ensure that this effect can be fully ruled out in the present measurements, the target was kept at ground potential for the experiments where the target x-rays were studied. For those experiments where we studied only the argon spectrum, we biased the sample in order to adjust the kinetic energy.

4. Data analysis

Following a standard procedure that is used for solid-state silicon detectors [38], the spectra were fitted with asymmetric line-shape functions that took into account the response function

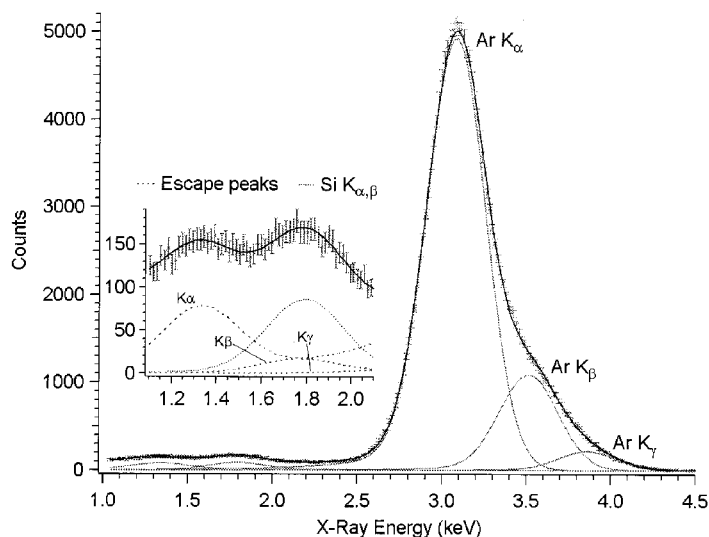


Figure 2. X-ray spectrum from the SiO₂ sample showing the projectile K x-ray peaks at around 3 keV and the silicon target K peaks at around 1.8 keV. The target x-ray peak partially overlaps the ‘escape’ components of the projectile peaks. The error bars indicate one-standard-deviation uncertainties associated with counting statistics.

of our detector. The line-shape consists of a Gaussian with an exponential low-energy tail and a so-called ‘escape peak’. The width of the Gaussian, the slope and intensity of the exponential tail and the position and intensity of the escape peak with respect to the main peak were treated as instrumental parameters and were held at the same value in all of the spectra. All the spectra were fitted simultaneously to determine these parameters. Only the positions and intensities of the Gaussian peaks were free parameters.

Although the 250 eV resolution of the x-ray detector did not allow us to separate the K α , K β and K γ components of the projectile peak, the shape of the argon K peak made it necessary to include all three components in the fits. A spectrum from the SiO₂ sample, together with the fitted curves, is shown in figure 2. The blending of the silicon K x-rays with the escape peaks of the K β and K γ lines of argon complicated the determination of the silicon x-ray intensity. However, the escape peak of the argon K α transition is fairly well separated from the silicon line, and the argon K α , K β and K γ structure is well separated from other features in the spectrum. Therefore, the information about the relative intensities of the argon K lines was used to determine the positions and intensities of the argon K escape peaks and to extract the intensity of the silicon line. The uncertainties of the results in our figures and text are one-standard-deviation uncertainties derived from the least-squares fit to the measured spectra, assuming that we have the correct functional form and that our noise is limited by counting statistics. Specifically, the uncertainties reported are the square root of the corresponding diagonal element of the covariance matrix, with the points in the spectra weighted as the square root of their intensities.

We calculated the contribution to the silicon K x-ray yield due to ‘x-ray-mediated vacancy transfer’ relative to the argon K x-ray yield as described in [26]. The fluorescence and the attenuation in all the layers were taken into account for both samples (SiO₂–Si and C–Mo–Si). In addition to the silicon x-rays, molybdenum L x-rays were present in the C–Mo–Si spectra around 2.4 keV. The intensity of the Mo L $\alpha\beta$ x-ray peak was 0.2% of the Ar K α peak and its inclusion in the analysis was necessary to fit the spectra.

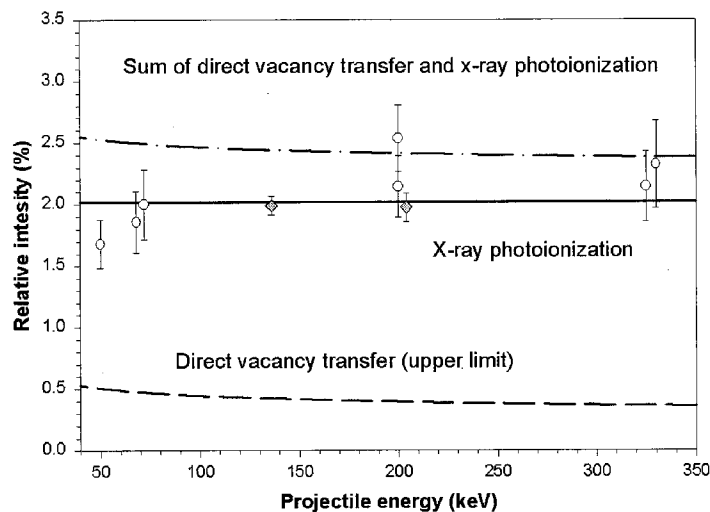


Figure 3. Contributions of the different silicon K-vacancy production mechanisms. The plot represents the ratios of the Si and Ar K x-ray peak intensities. The solid curve is a calculation of the contribution from x-ray photoionization. The upper limit of the ‘direct vacancy transfer’ contribution (dashed curve) is estimated using calculations of Stolterfoht *et al* [27]. The dot-dash curve is the sum of the other two. Grey diamonds, data obtained using the SiO₂-Si sample; open circles, data from [26].

5. Results

5.1. Experimental evidence for the importance of the ‘x-ray-mediated vacancy transfer’

As pointed out earlier, in the case of the C–Mo–Si multilayer sample, the sole origin of silicon x-rays was the photoionization caused by the penetration of energetic argon K x-rays into the silicon substrate. We found that the intensity of the silicon K x-rays relative to the intensity of the argon K x-rays was 0.0183(30). This experimental value agrees with the theoretical value of 0.016 calculated taking into account the attenuation of the incoming and outgoing x-ray intensities in the thin molybdenum and carbon films. This result is experimental verification that the x-ray fluorescence is indeed an important process for the K-vacancy transfer between the projectile argon and the target silicon atoms as suggested by Lehnert *et al* [26].

5.2. Upper limit for the ‘direct vacancy transfer’ contribution

Having shown that x-ray photoionization dominates the vacancy transfer, we wanted to set an upper limit for the ‘direct vacancy transfer’ contribution. In order to do this, we collected spectra using the uncoated sample and extracted relative line intensities from the fits. Figure 3 shows the measured ratio of the silicon K x-ray intensity to the argon K x-ray intensity for the SiO₂ sample. The experimental values from Lehnert *et al* [26] are also shown on the plot. These data are complementary to this paper because they span a wider energy range, even though their larger uncertainties do not allow one to rule out 25% or less ‘direct vacancy transfer’ contribution to the peak intensities. The calculated values for the contributions from the ‘x-ray-mediated vacancy transfer’ and from ‘direct vacancy transfer’ (discussed below) are also shown on the plot.

The calculation of silicon K x-ray yield from ‘x-ray-mediated vacancy transfer’ takes into account the effect of the 100 nm SiO₂ layer on the top of Si, which modifies the results only slightly. The calculated value, 2.02%, is independent of the projectile energy.

dynamics and successfully describes the projectile energy dependence of the structure within the $K\alpha$ line measured with high resolution in [24]. In this paper, the measured intensity ratios, $K\alpha/K\beta$ and $K\alpha/K\gamma$, are predicted by the theory to within 25% as shown in figure 4. Using a microcalorimeter, Legros *et al* [40] measured the ratio $(K\beta + K\gamma)/K\alpha$ to be 31%; the same ratio extracted from our spectra gives 29% and agrees well with this value. Our experiment shows essentially no energy dependence in either of the ratios, whereas the theory predicts a slight change in the case of $K\alpha/K\beta$ and a stronger change (about 40%) of the $K\alpha/K\gamma$ ratio over the measured energy range. If there is any change of the experimental ratio at the lowest projectile energies, it is hidden within the error bars of our measurement. In contrast, a ground state argon atom with a single K-vacancy emits only $K\alpha$ and $K\beta$ radiation (the intensity ratio, $K\alpha/K\beta$, is 9.5 [41]); $K\gamma$ radiation is absent because the N shell is empty. In the case of an HCI, however, any of these shells can be filled in a cascade from the high-lying states of the hollow atom.

6. Conclusions

We investigated the interaction of slow (kinetic energy less than 220 keV) hydrogen-like argon ions with silicon surfaces. We confirmed our earlier [23] and other [26] observations that target x-rays are indeed produced in this process. We used a novel technique to *experimentally* separate the mechanisms for vacancy transfer from the K-shell of the projectile to the K-shell of the target and found that ‘direct vacancy transfer’ is negligible compared with photoionization of the target atoms by x-rays originating from the decaying K-shell hole of the projectile. Based on this paper, we emphasize that, for a complete picture of the interaction of slow HCIs with surfaces, the interactions of secondary collision products with the target should be taken into account. These products (electrons and x-rays) can carry a significant part of the projectile’s potential energy; therefore, they can play a dominant role in the deposition of potential energy into the solid. As a result, they play a role in setting the timescale of the interaction and in the spatial distribution of the energy deposition into the target. The timescale and spatial distribution are important parameters for the further relaxation of the surface, and can determine whether the interaction causes only transient effects or permanent damage to the surface.

Acknowledgments

We wish to thank Douglas J Alderson for his excellent technical support. ET acknowledges the support of the Hungarian Science Fund (OTKA, F19336) and the US-Hungarian Joint-Fund (JFNo 562/96) for support. RM acknowledges support from the National Research Council. We would like to thank Cedric J Powell and Larry T Hudson for their critical reading of this manuscript.

References

- [1] Van Zant P 1990 *Microchip Fabrication: a Practical Guide to Semiconductor Processing* (New York: McGraw-Hill)
- [2] Brundle C R, Evans C A, Wilson S and Fitzpatrick L E 1992 *Encyclopedia of Materials Characterization* (Boston: Butterworth-Heinemann)
- [3] DeMarco A J and Melngailis J 1999 *J. Vac. Sci. Technol. B* **17** 3154–7
- [4] Chason E and Mayer T M 1993 *Appl. Phys. Lett.* **62** 363–5
- [5] Ziegler J F, Biersack J P and Littmark U 1985 *The Stopping and Range of Ions in Solids* (New York: Pergamon)
- [6] Young D A 1997 *Radiat. Meas.* **27** 575–86

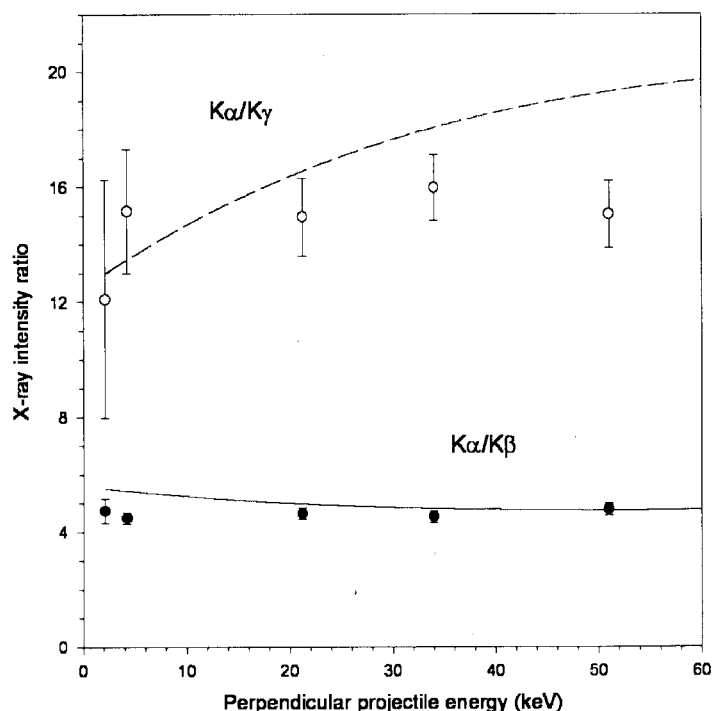


Figure 4. Measured intensity ratios of the different projectile K x-ray components. Open circles, $K\alpha/K\gamma$; full circles, $K\alpha/K\beta$. The theoretical curves are calculations based on [27].

The ‘direct vacancy transfer’ contribution for this particular sample (shown in figure 3) is an estimate for the upper limit of the dielectronic process proposed in [23]. In this process, the argon projectile K-vacancy is filled by a silicon K-shell electron and the excess energy is taken away by a second electron from the silicon L shell. In the calculation of the Si K-vacancy production, the rate for the dielectronic process was estimated using the Landau–Zener model as shown previously for L-shell vacancy transfer in the Ar–Si system [39]. To account for the filling of the hollow argon atom, a complex charge exchange and cascade model calculation, of the type described previously by Stolterfoht *et al* [27] was performed. The model was verified by complementary measurements in which the energy distribution and yield of the emitted electrons were measured in the same system [29].

From figure 3, we conclude that, even in the case of the SiO₂ sample where close collisions between the argon projectiles and the silicon surface atoms were possible, the contribution from the ‘direct vacancy transfer mechanism’ is less than 5% of the contribution from x-ray photoionization. This observation supports the suggestion of Lehnert *et al* [26]; however, in their measurement the error limits did not rule out the contribution from the ‘direct vacancy transfer mechanism’ within the limits of the theoretical estimates.

5.3. Ratios of projectile K emission lines

In addition to the silicon K radiation, we have studied the argon K radiation. We obtained intensity ratios for the $K\alpha$, $K\beta$ and $K\gamma$ x-ray lines in argon from the data fits described earlier and compared them with the charge exchange and cascade calculation [27]. The positions and relative strengths of these lines carry information about the number of electrons in the various shells at the time of the K transition and, in turn, about the dynamics of the electron capture and cascade. The charge exchange and cascade model calculation accounts for these

- [7] Dufour C, Audouard A, Beuneu F, Dural J, Girard J P, Hairie A, Levalois M, Paumier E and Toulemonde M 1993 *J. Phys.: Condens. Matter* **5** 4573–84
- [8] Schenkel T, Hamza A V, Barnes A V and Schneider D H 1999 *Prog. Surf. Sci.* **61** 23–84
- [9] Parks D C, Stockli M P, Bell E W, Ratliff L P, Schmieder R W, Serpa F G and Gillaspay J D 1998 *Nucl. Instrum. Methods B* **134** 46–52
- [10] Arnau A *et al* 1997 *Surf. Sci. Rep.* **27** 117–239
- [11] Sporn M, Libiseller G, Neidhart T, Schmid M, Aumayr F, Winter H P, Varga P, Grether M, Niemann D and Stolterfoht N 1997 *Phys. Rev. Lett.* **79** 945–8
- [12] Burgdorfer J, Lerner P and Meyer F W 1991 *Phys. Rev. A* **44** 5674–85
- [13] Hattass M, Schenkel T, Hamza A V, Barnes A V, Newman M W, McDonald J W, Niedermayr T R, Machicoane G A and Schneider D H 1999 *Phys. Rev. Lett.* **82** 4795–8
- [14] Stolterfoht N, Arnau A, Grether M, Kohrbruck R, Spieler A, Page R, Saal A, Thomaschewski J and Bleckneuhaus J 1995 *Phys. Rev. A* **52** 445–56
- [15] Snowdon K J, Havener C C, Meyer F W, Overbury S H, Zehner D M and Heiland W 1988 *Phys. Rev. A* **38** 2294–304
- [16] Limburg J, Schippers S, Hughes L, Hoekstra R and Morgenstern R 1996 *Phys. Rev. A* **53** 4228
- [17] Aumayr F, Kurz H, Schneider D, Briere M A, McDonald J W, Cunningham C E and Winter H P 1993 *Phys. Rev. Lett.* **71** 1943–6
- [18] Winecki S, Cocke C L, Fry D and Stockli M P 1996 *Phys. Rev. A* **53** 4228–37
- [19] Briand J P, Le Roux V, Bechu N, Dreuil S, Machicoane G, Prior M and Xie Z 1999 *Nucl. Instrum. Methods B* **154** 166–73
- [20] Meyer F W and Morozov V A 1999 *Phys. Scr. T* **80B** 226–7
- [21] Schenkel T, Barnes A V, Hamza A V, Schneider D H, Banks J C and Doyle B L 1998 *Phys. Rev. Lett.* **80** 4325–8
- [22] Briand J P, Debilly L, Charles P, Essabaa S, Briand P, Geller R, Desclaux J P, Bliman S and Ristori C 1990 *Phys. Rev. Lett.* **65** 159–62
- [23] Takács E, Ónodi-Szűcs Z, Ratliff L P, Gillaspay J D and Pálinskás J 1997 *Nucl. Instrum. Methods B* **124** 431–4
- [24] Briand J P *et al* 1996 *Phys. Rev. A* **54** 4136–9
- [25] Krause M O 1979 *J. Phys. Chem. Ref. Data* **8** 307
- [26] Lehnert U, Stockli M P and Cocke C L 1998 *J. Phys. B: At. Mol. Opt. Phys.* **31** 5117–22
- [27] Stolterfoht N, Bremer J H and Muino R D 1999 *Int. J. Mass Spectrom.* **192** 425–36
- [28] Khemliche H, Schlatholter T, Hoekstra R, Morgenstern R and Schippers S 1998 *Phys. Rev. Lett.* **81** 1219–22
- [29] Stolterfoht N, Grether M, Niemann D and Hoffmann V 1999 *21st Int. Conf. on Physics of Electronic and Atomic Collisions (Sendai, 1999) Book of Contributed Papers*
- [30] Ashley J C and Anderson V E 1981 *J. Electron Spectrosc.* **24** 127
- [31] Chantler C T 1995 *J. Phys. Chem. Ref. Data* **24** 71–591
- [32] Schenkel T, Hamza A V, Barnes A V, Schneider D H, Banks J C and Doyle B L 1998 *Phys. Rev. Lett.* **81** 2590–3
- [33] Cheng H P and Gillaspay J D 1998 *Comput. Mater. Sci.* **9** 285–94
- [34] Cheng H P and Gillaspay J D 1997 *Phys. Rev. B* **55** 2628–36
- [35] Bitenskii I S, Murakhmetov M N and Parilis E S 1979 *Zh. Tekh. Fiz.* **49** 1044
- [36] Pikin A I, Morgan C A, Bell E W, Ratliff L P, Church D A and Gillaspay J D 1996 *Rev. Sci. Instrum.* **67** 2528–33
- [37] Pedulla J and Deslattes R D 1993 Production of ion beam sputtered multilayers *Multilayer and Grazing Incidence X-Ray/EUV Optics (Proc. SPIE vol 2011)* ed R B Hoover and A B C Walker (Bellingham, WA: SPIE)
- [38] Campbell J L, Wang J X and Teesdale W J 1989 *Nucl. Instrum. Methods B* **43** 490–6
- [39] Stolterfoht N 1993 *Phys. Rev. A* **47** R763–6
- [40] Legros M, Silver E, Schneider D, McDonald J, Bardin S, Schuch R, Madden N and Beeman J 1995 *Nucl. Instrum. Methods A* **357** 110–4
- [41] Salem S I, Panossian S L and Krause R A 1974 *At. Data Nucl. Data Tables* **14** 91–109

In situ imaging of highly charged ion irradiated mica

L.P. Ratliff and J.D. Gillaspay

Atomic Physics Division, National Institute of Standards and Technology, Gaithersburg, MD 20899 USA

Abstract. We have studied the modification of mica surfaces due to the impact of Xe^{44+} ions by imaging the ion-exposed surfaces with atomic force microscopy in vacuum. By incorporating the microscope into the vacuum chamber where the samples are exposed to the ions, we rule out posterior modification of these features in air. The features, raised bumps 19(2) nm in diameter, are similar to those imaged previously in air, however, their heights appear to be larger than previously reported.

There is a growing interest in the interactions of highly charged ions (HCIs) with surfaces, which is driven by a basic scientific interest in the physical processes involved and by an increasing number of applications that are being developed [1,2]. This interest stems from the fact that HCIs carry massive amounts of potential energy (for example, the Xe^{44+} ions used in the present work have 51 keV of potential energy). Because this potential energy is released at the surface [3], while the kinetic energy is released along the ion's path through the solid, the processes that occur at the surface are dominated by the potential energy. This strong influence of the potential energy has been demonstrated in studies of particle emission during HCI impact [4-6] (for example, x-ray emission, sputtering, secondary ion emission and electron emission), and in studies of surface damage after ion exposure [7,8].

With these experiments, as well as theoretical investigations [9,10], we have learned a great deal about the evolution of the projectile as it approaches and penetrates the surface. As described in the 'classical over-the-barrier model' [9], the ion begins to extract electrons from the surface even before impact. Many of these electrons become bound in high-lying states of the projectile, forming a 'hollow atom' with many empty core states. As the ion nears the surface, it can begin to decay, for instance by Auger ionization. Upon penetration of the surface, the electrons that are weakly bound are 'peeled off' and replaced with electrons from inside the surface, forming a secondary hollow atom.

While the formation and decay of the hollow atom is well described by models, at least in a general sense, the response of the surface is still poorly understood.

Several models have been proposed to describe this situation. The first such model asserts that, if electrons are removed from the surface faster than they can be replaced from the bulk, there will be a localized charge imbalance which will cause a 'Coulomb explosion' [11]. This explosion can result in the sputtering of a large number of ions and neutral atoms or, in the case of mica, blistering [12]. A second model says that the ion leaves many excitations near its impact site [13]. These excitations promote atom pairs from bonding states to antibonding states. If the excitation density is above a threshold, they can lead to a destabilization of the crystal structure and permanent structural damage [14,15]. Materials that support self trapped excitons can be described by a third model. In this case, self-trapping can localize the excitations very near the surface until they decay into color centers, which migrate to the surface and result in sputtering [6].

One approach to studying the surface response to HCI impact is to image the impact sites after ion exposure in order to determine the size and morphology of the impact features. Such studies can give us information about the spatial extent of the ion-surface interaction and perhaps about the mechanism for their formation. In addition, for the various applications that are under development, it is useful, and in some cases necessary, to understand and characterize the damage left by the ion. Furthermore, if we can image these features, the morphology might suggest other applications that have not yet been considered. Because they are very small (approximately 20 nm in diameter and approximately 1 nm high), however, observation of the ion-induced features has been limited to a few materials on which atomically smooth surfaces can be prepared easily and

reliably. One such surface is mica. Because of its layered structure, mica is easily cleaved with adhesive tape to reveal large, single crystalline terraces. Such a freshly cleaved surface can be imaged with contact mode atomic force microscopy (AFM) in air to reveal crystal structure. Because of these favorable characteristics, mica was used as the target for the most extensive, systematic studies of HCI-induced surface damage [7,8,16].

The studies of surface damage on mica from HCI impact have shown that each ion impact leaves a bump on the surface and that the size of these bumps is independent of kinetic energy in the range, 4.4 to 880 keV (Xe^{44+} projectiles) [7,16]. Furthermore, the volume of the bumps increases monotonically with charge state, and therefore, potential energy [7,8]. In one study, where HCIs of various species and kinetic energies were used, it was found that the volume increased linearly with projectile charge state from an apparent threshold at $q = 30$. Another study used only xenon ions with 100 keV of kinetic energy so that the charge state (and therefore, potential energy) was the only independent variable. In this case, the volume increased more rapidly than the charge state. In fact, the volume correlated more strongly with the potential energy, which has a non-linear relation to the charge state. Although the variation of feature size with charge state seems to be different in the two studies, they are not inconsistent. All of the data points in these two studies that correspond to the same ion species and charge state agree to within the stated uncertainty limits. The apparent difference in slope might arise from the fact that the former work involved ions of different mass (note that the relationship between charge state and potential energy varies with mass).

Because the variation in the size of the observed features is systematic and reproducible, we believe that the method of measuring the features with AFM in air is sound and useful. That is, the dimensions being measured are physically meaningful. In order to better understand the nature of these features, however, we need to look carefully at the imaging technique. There are some aspects of imaging in air that can change the apparent features from their original form. First, exposing the samples to air allows the features themselves to be modified [17]. For example, the impact sites are likely to contain many broken bonds, which would make them more reactive than the surrounding single-crystalline material. When such a surface is exposed to air, hydrocarbons or other contaminants might preferentially attach to the impact site, significantly changing its morphology from that of the original feature. Second, in air, there is a layer of water adsorbed on the surface. The capillary forces

due to this water layer increase the force between the sample and the probe, possibly deforming the surface. The purpose of this study is to better understand the nature of the features as created by the HCIs. To this end, we have exposed mica surfaces with Xe^{44+} ions and imaged them in vacuum without allowing them to come into contact with air. We chose Xe^{44+} ions for our experiments because they were used in both of the previous experiments with which we compare our results. Because it has been established that the morphology of these features is independent of kinetic energy [7,16], we used a single kinetic energy, 350 keV, for all of our measurements.

Experimental

The ions are produced in the NIST electron beam ion trap (EBIT) and extracted into a beam line system that has been described previously [18]. The beam that reaches the target consists of approximately one million $^{136}\text{Xe}^{44+}$ ions per second at 350 keV in a diameter of 3 mm.

The mica samples were cleaved in air using adhesive tape and immediately inserted into a load lock chamber. From the load lock, they were passed between the various chambers of the apparatus while remaining under a vacuum of 10^{-7} Pa. This apparatus consists of a target chamber, where they are exposed to the ions and the imaging chamber, which is equipped with a scanning probe microscope. This microscope was used previously in scanning tunneling mode to image HOPG (highly oriented pyrolytic graphite) samples [19]. Because mica is a good insulator, all of the imaging was performed using AFM. We used contact mode AFM with an applied normal force of 1 nN. The samples were imaged, exposed to the HCIs, then imaged again without exposure to air. In order to study the effect of air exposure on the ion-induced features, the exposed samples were brought out of the vacuum, reinserted and imaged again.

Results and Discussion

Before exposure to the ions, the mica surfaces were featureless except for crystal structure observed in scans of small areas. In the exposed regions of the surfaces, we consistently found bumps that are 19(2) nm in diameter (the uncertainties given in this paper are single standard deviation and are based on repeated sampling) (see Figure 1) and each bump appears to correspond to a single ion impact; this is in agreement with previous measurements [7,8,16]. The fact that these features are convex, even before removal from the vacuum, means that this morphology is a direct result of the ion impact rather than, for

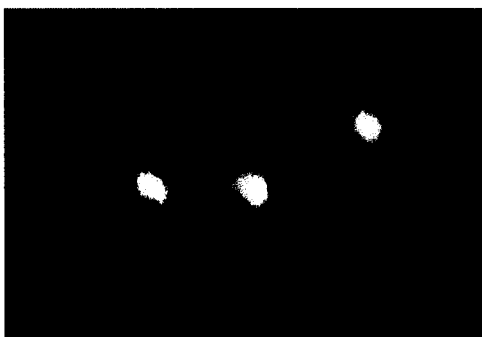


FIGURE 1. AFM image showing the topography of three Xe^{4+} impact sites on mica. The image is 50 nm x 80 nm and the features are approximately 20 nm in diameter and 1 nm high.

instance, contaminant adsorption at the impact sites [17]. Therefore, our observation is consistent with the interpretation of these features as blisters [7,16]. The heights measured in the current work, however, are somewhat larger than those previously reported. In the images taken before exposure to air, the features were 1.0(3) nm high, approximately double the heights measured previously with AFM in air [7,8,16]. The feature heights that were measured after the samples were exposed to air and returned to the vacuum for imaging, varied somewhat but remained in the range between the height of those not exposed to air (approximately 1 nm) and the height of those imaged in air (approximately 0.5 nm [7,8,16]). Quantitative measurement of feature height is difficult, however, because the topography is convoluted with other characteristics of the probe and of the surface, such as hardness and friction.

In order to correctly interpret the images, it is important to understand the lateral forces. The term lateral force refers to the torque exerted on the cantilever as it is scanned, for example, over a feature of elevated friction. When scanning in the forward direction (the direction perpendicular to the symmetry axis of the cantilever, referred to below as the 0° direction) this torque manifests itself as a lateral displacement of the beam of light in the 'bouncing beam' method of detection [20]. When imaging an area that is flat, but has a modified coefficient of friction, if the lateral force signal decreases when scanning in the forward direction it will increase when scanning in the reverse direction (this is because the frictional force is opposite to the direction of travel). If this surface is scanned in the direction along the axis of symmetry of the cantilever (90°), there will be no features in the lateral force image because the torque on the cantilever will tend to move it up and down, modifying the normal force, and thus mimicking

topography. Such an increase in friction has been observed in tracks formed in mica by fast ions [21]. While the lateral and normal forces are nominally independent, there can be a coupling between the two that interferes with the measurement of feature height. Parks *et al.* [16] found that, in imaging mica exposed with Xe^{4+} , the lateral force played an important role in the measurement of the heights of the ion induced features. The heights measured when scanning in one direction were larger than those measured when scanning in the opposite direction; the quoted height values are averages of the two measurements. In order to minimize this effect, the normal force was kept to its minimum stable value (recall that the magnitude of the frictional force is proportional to the normal force). Interestingly, Ruelicke *et al.* [7] did not observe this effect.

In the present work, we find that many of our lateral force images have an asymmetric character (see Figure 2) while others have the character of flat areas of modified friction (see Figure 3) that was seen by Parks *et al.* [16]. With respect to the asymmetric images, when the scanning direction is changed, their orientation does not rotate, as if the features are truly asymmetric. We interpret this phenomenon as resulting from the torque on the cantilever as it traverses the changing slope of the ion-induced bumps [20]. While many of our lateral force images show the type of frictional character seen in fig. 3, in addition to asymmetric character seen in fig. 2, the images taken before exposure to air are dominated by the later. With

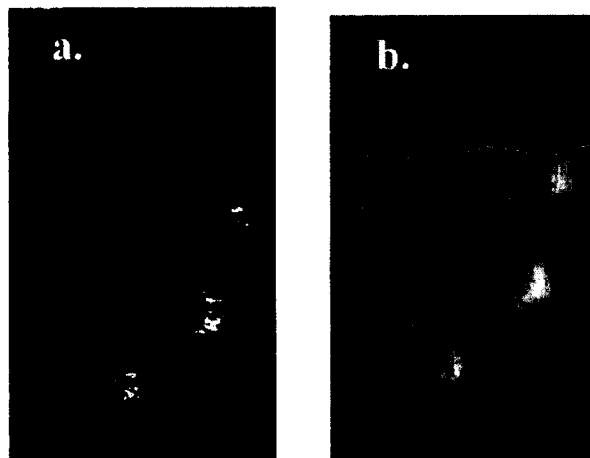


FIGURE 2. Lateral force images taken before the sample was exposed to air. The images are 100 nm across and were scanned at a) 0° and b) 90° . The asymmetric nature of these features is interpreted as resulting from a torque on the cantilever as it traverses the changing slope of the ion-induced bumps.

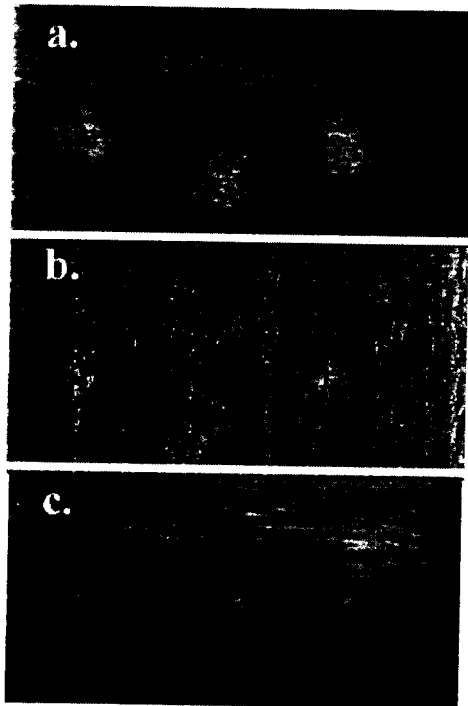


FIGURE 3. Lateral force images taken after the sample was exposed to air. The images are 100 nm across and were scanned at a) 0°, b) 90° and c) 180°. The features appear to have a modified coefficient of friction as compared to the background.

the possible exception of images taken very soon after exposure to air (less than one hour in the vacuum), we do not see the difference in forward and reverse heights observed by Parks *et al.* [16].

It was previously reported that repeated scanning tends to 'erase' the features; that is, the bumps flatten [16] or even peel open to reveal a crater [7]. While there were examples in the present work where slight modification in the features was observed after repeated scanning, generally the feature heights remained constant. One possible explanation for this discrepancy is that the adsorption of water and other contaminants in the air plays a role in the erasure. Alternatively, perhaps the imaging in the present work is done with a normal force that is sufficiently weak that the features are not significantly affected by the probe. It is not surprising that the effective normal force in vacuum is less than that in air because the capillary force due to adsorbed water is reduced. A weaker normal force could also explain the apparent increase in feature height over those measured in air; the tendency of the probe to compress the features

during scanning is reduced, allowing the true topography to be measured.

Conclusion

We have confirmed that the features created by HCI impact on mica are protrusions as previously observed in air. This supports the assertion that these features are in fact blisters, and that they are caused by a delamination of the layers of the mica due to the deposition of the ion's large potential energy [7,8,12,16]. The heights of the features appear larger than those measured previously in air. This difference could reflect an actual modification of the surface when in air or an artifact of the imaging. In either case, because the vacuum environment allows more control over atmospheric conditions that are known to influence imaging with AFM, images taken in vacuum are more likely to reflect the true topography of the features created by the ions. Because of the similarity of features imaged in vacuum to those imaged in air, this study supports the general conclusions of the previous systematic studies [7,8,16].

Acknowledgements

We thank Doug Alderson for his technical assistance.

References

1. Hamza, A.V. *et al.*, *J. Vac. Sci. Technol. A*, **17**, 303-305 (1999).
2. Marrs, R.E. *et al.*, *Rev. Sci. Instrum.*, **69**, 204-209 (1998).
3. Hattass, M. *et al.*, *Phys. Rev. Lett.*, **82**, 4795-4798 (1999).
4. Schenkel, T. *et al.*, *Prog. Surf. Sci.*, **61**, 23-84 (1999).
5. Arnau, A. *et al.*, *Surf. Sci. Rep.*, **27**, 117-239 (1997).
6. Aumayr, F. *et al.*, *Int. J. Mass Spectrom.*, **192**, 415-424 (1999).
7. Ruehlicke, C. *et al.*, *Nucl. Instrum. Methods B*, **99**, 528-531 (1995).
8. Parks, D.C. *et al.*, *Nucl. Instrum. Methods B*, **134**, 46-52 (1998).
9. Burgdorfer, J. *et al.*, *Phys. Rev. A*, **44**, 5674-5685 (1991).
10. Stolterfoht, N. *et al.*, *Int. J. Mass Spectrom.*, **192**, 425-436 (1999).
11. Parilis, E.S., in *Proceedings of the International Conference on Phenomena in Ionized Gasses*, edited by 1969, 94.
12. Parilis, E., *Nucl. Instrum. Methods B*, **116**, 478-481 (1996).
13. Schenkel, T. *et al.*, *Phys. Rev. Lett.*, **81**, 2590-2593 (1998).
14. Stampfli, P. and Bennemann, K.H., *Appl. Phys. A*, **60**, 191-196 (1995).
15. Herrmann, R.F.W. *et al.*, *Appl. Phys. A*, **66**, 35-42 (1998).
16. Parks, D.C. *et al.*, *J. Vac. Sci. Technol. B*, **13**, 941-948 (1995).
17. Neumann, R., *Nucl. Instrum. Methods B*, **151**, 42-55 (1999).
18. Ratliff, L.P. *et al.*, *Rev. Sci. Instrum.*, **68**, 1998-2002 (1997).
19. Minniti, R. *et al.*, *Physica Scripta*, , In Press (2000).
20. Colton, R.J. *et al.*, *Procedures in Scanning Probe Microscopies*, John Wiley and Sons, Chichester, 1998.
21. Hagen, T. *et al.*, *J. Vac. Sci. Technol. B*, **12**, 1555-1558 (1994).

***In-situ* Observation of Surface Modification Induced by Highly Charged Ion Bombardment**

R. Minniti, L. P. Ratliff, and J. D. Gillaspay

National Institute of Standards and Technology, Gaithersburg, MD 20899, USA

Received July 31, 2000; accepted September 29, 2000

Abstract

Nanoscale dots created on the surface of a highly oriented pyrolytic graphite sample by individual highly charged xenon projectile ions were observed using an *in-situ* scanning tunneling microscope. This is the first time that such features have been created and imaged without exposure to air. The dots vary in size with the charge state of the ion, up to a diameter of 6.6 nm for Xe^{44+} . The results are discussed in terms of the energy density deposited in the near surface region.

The interaction of ions with surfaces has been extensively studied and forms the basis of many powerful tools used in modern industrial processes [1], particularly in the area of microelectronics [2]. Until recently, however, this field of study virtually always involved ions of low charge state. In this regime, the mechanism underlying the ion-surface interaction involves the *kinetic* energy of the ion. The advent of compact sources of highly charged ions (HCIs) with reasonably high brightness has allowed investigators to study a new regime in which the internal *potential* energy dominates the interaction with the surface. The kinetic energy of ions extracted from these sources is generally in the range of several hundred keV but can be accelerated or decelerated to suit the experiment. Using an electron beam ion trap (EBIT), it is possible to produce ions with charge states beyond $q = 70+$ [3] with a device that is small enough to fit in a closet; a larger version of EBIT has been shown to produce even the highest possible charge state ion among the naturally occurring elements i.e. U^{92+} [4]. When a single such ion neutralizes itself on a surface, it releases approximately 700 keV of potential energy (the sum of the binding energies of all electrons removed in forming the HCI). In contrast, a conventional Ar^{1+} ion releases approximately 10 eV of potential energy. For the purposes of this paper, we refer to the “highly charged regime” as that for which the ion’s potential energy is at least a few percent of the U^{92+} potential energy. Most of the possible states of ionization on the periodic table fall into this regime, but relatively few of them have been investigated, leaving a vast territory unexplored. Because a single HCI deposits a tremendous amount of energy into a small volume (nanometers) in a very short time (femtoseconds) [5] it has been hypothesized that investigation of the high charge regime will reveal mechanisms of ion-surface interaction that rely on the ion’s potential energy rather than its kinetic energy. This is of fundamental interest and might have practical application [6,7].

As an HCI approaches a surface, it extracts many electrons. Some of these electrons become bound in high

lying states of the projectile, forming a so-called hollow atom. The formation and decay of the hollow atom have been the subject of a considerable amount of theoretical and experimental work [8–11]. In addition, one would expect a single HCI to produce a very substantial disruption on a surface that would be observable using modern scanning probe microscopy techniques. To date, however, microscopic evidence of such disruptions has been presented for only a few selected surfaces: polymers (CR-39 [12] and PMMA [13]), mica [14,15] and alkanethiols [16]. Of these, only mica and alkanethiols show features that are evident without chemically etching the surface after bombardment with ions. Only in mica has a systematic dependence of the feature size on potential energy been demonstrated. This dearth of evidence, coupled with the fact that other surfaces such as silicon have been studied in air with null results [17], leaves open the question of whether the formation of surface features is a general characteristic of HCI-surface interactions, or whether it is a phenomena which appears in only a few special types of surfaces.

Answering the question posed above has been hampered by the lack of appropriate tools. In the case of silicon, for example, oxide overgrowth can be expected to obscure any nanoscale surface features that might be induced by HCIs, unless the entire experiment is performed in vacuum. Furthermore, even for normally inert surfaces, the HCI impact site is likely to contain broken bonds to which atmospheric gasses might attach [18,19]. This nucleation could create bumps at impact sites that were originally craters. In order to overcome these limitations, we have recently developed a unique combination of tools in our laboratory at NIST: an EBIT [20] equipped with a highly efficient ion beamline [21] that terminates in a UHV chamber equipped with an *in-situ* scanning tunneling microscope (STM). This paper presents our first results using this system.

The surface we have chosen to study first with this system is highly oriented pyrolytic graphite (HOPG), both for its similarity to mica (layered structure) and for its ease of surface preparation. Many groups have studied single ion impact sites on HOPG with STM in air and have observed nanoscale features ([19,22–27], and the references therein), but none of these explored the highly charged regime. Furthermore, there is an apparent lack of reproducibility in the size of these features, perhaps due to the different atmospheric conditions under which the various experiments were carried out. In one study, the structures were studied as a function of charge state at a constant kinetic energy of 2 keV; the diameters (full width at half max) were observed

to increase from 0.23 nm to 0.67 nm as the potential energy was increased from 14 eV to 138 eV [26]. Our study extends this potential energy study by more than two orders of magnitude and reaches well into the highly charged regime, where mechanisms that depend on the projectile's potential energy have been hypothesized to dominate.

In the present work, HOPG samples were cleaved with adhesive tape and inserted into a load lock chamber. From the load lock they were transferred, under vacuum, to a target chamber, where they were exposed to the ion beam, and to a surface analysis chamber equipped with an STM. The pressure in the system was approximately 10^{-7} Pa (10^{-9} torr). The samples were imaged with the STM prior to exposure to the ion beam using Pt-Ir tips, with tunneling currents between 0.5 nA and 0.9 nA and gap voltages around 0.1 Volt. The unexposed surface displayed large flat terraces and atomic structure.

The samples were then transferred to the target chamber and exposed to beams of xenon ions from the NIST EBIT with 276 keV of kinetic energy and with charge states of $q = 23+$ and $q = 44+$ [20,21]. For a typical ion beam current, 10 pA (as measured with both a Faraday cup and a channel electron multiplier), the exposure time was approximately 60 minutes.

After exposure, the samples were again imaged with the STM. Figure 1(a) shows a typical image of an HOPG sample after exposure to a Xe^{44+} ion beam. A number of HCl-induced nanoscale protrusions, which we refer to hereafter as *dots*, can be observed. The density measured on several exposed regions is, on average, about 2500 dots/ μm^2 . This is in good agreement with the estimated ion fluence and is consistent with the assertion that each of the observed dots corresponds to a single ion impact. To confirm that we were observing topographical, as opposed to electrical, features, we imaged them at both positive and negative bias voltages and found that, in both cases, the features appeared convex [25]. In contrast, Mochiji *et al.* [26] found that their ion induced features were due, at least in part, to a modification of the partial density of states at the impact sites; they illustrate this with I - V curves from both the impact site and the background. Furthermore, they did not see any features

with contact mode AFM, and they concluded that the features were due to a sputtering of surface atoms which left a defect in the crystal. It is not surprising that our features are somewhat different from those seen by Mochiji *et al.* [26] because, in their case, the ion's kinetic energy and potential energy were both an order of magnitude less, and the surfaces were imaged in air.

Figure 1(b) is an image of a dot produced by a Xe^{44+} ion. The region around the dot is unperturbed, displaying the expected crystal structure. The image was obtained using a positive gap voltage of 0.095 V on the sample, a tunneling current of 0.6 nA and a scan speed of 1 line/s. Figure 2 shows cross sections of dots such as the one in Fig. 1(b); the dot produced by the higher charge state ion is considerably wider than that produced by the lower charge state ion. This is consistently observed for dots on different regions of the exposed surfaces as seen in the histograms of the basal widths of dots, plotted in Fig. 3. The mean basal widths and standard deviations of the dots produced by the Xe^{23+} ions are 3.0 (10) nm, while for those produced by Xe^{44+} is 6.6 (10) nm, indicating that the size of these dots is correlated with the charge state of the ion.

This variation in size can be understood in terms of the deposition of a high local potential energy density into the surface. The potential energy of a Xe^{44+} ion is 51.3 keV, nearly 8 times greater than the potential energy of a Xe^{23+} ion (6.58 keV); this energy is transferred to the solid, as the ion neutralizes, within several nanometers of the surface [5]. In contrast, assuming that the stopping power is independent of the ion's initial charge state, the 276 keV of kinetic energy is deposited over a region extending about 100 nm into the solid and only 16 keV is deposited in the first 5 nm of its path (4 keV in electronic stopping and 12 keV in nuclear stopping) [28]. This indicates that, in the near surface region, the Xe^{44+} ion deposits significantly more potential energy than kinetic energy, whereas the Xe^{23+} ion deposits mostly kinetic energy. As a result, the transfer of potential energy from the Xe^{44+} ion plays a dominant role during the ion-surface interaction, and is the expected cause of the observed change in the size of the dots.

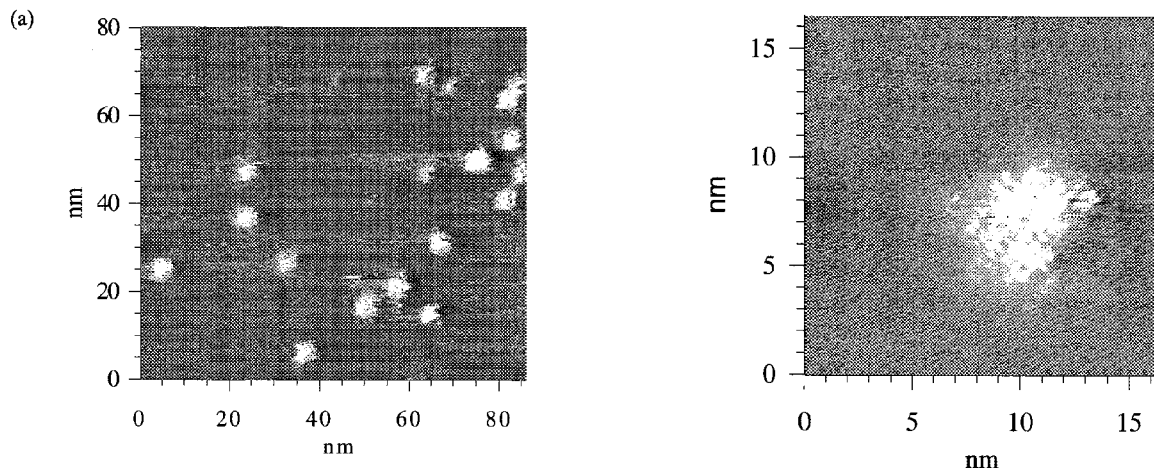


Fig. 1. STM images of an HOPG surface after exposure to a beam of Xe^{44+} ions (the lighter parts correspond to raised features). Figure 1(a) displays several dots in a 80 nm \times 80 nm image, while Fig. 1(b) displays a single dot in a 16.5 nm \times 16.5 nm image. In the unperturbed areas, crystal structure is observed.

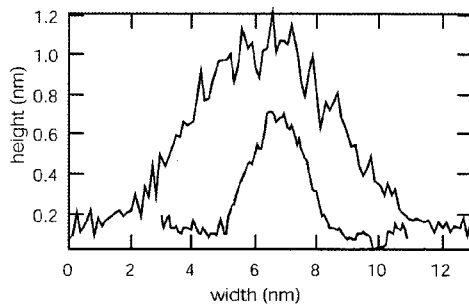


Fig. 2. Cross sectional cuts of STM images of dots produced by bombardment with a Xe^{23+} ion (lower curve) and a Xe^{44+} ion (upper curve).

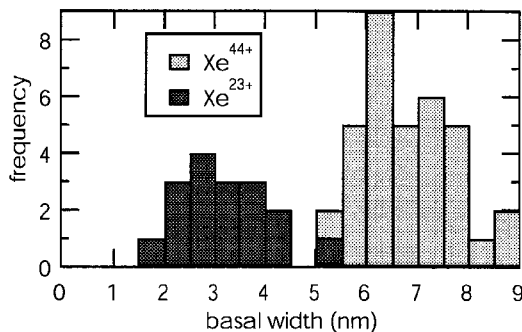


Fig. 3. Histograms of the basal widths of ion induced dots obtained from STM images.

Three models attempt to explain the response of surfaces to HCI impact. The first such model [29,30] asserts that the surface becomes locally charged because of the massive removal of electrons by the projectile. This charged volume can 'Coulomb explode', ejecting ions from the surface and initiating a shock wave which causes the sputtering of neutral surface atoms. This process was simulated in a molecular dynamics computation by Cheng and Gillaspay [31]. A second model is similar to the structural instability model used to describe surface sputtering by intense laser pulses [32]. In this model, the HCI impact produces a localized region of multiple electronic excitation. These excitations can cause the covalent bonds in the lattice to convert to antibonding potentials, leading to the expulsion of atoms from the surface. This mechanism was suggested as the cause of the high sputter yields observed from gallium arsenide under HCI impact [33]. A third model asserts that, in certain materials, HCIs can produce self-trapped excitons that decay into color centers leading to enhanced sputtering of surface particles [34]. This model was used to explain the observations on LiF, but appears to be relevant only to a limited class of materials such as alkali halides and SiO_2 . In the present work, it seems likely that the ion impact would leave both holes and excitations, so the Coulomb explosion model and the structural instability model should both be considered further.

All of the models predict the removal of material from the surface, and have been presumed to lead to the formation of craters. The data presented in this work show the formation of protrusions. Similar protrusions, observed

previously in mica after HCI impact, have been interpreted by Parilis as a result of potential energy deposition [35]. The model is an extension of the Coulomb explosion model in which the structure of the surface plays an important role. Mica has a layered structure and the layers are held together by ionic bonds. As the ion approaches, electrons are removed from between the surface layers leaving a net positive charge. The ionic bonds are thus destroyed, leading to delamination of the layers.

In extending the Coulomb explosion model to describe the response of HOPG to HCI impact, one needs to account for some differences between mica and HOPG. While both mica and HOPG have highly anisotropic layered structures, the nature of the bonds between the layers is different: in mica, the layers are held together by ionic bonds while in HOPG the layers are held together by much weaker van der Waals bonds. This might allow the delamination to occur even more readily in HOPG than in mica, and allow the Coulomb explosion to result in a protrusion as seen in the present work. A similar argument could be made with respect to the structural instability model; that is, a local expansion of the target due to stretching of bonds from electronic excitation could result in a delamination of the layers of HOPG. It remains to be determined if one of these mechanisms (or a combination of the two) is responsible for the observed dots. We therefore consider these models in more detail below.

With respect to the Coulomb explosion model, it is well established that the impact of an HCI can remove many electrons from a surface. In measurements of the total electron yields, it has been shown that a single HCI with an initial charge, q , can extract a number of electrons into the vacuum that is several times larger than q [36]. However, the Coulomb explosion can be quenched if the charged region is replenished with electrons before the target nuclei have been displaced. HOPG is a semimetal and its relatively high carrier density might make it susceptible to such a quenching. The time scale for the electron motion, as extracted from the plasma frequency, is less than one femtosecond. The highly anisotropic crystal structure, however, leads to a conductivity that is orders of magnitude larger in the plane of the surface than normal to the surface [37]. This anisotropy could affect the availability of electrons to neutralize the impact site. Furthermore, it is not clear that the properties measured for the bulk material are relevant on the time scales and length scales involved here. For example, the presence of two holes in a single atom of a solid can increase the hopping time of the holes by orders of magnitude [38]. This argument assumes that the two holes represent a small perturbation to the lattice and can not be directly applied to the situation here where tens or even hundreds of holes are created at the impact site. It has been observed, however, that when silicon is excited with high intensity picosecond laser pulses, carrier diffusion decreases with increasing fluence [39]. These examples illustrate the point that the Coulomb explosion model can not be ruled out simply on the basis of bulk properties such as conductivity.

In addition to the charge that the HCI impact creates on the surface, there is likely to be a large number of electronic excitations that could lead to a structural instability. It was shown recently that a single HCI impact on a silicon surface

can deposit as much as 40% of its potential energy in electronic excitations [40]. A critical issue that remains to be addressed is whether or not these excitations are highly localized. Stampfli predicted that structural instabilities occur in graphite when at least 7% of the valence electrons are excited, or at an excitation density of 32 excitations/nm³. This excitation density requires the full 51 keV of potential energy from the Xe⁴⁴⁺ ion to be deposited in excitations (assuming that the average excitation energy is 5 eV) within a hemisphere of radius 5.4 nm. Atomic displacement due to this instability can begin in as little as 50 femtoseconds, much faster than the time that it takes for the electrons and atoms to thermalize, which is about half of a picosecond [41]. Note that 50 fs is comparable to the response time indicated by the Coulomb explosion simulations [31]. Therefore, if the HCI's potential energy is converted to electronic excitations with sufficient efficiency, the surface could suffer a structural instability that would leave the surface locally deformed.

The conditions in the present work are right for both Coulomb explosion and structural instability and both of these processes can take place in the same ion impact event. Our experiment does not distinguish between these mechanisms because, at the level of precision that the models have achieved, both would result in the same type of surface damage. In order to determine the relative importance of the two mechanisms, one would need to do more extensive modeling and/or perform experiments specifically designed to address this issue.

Another component of the ion/surface interaction that can affect the size of the dots is a charge-state dependence in the stopping power. This can be understood in terms of a fast ion entering a solid; the kinetic energy is mainly deposited by ionizing atoms in the solid. The efficiency of this primary ionization is determined in a competition between the equilibrium charge state of the ion inside the solid, which increases with speed, and the time that the ion interacts with the target electron, which decreases with increasing speed. In the case of slow HCI impact, both the charge state and the impulse are large just as the ion reaches the surface, maximizing the primary ionization rate. Schenkel *et al.* studied this effect by passing ions of various charge states through thin carbon foils and measuring the (kinetic) energy loss; they found that the energy loss increased with increasing charge state for xenon and gold ions [42]. The energy loss of Xe³⁶⁺ is several keV less than that for Xe⁴⁴⁺; for Xe²³⁺, the energy loss is likely to be still less. While this measured energy discrepancy is small compared to the total energy, it is deposited in the first several nanometers so it contributes significantly to the local energy density, and it is likely to contribute to the creation of surface features.

According to the ion explosion spike model [43], which is used to explain tracks in solids from fast ions, the Coulomb repulsion between ionized target ions causes nuclear displacement and there is a threshold for track formation with respect to the primary ionization from a fast ion. This is similar to the Coulomb explosion model described above and, if the surface does suffer a Coulomb explosion, the charging might be due to both neutralization of the projectile and increased electronic stopping power. The

presently observed variation in feature size, therefore, might come, at least in part, from such a synergistic effect between the projectile's kinetic energy and charge state.

In summary, we bombarded HOPG samples alternately with slow xenon ions of the same kinetic energy but in two widely differing charge states. The observed ion-induced dots vary in size with the charge state of the ions. The damage formation is discussed in terms of Coulomb explosion and structural instability. We expect that both of these processes can be involved in a single ion impact event and we suggest that their relative importance should be the subject of further investigation. We also expect that a charge state dependence in the stopping power can contribute to the high energy density deposited at the surface and, thus, the damage observed. Our measurements provide the first in-situ images of direct surface modification due to a highly charged ion beam.

Acknowledgements

We thank Doug Alderson for his valuable technical assistance and Dan Parks and Larry Hudson for many fruitful discussions. R. Minniti gratefully acknowledges a fellowship from the National Research Council.

References

1. Brundle, C. R., Evans, C. A., Wilson, S. and Fitzpatrick, L. E., "Encyclopedia of Materials Characterization", (Butterworth-Heinemann, Boston, 1992).
2. Van Zant, P., "Microchip Fabrication: a Practical Guide to Semiconductor Processing", (McGraw-Hill, New York, 1990).
3. Marrs, R. E., Beiersdorfer, P. and Schneider, D., *Phys. Today* **47**, 27 (1994).
4. Schneider, D., *Hyperfine Interactions* **99**, 47 (1996); Marrs, R. E., Elliot, S. E. and Knapp, D. A., *Phys. Rev. Lett.* **72**, 4082 (1994).
5. Schenkel, T. *et al.*, *Phys. Rev. Lett.* **65**, 159 (1990).
6. Hughes, I., *Phys. World* **8**, 43 (1995).
7. Schenkel, T. *et al.*, *Progr. Surface Sci.* **61**, 23 (1999).
8. Briand, J.-P. *et al.*, *Phys. Rev. Lett.* **65**, 159 (1990).
9. Burgdorfer, J., Lerner, P. and Meyer, F. W., *Phys. Rev. A* **44**, 5674 (1991).
10. Ducrec, J., Andra, H. J. and Thumm, U., *Phys. Rev. A* **60**, 3029 (1997).
11. Arnau A. *et al.*, *Surf. Sci. Rep.* **27**, 117 (1997).
12. Schmieder, R. and Bastasz, R., *AIP Conference Proc.* **274**, 690 (1993).
13. Gillaspay, J. D., Parks, D. C. and Ratliff, L. P., *J. Vac. Sci. Technol. B* **16**, 3294 (1998).
14. Parks, D. C. *et al.*, *Nucl. Instrum. Meth. B* **134**, 46 (1998).
15. Schneider, D. H. G. and Briere, M. A., *Physica Scripta* **53**, 228 (1996).
16. Schenkel, T. *et al.*, *J. Vac. Sci. Technol. B* **16**, 3298 (1998).
17. Parks, D., private communications.
18. Lozovik, Y. E., Popov, A. M. and Letokhov, V. S., *J. Phys. Chem.* **99**, 13480 (1995).
19. Neumann, R., *Nucl. Instrum. Meth. B* **151**, 42 (1999).
20. Gillaspay, J. D. *et al.*, *Physica Scripta* **T59**, 392 (1995).
21. Pikin, A. I. *et al.*, *Rev. Sci. Instrum.* **67**, 2528 (1996); Ratliff, L. P. *et al.*, *Rev. Sci. Instrum.* **68**, 1998 (1997).
22. Matzukawa, T. *et al.*, *Appl. Surf. Sci.* **107**, 227 (1996).
23. Biro, L. P., Gyulai, J. and Havancsak, K., *Nucl. Instrum. Meth. B* **112**, 270 (1996).
24. Marton, D. *et al.*, *Surf. Sci.* **326**, L489 (1995).
25. Porte, L. *et al.*, *Nucl. Instrum. Meth. B* **44**, 116 (1989).
26. Mochiji, K. *et al.*, *J. Appl. Phys.* **82**, 6037 (1997).
27. Habenicht, S., Bolse, W. and Lieb, K.-P., *Rev. Sci. Instrum.* **69**, 2120 (1998).
28. "The Stopping and Range of Ions in Solids", (Eds J. F. Ziegler, J. P. Biersack and U. Littmark), (Pergamon Press, New York, 1985).
29. Parilis, E. S., *Proc. Intern. Conf. Phenomena in Ionized Gases*, Bucharest, p. 94, (1969); *Proc. Intern. Conf. Atomic Collision Phenomena in Solids*, Amsterdam, p. 324 (1970).

30. Bitenskii, I. S., Murakhmetov, M. N. and Parilis, E. S., *Sov. Phys. Tech. Phys.* **24**, 618 (1979).
31. Cheng, Hai-Ping and Gillaspay, J. D., *Phys. Rev. B* **55**, 2628 (1997).
32. Stampfli, P., *Nucl. Instrum. Meth. B* **107**, 138 (1996).
33. Schenkel, T. *et al.*, *Phys. Rev. Lett.* **81**, 2590 (1998).
34. Varga, P. *et al.*, *Physica Scripta* **T73**, 307 (1997).
35. Parilis, E., *Nucl. Instrum. Meth. B* **116**, 478 (1996).
36. Aumayr, F. *et al.*, *Phys. Rev. Lett.* **71**, 1943 (1993).
37. McClure, J. W., *IBM J. Res. Develop.* **8**, 255 (1964).
38. Young, D. A., *Radiat. Meas.* **27**, 575 (1997).
39. van Driel, H. M., *Phys. Rev. B* **35**, 8166 (1986).
40. Schenkel, T. *et al.*, *Phys. Rev. Lett.* **83**, 4273 (1999).
41. Bloembergen, N., *AIP Conference Proc.* **288**, 3 (1994).
42. Schenkel, T. *et al.*, *Phys. Rev. Lett.* **79**, 2030 (1997).
43. Fleischer, R. L., "Tracks to Innovation: Nuclear Tracks in Science and Technology", (Springer-Verlag, New York, 1998).